Neogene diatoms from the Southern Ocean; tiny fossils, big questions

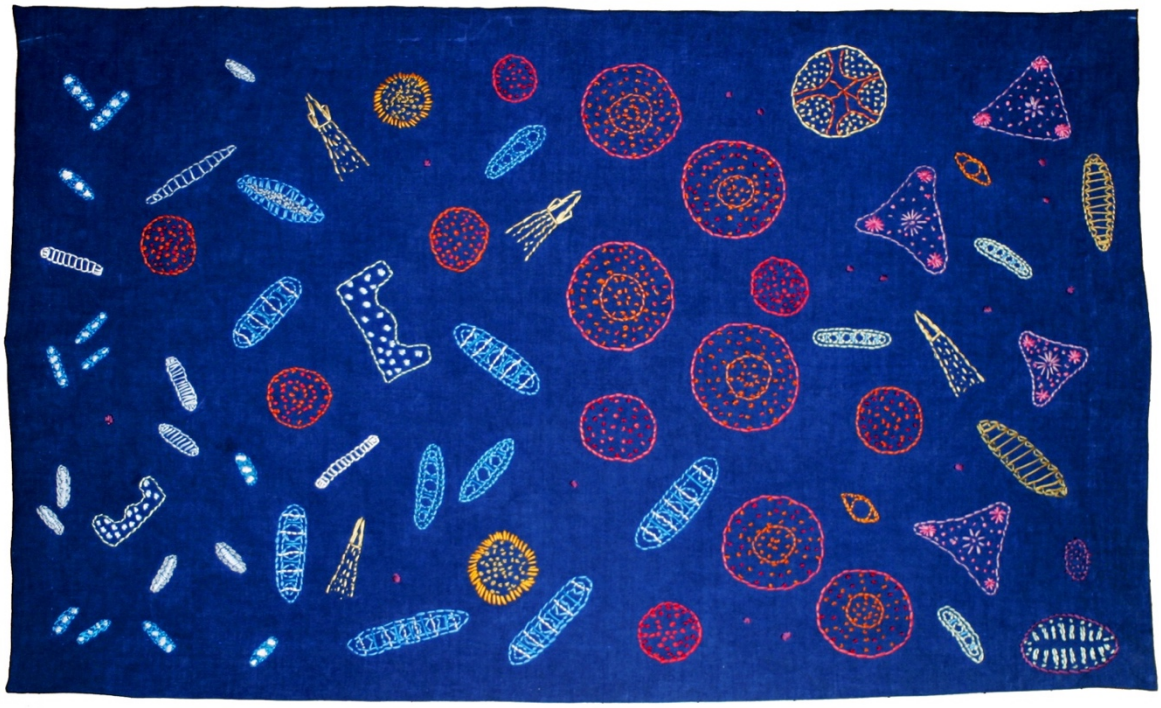

Freya Lorna Mitchison

Thesis submitted for the Degree of Doctor of Philosophy

Cardiff University

August 2019

CARDIFF UNIVERSITY

PRIFYSGOL CAERDYDD

Declaration

This work has not previously been accepted in substance for any degree and is not concurrently submitted in candidature for any degree.

Signed…… (candidate) Date……..

Statement 1

This thesis is being submitted in partial fulfilment of the requirements for the degree of Doctor of Philosophy (PhD).

Signed…… (candidate) Date……..

Statement 2

This thesis is a result of my own independent work and investigation, except where otherwise stated, and the thesis has not been edited by a third party beyond what is permitted by Cardiff University's policy on the Use of Third Party Editors by Research Degree Students. Other sources are acknowledged by explicit references. Views expressed here are my own.

Signed…… (candidate) Date……..

Statement 3

I hereby give consent for my thesis, if accepted, to be available online in the University's Open Access repository and for inter library loan, and for the title and summary to be made available to outside organisations.

Signed…… (candidate) Date……..

Statement 4

I hereby give consent for my thesis, if accepted, to be available online in the University's Open Access repository and for inter library loan, and for the title and summary to be made available to outside organisations after expiry of a bar on access previously approved by the Graduate Development Committee.

Signed…… (candidate) Date……..

Acknowledgements

I would firstly like to thank Jenny Pike, my main PhD supervisor, for the opportunity to do this PhD in the first place and for giving me the freedom to explore the things I was interested in, whilst providing invaluable guidance and support throughout my time at Cardiff. Also David Harwood, for sharing some of his vast diatom knowledge with me during my time in Nebraska. I would like to thank Steve Bohaty, who shared with me his unpublished diatom data, plates and biostratigraphic counts that helped evolve my understanding of my own data.

I would really like to thank James Williams, Jenny Pike and James Smith for sharing their unpublished $\delta^{18}O_{diatom}$ and Al/Si data with me, providing context for my own data in Chapter 8. Thanks also to James Williams for many useful conversations about diatom isotopes. I am very grateful to Mel Leng and, in particular, George Swann, for teaching me about diatom isotope analysis and for helping me to process and analyse my samples presented in Chapter 8. My diatom isotope work was funded by an Antarctic Science International Bursary, for which I am also very grateful.

I would like to thank the students who did projects with me, some of who's work is considered in this thesis. Ben Skinner, who did his MSc thesis, Jonatan Isaksson who did a CUROP project, Arianne Omana who did a Nuffield project and Laura Hunt, who did an undergraduate project and work experience helping to prepare samples for ice-rafted debris analysis. I also thank the technical staff at Cardiff who helped me with lab work at various stages; Lindsey Axe who helped with microscopy, Sandra Nederbragt and Lindsey Owen who helped with carbonate isotope analysis and general lab stuff, and Duncan Muir who helped me with SEM analysis.

Finally, thanks to my friends and family for supporting me throughout my PhD. Thanks to everyone in the Cardiff PhD community and paleoclimate office in particular, and also to Ewa and Dhobby for providing me with somewhere to stay whilst writing up! Special thanks also to my mother, Cathy Piccolo, who sewed the image on the front of this thesis showing the diatom assemblage transition across the Middle Miocene (based on the data presented in Chapter 6). Also, to my grandfather Av, for inspiring me to pursue science and for being possibly the only person not directly involved in this project who was always genuinely excited to hear about diatoms and what they can tell us!

Summary

The Neogene (c. 23-2.6 Ma) is the most recent period of Earth history in which atmospheric CO_2 was last >400 ppm; possibly associated with dramatic fluctuations in Antarctic ice volume and thus eustatic sea level. With continental configurations broadly similar to today, the Neogene therefore provides an opportunity to characterise and explore the different feedbacks and configurations of Earth's climate that occur under climatic forcing conditions either similar to today or to projected anthropogenic warming scenarios. However, many important questions in Neogene paleoclimatology remain unanswered. For example, the role in and response of the Southern Ocean, a key modulator of the Antarctic ice sheet and a disproportionately important player in the carbon cycle, to major episodes of climate change. In this thesis, diatom-based proxies, which tend to be well-preserved in the Southern Ocean, are developed and applied to some of the big questions in Neogene paleoclimatology.

Here, high resolution quantitative diatom assemblage records across the Middle Miocene Climate Transition (15-12 Ma) at a latitudinal transect of three Antarctic Zone ODP Sites (747, 744 and 1165), and a record at Site 1165 extending to the present, provide paleoceanographic insights. For example, the expansion of marine ice into Prydz Bay at 13.8 Ma, followed by eccentricity-paced Southern Ocean cooling and intensification of the Antarctic Circumpolar Current (ACC) at c. 13 Ma. Further cooling and full expression of the ACC during the Late Miocene was interspersed with transient warm intervals, possibly associated with ice sheet retreat. Unique Early Pliocene paleoceanography is indicated by diatom assemblages at high latitude circum-Antarctic sites, including Site 1165, dominated by *Thalassiothrix, Thalassionema* and *Trichotoxon* diatoms. These assemblages suggest substantially increased high latitude oceanic upwelling, which could have provided a source of heat contributing to Pliocene ice sheet retreat.

Finally, the first Pliocene Southern Ocean diatom silica stable oxygen isotope record ($\delta^{18}O_{diatom}$) at Site 1165 (3.45-3.75 Ma) explores the application of this proxy to Neogene material, alongside a geochemical assessment of sample purity. A strong correlation between Al/Si and $\delta^{18}O_{diatom}$ ($r=-0.89$, $p=<0.01$, $n=46$) suggests clay mineral-mediated secondary isotope exchange has overprinted the environmental signature at Site 1165 which, in the context of published and unpublished data, may be either age- or site-dependant. Any future study using $\delta^{18}O_{diatom}$, particularly within Neogene material, must therefore include a geochemical assessment of sample purity and carefully consider the correlation between $\delta^{18}O_{diatom}$ and Al/Si before interpreting $\delta^{18}O_{diatom}$ as a paleoenvironmental signal.

List of Acronyms

ACC	Antarctic Circumpolar Current
AAIW	Antarctic Intermediate Water
CCD	Carbonate compensation depth
CDW	Circumpolar Deep Water
CIE	Controlled isotope exchange
EAIS	East Antarctic Ice Sheet
EOT	Eocene/Oligocene Transition
HNLC	High nutrient-low chlorophyll
IODP	International Ocean Discovery Program
IRD	Ice-rafted debris
MECO	Middle Eocene Climate Transition
Mi1	Oligocene/Miocene boundary transient ice expansion event, 23.03 Ma
Mi3	Middle Miocene Climate Transition (glaciation), MMCT, c. 13.8 Ma
Mi3a	Miocene glaciation event, c. 14.6 Ma
Mi4	Miocene glaciation event, c. 13.1 Ma
Mi6	Miocene glaciation event, c. 10.5 Ma
Mi7	Miocene glaciation event, c. 9.4-9.3 Ma
MIS	Marine Isotope Stage
MLD	Mixed layer depth
MMCO	Middle Miocene Climatic Optimum, c. 17-15 Ma
MMCT	Middle Miocene Climate Transition, c. 13.8 Ma
NADW	North Atlantic Deep Water
ODP	Ocean Drilling Program
PF	Polar Front
PFZ	Polar Frontal Zone
PMOC	Pacific meridional overturning circulation
POC	Particulate organic carbon
s-ACC	Southern branch of the ACC
SACCF	Southern Antarctic Circumpolar Current Front
	SACCF-N and SACCF-S are northern and southern branch of SAACF, respectively
SAF	Subantarctic Front
SB	Southern Boundary

SEM	Scanning electron microscope
SLR	Sea level rise
SPT	Sodium polytungstate
SST	Sea surface temperature
SWF	Stepwise fluorination
SWW	Southern westerly winds
UCDW	Upper Circumpolar Deepwater
WAIS	West Antarctic Ice Sheet
XRF	X-ray fluorescence

Neogene diatoms from the Southern Ocean; tiny fossils, big questions

1. Introduction

This chapter provides the context and rationale for the thesis by outlining the reasons for investigating Neogene diatoms from the Southern Ocean (Sections 1.1-1.5), by defining the "big questions" that the thesis will address (Section 1.6) and by providing the thesis structure (Section 1.7).

1.1. Why investigate the Neogene period?

1.1.1. Cenozoic climate evolution

The Cenozoic, encompassing the most recent 66 million years of Earth history, saw the Earth transition from a greenhouse into an icehouse climate state. The progression has been extensively documented using stable isotopes preserved in foraminiferal calcite (Figure 1) that reveal a record of stepped transitions and transient climate events overlaying a gradual cooling since the Middle Eocene (e.g. Zachos et al., 2001; Zachos et al., 2008). During the early Cenozoic, beginning with the warm Paleocene and culminating in the Middle Eocene Climate Optimum (MECO), c. 40 Ma, there were palm trees on Antarctica and the global latitudinal temperature gradient was strongly reduced (Greenwood & Wing, 1995). Atmospheric CO_2 levels were very high, up to around 1500 ppm (Agnostou et al .2016; Figure 1), but evidence exists for a nascent Antarctic ice cap appearing during the Late Eocene cooling that followed the MECO (Scher et al., 2013; Carter et al., 2017), or perhaps even earlier (Bowman et al., 2013).

Despite conflicting evidence for the existence or extent of an Eocene Antarctic ice cap, proxy records generally agree that substantial Antarctic ice expansion occurred at the Eocene/Oligocene Transition (EOT), c. 34 Ma, with the ice sheet expanding to approximately its modern size (Petersen & Schrag, 2015; Galeotti et al., 2016). This expansion is clearly documented in Prydz Bay as well as Wilkes Land, the Ross Sea and possibly the Antarctic Peninsula (Barrett et al., 1989; Hambrey et al., 1991; Escutia & Brinkhuis, 2014; McKay et al., 2016). Primarily, the EOT was forced by a decrease in atmospheric CO_2, which fell below the ~780 ppm threshold required for the establishment of an ice sheet (DeConto & Pollard, 2003). However, associated changes in ocean circulation, for example increased high latitude thermal stratification and/or the inception of a circumpolar current in the Southern Ocean, likely acted as positive feedbacks, amplifying cooling (Goldner et al., 2014).

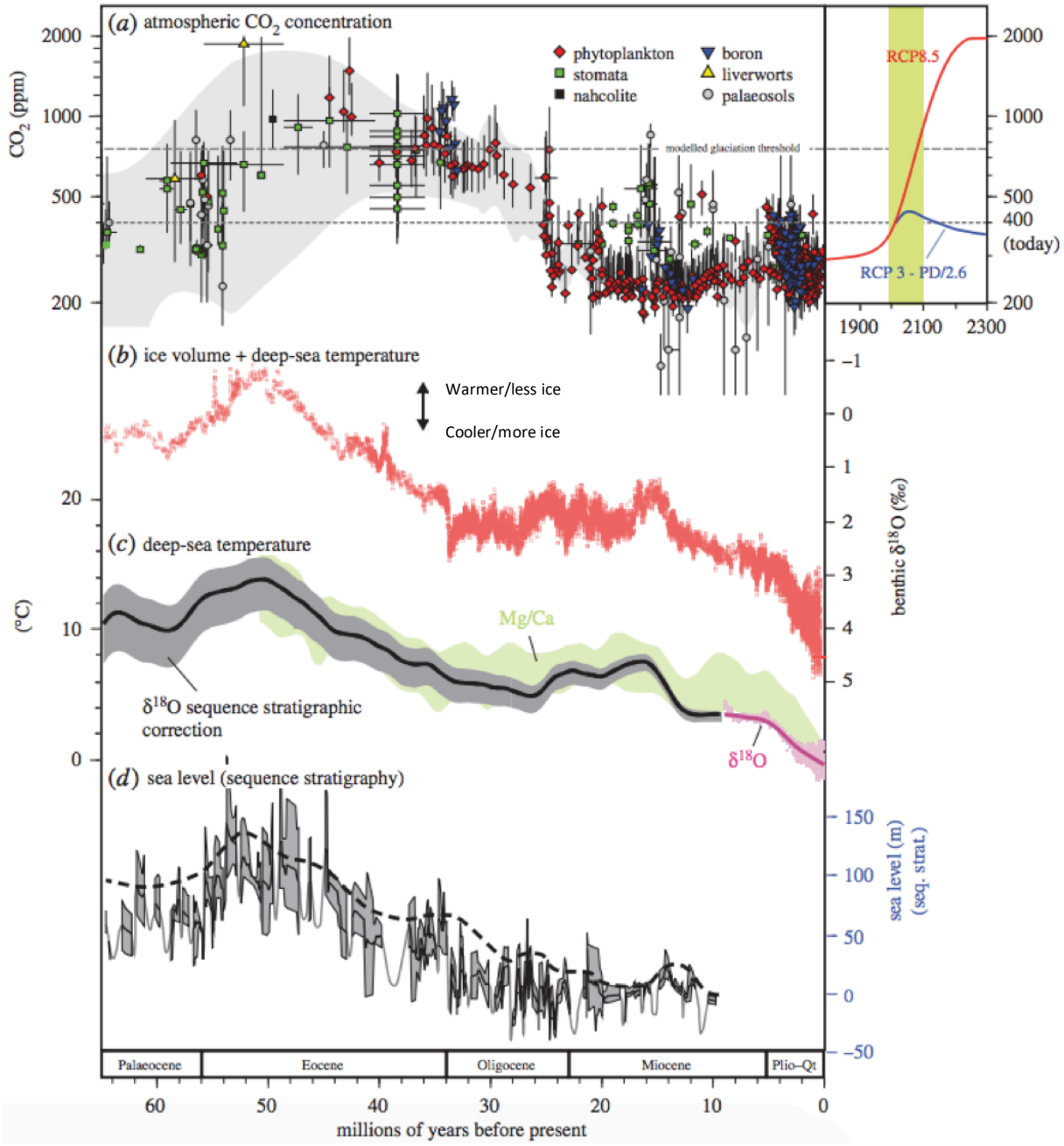

Figure 1. Summary of proxy climate records through the Cenozoic. A) Reconstructions of atmospheric CO_2 using various proxies (see McKay et al., 2016 for full list of references), including forward projections for best and worst case Representative Concentration Pathways for historic and future CO_2 emissions pathways (Meinshausen et al., 2011). B) composite of benthic $\delta^{18}O$ (Zachos et al., 2008). C) Record of deep-sea temperature calculated by stripping the ice volume component from the $\delta^{18}O$ signal using sequence stratigraphic records and Mg/Ca (Cramer et al., 2011; Miller et al., 2011). D) Reconstructed eustatic global sea level with minimum uncertainty ranges (grey shading) and smoothed trend (black dotted line) using

sequence stratigraphy from the New Jersey Margin (Kominz et al., 2008). Full figure from McKay et al. (2016).

Despite substantial ice expansion at the EOT, Oligocene ice sheets seem to have been more dynamic than their modern equivalents, with a dry-based interior but wet-based coastal regimes (McKay et al., 2016; Gulick et al., 2017). Dramatic oscillations of the Oligocene Antarctic ice cap have been inferred from far field marine isotope records, suggesting fluctuations of between 85-110% of modern ice volume during 110 kyr eccentricity-paced glacial/interglacial cycles (Leiband et al., 2017). During the warmest point of the Oligocene, at around 25 Ma, the Antarctic ice cap may even have returned to its much reduced Eocene configuration (McKay et al., 2016; Salabarnada et al., 2018), although other evidence suggests a large ice sheet persisted through the Late Oligocene (Hauptvogel et al., 2017).

Following the relatively warm Oligocene, the onset of the Neogene period was marked by an orbitally-induced, transient but substantial expansion of the Antarctic ice cap at the Oligocene/Miocene boundary at 23.03 Ma. This glaciation event coincided with an obliquity node; a 1.2 Ma minimum in the modulation of Earth's axial tilt and orbit, and a 400 kyr eccentricity minimum, both of which likely reduced seasonality and increased the persistence of snowfall during the summer (Coxall et al., 2005; Palike et al., 2006). However, coincident carbon isotope maxima and a Late Oligocene decrease in atmospheric CO_2 (Greenop et al., 2019) suggest a role for the carbon cycle in amplifying or even driving global cooling at the Oligocene/Miocene boundary.

The Early to early Middle Miocene was a period of global warmth that culminated in the Middle Miocene Climatic Optimum (MMCO) between c. 17-15 Ma. During the MMCO, global latitudinal temperature gradients were reduced in comparison to modern (Pound et al., 2012), and global sea levels were around 48 m higher than present (Frigola et al., 2018). The onset of the MMCO coincided with a massive perturbation of the global carbon cycle (Holbourn et al., 2015), followed by a subsequent broad positive $\delta^{13}C$ excursion known as the Monterey Excursion (Vincent & Berger, 1985), which indicates a role for the carbon cycle in forcing MMCO warmth. However, relatively low-amplitude $\delta^{18}O$ variability during atmospheric CO_2 fluctuations of between c. 300-500 ppm suggests decreased climate sensitivity to CO_2 forcing during this period in comparison to the Quaternary (Greenop et al., 2014). In Antarctica at least, the MMCO may have comprised a series of particularly warm events, for example at 15.7 Ma and 16.4 Ma

(Warny et al., 2009; Feakins et al., 2012), rather than a period of prolonged warmth. In any case, the warmth of the MMCO terminated in abrupt cooling at the Middle Miocene Climate Transition (MMCT), c. 13.8 Ma, during which the East Antarctic Ice Sheet (EAIS) re-expanded to larger than its modern volume (Lewis & Ashworth, 2015) but, this time, also shifted to a cold-based glacial regime (Lewis et al., 2007). During the MMCT, tundra biota became extinct on Antarctica (Lewis et al., 2008) and the Southern Ocean cooled by 6-7°C in surface waters (Shevenell et al., 2004) and by c. 2°C in bottom waters (Shevenell et al., 2008). The structure and nature of abrupt cooling at the MMCT forms one of the main themes of investigation in this thesis (Chapter 4.1).

Following the MMCT, a series of glaciations (named as numbered Mi events by Woodruff & Savin, 1991) punctuated the general global cooling trend of the Late Miocene, culminating in global sea surface temperatures (SSTs) first approaching modern levels by around 7 Ma (LaRivere et al., 2012; Herbert et al., 2016). This Late Miocene SST cooling coincided with an intensification of the Asian Monsoon (Ao et al., 2016; Holbourn et al. 2018) and the expansion of C4-pathway vegetation and grasslands (Cerling et al., 1993; Latorre et al., 1997). The role of atmospheric CO_2 in forcing Late Miocene climate remains unclear, with some proxy records suggesting a sharp decrease in CO_2 associated with decreasing extra-tropical SSTs (Mejia et al., 2017), but others suggesting a decoupling of CO_2 and global climate during this interval (Pagani et al. 1999; LaRivere et al., 2012; Sosdian et al., 2018).

Following the uncertain role of CO_2 in forcing Late Miocene climate, a better correlation between benthic $\delta^{18}O$ and reconstructed CO_2 is documented during the Pliocene (Sosdian et al., 2018), when climatic amelioration resulted in warmer global temperatures (c. 2-3°C above present; Dowsett et al., 2010), a smaller Antarctic ice cap and atmospheric CO_2 levels of >400 ppm (Figure 1; Seki et al., 2010). However, Early Pliocene warmth was terminated by Late Pliocene cooling, during which time large Northern Hemisphere ice sheets were established (Ravelo et al., 2004). It has been suggested that increasing Southern Ocean sea ice extent and SST cooling resulted in strengthened southern westerly winds and invigorated Southern Ocean circulation, in turn reducing Atlantic Meridional Overturning Circulation and, thus, heat transport to the high latitude North Atlantic during the Late Pliocene (McKay et al., 2012). However, declining CO_2 (Lunt et al., 2008), changing tectonic (Cane & Molnar, 2001) and/or orbital configurations (Maslin et al., 1998) also may have played a role in forcing Late Pliocene

cooling, which culminated in the large-amplitude glacial/interglacial cycles of the relatively well-studied Quaternary period.

This section has outlined how important trends in Neogene climate fit into the context of Cenozoic climate evolution. However, many central questions in Neogene paleoclimatology remain unanswered. The next section will address, in particular, the scientific controversy surrounding the stability of the Antarctic ice sheet(s) in response to climate forcing during the Neogene, and will outline the rationale for targeting the Neogene interval in particular.

1.1.2. Neogene history of the Antarctic ice cap

Oscillations in the size of the Antarctic ice cap through the Neogene period, particularly since 15 Ma, have been the subject of continuous scientific debate for over thirty years (see Barrett, 2013, for a full review of the discussion). A dominant school of thought has considered the Antarctic ice sheets, in particular the East Antarctic Ice Sheet (EAIS), as being relatively stable since its expansion and transition to a cold-based glacial regime at the Middle Miocene Climate Transition (MMCT), c. 13.8 Ma (Lewis et al., 2007). This view was largely based on the evidence of well-dated ash deposits and surfaces in the Dry Valleys that indicate a stable polar climate since 14 Ma (Sugden et al., 1993; Denton et al., 1993; Sugden, 1996; Sugden et al., 1999; Sugden & Denton, 2004). However, other more recent evidence indicates a much more dynamic ice sheet during warm Neogene intervals, such as the Pliocene, when atmospheric CO_2 concentration was last >400 ppm (Martínez-Botí et al., 2015). The rapid thinning of modern East Antarctic glaciers (Shepherd et al., 2019) also suggests a potential vulnerability of the EAIS to future anthropogenic climate warming. As such, better understanding the EAIS response to past climate change is of major societal relevance.

A raised awareness of potential EAIS instability began in the 1980s, when marine diatoms were discovered in the Transantarctic Mountains within terrestrial glacial deposits known as the Sirius Group, as far south as 86°S (Webb et al., 1984). The deposits contain reworked Pliocene and Miocene age marine diatoms, the in-situ deposition and transport of which would have required much higher sea levels and the ice sheet to have been reduced to around two thirds of its present volume. Webb et al. (1984) dated the Sirius Group deposits to the Pliocene using diatom biostratigraphy, and invoked substantial deglaciation and subsequent erosion and transport to explain their deposition. However, the diatom evidence has since been subject to intense scrutiny, with suggestions that the marine diatoms were instead wind-blown, or that the sieves

used to prepare the samples could have resulted in the loss of smaller freshwater diatom assemblages indicative of, alternatively, in-situ freshwater deposition (Barrett et al., 2013). Instead, Denton et al. (1984) invoked geomorphological evidence to date and attribute the deposits to Middle Miocene ice sheet overriding of the Transantarctic Mountains.

The Sirius Group is not the only terrestrial Antarctic deposit containing marine diatoms. The Pagodroma Group, uplifted into the Prince Charles mountains near Prydz Bay, also contains marine diatoms, indicating that the EAIS margin retreated up to 300 km inland several times during the late Neogene (Figure 2). The Pagodroma and Sirius Groups differ substantially; the Sirius Group is a predominantly terrestrial glacigenic succession of controversial age, while the Pagodroma Group is a marine-proximal fjordal sequence indicating different depositional processes. Marine molluscs, relatively high biogenic opal concentrations and a large proportion of benthic diatoms found in the Pagodroma deposits also strongly indicate marine deposition (Whitehead et al., 2004). As such, the Pagodroma Group provides robust evidence for substantial EAIS variability through the Neogene, although the total extent of EAIS retreat remains unresolved.

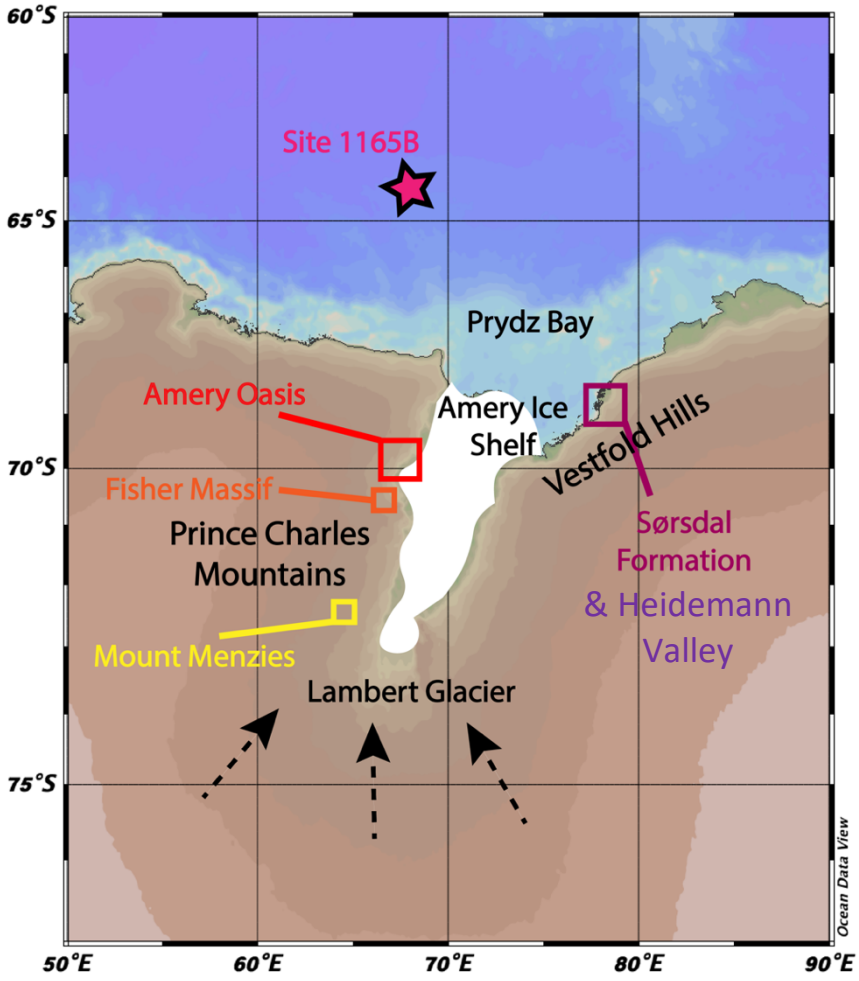

Figure 2. Map showing the location of the Pagodroma Group (Mount Menzies, Fisher Massif and the Amery Oasis) and Vestfold Hills deposits.

Over the past decade, numerical modelling efforts and physical evidence have increasingly supported the idea of a more dynamic EAIS (Figure 3). For example, orbitally-paced variability has been documented in the Wilkes Land sector of the EAIS during the Pliocene (Patterson et al., 2014), including times when open-marine conditions persisted on the continental shelf (Orejola et al., 2014; Reinardy et al., 2015) and the ice sheet margin retreated into the Aurora and Wilkes subglacial basins (Cook et al., 2013). ANDRILL cores show evidence for repeated advances and retreats of the Ross Ice Shelf across the continental shelf, suggesting the WAIS was also likely reduced to at least its terrestrial component during the warmest Pliocene (Naish et al., 2009). However, recent geophysical data from the Sabrina coast (Wilkes Land sector of the EAIS) indicates a transition to a cold-based permanent ice sheet during the Late Miocene, with minimal glacial response to Pliocene warmth (Gulick et al., 2017), raising the possibility of substantial heterogeneity in the pattern of EAIS retreat.

Far-field records have provided estimates for an Antarctic contribution to Pliocene sea level rise (SLR) of 15-20 ± 10 m, although significant uncertainty exists in paleo sea level reconstructions due problems estimating dynamic topographical changes (Miller et al., 2012; Dutton et al., 2015). Factoring in newly-considered processes such as hydrofracturing, marine ice cliff instability and marine ice sheet instability (Pollard et al., 2015), a new generation of ice sheet models produce simulations closer to the higher end of proposed Pliocene EAIS retreat and SLR constraints (DeConto & Pollard, 2016; Gasson et al., 2016; Golledge et al., 2017). However, recent cosmogenic isotope evidence showing minimal retreat of land-based sectors of the EAIS during at least the last 8 million years provides a likely upper bound for an Antarctic contribution to Pliocene SLR of around 22 m (Shakun et al., 2018; Escutia et al., 2019). These SLR constraints largely align with a recent effort to resolve the Sirius Group controversy using atmospheric modelling to show that substantial retreat of the EAIS into the Aurora and Wilkes subglacial basins could have created a shallow marine embayment and associated deposits, from which the marine assemblages could have been wind-blown into the Transantarctic Mountains (Scherer et al., 2016). However, significant questions still remain about the response of the EAIS to climate and ocean forcing during the Neogene period. If we are to predict the fate of the EAIS in response to future climate change, it is essential to first ground-truth forward-casting models

using paleodata, and to fully understand the dynamics of the EAIS through the Neogene, including its response to various different forcings, such as ocean dynamics.

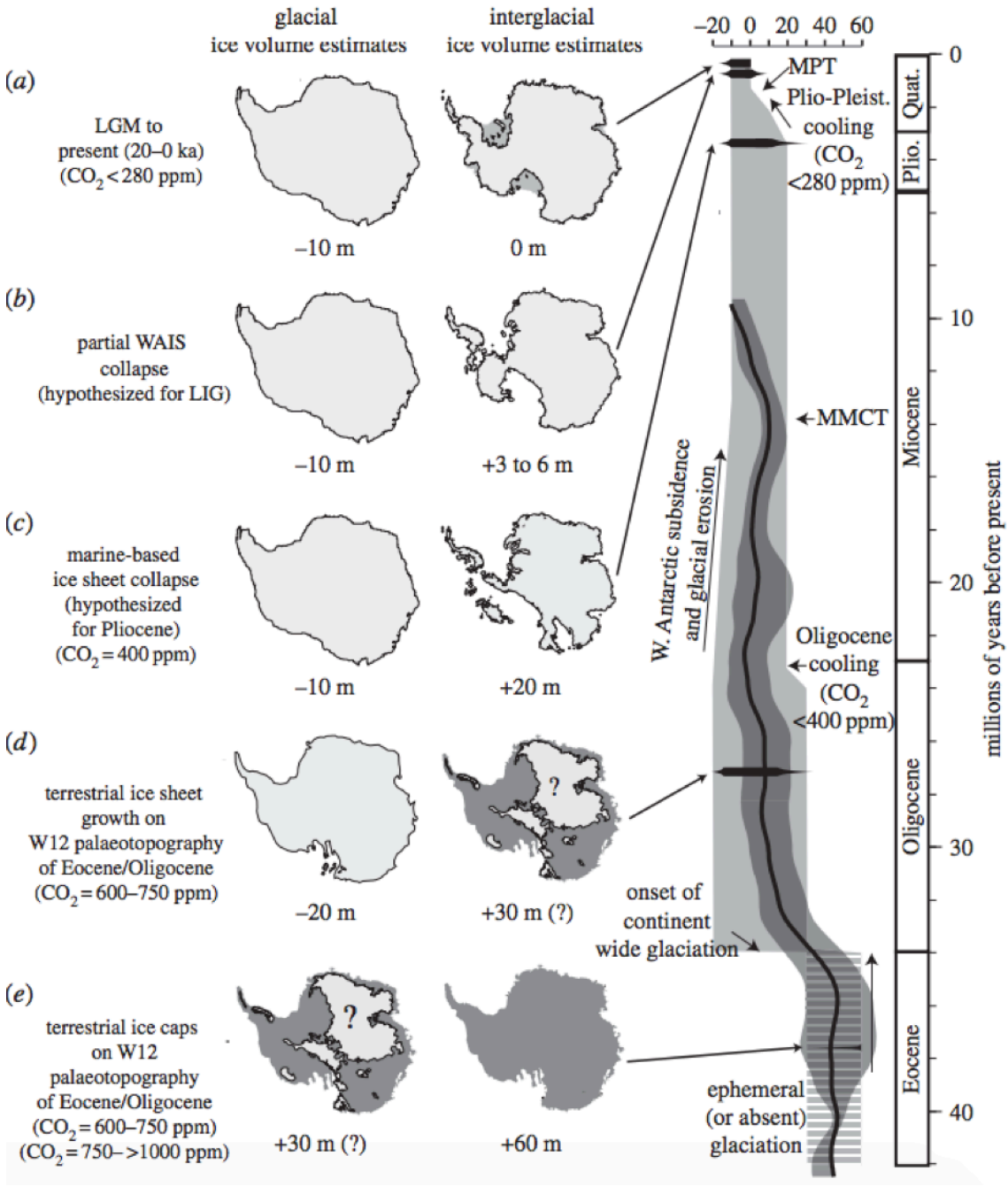

Figure 3. Hypothesized extent (and sea level contributions) of ice sheets during the Cenozoic. A-E) Modelled variations in ice sheet extent using modern day (Bedmap 2) topography and the ice sheet model of Golledge et al. (2016) to estimate sea level contributions. Superimposed on modelled sea level are sequence stratigraphic sea level reconstructions from New Jersey (Kominz et al., 2008; McKay et al., 2016). Oligocene glacial maximum scenarios are based on

reconstructions in Wilson et al. (2013) and DeConto & Pollard (2003). Figure from McKay et al. (2016).

Overall, with continental configurations broadly similar to today, the last 15 million years of Earth history represents an ideal interval within which to explore and understand Earth's different climate configurations. Neogene climatological fluctuations, including in the size of the Antarctic ice sheets, were likely of a higher amplitude than what has occurred during the Quaternary period, providing fertile ground for investigation. However, whilst the Quaternary has been relatively well studied, many questions in Neogene paleoclimatology remain. For example, how extensive was Antarctic sea ice, what role did it play in the climate system, and how did it respond to, for example, the transition away from a meltwater-dominated Antarctic glacial regime? What was the volume and extent of the Antarctic ice sheets, and how much, why, and when did they fluctuate? When did the Antarctic Circumpolar Current initiate and intensify, and what affect did this have on global ocean circulation? How much of a role did CO_2 play in climate forcing? How did ocean productivity vary, and how active was the biological pump in regulating atmospheric CO_2? Understanding Neogene climate is becoming increasingly relevant as modern atmospheric CO_2 concentrations approach values not seen since the Pliocene or even the Middle Miocene (Figure 1). As such, and given the number of fundamental, unanswered big questions, the Neogene period provides an important target for further scientific investigation.

1.2. Why investigate the Southern Ocean?

1.2.1. Ice/ocean interactions

Recent climate observations in both the Northern and Southern Hemispheres have highlighted the importance of oceanic forcing on ice sheet dynamics (Joughin et al., 2012). Given the enormous heat capacity of the oceans, relatively small changes in ocean forcing can have a substantial impact on ice sheets and, therefore, global sea level. The affect of ocean forcing is particularly outsize in Antarctica, where relatively cold atmospheric temperatures have less of an impact on ice melting (Joughin et al., 2012). The Antarctic ice sheets are also entirely surrounded by the Southern Ocean and, in many regions, are grounded below sea level and/or ocean terminating, sometimes with ice shelves protruding into the ocean that buttress a much greater quantity of continental ice (Figure 4). Ice shelves and marine-terminating margins provide the Southern Ocean with direct access to the ice, meaning increases in ocean temperature can directly melt ice. For example, relatively warm circumpolar deep water

upwelling beneath modern Antarctic ice shelves and glaciers, such as beneath the West Antarctic Pine Island Glacier and the East Antarctic Totten Glacier, is currently increasing ice melt and flow rates (Rignot et al., 2019). Conversely, a relatively warm ocean could also theoretically increase evaporation and subsequent precipitation, driving ice growth, as is proposed to have occurred at the Middle Miocene Climate Transition (Flower & Kennett, 1994; Kuhnert et al., 2009).

Direct ocean forcing can influence glacier calving, as well as reshaping and relocating glacial termini (Joughin et al., 2012). In turn, the shape and location of glacial termini can influence the balance of stresses acting upon ice streams, such that changes at the terminus can have a far-reaching effect on the continental ice cap. For example, if ocean-forced melting drives the disintegration of marine ice shelves, the continental ice that the ice shelves were buttressing may increase in flow rate towards the ocean. This was demonstrated by the collapse of the Larsen B ice shelf in 2002, following which anterior ice streams sped up; reducing local ice volume (Scambos et al., 2004). In Greenland, the warming-induced thinning and eventual loss of the Jakobshavn Isbrae glacial tongue resulted in increased terminal flow rates (Joughin et al., 2008; Joughin et al., 2012). While a build-up of melting calved ice can slow down glacial ice loss, in other locations ocean currents carry away calved ice, allowing it to melt elsewhere and for glacial ice loss to continue (Joughin, 2012).

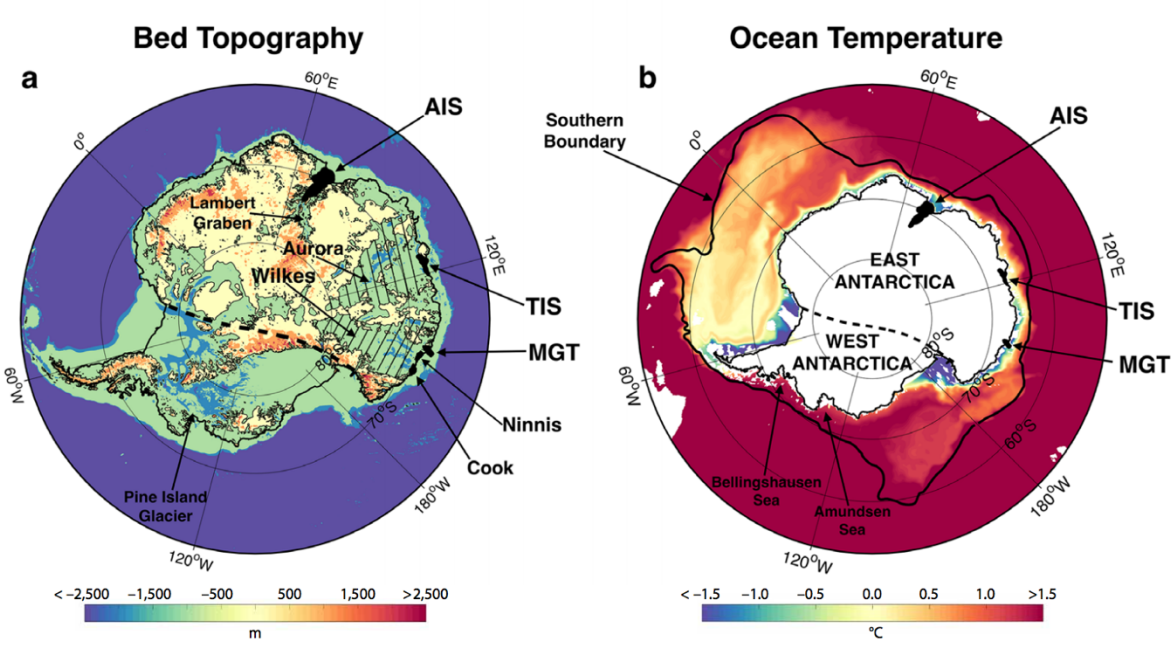

Figure 4. Map of Antarctica, showing A) modern bed topography, with many areas, even in East Antarctica, lying below sea level (Fretwell et al., 2013). B) Ocean temperatures at 438 m water depth – close to the core of Circumpolar Deep Water within the Antarctic Circumpolar Current, based on a six year (2005-2010) mean (Mazloff et al., 2010). Highlighted ice shelves include the Amery Ice Shelf (AIS), Totten Ice Shelf (TIS) and Mertz Glacier Tongue (MGT) (Silvano et al., 2016).

While the ocean influences ice dynamics, ice can also directly and indirectly influence the ocean. For example, the release of large quantities of freshwater via glacial discharge into the Southern Ocean upon substantial retreat of the Antarctic ice sheets would have a significant impact on local, and global, ocean circulation. In fact, the climate response to freshwater release has been identified as one of the largest uncertainties in future IPCC projections (Fogwill et al., 2015). Past episodes of substantial Antarctic ice sheet retreat offer an opportunity to better understand the Southern Ocean response to freshwater release. For example, the disintegration and melting of icebergs during the last glacial termination is suggested to have led to increased stratification in glacial calving bays, likely compromising bottom-water formation (Leventer et al., 2006). If massive ice sheet retreat occurred during the Pliocene, large quantities of freshwater would have been released into the Southern Ocean; providing a potential target interval within which the consequences of ice sheet retreat on ocean circulation could be investigated.

Another key component of ice/ocean interactions is sea ice. Antarctic sea ice is largely seasonal, with around 20 million km^2 surrounding the continent during the October maximum, but only 3 million km^2 during the February minimum (Figure 5; Thomas, 2007). In comparison to Arctic sea ice, much of which is perennial and >4 m thick, Antarctic sea ice is younger and thinner; usually only 1-2 m thick (Thomas, 2007). Sea ice at both poles plays a major role in the global climate system, influencing albedo and mediating the ocean/atmosphere exchange of energy and gases such as CO_2. However, ocean/atmosphere exchange is particularly important in the Southern Ocean, where the world's oceans upwell and are exposed to the atmosphere (are ventilated), before sinking to continue on their journey through global oceans. Winter Southern Ocean sea ice coverage currently blocks a large amount of air/sea exchange, preventing substantial oceanic CO_2 degassing (Butterworth & Miller, 2016).

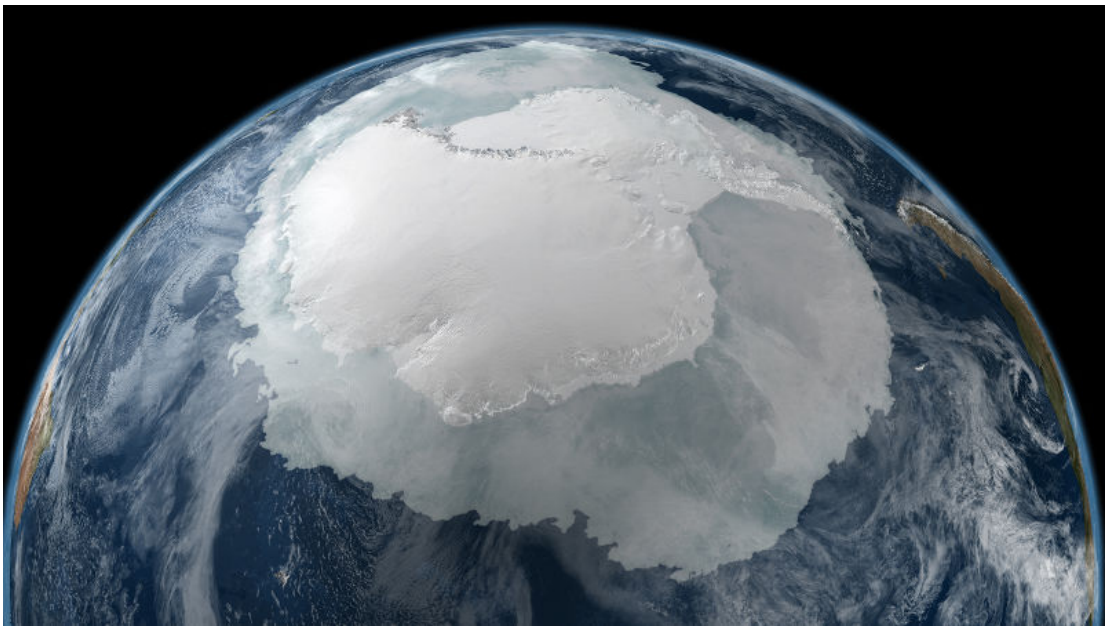

Figure 5. Photograph of Antarctica and its autumn sea ice on 21/05/2005, taken from the AMSR-E satellite (NASA).

Arctic sea ice has been steadily declining in recent decades (Serreze et al., 2015), however, the response of Southern Ocean sea ice has been less clear. Antarctic sea ice coverage had been increasing, although heterogeneously, since the late 1970s (Parkinson & Cavalieri, 2012), leading to the suggestion that meltwater from retreating Antarctic glaciers was causing more sea ice to form (Bronsalaer et al., 2018). However, Antarctic sea ice reached a record low in late 2016, forced by oscillations of the Southern Annular Mode and Interdecadal Pacific Oscillation (Meehl et al., 2019), operating on decadal timescales. Extending the record of sea ice dynamics beyond the satellite era is important in order to fully understand the role in, and response of, sea ice to climate change. While Quaternary Southern Ocean sea ice dynamics are relatively well-studied (e.g. Crosta et al., 1998), the behaviour of Neogene Southern Ocean sea ice remains almost entirely unknown despite substantial previous changes in Neogene climate, for example the transition from a meltwater-dominated glacial regime to a drier, more stable EAIS during the Middle-Late Miocene (Gulick et al. 2018), which presumably greatly affected sea ice cover. Reconstructing and understanding Neogene changes in sea ice may, therefore, improve understanding of Antarctic sea ice dynamics and the accuracy of future sea ice forecasts.

1.2.2. The role of the Southern Ocean in regulating global climate

The Southern Ocean plays a disproportionately important role in the global climate system. This is primarily due to its direct access to the world's largest ice sheet (discussed in Section 1.2.1), and also to its position as the locus of global deep water upwelling (Figure 6) and, thus, its role in the global carbon cycle. Southern Ocean meridional overturning circulation, driven by strong circumpolar winds and Ekman transport, forces much of modern global ocean circulation (Carter et al., 2009). The intense upwelling generated south of the Polar Front brings old, deep water to the surface where it interacts with the atmosphere. This older deep water is rich in dissolved organic carbon, as a result of remineralized organic matter and the dissolution of $CaCO_3$ on its path around the global ocean. Upon reaching the surface, the deep water is either: pushed south, where sea ice largely prevents substantial carbon exchange with the atmosphere (Hoppema et al., 2001; Butterwork & Miller, 2016) and the deep water is transformed into Antarctic Bottom Water upon freshening and cooling. Alternatively, the upwelled deep water is pushed northwards by Ekman transport and is subject to strong air/sea fluxes before being subducted as intermediate water (Carter et al., 2009).

The efficiency of Southern Ocean air/sea exchange is, at least in the open ocean, mediated by the biological pump, whereby photosynthetic organisms, such as diatoms, transform inorganic carbon into organic carbon in the surface ocean. This organic matter is subsequently exported to depth by a number of processes (Figure 7). In the Southern Ocean, biological productivity is primarily limited by micronutrient availability, specifically iron (Boyd et al., 2000). However, other factors such as light conditions, macronutrient (e.g. silica) availability and grazing pressure are also important (Boyd, 2002).

The biological pump can be defined as the ratio of preformed:regenerated nutrients. Preformed nutrients are nutrients unused by organisms before they are subducted during intermediate and deep water formation, representing essentially a missed opportunity for carbon drawdown, whilst regenerated nutrients are remineralized from organic matter. The ratio increases when nutrient use efficiency is low. In this sense, the Southern Ocean biological pump is currently highly inefficient, as a result of its micronutrient limitation, and a large amount of inorganic carbon remains unfixed. If iron limitation was ameliorated, as may have occurred during past glacial periods (Kumar et al., 1995; Watson et al., 2000; Martinez-Garcia et al., 2011; Shoenfelt et al., 2018), productivity and biological pump efficiency would increase, leading to a drawdown of atmospheric pCO_2.

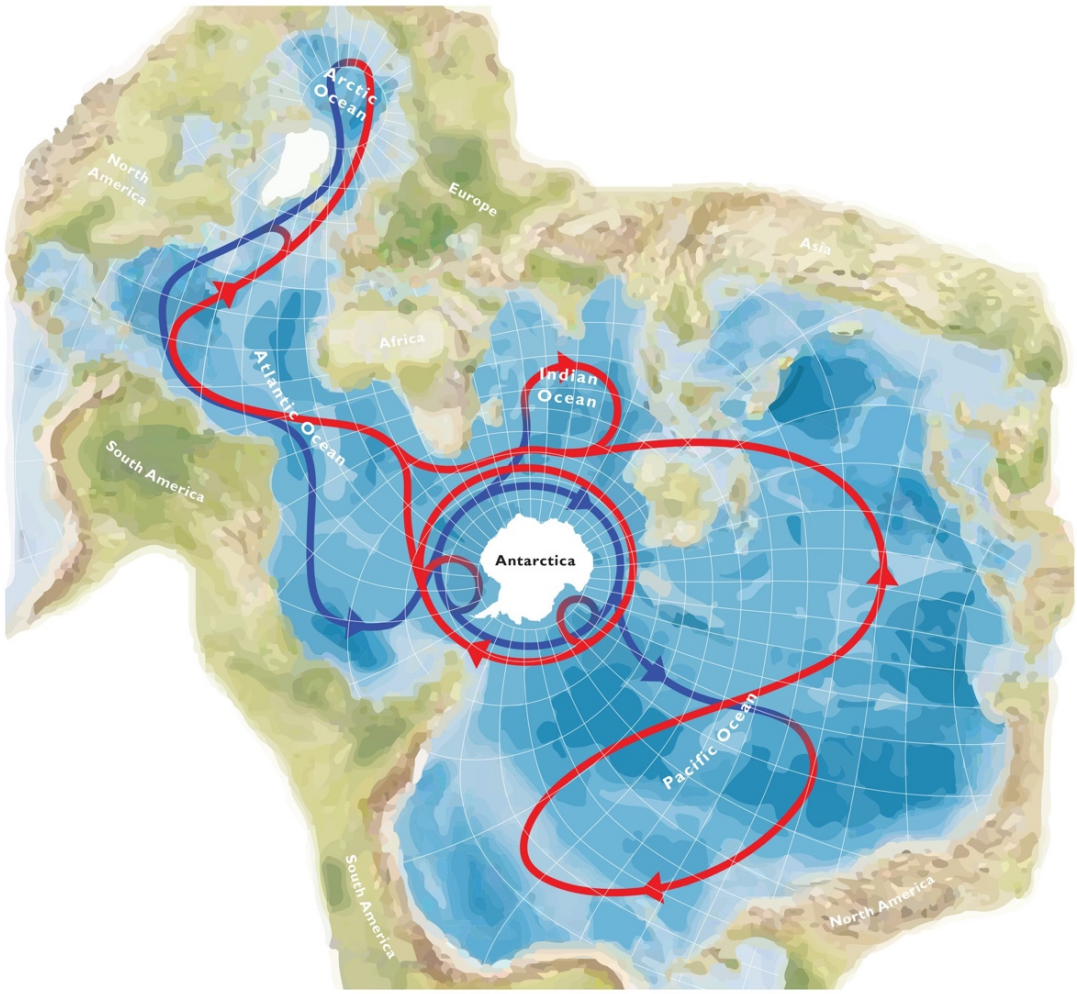

Figure 6. Global ocean circulation on a Spilhaus projection; emphasising the central role of the Southern Ocean. Upper flow is shown in red; deep water flow in blue (Meredith, 2019).

Southern Ocean waters are a source of nutrients to the low latitudes (Hayes et al., 2011). Thus, changes in Southern Ocean productivity also affect export production and the efficiency of the global biological pump, making Southern Ocean productivity an important regulator of atmospheric CO_2 (Primeau et al., 2013). However, Southern Ocean circulation patterns affect the ability of a given increase in productivity to affect atmospheric CO_2. For example, in numerical model simulations forced by increased nutrient utilization, the subantarctic is more efficient at decreasing low latitude export production because the upper ocean circulation is responsible for advecting nutrients to the low latitudes. However, the higher preformed nutrient content and volume of global Antarctic Bottom Water ventilation means the more southerly Antarctic zone is more efficient in lowering global CO_2 (Marinov et al., 2006). Given that Southern Ocean circulation patterns have varied substantially through time, the impact of past changes in Southern Ocean productivity on atmospheric CO_2 and the global carbon cycle during the Neogene period therefore remains largely unresolved.

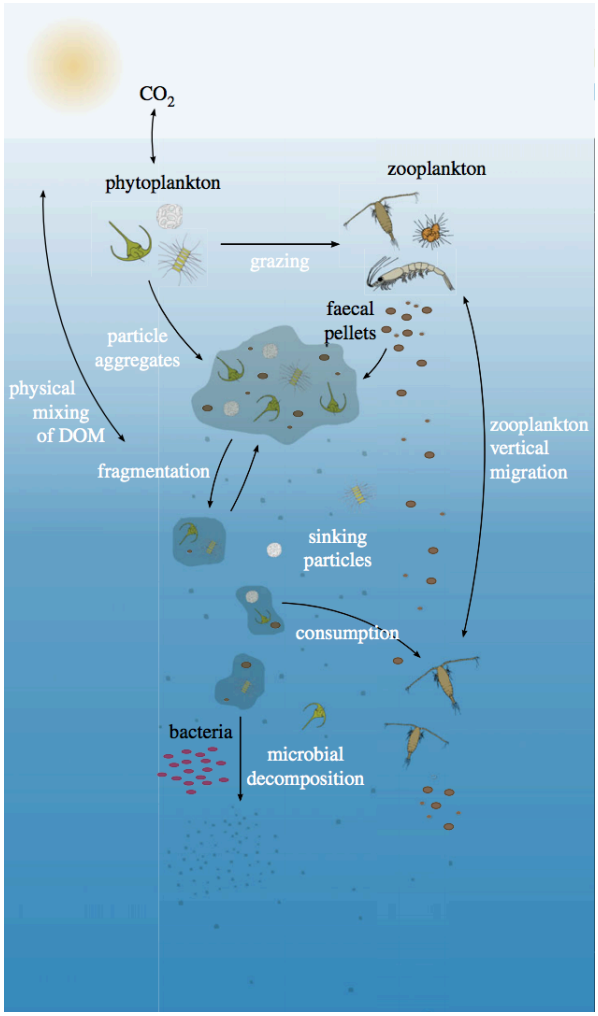

Figure 7. Carbon sequestration via the global ocean biological pump. Phytoplankton, including diatoms, photosynthesize in the surface ocean, transforming inorganic carbon into organic material. Phytoplankton are then grazed by heterotrophs, with a fraction exported as fecal pellets, via physical mixing and/or by the vertical migration of zooplankton. Image is drawn to proportion to the quantitative importance of the process (modified from Benoiston et al., 2017).

1.3. Why investigate Neogene Southern Ocean changes using diatoms?

1.3.1. How climate influences diatoms

Diatoms are siliceous microalgae which live in both marine and freshwater environments. In the oceans, planktonic diatoms living at the sea surface die and sink to the sea floor, eventually becoming ocean sediment. However, only a small proportion of valves ever reach the sea floor, with the remainder broken down or dissolved during sinking (Jordan & Stickley, 2010). Nonetheless, the sedimentary diatom record has been shown to closely reflect

paleoenvironmental trends (e.g. Gersonde & Zielinski, 2000). Within the confines of the fossil record, the primary tools available with which to assess the diatom response to environmental change are: records of overall diatom abundance and concentration within sediment, diatom assemblages and diatom morphologies. This section will outline how various environmental factors may influence these properties, and therefore, how diatom fossils may document environmental change.

Diatoms are extremely sensitive to the environmental conditions in the water column in which they live; for example, to macro- and micro-nutrient availability, light conditions, water temperature and salinity. They possess efficient signalling and sensing mechanisms, allowing them to respond to environmental change in three main ways (Figure 8):

1. Phenotypic plasticity, e.g. via a change in morphology, biochemical or physiological properties and/or behaviour within a species. This can widen the species' ecological niche, which has been shown to contribute towards increased persistence during global change (Nicotra et al. 2010);
2. Species sorting (generally after the limits of phenotypic plasticity are breached);
3. Genetic adaptation.

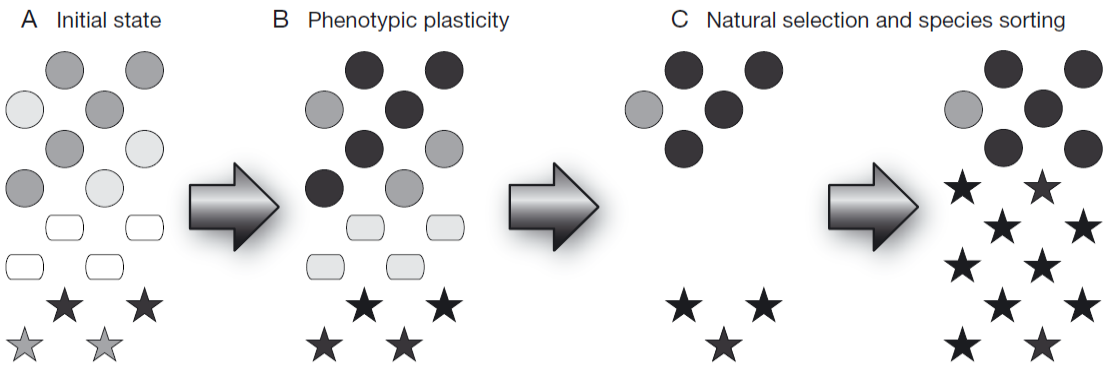

Figure 8. The succession of a diatom response to environmental change either over time or with increasing change. Different shapes represent different diatom species (Litchman et al., 2009).

Species sorting occurs because diatom species are each best adapted to specific environmental conditions in a number of ways. For example, larger species have a lower surface area:volume ratio, making them more likely to be diffusion-limited in accessing nutrients. However, larger cells tend to have superior storage capacities (Finkel et al., 2010) and an increased capacity for

biomass production (Verdy et al., 2009), allowing them to out-compete smaller cells under low or pulsed nutrient conditions despite the faster metabolic rates of smaller cells (Finkel et al., 2004). Shifts in cell shape, for example elongation along the apical axis, can also increase the cell surface area:volume ratio, allowing for increased nutrient uptake (Grover, 1989). Further, colony formation can play a role, whereby solitary cells have increased nutrient uptake capacities relative to those in chains, although turbulent flow could increase the nutrient flux to widely-spaced chain-forming cells relative to single cells (Pahlow et al., 1997).

Differences in diatom frustule morphology, often observed in the fossil record, could potentially be explained by nutrient-uptake strategies. For example, frustule microtomographies have been shown to concentrate nutrient-like particles around pore ridges, indicating that cells could sort and select nutrient particles (Hale & Mitchell, 2001). This result also suggests that variations in frustule microstructure could influence nutrient uptake, either via intra-species phenotypic plasticity, inter-species sorting, or potentially even by forcing evolutionary adaptation and/or speciation. In reality, nutrient supply to the natural environment can vary widely, allowing cells to exploit various different nutrient strategies (for example, bloom formers and larger, persistent background cells), which explains the heterogeneity of diatom and phytoplankton communities.

As photoautotrophic organisms, light is required for diatom growth. Fluctuations in the underwater light climate therefore have the potential to influence diatom species morphology, sorting, or even evolution if differences in photosynthetic capability are large. In the natural marine environment, light levels are dictated by, for example, latitude, seasonality, turbidity, sunshine hours, the extent of water column stratification and the presence of sea ice. As such, differences in the photo-protective capacity of various species (Lavaud et al., 2007) could influence their biogeography. There are also links to cell size; diatoms withstand fluctuating light levels better than larger phytoplankton, and cell size in marine centric diatoms affects photosynthetic activity as a result of the increased self-shading of larger cells, making smaller cells more photosynthetically-competitive (Key et al., 2010). However, larger cells are also less susceptible to photoinactivation, giving them an advantage within a fluctuating and/or high light regime (Key et al., 2010).

The depth of the mixed layer dictates the upper limit of phytoplankton crop size (Mitchell & Holm-Hansen, 1991); primary productivity in the Southern Ocean stops increasing when mixed

layer depths (MLD) deepen to >50 m, regardless of iron availability (Cassar et al., 2011). Phytoplankton in the open ocean (that is, not stabilized by meltwater) may only be able to utilize around 10% of available nutrients in high nutrient-low chlorophyll (HNLC) areas, at minimum loss rates, before they become self-shading (Mitchel et al., 1991). This would place bounds on any increase in productivity and subsequent CO_2 drawdown in response to, for example, Fe addition to the Southern Ocean during glacial periods, but has generally been neglected in quantification of glacial/interglacial productivity change (Hain et al., 2010; Ganopolski & Brovkin, 2017). As a further complication, photoacclimation at low light levels generally requires more Fe (Venables & Moore, 2010), whilst increased Fe availability has been shown to increase the photosynthetic capacity of photosystem II (Boyd & Abraham, 2001; Moore et al., 2007). In this sense, a poor response of diatoms to an initial deepening of the mixed layer might be expected due to Fe limitation (Queguiner, 2013), although light limitation may become dominant at MLD >50 m (Cassar et al., 2011). In any case, light conditions demonstrably affect diatoms in a number of ways, either directly and indirectly, via self-shading and/or a coupling with bioavailable Fe concentrations.

Interpreting the drivers of a diatom response from the fossil record is complex. For example, morphological changes in the Antarctic diatom *Thalassiosira torokina* over the course of the Neogene, including its decreased diameter (from 152 µm to 26 µm on average) and increased domeness, were found to correlate with various climate proxies including changes in sea ice (McLean, 2011). However, whilst the correlation indicates the changes may be related, it does not explain why or how sea ice cover could be driving each specific morphological change. Nonetheless, records of diatom assemblages, abundances, morphologies, and also frustule biogeochemistry (expanded upon in Chapter 8), preserve an important archive of paleoceanographic data if they can be correctly interpreted.

1.3.2. How diatoms influence climate

Section 1.3.1 described how diatoms are sensitive to climate and ocean conditions and, therefore, how diatoms can provide a record of past environmental change. A further reason for studying past fluctuations in diatom populations is the possible affect diatoms themselves can have on Earth's climate. This is because although they represent <1% of global biomass, diatoms account for up to 20% of global primary productivity (Nelson et al., 1995; Field et al., 1998). Diatom frustules are the most ubiquitous global biogenic sediment particle, but are most common in upwelling areas with a high macronutrient supply such as the Southern Ocean (Honjo

et al., 2008). Figure 9 illustrates the relationship between surface ocean silicic acid availability and sedimentary biogenic silica; both are concentrated in the Southern Ocean, particularly south of the Polar Front, where diatoms comprise a major part of the plankton (Deppeler & Davidson, 2017).

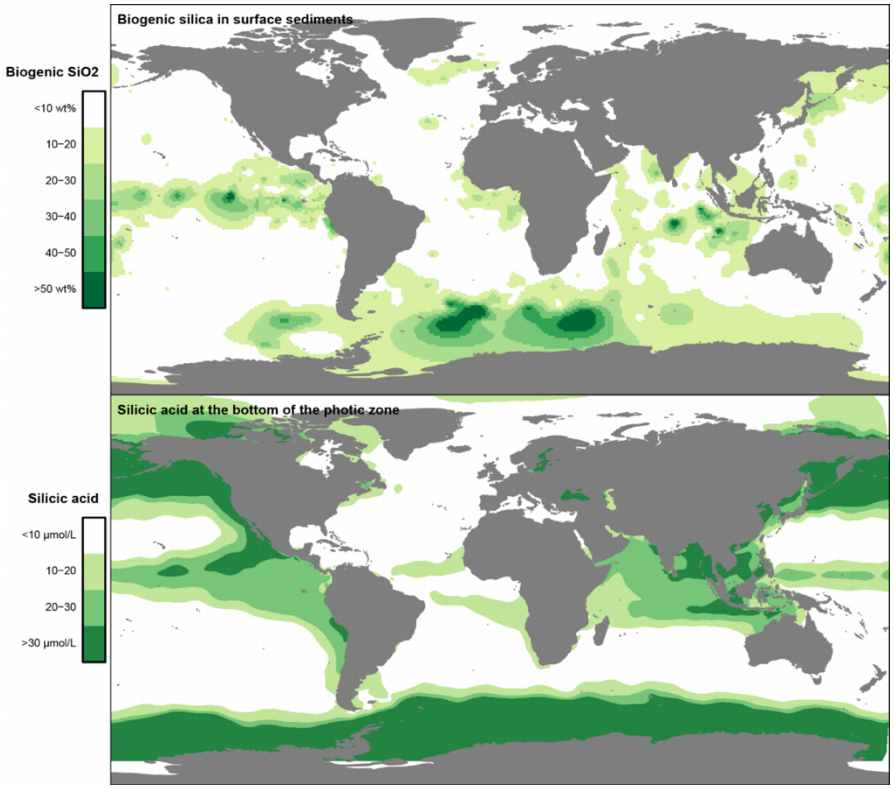

Figure 9. Top panel: biogenic opal in surface sediments (Archer, 1996). Lower panel: silicic acid concentrations at 200 m water depth, the lower limit of the euphotic zone (Garcia et al., 2010) (Renaudie, 2016).

Despite being most common in upwelling areas, diatoms are major contributors to organic carbon fluxes in all ocean basins (Buessler et al., 2007). However, porous silica frustules lower their specific gravity relative to higher density calcite shelled coccolithophores and may, therefore, provide less ballast for sinking carbon (Armstrong et al., 2002). Nonetheless, some combination of their relatively large size (Boyd & Newton, 1999), fast growth rates/efficient nutrient acquisition strategies (Goldman, 1993) and/or their tendency to aggregate, reducing their exposure to decay (De Le Rocha et al., 2008), makes diatoms key exporters of organic carbon (Buessler et al., 2007). It has also been suggested that diatom mats sinking out en-masse, for example at bloom terminations, could trap other suspended particles and aggregates, increasing their contribution to carbon sequestration relative to other phytoplankton groups

(Lampitt, 1985; Honjo et al., 2008). The TARA Oceans expedition dataset demonstrates that in the modern ocean at least, Bacillariophyta (including diatoms) show the strongest correlation with carbon export of all marine eukaryotic microbiota (Figure 10).

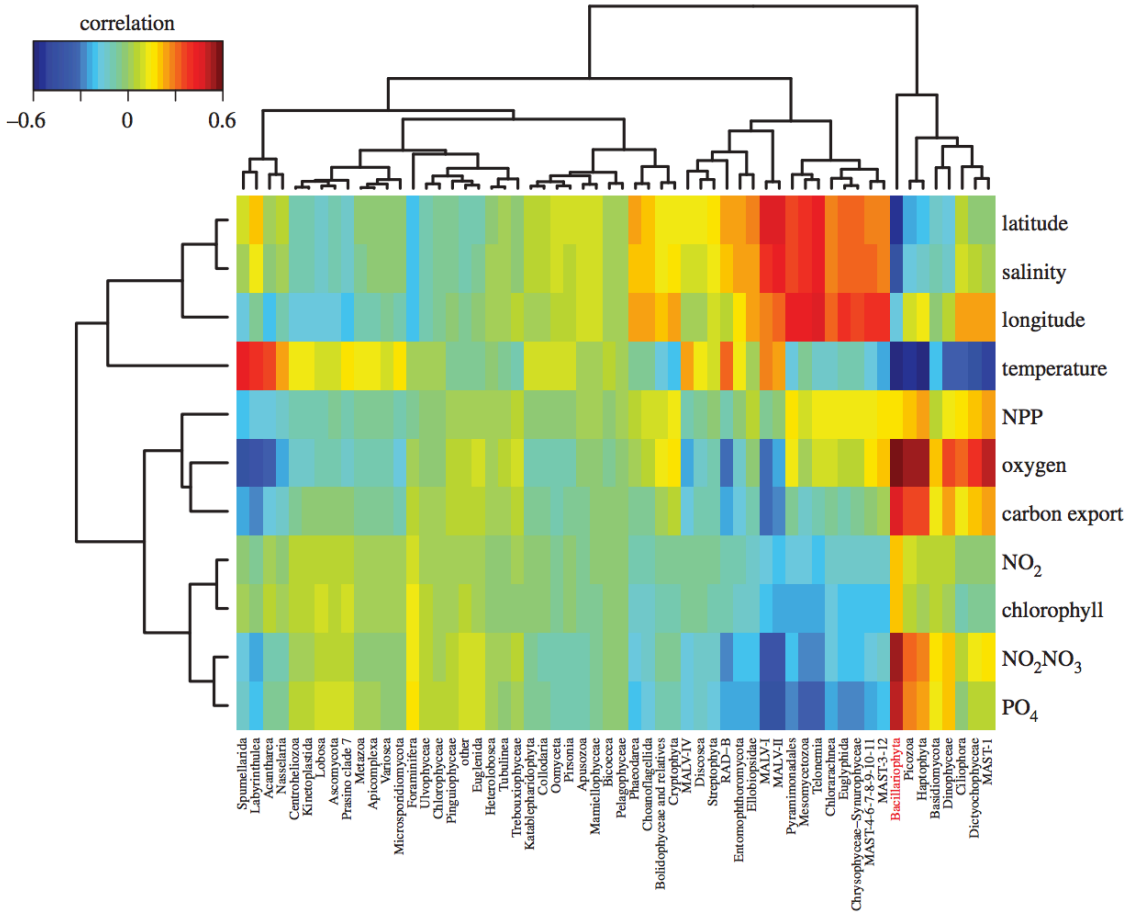

Figure 10. Regression-based modelling of high-throughput DNA sequence analysis of eukaryotic lineages and environmental parameters, using the TARA Oceans expedition global metabarcoding dataset. This figure also demonstrates the strong correlations between Bacillariophyta (including diatoms) and carbon export, nutrient availability, temperature, salinity and latitude (Benoiston et al., 2017).

Certain stages of the diatom life cycle may also contribute disproportionately to carbon export. For example, diatom resting spores, produced by some genera in response to a variety of environmental triggers, are more carbon-dense than their vegetative counterparts as a result of their increased density of carbohydrate and lipid storage compounds and their lack of a vacuole (Kuwata et al., 1993). Resting spores are also usually heavily silicified (French & Hargraves, 1980), making them relatively dissolution resistant. In the Southern Ocean, *Chaetoceros*

(Hyalochaete) and *Thalassiosira antarctica* resting spores were shown to contribute up to 60% of particulate organic carbon (POC) flux in naturally iron-fertilized waters near the Kerguelen plateau (Rembauville et al., 2014). Variability in the environmental triggers of resting spore/winter form production, as well as assemblage shifts in the contribution of species that produce these forms, could therefore have consequences for POC flux and the biological pump.

Species-specific variability in the volume of carbon per cell in both vegetative diatom cells and resting spores could also influence the magnitude of the biological pump. Cornet-Barthaux et al. (2007) demonstrated the variability in the amount of carbon per cell found in common modern Southern Ocean species using the carbon:volume equation (Eppley et al., 1970):

$$\log_{10}C\ (pg) = 0.76\ \log_{10}[\text{cell volume}\ (\mu m^3)] - 0.352 \qquad \text{(Equation 1)}$$

Their calculations show that carbon content per cell ranges from 10 pg in *Fragilariopsis pseudonana* to 3556 pg in *Thalassiothrix antarctica*. Changes in cell size can also affect sinking rates and, thus, the ability of diatoms to export carbon. For a given diatom concentration, species composition can greatly affect the amount of associated carbon that could be sequestered. For example, increased POC flux has been reported in association with a peak in *Thalassiothrix antarctica* abundance in sediment traps in the subantarctic zone of the Southern and the Si:C ratio (or frustule thickness/density), which differ between species and life cycle stage as well as with environmental context (Rigual-Hernandez et al., 2015). However, Equation 1 yields an almost linear relationship between cell size and volume that cannot account for variations in factors such as vacuole size.

Given that fluctuations in overall diatom productivity and inter-species variability have the potential to affect carbon drawdown, past changes in diatom populations, in particular in the Southern Ocean, could have played a role in past climate changes. The fossil record provides a key archive with which to investigate these associations. Many previous studies have linked changes in Southern Ocean diatom productivity to climatic variability during the Quaternary period, for example, iron fertilization causing increased siliceous productivity and CO_2 drawdown during glacial periods (Martin, 1990), or deposition of giant marine diatom (*Ethmodiscus rex*) mats in the Philippine Sea during the last glacial maximum being linked to CO_2 drawdown (Xiong et al., 2013). Some studies have also linked changes in diatom productivity to changes in climate through the Cenozoic. For example, an increase in siliceous productivity in

the Southern Ocean during the Late Eocene/Early Oligocene has been linked to increased CO_2 drawdown and climate cooling at the EOT (Egan et al., 2013) and peaks in global diatom abundance, for example during the Early Oligocene, the Oligocene/Miocene boundary and MMCT (Figure 11), have been associated with cooling periods through the Cenozoic (Renaudie, 2016).

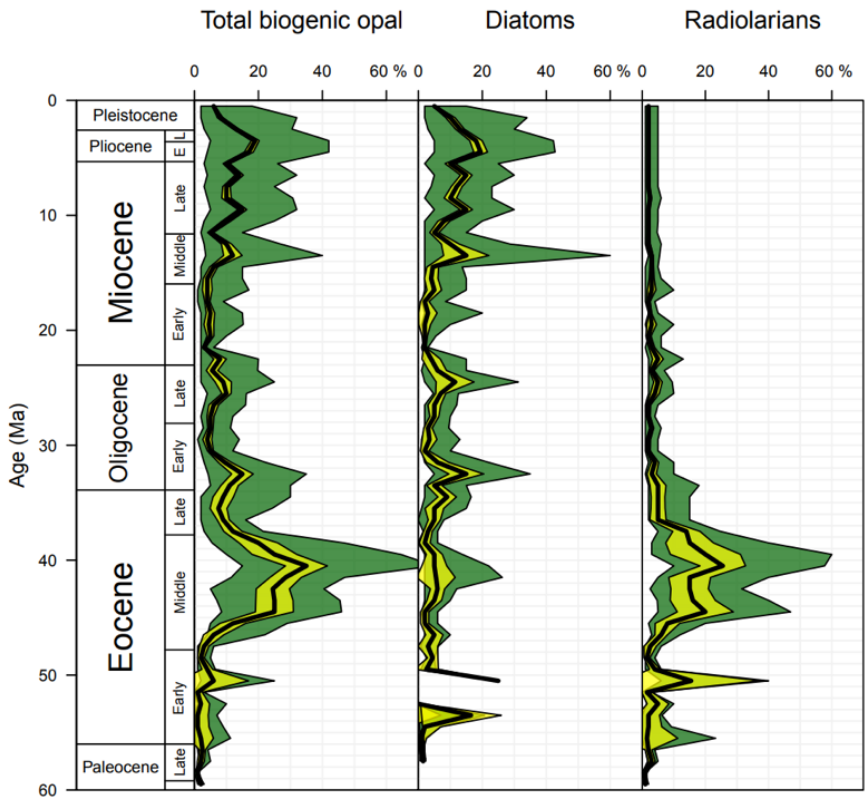

Figure 11. A history of biogenic opal deposition from a synthesis of global IODP/ODP/DSDP smear-slide and biochemical data. The black line represents the median value in each 1 Ma time bin, with the lime envelope denoting the 95% confidence interval and the dark green envelope indicating the interquartile range of the data (Renaudie, 2016).

In addition to changes in diatom concentrations, diatom diversity changes the Cenozoic provide further evidence of a link between diatoms and climate (Lazarus et al., 2014). Diatom diversity can act as a proxy for diatom productivity and, thus, an association between diatom diversity

and benthic foraminiferal $\delta^{18}O$ (Figure 12) is indicative of a role for diatom productivity in forcing, or at least amplifying, Cenozoic climate changes (Lazarus et al., 2014).

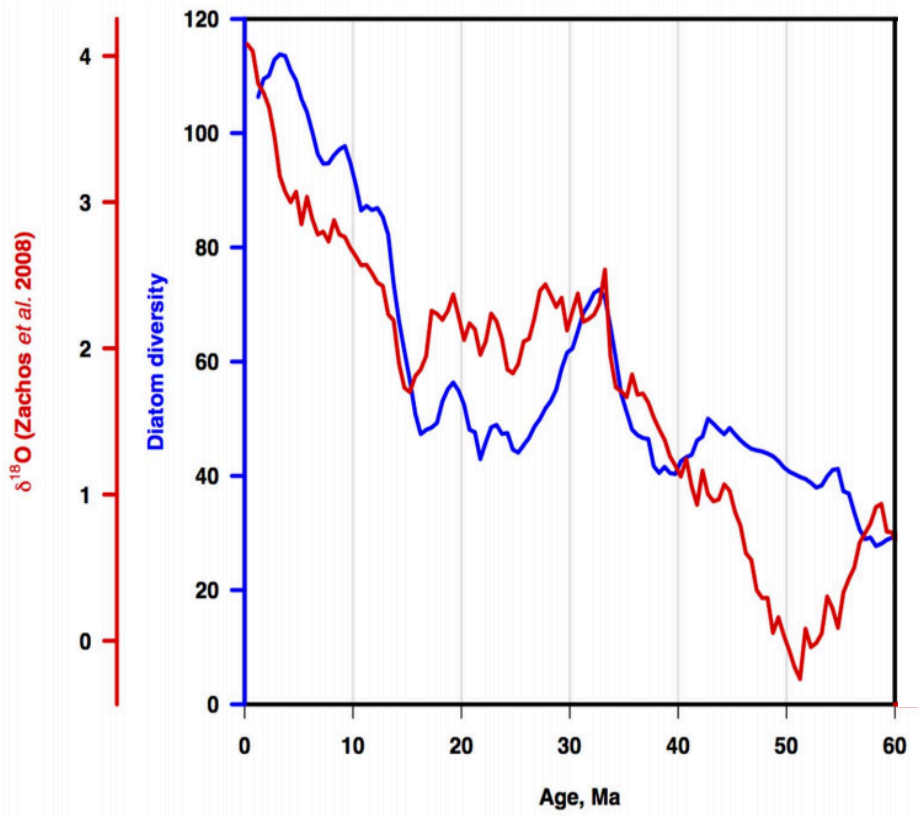

Figure 12. The relationship between diatom diversity and climate through the Cenozoic. Blue line represents three point moving average of diatom diversity; red line represents benthic foraminiferal $\delta^{18}O$ (Zachos et al., 2008) (Lazarus et al., 2014).

Finally, evolutionary turnover within Southern Ocean diatom populations also has been linked to Neogene cooling episodes (Crampton et al., 2016) (Figure 13). While Crampton et al. (2016) suggest diatom evolutionary turnover was largely driven by expansion of the sea ice zone, the fact that Miocene turnover pulses coincided with positive $\delta^{13}C$ excursions (Figure 13) indicates a possible role for the global carbon cycle and Southern Ocean diatoms in driving associated climatic cooling.

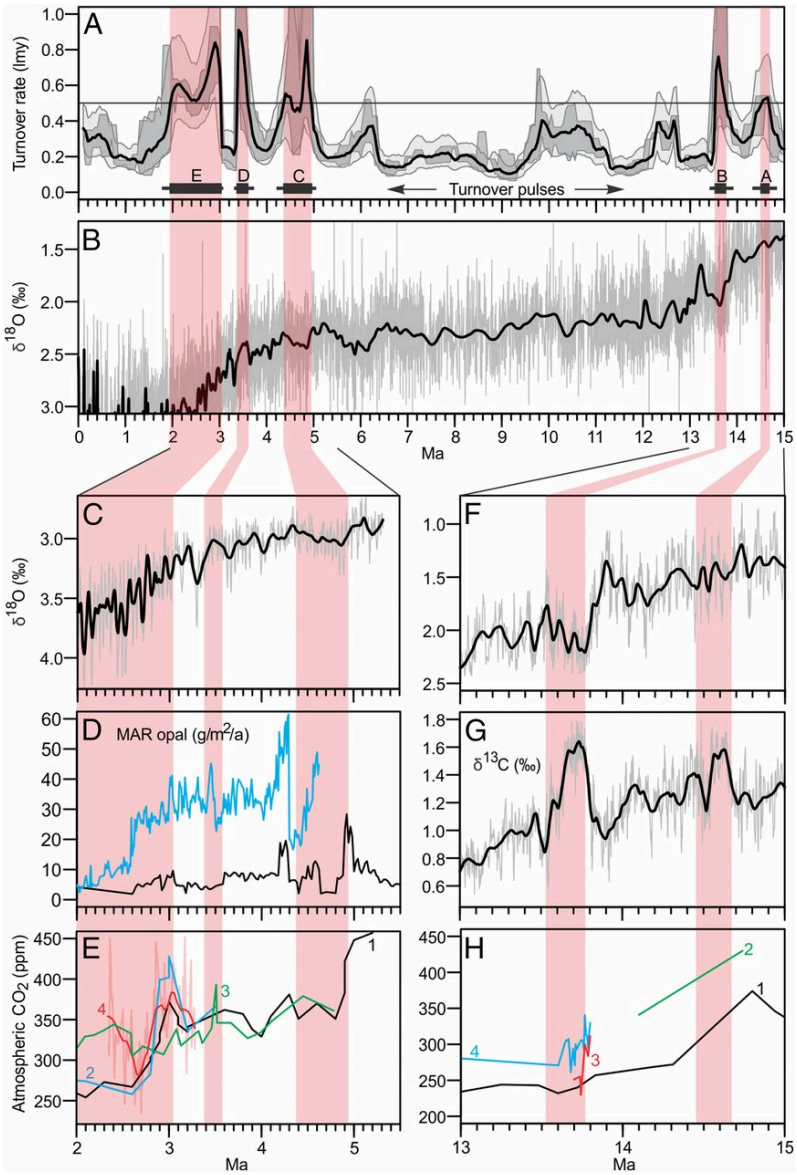

Figure 13. Pulses of Southern Ocean evolutionary turnover during the last 15 million years, calculated from first and last appearances using the CONOP model of Cody et al. (2008). A) Black line is the model ensemble and bootstrapped median; dark envelope is the non-bootstrapped model ensemble. Pink bars identify turnover pulses (labelled). B) Benthic $\delta^{18}O$ (Zachos et al., 2008) (black line represents loess smoothing of data). C) Benthic $\delta^{18}O$ curve, as for B. D) Opal accumulation rates from ODP Sites 1095 (black) and 1096 (blue) on the Antarctic Peninsula margin. E) Atmospheric CO_2 based on various proxy records; for full list of references see Seki et al. (2010). F-G) Benthic $\delta^{18}O$, as in B/C. H) Atmospheric CO_2 from (Foster et al., 2012; Zhang et al., 2013; Badger et al., 2013). Figure is from Crampton et al. (2016).

1.4. Neogene diatoms from the Southern Ocean – an under-exploited paleoceanographic archive

This chapter has outlined why studying the Neogene Southern Ocean is important, and how diatoms are both key archives of paleoceanographic data and potential drivers of climate change. A further reason for using diatoms to investigate Neogene Antarctic paleoclimatology is a practical one. Whilst traditional paleoceanographic studies have largely relied on proxy records using calcareous microfossil assemblages and geochemical analyses (Wefer, 2015), carbonate is poorly preserved in the modern Southern Ocean. This poor preservation has encouraged the development of alternative well-preserved proxies, e.g. using diatoms. Cortese et al. (2004) suggested that the Southern Ocean became a major sedimentary opal sink from around 2 Ma, however, biogenic opal increased substantially within Southern Ocean sediments from the Middle Miocene onwards (Figure 14; also addressed in Chapters 6 and 7), when diatoms took over from radiolarians as the dominant contributors to global sedimentary opal (Figure 11; Renaudie, 2016). If sedimentary abundance is linked to diatom productivity, Southern Ocean diatoms therefore may have played a more important role in the carbon cycle from the Middle Miocene onwards.

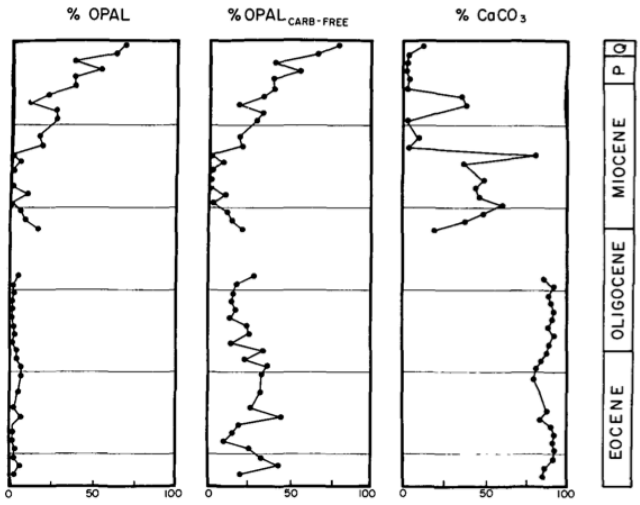

Figure 14. The combined biogenic silica and carbonate profiles of Southern Ocean DSDP Sites 266 and 277, showing the stepped decreases in carbonate content since the Oligocene and Middle Miocene, and the subsequent increase in biogenic opal (Brewster et al., 1980).

Numerous cores containing well-preserved Neogene diatom assemblages have been recovered from around Antarctica, however, these archives remain relatively unexploited from a paleoceanographic perspective. To date, studies of Cenozoic Southern Ocean diatoms have

largely focused on diatom biostratigraphy, because the well-preserved record of diatom evolution within Southern Ocean sediments can provide key chronological constraints (from DSDP/ODP/IODP expeditions: e.g., McCollum, 1975; Schrader, 1976; Gombos, 1976; Weaver and Gombos, 1981; Ciesielski, 1983; Gersonde, 1990; Gersonde and Burckle, 1990; Baldauf and Barron, 1991; Harwood and Maruyama, 1992; Censarek and Gersonde, 2002; Arney et al., 2003; Bohaty et al., 2003; Whitehead and Bohaty, 2003a; Farmer, 2011). Diatom records also exist from Antarctic drill cores (for example, McKelvey, 1981; Harwood, 1986; Harwood, 1989; Ishman and Reick, 1992; Winter and Harwood, 1997; Harwood et al., 1998; Scherer et al., 2000; Barrett et al., 2001; Harwood and Bohaty, 2001).

A few quantitative Southern Ocean diatom assemblage studies that focus on palaeoceanography, rather than biostratigraphy, exist that from the Pliocene (Sjunneskog & Winter, 2012; Winter et al., 2010; Taylor-Silva & Riesselmann, 2018). However, no fully quantitative Southern Ocean diatom assemblage records have yet been published for the Miocene, and no Neogene diatom silica isotope studies have been published from the Southern Ocean. Part of the reason for this limited exploitation of diatom records is a poor understanding of the palaeoecologies of extinct diatom palaeofloras and uncertainties in the reliability of diatom silica isotope proxies far back in time. However, careful analysis of paleo-biogeographical appearances, links to existing species and the comparison of abundances between sites (explored in Chapter 4.2) can facilitate interpretations of extinct assemblages, as has been possible for other microfossil groups (for example, Majewski, 2002; Jones et al., 2008). A robust assessment of oxygen isotopes preserved in biogenic silica (explored in Chapter 4.5) can also test the application of biogeochemical diatom proxies to Neogene environmental questions. The production of new Southern Ocean diatom assemblage and biogeochemical records for the last 15 million years therefore offers the potential to address key questions about Southern Ocean productivity, oceanography and climate during Neogene episodes of environmental change.

1.5. What are the big questions?

This thesis will address the following scientific questions:

1. How did the Southern Ocean and Antarctic Ice Sheets vary through the Neogene? Is there evidence of substantial warmth and/or retreat?
2. What role did the Southern Ocean play in forcing changes in the Antarctic ice sheets through the Neogene?
3. How was the Southern Ocean affected by changes in Antarctic ice sheet volume?

4. Did diatoms play a role in carbon drawdown during key episodes of Neogene climate change?
5. How can diatom proxies be exploited to answer key questions in Neogene paleoceanography?

Numbered questions are referred to in Section 1.6, below.

1.6. Outline of the thesis

The materials used, including the physical and oceanographic position of sites, are presented in Chapter 2. Following this, analytical methods are presented in Chapter 3, with the results and discussion presented in Chapters 4-8. Chapter 4 provides the chronology of the sites used in this thesis (ODP Sites 747, 744, 1165, 1138 and 1171), including presenting several new diatom biostratigraphic constraints. Chapter 5 reviews the paleoecological associations of diatom species encountered in the research, presenting diatom plates and three new diatom species (addressing question 5). Chapter 6 presents the first quantitative diatom assemblage records across the Middle Miocene Climate Transition (12-15 Ma) from a latitudinal transect of three Southern Ocean ODP Sites (Sites 747, 744 and 1165), as well as a new record of ice-rafted debris at Site 1165. The new records are compared with the high-resolution Southern Ocean sea surface temperature record available from ODP Site 1171, and interpreted to determine implications for Southern Ocean paleoceanography, Antarctic paleoclimatology and diatom productivity during this key episode of Neogene cooling (addressing questions 1-4). Chapter 7 presents a diatom assemblage and silicofossil concentration record from ODP Site 1165 between 15 Ma-present. This record is presented together with an unpublished record of diatom concentration and *Thalassiothrix/ Trichotoxon* spp. abundance over the same interval from ODP Site 1138 (data provided by A. Biddle, 2014). This chapter will address Southern Ocean paleoceanography and the development of the Antarctic Circumpolar Current through the Neogene in the context of additional published diatom and opal records from other Southern Ocean sites (addressing questions 1-4). Finally, Chapter 8 presents the first Pliocene (3.34-3.75 Ma) record of stable oxygen isotopes from Southern Ocean diatom silica, including a geochemical assessment of the validity of the proxy for use in Neogene sediments (addressing questions 1, 2 and 5). A summary and conclusions are presented in Chapter 9.

2. Materials, geographic and oceanographic settings

This chapter outlines the reasons for selecting the three primary sites investigated in this thesis, and describes the sites and their physical and oceanographic setting. Contextual information for unpublished and published data from additional sites presented and considered in this thesis are presented in the relevant chapters (Chapters 7 and 8).

2.1. Site selection

Three primary sites were selected for investigation in this thesis: ODP Sites 747 (54°S), 744 (61°S) and 1165 (64°S), which form an approximate latitudinal transect through the high latitude Southern Ocean. The modern Southern Ocean is strongly latitudinally differentiated by, for example, sea surface temperature, salinity and mixed-layer depth (Saleè et al., 2010), and as such the transect provides an opportunity to assess latitudinal palaeoceanographic variation. The transect also provides an opportunity to assess diatom assemblage changes associated with these latitudinal variations, for example, to determine cold-associated species that are presumably more abundant at the southerly and, therefore, cooler Site 1165 than at the northerly, presumably warmer, Site 747.

Hiatuses are a common problem when selecting sites for Neogene palaeoceanographic reconstructions at both continental shelf and deep-sea locations. ODP Site 1165 was chosen because it offers the most ice-proximal, complete Antarctic sediment sequence spanning the last 15 million years. It also contains relatively abundant diatoms throughout, and a robust paleomagnetostratigraphic record from the Late Miocene to present interval (Shipboard Science Party, 2001). ODP Site 747 comprises particularly well-preserved and abundant carbonate for such a southerly site and has, therefore, become a reference site for high latitude Neogene paleoceanography. As such, high resolution isotope records and a good age model, including robust paleomagnetostratigraphy, already exist for the Miocene interval at Site 747 (Majewski & Bohaty, 2010). ODP Site 744, situated between Sites 1165 and 747, contains well-preserved diatoms and has a relatively well-constrained age model (Florindo et al., 2013).

2.2. Geographic setting

ODP Sites 747, 744 and 1165 are located on or between the Kerguelen Plateau and the coast of Prydz Bay in East Antarctica. The Kerguelen Plateau is a large igneous province situated on the Antarctic Plate in the Southern Indian Ocean, spanning approximately 45-62°S and

standing c. 2 km above the surrounding ocean floor. The Kerguelen Plateau formed due to volcanism caused by the Kerguelen hotspot, which has produced magmatic lava since at least 130 Ma. Today, the plateau breaks sea level only at the Northern Plateau to form the Kergeulen Islands and the Heard and McDonald Islands, which still experience volcanic activity. ODP Site 747 was drilled on the central Kerguelen Plateau, and ODP Site 744 is located on the Southern Kerguelen Plateau. The geographical location of Sites 747, 744 and ODP 1165 with respect to Antarctica has not changed significantly since the early Miocene (Lawver et al., 1992).

ODP Site 1165 is situated on the continental rise of Prydz Bay. Today, the Lambert Glacier drains around 16% of Antarctic freshwater and 20% of the East Antarctic Ice Sheet (EAIS) (Florindo et al., 2013) into Prydz Bay and extends out into the Southern Ocean as the Amery Ice Shelf; the third largest in Antarctica and the largest single ice stream extending from the EAIS interior into the Southern Ocean (Florindo et al., 2013). The catchment area of the Lambert Glacier includes the Gamburtsev Mountains, a likely initial nucleation site for the early EAIS (Bo et al., 2009; O'Brien & Leitchenkov, 2009). Prydz Bay is a re-entrant in the East Antarctic margin, overlying a rift structure, active since the Cretaceous, that extends over 500 km into the continental interior (O'Brien & Leitchenkov, 2009).

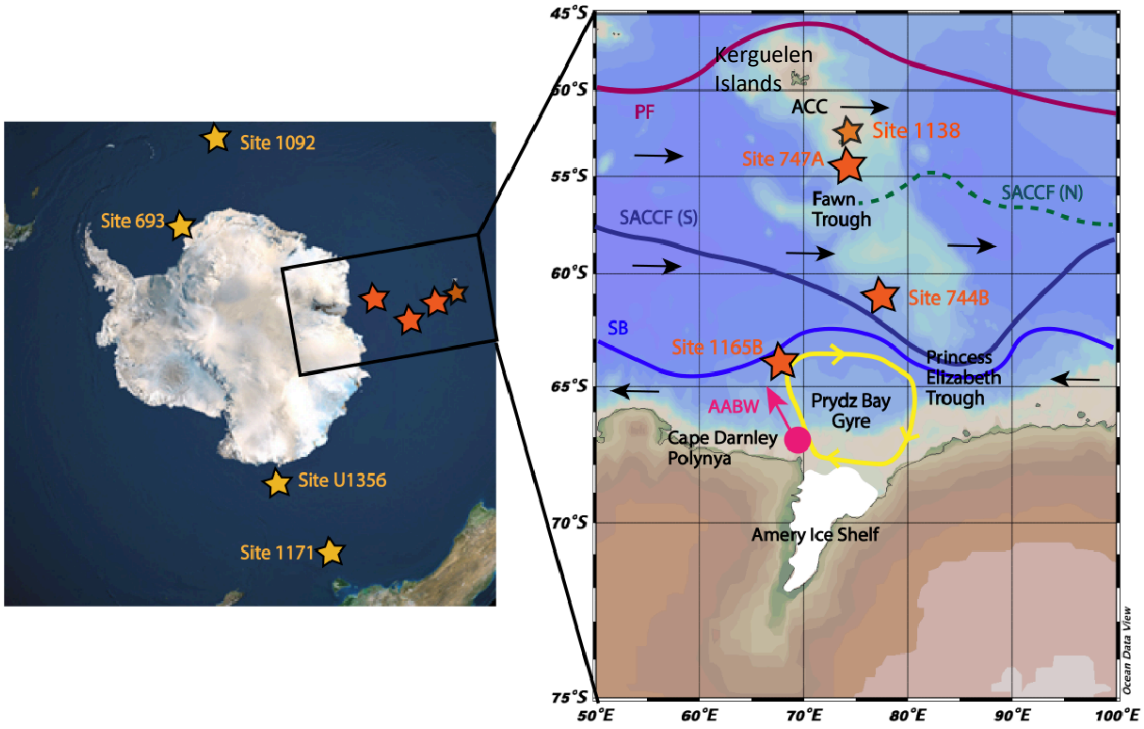

Figure 1. Map showing the location of the primary sites investigated in this thesis (ODP Sites 1165, 744 and 747), as well as other ODP and IODP Sites mentioned in the text. Bathymetry is included in the panel to the right, outlining the raised Kerguelen Plateau upon which Sites 747 and 744 were drilled.

Seismic data and drilling at ODP Sites 1166, 740 and 741 on the Prydz Bay continental shelf penetrated pre-glacial sediments which revealed Late Eocene fluvial to fluvial-deltaic sediments containing palynormophs indicative of coniferous woodland and a cool, humid climate (O'Brien & Leitchenkov, 2009). Sand-grain surface textures have also been linked to glacial erosion and breakage, suggesting the presence of valley glaciers (Cooper & O'Brien, 2004). Into the Oligocene and Early Miocene, Prydz Bay strata consist mostly of subglacial and glacimarine diamicts as well as interbedded diatomaceous units deposited during warmer periods (Hambrey et al., 1991; O'Brien & Leitchenkov, 2009). Seismic and drillcore evidence suggests repeated glaciation in Prydz Bay during the Oligocene and Miocene, with a likely wet-based ice sheet probably extending out to the shelf edge and supplying large volumes of eroded material since the Early Oligocene (O'Brien & Leitchenkov, 2009).

2.3. Oceanographic setting

Modern Southern Ocean circulation, particularly between latitudes of c. 40-60°S, is dominated by the Antarctic Circumpolar Current (ACC). The ACC is the world's only truly circumpolar current, circulating in an eastward direction around the Antarctic continent forced predominantly by Southern Hemisphere westerlies, Ekman transport and surface buoyancy (Wolfe & Cessi, 2011). This wind-stress is counterbalanced by bathymetry via bottom force stress (Rintoul & da Silva, 2019), while eastward ACC flow is balanced to the south by westward circulation of the Antarctic Coastal Current (ACoC). Ekman transport and wind stress also force Southern Ocean meridional overturning circulation, whereby deep waters upwell to the surface and interact with the atmosphere, exchanging both carbon and heat before either returning northward as intermediate or surface waters (Tamsitt et al., 2017) or flowing southwards where they cool and interact with sea ice to become Antarctic Bottom Water (see discussion in Chapter 1, Section 1.2.2). Thus, the ACC is a key feature of Southern Ocean circulation and global climate, playing an important role in regulating both the carbon cycle and heat transfer to the Antarctic Ice Cap.

The ACC extends 2-4 km below the ocean surface, and can be as wide as 2000 km (Smith et al., 2013). It is the world's strongest and most voluminous ocean current, transporting 137±8

x 10^6 m^3 s^{-1} of water through Drake Passage (Rintoul & da Silva, 2019). However, the bulk of ACC transport occurs within a few fast-moving jets, usually associated with deep reaching hydrographic fronts at water mass boundaries (Figure 2). These fronts tend to be around 85 km wide (Shao et al., 2015), and are often associated with higher biological productivity than surrounding regions due to the associated upwelling of nutrient-rich waters (Ward et al., 2002). Frontal systems create circumpolar gradients in temperature and salinity, which also forces a largely circumpolar latitudinal biological species distribution (Malinverno et al., 2016). Between the jets, flow speeds and volumetric transport are substantially reduced (Figure 2).

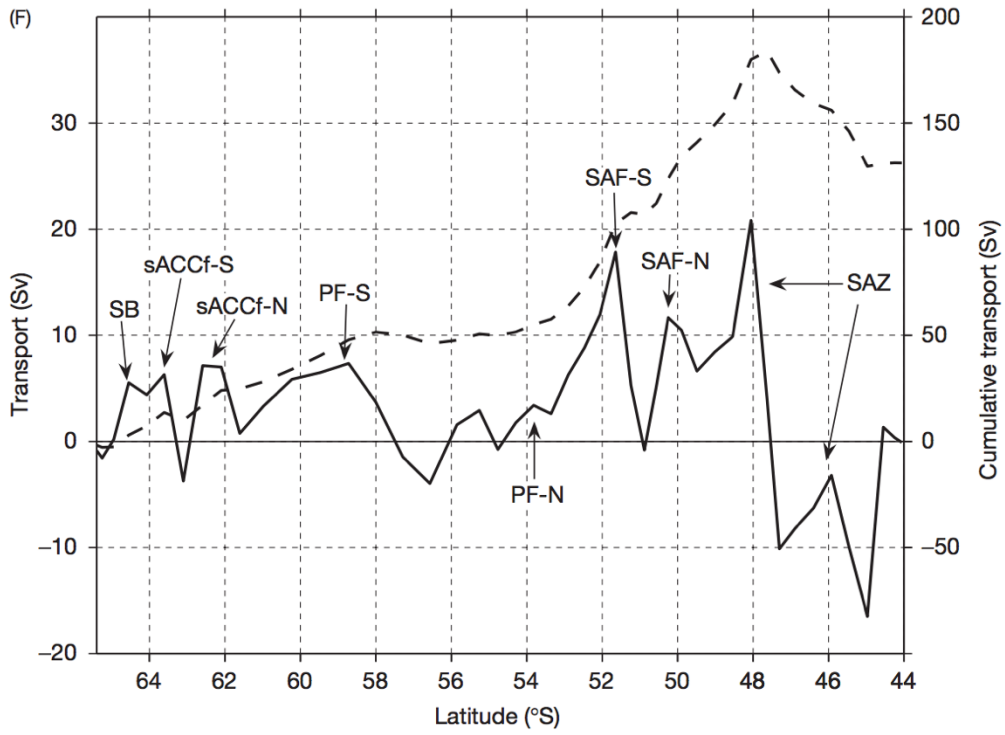

Figure 2. Cumulative Southern Ocean transport rates across a north-south transect at c. 140°E, approximately south of Australia. SB=Southern Boundary, sACCf-S= Southern Antarctic Circumpolar Front-southern branch, sACCf-N= Southern Antarctic Circumpolar Current- northern branch, PF-S=southern branch of the Polar Front, PF-N=northern branch of the Polar Front, SAF-S=southern branch of the Sub Antarctic Front, SAF-N=northern branch of the Sub Antarctic Front, SAZ=Sub Antarctic Zone. Solid line is transport at each location, dashed line is cumulative transport from south to north (Rintoul & da Silva, 2019).

Up to ten distinct oceanic frontal systems can be recognized in the Southern Ocean (Sokolov & Rintoul, 2007), but the four major fronts associated with the ACC are the Subantarctic

Front (SAF), the Polar Front (PF), the Southern ACC Front (SACCF) and the Southern Boundary (SB) (Orsi et al., 1995). The SAF defines the northern boundary of the ACC and acts as the boundary between upwelling Upper Circumpolar Deep Water (UCDW) to the south and downwelling Antarctic Intermediate Water (AAIW) to the north (Figure 3). South of the SAF, fresher and colder Antarctic surface waters are forced beneath relatively warm, salty subantarctic waters at the PF. The PF has been defined in the modern Southern Ocean as the 2°C isotherm at 200 m below the ocean surface. Further south still, the SACCF is defined by the properties of upwelling UCDW. Definitions of the SACCF include the 1.8°C isotherm at >500 m depth and salinities of 34.73 psu at >800 m depth (Orsi et al., 1995). The Southern Boundary denotes the southern limit of upwelling UCDW (Figure 3).

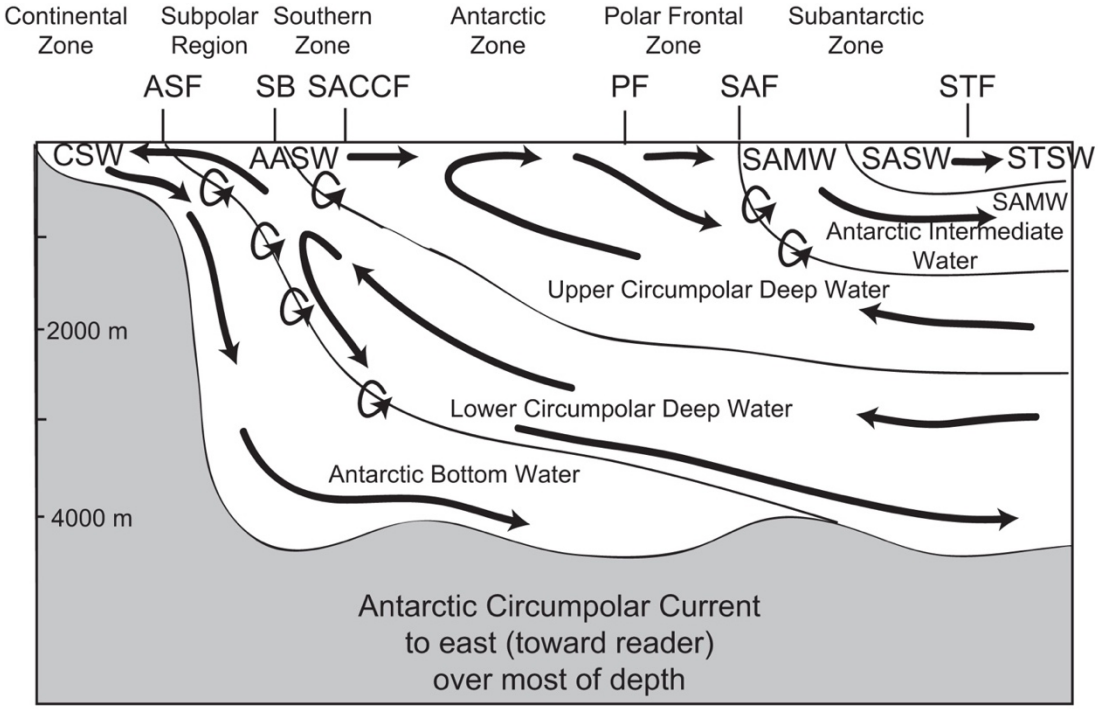

Figure 3. Schematic of Southern Ocean water masses, circulation, fronts and zones. Continental Shelf Water (CSW), Antarctic Surface Water (AASW), Subantarctic Mode Water (SAMW), Subantarctic Surface Water (SASW), Subtropical Surface Water (STSW), Antarctic Slope Front (ASF), Southern Boundary (SB), Southern ACC Front (SACCF), Polar Front (PF), Subantarctic Front (SAF), and Subtropical Front (STF). Talley (2011).

Today, ODP Sites 747, 744 and 1165 are all situated south of the PF, which is steered north of the Kerguelen Plateau. Sites 747 and 744 are situated directly beneath the ACC (Figure 1), while Site 1165, situated beneath the Southern Boundary, is also influenced by

oceanographic conditions in Prydz Bay. Modern circulation in Prydz Bay is dominated by the Prydz Bay Gyre (Figure 1), which channels water clockwise past the Amery Ice Shelf. To the east of the Prydz Bay Gyre is the Cape Darnley polynya (Figure 1), recently recognised as one of the four most important locations of Antarctic Bottom Water (AABW) production (Williams et al., 2016). Today, Cape Darnley AABW is channeled north towards Site 1165 (Figure 1). However, bottom water formation in most of Prydz Bay is suppressed by the melting of, and associated freshwater release from, the Amery Ice Shelf (Williams et al., 2016), highlighting the sensitivity of ocean circulation to ice dynamics in the region.

In the modern Prydz Bay, upwelling UCDW is mostly kept away from the Amery Ice Sheet by the Antarctic Slope Front. However, UCDW does reach the coast in some areas, likely playing a role in melting the underside of the ice shelf and reducing sea ice formation in coastal polynyas (Guo et al., 2019). Generally, winter sea ice formation in the Prydz Bay/Kerguelen Plateau region during the satellite era has extended northwards to around 58°S, covering Sites 744 and 1165, with summer sea ice restricted to inner coastal regions (Jenna et al., 2018). During the last glacial maximum, c. 20 ka, the winter sea ice edge is thought to have migrated northwards to around 48°S, covering all three sites investigated in this thesis (Gersonde et al. 2005).

2.4. ODP Site 747

ODP Site 747 (54°48.68'S, 76°47.64'E; 1698 mbsl) was drilled on the central Kerguelen Plateau during ODP Leg 120 (Schlich, Wise et al., 1989). Core recovery was close to 100% for ODP Hole 747A, on which this study focuses (Shipboard Science Party, 1989). The interval examined (79.89-62.03 mbsf; 14.90-12.27 Ma – see Chapter 4.2 for age model) primarily consists of nannofossil chalk with minor foraminiferal and biogenic opal components (Figure 4), suggesting that relatively oligotrophic and warm (>3°C) surface water conditions prevailed above the core site (Burckle et al., 1996; Diekmann et al., 2003). Nannofossil assemblages are low diversity and dominated by the cool water species *Coccolithus pelagicus* and *Reticulofenestra* spp. (Beaufort & Aubry, 1992). IRD was not observed in the study interval, however, due to its location downwind of several volcanic islands, sediments at Site 747 do contain discrete ash layers and volcanic shards dispersed throughout the sediment (Shipboard Science Party, 1989; Abrajevitch, 2014). Chemical analyses of volcanic ash at Site 747 suggest this mostly comes from the Kergeulen Islands, with minor components from the Heard Islands, Crozet Islands and South Sandwich Island Arc (Morche et al., 1992).

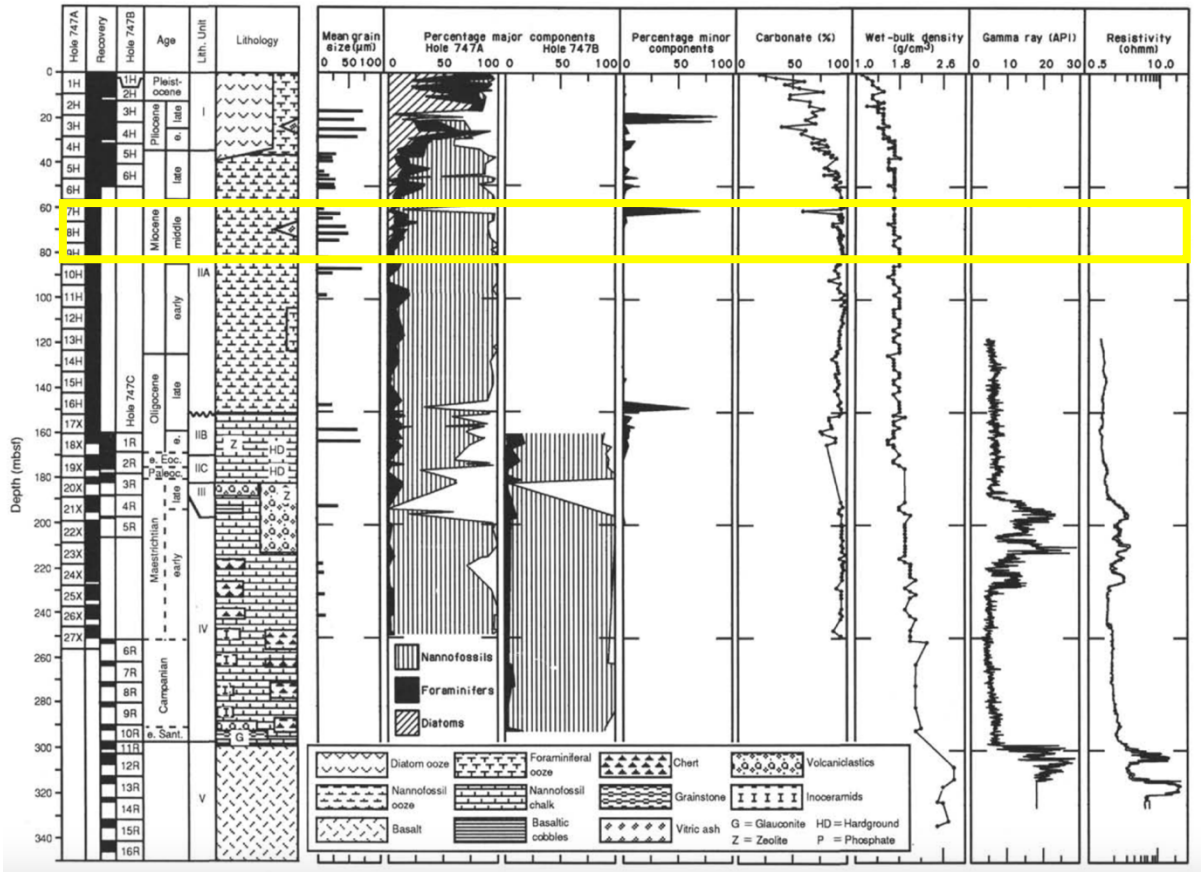

Figure 4. A summary log for ODP Site 747 (Figure from Schlich, Wise et al., 1989). The study interval at Hole 747A is indicated by the yellow box.

Site 747 lies beneath the flow path of the modern ACC and is therefore bathed in Circumpolar Deep Water. The proximity of the site to the northern boundary of the modern ACC (approximately 500 km north of the core site, Figure 1) makes it sensitive to climatically-induced fluctuations in the position of the ACC. However, the ACC flow path in the region is steered by the bathymetry of the Kerguelen Plateau and the Fawn Trough in particular (Figure 1), which lies directly south of Site 747. Today, up to one third of modern ACC transport flows through the Fawn Trough (Vivier et al., 2015), representing the northern branch of the SACCF (SACCF-N).

2.5. ODP Site 744

ODP Site 744 was drilled on the Southern Kerguelen Plateau (61°34.66'S, 80°35.46'E; 2300 mbsl) (Figure 1) during ODP Leg 119 (Barron, Larsen et al. 1989) with core recovery of 101.6% for ODP Hole 744B (Shipboard Science Party, 1989). Sediments in Hole 744B primarily consist of nannofossil chalk with minor foraminiferal components and a slightly higher opal content

than at ODP Site 747 (Figure 5). Carbonate content within the study interval (50.02-68.08 mcd; 14.89-12.10 Ma; see Chapter 4.3. for age model) remains mostly around 80%, but falls to approximately 20% in a few discreet intervals, most notably at c. 59 and 65 mbsf, when

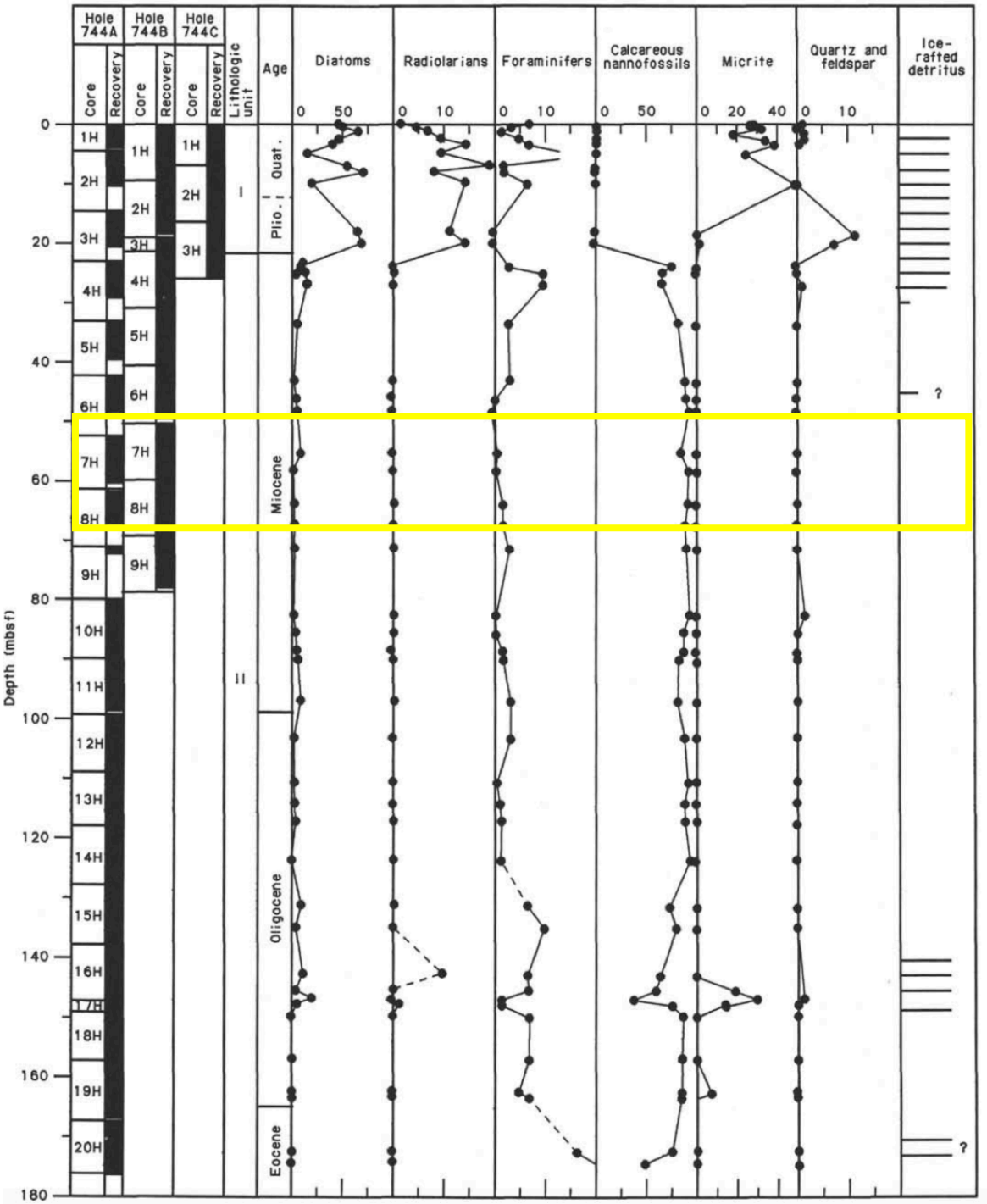

Figure 5. Summary log for Site 744 (Figure from Barron, Larsen et al., 1989). The study interval within Hole 744B is indicated by the yellow box.

siliceous microfossils increase in relative abundance (Dorn, 1991). Diatoms are the dominant siliceous microfossil in Hole 744B, but radiolarians, sponge spicules and silicoflagellates are also present (Figure 5).

Like Site 747, Site 744 lies beneath the flow path of the modern ACC and is bathed in Circumpolar Deep Water. However, Site 744 is situated closer to the Antarctic continent and lies just north of the southern branch of the modern SACCF (SACCF-S) and southern boundary (SB) (Figure 1). The SACCF-S is steered southwards through the Princess Elizabeth Trough by the Kerguelen Plateau, which restricts latitudinal drift of the ACC; to the east of the plateau, the ACC can migrate up to 7 degrees of latitude in response to climatic shifts (e.g. changes in the westerlies) (Florindo et al., 2013). The restricted flow path to the south of the plateau can also increase current speeds, with modern flow speeds of up to 39.5 cm s^{-1} detected at the base of the Princess Elizabeth Trough (Heywood et al., 1999). This flow speed is considered above the threshold for the erosion of non-cohesive sediments, and may well be responsible for sedimentary hiatuses in the region (Florindo et al., 2013).

2.6. ODP Site 1165

ODP Site 1165 was drilled on Wild Drift on the continental rise offshore of Prydz Bay (64°22.78'S, 67°13.14'E; 3525 mbsl) (Figure 1) during ODP Leg 188 (O'Brien, Cooper & Richter et al., 2001). Close to 1 km of contourite sediments were recovered, comprising a relatively complete Neogene sequence (Shipboard Science Party, 2001) with overall core recovery around 70% (Cooper & O'Brien, 2004). ODP Hole 1165B sediments, on which this study is based, comprise a mixed hemipelagic-pelagic deposit (Shipboard Science Party, 2001). As such, sediments at Site 1165 differ in character substantially from sediments at ODP Sites 747 and 744, with carbonate microfossils present only in a few discreet intervals (Shipboard Science Party, 2001). This suggests that Site 1165 was either mostly positioned below the carbonate compensation depth (CCD) during the Neogene, or that nutrient/ temperature conditions in the surface waters were not favorable to the growth or preservation of calcareous plankton. Siliceous microfossils are generally abundant and well-preserved within the study interval in Hole 1165B (332.80-0 mbsf; 15.06-0.01 Ma; see Chapter 4.4. for age model) (Figure 6).

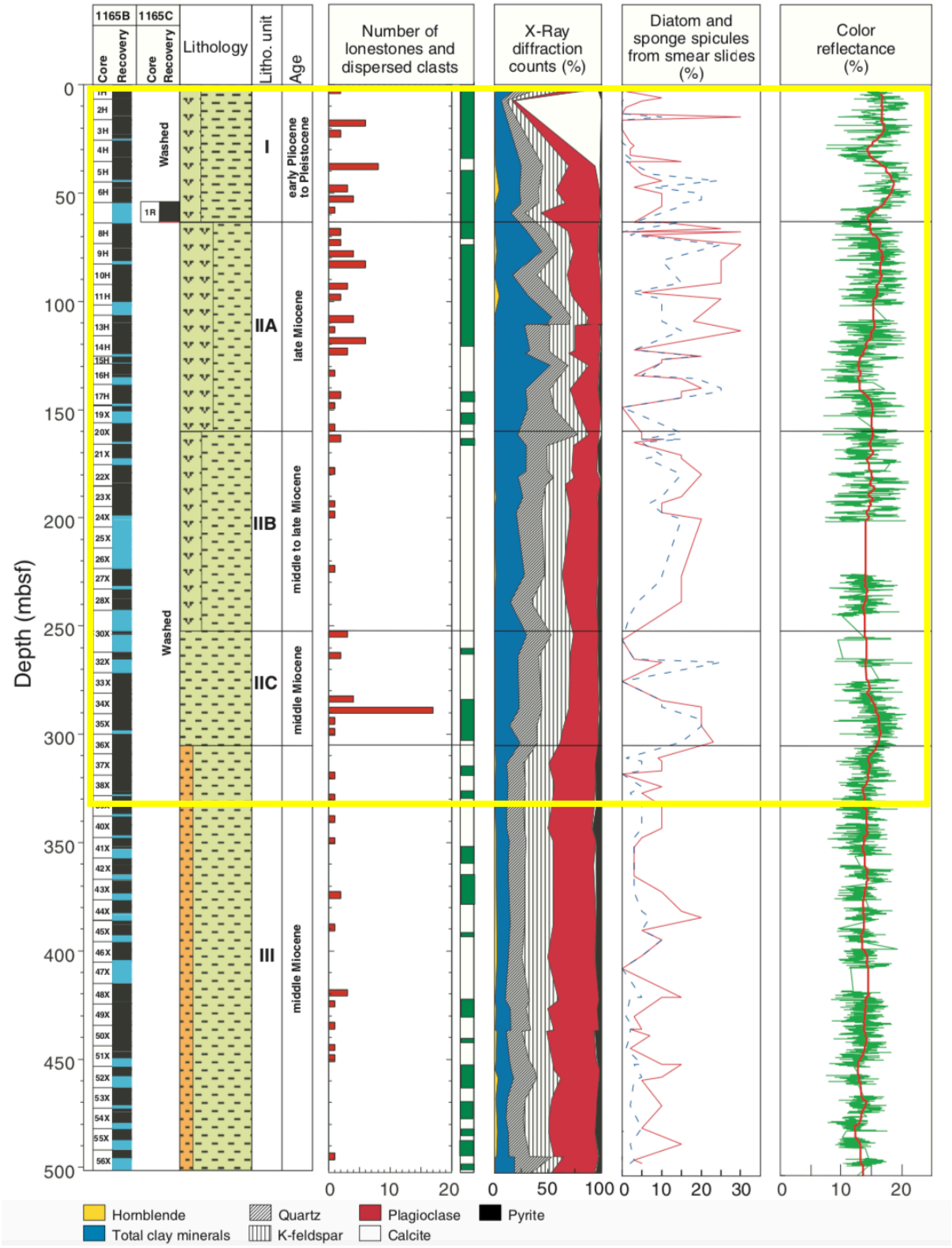

Figure 6. Summary log for Site 1165 (Figure from O'Brien, Cooper & Richter et al., 2001). The study interval (at Hole 1165B) is indicated by the yellow box.

Site 1165 is the most ice-proximal of the transect, located south of the ACC and SACCF and within 500 km of the Prydz Bay coastline (Figure 1). In the modern ocean, Site 1165 is bathed in downwelling AABW. However, it is also situated almost directly beneath the SB (or Antarctic Divergence), which acts as a series of cyclonic gyre systems forced by eastward circulation of the ACC to the north and westward circulation of the Polar Current to the south. Thus, Site 1165 was likely influenced by oceanographic conditions within both the ACC and the Antarctic coastal regime through the Neogene (Shipboard Scientific Party, 2001).

3. Methods

The sediments from cores ODP Site 747, 744 and 1165, analysed in this thesis, were requested from, and sampled by, staff at the Kochi Core Centre, Japan, and Gulf Coast Repository, USA (www.iodp.org/resources/core-repositories).

At ODP Site 747, 55 samples were processed and counted for diatom assemblages by Freya Mitchison at Cardiff University. Neogene diatom taxonomic and biostratigraphic training was provided to Freya Mitchison by David Harwood at the University of Nebraska-Lincoln, USA. Additional diatom assemblage counts at Site 747 were performed by Ben Skinner, who prepared and counted 40 samples as part of his MSc. project, supervised by Freya Mitchison, using the same method described in this chapter. Further, 25 diatom assemblage data points at Site 747 were provided by Steve Bohaty (University of Southampton, UK; unpublished data, 2014). All of the diatom assemblage counts at Site 747 were integrated and no obvious disparity in identified species was observed between observers. See Appendix 4 for full details of who counted each sample at site 747.

At ODP Site 744, 81 samples were processed and counted by Freya Mitchison for diatom assemblage analysis. In addition, 75 samples at Site 744 from the same interval were processed for isotope analysis by Freya Mitchison, with the isotope analysis itself conducted by Alexandra Nederbragt at Cardiff University, UK.

At ODP Site 1165, 188 samples were processed for diatom and silicofossil analysis by Freya Mitchison between 332.80 and 0.2 mbsf. In addition, Jonatan Isaksson prepared and counted 29 samples for diatom assemblages at Site 1165 between 291.45 and 278.35 mbsf as part of his CUROP project, supervised by Freya Mitchison, using the same methods described in this chapter. Appendix 4 contains details of who counted each sample; like at Site 747, no obvious disparity was identified between counters, including within two samples that were counted by both Freya Mitchison and Jonatan Isaksson as a comparison. 101 samples between 332.80 and 197 mbsf at Site 1165 were also prepared for sedimentary IRD analysis by Freya Mitchison and Laura Hunt, who was on work experience, at Cardiff University.

46 samples from Site 1165 and five samples from Site 744 were prepared for stable oxygen isotope analysis of diatom silica ($\delta^{18}O_{diatom}$) by Freya Mitchison and George Swann at the University of Nottingham, UK, with cleaned and purified silica samples sent to the NERC Stable

Isotope Facility at the British Geological Survey, UK, for $\delta^{18}O_{diatom}$ analysis (www.bgs.ac.uk/sciencefacilities/laboratories/geochemistry/sif/home.html). $\delta^{18}O_{diatom}$ analysis was funded by an Antarctic Science Bursary, awarded to Freya Mitchison (www.antarcticsciencebursary.org.uk/).

3.1. Quantitative diatom assemblage analysis

3.1.1. Sample preparation

In total, 217 sediment samples from ODP Site 1165 (0-333 mbsf; 0.1-15.08 Ma; see Chapter 4.4 for age model), 81 samples from ODP Site 744 (68-50 mbsf; 12.10-14.88 Ma; see Chapter 4.3 for age model) and 120 samples from ODP Site 747 (62-80 mbsf; 12.27-14.90 Ma; see Chapter 4.2 for age model) were processed for quantitative diatom analysis. Processing followed an established method for the analysis of absolute diatom concentration, described in Scherer (1994).

In order to achieve a layer of diatoms on the microscope slide that was neither too sparse nor too dense, 0.07 g of dry sediment per sample was used at Site 744, around 0.08 g at Site 1165, and 0.2 g dry sediment was used at Site 747 due to a lower concentration of diatoms than at the other sites. Sediment samples were first dried overnight in an oven at 40°C. Between 0.07-0.2 g dry sample mass was weighed, using a Sartorius HR120 balance accurate to four decimal places. Samples were subsequently boiled in 50 ml beakers with ~25 ml of distilled water and sufficient 37% HCl (~5 ml) and 30% H_2O_2 (~5 ml) to remove the organic and carbonate fractions. Samples were boiled until the reactions stopped; generally around 4 hours. Finally, the beaker was topped up with Calgon (2 g sodium hexametaphostphate in 100 ml distilled H_2O) and left to react for an hour, then samples were held in an ultrasonic water bath for no more than 4 seconds to disaggregate the sediment.

To ensure an even, random distribution of diatoms across each coverslip, each diatom sample was poured into, and settled through, a 10 cm distilled water column in a large 1 litre beaker. Diatoms were settled onto glass coverslips placed on an upturned petri dish on the bottom of the 1 L beaker (Figure 1). The water in the beakers was drained out slowly, from beneath the petri dish, by opening the taps at the end of the tubing (aiming for no more than one drip every one to two seconds). Once fully dry, the cover slips were glued to glass microscope slides using Norland Optical Adhesive 061, which was set under a UV lamp for 30 minutes.

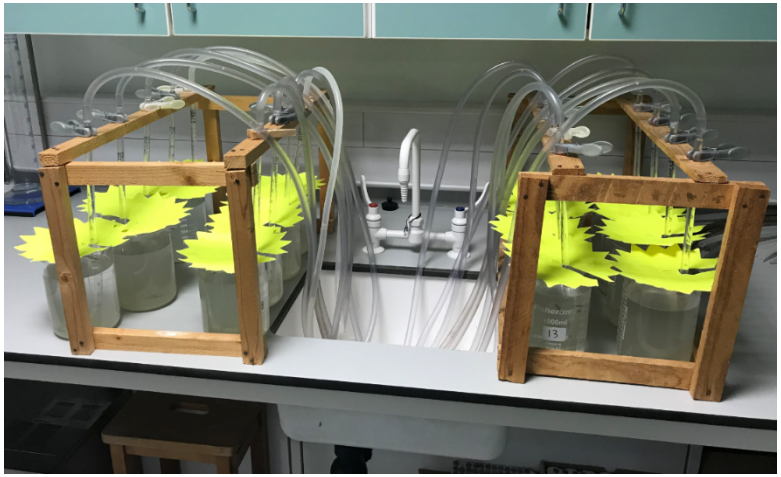

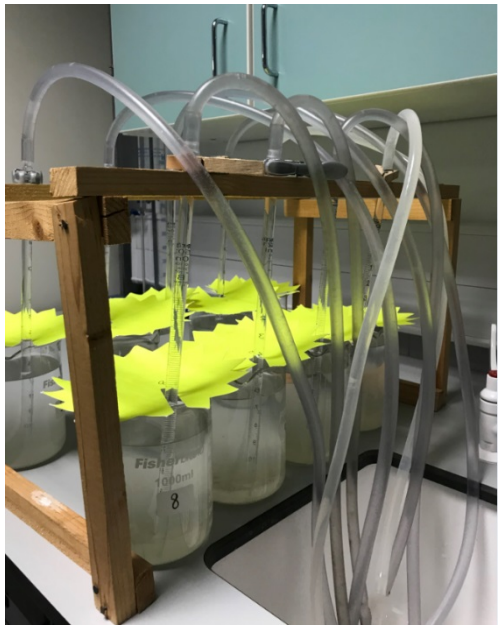

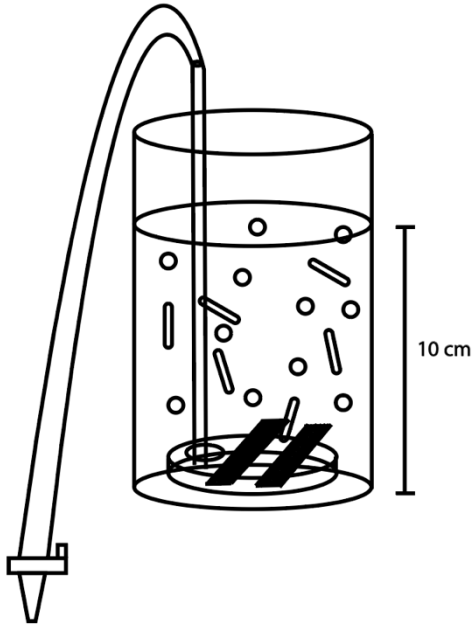

Figure 1. Settling beakers for diatom microscope slide preparation. Glass coverslips were laid on a petri dish beneath a 10 cm distilled water column. After chemical processing, diatoms were held in an ultrasonic bath for ~4 seconds to disaggregate and then poured into the beaker. Diatoms samples were left to settle for at least 5 hours. Following this, the taps on the end of the tubes were opened very slightly to allow the water to be siphoned out slowly (1 drop every 1-2 seconds). Once dry, cover slips were removed from the petri dishes and glued to microscope slides using Norland Optical Adhesive 061.

3.1.2. Diatom assemblage analysis

Individual diatoms were identified to species level, if possible, and counted at Cardiff University, UK, using a Leica DMR-X microscope with differential interference contrast at 1000x magnification. The quality of diatom preservation at each site varied, with assemblages typically more fragmented at ODP Site 1165 and more dissolved at ODP Site 747. For quantitative analysis, in most cases diatoms were counted only if more than half of the valve was present within the field of view (Figure 2). However, due to the particularly long, thin morphologies of certain species, that would not generally fit within one field of view, *Cavitatus miocenicus*, *Thalassionema* spp. (excluding *Thalassionema nitzschioides* var. *parva)*, *Thalassiothrix* spp. and *Trichotoxon* spp. were instead counted as 0.5 units for each pole present (Figure 2). In addition, any valves that were identifiable to species level but only encountered as fragments, including a pole, were recorded as 0.5 units (mostly only rare, finely silicified *Synedropsis* spp.). Although it is possible that this strategy resulted in an over-representation of taxa such as *Synedropsis* spp. and *Thalassiothrix* spp. relative to other rare species not identifiable by fragments alone, I considered this preferable to not recording the presence of *Synedropsis* spp. in a sample. Final valve counts for each sample were rounded up to whole numbers.

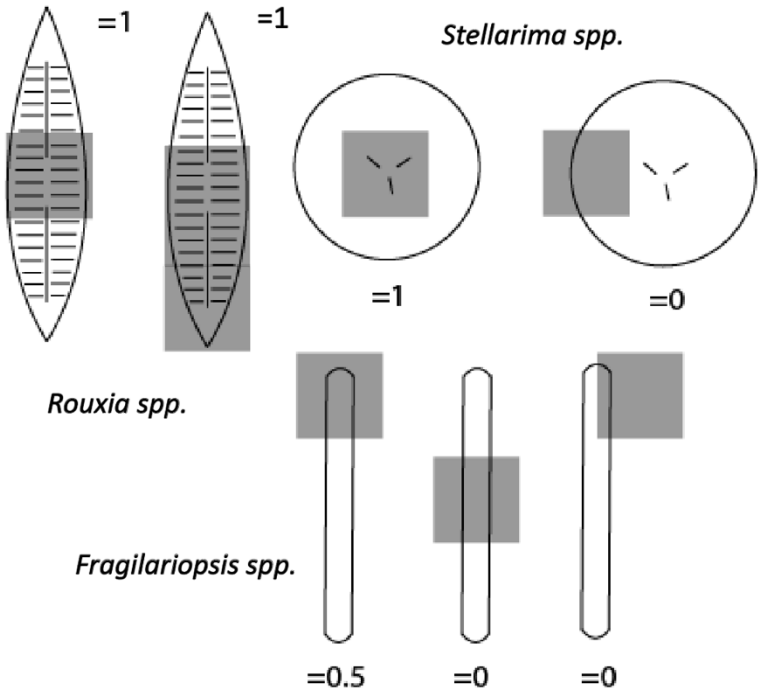

Figure 2. Schematic showing the diatom counting technique employed in this study, allowing for valve fragmentation. With centric diatoms e.g. *Stellarima microtrias*, if a recognizable center was present the valve was counted as one unit, even if the rest of the valve had dissolved/fragmented. For long, more finely silicified species such as *Rouxia spp.*, if over half of

the valve was present, it was counted as 0.5 units. This was also the case with more fragile, longer pennate species, e.g. *Thalassiothrix spp.*; if one end was present, the valve was counted as 0.5 units. All final counts were rounded to whole numbers.

For the Middle Miocene interval in Chapter 6, at least 500 diatoms were counted per sample. This number was chosen in order to capture the entire diatom diversity in each sample and was based on the result of rarefaction tests (Gotelli & Colwell, 2011) where 1500 diatom valves were counted in one sample (Figure 3).

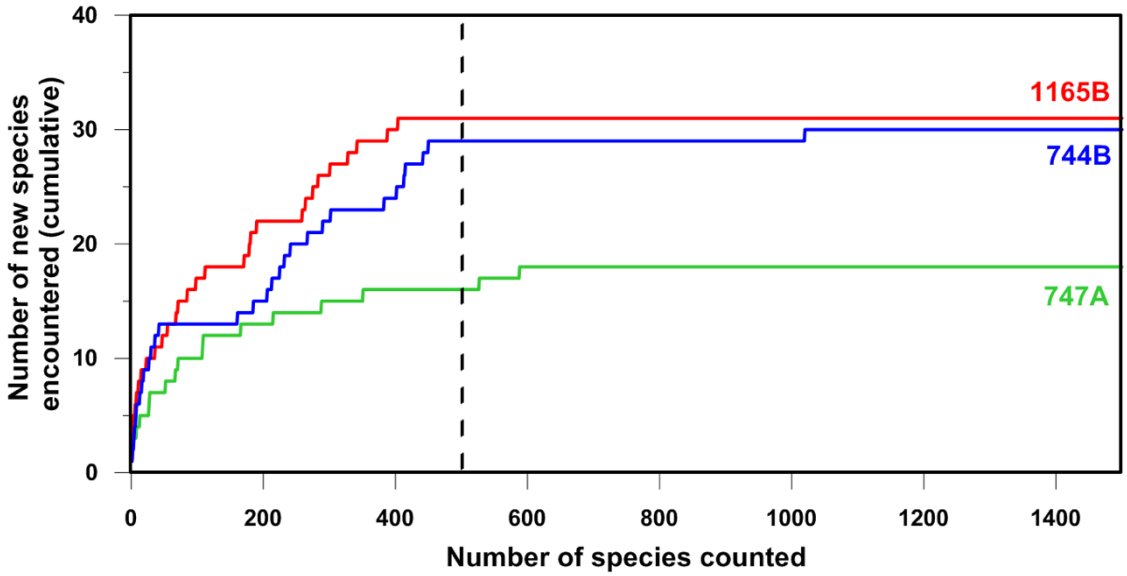

Figure 3. Rarefaction tests at ODP Sites 747 (red; sample 747A, 8H 1W 13 cm), 744 (blue; sample 744B 9H 2W 3 cm), and 1165 (green; sample 1165B 37X 3W 45 cm). Vertical dashed line indicates that diversity will be mostly captured by a 500 valve count.

A different strategy was employed for the lower resolution, whole Neogene record at ODP Site 1165 in Chapter 7. Diatom assemblages evolved significantly through the 12 million year interval, such that assemblages are almost entirely different in, for example, the Pleistocene versus the Late Miocene. Therefore, in order to accurately calculate a representative number of valves for the different assemblages in each sample, it would have been necessary to perform rarefaction tests for many different samples prior to counting. As such, 400 specimens per sample was chosen as a pragmatic compromise between the time available and capturing representative species diversity. However, in order to ensure no species was missed, two extra transects across each slide were scanned following the counting of each sample to find any species that were missed. In one sample (1165B-22X-3H, 45-46 cm), I encountered one

additional species (*Rhizosolenia hebetata*) in the subsequent two transects. In every other sample, no new species were encountered during these transects, confirming that 400 valves per sample were sufficient to assess the total diversity of the assemblages.

Diatom plates and a list of all species that I encountered during the analysis of ODP Sites 747, 744 and 1165, including taxonomic assignments and biostratigraphic ranges, can be found in Chapter 5 and Appendices 1 and 2. My study represents one of the first quantitative analyses of Miocene Southern Ocean diatom assemblages (as opposed to biostratigraphic analyses which tend to focus on biostratigraphically-useful species only), thus, I identified several new species which are described in Appendix 2.

3.1.3. Calculation of diatom concentration

Preparing microscope slides that have an even, random distribution of diatoms across each slide enables the calculation of quantitative diatom concentrations (Scherer 1994). Calculations are performed as follows:

$$\mathrm{T} = \frac{\mathrm{NB/AF}}{\mathrm{M}}$$

Equation 1

Where:

T = Total number of diatoms per gram of dry sediment (v/g); the concentration

N = Number of diatoms counted

B = Area of bottom of beaker (7854 mm^2)

A = Area of field of view (mm^2)

F = Number of fields of view to achieve N

M = Mass of sediment (g)

3.2. Ice-rafted debris at ODP Site 1165

101 sediment samples from ODP Site 1165 (333-197 mbsf; 11.2-15.08 Ma; see Chapter 5 for age model) were used to generate the record of ice rafted debris presented in Chapter 6. Pierce et al. (2017) documented a bimodal grain size distribution in Site 1165 sediments aged 14.4-13.5 Ma, mostly consisting of grains larger than 1 mm and smaller than 63 µm. Following the interpretation of Pierce et al. (2017), I consider IRD at Site 1165 as lithic grains >1 mm.

In order to obtain the >1 mm coarse fraction IRD, 5 g sediment samples were dried in an oven overnight at 40°C and weighed, using a Pioneer PA413C balance accurate to 3 decimal places. Samples were then disaggregated and the organic fraction digested by boiling in 30% H_2O_2 in 60 ml jars (c. 30 ml of H_2O_2 was used, topped up if necessary) for approximately 4 hours. After digestion, samples were wet-sieved through 63 µm and 1 mm sieves until the water ran clear. The two remaining fractions were washed into containers and settled, after which the water was carefully pipetted out and the samples dried in an oven at 40°C. Once dry, material from the >1 mm fraction was weighed, also using the Pioneer PA413C balance, and the grains counted to generate two complementary records of IRD – the number of grains of IRD per gramme of sediment (grains/g), and the percentage of IRD by mass of sediment (weight %).

3.3. Bulk sediment carbonate isotopes

78 sediment samples from ODP Site 744 (68-50 mbsf; 12.10-14.88 Ma; see Chapter 4 for age model) were analysed for bulk sediment carbonate stable isotopes ($\delta^{13}C$ and $\delta^{18}O$) from samples at the same depth as those used for diatom assemblage analysis. Only the sedimentary fine fraction was analysed (<63 µm), excluding larger foraminifera and other carbonate fossils. This was to capture primarily the nannofossil isotope signal, since nannofossils make up the bulk of the carbonate in the study interval at Site 744 (Shipboard Scientific Party, 1989). In order to separate the <63 µm fraction, all samples were left in the oven overnight at 40°C and then dry-sieved. The fine fraction was retained and then weighed out for isotope analysis alongside a pure carbonate standard (BCT 53-125). Stable isotope measurements were performed using a Thermo Delta V Advantage with Gasbench II at Cardiff University, UK.

3.4. Stable oxygen isotopes in biogenic silica

The application of diatom silica stable oxygen isotope analysis to marine sediments is relatively immature compared with lake sediments, and also marine calcite-based stable isotope methods. Thus, in this section, the development of the method will be briefly outlined, as well as the method that I used in my study (discussed in further detail in Chapter 8).

3.4.1. Method development

3.4.1.1. Particulate contamination

In order to obtain pure diatom silica samples from the sediment, cleaning techniques first use chemical methods such as HCl to remove sedimentary carbonate components and H_2O_2 to remove the organic fraction. Chemical methods can be followed by sieving (e.g. at 10 µm with

the coarse fraction retained) to remove clay particles and other contaminants such as siliceous sponges. Sieving can also be used successfully to obtain a particular diatom size fraction; for example, Swann et al. (2013) analysed the differences in $\delta^{18}O_{diatom}$ between the <10 µm and >10 µm fractions from spring laminations, and the <15 µm and >15 µm fractions from summer laminations, to investigate intra-seasonal variability in glacial discharge. Following, or as an alternative to, sieving, particulate contaminants can be removed via settling procedures and density separation using heavy liquids, for example, sodium polytungstate (Swann & Leng, 2009). Improvements in the quality of the $\delta^{18}O_{diatom}$ measurements with each sequential cleaning step have been demonstrated (Moreley et al., 2004).

Despite sequential cleaning, some external, or non-diatom, contaminants, particularly clay particles of a similar density to diatom silica, may be impossible to remove due to being hidden within, or electro-statically charged to, diatom frustules (Brewer et al., 2008). Such external contamination, particularly if it makes up >10% of the sample, could have a large impact on $\delta^{18}O_{diatom}$ (Morley et al., 2004). Mass-balancing equations have been used to isolate and remove the contamination signal within samples that could not be cleaned sufficiently using traditional methods (Morley et al., 2004; Leng & Swann, 2009). These calculations require the quantification of sample contamination. In early studies, point-counting of samples under a light microscope was performed in order to achieve this (Moreley et al., 2004). However, problems with point counting include the analysis of non-representative small subsamples of the original sample, the possibility of missing contaminants trapped within frustules and not accounting for the volumes of diatom silica versus contaminants (Lamb et al., 2007; Brewer et al., 2008).

Geochemical analyses may be used to improve mass balancing methods, for example, x-ray fluorescence (XRF), x-ray diffraction (XRD) and/or inductively coupled plasma atomic emission spectroscopy (ICP-AES) could provide more accurate estimates of sample purity (Brewer et al., 2008). Using these methods, Al/Si can be used to calculate the relative proportion of non-silica material within a sample; it has been suggested that samples containing <2.5% contamination can provide a robust $\delta^{18}O_{diatom}$ signal (Snelling et al., 2014; Abelmann et al., 2015). This assumption is based on the point at which the impact of particulate contamination on $\delta^{18}O_{diatom}$ becomes greater than analytical error. However, a more recent study (Maier et al., 2018) has analysed and presented $\delta^{18}O_{diatom}$ from samples containing up to 8% contamination. Thus, further substantive and/or quantitative assessment of the existence of a threshold Al/Si, below which samples can be considered sufficiently pure for $^{18}O_{diatom}$ analysis, is required.

If contamination cannot be removed via conventional cleaning methods, for example heavy liquid density separation (Swann & Leng, 2009), but can be measured as a percentage of the sample, and the relative $\delta^{18}O_{diatom}$ of contaminated material is known, the contaminated portion of the $\delta^{18}O_{diatom}$ signal can, in theory, be removed using simple mass balance equations. For example, if a sample contains 7% contaminated material which has a $\delta^{18}O_{contaminant}$ value of 10‰, and the primary diatom $\delta^{18}O$ is 40‰, the $\delta^{18}O$ of the sample will be decreased by 2.3‰ by the contaminant. This is higher than analytical error for the stepwise fluorination procedure employed by the NERC Stable Isotope Facility (used for analyses in my study), which is generally between ±0.2-0.5 ‰ (Swann & Leng, 2009). Mass-balancing is performed using equation 2 (Swann & Leng, 2009):

$$\Delta^{18}O_{corrected} = (\delta^{18}O_{sample} - (\%\ contamination/100) \times \delta^{18}O_{contaminant})/(\%\ purity/100) \quad \text{(Eqn. 2)}$$

Using equation 2 and the previous example, primary $\delta^{18}O_{diatom}$ is shown to be 40‰ rather than 42.3‰. Brewer et al. (2008) demonstrated that mass-balancing can substantially alter the original $\delta^{18}O_{diatom}$ signal, depending on the proportion and $\delta^{18}O$ of contaminated material. However, to date these mass-balancing efforts have mostly been applied in lacustrine settings. In a $\delta^{18}O_{diatom}$ record from the Bering Sea (Maier et al., 2018), mass balancing did not substantially affect the structure of the $\delta^{18}O_{diatom}$ record. Further, despite geochemical methods providing more accurate contamination estimates than point-counting, a certain amount of error still exists with mass-balancing, for example, due to an unknown amount of contamination being removed during the stepwise fluorination process (although that would over-estimate rather than under-estimate the influence of contamination).

3.4.1.2. Removal of the exchangeable silanol layer

In addition to the removal of particulate contamination, removal of the surficial, exchangeable –OH layer of biogenic silica is essential prior $\delta^{18}O_{diatom}$ analysis, but has proven technically challenging. Early attempts involved dehydrating samples under a vacuum at 800-1000°C in order to heat and energize the molecules (Mopper & Garlick, 1971; Labeyrie, 1974; 1979). While this did improve the accuracy and reproducibility of the $\delta^{18}O_{diatom}$ signal, a certain amount of exchangeable oxygen in the outer layer remained. More recent work has also highlighted a potential impact of post-depositional heating on $\delta^{18}O_{diatom}$ above 20°C; changes of up to 1‰ in samples dried at 40°C, and up to 12‰ for samples stored in a water bath at 80°C, have been

documented (Tyler et al., 2017). As such, lower temperature laboratory methods which can remove the entire outer exchangeable layer are required to extract a primary $\delta^{18}O_{diatom}$ signal.

Three techniques have been demonstrated to completely remove the exchangeable outer layer. These techniques are controlled isotope exchange (CIE) followed by fluorination (Labeyrie & Julliet, 1982; Julliett-Leclerc and Labeyrie, 1987), inductive high-temperature carbon reduction (iHTR) (Lucke et al., 2005), and stepwise fluorination (SWF) (Haimson & Knauth, 1983; Matheney & Knauth, 1989). SWF, employed in my study, involves using fluorine to extract oxygen from the different layers of the frustule in stages in order to avoid cross-contamination (Swann & Leng, 2009). First, the –Si–OH layer is stripped using bromine pentaflouride, leaving the uncontaminated –Si–O–Si layer to provide the $\delta^{18}O_{diatom}$ signal (Epstein & Taylor, 1971). This process is documented through continual measurement of the $\delta^{18}O_{diatom}$ signal, which increases as the –Si–OH layer is stripped until it plateaus within the –Si–O–Si layer. A further benefit of the SWF method is that it also removes a proportion of any non-diatom material, minimizing external contamination (Matheney & Knauth, 1989).

3.4.2. $\delta^{18}O_{diatom}$ measurements on samples from ODP Sites 1165 and 744

Samples from ODP Sites 1165 and 744 were prepared for diatom silica oxygen isotope analysis ($\delta^{18}O_{diatom}$) at the University Nottingham, UK, following an established method (Swann et al., 2013; Swann & Leng, 2009). First, sediment samples were placed in test tubes, to which 1 ml of 30% H_2O_2 was added. Samples were left to disaggregate in the test tubes for 3-4 hours, following which the H_2O_2 was removed and samples washed three times in a centrifuge using deionised water. Following centrifuging, diatoms were separated from contaminant material, for example clay and terrigenous particles, using a density separation method. Sodium polytungstate (SPT) was diluted to the desired density (2.25-2.3 SI; diatom density is 2.1 SI) using deionised water. SPT was added to the samples in the centrifuge tubes which were centrifuged again for 5 minutes. Following each density separation, the diatomaceous supernatant was carefully pipetted into fresh test tubes. This process was repeated three times to ensure all contaminants were removed, leaving diatomaceous material of maximum purity. Following SPT density separation, samples were again washed three times using deionised water in the centrifuge, with the diatom supernatant pipetted off each time. After washing, the organic and carbonate fractions were digested by soaking samples in 30% H_2O_2 for 3-5 days followed by 37% HCl for 24 hours. Samples were 'washed' by spinning with deionized water in the centrifuge three times and being left to settle, with the 'dirty' water then pipetted off each time, between each digestion.

In order to check the final purity of diatom samples prepared for isotope analysis, a small amount of each was pipetted onto a petri dish and assessed using a light microscope. These analyses showed no more than one clay particle per 100 diatom valves in any of the samples. Radiolarians and silicoflagellates were present in some samples, but only in very low abundances, e.g. c. 1 fragment per 200 diatoms. As such, I consider contamination from alternative sources of oxygen in my study to be minimal. Further investigation of this issue, including SEM images of select samples, is presented in Chapter 8.

Each processed sample was geochemically analysed using x-ray fluorescence at the University of Nottingham, UK, in order to check for contamination using Al/Si. The proportion of aluminum present in a sample is largely indicative of contamination, since diatom silica naturally contains only low levels of aluminum (Brewer, 2008). Below Al/Si ratios of 0.03 (3%), the effect of non-diatom contaminants on $\delta^{18}O$ is thought to be less than analytical error (Swann & Leng, 2009). Many samples in my study showed Al/Si ratios of <0.03, however, many at ODP Site 1165 also showed Al/Si ratios of up to 0.08 (Section 8.3.2.1). An attempt was made to further separate small, non-diatom contaminants (likely clays) from diatom material in these relatively high Al/Si samples by wet-sieving in deionised water at 10 µm, with the coarse fraction retained. However, in some test samples I found that sieving had little impact on Al/Si (Table 1), and a large amount of material was lost in the process, so sieving was discontinued. Since reducing Al/Si ratios proved difficult, it was decided that samples with relatively high Al/Si values would be analysed with error bars on final values increased accordingly (likely only slightly larger than analytical error of $\delta^{18}O_{diatom}$ at 0.3‰ VSMOW). Efforts to mass balance out the contaminated portion of the signal could then be made, as documented in Section 8.4.1.1.

Table 1. XRF Al/Si in diatom samples after purification for isotope analysis, and then the coarse fraction after wet-sieving using deionized water and a 10 µm mesh sieve. In two samples, all of the material was lost through the sieve.

Sample	XRF Al/Si before sieving	XRF Al/Si after seiving	Change in Al/Si
1165B-5H-1W-80	0.0417	0.0363	-0.0053
1165B-5H-1W-32	0.0379	0.0362	-0.0017
1165B-5H-1W-4	0.0484	0.0379	-0.0106
1165B-4H-6W-29	0.0392	Material lost	
1165B-4H-7W-50	0.0509	Material lost	

4. Chronology

4.1. Introduction

In this thesis, I have constructed and/or refined new age models for four ODP Sites; ODP Site 747, Site 744, Site 1165 and Site 1171. At Site 747, I refined the existing age model (Whitehead & Bohaty, 2010) by adding one new diatom tie-point based on the new high-resolution diatom assemblage counts presented in Chapter 6. My revised age model is supported by my new isotope stratigraphy and my additional refined diatom biostratigraphy, including several of my new diatom biostratigraphic datums (bioevents), both classical and based on quantitative assemblage data (presented in Section 4.2). At Site 744, the age model of Florindo et al. (2013) is used between 15-14 Ma, but I constructed a new age model between 14-12 Ma using diatom biostratigraphy based on the new high-resolution diatom assemblage records presented in Chapter 6. My revised age model is supported by new bulk carbonate isotope stratigraphy (presented in Section 4.3). At Site 1165, I constructed a new age model between 7-15 Ma using new diatom bioevents based on the new high-resolution diatom assemblage record presented in Chapters 6 and 7, with the 0-7 Ma age model based on the paleomagnetic record of Florindo et al. (2003). The paleomagnetic stratigraphy and new biostratigraphic tie-points are supported by my new diatom assemblage counts and associated biostratigraphic datums (revised age model presented in Section 4.4). I also propose a new age model for ODP Site 1171 between 12-15 Ma, which I construct by tuning the benthic stable isotope records of Shevenell et al. (2008) to the high-resolution, orbitally-tuned benthic isotope record at IODP Site U1338 (Holbourn et al., 2014). The existing age model for IODP Site U1138 (Section 4.4), at which unpublished data is presented in Chapter 7, is described here but not revised.

Bioevents in the new age models presented in this thesis are dated primarily using CONOP model run results based on age assignments of diatom bioevents at IODP Site U1356 in Wilkes Land, which is situated at a similar latitude (64˚S) to ODP Sites 747, 744 and 1165 (64-54˚S) (Sangiorgi et al., 2018). CONOP (CONstrained OPtimization) is a computational technique in which age models for a given site can be correlated with a series of existing integrated biostratigraphic, magnetostratigraphic and tephrostratigraphic Southern Ocean records to establish the most parsimonious sequence of events for a given location (Cody et al., 2008). I use some additional age assignments in this chapter from a limited CONOP run at Site 744 (Florindo et al., 2013) and also from David Harwood (personal communication; unpublished assignments used for diatom biostratigraphy during the recent Ross Sea IODP Expedition 374, collated from Harwood & Maruyama (1992), Gersonde & Barcena (1998), Censarek & Gersonde

(2002), Bohaty et al. (2003), Barron (2003), Cody et al. (2008), Barron (2010, unpublished data), Florindo et al. (2013), Cody et al. (2012)). I have tuned all magentostratigraphic and biostratigraphic age assignments in this chapter to the Gradstein et al. (2012) timescale where necessary.

4.2. ODP Site 747

Several different age/depth interpretations have been proposed for ODP Site 747 between 60-90 mbsf. Harwood & Maruyama (1992) first interpreted the presence of a hiatus at c. 68 mbsf as between 13.1-12.1 Ma, inferred from diatom biostratigraphy. Subsequently, Ramsay & Baldauf (1999) suggested continuous sedimentation through this interval, decreasing inferred sedimentation rates from 0.8 cm/kyr to 0.17 cm/kyr between 60-65.5 mbsf. Verducci et al. (2007) proposed that the two normal polarity intervals between 64.8-60.9 mbsf represented Chrons C5AAn (13.2 Ma) and C5An.1 (12.5 Ma). However, the refined diatom biostratigraphy of Majewski & Bohaty (2010) supported the presence of the hiatus recognised by Harwood & Maruyama (1992) and reinterpreted existing magnetostratigraphy (Heider et al., 1992) on that basis.

My newly refined diatom biostratigraphy best supports the age/depth interpretation of Bohaty & Majewski (2010), thus, I use their age/depth curve in my age model. The only difference in age model between mine and that of Bohaty & Majewski (2010) is that I have added one robust diatom biostratigraphic datum (FO of *Denticulopsis dimorpha*, 12.57 Ma, at 65.94 mbsf) as a tie-point to refine the position of the hiatus at 66 mbsf (Figure 5). I recognized four additional diatom datums, not included in Majewski & Bohaty (2010), at Site 747 and have included these in Figure 5 in support of my age/depth curve; FO of *Denticulopsis hyalina* (14.50 Ma) at 74.56 mbsf, LO *Denticulopsis maccollumii* (14.14 Ma) at 73.82 mbsf, LO *Cavitatus jouseanus* (14.12 Ma) at 75.96 Ma and LO *Nitzschia grossepunctata* (12.79 Ma) at 65.82 mbsf.

I have also created a new isotope stratigraphy for Site 747 by tuning the benthic foraminiferal records of Majewski & Bohaty (2010) to the astronomically-tuned benthic foraminiferal isotope record from IODP Site U1338, equatorial Pacific (Holbourn et al., 2014), using established isotope events (Woodruff & Savin, 1991; Shevenell et al., 2004b) (Figures 1-4). Similar to the majority of new diatom bioevents recognized at Site 747, the new isotope events are used only in support of my age/depth curve rather than as tie-points. However, the fact that they plot in

good agreement (Figure 8) is strong supporting evidence for both the validity of my age model at Site 747 and the utility of these isotope events in constructing age models at other sites.

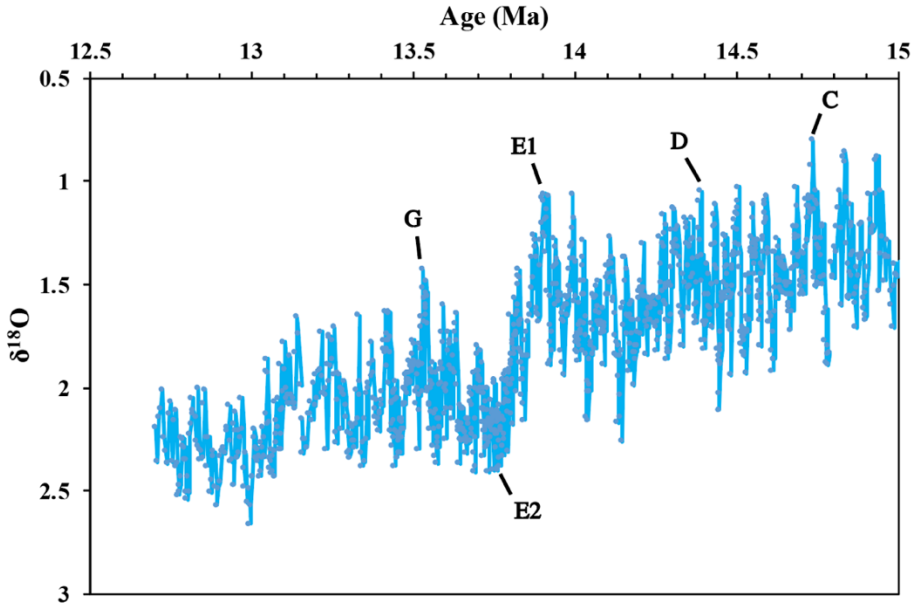

Figure 1. Benthic foraminiferal oxygen isotope record at IODP Site U1338 (Holbourn et al., 2014). Oxygen isotope events are indicated, based on work by Shevenell et al. (2004b) and Woodruff & Savin (1991).

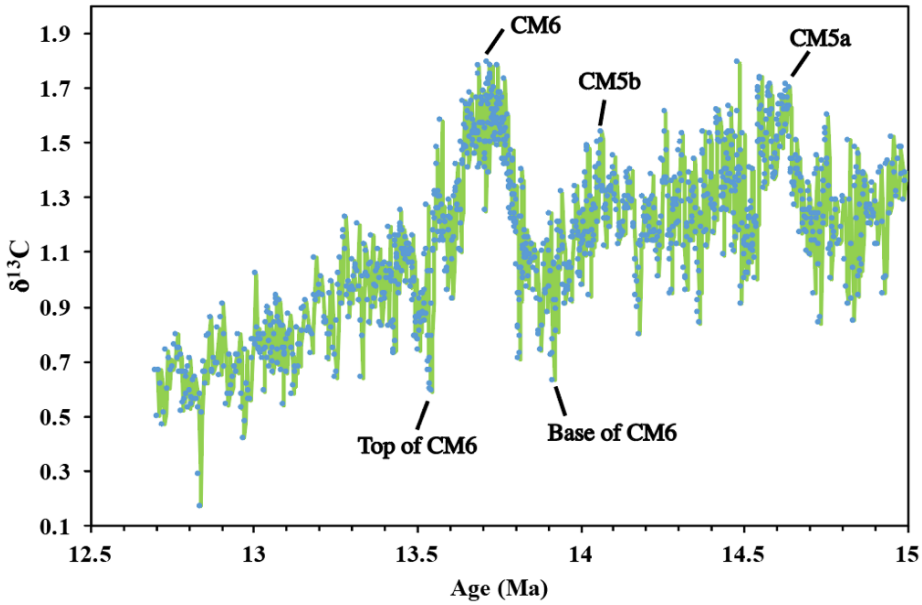

Figure 2. Benthic foraminiferal carbon isotope record at IODP Site U1338 (Holbourn et al., 2014). Carbon isotope events are indicated, based on work by Shevenell et al. (2004b) and Woodruff & Savin (1991).

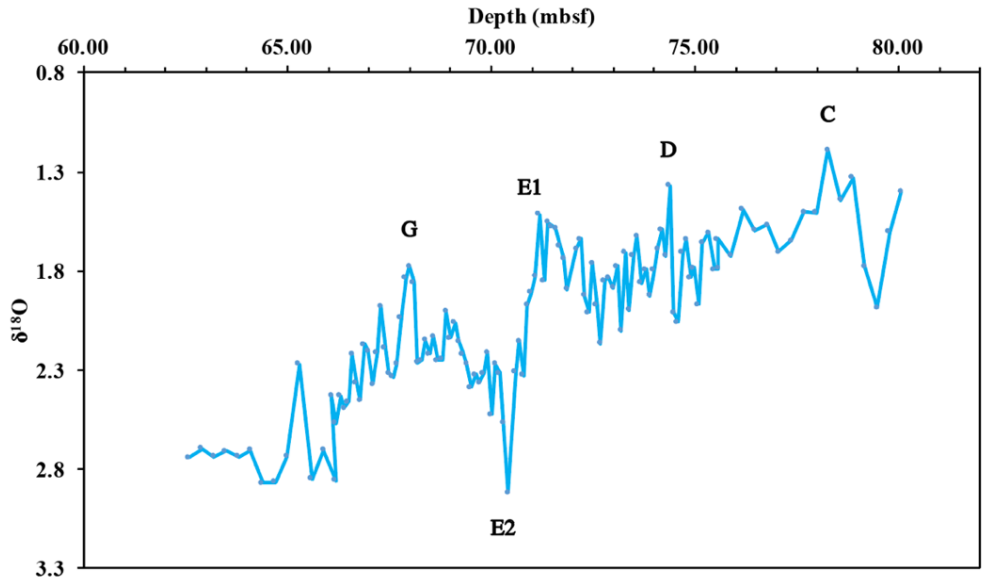

Figure 3. Benthic foraminiferal oxygen isotope record at ODP Site 747 (Bohaty & Majewski, 2010). Proposed oxygen isotope events (constrained by diatom biostratigraphy) are indicated (refer to Figure 1), based on work by Shevenell et al. (2004b) and Woodruff & Savin (1991).

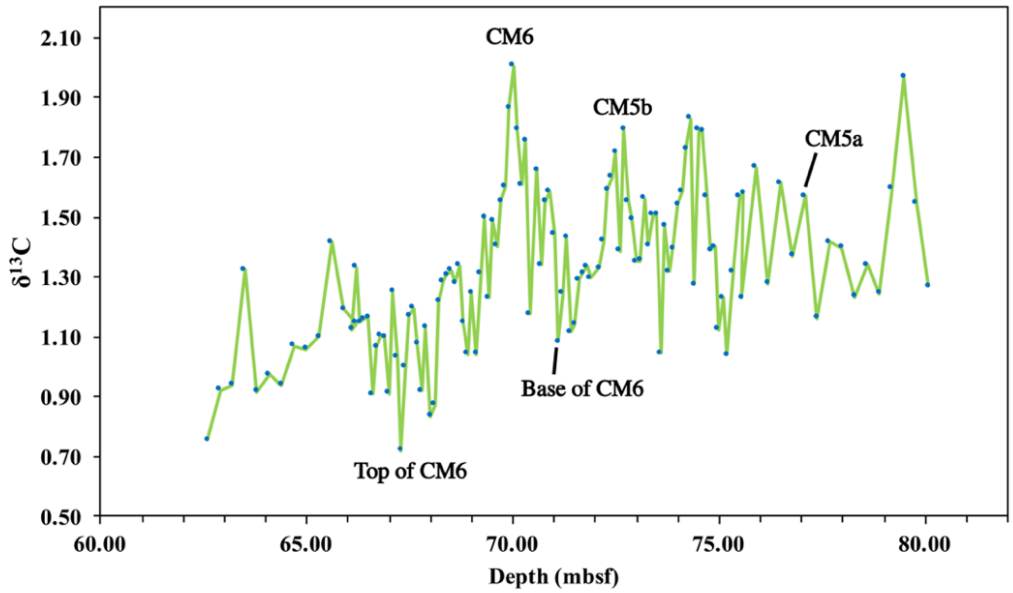

Figure 4. Benthic foraminiferal carbon isotopes at ODP Site 747 (Bohaty & Majewski, 2010). Carbon isotope events (constrained by diatom biostratigraphy) are indicated (refer to Figure 2), based on work by Shevenell et al. (2004b) and Woodruff & Savin (1991).

In addition to new isotope stratigraphy, I propose some new quantitative and classical diatom bioevents and biostratigraphic horizons for the Middle Miocene (12-15 Ma) based on my diatom assemblage records from ODP Sites 747, 744 and 1165. These new events and are calibrated using the robust, magnetostratigraphically-constrained age/depth curve at Site 747, with some of the new events subsequently being used in the age models for Sites 744 and 1165.

My first, newly-proposed quantitative diatom assemblage datum is a group of three peaks (<30%) in the abundance of *Actinocyclus ingens* var. *nodus* seen in the diatom assemblage record at both Sites 747 and 744 (Figure 5), and magnetostratigraphically-calibrated at Site 747 to 14.29 Ma, 14.24 Ma and 13.98 Ma. These *A. ingens* var. *nodus* abundance peaks are not seen at Site 1165, perhaps because it was situated further south and therefore subject to different oceanographic conditions prior to the Middle Miocene Climate Transition at 13.8 Ma. A relatively low magnitude (15%) *A. ingens* var. *nodus* abundance peak does occur at Site 1165 at 288.75 mbsf, however, other well-established diatom datums at Site 1165 strongly suggest 288 mbsf is younger than 14 Ma (Table 4).

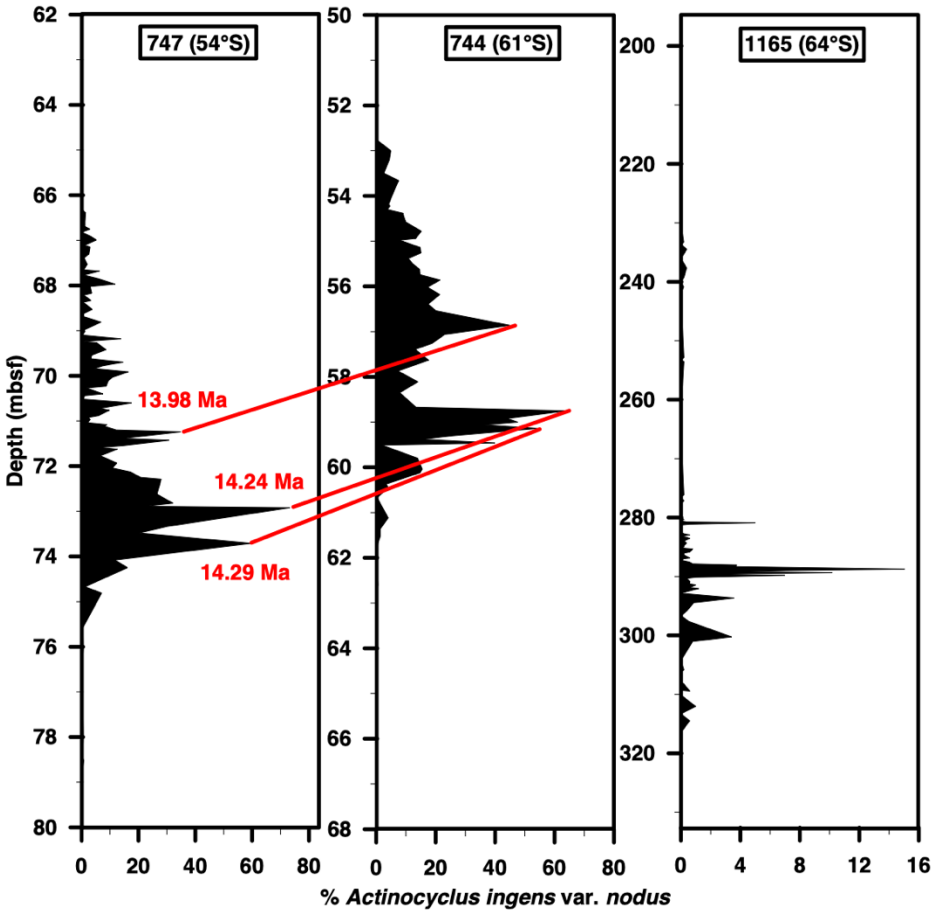

Figure 5. New quantitative diatom bioevent (three *Actinocyclus ingens* var. *nodus* abundance peaks at 14.29, 14.24 and 13.79 Ma, chronologically-calibrated at ODP Site 747) identified at ODP Sites 744 and 747.

My second new quantitative diatom assemblage datum is an abundance peak in *Denticulopsis hyalina*, seen at ODP Sites 747, 744 and 1165 (Figure 6) and calibrated to 13.79 Ma at Site 747. At Site 1165, two peaks in *D. hyalina* occur, the deeper being of greater magnitude (18%) than the shallower (5%). However, based on existing diatom datums (Table 4), the lower peak at 302.65 mbsf occurs closer to 14 Ma, and the shallower peak at 290.35 mbsf better corresponds to the peaks at Sites 744 and 747 at 13.79 Ma.

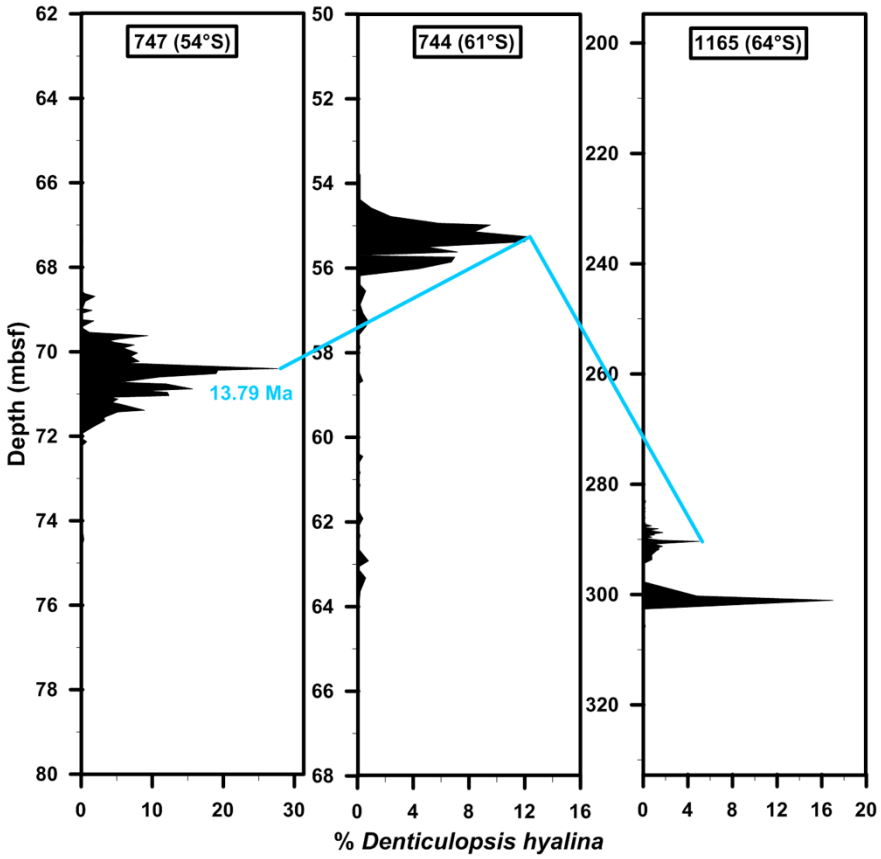

Figure 6. New quantitative diatom bioevent at 13.79 Ma (based *Denticulopsis hyalina* abundance peak and chronologically calibrated at ODP Site 747) identified at ODP Sites 744 and 747 and 1165.

My third newly identified quantitative diatom assemblage bioevent is a peak in the abundance of a new species, *Actinocyclus* sp. nov #1 (see Appendix 2 for description),

magnetostratigraphically-calibrated at ODP Site 747 to 13.47 Ma and also identified at ODP Sites 744 and 1165 (Figure 7).

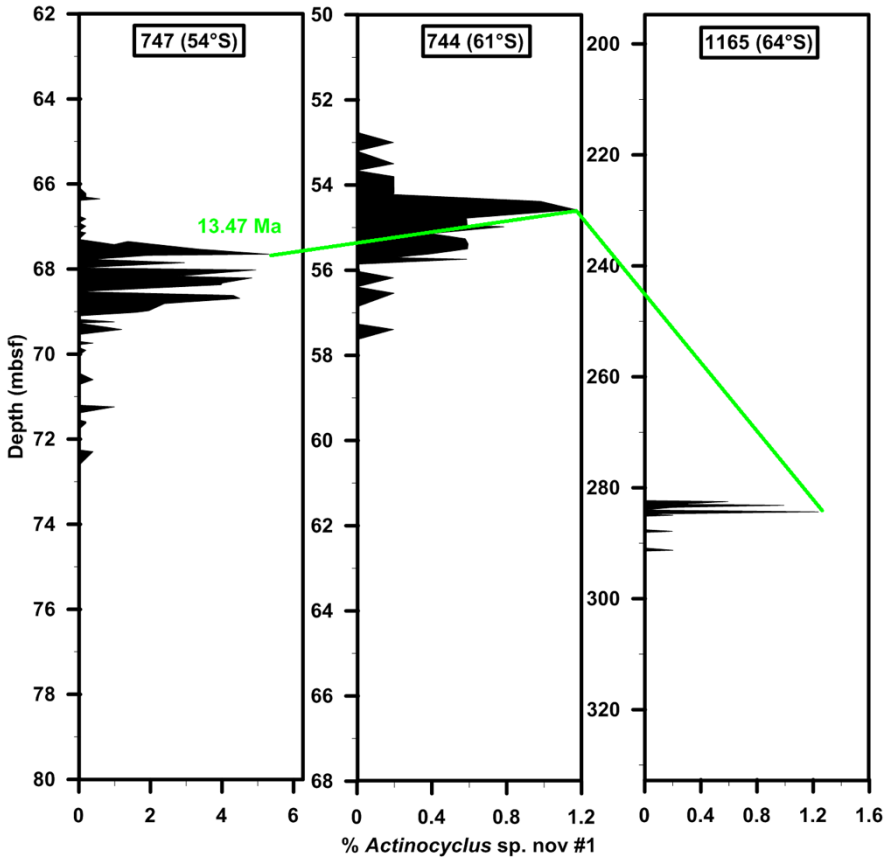

Figure 7. New quantitative diatom bioevent at 13.47 Ma (*Actinocyclus* sp. nov #1 abundance peak, chronologically calibrated at Site 747) identified at ODP Sites 744, 747 and 1165.

Finally, I also recognized additional classical biostratigraphic horizons at Sites 747, 744 and 1165, based on the high resolution diatom assemblage records presented in Chapters 6 and 7, which I have magnetostratigraphically calibrated at Site 747. These newly-calibrated datums are: the FO of *Fragilariopsis donahuensis*, calibrated at 14.19 Ma, identified at all three sites, and the FO and LO of a second new species, *Thalassiosira* sp. nov (see Appendix 2 for description) at 13.71 Ma and 13.35 Ma, respectively, observed at Sites 744 and 1165. While diachrony must be considered when proposing new bioevents and datums, I excluded this possibility for both the quantitative and classical bioevents by first assessing new bioevents using age models based on the more established datums at each site, and only proposed those new events that appeared to be synchronous between at least two sites.

Table 1. Stratigraphic bioevents and datums recognized at ODP Hole 747A, including from magnetostratigraphy, isotope stratigraphy and diatom biostratigraphy. Diatom biostratigraphic datums are updated from Bohaty & Majewski (2010) using the higher-resolution diatom assemblage record presented in this thesis. Tie-points used to calculate the age/depth curve (constructed via linear interpolation) are shaded grey. Age references include Heider et al. (1992) (H02), Sangiorgi et al. (2018) (S18), Florindo et al. (2013) (F13), Gradstein et al. (2012) (G12), Holbourn et al. (2014) (H14) and David Harwood, unpublished data (HUP). CIE= carbon isotope event, OIE= oxygen isotope event.

Bioevent	Age (Ma)	Age reference	Mid-depth (mbsf)	Depth Error (mbsf +/-)
Top C5An.1n	12.05	G12, H92	60.92	
Base C5An.1n	12.17	G12, H92	61.67	
Top C5An.2n	12.27	G12, H92	61.97	
Base C5An.2n	12.47	G12, H92	64.82	
FO *Denticulopsis dimorpha*	12.57	S18	65.94	0.04
LO *Actinocyclus ingens* var. *nodus*	12.60	F13	66.30	0.08
LO *Crucidenticula nicobarica*	12.63	F13	65.95	0.05
FO *Denticulopsis praedimorpha*	12.76	S18	66.03	0.04
LO *Nitzschia grossepuntata*	12.79	S18	65.82	0.10
LO *Thalassiosira* sp. nov	13.35	This study	66.33	0.02
Top C5ABn	13.36	G12, H92	66.81	
Abundance peak *Actinocyclus* sp. nov #1	13.47	This study	67.68	
OIE G	13.54	H14, This study	67.83	
Top CIE CM6	13.55	H14, This study	67.83	
Base C5ABn	13.61	G12, H92	68.84	
FO *Thalassiosira* sp. nov	13.71	This study	69.81	0.03
CIE CM6	13.79	H14, This study	69.84	
Top C5ACn	13.74	G12, H92	69.91	

Top OIE E	13.76	H14, This study	70.24	
Abundance peak *Denticulopsis hyalina*	13.79	This study	70.40	
Base OIE E	13.91	H14, This study	71.02	
Base CIE CM6	13.92	H14, This study	71.22	
Third *Actinocyclus ingens* var. *nodus* abundance peak	13.98	This study	71.24	
Base C5ACn	14.07	G12, H92	71.79	
CIE CM5b	14.07	H14, This study	72.39	
LO *Cavitatus jouseanus*	14.12	S18	75.96	0.38
LO *Denticulopsis maccollumii*	14.14	S18	73.82	0.11
Top C5ADn	14.16	G12, H92	72.42	
FO *Fragilariopsis donahuensis*	14.19	This study	72.27	0.02
FO *Nitzschia denticuloides*	14.25	S18	72.19	0.06
Second *Actinocyclus ingens* var. *nodus* abundance peak	14.24	This study	72.92	
First *Actinocyclus ingens* var. *nodus* abundance peak	14.29	This study	73.71	
FO *Denticulopsis simonsenii*	14.35	S18	73.13	0.21
OIE D	14.39	H14, This study	74.08	
FO *Actinocyclus ingens* var. *nodus*	14.56	S18	78.36	0.17
CIE CM5a	14.64	H14, This study	76.89	
FO *Denticulopsis hyalina*	14.50	HUP	74.56	0.11
CIE C	14.74	H14, This study	78.09	
Top C5Bn.2n	15.03	G12, H92	81.15	

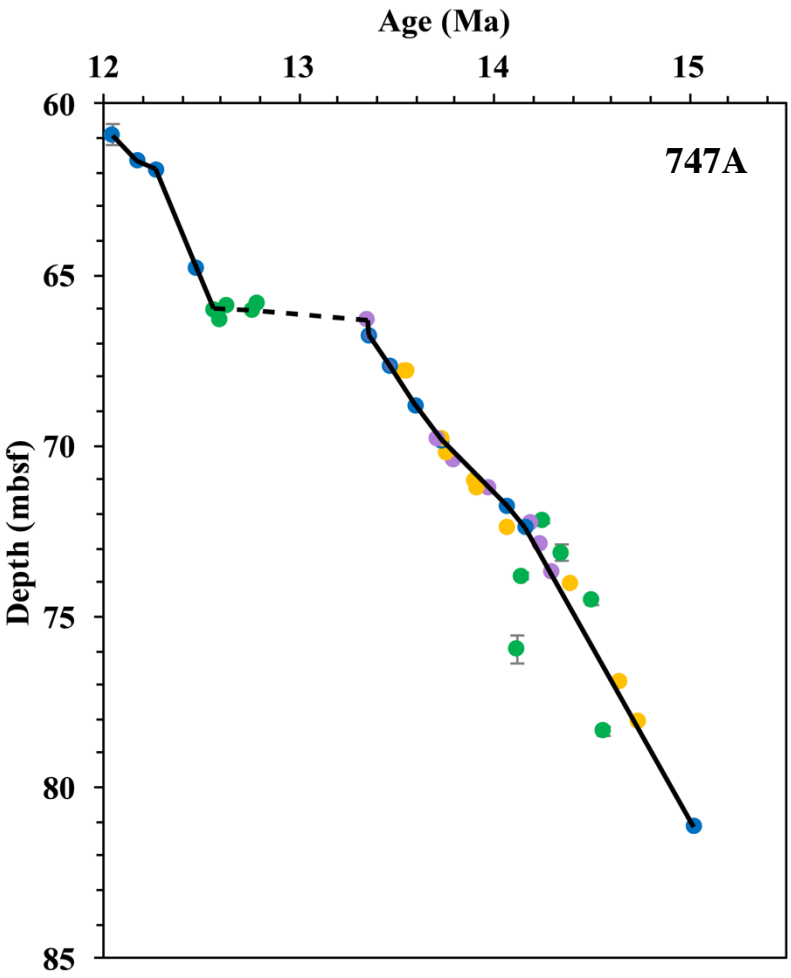

Figure 8. Age-depth model at ODP Hole 747A (see Table 1 for details). Blue dots are paleomagnetic reversals (Majewski & Bohaty, 2010; Heider et al., 1992), yellow dots are isotope events (Majewski & Bohaty, 2010; this study), purple dots are new proposed diatom bioevents, including both abundance events and biostratigraphic horizons (this study), green dots = previously existing diatom bioevents which have been refined for study. Black line joins tie-points (Table 1) used in age model using linear interpolation. Dotted line indicates a hiatus/strongly condensed interval between 13.36-12.97 Ma (66.81-65.94 mbsf).

4.3. ODP Site 744

The existing age model of Florindo et al. (2013) is used between 58-68 mbsf (c. 14-15 Ma) at ODP Site 744. This age model consists of linear interpolation between magnetostratigraphic tie-points, constrained by high-resolution, qualitative diatom biostratigraphic data of Farmer (2011) between c. 57-100 mbsf. The diatom biostratigraphy (Farmer, 2011) was refined using a CONOP model run (Florindo et al., 2013), which produced placed depths as well as ages for each Site

744 diatom biostratigraphic horizon, that are theoretically more accurate than observed depths. However, none of the biostratigraphic events are used as tie-points in my revised age model between 58-68 mbsf, at Site 744; rather, I use them to provide support for my proposed age/depth curve (Figure 11).

Magnetic reversals are not identified above 56 mbsf at Site 744 (Florindo et al., 2013), and existing diatom counts also do not extend above this depth (Farmer, 2011). As such, I construct a new age model at Site 744 between 56-50 mbsf, based on linear interpolation between biostratigraphic tie-points. The tie-points that I selected (Table 2) are diatom bioevents identified from the new diatom assemblage data at Site 744 (Chapter 6). I use my new quantitative abundance datums, refined at Site 747, as tie-points, as well as other established bioevents. One radiolarian datum is also used as a tie-point at 50.35 mbsf (LAO Cyrtocapsella tetrapera, 12.16 Ma) (Florindo et al., 2013). Other diatom bioevents recognised at Site 744 are included as support for the interpreted age/depth curve, but I do not use them as tie-points (Table 2; Figure 11).

In support of my proposed age/depth curve at Site 744, I also generated a new bulk carbonate (due to insufficient foraminifera) stable isotope record at Site 744, to compare with the isotope records from ODP Sites 747 (Majewski & Bohaty, 2010) and 1171 (Shevenell et al., 2008). My aim was to identify equivalent isotope events, which would further support my new age model at Site 744, as well as facilitating robust comparisons with Site 747. The new isotope record did improve upon the resolution of an existing multi-species benthic isotope record from Site 744 (Woodruff & Chambers, 1991; Figures 6 & 7), and facilitated the identification of isotope events. Although bulk carbonate isotope records, primarily consisting of surface-dwelling coccolithophores (e.g. *Coccolithus pelagicus* and *Reticulofenestra* spp.) at Site 744, may differ from benthic foraminifera isotope records, planktonic and benthic carbonate isotope records at Site 747 across the Middle Miocene interval both reflect major isotope trends (Majewski & Bohaty, 2010; Bohaty, unpublished data 2014).

I identify isotope events E1, E2 and CM6 at Site 744 in both the bulk carbonate and benthic foraminiferal records (Figures 9 and 10; Table 2). However, like the diatom biostratigraphy in the lower section, I do not use these isotope events as tie-points in generating the new age/depth curve. Instead, they plot close to the modelled age/depth line (Figure 11), supporting my new age model.

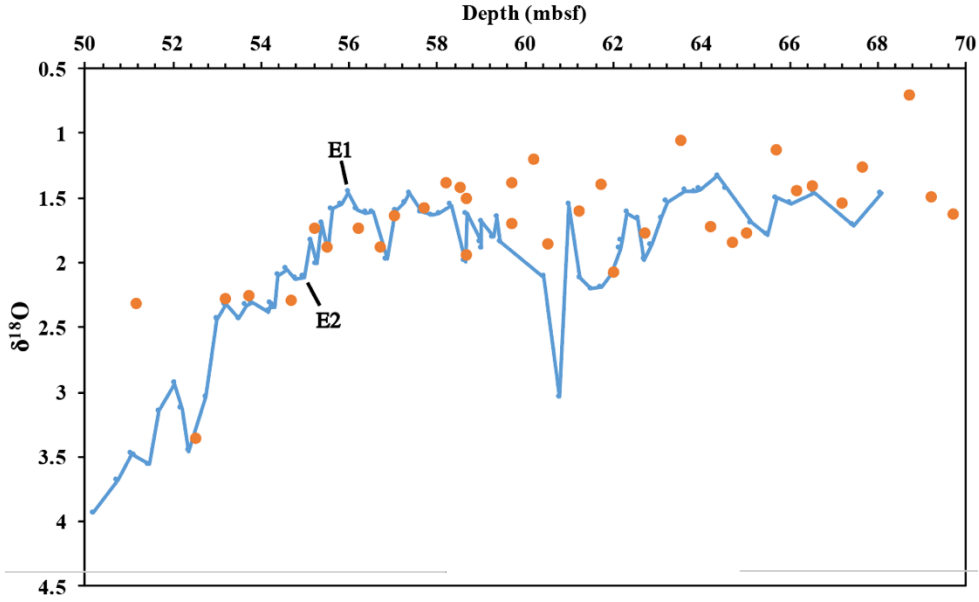

Figure 9. Stable oxygen isotope records from ODP Site 744. Blue line is new bulk carbonate data generated for this study; orange dots are benthic foraminiferal data from Woodruff & Chambers (1991). Oxygen isotope events are indicated, constrained by diatom biostratigraphy.

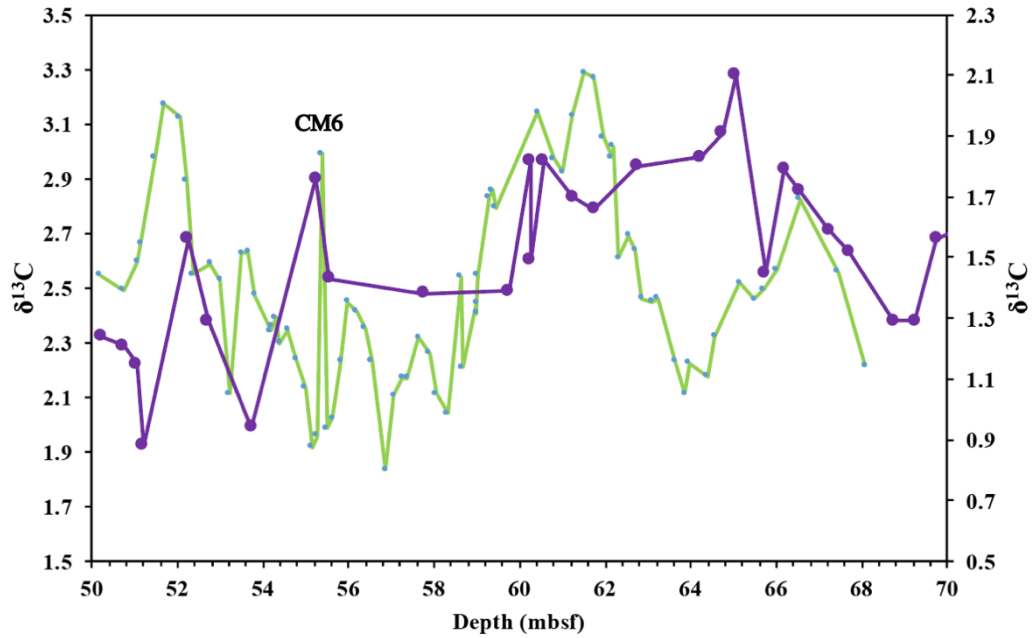

Figure 10. Carbon isotope records from ODP Site 744. Green line is new bulk carbonate data generated for this study; purple line is benthic foraminiferal data from Woodruff & Chambers (1991). Carbon isotope event CM6 is indicated, constrained by diatom biostratigraphy.

Table 2. Bioevents and datums recognized at ODP Hole 744B including magnetostratigraphy, diatom and radiolarian biostratigraphy and isotope stratigraphy. Bioevents are included from Florindo et al. (2013) (F13) as well as from this study, with age-assignments from Sangiorgi et al. (2018) (S18), Florindo et al. (2013) and David Harwood (personal communication) (HUP). New quantitative diatom assemblage bioevents and biostratigraphic datums are included, chronologically-calibrated at ODP Site 747 (Section 4.1.1). Isotope events are based on bulk isotope stratigraphy from data presented in this thesis and in Woodruff & Chambers (1991) and Shevenell et al. (2004b) (Figures 6 and 7). The age model was constructed using linear interpolation between selected tie-points (shaded grey) (Figure 11).

Bioevent	**Age (Ma)**	**Age reference**	**Mid-depth (mbsf)**	**Depth Error (mbsf +/-)**
LAO *Cyrtocapsella tetrapera* (radiolarian)	12.16	F13	50.35	placed
FAO *Cycladophora spongothax* (radiolarian)	12.23	F13	50.35	placed
FO *Denticulopsis dimorpha*	12.57	S18	52.91	0.17
LO *Actinocyclus ingens* var. *nodus*	12.60	F13	52.93	0.17
LO *Crucidenticula nicobarica*	12.63	F13	53.30	0.20
FO *Denticulopsis praedimorpha*	12.76	S18	53.70	0.19
LO *Nitzchia grossepunctata*	12.79	S18	53.70	0.19
FO Unidentified centric sp. 3	13.35	This study	53.80	0.26
Peak abundance *Actinocyclus* sp. nov #1	13.47	This study	54.54	0.18
LO *Thalassiosira* sp. nov	13.71	This study	55.58	0.10
Top OIE E	13.76	S04	56.74	0.10
Peak abundance *Denticulopsis hyalina*	13.79	This study	55.22	0.12
FO *Denticulopsis delicata*	13.91	S18	54.22	0.06
Base OIE E	13.91	S04	57.75	0.16
Third abundance peak; *Actinocyclus ingens* var. *nodus*	13.98	This study	56.86	0.26
Base C5ACn	14.07	G12, F13	57.18	
LO *Cavitatus jouseanus*	14.12	S18	59.38	0.08
LO *Denticulopsis maccollumii*	14.14	S18	56.96	0.10

LO *Nitzschia* sp. 17 Schrader	14.17	S18	57.39	0.13
Top C5ADn	14.16	G12, F13	59.87	
FO *Fragilariopsis donahuensis*	14.19	This study	57.76	0.24
FO *Nitzschia denticuloides*	14.25	S18	58.32	0.14
Second *Actinocyclus ingens* var. *nodus* abundance peak	14.24	This study	59.30	0.12
First *Actinocyclus ingens* var. *nodus* abundance peak	14.29	This study	59.76	0.52
FO *Denticulopsis simonsenii*	14.35	S18	60.16	placed
FO *Araniscus lewisianus*	14.46	S18	60.16	placed
FO Denticulopsis hyalina	14.50	HUP	63.10	Placed
FO *Actinocyclus ingens* var. *nodus*	14.56	S18	64.72	placed
LO *Cavitatus miocenicus*	14.61	F13	62.11	placed
Base C5ADn	14.61	F13	61.50	
Top C5Bn.1n	14.78	F13	65.11	
LO *Crucidenticula kanaye*	14.82	F13	64.52	TRM placed
Base C5Bn.1n	14.87	F13	66.82	
FO *Denticulopsis lauta*	14.95	S18	64.52	TRM placed
Top C5Bn.2n	15.03	F13	68.29	
LO *Raphodiscus marylandicus*	15.10	F13	67.79	TRM placed

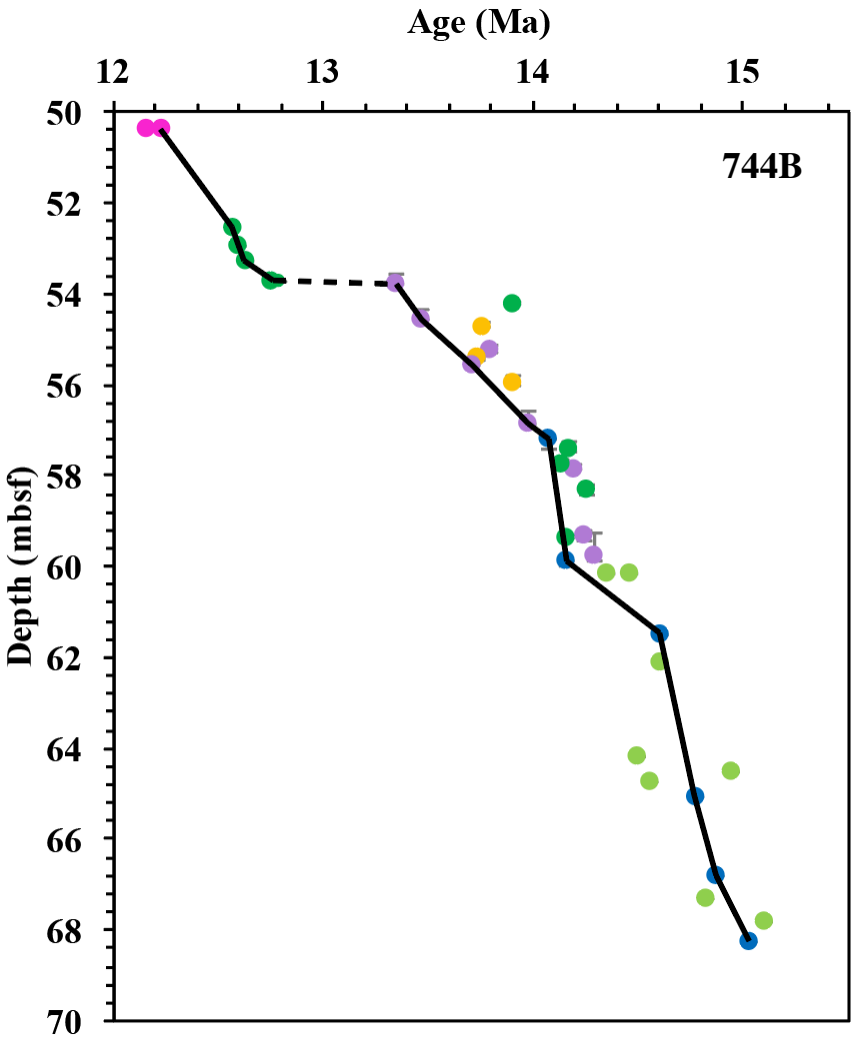

Figure 11. Age-depth model for ODP Hole 744B (see Table 1 for details). Blue dots are magnetic reversals (Florindo et al., 2013), yellow dots are isotope events (this study), purple dots are new quantitative diatom bioevents chronologically-calibrated at ODP Site 747 (this study), pink dots are radiolarian bioevents (Florindo et al., 2013), light green dots are placed diatom bioevents from Florindo et al. (2013) (Total Range Model depths- converted to mbsf), dark green dots are established diatom bioevents recognized at Site 744 based on assemblage counts in this study. Black line joins tie-points used in the age model (see Table 1), dotted line indicates a hiatus at ODP Site 744.

4.4. ODP Site 1165

I generated a new age/depth curve for ODP Site 1165 using linear interpolation between tie-points (Table 4, Figure 12). Tie-points used in my new age model are magnetostratigraphic above 89 mbsf, 7.14 Ma (Grutzner et al., 2003; Hilgen et al., 2003; Florindo et al., 2013; Teitler et al., 2015). Below this depth, the most reliable diatom bioevents were chosen as tie-points. As in the

choice of tie-points at other sites presented in this chapter, I prioritised the first occurrences of species, bioevents for which age-assignments show minimal spread between different studies, and bioevents that seem to best reflect the trends of supporting bioevents. All of the diatom bioevents (Table 4) have been revised from the original biomagnetostratigraphic age model of Florindo et al. (2003) using my new higher-resolution quantitative diatom assemblage record at Site 1165 (see Appendix 3 for full diatom tables) and unpublished biostratigraphic counts from Site 1165 (S. Bohaty, unpublished data, 2014). However, I have also included five radiolarian bioevents from Florindo et al. (2003) as supporting bioevents, using revised age-assignments from Sangiorgi et al. (2018). The lack of carbonate preserved at Site 1165 (Shipboard Science Party, 2001) precluded isotope stratigraphy.

Supporting bioevents provide ages that are generally consistent with my age-depth model at Site 1165 (Figure 12), however, a greater spread away from the model is seen in the Late Miocene. A CONOP (Cody et al., 2008) run for Site 1165 could possibly reduce the spread with site-specific age assignments. Perhaps more likely, the spread may suggest that more Late Miocene records calibrated to magnetostratigraphy are needed from the Southern Ocean, particularly at higher latitudes, in order to better constrain the age assignments of diatom bioevents from this time period.

Table 4. Biostratigraphic events and paleomagnetic reversals used in the construction of the age model at ODP Site 1165. Tie-points used in the age model are shaded grey; others are used as supporting data. Paleomagnetic data come from Grutzner et al. (2003) (G03), Teitler et al. (2015) (T15), Hilgen et al. (2003) (H03) and Shipboard Science Party (2001) (S01). Radiolarian data are from Florindo et al. (2003) (F03) with some age assignments adjusted to Sangiorgi et al. (2018). All diatom bioevents are from this study, with age assignments from Sangiorgi et al. (2018) (S18) and D. Harwood, unpublished data (HUP).

Bioevent	**Age (Ma)**	**Age reference**	**Mid-depth (mbsf)**	**Depth Error (mbsf +/-)**
LO *Actinocyclus ingens*	0.11	S18	3.20	0.75
PMAG	0.78	S01	5.37	
LO *Fragilariopsis barronii*	0.86	S18	5.80	0.43
PMAG	0.99	T15	6.97	
FO *Fragilariopsis separanda*	1.40	HUP	6.22	0.02

LO *Thalassiosira inura*	1.90	HUP	7.75	0.75
LO *Thalassiosira torokina*	1.90	HUP	6.91	0.10
PMAG	1.95	G03	14.10	
LO *Thalassiosira kolbei*	2.14	S18	13.25	2.00
PMAG	2.14	G03	14.66	
LO *Thalassiosira vulnifica*	2.20	HUP	15.63	0.38
LO *Actinocyclus fasciculatus*	2.26	S18	15.63	0.38
FO *Shionodiscus oestrupii* var. *reimeri*	2.30	HUP	18.28	0.09
LO *Fragilariopsis weaverii*	2.32	S18	17.16	0.09
LO *Thalassiosira insigna*	2.34	S18	17.36	0.11
LO *Actinocyclus maccollumii*	2.36	S18	17.16	0.09
FO *Fragilariopsis kerguelensis*	2.38	S18	17.22	0.15
LO *Fragilariopsis praeinterfrigidaria*	2.40	HUP	15.63	0.38
FO *Fragilariopsis mutayame*	2.40	HUP	17.36	0.11
LO *Rouxia diploneides*	2.40	HUP	17.36	0.11
LO *Helothus vema* (radiolarian)	2.42	F03	19.87	1.13
LO *Thalassiosira complicata*	2.52	S18	18.42	0.05
LO *Actinocyclus fasciculatus*	2.65	S18	18.99	0.52
FO *Actinocyclus actinochillus*	2.72	S18	18.04	0.04
LO *Fragilariopsis reinholdii*	3.00	HUP	21.75	0.75
PMAG	3.03	G03	19.23	
PMAG	3.12	G03	20.91	
FO *Thalassiosira vulnifica*	3.20	HUP	26.01	0.43
PMAG	3.21	G03	25.96	
PMAG	3.33	G03	30.76	
FAO *Thalassiosira insigna*	3.40	HUP	25.44	0.43
FO *Fragilariopsis weaverii*	3.49	S18	27.28	0.32
LO *Fragilariopsis praeinterfrigidaria*	3.50	HUP	25.93	0.07
PMAG	3.60	G03	36.46	
LO *Fragilariopsis arcula*	3.71	S18	38.88	0.38
FO *Thalassiosira kolbei*	3.95	S18	38.88	0.38
FO *Thalassiosira lentiginosa*	4.07	S18	36.38	0.63
PMAG	4.18	G03	42.06	

LO *Fragilariopsis praecurta*	4.20	HUP	31.63	0.38
LO *Fragilariopsis aurica*	4.20	HUP	39.63	0.38
LO *Rouxia californica*	4.20	HUP	39.63	0.38
PMAG	4.29	G03	43.19	
FO *Thalassiosira striata*	4.36	S18	43.00	0.22
FO *Fragilariopsis barronii*	4.41	S18	41.85	0.07
LO *Rouxia peragalii*	4.60	HUP	54.36	0.39
PMAG	4.62	G03	45.75	
FO *Helotholus vema* (radiolarian)	4.69	F03	51.37	1.88
PMAG	4.80	G03	46.96	
FO *Thalassiosira tumida*	4.84	S18	45.30	0.45
PMAG	4.89	G03	48.80	
PMAG	4.98	G03	49.12	
LCO *Lychnocanoma grande* (radiolarian)	5.02	F03	65.09	1.94
LO *Nitzschia miocenica*	5.10	HUP	62.65	0.95
PMAG	5.23	G03	54.26	
FO *Thalassiosira complicata*	5.46	S18	59.17	2.63
FO *Thalassiosira inura*	5.50	HUP	51.31	0.36
LO *Fragilariopsis donahuensis*	5.50	HUP	59.30	4.71
FAO *Rouxia diploneides*	5.52	S18	54.56	4.94
FO *Shionodiscus oestrupii*	5.70	HUP	54.56	4.94
LO *Hemidiscus triangularis*	5.81	S18	77.63	0.38
LO *Fragilariopsis januaria*	5.92	S18	64.38	0.38
LO *Amphymenium challengerae* (radiolarian)	6.10	F03	65.45	2.26
FO *Thalassiosira miocenica*	6.40	HUP	73.88	0.40
LO *Actinocyclus ingens* var. *ovalis*	6.50	HUP	64.38	0.38
FO *Amphymenium challengerae* (radiolarian)	6.65	F03	72.87	1.38
PMAG	6.67	G03	73.52	
FO *Fragilariopsis praeinterfrigidaria*	6.99	S18	78.13	0.28
FO *Hemidiscus triangularis*	7.00	HUP	82.20	0.62
FAD *Thalassiosira oliverana*	7.00	HUP	95.88	0.40

PMAG	7.14	H03	89.2	
LO *Thalassiosira mahoodii*	7.70	HUP	67.38	0.38
FO *Acrosphaera labrata* (radiolarian)	8.34	F03, S18	103.22	4.78
FO *Fragilariopsis aurica*	8.40	HUP	92.45	0.24
FO *Fragliariopsis arcula*	8.50	HUP	87.13	0.40
FO *Fragilariopsis reinholdii*	8.50	HUP	92.15	0.08
FO *Nitzschia miocenica*	8.60	S18/ HUP	96.63	0.40
FO *Actinocyclus ingens* var. *ovalis*	8.68	S18	100.62	0.81
FO *Thalassiosira oliverana* var. *sparsa*	8.71	S18	125.85	0.38
FO *Thalassiosira mahoodii*	8.80	HUP	127.30	0.44
FO *Thalassiosira torokina*	9.00	HUP	107.63	0.19
LO *Cycladophora spongothorax* (radiolarian)	9.12	F03	114.45	3.46
FO *Hemidiscus karstenii*	9.75	HUP	119.38	0.40
FAD *Thalassiosira nativa*	10.00	HUP	147.46	9.76
FO *Hemidiscus cuneiformis*	10.11	S18	162.83	0.16
LO *Fragilariopsis claviceps*	10.20	HUP	157.15	0.75
FO *Thalassiosira gersondeii*	10.30	HUP	125.88	0.40
FO *Asteromphalus kennettii*	10.30	HUP	189.05	0.38
FO *Acrosphaera australis* (radiolarian)	10.27	F03, HUP, S18	182.07	2.63
LO *Denticulopsis dimorpha*	10.60	HUP	185.70	0.40
LO *Denticulopsis dimorpha* var. *areolata*	10.71	S18	192.43	0.38
LO *Actinomma golownini* (radiolarian)	10.77	F03	190.54	5.85
LO *Denticulopsis praedimorpha*	11.20	HUP	195.95	1.05
LO *Nitzschia denticuloides*	11.75	HUP	211.11	12.61
FO *Denticulopsis ovata*	12.14	S18	206.28	3.81
FO *Cycladophora spongothorax* (radiolarian)	12.29	F03, S18	225.62	26.98
LO *Crucidenticula nicobarica*	12.33	S18	233.87	0.40
FO *Denticulopsis dimorpha*	12.57	S18	235.28	0.39
LO *Actinocyclus ingens* var. *nodus*	12.60	F13	233.28	1.54
LCO *Crucidenticula nicobarica*	12.63	S18, F13	234.48	0.80

FO *Denticulopsis praedimorpha*	12.76	S18	237.66	1.60
LO *Nitzschia grossepunctata*	12.79	S18	237.66	0.80
LO Thalassiosira sp. nov	13.35	This study	270.89	5.28
Abundance peak *Actinocyclus* sp. nov #1	13.47	This study	283.36	0.80
FO *Thalassiosira* sp. nov	13.71	This study	283.56	0.22
Abundance peak *Denticulopsis hyalina*	13.79	This study	290.35	0.10
IRD Peak	13.90	P17	290.50	0.27
FO *Denticulopsis delicata*	13.91	S18	283.16	0.10
LO *Denticulopsis maccollumii*	14.14	S18	285.35	0.10
LO *Nitzschia* sp. 17 Schrader	14.17	S18	285.35	0.10
FAO *Fragilariopsis donahuensis*	14.19	S18	300.25	0.40
FO *Nitzschia denticuloides*	14.25	S18	285.35	0.25
FAO *Cycladophora humerus* (radiolarian)	14.30	S18, F03	287.20	3.00
FO *Denticulopsis simonsenii*	14.35	S18	300.25	0.40
FO *Denticulopsis hyalina*	14.50	HUP	305.85	0.20
FO *Actinocyclus ingens* var. *nodus*	14.56	S18	315.50	1.00
FO *Denticulopsis lauta*	14.95	S18	328.6	1.45

For the 15-13 Ma interval at Site 1165, a spread exists between bioevents in the lower section (below 280 mbsf) and, as such, I consider two possible age/depth models. One age model indicates a hiatus/strongly condensed interval between 14.3-13.4 Ma (Figure 13), not recognised by either of the two previous age models for this section at ODP Hole 1165B (Shipboard Science Party, 2001; Florindo et al., 2003). The age/depth model without the hiatus agrees with several of my newly-proposed diatom bioevents, and I prefer this non-hiatus age model for the following reasons:

1. The bioevent at 14.19 Ma, FO *Fragilariopsis donahuensis*, is calibrated at Site 747 and appears to be a robust tie-point between Sites 747, 744 and 1165.
2. The bioevent at 13.79 Ma, a peak in *Denticulopsis hyalina* abundance (a cool water species; Chapter 5), also occurs at Sites 747 and 744, and coincides precisely with peak Middle Miocene Climatic Transition cooling (Shevenell et al., 2004).
3. A 290.80 mbsf peak in IRD at Site 1165 is constrained to 13.90 Ma by the non-hiatus age model, but c. 14.30 Ma if the hiatus is included. An IRD peak is also documented at IODP Site U1356 in Wilkes Land at 13.90 Ma and deposition is proposed to be synchronous at

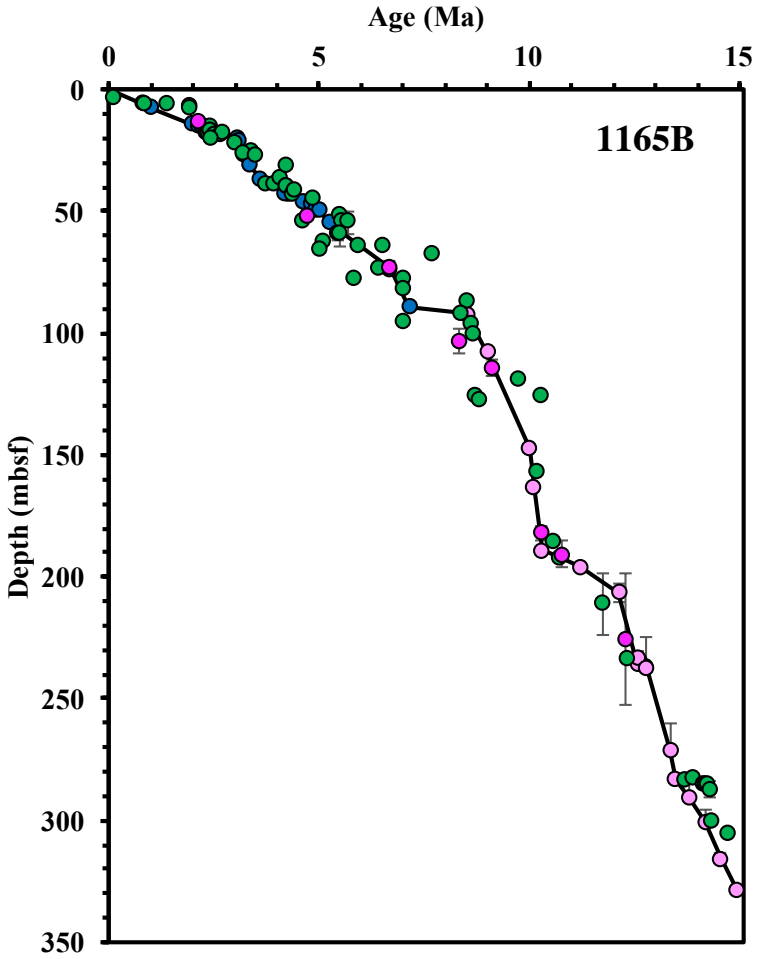

Figure 12. New proposed age model for ODP Site 1165 (15-0 Ma). Dark pink dots are radiolarian bioevents (Florindo et al., 2003), green dots are diatom bioevents (this study), light pink dots are diatom bioevents used as tie points (this study), blue dots are magnetostratigraphy (Florindo et al., 2003; Teitler et al., 2015; Grutzner et al., 2003). Solid black line joins age model tie-points (see Table 4).

both sites, linked to coincident climatic cooling (Pierce et al., 2017) since it occurs immediately prior to the Middle Miocene Climate Transition at 13.8 Ma (Shevenell et al., 2004).

4. Two of the bioevents which suggest the hiatus (LO *Nitzschia* sp. 17 at 14.17 Ma and LO *Denticulopsis maccollumii* at 14.14 Ma) are last occurrences, which are subject to error through reworking which can make it difficult to accurately place LO datums. As such, the first occurrences of species are generally considered more reliable biostratigraphic indicators (Whitehead et al., 2004).

5. The final diatom bioevent that indicates the hiatus, FO *Nitzschia denticuloides*, was assigned an age of 14.25 Ma by Sangiorgi et al. (2018). This age assignment aligns well with age/depth models at Site 747 and 744, but the same event is assigned an age of 13.5 Ma by D. Harwood (unpublished tables, based on a review of published data- see Section 4.1 for details), suggesting uncertainty exists with regards to dating this event, possibly due to latitudinal differences in Southern Ocean conditions.
6. Sea surface temperature trends at Site 1165, inferred from the abundance of *Actinocyclus ingens* group (Chapter 5), more closely align with trends at Sites 744 and 747 with the non-hiatus age/depth model (Appendix 3).

Despite outlined evidence supporting the absence of the hiatus, it cannot be definitively ruled out, hence, data from the relevant interval (12-15 Ma) at Site 1165 (as presented and discussed in Chapter 6) are plotted using both age models (see Appendix 3).

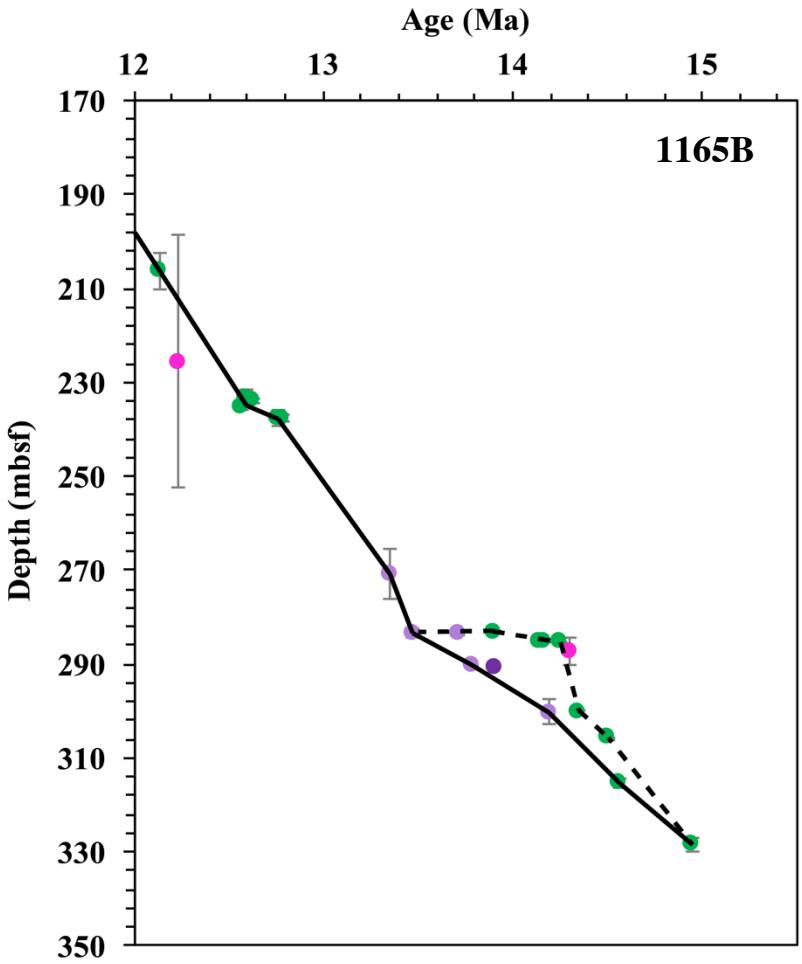

Figure 13. New proposed age model for ODP Site 1165 (15-12 Ma). Pink dots are radiolarian bioevents (Florindo et al., 2003), green dots are diatom bioevents (this study), lilac dots are new

quantitative diatom bioevents (this study; chronologically constrained at ODP Site 747), dark purple dot is IRD peak, chronologically-constrained at IODP Site U1356 (Pierce et al., 2017). Solid black line joins preferred tie-points (see Table 4). Dotted black line represents an alternative, less preferred age model for the Miocene interval at ODP Site 1165 (see text for discussion).

4.5. ODP Site 1171

The published age model for ODP Site 1171 (Shevenell et al., 2004; 2004b) shows disparities in the timing of major isotope events, such as the Middle Miocene Climate Transition, from other high resolution, astronomically-tuned global Middle Miocene reference sites such as IODP Site U1338 (Holbourn et al., 2014) and ODP Site 1146 (Holbourn et al., 2013). Therefore, I have revised the age model of ODP Site 1171 to facilitate accurate comparisons with Sites 747, 744 and 1165 and the high-resolution sea surface temperature record available at Site 1171 on the Tasman Rise (Shevenell et al., 2004). My new age model was constructed by tuning the high-resolution benthic oxygen and carbon isotope records from Site 1171 (Shevenell et al., 2008) to the high-resolution, astronomically-tuned benthic oxygen isotope record from IODP Site U1338 in the eastern equatorial Pacific (Holbourn et al., 2014) (Figures 14-15).

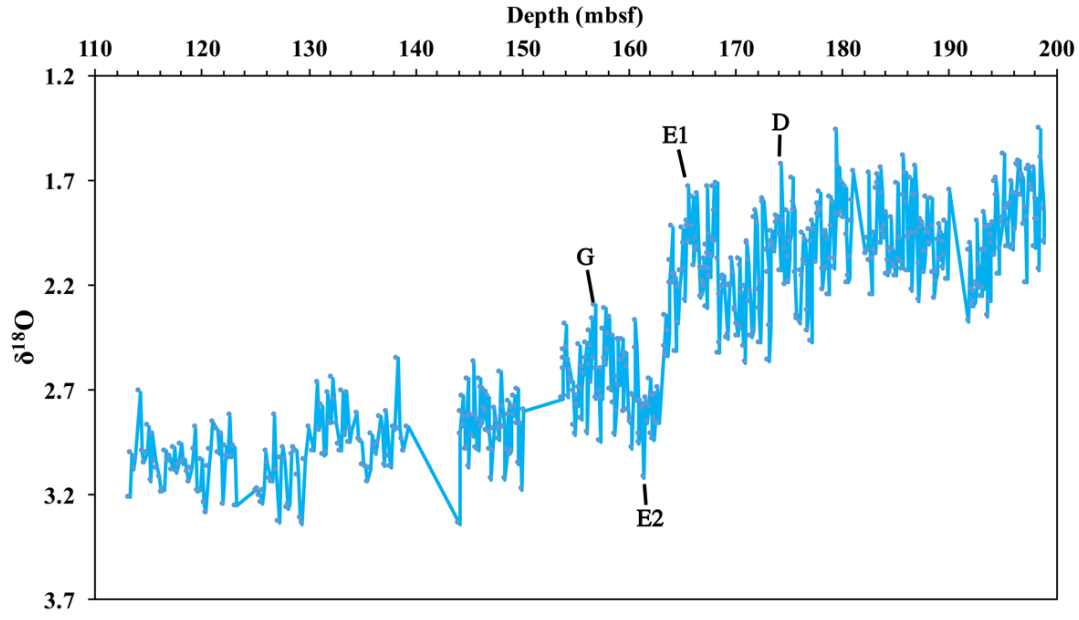

Figure 14. Benthic foraminiferal oxygen isotope record from ODP Site 1171 (Shevenell et al., 2008). Oxygen isotope events are indicated and constrained by biostratigraphy (Stickley et al., 2004).

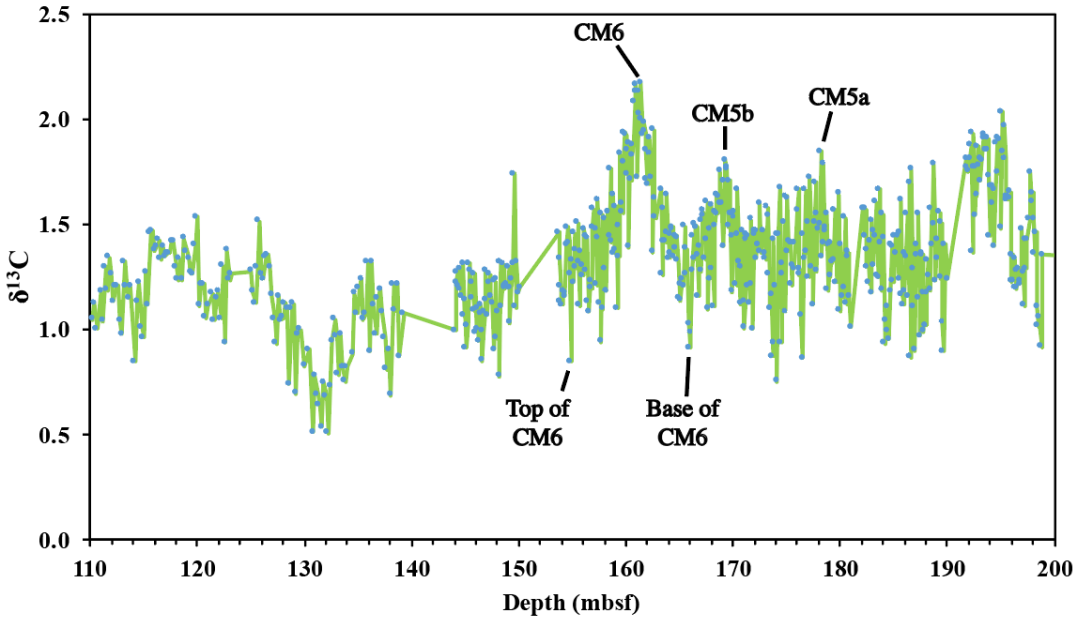

Figure 15. Benthic foraminiferal carbon isotope record from ODP Site 1171 (Shevenell et al., 2008). Carbon isotope events are indicated and constrained by biostratigraphy (Stickley et al., 2004).

Constrained by the revised isotope tie-points, I redefine the two normal polarity intervals below the section of no recovery between c.140-150 mbsf (originally identified as C5ACn and C5ADn, 167.2-156 mbsf; Stickley et al., 2004) as C5ABn and C5ACn, respectively. Thus, my new age model for Site 1171 is linear, with an R^2 of 0.99 (Figure 16). Using my new linear age model, benthic stable isotope events at Site 1171 better align chronologically with the same events at Site 747 (Majewski & Bohaty, 2010) and at other far-field, astronomically-tuned sites, for example ODP Site 1146 (Holbourn et al., 2013).

Table 3. Bioevents and datums recognized at ODP Hole 1171C, including magnetostratigraphy, biostratigraphy and isotope stratigraphy. Bioevents are included from Stickley et al. (2004) (S04), with age-assignments from Sangiorgi et al. (2018) (S18) and Stickley et al. (2004). Magnetostratigraphy is included and, in some cases, reinterpreted from Stickley et al. (2004) (see discussion in text). Isotope events are newly identified in isotope records of Shevenell et al. (2008) (Figures 9 and 10). The proposed age model at Site 1171 is linear (Figure 11).

Bioevent	Age (Ma)	Age reference	Mid-depth (mbsf)	Depth Error (mbsf +/-)

Top C5An.1n	12.05	S04, G12	129.75	
Base C5An.1n	12.17	S04, G12	130.60	
LAO *Cyrtocapsella tetrapera*	12.16	S04, S18	134.41	0.09
Top C5An.2n	12.27	S04, G12	133.40	
Base C5An.2n	12.47	S04, G12	134.50	
LO *Actinocyclus ingens* var. *nodus*	12.60	S04, S18	134.41	0.09
OIE F	12.74	S08, Sh04, This study	144.10	
LO *Calciduscus premacintyrei* (nannofossil)	12.76	S04	145.01	0.75
Top C5ABn	13.36	S04, G12	156.00	
OIE G	13.54	S08, Sh04, This study	156.78	
CIC Top CM6	13.55	S08, Sh04, This study	157.50	
Base C5ABn	13.61	S04, G12	159.35	
CIE CM6	13.73	S08, Sh04, This study	160.90	
Top C5ACn	13.74	S04, G12	161.30	
OIE end shift E	13.76	S08, Sh04, This study	162.77	
OIE start shift E	13.91	S08, Sh04, This study	166	
CIE Base of CM6	13.92	S08, Sh04, This study	166.00	
Base C5ACn	14.07	S04, G12	169.30	
CIE CM5b	14.07	S08, Sh04, This study	169.30	
OIE D	14.39	S08, Sh04, This study	174.83	
CIE CM5a	14.64	S08, Sh04, This study	178.20	
FO *Orbulina suturalis*	15.10	S04	1855.55	4.50

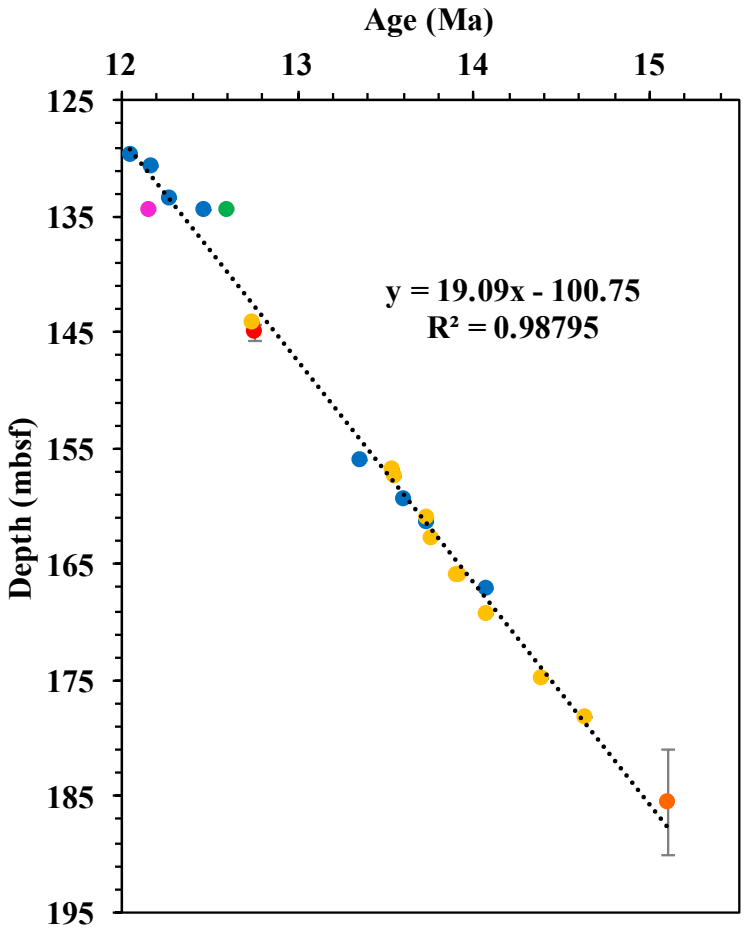

Figure 16. Proposed age model for ODP Site 1171. Blue dots are paleomagnetic reversals (Stickley et al., 2004), yellow dots are isotope events (this study), pink dots are radiolarian bioevents (Stickley et al., 2004), red dots are planktonic foraminifera bioevents (Stickley et al., 2004), orange dots are nannofossil bioevents (Stickley et al., 2004), green dots are diatom bioevents (Stickley et al., 2004). Dotted line represents linear age model for ODP Site 1171.

4.6. ODP Site 1138

New records of *Thalassiothrix* and *Trichotoxon* spp. (*Thlx* group) abundance and diatom concentration from ODP Site 1138, situated on the Kerguelen Plateau and presented in this thesis (Chapter 7), use the well-resolved biomagnetostratigraphic age model of Backman et al. (2013).

5. Neogene Diatom Palaeoecology

5.1. Introduction

Diatoms are sensitive to the environmental parameters of the water column in which they live (Section 1.3), making them useful palaeoceanographic sedimentary archives. The ecological preferences of extant species can be inferred from their associations with modern environmental variables, for example, water column temperature, stratification, salinity, nutrient availability and the presence of sea ice (e.g. Armand et al., 2005; Crosta et al., 2005; Romero et al., 2005). However, inferring the paleoecology of extinct diatom species is more challenging. Inferences of extinct species paleoecology can be made using:

- Paleobiogeographical distributions and occurrences. For example, a species that is much more abundant at low latitudes can be assumed to prefer warmer waters, with equivalent high latitude species assumed to prefer cooler waters.
- Paleoenvironmental conditions during evolution or extinction. If a species evolves during a particularly warm period, or goes extinct during a particularly cool interval, it may be assumed that the species prefers warm conditions.
- Co-occurrences with other species; particularly, but not exclusively, with extant species of known ecological affinity. For example, if a species of unknown paleo-ecology consistently co-occurs in the fossil record with an extant species known to proliferate within a stratified water column, it can be inferred that the extinct species may also prefer stratified conditions. Inferences can also be made on the basis of co-occurrences with extinct species of well-evidenced inferred ecological preferences, for example, with low-latitude species which are assumed to prefer warm sea surface temperatures, although such indirect inferences are more tenuous.
- Taxonomic relationships and morphological similarities to other species particularly, but not exclusively, with extant species of known ecological affinities. For example, evidence for the first Eocene Arctic sea ice comes from abundant, exceptionally-preserved *Synedropsis* diatoms documented from the central Arctic IODP ACEX core. Stickley et al. (2009) inferred the presence of sea ice based on the close taxonomic relationship and morphological similarity of the extinct *Synedropsis* species to extant sea-ice associated *Synedropsis* species (Hasle et al., 1994). Further evidence for the sea-ice association came from the co-occurrence of the fossil *Synedropsis* with IRD. However, interpretations are complicated by species from within the same genus sometimes exhibiting contrasting ecological preferences. For example, *Fragilariopsis curta* is

associated with sea ice (Armand et al., 2005), while *Fragilariopsis doliolus* thrives in warm waters at low latitudes (Hasle, 1976).

- Correlations with other paleoproxies. If species abundance correlates with independent proxies for sea surface temperature, it can be assumed that the presence of the species is related to sea surface temperature. Significant potential exists in this area; for example, assessing diatom species occurrences alongside proxy records for nutrient status and productivity, temperature or sea ice. However, no such studies have been published to date using Neogene Southern Ocean diatoms, other than a few Pliocene diatom assemblage studies (Winter et al., 2010; Sjunneskog & Winter, 2012; Taylor-Silva & Riesselmann, 2018) that compare Southern Ocean diatom assemblages with other proxy records.

Despite being able to infer the paleoecological niches of extinct diatoms using the methods described above, several limitations remain. Fossil diatom ecology is often not limited by only one environmental variable, but rather reflects a suite of intersecting conditions, as with modern species (Armand et al., 2005; Crosta et al., 2005; Romero et al., 2005). For example, even if ideal temperature conditions are met, a species that proliferates when temperature and nutrient conditions fall within a particular range may not proliferate under ideal temperatures if insufficient nutrients are available. Thus, care must be taken when interpreting associations with single ecological variables from the presence of a particular species. Further, the balance of species within an assemblage could affect individual species niches. For example, one species may out-compete others within a given assemblage at particular nutrient concentrations, but the same species may be out-competed by extinct species with more efficient nutrient conversion strategies within an older assemblage. As such, that species would show different abundances at the same nutrient concentrations. Another important consideration is that species niches may change through time. If a modern species is associated with sea ice, it may only have evolved to tolerate sea ice later in its evolutionary history and, thus, early occurrences may represent different environmental conditions. However, despite these limitations, variability within ancient microfossil assemblages, including diatom assemblages, still closely corresponds with and has been used to document environmental change during the Cenozoic era (e.g., Winter et al., 2010; Villa et al., 2014; Lyle & Baldauf, 2015).

5.2. The paleoecology of Neogene Southern Ocean diatoms at ODP Sites 747, 744 and 1165

The interpretation of diatom species paleoecology in this thesis is based on the principles outlined in Section 5.1. A number of records exist with which to contextualise ecological interpretations for diatom species within different time intervals between 15 Ma and present. Between 15-12 Ma, the latitudinal transect of three high-resolution diatom assemblage records presented in this thesis (ODP Sites 747, 744 and 1165) can be used to assess latitudinal distributions and, therefore, to infer species sea surface temperature (SST) preferences, since SST varies strongly by latitude in the Southern Ocean (Figure 1). From 12 Ma to present, only the diatom assemblage record from Site 1165 is presented, therefore, interpretations from

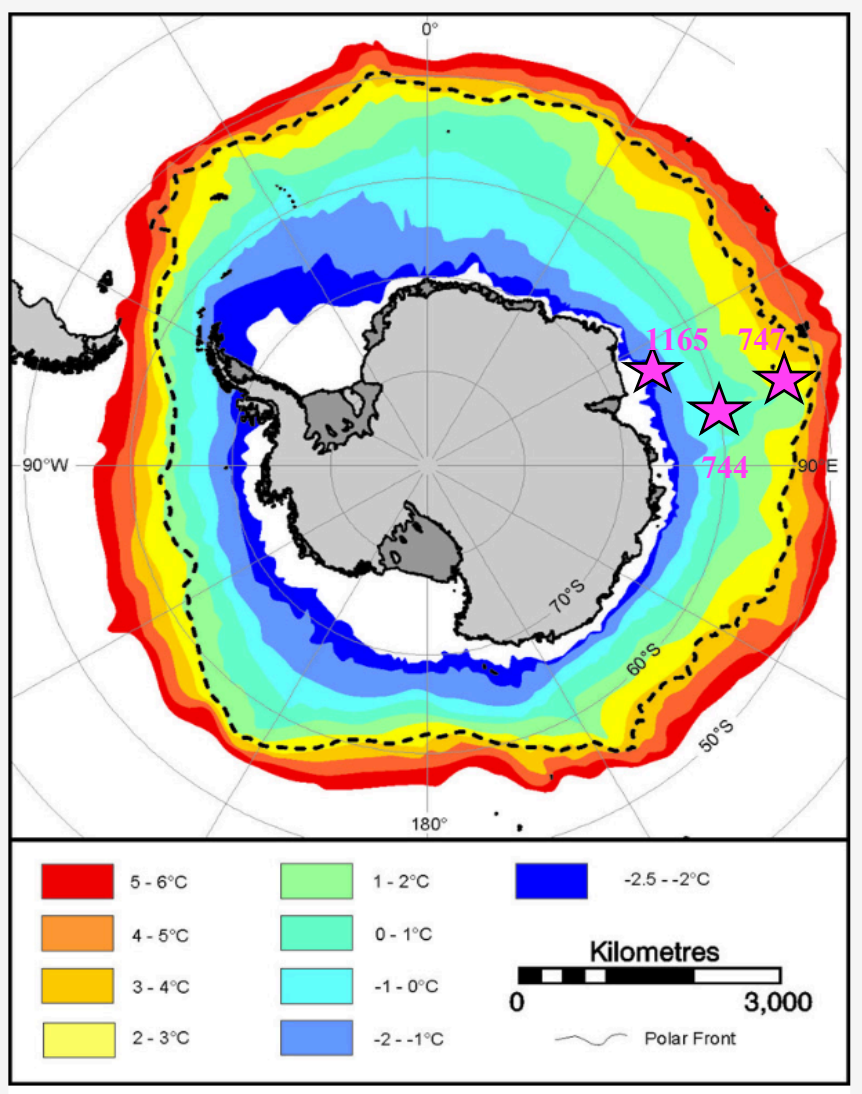

Figure 1. Modern Summer Southern Ocean sea surface temperatures (2002-2015); pink stars and numbers indicate the core sites at which diatom assemblages are investigated in this thesis. Figure modified from the British Antarctic Survey.

this interval will also rely upon co-varying species within the same record and published studies documenting paleo-occurrences. Many Pleistocene species are extant and have well established paleoecological preferences. Several previously published diatom assemblage studies also provide context for Pliocene diatom species ecology (Winter et al., 2010; Sjunneskog & Winter, 2012; Taylor-Silva & Riesselman, 2018). However, no Southern Ocean diatom assemblage studies have yet focused on the palaeoecologies of Late Miocene diatom assemblages, other than the PhD thesis of Censarek (2002) and, as such, the evidence for species preferences from this interval is weakest. Nonetheless, many biostratigraphic studies have documented paleo-occurrences within the Southern Ocean and globally during the Late Miocene and, as such, some robust conclusions can still be drawn from this interval.

For ease of interpretation, I have separated the planktonic species identified at Sites 747, 744 and 1165 by inferred paleoecological preferences into nine groups: warm; cool; high productivity; stratification; sea ice; reworked; neritic; benthic; and other. Planktonic diatom species are found throughout the 15-12 Ma interval at Sites 744, 747 and 1165, dominating the assemblage particularly after c. 13.8 Ma. Between 15-12 Ma, species abundances are assessed relative to the more northerly and, therefore, warmer Site 747 and the more southerly, cooler, Site 1165.

From 12 Ma to present, ecological preferences are assessed relative only to the position of Site 1165 at 64°S on the continental rise, offshore of Prydz Bay and south of the SACCF, with assumptions primarily based on paleo-occurrences documented within the literature. In general, cosmopolitan or subantarctic species are considered relatively warm, while species primarily documented south of the Polar Front are assigned to the cool group. Unfortunately, this removes some nuance with regards to those diatom species most abundant within the Polar Frontal Zone (PFZ), since the PFZ occurs to the north of Site 1165 and, thus, could be considered relatively warm. This is also a consideration when assigning species to groups based on increased abundances at the relatively northerly Site 747, which is still positioned south of the Polar Front. However, most of the species associated with the modern PFZ are endemic to the Southern Ocean; for example *Fragliariopsis kerguelensis* and *Thalassiosira lentiginosa* and, in the context of the 15 Ma record, evolved following global cooling and increasing Antarctic thermal isolation the Middle Miocene Climatic Transition (13.8 Ma), and so are assigned to the cool group.

5.2.1. Paleoecological groups

The paleoecological preferences of the diatoms encountered in this study are tabulated below. Full details, reasoning and evidence behind the inclusion of each species into its designated ecological group can be found in Appendix 1.

Table 1. Warm water species

Warm water species	
Extant	**Extinct**
Actinocyclus ehrenbergii	*Actinocyclus ingens group*
Dactyliosolen aantarcticus	*Actinocyclus ingens* var. *nodus*
Fragilariopsis rhombica	*Actinocyclus ingens* var. *ovalis*
Fragilariopsis pseudonana	*Actinocyclus* sp. *nov* #1
Hemidiscus cuneiformis	*Actinoptychus senarius*
Hemidiscus karstenii	*Azpeitia endoi*
Hemidiscus ovalis	*Azpeitia* spp.
Hemidiscus triangularis	*Azpeitia tabularis*
Shionodiscus tetraoestrupii	*Cavitatus jouseanus*
Shionodiscus tetraoestrupii var. reimerii	*Coscinodiscus marginatus*
Stellarima stellaris	*Crucidenticula nicobarica*
Thalassionema nitzschioides var. *parva*	*Fragilariopsis praeinterfrigidaria*
	Fragilariopsis reinholdii
	Fragliariopsis clementia
	Fragliariopsis interfrigidaria
	Fragliariopsis miocenica
	Fragliariopsis mutayamae
	Fragliariopsis porteri
	Fragliariopsis weaveri
	Rouxia californica
	Rouxia peragalli
	Shionodiscus praeoestrupii
	Thalassiosira complicata
	Thalassiosira convexa var. *aspinosa*
	Thalassiosira elliptipora

	Thalassiosira insigna
	Thalassiosira inura
	Thalassiosira miocenica
	Thalassiosira nativa
	Thalassiosira torokina
	Thalassiosira vulnifica
	Trinacria excavata

Table 2. Cool water species

Cool water species	
Extant	**Extinct**
Eucampia antarctica var. *recta*	*Actinocyclus karstenii*
Fragilariopsis separanda	*Denticulopsis crassa*
Fragliariopsis kerguelensis	*Denticulopsis delicata*
Thalassiosira lentiginosa	*Denticulopsis dimorpha*
Thalassiosira oliveriana	*Denticulopsis dimorpha* var. *areolata*
Coscinodiscus oculus-iridus/asteromphalus	*Denticulopsis hustedii* var. *aspera*
	Denticulopsis hutedii
	Denticulopsis hyalina
	Denticulopsis lauta
	Denticulopsis maccollumii
	Denticulopsis maccollumii var. *A*
	Denticulopsis ovata
	Denticulopsis praedimorpha
	Denticulopsis simonsenii/vulgaris
	Denticulopsis sp. 3
	Eucampia antarctica var. *twista*
	Fragilariopsis arcula
	Fragilariopsis aurica
	Fragilariopsis barronii
	Fragilariopsis claviceps
	Fragilariopsis donahuensis

	Fragilariopsis efferans
	Fragilariopsis januaria
	Fragilariopsis januaria var. A
	Fragilariopsis lacrima
	Fragilariopsis pseudokerguelensis
	Fragilariopsis sp. A
	Fragilariopsis sp. nov #1
	Fragilariopsis sp. nov #2
	Fragilariopsis sp. nov #3
	Fragilariopsis sp. nov #4
	Fragilariopsis spp.
	Nitzschia denticuloides
	Nitzschia denticuloides var. 17
	Nitzschia grossepunctata
	Rouxia isopolica
	Rouxia spp.
	Thalassiosira cf. *antarctica*
	Thalassiosira kolbei
	Thalassiosira mahoodii
	Thalassiosira oliveriana var. *sparsa*
	Thalassiosira striata
	Thalassiosira torokina

Table 3. High productivity species

High productivity species	
Extant	**Extinct**
Chaetoceros (Hyalochaete) resting spores	*Liradiscus* resting spores
Thalassionema nitzschioides var. *nitzschioides*	
Thalassiothrix spp.	
Trichotoxon reinboldii	

Table 4. Sea ice species

Sea ice species	
Extant	**Extinct**
Actinocyclus actinochilus	*Fragilariopsis bohatyii*
Fragilariopsis cf. curta	*Fragilariopsis maleinterpretaria*
Fragilariopsis cf. linearis	*Fragilariopsis praecurta*
Fragilariopsis cf. vanheurckii	*Fragilariopsis pusilla*
Fragilariopsis curta	*Fragilariopsis robusta*
Fragilariopsis obliquecostata	*Fragilariopsis truncata*
Fragilariopsis ritscherii	*Rouxia antarctica*
Fragilariopsis sublinearis	*Rouxia diploneides*
Fragilariopsis vanheurckii	*Rouxia naviculoides*
Stellarima microtrias	*Synedropsis* sp. 1
Thalassiosira tumida	*Synedropsis* sp. A
	Synedropsis sp. B
	Synedropsis sp. C
	Synedropsis spp.

Table 5. Stratification species

Stratification species	
Extant	**Extinct**
Corethron pennatum	*Rhizosolenia costata*
Rhizosolenia hebetata	*Rhizosolenia harwoodii*
Rhizosolenia hebetata var. *hiemalis*	*Rhizosolenia* sp. 1
Rhizosolenia styliformis	*Rhizosolenia* sp. 3
	Rhizosolenia sp. 2
	Rhizosolenia spp.

Table 6. Neritic species

Neritic species	
Extant	**Extinct**

Delphineis spp.	*Stephanopyxis* sp. B
Ellerbeckia sol	*Actinocyclus* sp. nov #2
Paralia sulcata	
Stephanopyxis turris	

Table 7. Benthic species

Benthic species	
Extant	**Extinct**
Arachnodiscus spp.	*Isthmia* spp.
Cocconeis spp.	*Kisseleviella* spp.
Cymatosira spp.	*Lithodesmium* cf. *minisculum*
Diploneis spp.	*Sphynctolethus* spp.
Entopyla spp.	
Grammatophora spp.	
Melosira spp.	
Navicula spp.	
Pleurosigma spp.	
Raphonies spp.	
Rhabdonema japonicum	
Rhabdonema spp.	
Synedra spp.	
Trigonium antarcticum	

Table 8. Reworked species.

Reworked species (all extinct)
Hemiaulus spp.
Rocella gelida
Pyxilla spp.

5.2.2. Group 9: other species

It was not possible to assign a number of species to paleoecological groups on the basis of existing evidence. However, none of these species make up >6% of the assemblage, and as such

their exclusion does not preclude the palaeoceanographic interpretation of diatom assemblage records presented in this thesis. The species included in this 'other' group are:

***Actinocyclus fasciculatus* (2%; 2.80-1.88 Ma), *Actinocyclus fryxellae* (5%; 10.73-3.15 Ma), *Actinocyclus maccollumii* (1%; 2.80 Ma), *Actinocyclus octonarius var. asteriscus* (<1%; 9.04 Ma), *Actinocyclus spp.* (6%; present throughout the entire 15 Ma interval), *Asterolampra punctifiora* (<1%; 14.14 Ma), *Asteromphalus kenettii* (1%; 10.31-9.16 Ma), *Asteromphalus cf. parvalus (*<1%; 14.08-6.20 Ma), *Cavitatus miocenicus* (1%; present from the beginning of the record until 4.52 Ma), *Entopyla* spp. (<1%; present from the beginning of the record until 14.36 Ma), *Eurossia* spp. (<1%; 14.53-14.30 Ma), *Lisitznia ornata* (<1%; 9.04 Ma), *Nitzschia* cf. *challengerii* (<1%; 14-13.98 Ma), *Proboscia praebarboi/barboi* (<1%; 10.73-3.39 Ma), *Thalassiosira cf. eccentrica* (<1%; 9.40-3.11 Ma), *Thalassiosira gersondeii* (2%; 9.16-4.39 Ma), *Thalassiosira jacksonii* (<1%; 5.21-3.11 Ma), *Thalassiosira maculata* (1%; 8.81 Ma- present), *Thalassiosira nansenii* (<1%; 10.66 Ma), *Thalassiosira praelineata* (3%; 9.10-5.77 Ma), *Unidentified centric* sp. 3 (<1%; 13.92-13.78 Ma), plus *Thalassiosira sp. 1-14 & Thalassiosira spp.* (4%),**

5.2.3. *Actinocyclus ingens* abundance; a proxy for sea surface temperature

The *Actinocyclus ingens* group was assigned warm-water preferences (Table 1) based on its cosmopolitan, including frequently low-latitude, distribution (Barron, 1985; Lazarus, 1994) and greater abundance at ODP Site 747 (83%) than ODP Site 1165 (54%) between 15-12 Ma. In support of this palaeoecological interpretation, *Actinocyclus ingens* group abundance varies closely with the planktonic $\delta^{18}O$ record at Site 747 (Figure 2) (Majewski & Bohaty, 2010). Between 15-14.6 Ma (78-76 mbsf) and 14-13.2 Ma (70-65 mbsf), *A. ingens* abundance varies more closely with *Globigerina bulloides* $\delta^{18}O$ (Bohaty & Majewski, 2010), while in the other sections it varies more closely with G*loborotalia praescitula* $\delta^{18}O$. Differences between *A. ingens* group abundance and $\delta^{18}O$, in general, may be attributed to the ice volume component of the $\delta^{18}O$ signal, while differences between *A. ingens* group abundance and the $\delta^{18}O$ records of different planktonic foraminifera species could plausibly represent changing depth-habitats or seasonal preferences of either the two planktonic foraminifera species, or of *A. ingens*. Either way, the close variation between *A. ingens* group and $\delta^{18}O$ suggests *A. ingens* group abundance can be considered a proxy for sea surface temperature.

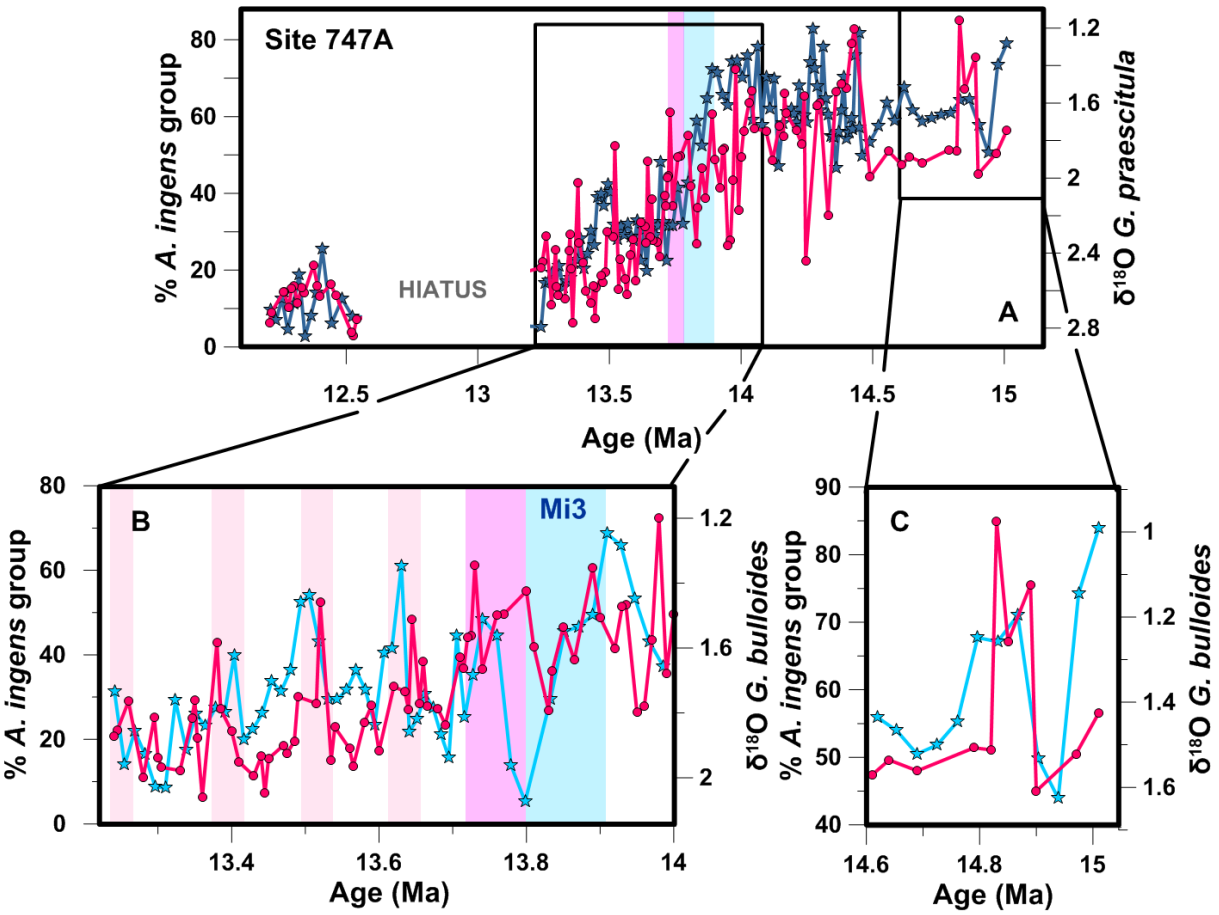

Figure 2. *Actinocyclus ingens* group (including *Actinocyclus ingens* var. *nodus* and *Actinocyclus* aff. *ingens)* abundance (pink) with foraminiferal planktonic $\delta^{18}O$ (dark blue - *Globorotalia praescitula*, light blue - *Globigerina bulliodes*) from ODP Site 747 (Bohaty & Majewski, 2010).

5.2.4. Diatom plates

In this section, plates are presented illustrating all of the abundant taxa identified in this thesis.

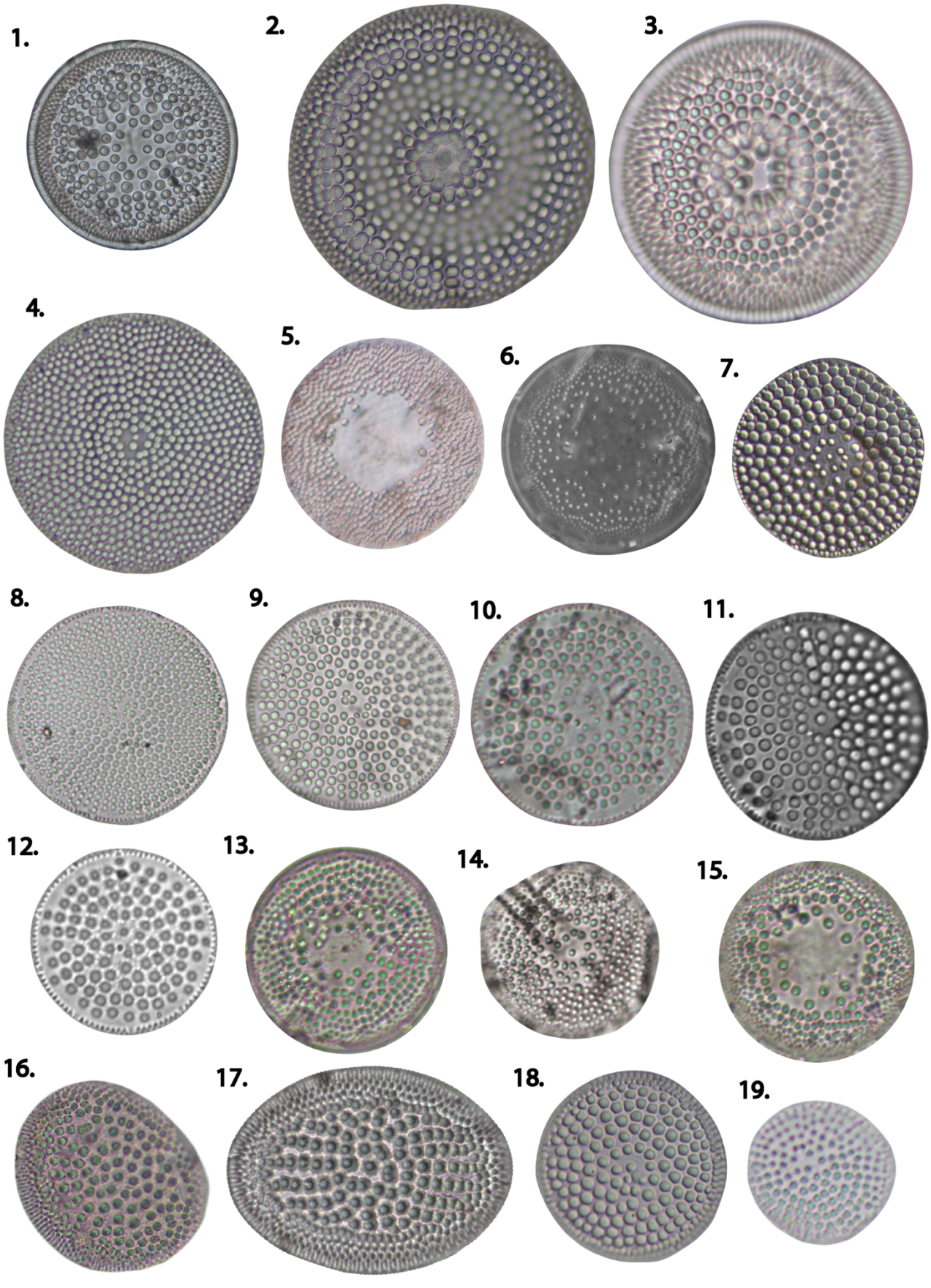
1.
2.
3.
4.
5.
6.
7.
8.
9.
10.
11.
12.
13.
14.
15.
16.
17.
18.
19.
20 µm

Plate 1

1. *Actinocyclus ingens* (1165B-36X-6W, 95-96 cm), **2**. *Actinocyclus ingens* var. *nodus* (744B-8H-2W, 104-105 cm), **3**. *Actinocyclus ingens* var. *nodus* (744B-7H-5W, 126-127 cm), **4**. *Actinocyclus octonarius* (744B-8H-3W, 62-63 cm) **5**. *Actinocyclus ingens* var. 4 (1165B-34X-3W-55-56 cm), **6**. *Actinocyclus* sp. nov #1 (Bohaty plate 13 Fig. 3) (747A-8H-2W, 83-84 cm), **7**. *Azpeitia* spp. (744B-7H-4W, 108-109 cm) **8**. *Azpeitia tabularis* (747A-8H-2W, 103-104 cm) **9**. *Azpetia endoi/tabularis* (1165B-33X-4W, 105-106 cm), **10**. *Azpeitia* sp. (1165B-39X-2W, 140-141 cm), **11-12**. *Azpeitia endoi* (744B-7H-4W, 132-133 cm), **13-14**. *Actinocyclus* sp. nov #2 (1165B-30X-1W, 86-87 cm), **15**. *Actinocyclus* sp. nov #2 (1165B-34X-6W, 85-86 cm), **16**. *A. ingens* var. *ovalis* (747A-8H-4W, 10-11 cm), **17**. *Araniscus lewisianus* (744B-8H-5W, 84-85 cm) **18**. *Azpeitia harwoodii* (744B-8H-2W, 100-101 cm) **19**. *Actinocyclus* sp. (744B-8H-2W, 140-141 cm)

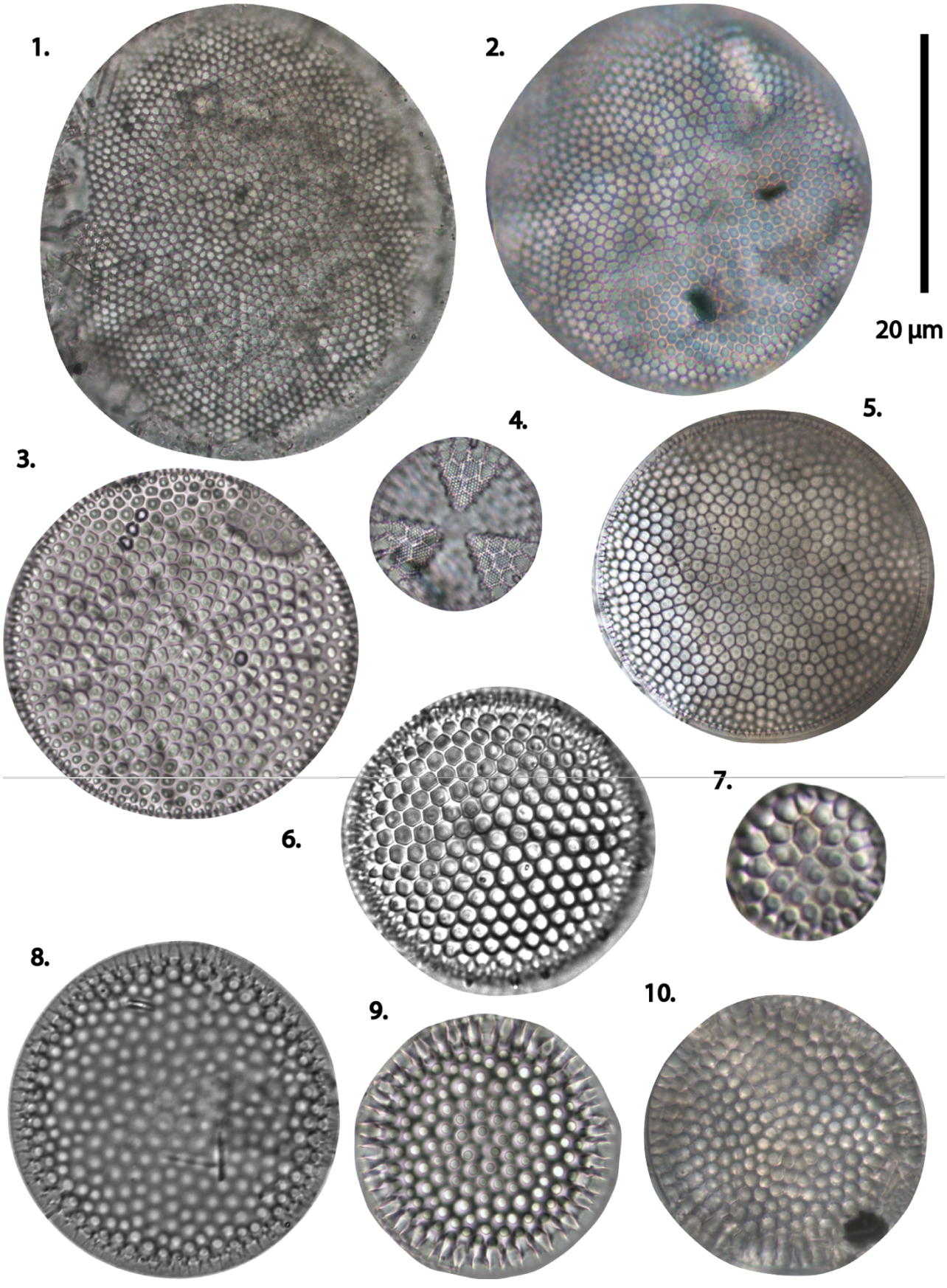
1.
2.
20 µm
3.
4.
5.
6.
7.
8.
9.
10.

Plate 2

1. *Coscinodiscus oculus-iridus/astermophalus* (1165B-28X-5W, 96-97 cm), **2.** *Coscinodiscus oculus-iridus/asteromphalus* (1165-32X-2W, 92-93 cm), **3.** *Coscinodiscus radiatus* (1165B-38X-1W, 135-136 cm), **4.** *Actinoptychus senarius* (744B-8H-5W, 84-85 cm) **5.** *Coscinodiscus radiatus* (1165B-34X-3W, 115-116 cm), **6.** *Thalassiosira* sp. nov (1165B-33X-4W, 5-6 cm), **7.** *Coscinodiscus* sp. A (744B-7H-3W, 10-11 cm) **8.** *Coscinodiscus marginatus* (744B-7H-5W, 18-19 cm), **9-10.** *Cosconidiscus marginatus* (744B-7H-4W, 120-121 cm)

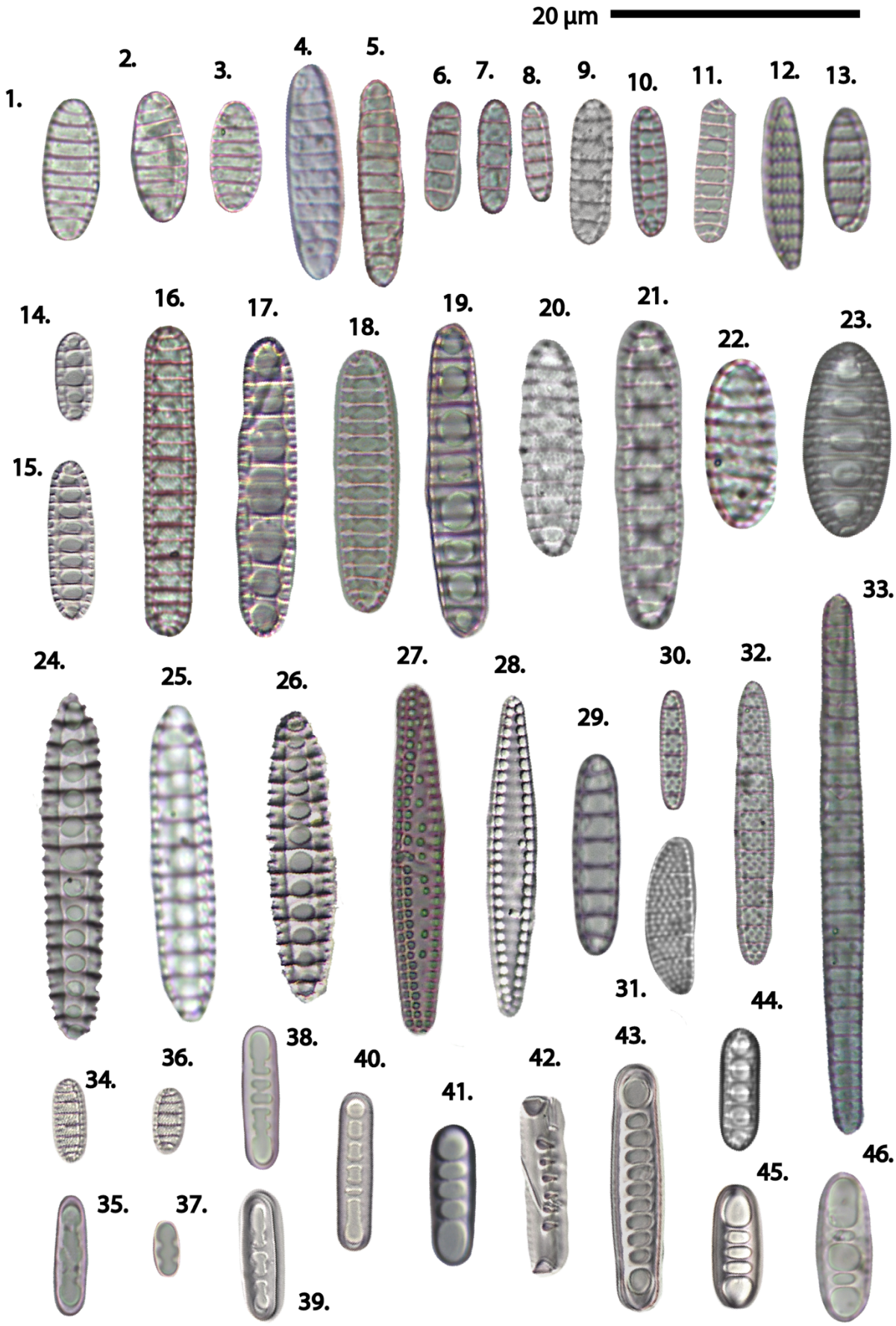
20 µm
1.
2.
3.
4.
5.
6.
7.
8.
9.
10.
11.
12.
13.
14.
15.
16.
17.
18.
19.
20.
21.
22.
23.
24.
25.
26.
27.
28.
29.
30.
31.
32.
33.
34.
35.
36.
37.
38.
39.
40.
41.
42.
43.
44.
45.
46.

Plate 3

1. *Denticulopsis* cf. *lauta* (1165B-36X-1W, 45-46 cm), **2.** *Denticulopsis* cf. *lauta* (1165B-33X-6W, 45-46 cm), **3.** *Denticulopsis* cf. *lauta* (1165B-36X-1W, 45-46 cm), **4.** *Denticulopsis* cf. *lauta* (1165B-34X-5W, 35-36 cm) **5.** *Denticulopsis* cf. *lauta* (1165B-34X-5W, 35-36 cm), **6.** *Denticulopsis* cf. *lauta* (1165B-39X-2W, 140-141 cm), **7.** *Denticulopsis praelauta* (1165B-39X-2W, 140-141 cm), **8.** *Denticulopsis lauta* (744B-8H-2W, 100-101), **9**. *Denticulopsis lauta* (744B-8H-2W, 78-79 cm), **10-11**. *Denticulopsis lauta* (744B-7H-5W, 106-107 cm; 744B-8H-2W, 100-101 cm), **12.** *Denticulopsis/Fragliariopsis* (744B-7H-3W, 138-139 cm), **13.** *Denticulopsis/Fragliariopsis* (744B-7H-3W, 66-67 cm), **14-15.** *Denticulopsis praehyalina* (744B-7H-5W, 106-107 cm), **16.** *Denticulopsis simonsenii/vulgaris* (1165B-34X-5W, 35-36 cm), **17.** *Denticulopsis vulgaris* (747A-8H-3W, 14-15 cm), **18.** *Denticulopsis vulgaris* (1165B-30X-1W, 86-87), **19.** *Denticulopsis simonsenii/vulgaris* (1165B-27X-2W, 120-121 cm), **20.** *Denticulopsis simonsenii/vulgaris* (747-8H-3W, 127), **21.** *Denticulopsis simonsenii* (744B-7H-5W, 106-107) **22.** *Denticulopsis vulgaris* (1165B-28X-4W, 6-7), **23.** *Denticulopsis crassa* (744B-8H-1W, 34-35) **24-26.** *Denticulopsis hyalina* (744B-7H-5W, 106-107 cm; 744B-7H-4W, 132-133 cm) **27.** *Denticulopsis maccollumii* var. A (744B-8H-4W, 62-63 cm), **28.** *Denticulopsis maccollumii* var. A (744B-8H-5W, 84-85 cm) **29.** *Denticulopsis maccollumii* sp. 1 (744B-8H-2W, 140-141 cm), **30.** *Crucidenticula nicobarica* (747A-8H-2W, 103-104 cm), **31.** *Crucidenticula* cf. *nicobarica* (747-8H-3W, 143-144 cm), **32.** *Crucidenticula nicobarica* (744B-7H-4W, 4-5 cm), **33.** *Denticulopsis delicata* (1165B-27X-1W, 121-122 cm), **34.** *Denticulopsis dimorpha* (744B-7H-1W, 2-3 cm), **35.** *Denticulopsis praedimorpha* (744B-7H-1W, 2-3 cm) **36.** *Denticulopsis praedimorpha* (744B-7H-1W, 2-3 cm), **37.** *Denticulopsis praedimorpha* (744B-7H-1W, 2-3 cm), **38-40.** *Denticulopsis praedimorpha* var. *intermedia* (744B-7H-1W, 2-3 cm), **41.** *Denticulopsis dimorpha* (744B-7H-1W, 2-3 cm) **42.** *Denticulopsis dimorpha*, girdle view (744B-7H-1W, 2-3 cm), **43.** *Denticulopsis dimorpha* (744B-7H-1W, 2-3 cm), **44.** *Denticulopsis dimorpha* (744B-7H-4W, 132-133 cm), **45.** *Denticulopsis dimorpha* (744B-7H-1W, 2-3 cm), **46.** *Denticulopsis ovata* (1165B-24X-2W, 80-81 cm)

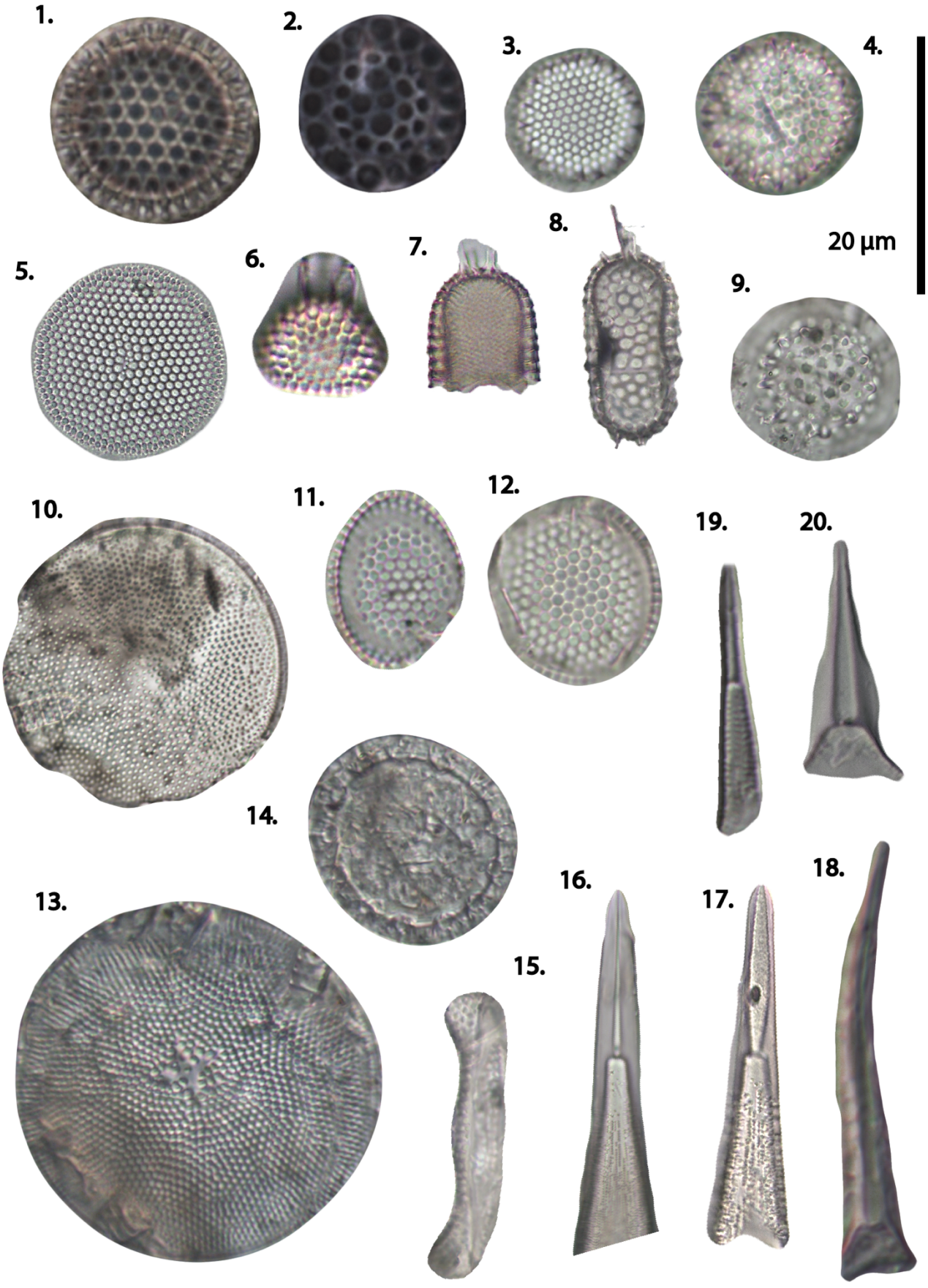
1.
2.
3.
4.
20 µm
5.
6.
7.
8.
9.
10.
11.
12.
19.
20.
14.
13.
16.
17.
18.
15.

Plate 4

1. *Stephanopyxis* sp. (747A-8H-3W, 139-140 cm), **2.** *Macrora barbadensis?* (747A-8H-3W, 139-140 cm), **3.** *Stephanopyxis* sp. (1165B-38X-2W, 135-136 cm), **4.** *Stephanopyxis* sp. (1165B-36X-1W, 45-46 cm), **5.** *Thalassiosira* cf. *antarctica* (747A-8H-4W, 118-119 cm), **6.** *Stephanopyxis turris* (744B-7H-5W, 106-107 cm), **7.** *Stephanopyxis turris* (747A-8H-4W, 90-91 cm), **8.** *Stephanopyxis turris* (1165B-35X-3W, 15-16 cm), **9.** *Macrora stella*? (1165B-36X-CCW, 15-16 cm), **10.** *Actinocyclus karstenii* (1165B-33X-6W, 85-86 cm), **11-12.** *Stephanopyxis* sp. B (1165B-4W, 105-106 cm), **13.** *Stellarima microtrias* (1165B-20X-3H, 21-22 cm), **14.** *Corethron pennatum* (1165B-20X-3H-21-22 cm), **15.** *Eucampia antarctica* var. *recta* (1165B-39X-2W, 90-91 cm), **16.** *Rhizosolenia hebetata* var. *hiemalis* (1165B-24X-2W, 80-81 cm), **17.** *Rhizosolenia hebetata* var. *hiemalis* (744B-7H-1W, 2-3 cm), **18.** *Rhizosolenia* sp. 1 (1165B-34X-2W, 5-6 cm), **19.** *Rhizosolenia hebetata* (744B-4W-84-85 cm), **20.** *Rhizosolenia styliformis* (744B-8H-2W, 100-101 cm)

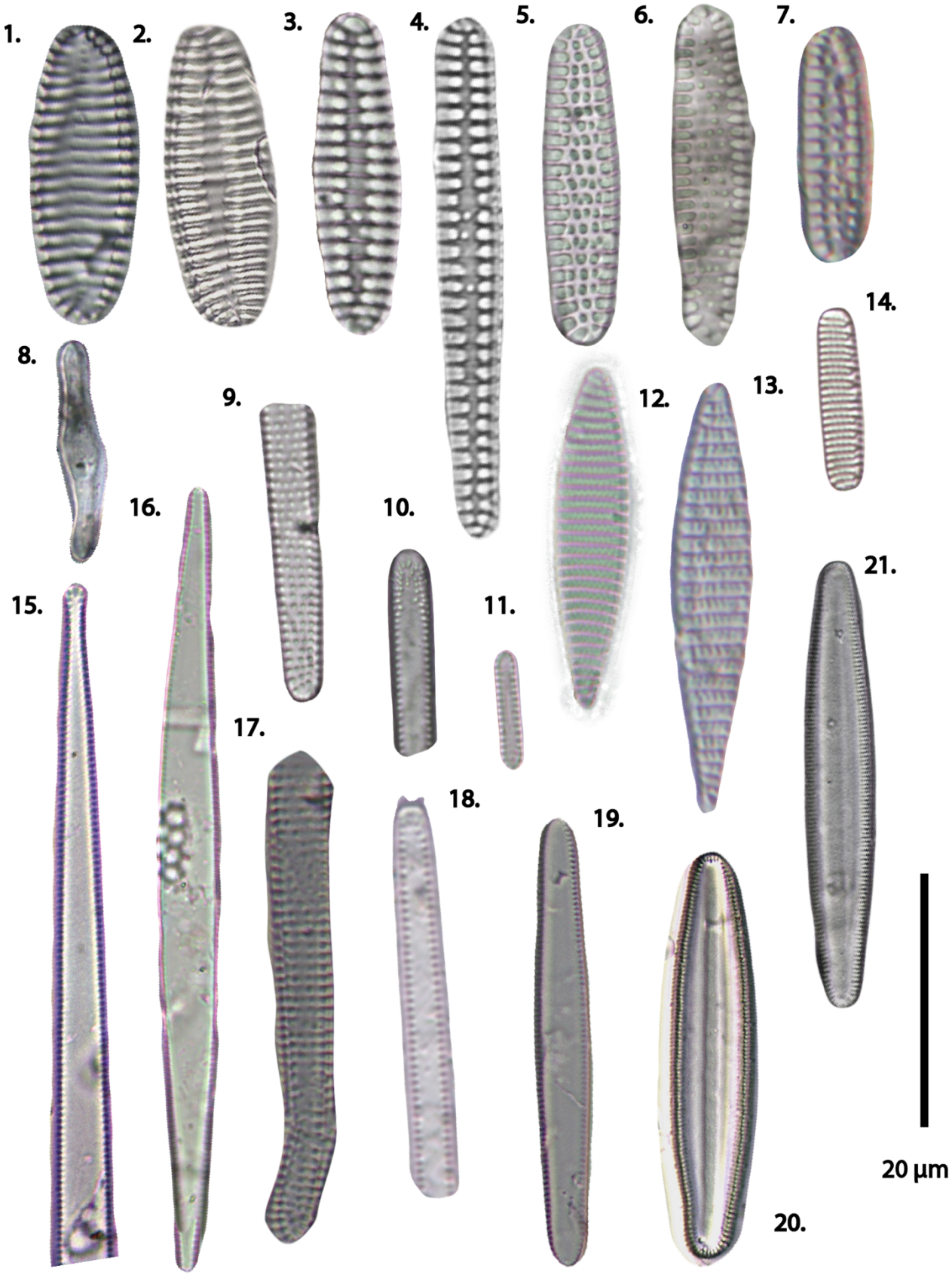
1.
2.
3.
4.
5.
6.
7.
8.
9.
10.
11.
12.
13.
14.
15.
16.
17.
18.
19.
20.
21.
20 µm

Plate 5

1-2. *Nitzschia denticuloides* (744B-7H-1W, 2-3 cm), **3.** *Nitzschia* sp. 17 (744B-7H-4W, 120-121 cm), **4.** *Nitzschia* sp. 17 (744B-7H-4W, 116-117 cm), **5.** *Nitzschia grossepunctata* (744B-7H-4W, 120-121 cm), **6.** *Niztschia grossepunctata* (744B-8H-5W, 19-20 cm), **7.** *Nitzschia grossepunctata* (1165B-34X-2W, 55-56 cm), **8.** *Thalassionema* sp. (1165B-39X-2W, 90-91 cm), **9.** *Nitzschia* sp. 3 (Farmer) (744B-8H-3W, 78-79 cm), **10**. *Trichotoxon reinboldii* (744B-8H-5W, 84-85 cm), **11.** *Thalassionema nitzschioides* var. *parva* (744B-7H-5W, 126-127 cm), **12.** *Fragilariopsis donaghensis* (747-8H-3W, 127 cm), **13.** *Fragilariopsis pseudokerguelensis* (747A-8H-2W, 43-44 cm), **14.** *Nitzschia* cf. *challengeri* (744B-8H-2W, 12-13 cm), **15.** *Cavitatus miocenicus* (744B-7H-05W, 38-39 cm), **16.** *Cavitatus miocenicus* (1165B-36X-1W, 45-46 cm), **17.** *Nitzschia* sp. 3 (744B-8H-2W, 100-101) **18.** *Thalassiothrix* sp. (744B-7H-5W, 106-107 cm), **19.** *Caviatus jouseanus* (744B-8H-3W, 102-109), **20.** *Cavitatus jouseanus* (744B-8H-5W, 84-85 cm), **21**. *Cavitatus jouseanus* (744B-8H-5W, 84-85 cm).

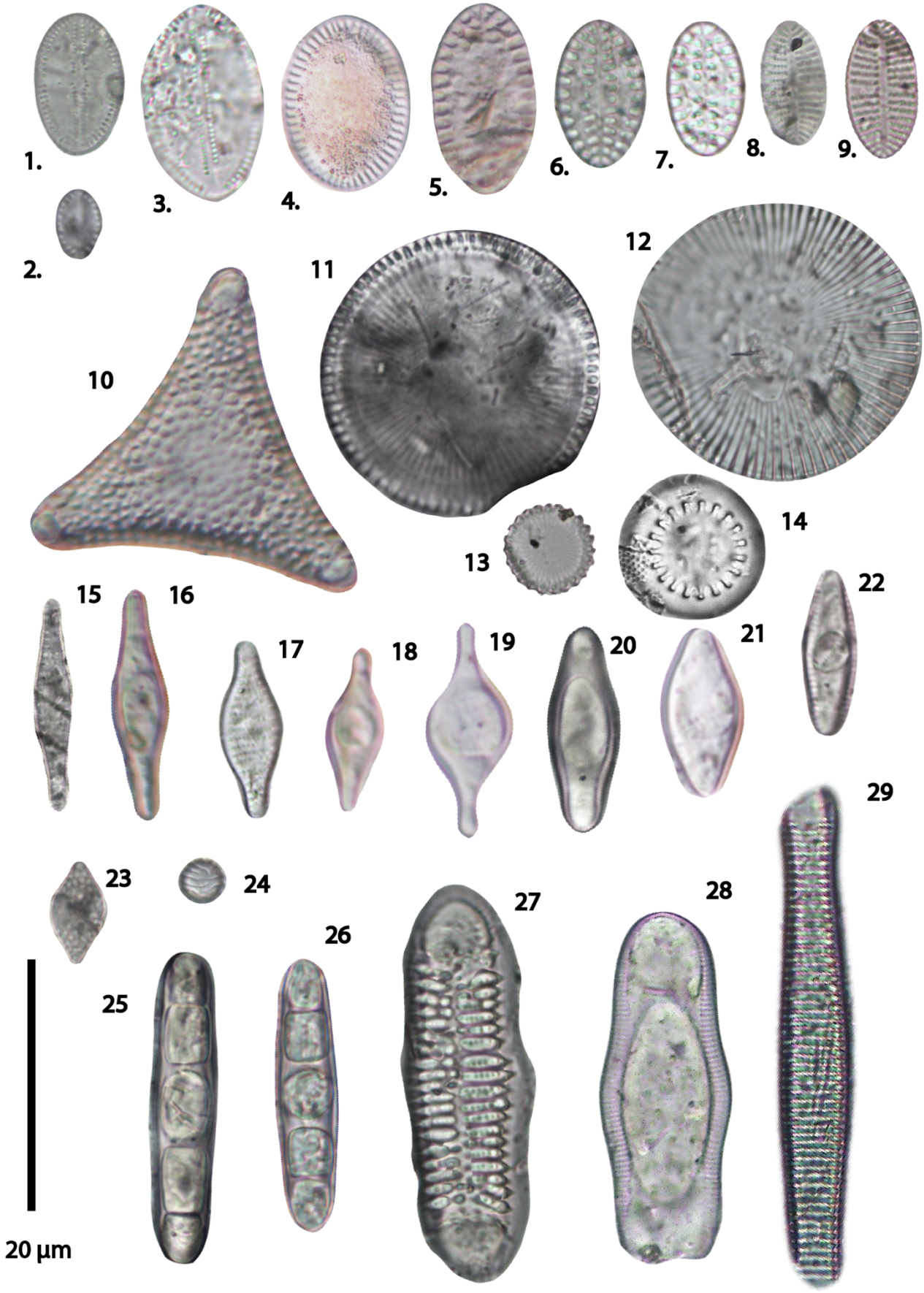
1.
2.
3.
4.
5.
6.
7.
8.
9.
10
11
12
13
14
15
16
17
18
19
20
21
22
23
24
25
26
27
28
29
20 µm

Plate 6

1. 2. *Cocconeis* sp. cf. *Cocconeis californica* (1165B-35X-4W, 85-86 cm), **3.** *Cocconeis* sp. cf. *Cocconeis californica* (1165B-36X-6W, 55-56 cm), **4.** *Cocconeis* sp. ? (1165B-35X-1W, 115-116 cm) **5.** *Cocconeis* sp. (1165B-33X-7W, 15-16 cm), **6.** *Cocconeis* sp. (1165B-37X-3W, 120-121 cm), **7.** *Cocconeis sp.* (1165B-39X-2W, 140-141 cm), **8.** *Cocconeis costata* (1165B-36X-6W, 95-95 cm), **9.** Cocconeis *costata* (1165B-38X-1W, 135-136 cm), **10.** *Trinacria excavata* (1165B-36X-1W, 45-46 cm), **11.** *Paralia* sp. (1165B-35X-4W, 85-86 cm), **12.** *Ellerbeckia* sp. (1165-37X-5W, 140-141 cm), **13.** *Paralia* sp. (744B-7H-4W, 120-121 cm), **14.** *Melosira* sp. (1165B-38X-1W, 85-86 cm), **15.** *Rhabdonema* sp. (1165B-37X-2W, 145-146 cm), **16.** *Rhabdonema* sp. (1165B-34X-2W, 5-6 cm), **17.** *Rhabdonema* sp. (1165B-36X-5W, 45-46 cm), **18.** *Rhabdonema* sp. (1165B-34X-6W, 85-86 cm), **19.** *Rhabdonema* sp. (1165B-35X-1W, 115-116 cm), **20**. *Rhabdonema* sp. (1165B-34X-6W, 115-116 cm), **21.** *Rhabdonema* sp. (1165B-34X-2W, 85-86 cm) **22.** *Rhabdonema* sp. (1165B-38X-1W, 135-136 cm), **23.** *Cymatosira/Kisseleviella* sp. (1165B-35X-5W, 15-16 cm), **24.** Crysophyte cyst (1165B-39X-2W, 90-91 cm), **25.** *Grammatophora* sp. (1165B-34X-6W, 115-116 cm), **26.** *Grammatophora* sp. (1165B-35X-5W, 15-16 cm) **27.** *Rhabdonema japonicum* (1165B-39X-2W, 140-141 cm), **28.** *Rhabdonema japonicum* girdle band (1165B-39X-2W, 140-141 cm), **29.** *Rhabdonema* cf. *elegans* (1165B-37X-1W, 60-61 cm).

6. Evolution of the Southern Ocean and East Antarctic Ice Sheet During Middle Miocene Cooling

6.1. Introduction

Globally, terrestrial (Jimenez-Moreno et al., 2006; Hayashi et al., 2018) and marine (Woodruff & Savin, 1991; Krylov et al., 2008) proxy climate records indicate large-scale, step-wise cooling in the Middle Miocene (Holbourn et al., 2013). The stepped cooling pattern is punctuated by oxygen isotope events interpreted as glaciations; within the study interval (15-12 Ma), these include Mi3a (c. 14.6 Ma), Mi3 (c. 13.8 Ma) and Mi4 (c. 13.1 Ma) (Miller et al., 1991). During this Middle Miocene interval, the Antarctic Ice Sheet expanded to at least its modern size (Lear et al., 2015; Lewis & Ashworth, 2016), eustatic sea level decreased by 59±6 m (John et al., 2011), and benthic oxygen isotope ratios increased by c. 1‰ (Zachos et al., 2001).

Hypotheses for the cause of the Mi3 event (or Middle Miocene Climate Transition, MMCT, at 13.8 Ma) have focused on changes in ocean gateways (Hamon et al., 2013) or CO_2 drawdown into the terrestrial (Diester-Haas et al., 2009; Ma et al., 2018) or oceanic (Vincent & Berger, 1985; Holbourn et al., 2014; Carter et al., 2016) realms. Whatever the cause of the Mi3 event in particular, a close correlation between CO_2-forcing and benthic $\delta^{18}O$ suggests an important role for CO_2 in forcing during the Middle Miocene (Sosdian et al., 2018).

On the Antarctic continent, ice growth during Mi3, and other Middle Miocene glaciation events, was likely focused on East Antarctica (Flower & Kennett, 1994). However, the West Antarctic Ice Sheet also expanded onto the continental shelf during the Middle Miocene (Chow & Bart, 2003; Rocchi et al., 2006; Levy et al., 2016), as atmospheric CO_2 concentrations passed the threshold below which WAIS formation could occur (400 ppm) (Foster et al., 2012; Super et al., 2018). A decrease of close to 8°C in atmospheric temperatures over continental Antarctica, which accompanied Mi3 ice growth, also lead to the final extinction of Antarctic tundra biota (Lewis et al., 2008).

In the Southern Ocean, oceanic temperatures in the Ross Sea were between 1 and 11°C prior to Mi3 (Warny et al., 2009; Feakins et al., 2012); warm enough to prevent the formation of perennial sea ice. Modelling studies show similar conditions could also have existed in other Antarctic marginal seas, such as the Weddell Sea (Huang et al., 2017). During Mi3, deep water temperatures decreased by 2-3°C and surface waters decreased by 6-7°C overall (Shevenell et

al., 2008; 2004). However, Mi3 ice growth was also accompanied by a transient sea surface temperature (SST) increase at ODP Site 1171 (Shevenell et al., 2004; Shevenell et al., 2008), which modelling suggests was caused by changes in the wind field associated with changing ice surface elevation (Knorr & Lohmann, 2014). The subantarctic position of Site 1171 puts it away from the greatest modelled relative SST increase, which is generally highest towards the Antarctic coastline. Additional ice–proximal records are therefore needed to explore and confirm the nature and pattern of the transient increase in SST at Mi3.

Middle Miocene cooling, and the Mi3 event in particular, was clearly a profound period of Cenozoic climatic change in Antarctica and worldwide. However, the role of the Southern Ocean in, and its response to, such large changes in Antarctic ice volume remains relatively unconstrained, particularly at the highest latitudes. Here I will present three high-resolution quantitative diatom assemblage records for the period between 15 and 12 Ma from the Southern Ocean and Antarctic region at ODP Sites 747, 744 and 1165, located on a transect spanning 10 degrees of latitude across the Indian Ocean sector of the Southern Ocean. In addition, a new record of ice rafted debris (IRD) is presented from the southern-most site, Site 1165, which expands upon the IRD record of Pierce et al. (2017) at Site 1165 to encompass the entire 15-12 Ma interval. The comparison of IRD records and quantitative diatom assemblages provides new insight into Antarctic zone palaeoceanography as well as ice dynamics in the ice-proximal Prydz Bay region during the Middle Miocene.

6.2. Results

6.2.1. Diatoms at ODP Site 747

Diatom preservation, assessed following the method of Barron & Gladenkov (1995), was generally moderate at ODP Site 747. Dissolution was more prominent than fragmentation, and in five samples (at 79.89, 79.59, 78.99, 78.39 and 72.29 mbsf), where dissolution was strongest, it was possible to count only 200 diatom valves per slide. Despite this, over 100 diatom species were identified at Site 747 (full diatom assemblage data are in Appendix 4), with the *Actinocyclus ingens* group and several species of *Denticulopsis* accounting for between 20 and 96% of the assemblage overall (Figure 1).

Prior to Mi3 at 13.8 Ma (70.27 mbsf), diatom assemblages at Site 747 are dominated by the *Actinocyclus ingens* group (up to 90% of the assemblage). However, the highest abundances of *Denticulopsis maccollumii* (up to c. 20%), *Thalassionema nitzschioides* var. *parva* (up to c. 16%)

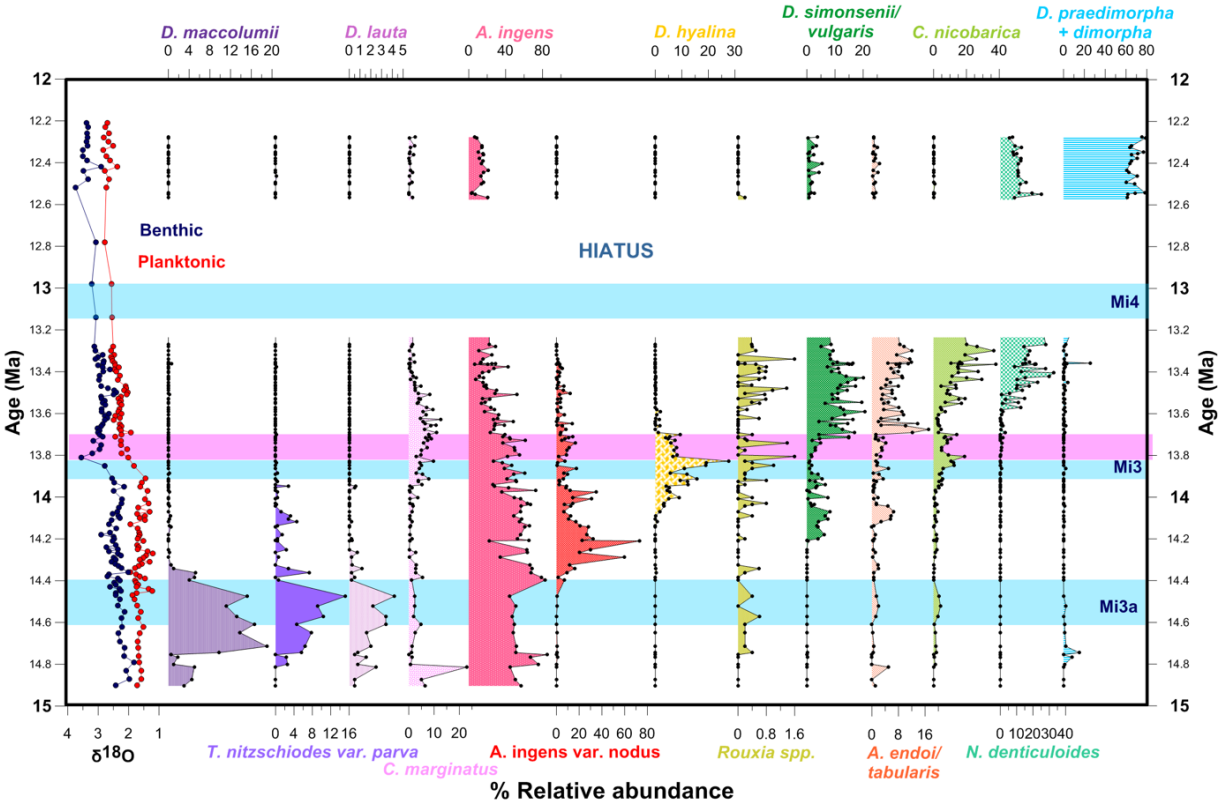

Figure 1. Diatom relative abundances at ODP Site 747 between 15-12 Ma. Site 747 planktonic and benthic foraminiferal $\delta^{18}O$ is from Majewski & Bohaty (2010). Blue and pink horizontal shading indicates Miocene glaciation events (Mi3a, Mi, Mi4) and the transient increase in SSTs following Mi3, respectively.

and *Denticulopsis lauta* (up to c. 4%) are observed before c. 14.4 Ma (74.81 mbsf). Following 14.4 Ma, *A. ingens* var. *nodus* abundance increases, peaking at c. 14.2 Ma, 72.92 mbsf (73%), and 14 Ma, 71.43 mbsf (35%), with subsequent assemblages shifting from being dominated by the *A. ingens* group to containing increasing abundances of *Denticulopsis simonsenii/vulgaris* and *Denticulopsis hyalina*. At 13.8 Ma (70.27 mbsf), a peak in *D. hyalina* (>30%) and *Rouxia* spp. (2%) is observed. After 13.7 Ma (69.62 mbsf), *D. simonsenii/vulgaris* abundance increases substantially to around 20%, whilst *Crucidenticula nicobarica, Nitzschia denticuloides,* and *Azpeitia endoi/tabularis* also begin to increase, peaking at a combined abundance of c. 70% immediately prior to the hiatus beginning at 13.3 Ma (66.22 msf).

Above the hiatus at 12.6 Ma (66 mbsf), *Denticulopsis praedimorpha* and *Denticulopsis dimorpha* are dominant (combined abundance up to c. 80%) at Site 747. A few *D. dimorpha* and *D. praedimorpha* valves are also documented in samples below the hiatus, indicating either minor laboratory contamination or reworking at Site 747. No benthic diatoms were identified at Site

747, although a few valves of neritic species, such as *Paralia sulcata*, are encountered throughout the record. The highest abundances of a new but as yet undescribed species, *Actinocyclus* sp. nov #1 (described in Appendix 2), was also found at this site (5% at 13.56 Ma; 68.37 mbsf), and proved to be biostratigraphically useful (Chapter 4).

6.2.2. Diatoms at ODP Site 744

The more southerly position of ODP Site 744 resulted in generally better preserved and more abundant diatoms than at ODP Site 747. Over 110 diatom species were identified at Site 744, mostly consisting of planktonic diatoms including the *Actinocyclus ingens* and *Denticulopsis* spp. groups (combined abundances of 33-99%; Figure 3), although several neritic species such as *Paralia sulcata* were also documented. A few benthic diatoms (most notably *Cocconeis* spp.) were also identified in sediments older than 13.8 Ma (55.34 mbsf), but never at >1% abundance. Abundances of *Denticulopsis maccollumii* (up to c. 80%) and *Denticulopsis lauta* (up to 8%) at Site 744 are higher than at Site 747 prior to 14.6 Ma (62.70 mbsf), after which *D. maccollumii* abundance falls to <20% (Figure 3). Following 14.6 Ma, the *Actinocyclus ingens* var. *nodus* abundance pattern at Site 744 is nearly identical to Site 747, peaking at c. 14.2, 58.80 mbsf (64%) and 14 Ma, 56.86 mbsf (54%). These peaks are used as a new quantitative biostratigraphic markers (Chapter 4). *Denticulopsis hyalina* peaks at 13.8 Ma, 55.34 mbsf (c. 12%), coincident

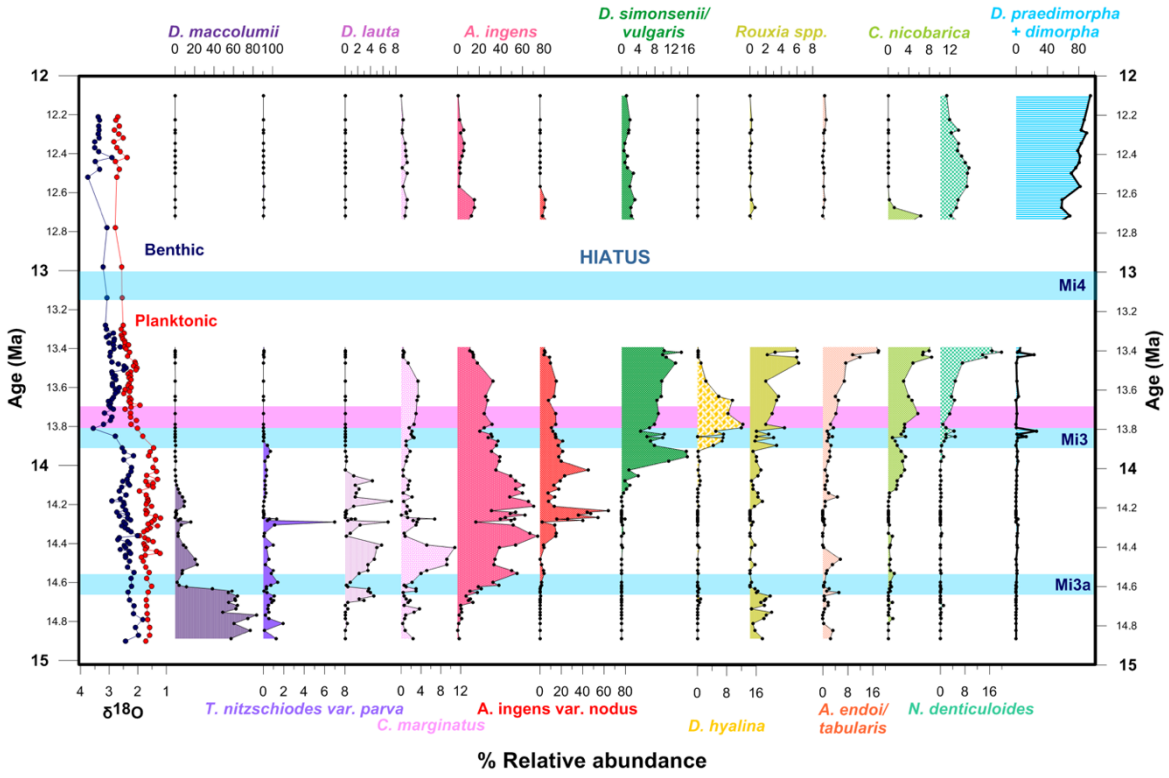

Figure 2. Diatom relative abundance at ODP Site 744 between 15-12 Ma. Planktonic and benthic $\delta^{18}O$ is from Site 747 (Majewski & Bohaty, 2010). Blue and pink horizontal shading indicates Miocene glaciation events (Mi3a, Mi, Mi4) and the transient increase in SSTs following Mi3, respectively.

with, but at a lower magnitude than, its abundance peak at Site 747. *Denticulopsis simonsenii/ vulgaris* increases in abundance (up to 16%) after c. 13.9 Ma, 55.98 mbsf, with its abundance remaining high until the hiatus at 13.4 Ma, 54.18 mbsf. *Rouxia* spp., *Crucidenticula nicobarica* and *Azpeitia tabularis/endoi* also increase after 13.8 Ma, 55.34 mbsf, to a maximum combined abundance of c. 35% prior to the hiatus. Above the hiatus at c. 12.8 Ma, 53.80 mbsf, diatom assemblages are dominated by *Denticulopsis dimorpha* and *Denticulopsis praedimorpha* (combined abundance >80%), as at Site 747. Similar to Site 747, a few valves of *D. praedimorpha* and *D. dimorpha* were also found in samples from below the hiatus, possibly indicating minor reworking at Site 744 or laboratory contamination.

6.2.3. Diatoms at ODP Site 1165

Diatoms were abundant at ODP Site 1165 and preservation was generally good with minimal dissolution. Fragmentation was more prevalent than at the two northern sites, perhaps reflecting glacial processes at the continental margin e.g. subglacial compaction and shearing (Scherer et al., 2004), and transport from the continental shelf to the site. Over 140 species were identified at Site 1165, making this southern-most site the most diverse in the latitudinal transect. A new species, *Actinocyclus* sp. nov. #2 (described in Appendix 2), was present at up to >17% relative abundance in the lower sections at Site 1165.

Prior to 14.6 Ma, 316.50 mbsf, diatom assemblages at Site 1165 contain relatively high abundances of *Denticulopsis maccollumii* (>16%), *Denticulopsis lauta* (>20%) and *Thalassionema nitzschiodes* var. *parva* (>2%) (Figure 4) and, prior to 13.8 Ma, 290.85 mbsf, also high abundances of the subgenus *Chaetoceros (Hyalochaete)* resting spores (up to 36%) and *Liradiscus* spp. resting spores (>15%). Diatom assemblages at Site 1165 also contain neritic diatom taxa at their highest abundances prior to 13.8 Ma, 290.85 mbsf, including *Stephanopyxis turris* and *Ellerbeckia sol* (up to 10 % combined abundance). Site 1165 also differed from Sites 747 and 744 in containing a diverse benthic diatom assemblage prior to 13.8 Ma, including *Cocconeis*, *Rhabdonema* and *Grammatophora* species at combined abundance of up to 3% (Figure 3).

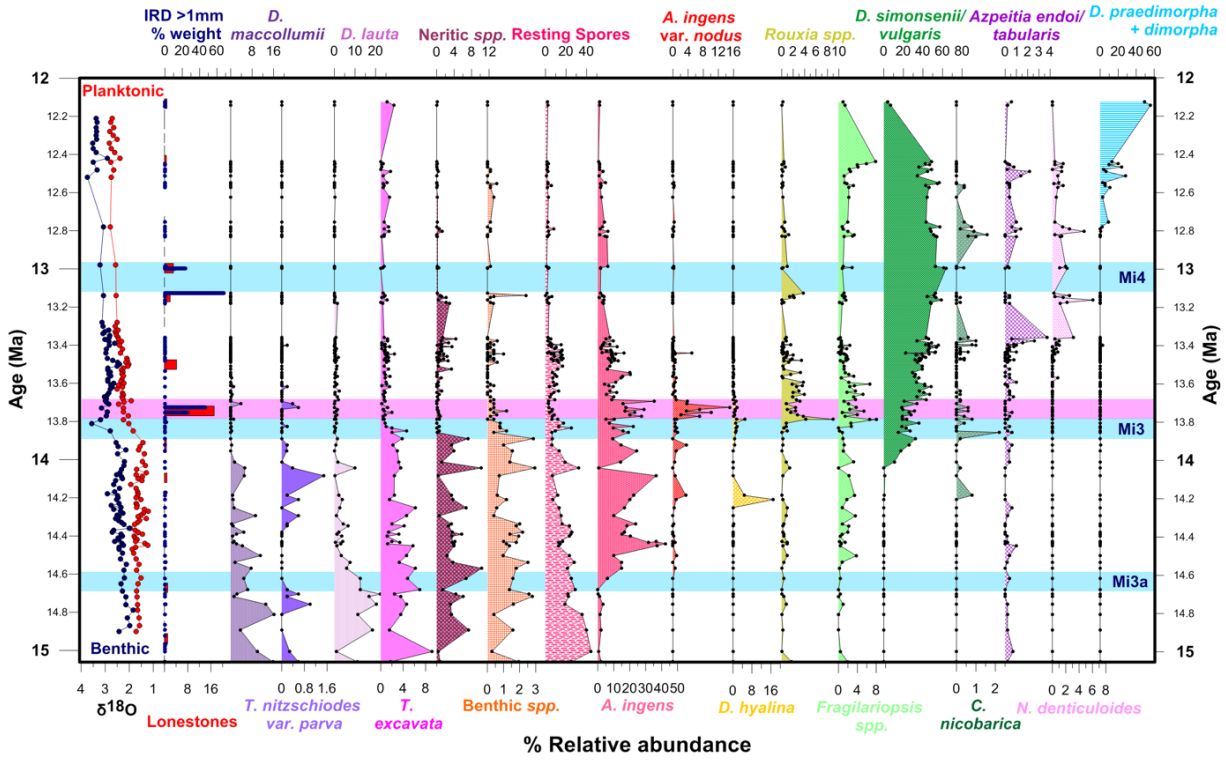

Figure 3. Diatom relative abundance at ODP Site 1165 between 15-12 Ma. Planktonic and benthic $\delta^{18}O$ is from Site 747 (Majewski & Bohaty, 2010), and IRD at Site 1165 is from this study (purple bars) and lonestones from the Shipboard Scientific Party (2001) (red bars). Blue and pink horizontal shading indicates Miocene glaciation events (Mi3a, Mi3, Mi4) and the transient increase in SSTs following Mi3, respectively.

The abundance of *Actinocyclus ingens* var. *nodus* was low (<4%) prior to 13.8 Ma at Site 1165, and the 14.24, 14.29 and 13.98 Ma peaks in *A. ingens* var. *nodus* abundance seen at Sites 747 and 744 (Figures 1 and 2) are not observed at Site 1165 (Figure 3). *Denticulopsis hyalina* peaked at c. 14.2 Ma, 301.05 mbsf, at Site 1165 (86%), but a second lower abundance (35%) at 290.85 mbsf likely corresponds to the 13.79 Ma abundance peak at Sites 744 and 747 (Figures 1 and 2; Chapter 4). A combined abundance peak (c. 20%) of *Rouxia* spp. and *Fragilariopsis* spp. also occurred at 289.75 mbsf, 13.79 Ma; not seen at Sites 747 and 744. *A. ingens* var. *nodus* abundance peaked (>12%) at Site 1165 at c. 13.70 Ma, 288.35 mbsf, again not seen at Sites 747 and 744, although Site 747 did show increased *A. ingens* abundances during this interval (Figure 1).

From 14.2 Ma, 301.05 mbsf, but in particular after 14 Ma, 295.86 mbsf, *Denticulopsis simonsenii/vulgaris* increases in abundance to dominate the assemblage at Site 1165 (>70%

abundance). The *Denticulopsis* group also diversifies to include *Denticulopsis* sp. 3, a new species (described in Appendix 2) which is not seen at Sites 747 and 744. *D. simonsenii/vulgaris* continues to dominate the diatom assemblages at Site 1165 until after 12.4 Ma, 223.72 mbsf, when *Denticulopsis praedimorpha* and *Denticulopsis dimorpha* appear and increase in abundance (up to c. 60%; Figure 3), as they do at Sites 747 and 744 from c. 12.8 Ma (Figures 1 & 2).

Overall, diatom assemblages suggest surface water conditions were substantially different at Site 1165 than at Sites 747 and 744 throughout the record, but most clearly prior to 13.8 Ma. After 13.8 Ma, diatom assemblages at Site 1165 gradually become more similar to the two northerly sites by the end of the records.

6.2.4. IRD at ODP Site 1165

The extended IRD record generated at Site 1165 between 332.8 and 197.0 mbsf expands on, and is presented alongside, the high-resolution record of Pierce et al. (2017), who documented IRD at the same site between 280-292 mbsf (Figure 4).

Three samples in the early record containing a maximum of 4.8 grains/g occurr at 14.9 Ma (326.55 mbsf), 14.45 Ma (310.10 mbsf) and 14.2 Ma (301.05 mbsf), within an otherwise IRD-free interval (291-332 mbsf). However, these samples contain less than 1 wt % IRD (Figure 4). Similar to the results of Pierce et al. (2017), I find a peak in IRD abundance (5 grains/g, 46 wt% IRD) at c. 290 mbsf, 13.8 Ma, which coincides with peak numbers of lonestones (>5 mm) documented at Site 1165 by the Shipboard Scientific Party (2001) (Figure 4). I also find a second, more prominent peak in IRD (10 grains/g, 68 wt% IRD) at 262.03 mbsf, c. 13.1 Ma (Figure 4), although fewer lonestones were associated with this peak than at 13.8 Ma (Shipboard Scientific Party, 2001). After 13 Ma, 262 mbsf, IRD abundance remains negligible for the remaining record.

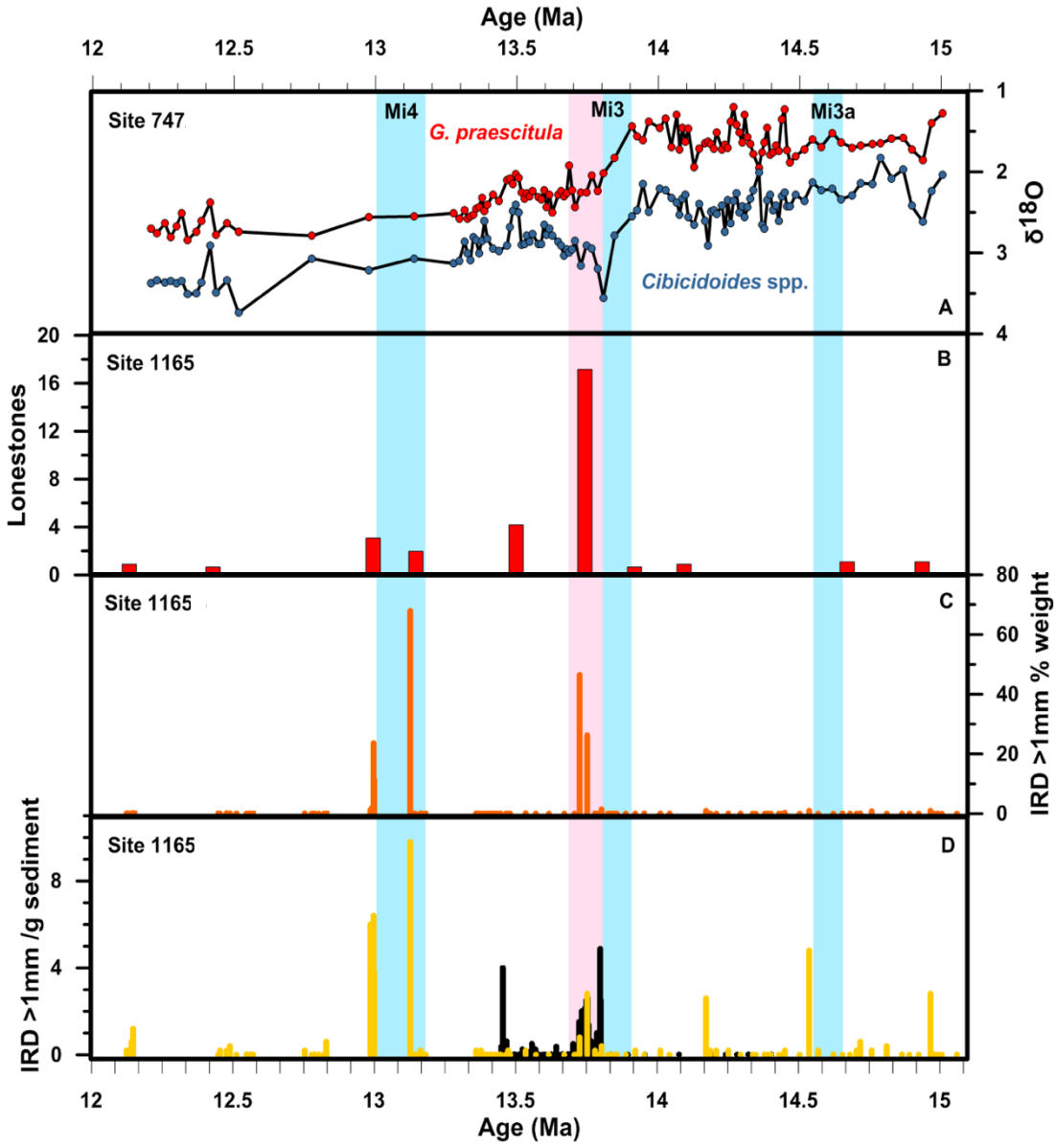

Figure 4. IRD at ODP Site 1165. D) IRD generated in this study (yellow bars) and by Pierce et al., 2017 (black bars) in terms of the number of IRD grains per gram of sediment. C) IRD grains found in this study in each sample by weight (orange bars), B) lonestones (>5mm grains) identified at Site 1165 by the Shipboard Scientific Party (2001). A) planktonic (red) and benthic (blue) stable oxygen isotope records at ODP Site 747 (Majewski & Bohaty, 2010).

6.2.5. Diatom Diversity

Diatom diversity at ODP Sites 747, 744 and 1165 is presented in terms of the Simpson's diversity index (SDI) and Shannon's H (SH), both numerical diversity models that calculate the diversity of a given sample assemblage based on the evenness and number of species present. Both indices

correlate well throughout all three records (Figure 5), suggesting they robustly describe true diatom assemblage diversity.

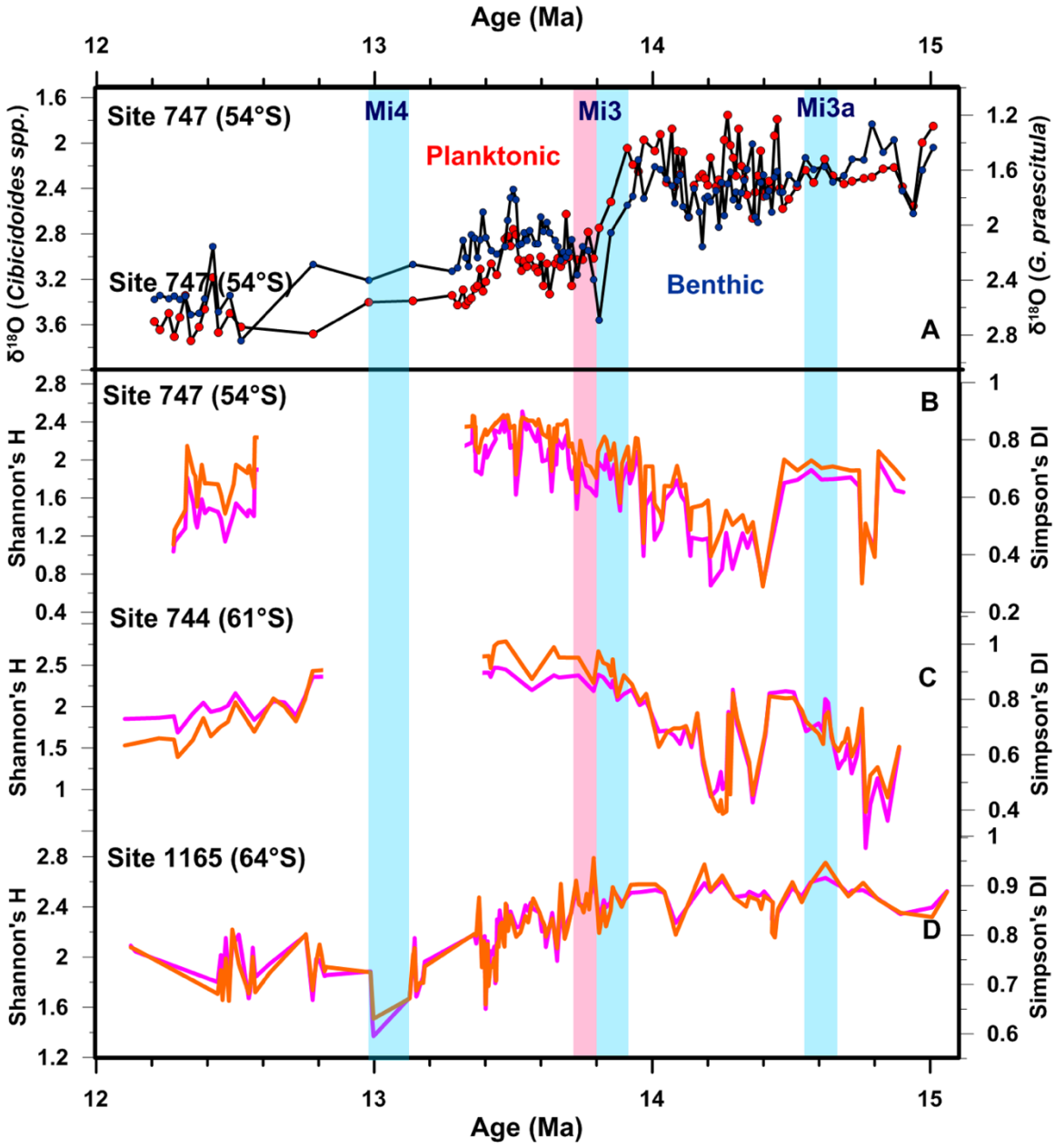

Figure 5. Diatom diversity at ODP Sites 747, 744 and 1165. A) planktonic (red) and benthic (blue) stable oxygen isotope records at Site 747 (Majewski & Bohaty, 2010). B-D) Diatom diversity expressed in terms of both the Simpson's Diversity Index (pink line) and Shannon's H (orange line) at ODP Sites 747, 744 and 1165. Blue shaded bars indicate Miocene isotope events, pink shaded bar indicates SST warming following the MMCT.

Prior to 13.8 Ma, diatom diversity is highest at the southerly Site 1165 (>0.9 SDI; >2.5 SH) and lowest at northerly Site 747 (<0.4 SDI, 0.8 SH) (Figure 5). Dissolution (Barron & Gladenkov, 1995), which is strongest in the older sections at Site 747, could have artificially reduced species diversity at Site 747, although diversity at Site 744 closely resembles Site 747, suggesting this is not the case. Trends in diatom diversity diverge from 13.8 Ma, after which diatom diversity increases at Sites 747 and 744 by c. 0.6 SDI and 1 SH, but decreases by c. 0.3 SDI and 1.2 SH at Site 1165, bringing diatom diversity to a similar level at all three sites (c. 0.7 SDI, 1.7 SH) by 12 Ma. These trends largely reflect the increasing abundance of *D. simonsenii/vulgaris* followed by *D. praedimorpha /D.dimorpha* at all three sites.

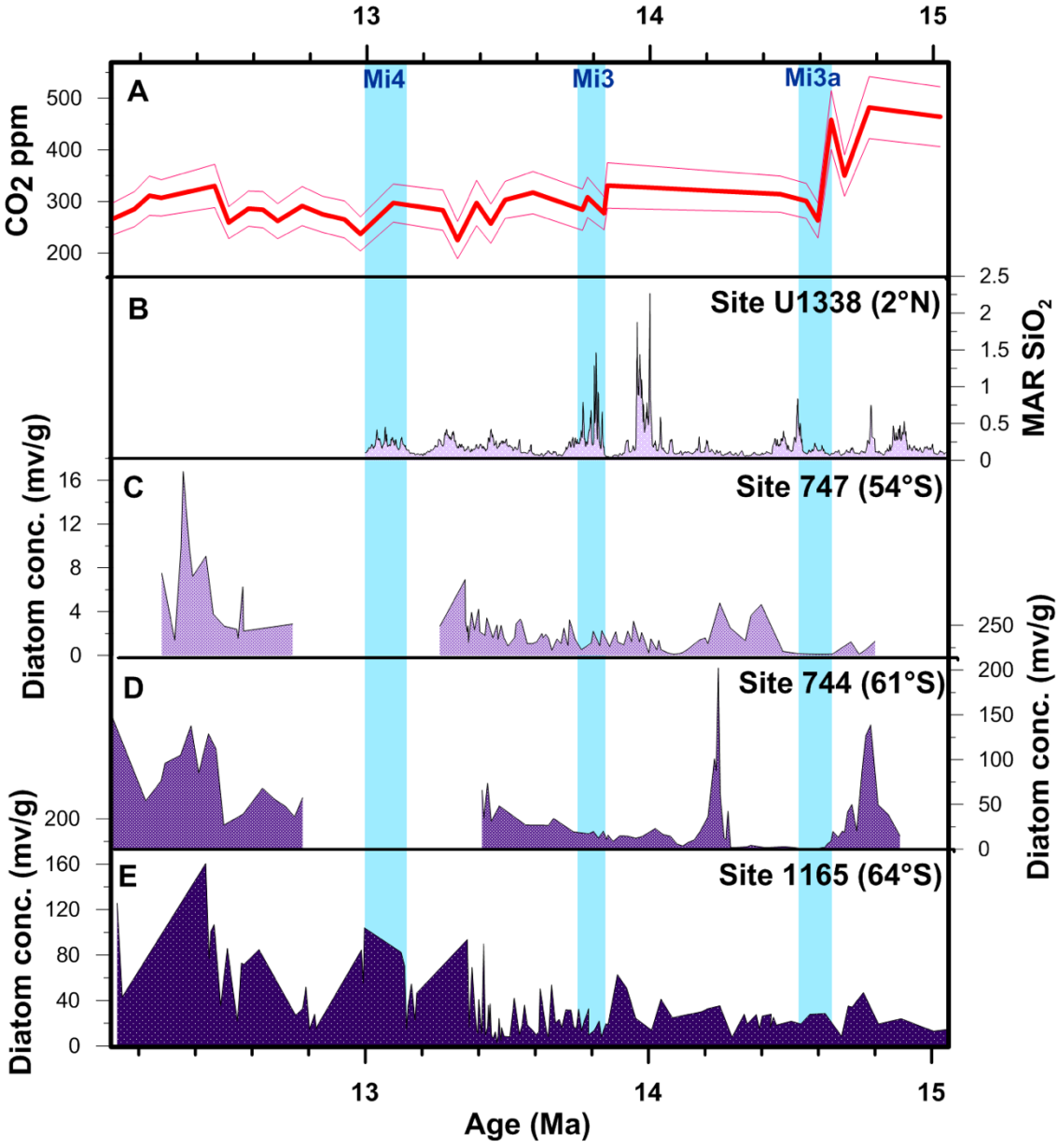

Figure 6. A) Alkenone atmospheric CO_2 reconstructions (Super et al., 2018; Pagani et al., 1999). B) Equatorial Pacific Ocean SiO_2 mass accumulation rates at IODP U1338 (Holbourn et al., 2014). C-E) Diatom concentration (v/gds) at ODP Site 747, 744 and 1165, this study. Blue horizontal shading indicates Miocene isotope events.

6.2.6. Diatom concentration

Diatom concentration, which can be considered a proxy for diatom productivity, was up to an order of magnitude greater at the southern ODP Site 1165 (>160 mv/g) than at northern ODP Site 747 (<16 mv/g) (Figure 6). ODP Site 744 shows similar diatom concentrations to Site 1165, but also greater amplitude variability (e.g. peaking at >200 mv/gds and falling to below 20 mv/gds). There are two prominent peaks in diatom concentration at Site 744 at 14.78 Ma, 65.22 mbsf, and 14.24 Ma, 59.22 mbsf, both dominated by *Actinocyclus ingens* and *Actinocyclus ingens* var. *nodus*. These peaks are higher than diatom concentrations in the remaining, younger record at Site 744, and also any peaks in Sites 747 and 1165. However, the two peaks are somewhat reflected at Site 1165 for the 14.78 Ma peak, and at both Site 747 and to a lesser extent 1165 for the 14.24 Ma peak. Diatom concentration stays low until c. 13.5 Ma, after which diatom concentration increases, and again at 12.5 Ma, at all three sites.

6.3. Discussion

6.3.1. The Mi3a event (15-14.6 Ma)

Between 15 and 14.6 Ma, *Denticulopsis maccollumi/D. maccollumii* var. *A*, both endemic Southern Ocean diatom species, reached their highest abundances at ODP Sites 747, 744 and 1165 along with *Denticulopsis lauta* at Sites 1165 and 747. *D. maccollumii/D. maccollumii* var. A and *D. lauta* indicate relatively cool, open water conditions (Chapter 5) across the Southern Ocean between 15 and 14.6 Ma. However, coexisting peak abundances of warm-indicator *Thalassionema nitzschiodes* var. *parva,* common in modern (Romero et al., 2009) and Neogene (Lyle & Baldauf, 2015) equatorial oceans, at all three sites suggests latitudinal sea surface temperature (SST) gradients were reduced, and/or oceanic circulation was different, from modern. This agrees with the existence of reduced SST latitudinal gradients in the Wilkes Land sector of the Southern Ocean during this period (Sangiorgi et al., 2018), and/or possibly suggests mixed or variable oceanographic conditions, e.g. particularly strong seasonality.

At c. 14.6 Ma, a shift in diatom assemblages occurred at Sites 744 and 1165, whereby *Denticulopsis maccollumii/D. maccollumii* var. *A* and *Denticulopsis lauta* were largely replaced

by *Actinocyclus ingens* and *Actinocyclus ingens* var*. nodus*. Several endemic Southern Ocean *Fragilariopsis* species also appeared from 14.6 Ma, in particular at Site 1165 (Figure 3). A similar diatom assemblage shift is documented at Site 747 at c. 14.4 Ma, but, based on the similarity of the diatom assemblages at Sites 747 and 744, the c. 200 kyr delay could be attributed to a lack of age model precision in the early part of the Site 747 record (Section 4.2). The diatom assemblage shift at 14.6 Ma coincided with a major Southern Ocean diatom evolutionary turnover event, which was linked with high benthic $\delta^{13}C$ and decreasing atmospheric CO_2 (Crampton et al., 2016). The assemblage shift/turnover event at 14.6 Ma also coincided with the Mi3a glaciation (Holbourn et al., 2013), during which eustatic sea level decreased by 33±5 m (John et al., 2011) and the MISA-3 ice advance event occurred in the Ross Sea (Levy et al. 2016). Proxy climate records indicate a shift from eccentricity (100 kyr) to obliquity (41 kyr) paced cyclicity around the time of Mi3a (Holbourn et al., 2014; Ohneiser & Wilson, 2018), suggesting the diatom assemblage shift may have been forced by orbitally-induced changes in high latitude seasonality (Holbourn et al., 2014).

6.3.2. Peak Southern Ocean warmth (14.6-14.2 Ma)

Following Mi3a and the assemblage shift at 14.6 Ma, *Actinocyclus ingens* and *A. ingens* var*. nodus* relative abundance continued to increase at ODP Sites 747, 744 and 1165, peaking by c. 14.2 Ma (Figure 7). Given the close relationship between % *A. ingens* group abundance and planktonic $\delta^{18}O$ at Site 747 (Section 5.2.3), % *A. ingens* group abundance indicates that all three sites experienced peak SSTs between c. 14.4 and 14.2 Ma, though trends are more erraticSite 1165. This corresponds with peak SSTs recorded at subantarctic ODP Site 1171 (Figure 7) (c. 20°C; Shevenell et al., 2004) and at Polar Frontal Zone ODP Site 1092 (c. 19°C; Kuhnert et al., 2009). These high SSTs are hypothesised to have been driven by upwelling warm deep waters, possibly sourced from the equatorial Tethys region (Flower & Kennett, 1994; Shevenell et al, 2004). However, despite peak SSTs, IRD deposition, particularly in terms of weight % IRD, remained low at Site 1165 during this period (Figure 7). A few samples between 15.0 and 13.8 Ma contained IRD (most notably at 14.92, 14.54 and 14.17 Ma), however, none were >1 wt% IRD; relatively low compared with samples that reach >65 wt% IRD later in the record (Figure 7). This lack of IRD deposition, despite peak SSTs, suggests either that ocean temperatures were so warm that icebergs all melted before reaching and depositing IRD at Site 1165, or that the Amery ice sheet was relatively insensitive to changes in ocean temperature, perhaps because it terminated mostly inland/did not have a calving front prior to Mi3.

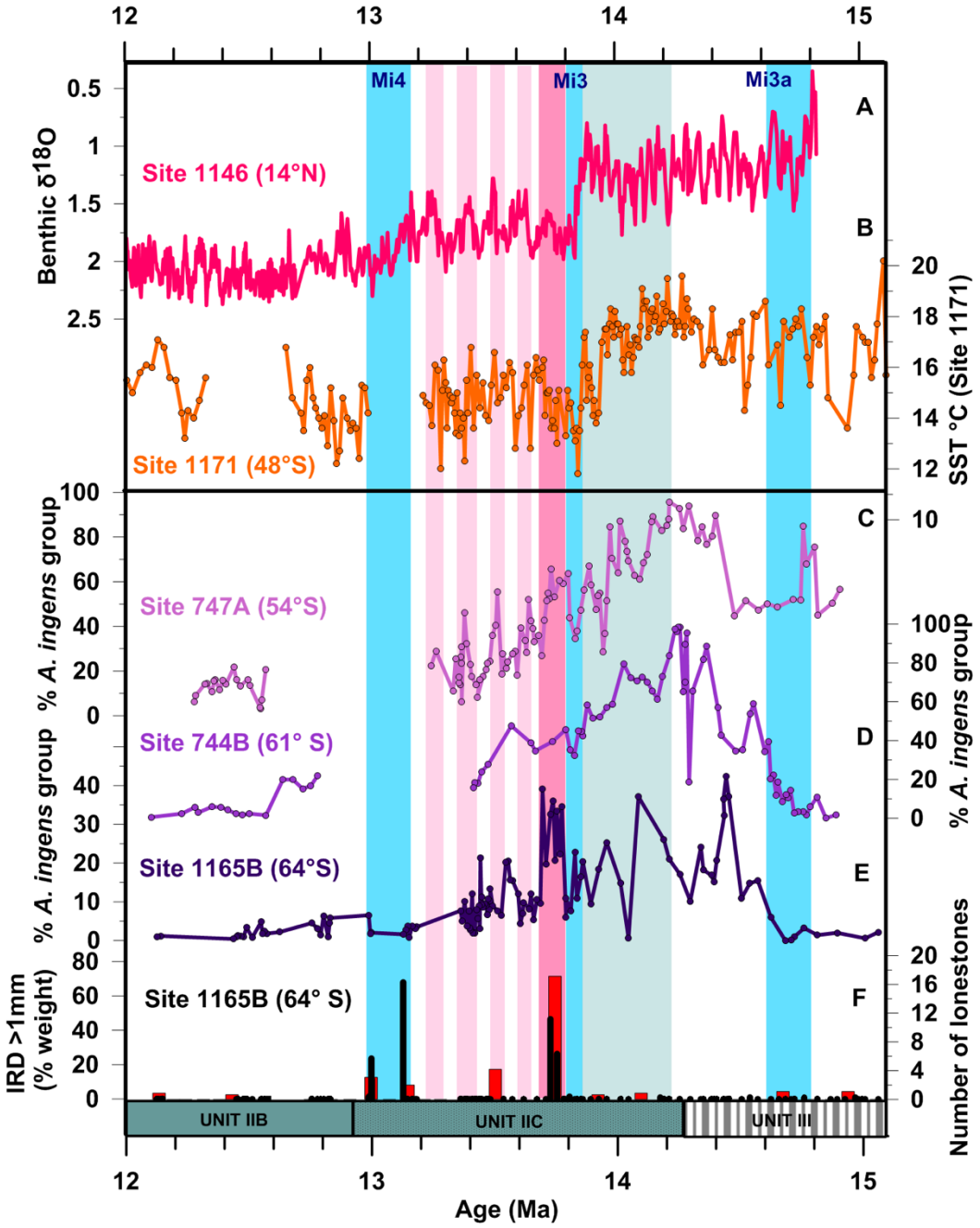

Figure 7. A: ODP Site 1146 benthic oxygen isotopes (Holbourn et al., 2013), B: ODP Site 1171 SST record (Shevenell et al., 2004), C-E: *Actinocyclus ingens* group abundance, as a proxy for SST, from ODP Sites 747, 744 and 1165 (this study). F: IRD at Site 1165. Black bars= this study, red bars= lonestones (Shipboard Science Pary, 2001). Vertical blue shaded bars indicate Miocene isotope glaciation events. Vertical dark pink shaded box represents SST warming following Mi3. Pale pink shaded bars indicate four subsequent interglacials that seem to be paced by 100 kyr-eccentricity cycles. The bottom panel shows the lithological transitions at Site 1165 from Unit II (thinly bedded, laminated fissile claystones with minimal bioturbation) to Unit III (moderately

bioturbated structureless clays with increased clay mineral content, shelf-derived foraminifers and glauconite).

In support of the land-terminating ice sheet hypothesis, neritic diatoms such as *Stephanopyxis turris* and *Paralia sulcata*, indicative of open-water coastal environments, showed high abundances at Site 1165 prior to Mi3 (Figure 8). Sediments at Site 1165 also consistently contained epiphytic benthic diatoms such as *Cocconeis* spp*., Rhabdonema* spp., *Raphoneis* spp., *Isthmia* spp. and *Grammatophora* spp. at combined abundances of up to 4%. These benthic species require stretches of ice-free coastline to survive, and many of the genera are epiphytic, attached to macrophyte seaweeds growing in shallow coastal waters, which may become dislodged and rafted to deeper water sites. Whilst it is possible that reduced perennial sea ice alone could account for the persistence of benthic diatoms at the coast, significantly reduced sea ice coverage would more likely have occurred alongside a smaller, or absent, marine ice sheet (DeConto et al., 2007). The presence of benthic diatoms such as *Cocconeis* spp. and *Grammatophora* spp. at ODP Site 693 in the Weddell Sea (Figure 1 of Chapter 2) during the Late Oligocene and Early-Middle Miocene were also interpreted as representing at least 50 m of ice-free coastline (Barker & Kennet, 1988). This suggests conditions in the Weddell Sea were similar to those in Prydz Bay during the Early-Middle Miocene, although unfortunately the low resolution of the age model and diatom data prevent a precise determination of when benthic diatom deposition ceased at Site 693.

Diatom assemblages at Site 1165 provide further insight into near-shore Antarctic paleoceanography during peak Southern Ocean warmth. For example, taxa that exhibit relatively high abundances during this period include extant *Chaetoceros (Hyalochaete)* (36% abundance), which bloom in the modern Southern Ocean in stratified water columns with abundant nutrients – conditions usually associated with sea ice melt and/or spring/summer glacial discharge in coastal areas of Antarctica, with resting spores (*Chaetoceros (Hyalochaete)* resting spores- CRS) produced towards the end of the bloom in response to nutrient depletion (Crosta et al., 1997). Extinct *Liradiscus* resting spores (up to 12%) may also proliferate during similar paleoceanographic conditions to CRS (Suto, 2004). Further, *Eucampia antarctica* (up to 4%) proliferates in response to high nutrient concentrations within glacial discharge (Allen et al., 2010; Conway et al., 2016), with its extinct relative *Eucampia antarctica* var*. twista* (2%) likely to have responded similarly. Species of *Rhizosolenia*, a genus able to migrate vertically within

the water column to access nutrients at depth and, therefore, to potentially thrive under stratified conditions (Leventer et al., 2002), also show peak abundances (34%) at 14.29 Ma.

Diatom assemblages at Site 1165 therefore indicate the prevalence of a stratified water column with generally high amounts of bioavailable nutrients prior to Mi3. The low abundance of potential sea ice indicator diatoms (combined *Synedropsis* spp. and *Fragilariopsis* spp. abundance at all three sites is never >4%) suggests sea ice melt is not responsible for stratifying the water column and delivering nutrients during this period. Rather, fluvial or meltwater discharge from a wet-based, predominantly land-terminating EAIS was likely responsible for stratifying the coastal ocean and supplying nutrients to Site 1165, and the wider Southern Ocean, prior to Mi3.

The new diatom-based reconstructions indicate that the palaeoceanography of Prydz Bay was comparable to conditions in the Ross Sea prior to Mi3, where coastal SSTs of 0-10°C, tidewater glaciers that periodically retreated inland and tundra growing along the coastline are inferred by ANDRILL depositional motifs 3 and 4 (Levy et al., 2016). A smaller, land-terminating EAIS has also been inferred in the Wilkes Land sector prior to 14.8 Ma, based on the high soil content of sediments at IODP Site U1356 (Figure 1 of Chapter 2) (Sangiorgi et al., 2018), while numerical models simulate the potential for a substantially retreated ice sheet margin around Antarctica, including the absence of the Amery Ice Shelf, during the Middle Miocene Climatic Optimum (Gasson et al., 2016). Existing evidence, therefore, clearly supports that much of the EAIS (and WAIS), including the Lambert Glacier, was retreated inland prior to Mi3.

6.3.3. Onset of Southern Ocean cooling (14.2 Ma- 13.9 Ma)

From 14.2 Ma, SST records at ODP Sites 1092 and 1171 record the onset of Southern Ocean cooling (Shevenell et al., 2004; Kuhnert et al., 2009), culminating in major ice growth at 13.8 Ma during Mi3. The diatom records presented in this chapter support this interpretation; in particular, the excellent correspondence between % *Actinocyclus ingens* group abundance at ODP Site 747 and Mg/Ca SST at Site 1171 (Shevenell et al., 2004) during this interval (Figure 7). Diatom assemblages at ODP Sites 747, 744 and 1165 all document the appearance of cool water indicator *Denticulopsis simonsenii/vulgaris* after c. 14.2 Ma; most abundantly at Site 1165, where cold water *Denticulopsis hyalina* also peaked at c. 14.1 Ma (Figure 3).

The onset of cooling at 14.2 Ma coincides with reduced obliquity forcing and increased current speeds in the South Pacific (Ohneiser & Wilson, 2018). A major lithological transition also occurs at Site 1165 between c. 14.5-14.2 Ma; going from thinly bedded, laminated fissile claystones with minimal bioturbation to moderately bioturbated, structureless clays with increased clay

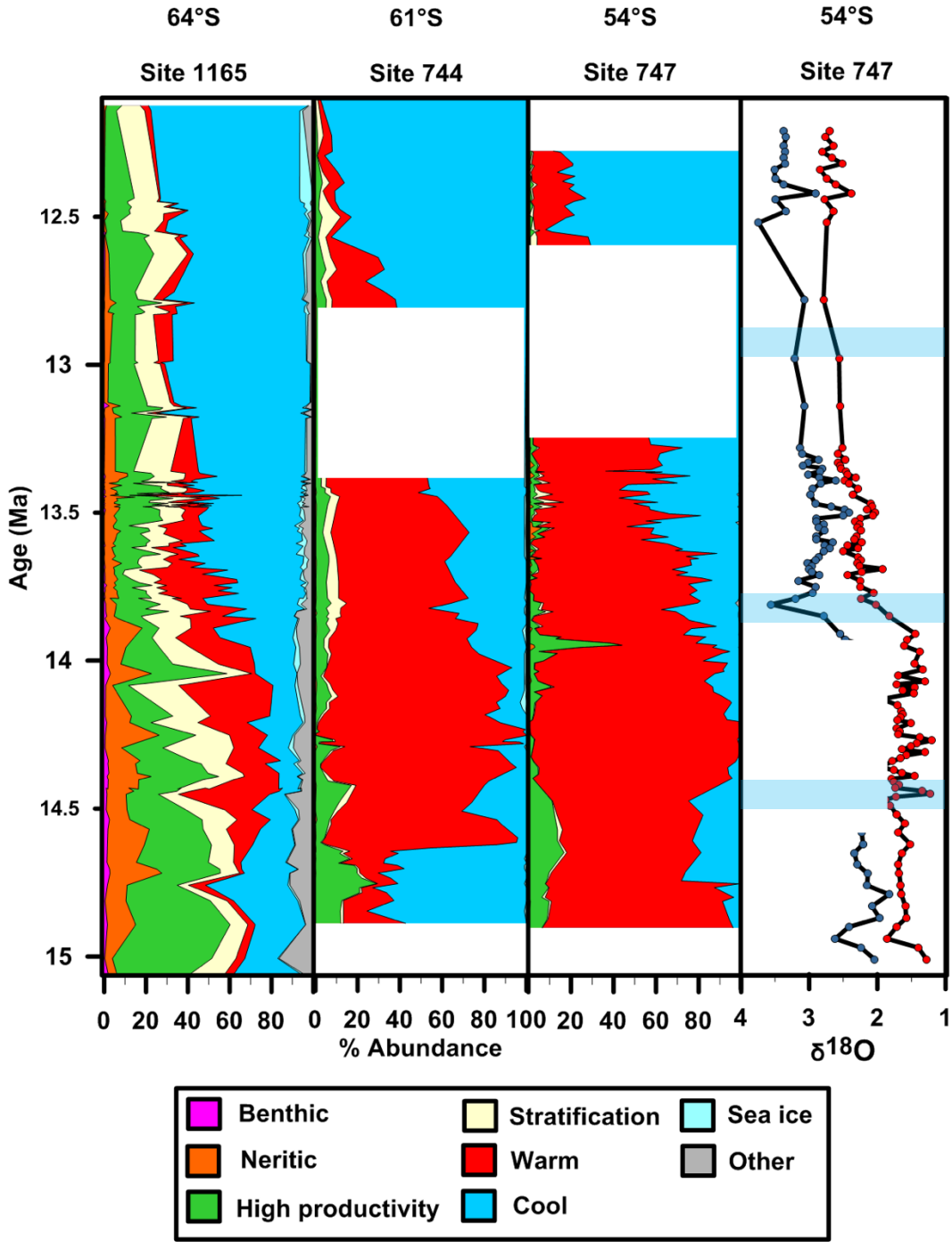

Figure 8. Diatom species at ODP Sites 747, 744 and 1165, group by inferred palaeoecological preferences (see Chapter 5 and Appendix 1). In the right-hand panel, benthic (blue) and planktonic (red) Site 747 stable oxygen isotope records are shown (Majewski & Bohaty, 2010).

mineral content, shelf-derived foraminifers and glauconite (Figure 7; Shipboard Science Party, 2001). The lithological change is indicative of increased bottom water oxygenation, perhaps due to invigorated bottom water production and/or a change in water mass above the site that contributed to SST cooling.

Despite the onset of sea surface cooling at 14.2 Ma, the abundance of neritic and benthic diatoms at Site 1165 does not decrease noticeably until 13.8 Ma (Figure 3, Figure 8), suggesting substantial marine ice did not appear in Prydz Bay until 13.8 Ma. Instead, sea surface cooling and a change in climate forcing and depositional regime at Site 1165 from 14.2 Ma primed the environment, over a period of c. 400 kyr, for major EAIS expansion at 13.8 Ma. This threshold response of major ice growth at 13.8 Ma could be largely explained by ice sheet hysteresis, whereby the snowline must descend right to the ice-free surface before ice sheet expansion can take place (Pollard & DeConto, 2005).

6.3.4. The Mi3 event (13.9-13.7 Ma)

The new IRD record from ODP Site 1165 complements and extends that of Pierce et al. (2017), and the record of lonestones from the same site (Shipboard Science Party, 2001), in finding the same substantial IRD peaks between 13.8 Ma and 13.7 Ma. These IRD peaks at Site 1165 coincided with the Mi3 glaciation at 13.8 Ma (Holbourn et al., 2013a), as well as with IRD peaks at IODP Site U1356 offshore of Wilkes Land (Pierce et al., 2017) and the MISA-4 episode of significant ice advance in the Ross Sea (Levy et al., 2016). This suggests that processes related to ice expansion were responsible for this episode of IRD deposition at Site 1165. Several potential mechanisms for the IRD deposition have been suggested (Pierce et al., 2017), however, comparing the extended IRD record with the new quantitative diatom assemblage records provides fresh insight.

An initial IRD peak at 13.8 Ma correlates with Mi3 SST cooling, recorded at Site 1165 by peaks in *Rouxia* spp. and *Fragilariopsis* spp. abundance (Figure 9); both cold water and potentially sea ice-associated diatom genera (Chapter 5). At Sites 744 and 747, SST cooling is reflected by transient peaks in *Denticulopsis hyalina* at c. 13.8 Ma (Figures 1-2). *D. hyalina* is a bipolar mid-high latitude species which, based on its peak abundance during Mi3 ice growth, may show colder sea surface temperature preferences than *Denticulopsis simonsenii/vulgaris*. The high abundance of cold-water diatoms at all three sites during this 13.8 Ma peak in IRD concentrations suggests that the initial phase of IRD deposition occurred during cooling, for

example as the expanding EAIS reached the continental shelf and delivered regolith eroded from the Antarctic continent into the surrounding marine waters (Pierce et al., 2017).

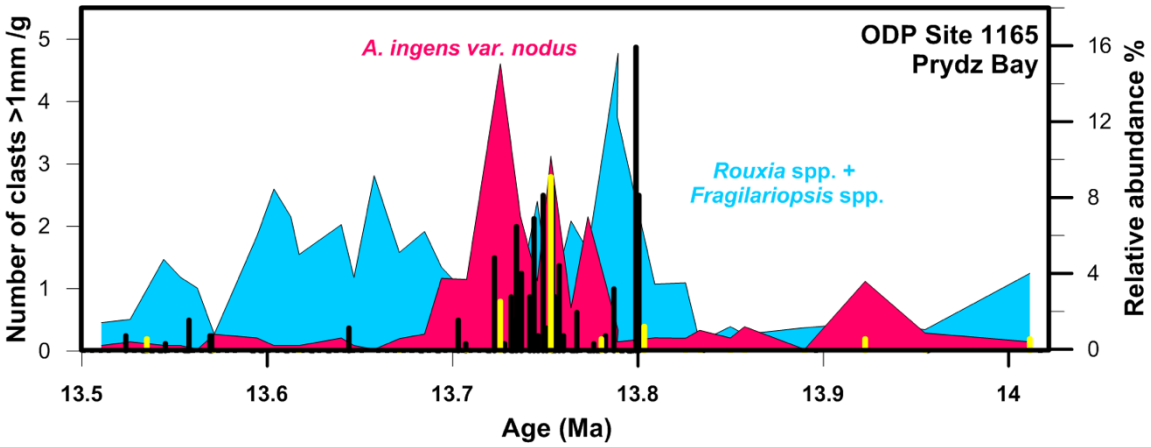

Figure 9. IRD and diatom abundances at ODP Site 1165 during the Mi3 pulse of IRD that occurs first alongside increased cool water *Fragilariopsis* and *Rouxia* spp (blue) and then alongside *Actinocyclus ingens* var. *nodus* (pink), which may represent the SST warming that occurs following initial MMCT ice growth (Knorr & Lohmann, 2014). IRD record includes data from Pierce et al. (2017) (black bars) and from this study (yellow bars).

A second, higher magnitude (in terms of weight percent and lonestones), pulse of IRD subsequently occurred at Site 1165 between 13.77 and 13.70 Ma. Geochemical analyses of IRD from this section suggests the IRD was sourced from the local Lambert Glacier graben as well as the distant Aurora Subglacial Basin, indicating widespread EAIS iceberg discharge (Pierce et al., 2017). This second peak coincided with peaks in the relatively warm water indicator *Actinocyclus ingens* var. *nodus* at Site 1165 (Figure 9), while warm water is also documented at Site 747 by the increased abundance of *A. ingens* group (Figure 7). This warm water episode, which lasted for around 70 kyr, is likely the same SST warming first identified following Mi3 at subantarctic ODP Site 1171 (Shevenell et al., 2004). Modelling suggests the SST increase, which occurred whilst bottom waters continued to cool following Mi3 (Shevenell et al., 2008), was generated by changes in ice topography and, subsequently, changes in the wind field and surface flow throughout the Southern Ocean (Knorr & Lohmann, 2014). Data presented in this chapter show that the SST increase was most pronounced at the highest latitudes, as predicted by the model of Knorr & Lohmann (2014), and was of a sufficient magnitude to generate large volumes of iceberg discharge.

6.3.5. Eccentricity-paced cooling at ODP Site 747 (13.8-13.2 Ma)

Following the Mi3 event, *Actinocyclus ingens* group abundance and, thus, inferred SST, at ODP Sites 747, 744 and 1165, continued to decrease until at least 13.2 Ma (Figure 7). Reconstructed SSTs at Subantarctic ODP Site 1171 and Polar Frontal Zone ODP Site 1092 do not exhibit the same decreasing temperature trend, suggesting Southern Ocean latitudinal SST gradients and thermal isolation of the Antarctic continent continued to increase between the end of Mi3 and beginning of Mi4 (c. 13.7-13.2 Ma). *A. ingens* abundance at Site 747 appears to decrease cyclically, paced by the 100 kyr eccentricity cycle, and closely corresponds to the benthic oxygen isotope record from western equatorial Pacific ODP Site 1146 (Holbourn et al., 2013) (Figure 7). The % *A. ingens* group record at Site 747 is the first Southern Ocean climate record clearly exhibiting 100 kyr cyclicity post-Mi3, following the suggestion of orbital cyclicity in the SST record at Site 1171 (Figure 7; Shevenell et al., 2004). However, proxy climate records from other locations do indicate 100 kyr periodicities following Mi3. Most notably, benthic oxygen isotope records from the eastern equatorial Pacific Ocean (e.g. ODP Sites 1237 and 1236) and southwest Pacific (e.g. DSDP Sites 588, 806 and 574) (Holbourn et al., 2013b), but also monsoonal variability inferred from lake records in NE Tibet (Wang et al., 2018). Together, these records indicate that elements of the global climate system were paced primarily by eccentricity between 13.8-13.2 Ma.

The observed c. 100 kyr cycle in diatom-inferred SST at Site 747 (Figure 7) is not seen at the more southerly Sites 744 and 1165. At Site 744, this is likely because the sample resolution (between 20 and 80 kyr) is insufficient to capture 100 kyr cyclicity, since diatom assemblage patterns at Site 744 otherwise closely follow those at Site 747 during this period. However, the sample resolution at Site 1165 (10-20 kyr) is adequate to capture 100 kyr cyclicity, so this is not the cause for the lack of 100 kyr cyclicity closer to the Antarctic continent. The prominent 100 kyr cyclicity at the Pacific sites has been linked to enhanced Pacific Meridional Overturning Circulation (PMOC) during glacial periods following Mi3 (Holbourn et al., 2013). The Site 747 record demonstrates that the 100 kyr cyclicity was not limited to the Pacific sector, but that enhanced PMOC could have been driven by cyclical glacial equatorward shifts of the southern westerly wind (SWW) belt (Sijp & England, 2009) and, in turn, the Polar Front, similar to what probably occurred during Quaternary glacial cycles (Kohfield et al., 2013). The lack of 100 kyr cyclicity in both the diatom and IRD records at Site 1165 suggest the 100 kyr forcing of the SWW belt came from the north rather than from Antarctica. For example, alternative potential forcing mechanisms include changes in latitudinal temperature gradients (Flower & Kennett, 1990; Sime

et al., 2013) and/or teleconnections to the tropics or even the Northern Hemisphere (Ceppi et al., 2013; Montade et al., 2015), although the nature of such teleconnections is poorly constrained in the Miocene. However, these suggestions are highly speculative, and it cannot be ruled out that further age model refinement at Site 1165 could identify 100 kyr cyclicity within the record.

6.3.6. The Mi4 event

A third large peak in >1 mm IRD was recorded at ODP Site 1165 between 13.1-13 Ma, and was of a greater magnitude than the earlier peaks associated with Mi3 in terms of both wt% and grains/g (Figure 4), although fewer associated lonestones were observed (Shipboard Science Party, 2001). At 13.1 Ma, the IRD peak aligns with the Mi4 glaciation event that is associated with an almost equivalent decrease in benthic $\delta^{18}O$ (0.4‰) as occurred during Mi3 (0.5‰) (Holbourn et al., 2013a). A core gap at Site 1165 makes it more difficult to compare the Mi4 IRD peak with trends in diatom abundance, however, the IRD peak is not associated with high *Actinocyclus ingens* var. *nodus* abundance, because this species is not seen at Site 1165 after 13.48 Ma. Rather, *Denticulopsis simonsenii/vulgaris* reached its highest abundance (almost 80%) around 13.1 Ma, indicating particularly cool open water conditions at Site 1165. At c. 12.9 Ma (252.4 mbsf), a lithological transition also occurs at Site 1165, whereby the dominance of structureless, homogenous greenish clay and the abundance of >2mm grains decreases upwards (Shipboard Science Party, 2001). This suggests decreased siliciclastic sediment input and decreased current activity (Shipboard Science Party, 2001), perhaps as a result of an expanded, more stable ice sheet and reduced climate variability following Mi4 (Holbourn et al., 2013).

The Mi4 glaciation falls within the hiatus between c. 13.4-12.8 Ma at ODP Sites 747 and 744. The hiatus approximately corresponds with NH3, a global hiatus identified between 13.5 and 12.5 Ma in the Pacific Ocean, equatorial Indian Ocean and eastern North Atlantic (Keller & Barron, 1983). NH3 can also be recognised at Southern Ocean ODP Sites 751 and 748 (Harwood & Marayuma, 1992), ODP Site 1092 (Diekmann et al., 2003) and IODP Site U1356 (13.4-10.8 Ma; Sangiorgi et al., 2018). The most important factor responsible for pelagic Southern Ocean hiatuses at latitudes similar to Sites 747 and 744 is Antarctic Circumpolar Current (ACC) circulation (Diekmann et al., 2003). Sites 744 and 747 are particularly sensitive to changes in ACC flow strength because bathymetric constraints in the Kerguelen Plateau region focus ACC flow through the Princess Elizabeth Trough and the Fawn Trough (Figure 1 in Chapter 2), leading to particularly high flow speeds (Florindo et al., 2013; Vivier et al., 2014) and, thus, the erosion or

non-deposition of sediment. It therefore seems likely that the hiatuses at Sites 747 and 744 are caused by invigorated ACC circulation and increased flow speeds, which led to the erosion or non-deposition of sediment at these sites. In support of this hypothesis, a period of significantly increased Pacific Deep Water Boundary Current (an offshoot of the ACC) flow speeds was identified between 13.6 and 12.7 Ma at ODP Site 1123, located east of New Zealand (Hall et al., 2003). Peaking at 13.2 Ma, the increase was linked to increased wind strength over the Southern Ocean (Hall et al., 2003). Benthic $\delta^{18}O$ at ODP Site 1085 in the SE Atlantic also shows a sharp decrease beginning at 13.35 Ma, immediately prior to Mi4 (Westerhold et al., 2005). This benthic $\delta^{18}O$ decrease correlates with the beginning of the hiatuses at Site 747 and 744, suggesting global deep water cooling and associated invigorated ACC circulation likely played an important role in driving Mi4 ice growth.

The timing of ACC evolution is still debated. Some form of circumpolar current probably initiated in the early Oligocene following the opening of the Tasmanian Gateway and possibly Drake Passage (Katz et al., 2011; Scher et al., 2015), and intensified during the late Oligocene (Lyle et al., 2007). However, full ACC circulation may not have been established until the Middle Miocene (Poulin et al., 2014), or even later (Dalziel et al., 2013). Whether or not Mi4 represents the development of full ACC circulation, the diatom and IRD data clearly show that Mi4 was associated with a large strengthening of the ACC, as well as substantial cold-driven iceberg discharge. Invigorated ACC circulation during Mi4 probably also impacted the global climate system. For example, it seems likely that the coincident onset of upwelling in the Arabian Sea (Gupta et al., 2015), the resulting expansion of the Indian Ocean oxygen minimum zone and the proposed abrupt onset of the South Asian Monsoon at 12.9 Ma (Betzler et al., 2016) are associated with increased ACC circulation. The Neogene development of the ACC will be discussed in greater detail in Chapter 7.

6.3.7. Did Southern Ocean diatom productivity play a role in CO_2 drawdown during the Middle Miocene?

Recent studies have identified periods of increased siliceous productivity in the equatorial Pacific Ocean, linked to CO_2 drawdown and subsequent Mi3 global cooling (Holbourn et al., 2014; Carter et al., 2016). Sustained increases in siliceous productivity in the equatorial Pacific require a sufficient nutrient supply which, in the modern equatorial Pacific, mostly comes from upwelling Antarctic Intermediate Water (AAIW). The nutrient content of AAIW is modulated by biological productivity in the Southern Ocean where AAIW forms; increased biological

productivity in the Southern Ocean reduces the nutrient content of AAIW and vice versa (see Section 1.1.2). Substantially increased productivity in the equatorial Pacific should, therefore, be linked to parallel changes in Southern Ocean productivity.

The diatom concentration records presented in this chapter show two prominent peaks at 14.8 and 14.2 Ma at ODP Site 744, and to a lesser extent at ODP Sites 747 and 1165 (Figure 6). Both peaks are dominated by *Actinocyclus ingens* and the related *Actinocyclus ingens* var*. nodus* – a particularly large (35-65 μm; Baldauf & Barron, 1980), strongly silicified centric diatom whose abundance and nutrient uptake, if replicated throughout the Southern Ocean, would presumably have decreased AAIW nutrient concentrations and even increased carbon sequestration in the Southern Ocean. It is therefore possible that the decrease in relative and absolute abundances of *A. ingens* and *A. ingens* var. *nodus* (warm water diatoms - Chapter 5) following the onset of Southern Ocean cooling from 14.2 Ma (Figure 8) could therefore have increased the supply of available nutrients to the equatorial Pacific, facilitating the increased siliceous productivity documented there between 14.0 and 13.7 Ma (Holbourn et al., 2014; Carter et al., 2016).

Diatom concentrations at ODP Sites 747, 744 and 1165 then increase again from c. 13.5 Ma (Figure 6). This potentially represents a further shift in the locus of siliceous productivity away from the equatorial Pacific, where opal accumulation remains lower after c. 13.6 Ma (Holbourn et al., 2014), back to the Southern Ocean; coherent in timing with proposed invigorated ACC circulation and, therefore, increased nutrient supply to the Southern Ocean.

6.4. Summary and conclusions

The Southern Ocean is a key modulator of global climate, in part via its role as a moisture and heat source to the Antarctic Ice Sheet. However, relatively little is known about how the Southern Ocean contributed, and responded, to the growth of the Antarctic ice cap to near modern size during the Middle Miocene; a period of major global cooling. Here I have presented the first latitudinal transect of quantitative Southern Ocean diatom assemblage records from ODP Sites 747, 744 and 1165 from between 15-12 Ma, together with an ice rafted debris (IRD) record from Site 1165. These records have shown that prior to the Mi3 event (the Middle Miocene Climate Transition, c. 13.8 Ma), diatom assemblages from all three sites indicate a warm Southern Ocean, with water column stratification and negligible marine ice in Prydz Bay. Maximum warmth occurs at all three sites between 14.5 and 14.2 Ma, but minimal IRD

deposition during this period suggests a relatively insensitive, predominantly land-terminating, EAIS. At 13.8 Ma, peak IRD deposition and increased abundances of cool water diatoms such as *Rouxia* spp. and *Fragilariopsis* spp., as well as a sharp decrease in benthic and neritic diatom abundance at Site 1165, indicate the expansion of marine ice into Prydz Bay during peak cooling. This is followed by a c. 70 kyr period of consistent IRD deposition between c. 13.77-13.70 Ma, correlated with increased *Actinocyclus ingens* var. *nodus* abundance at Site 1165. This likely reflects surface ocean warming associated with changes in ice elevation and the wind field, which resulted in significant iceberg discharge and melting. Progressive cooling between 13.7 and 13.2 Ma, not seen at more northerly sites, suggests an increasing latitudinal temperature gradient and Antarctic thermal isolation between Mi3 and Mi4. The diatom record at Site 747 shows c. 100 kyr cyclicity during this interval, possibility reflecting orbitally-forced fluctuations of an oceanic frontal boundary. Finally, further IRD deposition during Mi4 (c. 13.1 Ma) at Site 1165 is coincident with hiatuses recorded at Sites 747 and 744. The hiatuses represent an intensification of the Antarctic Circumpolar Current between 13.4 and 12.7 Ma, which likely contributed to further Antarctic cooling and ice growth during Mi4.

7. Neogene palaeoceanography of the Southern Ocean & evolution of the Antarctic Circumpolar Current

7.1. Introduction

This chapter will present, analyse and discuss quantitative diatom assemblages as well as diatom and other silicofossil concentrations at ODP Site 1165 over the last fifteen million years. These data will be interpreted in the context of unpublished quantitative *Thalassiothrix/Trichotoxon* (*Thlx* group) abundances and diatom concentrations from ODP Site 1138 (A. Biddle, unpublished data, 2012) and published weight percent biogenic silica (% BSi) and diatom assemblage records from other Southern Ocean sites in order to better constrain Neogene Antarctic climate evolution and, in particular, the development of the Antarctic Circumpolar Current (ACC). The ACC, previously discussed in Chapters 1 and 6, is the strongest, most voluminous ocean current in the world (Donoghue et al., 2016), and is the most important component of modern Southern Ocean circulation. Constraining its evolution is therefore essential to understanding Southern Ocean palaeoceanography and, in turn, the relationship between the Southern Ocean and the Antarctic Ice Sheets through the Neogene.

7.1.1. Proxies for tracking past fluctuations of the ACC

North of the Polar Front (PF), higher temperature, lower nutrient ocean conditions result in marine sediments which are dominated by calcareous plankton (Barker & Thomas, 2004; Flores & Sierro, 2007). To the south, larger R-strategist siliceous plankton, e.g. diatoms, have a competitive advantage in higher nutrient conditions and so are more abundant in sediments (Smetacek, 2012). Given these associations, it is possible to track the evolution of the PF, and thus the ACC, using the marine sedimentary record; by reconstructing the abundance of biogenic opal vs. carbonate in marine sediment cores to determine the boundary between calcareous sediment north of the PF and opal-dominated sediment to the south (Burckle et al., 1996; Anderson et al., 2009; Kemp et al., 2010; Tang et al., 2016). In the open Southern Ocean away from the continental shelf terrigenous input is generally low (Diekmann et al., 2003), so carbonate and biogenic silica are the two primary components of marine sediment. Reconstructing only % Biogenic Silica (% BSi) or % $CaCO_3$ can therefore still be useful in determining the position of the PF. Microfossil assemblages can also be used to reconstruct changes in the position of the PF because different species proliferate in the different oceanographic conditions either side of the front (Barron, 1996; Cortese & Gersonde, 2008; Bart & Iwai, 2012; Taylor-Silva & Reisselman, 2018).

In addition to biogenic proxies, ACC evolution can be tracked using physical proxies, for example, grain size analysis as a proxy for paleo-current speeds. Studies utilising grain size analysis to track ACC circulation reconstruct the initiation of the ACC at 24 Ma, and its intensification associated with expansion of the East Antarctic Ice Sheet (EAIS) during the Middle Miocene (Hall et al., 2003; Pfuhl & McCave, 2005). McCave et al. (2014) also used grain size to infer minimal changes in ACC flow speeds between the last glacial maximum and the Holocene. The paleo-ACC can also be reconstructed using erosional surfaces and sedimentary hiatuses, since particularly high flow speeds can breech the threshold for the non-deposition or erosion of non-cohesive sediments (Barker & Thomas, 2004). For example, erosional surfaces on the Falkland Plateau, sedimentation rates and seismic correlation studies have all been used to infer ACC initiation from the Oligocene and Early Miocene (Koenitz et al., 2008; Perez et al., 2015; Nicholson & Stow, 2019). Hiatuses within Polar Frontal Zone cores have been used to suggest intensification of the ACC during the Middle and Late Miocene (Diekmann et al., 2003). In Chapter 6, I used the presence of hiatuses at ODP Sites 744 and 747 to infer increased flow speeds of the ACC coinciding with Mi4 at c. 13 Ma. However, care must be taken when interpreting the palaeoceanographic significance of hiatuses and features at single core sites, because the passage over a site of a frontal system such as the PF, associated with particularly high flow speeds, could result in hiatuses despite no overall change in flow speed. As such, single records should ideally be evaluated in the context of other records.

7.1.2. Cenozoic evolution of the Southern Ocean and ACC

Early workers suggested the ACC first initiated in the late Eocene, facilitated by the opening of the Tasman Gateway between c. 35.5 and 30.2 Ma (Stickley et al., 2004 and references therein). This theory proposes that initiation of the ACC helped to thermally isolate Antarctica, forcing the Cenozoic onset of large-scale Antarctic glaciation at the Eocene/Oligocene transition (EOT), c. 34 Ma (Kennett, 1977; Zachos et al., 1996). This early theory is supported by a recent study which documented erosional surfaces on the Falkland Plateau from 34 Ma (Nicholson & Stow, 2019). However, other studies have questioned this narrative, and suggested that the ACC initiated, or at least first strengthened to its full capacity, at a later date. For example, neodymium ratios in cores from the Tasmanian Margin and Hikurangi Plateau have been used to document the large-scale homogenisation of water masses that suggests full ACC development by 30 Ma (Scher et al., 2015); around 4 Ma after the EOT. Water mass homogenisation is proposed to have followed the opening of the Tasman Seaway at 33.5 Ma, and the subsequent drift of the northern margin of the Tasmanian Gateway into the mid latitude

westerly wind band. Other studies show no change in water mass composition and, therefore, Southern Ocean circulation in the Kerguelen Plateau region during the entire Eocene and Oligocene (Wright et al., 2018), while climate model studies suggest a circumpolar deep water circulation pathway could not have existed during the Oligocene due to Australian paleogeography (Hill et al., 2013). The opening of Drake Passage, essential for a circumpolar deep water flow path, also remains chronologically unconstrained, with estimates ranging from the Early Eocene to as late as the earliest Miocene (Lawver and Gahagan, 2003; Lyle et al., 2007). Barker (2001) suggested that during the early stages of its opening, the bathymetry of Drake Passage would have been rougher and shallower, potentially prohibiting full ACC development until the Middle Miocene. However, even the opening of these gateways may not have been sufficient to initiate the ACC in isolation; it has been suggested that a background cooling climate may also have been required for full expression of the ACC (Pfuhl & McCave, 2005; Lefebvre et al., 2013).

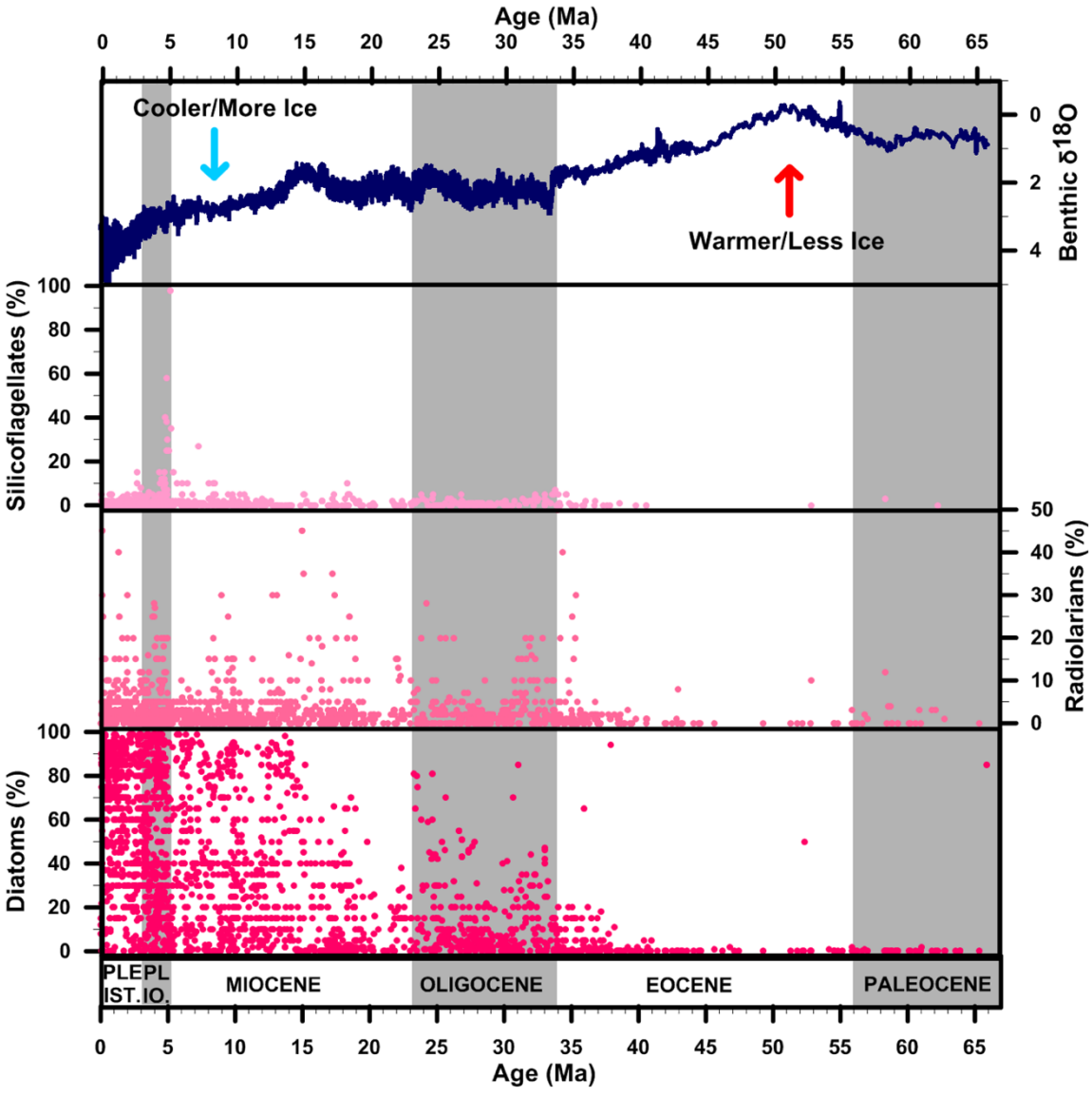

Figure 1. The proportion of silicofossils in smear slides from ODP Sites drilled in the Southern Ocean through the Cenozoic. Silicofossil data (from cores South of 40°S) is taken from the global dataset of Renaudie (2016) and benthic oxygen isotope data in the top panel is from Zachos et al. (2001).

Southern Ocean sediments contain more siliceous microfossils from c. 38 Ma, increasing again from c. 33 Ma (Renaudie, 2016), which suggests the intensification of Southern Ocean upwelling during the Late Eocene and Early Oligocene (Figure 1). However, silicofossils, and in particular diatoms, do not reach modern abundances in Southern Ocean sediments until the Middle-Late Miocene (Figure 1). Microfossil assemblage studies also demonstrate that a large proportion of microfossils in Southern Ocean sediments were of relatively cosmopolitan distributions during the Neogene. For example, diatom species dominating Oligocene Southern Ocean sediments include the cosmopolitan diatom species *Coscinodiscus marginatus, Cestodiscus pulchellus* and *Rocella* spp. (Harwood & Maruyama, 1992).

The new diatom records presented in Chapter 6 also show that prior to the Middle Miocene Climatic Transition at c. 13.8 Ma, cores south of the modern PF, e.g. Sites 747 (54°S) and 744 (61°S), were dominated by the cosmopolitan diatom *Actinocyclus ingens*. These cores, as well as other sites situated south of the modern PF, e.g. ODP Sites 1138 (53°S) and 751 (57°S), also remain primarily composed of carbonate rather than biosilica until at least the Late Miocene (Shipboard Scientific Party, 1989; Shipboard Scientific Party, 2000). This suggests either that the PF was located far south of its current position, or that the ACC and PF were not fully developed until after this time. Thus, while the ACC likely initiated in some form during the Early Oligocene, perhaps during the EOT (Nicholson & Stow, 2019), it probably did not reach its full strength and capacity until at least the Middle-Late Miocene. In this chapter, I will present new insights into ACC development over the last 15 million years to better constrain its evolution and relationship to the Antarctic Ice Sheet and global climate.

7.2. Core sites: new data and published palaeoceanographic proxy records

7.2.1. New quantitative diatom records from ODP Site 1165

Quantitative diatom assemblages at ODP Site 1165 between 12-0 Ma are presented and analysed alongside the 15-12 Ma Site 1165 record that was presented in Chapter 6, thereby reconstructing a 15 million year interval of Southern Ocean history. For details on the methodology for quantitative diatom analysis at Site 1165, see Section 3.1.

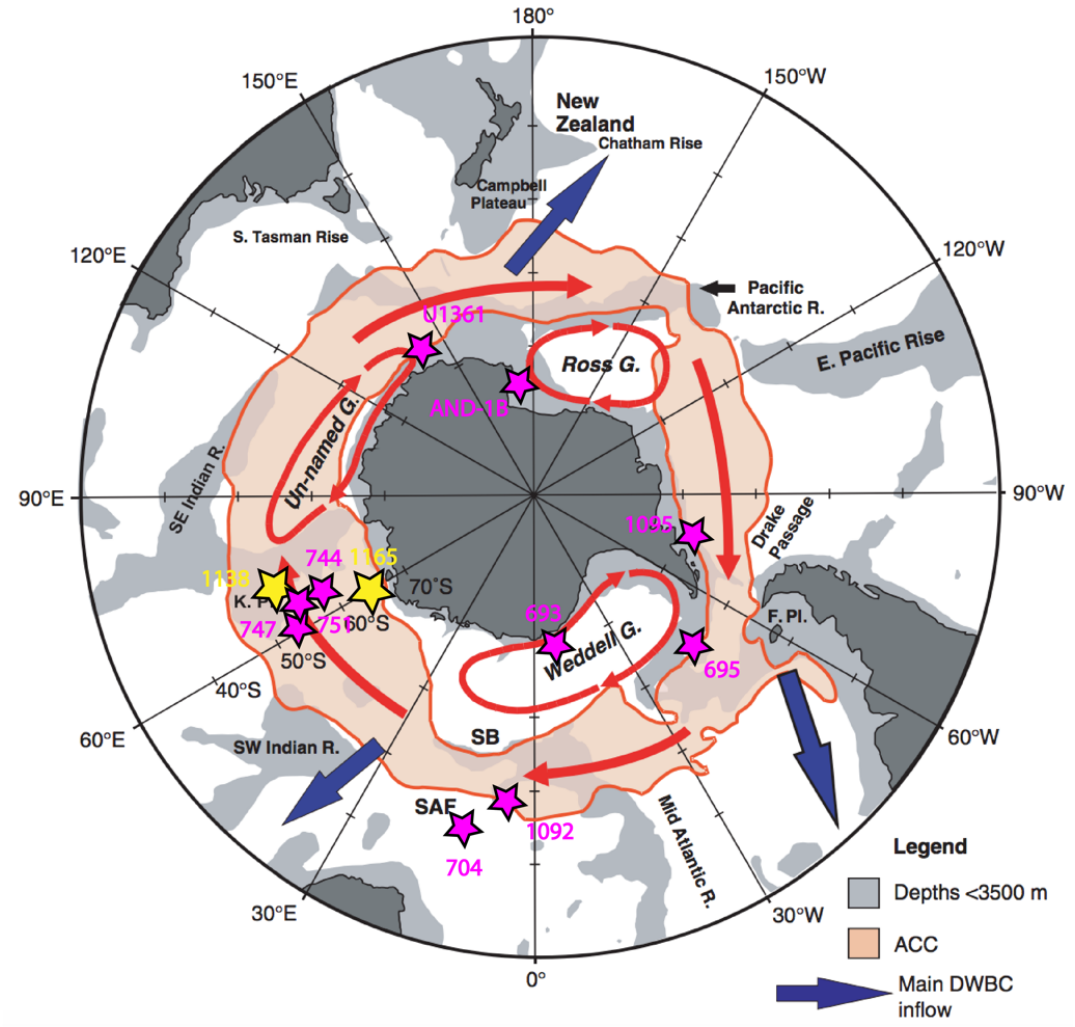

Figure 2. Sites investigated in this Chapter. New records in yellow, published records in pink (modified from Carter et al. (2008) and Orsi & Whitworth (2005)). SAF= Sub Antarctic Front, SB= Southern Boundary; the orange coloured area represents the limits of modern Circumpolar Deep Water upwelling.

7.2.2. New quantitative silicofossil concentration records from ODP 1165

Quantitative sedimentary diatom, radiolarian, silicoflagellate and crysophyte cyst concentrations from ODP Site 1165 are presented between 15-0 Ma (diatom concentrations between 12-15 Ma are also discussed in Chapter 6). The methodology for generating radiolarian, silicoflagellate and crysophyte cyst concentrations is the same as used for generating diatom concentrations (see Section 3.1).

7.2.3. New diatom records from ODP Site 1138

A new quantitative diatom assemblage record from 15-0 Ma (A. Biddle, unpublished data, 2012) at ODP Site 1138 (Figure 2) is also presented in this chapter, generated using the same methods as used at Site 1165. However, only total diatom concentrations and relative abundances of the *Thalassiothrix spp./Trichotoxon reinboldii* group (hereafter the *Thlx* group) are utilised in this chapter in order to avoid potential differences in species identification between observers. The *Thlx* group are easily distinguished from other diatoms due to their long, thin, needle-like valves and, therefore, the risk of confusion with other diatom genera is low.

7.2.4. Published weight percent biogenic silica and diatom records

Published records of weight percent biogenic silica (% BSi), diatom concentrations and diatom assemblages from ODP Sites 751, 747, 704, 693 and 695 (Figure 2) (Renaudie, 2016) are used in this chapter to contextualize the new diatom and silicofossil records at ODP Sites 1165 and 1138. Renaudie (2016) utilized data published in Initial Reports from each Ocean Drilling Program Leg, as well as data from the Janus database (Mithal & Becker, 2006) and the National Geophysical Data Centre, 2001 and 2002. For details of the age models used in these records, see Renaudie (2016).

Records included in this chapter in addition to those from Renaudie (2016) are: % BSi at ODP Site 1092 (Diekmann et al., 2003); % BSi and diatom assemblages at Site U1356 (Cook et al., 2013); diatom concentration and assemblages at ODP Site 1095 (Bart & Iwai, 2012); and diatom assemblages at AND-1B (McKay et al., 2012) (Figure 2). The published age models used in these studies are also used here.

7.3. Results

7.3.1. Diatom assemblages at ODP Site 1165

Over 226 diatom species are identified at ODP Site 1165 from 15 Ma to the present. Preservation, according to the preservation index of Barron & Gladenokov (1992), is generally moderate-good, although several intervals with poor preservation were encountered; c. 5-17 mbsf, 78-84 mbsf, and c. 119 mbsf, which generally coincided with low sedimentary diatom concentrations. However, it was always possible to count at least 400 valves in each sample. Diatom preservation was best where diatom concentration was highest. Planktonic, neritic and benthic diatoms are identified at Site 1165, but the number of planktonic species far outweighs the proportion of benthic or neritic diatoms; as expected at a continental rise site. The

planktonic diatoms encountered at Site 1165 are grouped into palaeoecological categories defined in Chapter 5 and Appendix 1.

Diatom assemblages between 15 and 12 Ma at Site 1165 are described in Chapter 6. A core gap due to low recovery then exists between 12.39-11.43 Ma (223.72 to 198.50 mbsf; See Chapter 4 for details of Site 1165 chronology). Directly above the core gap, the samples at 198.50 and 197 mbsf (11.43 Ma and 11.29 Ma) are dominated (40-50%) by *Denticulopsis dimorpha*, followed by the sample at 193.55 mbsf (10.87 Ma), which is dominated (49%) by *Denticulopsis ovata* (Figure 3). After this point, diatom assemblages at Site 1165 again become overwhelmingly dominated by *Denticulopsis simonsenii/vulgaris* between 191.30-121.10 mbsf (10.58-9.47 Ma), which generally represents 50-70% of the diatom assemblage (Figure 3). During this *D. simonsenii/vulgaris*-dominated interval, the cool water diatoms *Denticulopsis delicata* and *Fragliariopsis donaghuensis*, which show similar abundance patterns throughout the core, peak at 40% and 5%, respectively, between 186.06-177.95 mbsf (10.27-10.21 Ma), also coinciding with relatively high *CRS* abundance (18%) between 187.55-179.45 mbsf (10.28-10.22 Ma). A transient *Actinocyclus ingens* peak (14%) occurs at 176.45 mbsf (10.20 Ma). *Rhizosolenia styliformis* first increases in abundance to >4% upcore from 186.06 mbsf (10.27 Ma), and *Actinocyclus ehrenbergii* first occurs at 177.95 mbsf (10.21 Ma), peaking, although still rare (1%), at 150.75 mbsf (10.03 Ma). The *A. ehrenbergii* peak is immediately followed by the first appearance and peak abundance of *Thalassiosira nativa* (5%) at 146.75 mbsf (9.98 Ma) (Figure 3).

From c. 121.10 mbsf (9.32 Ma), *Denticulopsis simonsenii/vulgaris* begins to decrease in abundance at Site 1165, decreasing again from 92.50 mbsf (8.51 Ma) and falling to <10% by 73.50 mbsf (6.67 Ma) (Figures 3 & 6). Above a core gap between 107.25-99.84 mbsf (8.98-8.74 Ma), a peak in *A. ingens* between 92.40-89.75 mbsf (8.51-7.39 Ma) marks the end of *D. simonsenii/vulgaris* dominance. Following this *A. ingens* peak, *Thalassiosira oliveriana* var. *sparsa* abundance is highest (>5%) between 89.75-86 mbsf (7.39-7.04 Ma), while *Rouxia isopolica* and *Thalassiosira mahoodii* also peak (8% and 6%, respectively) at 85.25 mbsf (7.02 Ma) (Figures 3, 4 & 5). *Thalassiosira torokina* and *Thalassiosira* cf. *antarctica* first appear at 107.25 mbsf (8.99 Ma) and 145.25 mbsf (9.94 Ma), respectively, and become relatively abundant (>4%) from 81.23 mbsf (6.90 Ma) (Figures 3 & 5). The peak abundance of these four *Thalassiosira* species occurs within the *Actinocyclus ingens* var. *ovalis* range; a short-lived species only found

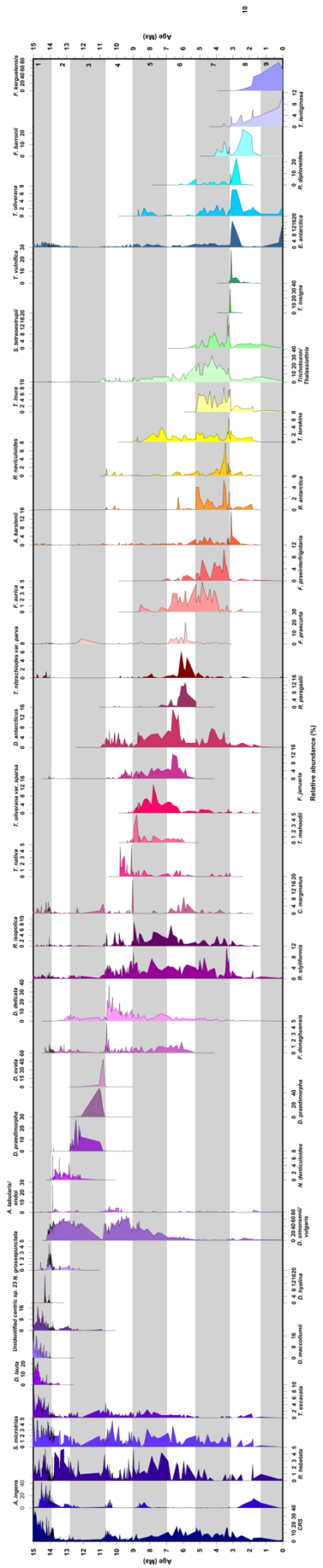

Figure 3. Relative diatom abundances (>5%) at ODP Site 1165.

at Site 1165 between 97.75-65.51 mbsf (8.68-6.07 Ma), and which peaks (2%) in abundance at 78.01 mbf (6.81 Ma) (Figures 3, 4 & 5).

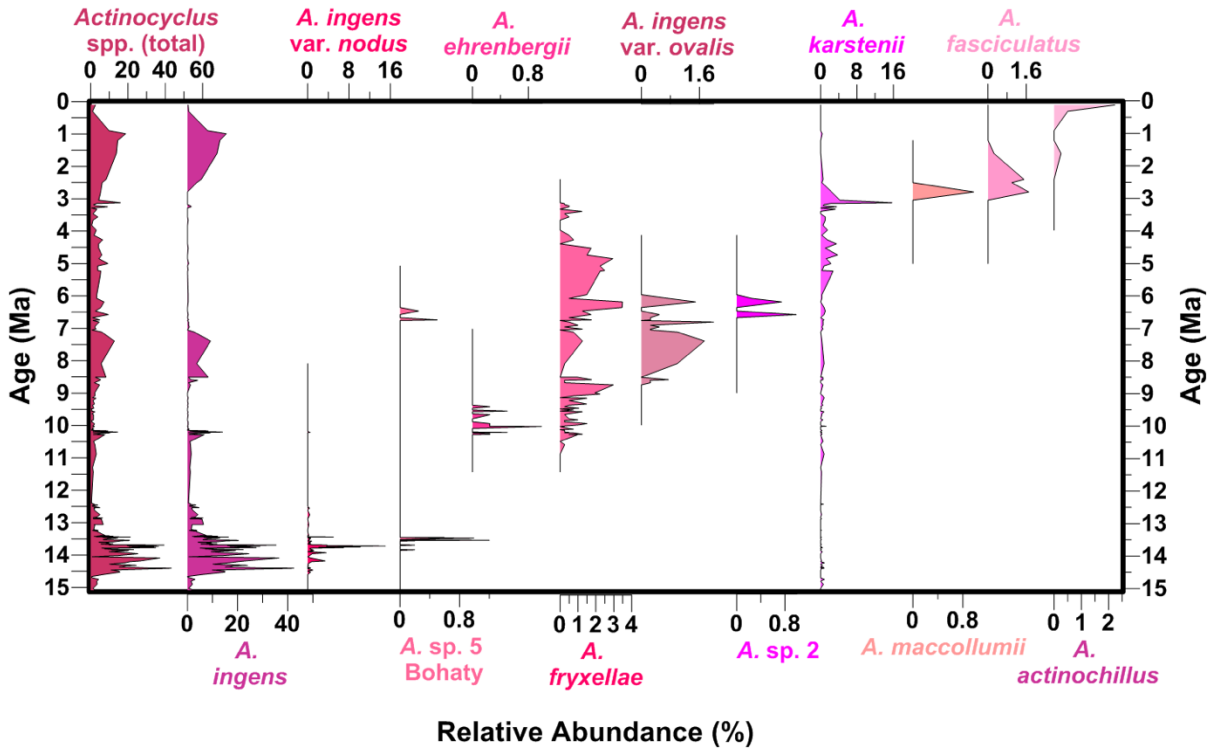

Figure 4. *Actinocyclus* species abundance at ODP Site 1165, species arranged chronologically by peak abundance. The total abundance of *Actinocyclus* spp. as a proportion of the diatom assemblage is shown in the left-hand column.

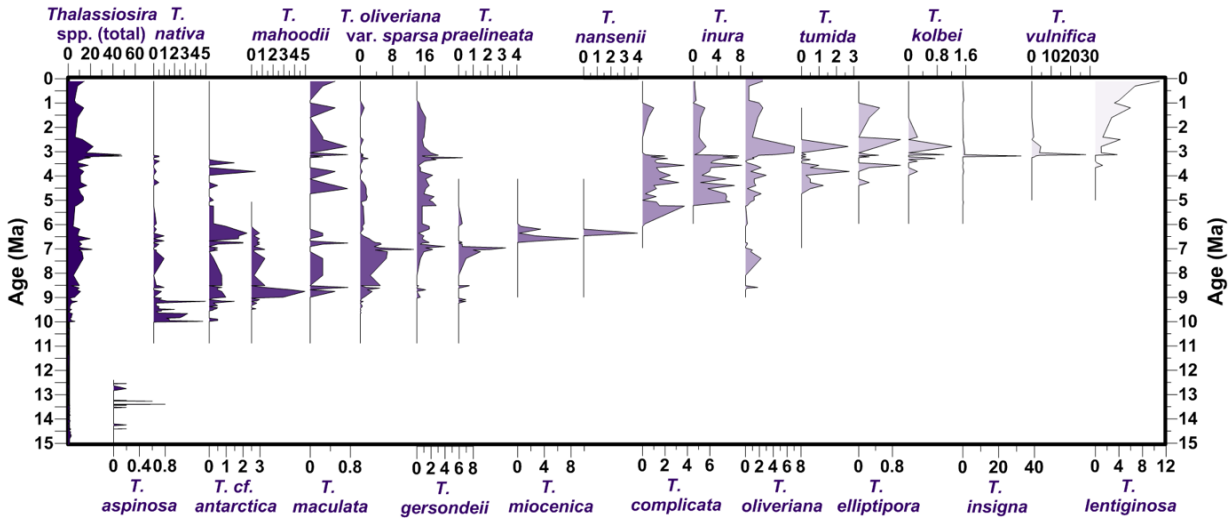

Figure 5. *Thalassiosira* species at ODP Site 1165, species arranged chronologically by peak abundance. The total abundance of *Thalassiosira* spp. as a proportion of the diatom assemblage is shown in the left-hand column.

Immediately following the *A. ingens* var. *ovalis* peak, the total abundance of *Fragilariopsis spp*. first reaches >30% by 73.50 mbsf (6.67 Ma), which approximately coincides with the first appearance of *Fragilariopsis aurica, Fragilariopsis arcula* and *Fragilariopsis praeinterfrigidaria*, although *F. praeinterfrigidaria* abundance remains low (<4%) until c. 5 Ma (Figures 3 & 7). *Fragilariopsis* cf. *vanheurckii* first increases to >4% from 113.25 mbsf (9.14 Ma) and peaks at 73.50 (6.67 Ma), with *Fragilariopsis januaria* showing almost identical abundance patterns to *F.* cf. *vanheurckii*, peaking at 13% at 73.50 mbsf (6.67 Ma). *Fragilariopsis praecurta* also increases in abundance during this interval, although it increases to its highest abundance of the entire record (20%) slightly later, at 65.61 mbsf (6.08 Ma). The sample at 65.61 mbsf also contains peak (15%) abundances of *Rouxia peragalli*, while *Thalassionema* var. *parva* also peaks (5%) between 69.25-64 mbsf (6.35-5.96 Ma).

Early Pliocene (5.33-3.60 Ma) diatom assemblages at Site 1165 show a large increase in the abundance of the *Thalassiothrix/Trichotoxon* (*Thlx*) group (Figure 3) between 54.33-29 mbsf (5.24-3.29 Ma), peaking in abundance (32%) at 43 mbsf (4.27 Ma). Diatom preservation is also very good during this 54.33-29 mbsf interval. *Rouxia antarctica* abundance peaks (4%) at 54.24 mbsf (5.21 Ma), approximately coinciding with the first occurrences of *Thalassiosira inura*, *Shionodiscus tetraoestrupii* and *Fragilariopsis reinholdii* (Figure 3). *Fragilariopsis aurica* abundance is also highest during the Early Pliocene, peaking (5%) at 48.01 mbsf (4.85 Ma).

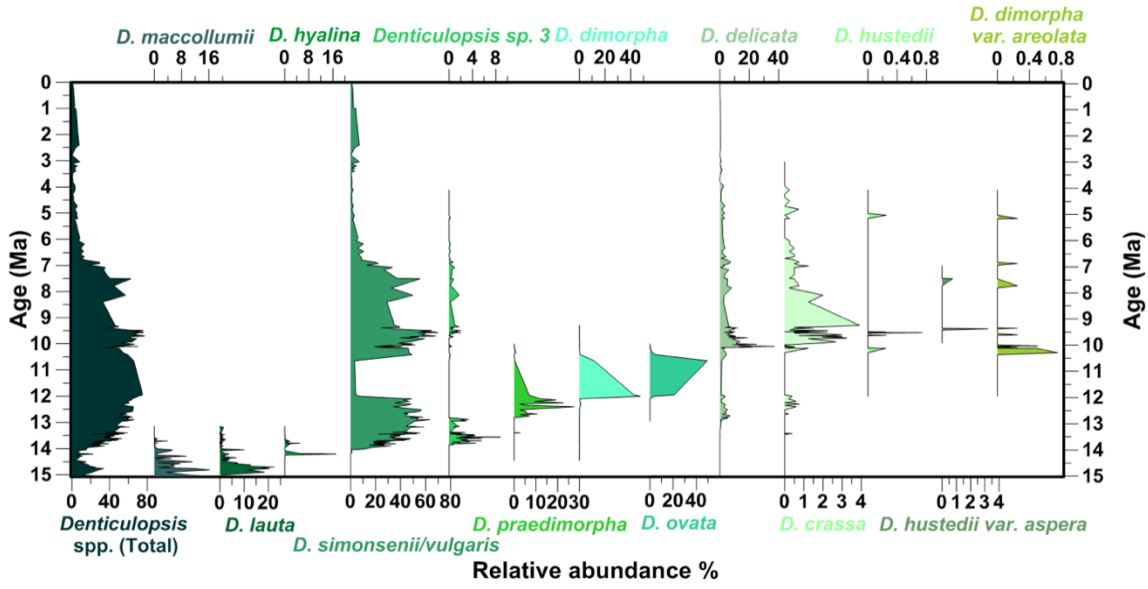

Figure 6. *Denticulopsis* species at Site 1165, species arranged chronologically by peak abundance. The total abundance of *Denticulopsis* spp. as a proportion of the diatom assemblage is shown in the left hand column.

During the Late Pliocene (3.6-2.58 Ma), following a reduction in the prominence of the *Thlx* group, diatom assemblages at Site 1165 undergo a period of substantial variability. Peaks in *Rouxia antarctica* (5%) at 35.64 mbsf (3.54 Ma), *Rouxia naviculoides* (8%) at 33.50 mbsf (3.45 Ma), and *Shionodiscus tetraoestrupii* (20%) at 30.31 mbsf (3.32 Ma) are closely followed by isolated peaks in *Thalassiosira torokina* (7%) at 27.50 mbsf (3.25 Ma), *Thalassiosira insigna* (33%) at 24.01 mbsf (3.17 Ma), *Actinocyclus karstenii* (16%) and *Thalassiosira vulnificana* (28%) at 24.01 mbsf (3.11 Ma) and *Thalassiosira oliveriana* (7%) between 19.50-18 mbsf (3.05-2.80 Ma). *Eucampia antarctica* is also at its highest abundance of the entire record between 21.02-18 mbsf (3.11-2.80 Ma), peaking (17%) at 19.50 mbsf (3.05 Ma). *Actinocyclus fasciculatus* first appears at 18 mbsf (2.80 Ma), and *Rouxia diploneides* peaks (20%) at 18 mbsf (2.79 Ma). The Late Pliocene is notable for the presence of *Fragilariopsis weaverii* which, although rare (<2%) at Site 1165, peaked in abundance between 26-16.50 mbsf (3.22-2.50 Ma).

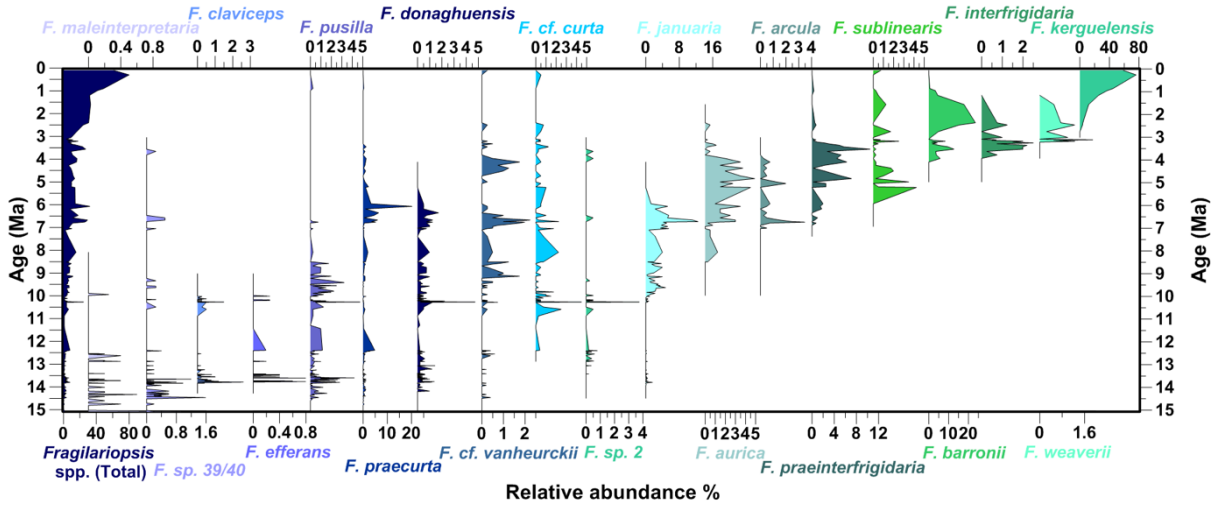

Figure 7. *Fragilariopsis* species at Site 1165, species arranged chronologically by peak abundance. The total abundance of *Fragilariopsis* spp. as a proportion of the diatom assemblage is shown in the left hand column.

Fragilariopsis spp. begin to dominate the Site 1165 diatom assemblage at the onset of the Pleistocene, 2.58 Ma, reaching up to 80% abundance in the youngest samples at Site 1165. The most abundant *Fragilariopsis* species during this period are *Fragilariopsis barronii* and its descendent *Fragilariopsis kerguelensis* (Figures 3 & 7). *F. barronii* is most abundant (23%), with an early form of *F. kerguelensis*, at 16.01 mbsf (2.40 Ma), followed by the modern form of *F. kerguelensis,* which peaks at 76% abundance by 1.70 mbsf (0.24 Ma). *Thalassiosira lentiginosa* first appeared at 3.11 Ma, but peaks in abundance (11%) only in the youngest samples at Site 1165, as does *Actinocyclus actinochilus* (<2%). Other notable occurrences of the Pleistocene

diatom assemblages at Site 1165 include a final peak (15%) in *A. ingens* at 7 mbsf (c. 0.99 Ma), although the sample resolution for this interval is relatively low. The sample containing peak *A. ingens* (15%) likely represents MIS 31 at Site 1165 (Teitler et al., 2015).

7.3.2. Diatom diversity

As in the previous chapter (Chapter 6), diatom diversity at Site 1165 is assessed in terms of the Simpson's Diversity Index (SDI) and Shannon's H (SH), both of which calculate the evenness and abundance of diatom species within a given sample using slightly different statistical models (Figure 8). Prior to Mi3 cooling at c. 13.8 Ma, diatom diversity at ODP Site 1165 is relatively high (>0.8 SDI, c. 2.50 SH). However, after Mi3 cooling diatom diversity drops to around 0.6 SDI and 0.50 SH by 13 Ma, remaining low until at least 223.72 mbsf (12.39 Ma). Above the core gap at Site 1165 (223.72-198.50 mbsf, 12.39-11.43 Ma), diatom diversity remains at similar levels to below the gap, but increases to 0.85 SDI and 2.50 SH by 182.81 mbsf (10.23 Ma). This increase in diversity is short-lived, decreasing again over the subsequent c. 400 kyr to its lowest levels of the entire 15 Ma record; reaching 0.45 SDI and 1.21 SH by 143.01 mbsf (9.89 Ma).

Following minimum diatom diversity at c. 9.5 Ma, diatom diversity increases sharply at Site 1165, peaking (0.96 SDI, 3.34 SH) at 72.25 mbsf (6.58 Ma). Diatom diversity remains relatively high and stable throughout the rest of the Late Miocene, Pliocene and early Pleistocene. Diatom diversity at Site 1165 then drops sharply above 1.81 mbsf (1.19 Ma), reaching its lowest levels (0.45 SDI, 1.24 SH) in the second youngest sample at 1.70 mbsf (0.25 Ma). Taphonomic and preservational bias likely affected diatom preservation in all samples at Site 1165, but intervals with poor preservation (c. 5-17 mbsf, 78-84 mbsf, and c. 119 mbsf) do not show particularly low diversity, suggesting any preservational bias on diversity calculations is minimal.

Overall, the Shannon's H (SH) and Simpson's diversity indices (SDI) largely align at Site 1165, reflecting the same trends in the diatom assemblages. The main difference between the indices is that SH suggests a slightly larger increase in diversity after c. 7 Ma, lasting through the latest Late Miocene and Pliocene, relative to diatom diversity in the preceding Middle/Late Miocene interval (Figure 8). SH also shows a decrease in diatom diversity beginning at 22.50 mbsf (3.14 Ma), not seen in the SDI record, although both indices record a sharp decrease in diversity after 8.50 mbsf (1.20 Ma). Despite these minor differences, the congruence of diversity indices, similar to the diversity records presented in Chapter 6, supports the robustness of the trends in diatom diversity at Site 1165.

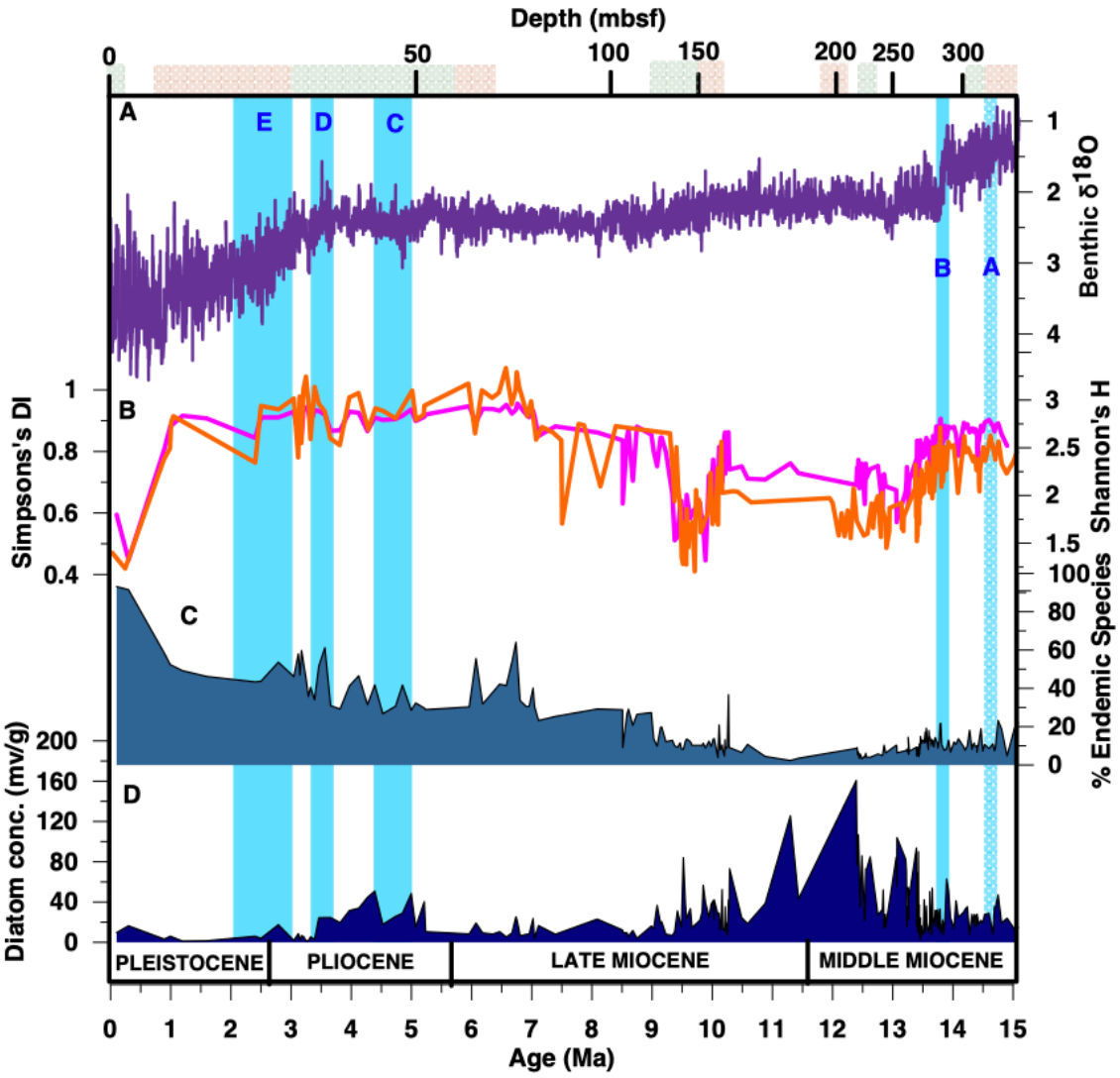

Figure 8. A) Benthic foraminiferal $\delta^{18}O$ stack (De Vleeschouwer et al., 2017). B) Diatom diversity at ODP Site 1165, quantified in terms of Simpson's Diversity Index (SDI). C) The proportion of the diatom assemblage at ODP Site 1165 made up of endemic Southern Ocean species. D) Diatom concentrations (mv/g) at ODP Site 1165. Vertical blue shading indicates Southern Ocean diatom evolutionary turnover events identified by Crampton et al. (2016), green and brown shaded boxes on upper axis indicate periods of particularly good or particularly poor preservation, respectively.

7.3.3. Endemic diatom species

The proportion of diatom species that are endemic to the Southern Ocean, as opposed to bipolar, mid latitude and/or cosmopolitan species, was calculated in order to assess relative Southern Ocean thermal and/or physical isolation. Results show that the proportion of endemic species remains low (generally <20%) until 166 mbsf, between c. 15-10 Ma, at Site 1165 (Figure 8), with an isolated peak (37%) at 186.06 mbsf (10.27 Ma). However, above this point, the

proportion of endemic diatom species slowly begins to increase, reaching a peak of 64% at 75.76 mbsf (6.74 Ma). The proportion of endemic species then decreases and largely remains between 30-50% for most the Pliocene. However, above 37 mbsf (3.64 Ma), the number of endemic Southern Ocean diatom species at Site 1165 increases again, eventually reaching >90% above 6 mbsf (c. 1 Ma).

7.3.4. Diatom concentrations

Diatom concentrations at ODP Site 1165 generally remain relatively low (<40 mv/g) until 300 mbsf, prior to c. 14 Ma (Figure 9). However, during an isolated peak at 292.85 mbsf (13.90 Ma), diatom concentrations reach >60 mv/g. A step-wise increase in diatom concentration occurs at Site 1165 above 279.55 mbsf (13.43 Ma) after which, diatom concentrations reach almost 90 mv/g. Following this increase, diatom concentrations fluctuate substantially, between <20-110 mv/g, until 223.72 mbsf (12.39 Ma) when diatom concentrations reach 160 mv/g, representing the highest value of the entire record. Above the core gap between 223.72-198.50 mbsf (12.39-11.43 Ma), diatom concentrations begin to decrease again, reaching 4 mv/g by 7.67 Ma. Concentrations then remain low (4-25 mv/g) until 54.33 mbsf (5.24 Ma), but then increase to >40 mv/g by 40.01 mbsf (3.95 Ma). Above 40 mbsf diatom concentrations at Site 1165 remain low (<20 mv/g) for remaining Late Pliocene and Quaternary periods.

7.3.5. Radiolarian concentrations

Radiolarian concentrations at ODP Site 1165 are low (<0.1 million tests per gram- mt/g) until 300 mbsf, c. 14 Ma (Figure 9). Following a relatively isolated peak (0.3 mt/g) at 287.85 mbsf (13.69 Ma), radiolarian concentrations at Site 1165 reach 0.4 mt/v by 253.55 mbsf (13.07 Ma), increasing again to 0.8 mt/g by 235.28 mbsf (12.56 Ma). Radiolarian concentrations remain high (notwithstanding the core gap between 223.72-198.50 mbsf, 12.39-11.43 Ma), reaching peak concentrations of the entire record of 0.9 mt/g at 197 mbsf (11.30 Ma). Above 197 mbsf, radiolarian concentrations decrease, reaching their lowest levels by c. 100 mbsf (7.5 Ma), with an isolated peak (0.5 mt/g) at 85.25 mbsf (7.02 Ma). After 85.25 mbsf, radiolarian concentrations begin to increase again, remaining fairly high during the Pliocene and peaking at 0.6 mt/g by 41.50 mbsf (4.11 Ma). After this peak, radiolarian concentrations decrease at Site 1165 to <0.3 mt/g for the remaining record.

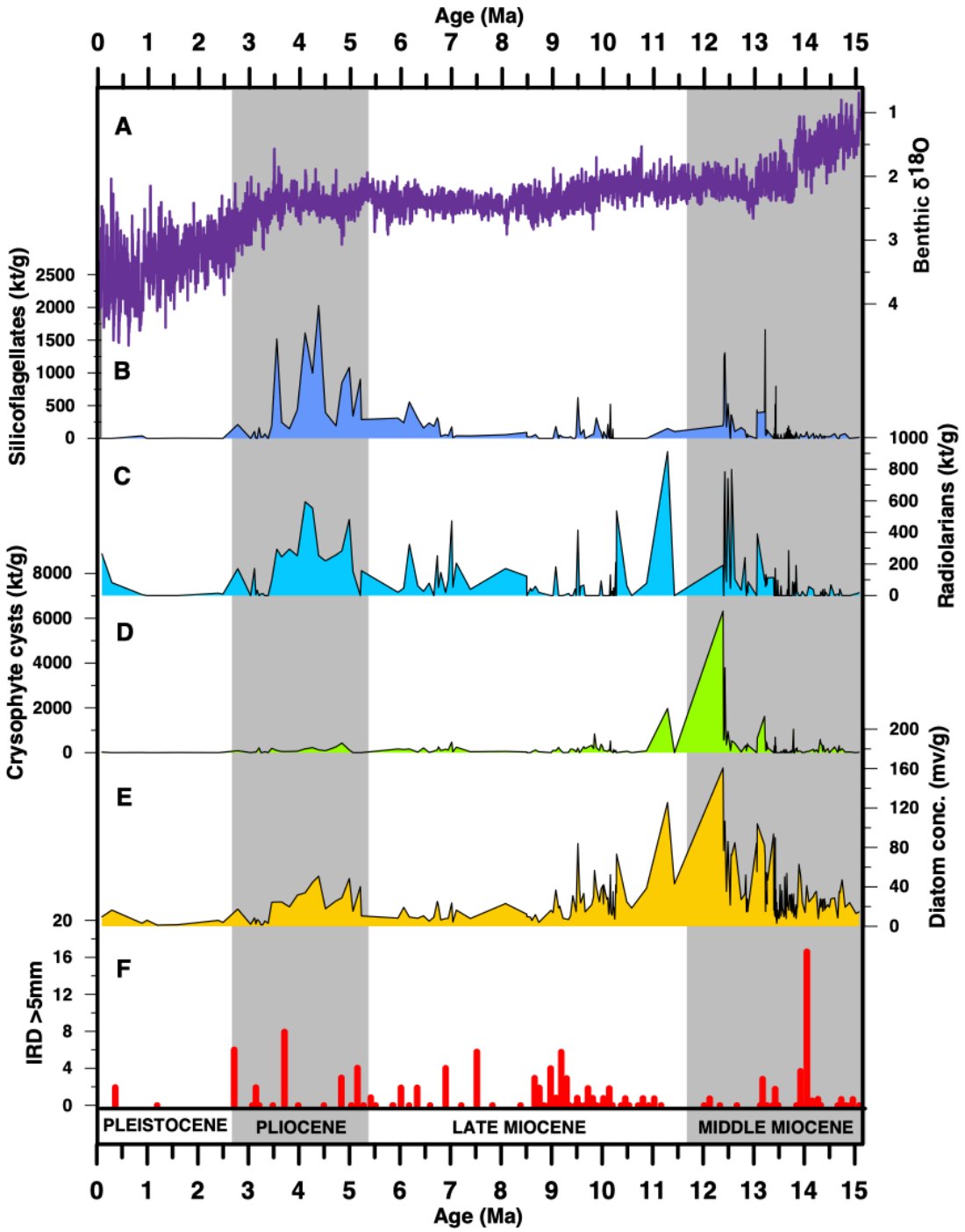

Figure 9. A) Benthic foraminiferal $\delta^{18}O$ stack (De Vleeschouwer et al., 2017). B-E) Quantitative silicofossil concentrations at ODP Site 1165. F) Lonestones at ODP Site 1165 (Shipboard Scientific Party, 2001)

7.3.6. Silicoflagellate concentrations

Like radiolarians and diatoms, silicoflagellate concentrations at ODP Site 1165 are relatively low (<0.05 mt/g) until 280 mbsf (13.43 Ma). They then increase, peaking (>1.5 mt/g) at 262.82 mbsf

(13.23 Ma) (Figure 9). Silicoflagellate concentrations remain high prior to the core gap at Site 1165 (223.72-198.50 mbsf, 12.39-11.43 Ma), after which concentrations decreased, reaching low concentrations (<0.01 mt/g), not seen since prior to 13.40 Ma, between 99.84-78.01 mbsf (7.67-6.69 Ma). Above 78.01 mbsf, silicoflagellate concentrations increase again, reaching a peak (>0.2 mt/g) at 43.97 mbsf (4.39 Ma), the highest concentrations of the entire record. This peak approximately corresponds with peak silicoflagellate abundance in the Southern Ocean during the Early Pliocene (Figure 1; Renaudie, 2016), and with high radiolarian concentrations at Site 1165 (Figure 9). Silicoflagellate concentrations at Site 1165 then remain relatively high until 35.64 mbsf (3.54 Ma), before decreasing to <0.02 mt/g for the remaining record.

7.3.7. Crysophyte cyst concentrations

Chrysophyte cysts are siliceous spores produced by chrysophyte algae. Crysophyte cyst concentrations at ODP Site 1165 generally remain low throughout the 15-0 Ma record, although a few samples containing increased (c. 1 million cysts per gram- mc/g) numbers of crysophyte cysts do occur, for example at 290.15 mbsf (13.78 Ma) and 262.03 (13.21 Ma) (Figure 10). The highest magnitude peak in crysophyte cyst concentrations (>6 mc/g) occurs at 223.72 mbsf (12.39 Ma), immediately prior to the core gap at Site 1165 between 223.72-198.50 (12.39-11.43 Ma). Other samples containing relatively high (>2 mc/g) cyst concentrations occur either side of the 223.72 mbsf (12.39 Ma) peak, at 226.21 mbsf (12.43 Ma) and 197 mbsf (11.29 Ma), showing that the substantial peak is not isolated. High crysophyte cyst concentrations at Site 1165 coincide with peak abundances of the other silicofossil groups at Site 1165 (Figure 9). Above 197 mbsf (11.29 Ma), crysophyte cyst abundances sharply decrease, remaining low (<0.1 mc/g) for the entire remaining record.

7.4. Discussion

7.4.1. Middle Miocene (15-11.6 Ma)

Global cooling during the Middle Miocene represents the first time during the Cenozoic that the EAIS transitioned to a fully cold-based, as opposed to wet-based, glacial regime (Lewis et al., 2007). The evolution of sea surface temperatures and paleoceanography at ODP Site 1165 between 15-12 Ma are described in detail in Chapter 6, so will be discussed only briefly here in regards to ACC evolution. However, a key finding is the decrease in benthic and neritic diatom

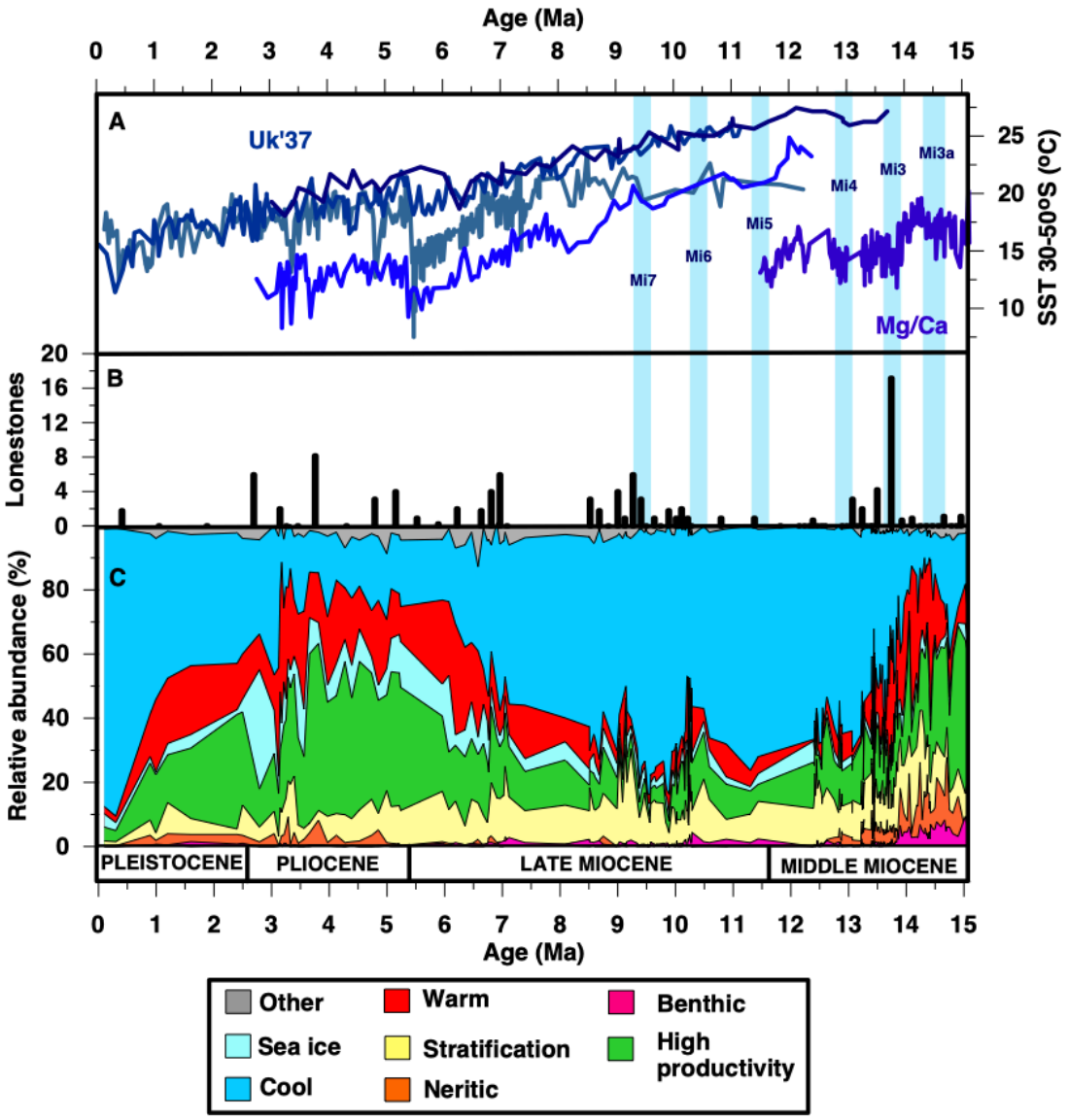

Figure 10. A: Southern Ocean (30-50°S) sea surface temperature records (alkenone data from Herbert et al., 2016; Mg/Ca data from Shevenell et al., 2004). B) Lonestones at ODP Site 1165 (Shipboard Scientific Party, 2001). C) Diatom assemblages at ODP Site 1165, grouped by ecological preferences. For details of each species group see Chapter 5 and Appendix 1). Mi glaciation events referred to in the text are shaded in blue.

species, *Chaetoceros* (*Hyalochaete*) resting spores and warm water species after 13.8 Ma, indicating the expansion of marine ice into Prydz Bay and a subsequent reduction in sea surface temperature (SST) and/or freshwater discharge (Figure 10; Chapter 6).

A role for enhanced ACC circulation during the 13.8 Ma Mi3 event has been suggested based on a decrease in SST from 14.2 Ma at subantarctic ODP Site 1171 (Shevenell et al., 2004) and Polar

Frontal Zone ODP Site 1092, where salinity also decreases from 14.2 Ma (Kuhnert et al., 2009). In Chapter 6, I have also documented this temperature decrease from 14.2 Ma using diatom data from ODP Sites 747 and 744, within the Polar Frontal Zone. However, changes in ocean temperature and salinity alone are not necessarily enough to infer movement of the PF. Instead, a sustained increase in diatom, radiolarian and silicoflagellate concentrations at Site 1165 between 13.4-12.39 Ma (Figure 9), indicative of a higher nutrient supply from, for example, upwelling, as well as hiatuses at several Southern Ocean sites between c.13.4-12.6 Ma, including at Sites 747 and 744 (Chapter 6), suggest the intensification of Southern Ocean upwelling and Antarctic Circumpolar Current circulation was associated with the Mi4 glaciation at c. 13 Ma. Further high-resolution silicofossil concentration and/or %BSi records are required in order to demarcate the limits of upwelling and, therefore, the ACC during this period.

Following Mi4 at c. 13 Ma, the large peak in chrysophyte cysts (>6 mc/g) at Site 1165 at 12.39 Ma is intriguing. Previous work has suggested crysophyte cysts may be associated with sea ice in high latitude marine settings (Lipps & McCartney, 1993), but their paleoecology is not well constrained. *Fragilariopsis praecurta*, likely a sea-ice associated diatom, does increase to 5% abundance in the same sample as peak crysophyte cyst abundances. However, the negligible abundance of sea ice diatoms at Site 1165 overall during this interval suggests sea ice is not likely the explanation for such high crysophyte cyst concentrations. Alternatively, crysophyte cysts may also be associated with glacial discharge in the Southern Ocean (Sjunneskog & Winter, 2012) and with terrestrial runoff in freshwater lakes (Nicholls & Wujek, 2003). Given the low amount of sedimentary IRD at Site 1165 around 12.39 Ma, which suggests icebergs are not the source of freshwater, a potential explanation for high crysophyte cyst abundances at 12.39 Ma could be a substantial episode of freshwater discharge, e.g. an outburst flood, as has been proposed in the Wilkes Land region during the Middle Miocene (Jordan et al., 2010). However, the co-occurrence of peak cyst concentrations with high concentrations of other silicofossil groups during this period, a trend beginning at 13.4 Ma, suggests that chrysophyte cysts may, in fact, have increased in response to an abundant nutrient supply, for example, increased upwelling. Whilst high silicofossil concentrations could be an artefact of decreased terrigenous material input at Site 1165, the simultaneous relative abundance of high productivity-indicator diatom species *Thalassionema nitzschiodes* during this interval, and the steady sedimentation rate, suggests silicofossil concentrations are reflecting an increase in nutrient supply and productivity.

Based on the new data presented here, the inferred reorganization of global ocean circulation and intensification of the ACC associated with Mi4, c. 13 Ma, coincided with significant changes in the global climate system, for example the onset of the South Asian Monsoon at 12.9 Ma (Betzler et al., 2016) (discussed in Chapter 6). However, even after Mi4, the proportion of endemic Southern Ocean diatom species at Site 1165 remained relatively low (generally <20%; Figure 8). As such, over 80% of Middle Miocene diatom species at Site 1165 were cosmopolitan or bipolar, whereas in the uppermost Late Quaternary samples at Site 1165, up to 90% of the diatom species were endemic to the Southern Ocean. This suggests that Antarctic thermal isolation and/or ACC circulation was still much reduced during at the Middle Miocene in comparison to the Quaternary/Holocene.

7.4.2. Late Miocene

7.4.2.1. Tortonian (11.6-7.3 Ma)

A core gap at ODP Site 1165 between c. 12.39-11.43 Ma prevents an assessment of palaeoceanographic conditions during that time. However, in three samples above the interval (11.43 Ma, 11.29 Ma, 10.87 Ma), the abundance of *Denticulopsis simonsenii/vulgaris* fell to <4% (Figures 6 and 11), the only time between c.13 and 7 Ma that the abundance of this diatom species fell below 50%. Instead, these three samples contained high abundances of *Denticulopsis dimorpha* (>40%) and *Denticulopsis ovata* (>40%), indicating a change in paleoenvironmental conditions that seems to begin during the core gap. While it is only possible to speculate how or why sea surface conditions changed at Site 1165 during this interval, the Mi5 glaciation event at c. 11.5 Ma was associated with cool conditions and increased productivity at South Atlantic ODP Site 1085, interpreted as a period of enhanced Benguela upwelling (Heinrich et al., 2011). Both *D. ovata* and *D. dimorpha* have longer ranges and are more abundant at more southerly ODP Sites 689/690 (located at around 65°S) than at more northerly ODP Sites 1088/1092 (46-43°S) (Censarek, 2002) and, as such, are assumed to represent relatively cool conditions at Site 1165. These diatoms dominate sediments at Site 689/690 during the 12.39-11.43 Ma interval, indicative of particularly cool conditions at Maud Rise (Censarek, 2002). However, during a similar time interval at IODP Site U1338 in the Equatorial Pacific, *Thalassionema nitzschiodes* var. *parva*, a warm water indicator diatom, increased in abundance (Figure 11) (Lyle & Baldauf, 2015). It is therefore possible that global latitudinal temperature gradients were increased between around 12-11 Ma, although this remains speculative.

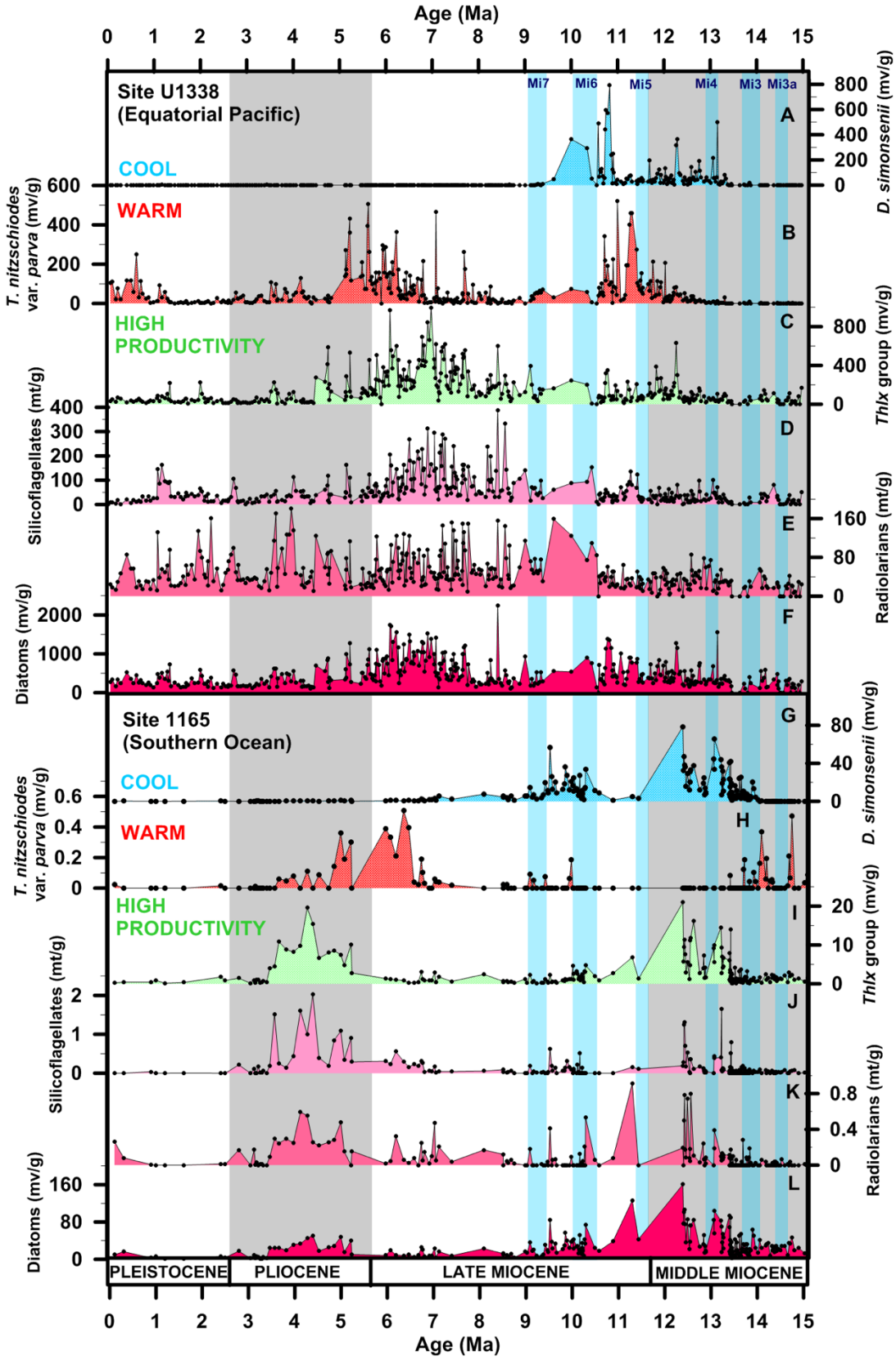

Figure 11. Selected diatom species abundances and silicofossil concentrations at ODP Site 1165 (G-L), presented alongside equivalent records at IODP Site U1338 from the equatorial Pacific (Lyle & Baldauf, 2015) (A-F). Mi glaciation events referred to in the text are shaded in blue.

Between c. 13.5-7 Ma, diatom assemblages at Site 1165 were dominated by *Denticulopsis simonsenii/vulgaris*. The relatively consistent high abundance (40-60%) of this species between c. 13.5-12 Ma and 11-7 Ma at Site 1165 suggests sea surface conditions were similar during those times. Between 11-10 Ma, *Denticulopsis simsonsenii* also increased in abundance at Site U1338 in the equatorial Pacific (Figure 12), suggesting coincident equatorial cooling. Peaks in other diatom species at Site 1165, e.g. *Fragilariopsis donahuensis, Fragilariopsis pusilla* and *Denticulopsis delicata*, that are likely associated with even cooler waters than *D. simonsenii/vulgaris* (Chapter 5), and possibly sea ice in the case of *F. pusilla*, occur between 10.27-10.21 Ma (Figures 6 & 7). Diatom diversity also peaks at Site 1165 at 10.23 Ma (Figure 8). This particularly cool interval approximately coincides with the Mi6 glaciation event (Heinrich et al., 2011), and possibly the lowest eustatic sea levels of the Miocene (Haq et al., 1987), although more recent sea level reconstructions show a reduced-amplitude decrease at this time (Kominz et al., 2008). As such, the period between 10.2-11 Ma was likely associated with low SSTs in the polar and equatorial regions, as well as a significant expansion of the East Antarctic Ice Sheet and possibly sea ice in Prydz Bay.

In a wider context, Mi6 coincided with a short-duration, moderate increase in diatom concentration at ODP Sites 1138 (53°S) and % BSi at ODP Site 751 (57°S) and Site 744 (61°S) (Figure 12), with high diatom concentrations also documented at ODP Sites 690 and 689 (65°S and 64°S, respectively) between 10 and 11 Ma (Censarek, 2002). This interval coincides with the first peak in *Thalassionema nitzschiodes* abundance at ODP Site 1092 (Figure 13), possibly reflecting enhanced upwelling (Baldauf & Lyle, 2015). It has been suggested, based on records of calcareous dinoflagellate cysts at ODP Site 1085, that the Benguella upwelling regime was also permanently established from this time (Heinrich et al., 2011), although perhaps only in warm mode (Diester-Haas et al., 1992). The proportion of endemic diatom species at Site 1165 peaks at 37% at 10.27 Ma, suggesting an increase in the thermal/physical isolation of the Southern Ocean. As such, the c. 11-10 Ma interval (including Mi6) likely represents a further intensification of upwelling in the Southern Ocean. However, the relatively low levels of biogenic silica deposited at other Southern Ocean sites suggest this period does not represent a full establishment of the ACC (Figure 12 and references therein).

The Mi7 glaciation event occurred at c. 9.4-9.3 Ma (Cook et al., 2008), representing further Miocene cooling. This coincided with a peak (3%) in *Fragilariopsis pusilla* at 9.41 Ma and *Fragilariopsis* cf. *vanheurckii* (2%) at 9.14 Ma, perhaps representing an expansion of sea ice at

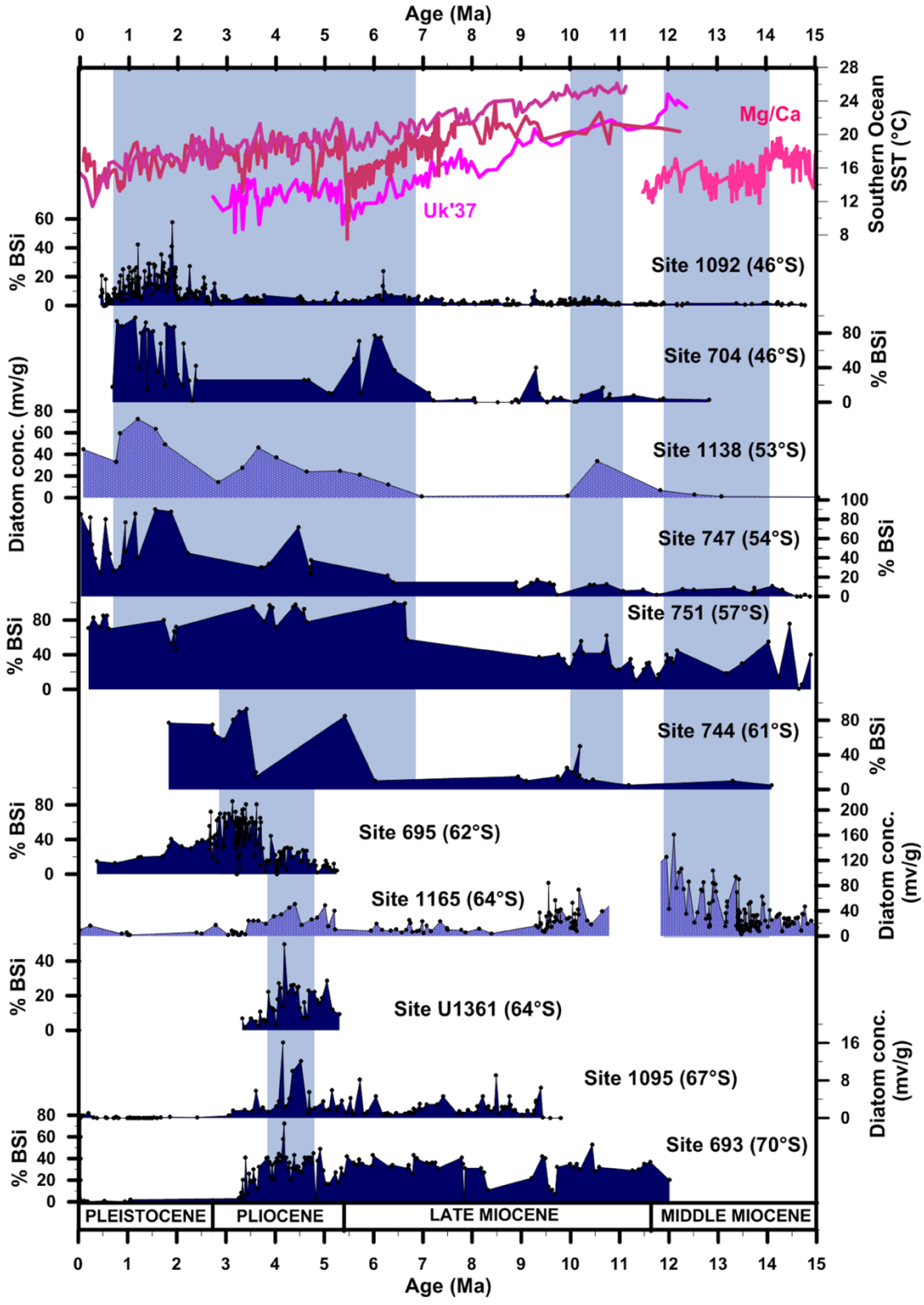

Figure 12. Published Southern Ocean % BSi and diatom concentration (mv/g) records. Data from ODP Sites 693, 695, 744, 747, 751 and 704 is from Renaudie (2016), ODP Site 1092 from Diekmann et al. (2003), IODP Site U1361 from Cook et al. (2013) and ODP Site 1095 from Bart & Iwai (2012). New records at from ODP Site 1165 and ODP Site 1138, this study. Sites are arranged

by latitude, with the most southerly at the bottom. The top panel shows Southern Ocean (30-50°S) sea surface temperature records (alkenone data from Herbert et al. (2016), Mg/Ca data from Shevenell et al. (2004). Vertical blue shaded areas indicate periods of Southern Ocean upwelling.

Site 1165 associated with Mi7, although the abundance of sea ice indicator diatoms remained low overall (<5%). Mi7 also coincides with a peak in the number of lonestones (Figure 10) and a subsequent decrease in diatom concentrations at Site 1165, likely in part a result of increased terrestrial sediment flux at the site (Shipboard Scientific Party, 2001). Increased IRD deposition and glacially-triggered turbidites have also been documented in the Weddell and Bellingshausen Seas between 10-8 Ma, suggesting simultaneous ice build-up in East and West Antarctica during this period (Cielski & Weaver, 1984; Kennet & Barker, 1990; Hillenbrand & Ehrmann, 2001). Further, a peak in diatom species indicating stratification, primarily *Rhizosolenia* spp., at this time (Figure 10 & Chapter 5) could indicate Southern Ocean stratification caused by substantial freshwater discharge in the form of icebergs associated with Mi7. Far-field ice volume/deep water temperature reconstructions suggest that global ice volume was greatest at this time within the last 17 million years and, in fact, substantially greater than present (Lear et al., 2015).

Although the Tortonian stage generally represents Antarctic cooling and crysopheric expansion, as described in this section, the diatom record at Site 1165 identifies two transient *Actinocyclus ingens* peaks at 10.20 Ma (14%) and c. 7.5 Ma (9%) (Figures 3-4). Since *A. ingens* can be considered a proxy for sea surface temperature (Section 5.2.3), this suggests short episodes of climatic amelioration and sea surface warming, during which palaeoceanographic conditions approached those prior to Mi3, when *A. ingens* was dominant (up to 40%). One of the Pagodroma group formations outcropping in the Prince Charles Mountains surrounding Prydz Bay, the Fisher Bench formation, has been dated using diatom biostratigraphy to between 9-10.7 Ma by Whitehead et al. (2004). Located 300 km inland of the modern coastline, deposition of this formation requires a >300 km inland retreat of the EAIS. The most abundant species within Fisher Bench planktonic diatom assemblages is *Actinocyclus ingens* (28%) (Whitehead et al., 2004). In comparison with the diatom record at Site 1165, it therefore seems most likely that deposition of the Fisher Bench formation occurred at c. 10.20 Ma, coincident with the increase in *A. ingens* at Site 1165. The fact that this short interval of oceanic warmth may have been associated with a >300 km inland retreat of the EAIS emphasises the vulnerability of the EAIS, at least in the Prydz Bay sector, to transient ocean warming.

7.4.2.2. Messinian (7.2-5.3 Ma)

The interval between 7.2-5.3 Ma has been identified as a period of major cooling both globally and in the Southern Ocean, with sea surface temperatures reaching near-modern levels for the first time, in both hemispheres, by 5.4 Ma (Herbert et al., 2016). Global cooling coincided with the intensification of both the east Asian summer monsoon (Ao et al., 2016) and the southeast Asian winter monsoon between 7-5.5 Ma, as well as ephemeral glaciations of the Northern Hemisphere between 6 and 5.5 Ma (Holbourn et al., 2018). A 50% decrease in sedimentation rates in the Bermejo foreland basin in the southern Andes also suggests aridification and cooling of the Southern Hemisphere between 5-6 Ma (Stevens-Goddard & Carrapa, 2018).

In Antarctica, frequent episodes of ice advance to the continental shelf break are documented on the Antarctic Peninsula between 7.2-5.3 Ma (Bart et al., 2005; Hernandez-Molina et al. 2017). A step-change in glacial regime has also been inferred along the Sabrina Coast, dated using diatom biostratigraphy to between 6.9 and 5.6 Ma (Gulick et al., 2017); a shift from a warm, wet-based glacial regime with substantial meltwater discharge to a cold, stable polar climate was interpreted from the absence of meltwater tunnel valleys on the Wilkes Land continental shelf after this time. Evidence of glacial advance more local to ODP Site 1165 includes the ice loading of sediments on the Prydz Bay continental shelf at ODP Site 739 at c. 6.3 Ma (ice-loading II event of Solheim et al. (1991) in Whitehead et al., 2006), confirming that the Messinian period represented global cooling and glacial advance around the circum-Antarctic.

Diatom assemblages at Site 1165 during the Messinian show increased *Thalassiosira* abundance between 6.97-6.77 Ma, including *T. oliveriana* var. *sparsa, T. mahoodii, T. torokina* and *T.* cf. *antarctica* (Figure. 5)*. Thalassiosira* is a genus often associated with mixed/unstratified surface waters in the modern Southern Ocean (Allen et al., 2010). A radiation of *Thalassiosira* species. could, therefore, suggest increased mixing of the Southern Ocean during this period. Alternatively, *Thalassiosira* spp. has also been associated in some studies with late summer productivity in the Southern Ocean (e.g. Stickley et al., 2006), so a lengthening of the summer season could also have opened this ecological niche, facilitating a radiation of the genus. Given the context of a climate cooling, and the coincident increase in *Rouxia isopolica* abundance (a cool water species, Chapter 5), the former hypothesis seems most likely.

The relatively short period of increased *Thalassiosira* abundance is followed by an increase in total *Fragilariopsis* spp. at Site 1165, first reaching >30% abundance at 6.67 Ma. This coincides

with the first occurrences of *F. arcula, F. aurica* and *F. praeinterfrigidaria* (Figure 7). Highest abundances of *F.* cf. *vanheruckii* within the entire record are seen at 6.67 Ma and *F. januaria*, which co-varies closely with *F.* cf. *vanheurckii* at Site 1165, also peaked in abundance at this time. *Fragilariopsis praecurta* also increases from 6.67 Ma, but peaks (20%) slightly later at 6.07 Ma; its highest abundance throughout the record. The abundance of these *Fragilariopsis* spp. is indicative of the proliferation of sea ice at Site 1165 between c. 6.5-6 Ma, coinciding with a decrease in global sea surface temperatures to near-modern levels (Herbert et al., 2016). An increase in Antarctic sea ice would have exacerbated global cooling during this time, and would likely have influenced the global climate system. For example, modern observational studies have suggested a teleconnection between Antarctic sea ice extent and the Asian monsoon (Dugam & Kakade, 2004; Prabhu et al., 2008). Expanded Antarctic sea ice coverage during the Messinian period could, therefore, be linked to the intensification of the Asian monsoon documented at this time (Ao et al., 2016; Holbourn et al., 2018).

Based on the records of siliceous marine productivity presented in this chapter, ACC circulation evolved close to its modern configuration during the Messinian, coincident with the proposed expansion of sea ice. Increased % BSi at ODP Sites 704 (46°S), 1092 (46°S), 751 (57°S) and 744 (61°S) (Figure 12), increased foraminifera and reduced nannofossil abundance at Site 1092 (46°S), and hiatuses at ODP Sites 689 (64°S), 690 (65°S) and 1088 (41°S) (Censarek, 2002) and Sites 747 (54°S) and 748 (58°S) (Harwood et al., 1992), all indicate an increase in Southern Ocean upwelling and flow speeds between 6.5-5 Ma (Dieckmann et al., 2003). Diatom assemblage records further document the onset of substantial upwelling from c. 7 Ma at ODP Sites 1138 (53°S) and 1092 (46°S), based on the first significant deposition of *Thlx* group diatoms at the Site 1138 and increased *T. nitzchiodes* abundance at Site 1092 (Censarek & Gersonde, 2002) (Figure 13). An increase in diatom concentration or *Thlx* group abundance is not recorded at Site 1165 during this period, suggesting that the site remained south of the ACC and Polar Front, as it is today. However, a peak (64%) in the proportion of endemic Southern Ocean species at Site 1165 at 6.73 Ma indicates increased Southern Ocean thermal and/or physical isolation. All of this evidence suggests an intensification of ACC circulation during the Messinian period, and that the Polar Front was located between c. 46-61°S, similar to its modern position between c. 44-64°S (Freeman & Lovendunski, 2016).

The proposed initiation of a near-modern ACC coincides with a strengthening of North Atlantic Deep Water (NADW) formation during the Late Miocene, leading to modern volumes of NADW

reaching the Southern Ocean by 6.6 Ma (Wright et al., 1991; Billups, 2002). Since NADW forms an important component of ACC circulation today (Figure 2 of Chapter 3), it follows that full-volume NADW upwelling would have been associated with the development of a near-modern ACC. The deposition of *Thalassiothrix-Thalassionema* diatom mats in the equatorial and North Pacific during the Late Miocene (Kemp & Baldauf, 1993; Dickens & Barron, 1997) also suggests that thermohaline circulation during the Messinian period was invigorated globally, not just in the Southern Ocean. Invigorated global ocean circulation and the establishment of a near-modern ACC would have acted as a positive feedback for global cooling and Antarctic thermal isolation during the Late Miocene.

7.4.3. Early Pliocene (5.3-3.6 Ma)

In contrast to the cool Late Miocene, the Early Pliocene saw a rise in global and Southern Ocean sea surface temperatures (Herbert et al., 2016), significantly reduced meridional temperature gradients (Fedorov et al., 2013) and a reversal of late Neogene aridification, with increased precipitation documented throughout the Southern Hemisphere (Sniderman et al., 2015). On the Antarctic continent, both the EAIS (O'Brien et al., 2004; Cook et al., 2013; Patterson et al., 2014; Reinardy et al., 2015) and WAIS (Naish et al., 2009; McKay et al., 2012) were dynamic, with the latter possibly absent for long periods (Haywood et al., 2008). As discussed in Chapter 1, estimates for Pliocene sea level rise vary, with uncertainty partially a result of dynamic topography. However, recent studies have converged around an upper bound of c. 22 m for an Antarctic contribution to Pliocene global sea level rise, allowing for substantial EAIS retreat (Escutia et al., 2019).

Terrestrial evidence documents the warmest episode of the late Neogene between c. 4.6-3.3 Ma on the Antarctic continent (Clark et al., 2013), which coincides with lowest modelled ice volumes (DeConto & Pollard, 2009). Seasonality was also increased during this period as a result of increased summer temperatures (up to 5°C above present), corroborated by bivalve evidence of coincident increased seasonality in the Weddell Sea (Clark et al., 2010). Ross Sea temperatures were >5°C above present (McKay et al., 2012). Records from ODP Site 1165 indicate a >60% reduction in sea ice coverage (*Eucampia antarctica* sea ice diatom proxy record; Whitehead et al., 2004) and temperatures of >4°C above present (silicoflagellate assemblages; Whitehead & Bohaty, 2003). These conditions would have effectively prevented or limited circum-Antarctic sea ice formation during the Early Pliocene. This interpretation is supported by

reduced sea ice in model simulations that show no perennial sea ice and very little seasonal sea ice during the warm early Pliocene in marginal Antarctic seas (Haywood et al., 2013).

The exact cause of Early Pliocene warming is not known, but hypotheses include: the loss of permanent Arctic sea ice (Raymo et al. 1990); lower mountain altitudes in North America and Tibet (Rind and Chandler 1991); increased northwards heat transport by the oceans (Dowsett et al. 1992; Billups, 2002); closure of the Panama ocean gateway (Haug and Tiedemann 1998); opening of the Indonesian seaway (Cane and Molnar 2001); changes in global ice cover (Haywood and Valdes 2004); permanent El Niño in the tropical Pacific (Wara et al. 2005); vegetation feedbacks (Haywood & Valdes 2006), perhaps associated with changes in terrestrial biomass (Mudelsee and Raymo 2005); elevated atmospheric CO_2 (Crowley et al., 1991; Haywood et al., 2007), which varied between c. 400-500 ppm (Seki et al., 2010; Zhang et al., 2013); feedbacks associated with significant ice sheet melting during the Early Pliocene (Clark et al., 2013); and an ACC shifted poleward by up to 900 km (Whitehead & McMinn, 2002; Bart & Iwai, 2012), although bathymetry in certain regions, e.g. the Kerguelen Plateau, makes the large migration of frontal systems less feasible. Numerical modelling investigations into the mechanisms of Early Pliocene warmth have not revealed a single driving mechanism; rather, Federov et al. (2013) suggest it was caused by a number of factors such as dynamical mixing by increased tropical storms and reduced cloud feedbacks.

Early Pliocene warmth coincided with a substantial shift in diatom assemblages at ODP Site 1165 (Figures 3, 10 and 13). *Denticulopsis* spp. decreased in abundance after the Late Miocene (Figure 6), and diatom assemblages instead became dominated by *Trichotoxon reinboldii/Thalassiothrix* spp. (*Thlx* group), reaching 15-32% abundance between c. 5.2-3.2 Ma at Site 1165 (Figure 13). The Early Pliocene *Thlx* group assemblage shift at Site 1165 coincided with peak *Thlx* group abundances at other high latitude Southern Ocean sites (Figure 13), for example, ODP Sites 1095 and 1096 on the Antarctic Peninsula (Bart & Iwai, 2012), ODP Sites 693, 695 and 696 in the Weddell Sea (Gersonde & Burckle, 1990), IODP Site U1358 on the Wilkes Land continental shelf (Reinardy et al., 2015), IODP Site U1356 on the Wilkes Land continental rise (Cook et al., 2013), Site 1138 on Kerguelen Plateau (this study) and AND-1B on the Ross Sea continental shelf (McKay et al., 2012). Where both diatom assemblage and % BSi records are available, peak *Thlx* group abundance correlates with peak BSi % (Figures 12 and 13).

A terrestrial outcrop within the Transantarctic Mountains surrounding Prydz Bay (Bardin Bluffs, within the Pagodroma Group) is also dominated (>50%) by *Thlx* species (Figure 14). Biostratigraphy dates this outcrop to the Pleistocene based on the presence of benthic foraminifera *Globigerina cf. G. antarctica* (range 2.6-0.99 Ma) and five valves of *Fragilariopsis kerguelensis* (FO 2.38 Ma) (Whitehead et al., 2004). However, given the high chance of aerial contamination within these terrestrial assemblages (Whitehead et al., 2004), the dominance of *Thlx* species suggests that the terrestrial formation could, instead, have been deposited during the circum-Antarctic Early Pliocene *Thlx* group peak, which would mean the EAIS retreated at least 250 km inland during this period. Indeed, another terrestrial deposit containing marine diatoms, the Sørsdal Formation outcropping in the Vestfold Hills to the east of Prydz Bay, has been dated using diatom biostratigraphy to between 4.5-4.1 Ma (Harwood et al., 2001). *Thlx* group diatoms are also 'common' in diatom assemblages from this formation (Harwood et al., 2001), the deposition of which requires EAIS retreat of >50 km.

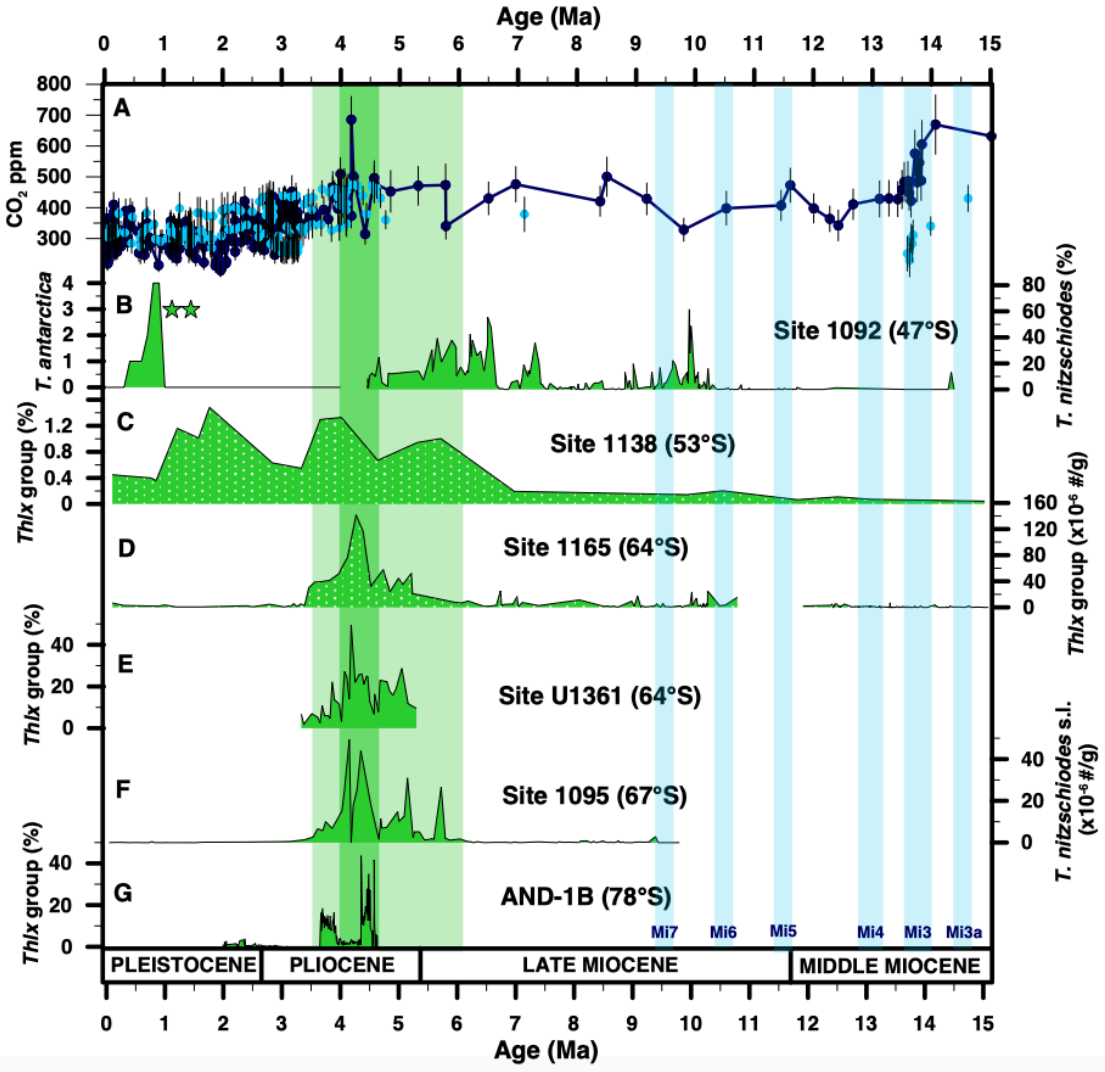

Figure 13. Southern Ocean records of *Thalassionema nitzschiodes* and *Thlx* group (*Thalassiothrix* spp. & *Trichotoxon reinboldii*) abundance. New data from ODP Sites 1165 and 1138 are presented alongside published records from other sites, presented by latitude with the most southerly site at the bottom. Published records are from: AND-1B (McKay et al., 2012); Site 1095 (Bart & Iwai, 2012); Site U1361 (Cook et al., 2013); Site 1092 (Censarek & Gersonde, 2004; Cortese & Gersonde, 2008). The top panel shows atmospheric CO_2 reconstructed using boron isotopes in planktonic foraminifera (dark blue- Sosdian et al., 2018 and references therein) and alkenones (light blue- see www.p-co2.org for full list of references). Vertical green shaded box indicates periods of increased *Thlx* group abundance at circum-Antarctic sites, coinciding with increased atmospheric CO_2 during the Early Pliocene. Mi glaciation events are shaded in blue.

The largest Early Pliocene peak in *Thlx* group abundances (32%) at Site 1165 between 4.2-4.3 Ma correlates with peaks in both % BSi and *Thlx* group abundance at other sites south of the modern Polar Front, for example, ODP Site 1095 (Antarctic Peninsula), IODP Site U1361 (Wilkes Land), ODP Site 693 (Weddell Sea) and, possibly, AND-1B within age-model error (Figure 13 and references therein). This event coincides with an Early Pliocene interglacial at 4.23 Ma, identified as one of the warmest periods of the Early Pliocene, which corresponded with peak austral insolation and atmospheric CO_2 of 400-700 ppm (Figure 13 and Golledge et al., 2017). During this interglacial, the WAIS collapsed and the EAIS margin retreated into the Wilkes subglacial basin, with a total modelled contribution of c. 8.6 m of sea level rise from the Antarctic Ice Sheet (Golledge et al., 2017).

Early Pliocene increased % BSi, documented in several high latitude records (Figure 12), has previously been interpreted solely as a consequence of reduced sea ice cover, with increasing sea ice cover then assumed to be causing a reduction in % BSi during Late Pliocene cooling (Grutzner et al., 2005; Hillenbrand & Ehrmann, 2005; Hillenbrand & Cortese, 2006). However, the analysis of diatom assemblages from Site 1165 reveals a more complex story. *Thlx* group diatoms were present in low abundances throughout the entire 15-0 Ma interval analysed, but only became abundant at Site 1165 (and other high latitude circum-Antarctic sites) during the Early Pliocene, and not during other warm periods such as prior to the Middle Miocene Climate Transition, c. 13.8 Ma. This suggests a fundamental change in Southern Ocean paleoceanography during the Early Pliocene. *Thalassiothrix* is associated with high productivity and frontal systems in the global ocean, including in the equatorial Pacific (Kemp et al., 1995; Kemp & Baldauf, 1993) and North Atlantic (Bodén & Backman, 1996; Romero et al., 2011).

Thalassiothrix is generally concentrated on the warm side of frontal boundaries for physical reasons; cells proliferate in colder, nutrient-rich waters but, as the cooler waters are subducted beneath warmer waters at frontal boundaries, *Thalssiothrix* cells, often grouped as tangled mats, pop up at the surface to access light for photosynthesis and then die due to the lower nutrient conditions, sinking to the sea floor (Leventer et al. 2010, and references therein). In the modern Southern Ocean, maximum *Thalassiothrix* abundance occurs between the sea ice edge and the SAF, at SSTs between 1-3°C and with a clear decrease in abundance associated with sea ice (Crosta et al., 2005). However, *Thalassiothrix* is particularly concentrated within the Polar Frontal Zone, where most upwelling occurs (Tremblay et al., 2002; Grigorov et al., 2002). An endemic Southern Ocean species, *Trichotoxon reinboldii* exhibits similar ecological preferences to *Thalassiothrix* in the Southern Ocean (Crosta et al., 2005; Hasle, 1987). *Thalassionema nitzschioides*, also linked to upwelling and high productivity in the global ocean (Chapter 5), is also abundant (28%) during the Early Pliocene at Site 1165. However, unlike the *Thlx* group, *T. nitzschioides* was also abundant (20%) between c. 13-12 Ma.

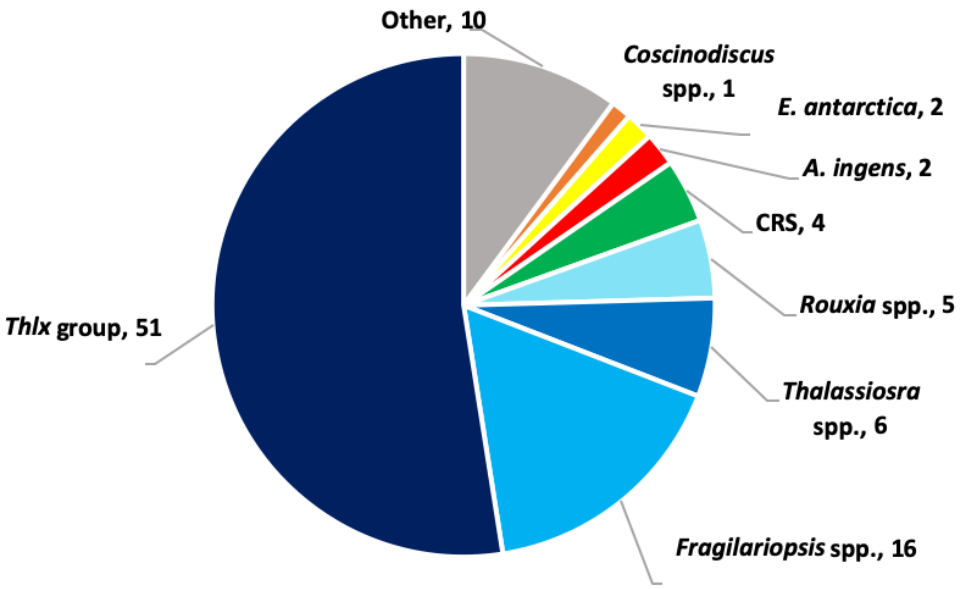

Figure 14. Diatom assemblages (planktonic species only) in samples from the Bardin Bluffs; within Pagodroma Group outcrops situated up to 250 km inland from the Prydz Bay. Species within the 'other' group represent <1% of the assemblage each.

Given the association of *Thlx* group species with frontal systems, the occurrence of *Thalassiothrix* and *Thalassionema nitzschioides* in Southern Ocean sediment cores have been used to track paleo-fluctuations of the PF through the Plio/Pleistocene, for example, at ODP Leg 177 Sites in the South Atlantic (Cortese & Gersonde, 2008). Coincident peaks of *Thalassiothrix*

antarctica and *T. nitzschioides* during the Early Pliocene at Site 1095 were interpreted as representing a southward shift of the PF (Bart & Iwai, 2012). However, *Thlx* group also shows an abundance peak (>40%) at the AND-1B site (78°S) (Figures 13 and 2) during the Early Pliocene- it seems impossible that the PF, or even the SACCF, migrated as far south as the inner Ross Sea continental shelf. Further, the general absence of carbonate microfossils at these sites during the Early Pliocene, despite carbonate being deposited at Site 1165 at other times (e.g. during MIS 31, c. 1 Ma; Teitler et al., 2015), suggests that either the sites remained south of the PF during the Early Pliocene, or that conditions remained hostile to calcareous plankton, which prefer higher temperature (>3°C) and lower nutrient conditions (Burckle et al., 1996).

Peak *Thlx* group abundances between c. 5.2-3.5 Ma co-occurred with high relative abundances of *Thalassionema nitzschioides* (28%), *Shionodiscus tetraoestrupii* (9%), *Thalassiosira inura* (7%), *Fragilariopsis praeinterfrigidaria* (7%), *Fragilariopsis aurica* (5%) and *Fragilariopsis reinholdii* (3%). All of these species are associated with or tolerant of relatively warm waters at Site 1165 (Chapter 5), implying that warm waters prevailed above the core site during the Early Pliocene. Similar warm-associated diatom species also co-occurred with *Thlx* group species at other sites (McKay et al., 2012; Reinardy et al., 2015), while low-resolution TEX_{86} sea surface temperature estimates at AND-1B (McKay et al., 2012) and numerical modelling studies (Haywood et al., 2013) suggest the Early Pliocene was associated with high sea surface temperatures (c. 5°C) and minimal sea ice close to the Antarctic continent. However, *Actinocyclus ingens* abundance, which is closely associated with warmer sea surface temperatures (Chapters 5 and 6), does not increase during the Early Pliocene at Site 1165, despite remaining present in the Southern Ocean for almost the entire 15 million year record. The lack of a peak in *A. ingens* abundance suggests that despite relatively warm sea surface temperatures, oceanographic conditions were substantially different during the Early Pliocene than during other warm periods of the Neogene, for example 14-15 Ma, c.10 Ma, c.7 Ma and during MIS 31, when *A. ingens* abundance did increase (Figures 3 and 4).

Given the available evidence, two mechanisms are proposed to explain the occurrence of high abundances of *Thlx* group diatoms at circum-Antarctic high latitude sites during the Early Pliocene:

- **Increased upwelling of Circumpolar Deep Water at high latitudes**

  In recent decades, relatively warm, nutrient-rich Circumpolar Deep Water (CDW) has been observed upwelling onto the Antarctic continental shelf, for example, beneath the Totten

Ice Shelf (Rintoul et al., 2016) or Pine Island Glacier (Jacobs et al., 2011), via mechanisms such as eddy transport from the ACC (Martinson, 2011; Schmidtko et al., 2014). Basal melt rates beneath ice shelves are increased by sub-ice shelf circulation of CDW via increased heat content and/or increased volume flux due to changes in wind or buoyancy forcing (Schmidtko et al., 2014). It is possible that increased CDW upwelling at high latitudes, e.g. perhaps onto Antarctic continental shelves, during the Early Pliocene could explain the dominance of *Thlx* group diatoms in high latitude sediments and, if this is the case, increased upwelling could also have played a major role in forcing Antarctic Ice Sheet retreat during the Early Pliocene. *Thlx* group abundances began to increase from c. 5.2 Ma at Site 1165 (Figure 13), coincident with decreasing Antarctic ice volumes (Lear et al., 2015).

Increased CDW upwelling onto the George IV continental shelf has been previously suggested during the Early Pliocene based on increased barite accumulation, and thus marine productivity, from c. 4.5 Ma at IODP Site U1359 (Wilkes Land) (Hansen & Passchier, 2016), however, no mechanism was suggested by which CDW upwelling was increased (Hansen & Passchier, 2016). Increased CDW upwelling onto the Amundsen continental shelf during the Early Holocene has been suggested based on benthic and planktonic $\delta^{13}C$ records as well as foraminiferal assemblage changes (Hillenbrand et al., 2017), linked to a strengthened or poleward-shifted westerly wind belt. However, Early Holocene diatom records from the Amundsen Sea do not show higher *Thlx* abundances during increased CDW upwelling (Mitchison, 2014), which implies that Early Pliocene CDW upwelling was either on a much larger scale, or that the oceanographic consequences of the upwelling were different. For example, if sea ice and ice shelf cover were substantially reduced during the Early Pliocene, upwelling CDW may not have generated an extensive melt-related surficial freshwater lens, as presumably occurred during the Holocene (Nakayama et al., 2014); the lack of a freshwater lens would have created substantially different oceanographic conditions on the shelf, leading to different diatom assemblages.

Any mechanisms proposed here to explain increased CDW upwelling during the Early Pliocene are speculative, however, perhaps the most likely mechanism involves a poleward-shifted westerly wind belt, which has been simulated by several Pliocene climate model studies (Zhang et al., 2013; Li et al., 2015). Additionally, a near absence of Early Pliocene sea ice (Whitehead et al., 2004; Haywood et al., 2013) could have led to freshening of surface waters from glacial runoff and strong easterly winds (also consistent with simulated Pliocene

ocean dynamics), which could have increased southward Ekman transport (Zhang et al., 2013) and therefore increased CDW upwelling onto continental shelves (Colloni et al., 2018). Big changes in sea ice coverage, ice volume and freshwater discharge would also have been accompanied by simultaneous changes in the atmospheric dynamics which regulate modern near-shore Southern Ocean circulation (Carter et al., 2008). Changes in Early Pliocene atmospheric dynamics could have perturbed the predominantly wind-driven Southern Ocean gyre systems and/or the Antarctic Coastal Current (ACoC), which balance eastward ACC circulation and keep upwelling CDW away from the continental shelf in the modern ocean (Smedsrud et al., 2006*; Nu*ñez-Riboni & Fahrbach, 2009*)*. A reduction or breakdown of gyre and/or ACoC circulation would have given upwelling CDW access to the Antarctic margin.

The production of North Atlantic Deep Water (NADW), which plays a key role in ACC circulation and reached modern volumes by the Late Miocene, was enhanced during the Early Pliocene (Kwiek & Ravelo, 1999; Ravelo & Andreasen, 2000). This enhancement has been linked to Early Pliocene warmth via greater transport of warm subtropical waters to the high latitudes (Billups, 2002). However, increased NADW formation on its own would have increased the volume of the warmer NADW component of CDW that upwells at high latitudes (Figure 2). Increased NADW-enhanced CDW upwelling could therefore have indirectly further increased shelfal CDW upwelling. Whatever the mechanism, any scenario in which high latitude CDW upwelling was substantially increased would also have had major implications for the formation of AABW and, therefore, global ocean circulation and the global climate system during the Early Pliocene.

- **Increased summer stratification and the diatom fall dump**

A second mechanism which could explain the dominance of *Thlx* group diatoms in high latitude Antarctic shelf sediments during the Early Pliocene is increased stratification of the summer water column. Species of *Thalassiothrix* may be able to adjust their buoyancy, similar to *Rhizosolenia* and *Corethron* species, enabling them to take advantage of nutrients at depth and, therefore, thrive within a stratified water column (Kemp et al., 2000). Indeed, a seasonally-recurrent patch of *Thalassiothrix spp.* has been documented suspended at the thermocline on the continental rise of Prydz Bay, not far from Site 1165 (Quilty et al., 1985). The deposition of high concentrations of *Thalassiothrix* spp. could be triggered by a breakdown in water column stratification at the onset of autumn, leading to a diatom ‘fall

dump' (Kemp et al., 2000). The fall dump of *Thalassiothrix* spp. would be enhanced by their morphology that leads to an entanglement of valves and their deposition as mats (Kemp et al., 2000). Leventer et al. (2002) invoked this mechanism to explain the formation of *Thalassiothrix*-dominated laminations, interspersed with laminations composed of other diatom genera e.g. *Corethron, Rhizosolenia* and *Proboscia*, in Holocene sediments from Palmer Deep, Antarctic Peninsula.

Evidence of increased Antarctic seasonality and particularly warm summers (>5°C above present) during the Early Pliocene (Clark et al., 2010; 2013) supports the summer stratification/fall dump hypothesis; thermal stratification would be enhanced as a result of higher summer temperatures and/or salinity stratification due to increased freshwater discharge from a more active hydrological cycle and more dynamic Early Pliocene ice sheet (Naish et al., 2009; Reinardy et al., 2015). Substantially reduced Pliocene sea ice concentrations could also have affected ocean circulation at the highest latitudes (Whitehead et al., 2004; Haywood et al., 2013). Seasonal sea ice maxima correspond with ACoC speed maxima in the Weddell Sea, where combined wind and sea ice concentrations account for 66% of baroclinic ACoC circulation (Nuñez-Riboni & Fahrbach, 2009). It is possible, therefore, that reduced sea ice coverage could have decreased ACoC speed, although unconstrained freshwater and atmospheric dynamics play a quantitatively more important role in forcing modern ACoC circulation (Nuñez-Riboni & Fahrbach, 2009). Whatever the mechanism, sluggish ACoC circulation could have facilitated summer stratification of the high latitude water column, followed by its seasonal breakdown, creating a fall dump scenario during which *Thlx* group diatoms were deposited.

Overall, it seems most likely that the first hypothesis (increased upwelling of CDW at the highest latitudes, e.g. perhaps onto continental shelves) describes Southern Ocean paleoceanography during the Early Pliocene. The evidence linking high *Thlx* group abundances to upwelling in the global ocean is strong (e.g. , while the absence of carbonate microfossils at Site 1165 and the coincident increase of silicoflagellates and radiolarians in the wider Southern Ocean and at ODP Site 1165 (Figures 1 and 9) during the Early Pliocene also suggest high nutrient conditions related to upwelling. The absence of *Thlx* spp. during other warm, stratified periods of the Neogene, for example, as proposed prior to the MMCT (Chapter 6), suggests that the oceanic conditions responsible for Early Pliocene *Thlx* deposition were unique within at least the last 15 Ma. Finally, limited evidence of increased summer stratification is documented in the remaining diatom

assemblage at Site 1165 during the Early Pliocene (Figure 10). Therefore, while both the early Middle Miocene and Early Pliocene were likely warmer than present with substantially reduced ice volume and sea ice compared to today, Southern Ocean paleoceanography, and therefore ice/ocean interactions, were substantially different during each. These differences may be explained by the Neogene development of the ACC. If the ACC, and the volume of NADW upwelling around Antarctica, were not comparable to modern configurations until the Late Miocene (Ravelo & Andreason, 2000), reduced ice volume and sea ice coverage (e.g. due to increased CO_2) would have had a significantly different impact on Southern Ocean circulation during the Middle Miocene in comparison to the perturbation of a near-modern system during the Early Pliocene.

7.4.4. Late Pliocene (3.6-2.6 Ma)

Global (Ravelo et al., 2004) and Southern Ocean (McKay et al., 2012) cooling followed the warm Early Pliocene. The driver of this temperature decrease has not been unequivocally demonstrated, however, closure of the Isthmus of Panama between 5.6-3 Ma may have affected ocean circulation (Diekmann et al., 2003) and could have reduced sea surface temperatures in the Ross Sea region alone by up to 2°C (Lunt et al., 2008). Siliceous productivity records suggest that after c. 3.5 Ma, the locus of Southern Ocean siliceous deposition began to migrate northwards (Figures 12). Between c. 3.5 and 2 Ma, peak % BSi occurs at ODP Site 695 (62°S) and Site 744 (61°S), and % BSi is reduced at the higher latitude sites which experienced Early Pliocene peaks % BSi. Hiatuses also occurred at ODP Sites 751 (57°S), 747 (54°S) and 704 (46°S) during the Late Pliocene, indicating that the position of the ACC at this time was between c. 46-62°S. Peaks in % BSi and *Thalassiothrix* spp. abundances also occur further north at ODP Site 1088 (35°S) (Diekmann et al., 2003) and Site 1084 (25°S) on the Benguela margin (Marlow et al., 2001) during the Late Pliocene, possibly indicating the position of the Subtropical Front.

Close to the Antarctic continent, a cooling trend commenced from c. 3.7 Ma, suggested by prograding glacial sequences on the Antarctic Peninsula (Hernandez-Molina et al., 2017) and increased IRD deposition at ODP Sites 1165, 1095, 1096 and IODP Site U1356, that increased in magnitude again from 3.3 Ma (Passchier, 2011). This episode of cryospheric expansion occurred during a period of substantial instability indicated by diatom assemblages at Site 1165. After 3.8 Ma, and particularly from 3.3 Ma, *Thlx* group abundance decreased to be replaced by transient peaks in *Rouxia antarctica* (5%) at 3.54 Ma, *Rouxia naviculoides* (8%) at 3.45 Ma, *Shionodiscus tetraoestrupii* (20%) at 3.32 Ma, *Thalassiosira torokina* (7%) at 3.25 Ma, *Thalassiosira insigna*

(33%) at 3.17 Ma, *Actinocyclus karstenii* (16%) and *Thalassiosira vulnifica* (28%) at 3.11 Ma, *Eucampia antarctica* (17%) at 3.05 Ma, *Thalassiosira oliveriana* (7%) between 3.05-2.80 Ma and *Rouxia diploneides* (20%) at 2.79 Ma. These species represent various palaeoecological conditions; *R. antarctica, R. naviculoides* and *R. diploneides* are associated with sea ice, *S. tetraoestrupii, T. insigna* and *T. vulnifica* with warm water, and *A. karstenii, T. torokina, T. oliveriana* and *E. antarctica* with cool waters (Chapter 5, Appendix 1). As such, this interval likely reflects highly fluctuating oceanographic conditions at Site 1165 following the equatorward migration of the ACC during Late Pliocene Southern Ocean cooling. The evolutionary radiation and relatively high abundance of *Thalassiosira* spp. during this period (Figure 5) could also indicate increasingly well-mixed surface waters, as occurred during the Late Miocene (see Section 7.4.2.2 for discussion). In the Ross Sea, a period of polynya-style deep mixing has been suggested following a major episode of ice sheet growth at 3.3 Ma, sea surface cooling and an expansion of sea ice between 3.3-2.5 Ma (McKay et al., 2012). Further cooling steps are also documented in the ANDRILL record at 2.5 and 2.9 Ma (McKay et al., 2012), after which time the Benguela upwelling system switched to its cold mode (Marlow et al., 2001) and arid climatic conditions commenced in South Africa (Diekmann et al., 2003).

7.4.5. The Pleistocene (2.6-0.1 Ma)

The Pleistocene represents a final shift in global cooling and the development of the ACC. Several studies have suggested that the Southern Ocean opal belt became fully established as the locus of global silica deposition from c. 2 Ma, based on % BSi records at ODP Site 1092 (Cortese & Gersonde, 2004) and at other ODP Leg 177 sites (Cortese & Gersonde, 2008). However, these records span only 40-53°S, and only extend beyond 4 Ma at Site 1092 (46°S). Within the context of other Neogene Southern Ocean siliceous productivity records (Figures 12 and 13), rather than indicating the onset of full-strength ACC circulation, the peak % BSi at Leg 177 Sites from 2 Ma may instead represent an equator-ward shift in the locus of siliceous deposition associated with the ACC during Pleistocene cooling. Coincident % BSi peaks at Sites 751 (57°S), 747 (54 °S), 1138 (53°S) and 704 (46°S), as well as peak *Thlx* group abundances at ODP Sites 1092 (46°S), 704 (Ciesielski, 1991; Cortese & Gersonde, 2008) and 1138 (Figure 14) suggest that the locus of Southern Ocean upwelling and siliceous deposition occurred between c. 57-46°S during the Pleistocene. Sites south of 57°S, for example, Site 695 (62°S) and Site 1165 (64°S), do not exhibit peaks in biosilica or *Thlx* abundance during this time, although other sites situated at latitudes of between 62-54°S are needed to confirm whether substantial siliceous deposition occurred within these latitudes during the Pleistocene.

7.4.5.1. MIS 31

Diatom records from ODP Site 1165 reveal an episode of warmth that likely represents Marine Isotope Stage (MIS) 31, at 1.08 Ma (Teitler et al., 2015). This interglacial was as an episode of remarkable circum-Antarctic warmth, during which a major retreat of the WAIS (Scherer et al., 1998), and possibly the EAIS (DeConto & Pollard, 2009), occurred. Sample resolution at Site 1165 in this study is low after 2 Ma, however, peak *Actinocyclus ingens* abundance (15 %) at 7 mbsf coincides with maximum $CaCO_3$ deposition and minimal IRD at Site 1165 (Figure 15; Teitler et al., 2015). The deposition of carbonate suggests a period of sea surface temperatures >3°C (Diekmann et al., 2003) and relatively low nutrient concentrations, while minimal IRD suggests reduced glacial activity at Site 1165. The presence of *A. ingens* suggests sea surface conditions were comparable to those prior to the Middle Miocene Climate Transition (MMCT) at 13.8 Ma, when *A. ingens* was dominant (up to 42%) and the Amery Ice Shelf is inferred to have been absent (Chapter 6).

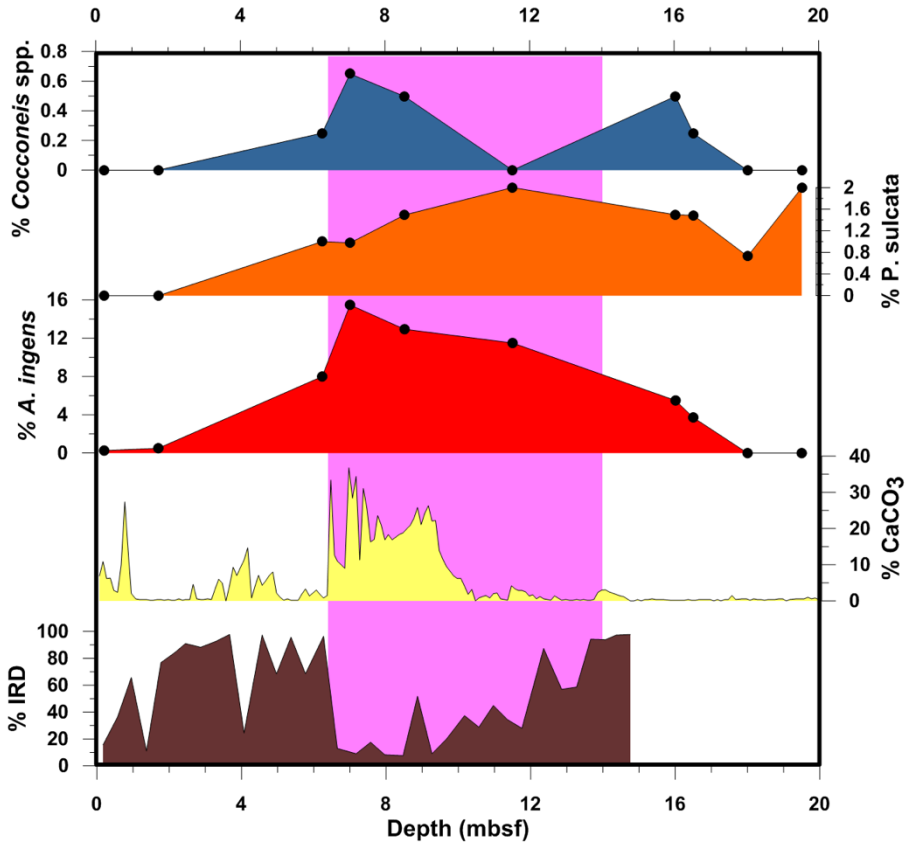

Figure 15. MIS 31 at ODP Site 1165B. Low resolution diatom assemblages (top three panels) are from this study; % $CaCO_3$ and % IRD are from Teitler et al. (2015).

Within age model constraints (Teitler et al., 2015), the interval between 6-10 mbsf at Site 1165 has been suggested to represent a 52 kyr period of peak warmth during MIS 31, which coincides

with peak warmth at ODP Site 1090 (Teitler et al., 2015). *Paralia sulcata* (<1.6 %), a neritic species, and *Cocconeis* spp. (c.1%), a benthic species, are recorded at Site 1165 at this time (Figure 15). Relative abundance peaks are low, however, they represent the highest abundances of these species recorded at Site 1165 since 13.8 Ma, prior to which the Amery Ice Shelf was likely absent. As such, the EAIS likely retreated in the Prydz Bay region during MIS 31 including, perhaps, a collapse of the Amery Ice Shelf. However, other benthic species at Site 1165 are less diverse and numerous during MIS 31 than they were prior to 13.8 Ma, suggesting the retreat may not have been as substantial, although this may also be because ice shelf retreat during MIS 31 was relatively short-lived.

7.4.6. Did high latitude Southern Ocean diatoms play a role in CO_2 drawdown during the Neogene?

Two modes in the relationship between Southern Ocean productivity and atmospheric CO_2 are identified during the Neogene. The first mode describes the late Middle-Late Miocene and Late Pliocene-Quaternary, in particular between 12-13.5 Ma, c. 10 Ma, 5.5-7 Ma and 3-0 Ma. During these times, increased Southern Ocean siliceous productivity was generally associated with decreasing atmospheric CO_2, hinting at a role for diatom productivity in contributing to CO_2 drawdown (Figures 12 and 13). Alternatively, and/or in addition, increased siliceous productivity during these periods was largely concentrated in the vicinity the modern PFZ. Associated inferred step-wise intensifications of the ACC and increased Antarctic sea ice coverage during these periods could, therefore, suggest a possible role for intensified ACC circulation and upwelling as well as expanded sea ice in contributing to CO_2 drawdown during this mode.

The second mode identified in the relationship between Southern Ocean productivity and atmospheric CO_2 occurred during the Early Pliocene, which saw a proposed expansion of Southern Ocean upwelling at the highest latitudes (Figures 12 and 13), which coincided with a rise in atmospheric CO_2 (Figure 13). Peak % *Thlx* group and % BSi at circum-Antarctic Sites between 4.20-4.30 Ma (Figure 13) also approximately coincided with the highest CO_2 documented for the Early Pliocene; 658 ppm at 4.19 Ma (Martinez-Boti et al., 2011; Sosdian et al., 2018), although this peak CO_2 value is so far only documented in one sample.

Sea ice coverage physically blocks the outgassing of oceanic CO_2 in the modern Antarctic Zone (Butterworth & Miller, 2016). Increased upwelling and reduced sea ice coverage during the Early Pliocene could therefore have increased outgassing of CO_2 from the deep ocean, contributing

to higher atmospheric CO_2; similar to during the last deglaciation (Anderson et al., 2012). In this sense, Early Pliocene increased upwelling at high latitudes could have provided a major positive climate feedback to Pliocene warmth both by increasing oceanic heat delivery to the Antarctic ice margin, driving ice sheet retreat and a reduction in sea ice, but also by increasing CO_2 outgassing. However, given the large carbon content of *Thlx* group diatoms (Chapter 1, Section 1.3.2), diatom-based carbon drawdown could actually have increased in the highest southern latitudes during the Early Pliocene, providing a negative feedback, but which was negated by increased positive feedbacks associated with upwelling.

7.5. Summary & conclusions

This chapter documents the evolution of the ACC and Southern Ocean paleoceanography between 15 Ma and present. The major events and findings presented and discussed in this Chapter, as well as in Chapter 6, are summarised in Table 1, below.

Table 1. A summary of the major events documented and described in Chapters 6 and 7 of this thesis.

Epoch	Stage	Age (Ma)	Major events documented in this thesis
Middle Miocene	Langhian	15-13.82	• Mi3a event at c. 14.6 Ma coincides with a shift in Southern Ocean diatom assemblages, possibly forced by changes in high latitude seasonality • SSTs then increased at Sites 1165, 744 and 747, peaking by c. 14.2 Ma • Substantially different sea surface conditions at Site 1165 (more stratified, cooler, diatom resting spores produced) than at Sites 747 and 744 (dominated by warm, planktonic species) prior to 13.8 Ma • Amery ice shelf proposed to be absent prior to Mi3 (13.8 Ma) based on benthic diatom species at Site 1165 and minimal IRD deposition despite warm SSTs • Southern Ocean cooling commenced from 14.2 Ma, with % *A. ingens* at Site 747 closely reflecting Mg/Ca SST trends documented at Site 1171 (Shevenell et

			al., 2004); major ice growth does not occur until 13.8 Ma
Middle Miocene	Serravalian	13.82-11.63	• Diatom concentrations increase at Sites 1165, 747 and 744 from c. 13.4 Ma (as do silicoflagellate, radiolarian and crysophyte cyst concentrations at Site 1165), indicative of an increased nutrient supply • Coincides with proposed intensification of the ACC (based on hiatuses at Sites 747 and 744), coinciding with Mi4 and the onset of the South Asian Monsoon (Betzler et al., 2016).
Late Miocene	Tortonian	11.63-7.25	• Increased global latitudinal temperature gradients between c. 10-11 Ma • Increased sea ice diatom abundance at Site 1165 at 10.25 Ma and 9.40-9.10 Ma • Possible deposition of the *Actinocyclus ingens*-dominated (Whitehead et al., 2004) Fisher Bench formation during a transient warm interval at 10.20 Ma, associated with >300 km EAIS retreat
Late Miocene	Messinian	7.25-5.33	• Onset of *Thlx* group deposition at Site 1138 from c. 6.8 Ma • Peak in sea ice diatoms at Site 1165 between 6.7-6.1 Ma • Coincides with increased silica deposition at circum-Antarctic sites, modern-volume NADW upwelling (Billups, 2002) and near-modern SSTs in the Southern Ocean (Herbert et al., 2016), indicating the onset of a near-modern ACC • Overall, mixed diatom assemblages at Site 1165 suggest Late Miocene diatoms require further ecological characterization
Early Pliocene	Zanclean	5.33-3.6	• Onset of *Thlx*-dominated assemblages at Site 1165, alongside other warm- and high-productivity-indicator species e.g. *T. nitzschioides*

			• Also see *Thlx*-dominated assemblages at other circum-Antarctic sites, including AND-1B (McKay et al., 2012) • Increased silicoflagellate and radiolarian concentrations at Site 1165 • Indicative of increased high-latitude upwelling, e.g. onto continental shelves → could have provided source of heat to melt ice shelves and/or increase CO_2 outgassing • Coincides with deposition of the Sørsdal Formation and possibly the Bardin Bluffs, indicating substantial EAIS retreat
Late Pliocene	Piacenzian	3.6-2.58	• Highly variable diatom assemblages at Site 1165 suggest highly variable paleoceanography, but overall cooling/sea ice formation • Northward migration of siliceous Southern Ocean deposition based on circum-Antarctic records
Pleistocene	Gelasian	2.58-0.01	• Overall cooling of diatom assemblages at Site 1165 • Peak number of endemic diatom species (>90%) • Locus of Southern Ocean siliceous deposition reaches modern latitudes → modern ACC • MIS 31 represented as warm interval with increased *A. ingens* abundance and a small increase in benthic species at Site 1165, hinting at retreat of the Amery ice shelf

8. Developing the use of stable oxygen isotopes in diatom silica as a Neogene palaeoceanographic proxy

8.1. Introduction

8.1.1. Oxygen isotopes in diatom silica as a palaeoenvironmental proxy

The measurement of oxygen isotopes in foraminiferal calcite is one of the longest-established proxies in palaeoceanography (see Pearson, 2012, and references therein). As a record of water temperature and ice volume, both benthic and planktonic foraminifera have provided a roadmap for our understanding of fundamental changes in Cenozoic climate (Zachos et al., 2008). Oxygen isotope ratios are generally expressed in palaeoceanography using the delta notation (δ) in relation to an agreed standard, whereby R is the oxygen isotope ratio $^{18}O/^{16}O$ and the reference standard is Vienna Pee Dee Belemnite (VPDB) for carbonate and Vienna Standard Mean Ocean Water (VSMOW) for silica (Swann & Leng, 2009):

$$\delta = [(R_{sample}/R_{reference}) - 1] \bullet 1000 \text{ ‰} \quad \text{(equation 1)}$$

However, carbonate is not well preserved in sediments from the southern high latitudes and, as such, interest in the use of oxygen isotopes within biogenic silica, which is well preserved in this region, has increased. To date, the majority of work on oxygen isotopes within biogenic silica has focused on diatom silica ($\delta^{18}O_{diatom}$), since the biogeochemistry of other siliceous organisms such as radiolarians, silicoflagellates and sponges is less well understood. Initial evidence also suggested that radiolarians may isotopically equilibrate with bottom waters over millennial timescales (Mopper & Garlick, 1971; Matheney & Knauth, 1989), although more recently Abelmann et al. (2015) used $\delta^{18}O_{radiolarian}$ to reconstruct subsurface Southern Ocean conditions across the last glacial transition, with the $\delta^{18}O_{radiolarian}$ record shown to be structurally similar to $\delta^{18}O_{diatom}$ from the same site.

Studies using oxygen isotopes within diatom silica initially focused on marine environments (reviewed in Swann & Leng, 2009) and the development of $\delta^{18}O_{diatom}$ as a proxy for surface water temperature and salinity. Since the 1990s, palaeolimnological applications have affirmed initial marine proxy development (Leng & Barker, 2006; Mackay et al., 2013). Diatom silica seems to preserve $\delta^{18}O_{diatom}$ approximately coherent with foraminiferal calcite, which has a mineral-water fractionation of around -0.2 ‰/°C (Brandriss et al., 1998; Moschen et al., 2005; Ravelo & Hillaire-

Marcel, 2007). Section 8.1.2, below, further explores the relationship between temperature and $\delta^{18}O_{diatom}$.

8.1.2. The chemical structure of diatom silica

Diatom silica is composed of silica tetrahedrons formed of covalent –Si–O–Si bonds via the condensation of Si–OH groups to form SiO_2 (equation 2) (Swann & Leng, 2009).

$$–Si–OH + –Si–OH \rightarrow –Si–O–Si + H_2O \qquad \text{(equation 2)}$$

The isotopically homogenous silica at the centre of diatom frustules is assumed to reflect the $\delta^{18}O$ of the water in which it formed (Julliet & Labeyrie, 1980; Leng & Swann, 2009). However, surrounding the frustule are loosely bonded –Si–O groups, which exchange with water in the photic zone after silica precipitation to form a –Si–OH molecule (Figure 1). Due to the high macro-porosity of most diatoms, e.g. due to areolae and frustule cavities, this also likely occurs during sinking and upon burial (Labeyrie and Julliet, 1982; Frohlich, 1989; Leng & Swann, 2009). In fact, it has been estimated that up to 40% of diatom frustule silica can be affected by these processes (Knauth, 1973; Labeyrie, 1979; Labeyrie and Julliet, 1982; Leng et al., 2001; Swann et al., 2008; Leng & Sloane, 2008; Swann & Leng, 2009), although the proportion of this outer layer is probably reduced during dissolution over long (>5-10 Ma) timescales (Hurd et al., 1981; Swann & Leng, 2009) and likely varies between species (Swann et al., 2008). Nonetheless, this outer layer presents a significant problem for the analysis of $\delta^{18}O_{diatom}$, and must be entirely removed in order to obtain an accurate reflection of water conditions upon initial precipitation of the silica.

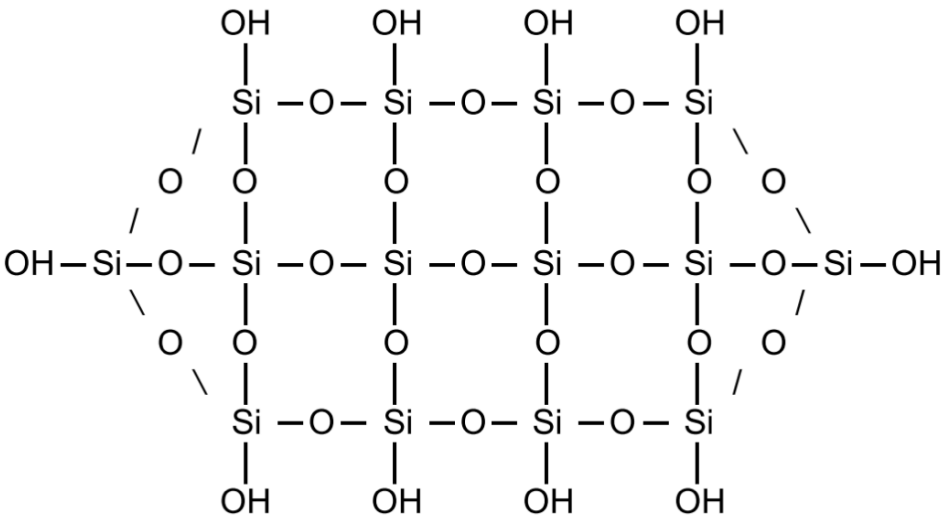

Figure 1. Schematic structure of diatom silica showing the isotopically homogenous inner Si–O–Si layer (siloxane groups) and outer –Si–O layer (silanol groups) which forms –Si–OH hydroxyl bonds (Swann & Leng, 2009).

8.1.3. Complications of measuring $\delta^{18}O_{diatom}$

Development of the method used in this chapter to obtain measurements of $\delta^{18}O_{diatom}$ are described in Chapter 3 (Section 3.4.1); including the cleaning technique used to achieve pure diatom silica, the stepwise fluorination technique used to remove the possibly contaminated outer oxygen layer, and the measurement of $\delta^{18}O_{diatom}$ from the inner, supposedly stable, oxygen layer. However, issues relating to dissolution, diagenesis and vital effects on $\delta^{18}O_{diatom}$ remain unresolved. The impact of dissolution, at least, on $\delta^{18}O_{diatom}$ is thought to be small; $\delta^{18}O_{diatom}$ was not substantially affected in Holocene-Miocene age samples aged in a weak alkaline solution at 20°C and 4°C by Smith et al. (2016). $\delta^{18}O_{diatom}$ decreased, but not in proportion to the degree of dissolution determined using SEM images (greatest in younger samples). Further, the reduction in $\delta^{18}O_{diatom}$ (up to 0.59‰) was greater than analytical error (0.46‰) in only half of the samples. If dissolution was to be an obstacle for $\delta^{18}O_{diatom}$ analysis at a particular site, the dissolution would therefore likely be identifiable upon inspection of samples using a microscope.

It is reasonable to assume that diatoms, like foraminifera, may exhibit vital effects which impact upon $\delta^{18}O_{diatom}$. Vital effects are biological processes that override the environmental $\delta^{18}O_{diatom}$ signal. Foraminifera vital effects differ by species due to, for example, differences in growth rates, nutrient utilization and calcification (Spero et al., 1997; Duplessy et al., 1970) and can be overcome by collecting single-species samples for analysis. Diatoms are generally too small to individually select for single-species records, however, studies have shown minimal vital effects within cultured, fossil, marine or lacustrine diatom silica $\delta^{18}O_{diatom}$ (Schiff et al., 2009; Shemesh et al., 1995; Julliet-Leclerc & Labeyrie, 1987). As such, it has been assumed that any vital effects likely fall within analytical error (Swann & Leng, 2009). However, other evidence of more substantial (up to 3.5‰) differences between different size-fractions of purified diatom silica (Swann et al., 2008; Swann et al., 2007; Swann et al., 2013) suggest further investigations in this area are needed. These offsets in $\delta^{18}O_{diatom}$ between size fractions are likely explained by environmental factors, since each size fraction contains different species with different environmental preferences. For example, Swann et al. (2013) noted that offsets between different size fractions within seasonal laminae, e.g. the spring <10 µm fraction, dominated by *Chaetoceros* resting spores, vs. the >10 µm fraction containing larger diatom species, could be

explained by differences in diatom depth habitat and the magnitude of seasonal glacial discharge.

8.1.4. Interpreting $\delta^{18}O_{diatom}$ as a paleoenvironmental proxy

8.1.4.1. Quantifying the effect of sea surface temperature on $\delta^{18}O_{diatom}$

Like $\delta^{18}O_{foram}$, oxygen isotope fractionation within diatom silica is thought to depend upon temperature and the $\delta^{18}O$ of the water in which it formed, which in turn depends on global ice volume and the hydrological cycle. In theory, it should be possible to quantify $\delta^{18}O_{diatom}$ fractionation in order to provide quantitative sea surface temperature (SST) estimates in the same way as is possible for $\delta^{18}O_{foram}$, however, to date, this has been unsuccessful. Early attempts to develop an isotope-equilibrium curve to back-calculate SST, which showed similar results to that of calcite (Epstein et al., 1953; Labeyrie, 1974), were developed using potentially contaminated material. Subsequent attempts have produced global calibrations equivalent to c. –0.2‰/°C (Julliet-Leclerc & Labeyrie, 1987). However, the complex oceanography of high latitude regions, where localized upwelling can have a large impact on $\delta^{18}O_{diatom}$, has necessitated the development of regional calibrations, equivalent to c. –0.5‰/°C in the Southern Ocean (Shemesh et al., 1992). Substantial differences also exist in temperature calibrations between lacustrine and marine environments. These differences result either from improved analytical methods, since the lacustrine temperature calibration work is more recent than that for the ocean, or from environment-specific vital effects (Swann & Leng, 2009). In the interim, end-members of –0.2 to –0.5 ‰ per °C can be assumed as the effect of SST on $\delta^{18}O_{diatom}$.

8.1.4.2. The effect of changes in source water $\delta^{18}O$ on $\delta^{18}O_{diatom}$

While temperature has been shown to affect oxygen isotope fractionation in diatom silica, the $\delta^{18}O$ of water in which the silica precipitated also affects $\delta^{18}O_{diatom}$. Around the coastal and shelf regions of Antarctica, meteoric water (ice and melt water from glaciers plus snow melt) has a mean signature of +20‰, while oceanic water (predominantly Upper Circumpolar Deepwater, UCDW) has a signature of c. –0.08‰ (Meredith et al., 2008). As such, the presence of even a small amount of freshwater can have a substantial impact on $\delta^{18}O_{seawater}$ and therefore $\delta^{18}O_{diatom}$, potentially overwhelming the temperature signal. This has led to studies around the Antarctic margin interpreting $\delta^{18}O_{diatom}$ as primarily forced by meteoric water, of which glacial discharge is the largest component (Pike et al., 2013; Swann et al., 2013). In high latitude regions, other sources of freshwater, such as melting sea ice which has a $\delta^{18}O$ of +2.1 ‰ (Meredith et al., 2008), could influence $\delta^{18}O_{diatom}$. However, modelling has suggested that the isotopic impact of sea ice

melt on $\delta^{18}O_{seawater}$ is minimal (<0.14%) on at least glacial/interglacial timescales (Brennan et al., 2013). Indeed, glacial discharge was interpreted as volumetrically the most important source of freshwater forcing a West Antarctic Peninsula Holocene $\delta^{18}O_{diatom}$ record (Pike et al., 2013), as opposed to minimal impacts from precipitation or the melting of a snow layer on top of sea ice.

8.1.5. Applications of $\delta^{18}O_{diatom}$ in palaeoceanography

8.1.5.1. Pleistocene and Holocene

To date, most studies using the $\delta^{18}O_{diatom}$ proxy have used Pleistocene and Holocene age sediments. Initial palaeoceanographic reconstructions using $\delta^{18}O_{diatom}$ suffered from incomplete removal of the contaminated outer –Si–OH– layer (Labeyrie, 1974; Mikkelsen et al., 1978; Wang & Yeh, 1985). However, following the development of the controlled isotope exchange (CIE) technique in the 1980s (Section 3.4), several studies have linked changes in $\delta^{18}O_{diatom}$ to global palaeoceanographic change during the Pleistocene and Holocene. For example, large (5-10‰) $\delta^{18}O_{diatom}$ fluctuations have been attributed to meltwater and sea ice events in the Bering Sea since the last glacial maximum (Sancetta et al., 1985) and, over the past 3 kyr, $\delta^{18}O_{diatom}$ in combination with diatom assemblages have been linked to changes in El Niño forcing in the Gulf of California (Juillet-Leclerc & Schrader, 1987).

Since the 1990s, records documenting both $\delta^{18}O_{diatom}$ and $\delta^{18}O_{foram}$ from the same cores provided further constraints for $\delta^{18}O_{diatom}$. For example, paired $\delta^{18}O_{diatom}$ and $\delta^{18}O_{foram}$ records from the Southern Ocean, Atlantic Sector (51°S), were used to document changes in SST over the last 300 kyrs (Shemesh et al., 1992). However, direct comparisons of $\delta^{18}O_{diatom}$ and $\delta^{18}O_{foram}$ are complicated by differences in the seasonality and water column depth habitat of the organisms providing the signal (e.g. diatoms tend to remain within the euphotic zone to photosynthesize, while foraminifera may migrate to greater depths). Last deglaciation and Holocene $\delta^{18}O_{diatom}$ records from the Antarctic Polar Frontal Zone (PFZ, Atlantic Sector) have also been interpreted as documenting substantial meltwater discharge to the Southern Ocean (varying between +46 and +38‰ $\delta^{18}O_{diatom}$; Shemesh et al., 1994, 1995; Hodell et al., 2001). Cores drilled closer to the continent showed lower isotope values (approaching +38‰ $\delta^{18}O_{diatom}$), pointing to an Antarctic source for the low $\delta^{18}O_{diatom}$ at the PFZ (Shemesh et al., 1994, 1995). In the last decade, deglacial and Holocene $\delta^{18}O_{diatom}$ records from Palmer Deep, western Antarctic Peninsula continental shelf, have demonstrated the potential of $\delta^{18}O_{diatom}$ to resolve seasonal- to centennial-scale differences in freshwater influx to the coastal zone (Pike et al., 2013; Swann et al., 2013). Samples for both of these records were analysed using the heavy-

liquid separation procedure I have used in my research (Section 3.4), however, while most of these Pleistocene/Holocene records were inspected for contaminant phases using the light microscope, none were published with accompanying geochemical analyses of contamination.

8.1.5.2. Neogene

In theory, $\delta^{18}O_{diatom}$ should be useful as a proxy for temperature, ice volume and salinity for as long a time period as $\delta^{18}O_{foram}$, which has been used to reconstruct changes in palaeoceanography over at least the last 100 million years. However, there are a number of challenges when reconstructing palaeoceanographic variability using $\delta^{18}O_{diatom}$ over Neogene or longer timescales. These include: (1) the effect of silica maturation (Menicucci et al., 2017), although the full impact of silica maturation on the $\delta^{18}O_{diatom}$ signal remains unclear; and (2) changes in the isotopic composition of Antarctic ice sheets when using $\delta^{18}O_{diatom}$ to reconstruct Antarctic freshwater discharge over longer timescales, however, modelled offsets in $\delta^{18}O_{ice}$ between modern and Mid Pliocene Warm Period values of c. 3‰ (Gasson et al., 2016) suggest such changes would have had a negligible impact upon my study at ODP Site 1165, which ranges in age between 3.75-3.45 Ma.

Despite potential concerns about silica maturation, several $\delta^{18}O_{diatom}$ studies have been published using Late Pliocene/early Pleistocene material from the North Pacific. $\delta^{18}O_{diatom}$ from ODP Site 882, between 2.85-2.39 Ma, has been presented with an independent Uk_{37}' SST record from the same site (Haug et al., 2005; Swann et al., 2006). Both records showed freshening of the surface layer at the onset of major Northern Hemisphere glaciation c. 2.73 Ma. $\delta^{18}O_{diatom}$ ranged between +46 and +33‰; including notably lower values than other Pleistocene and Holocene records published to date. A second $\delta^{18}O_{diatom}$ record from the same site, between 2.73-2.52 Ma, documented $\delta^{18}O_{diatom}$ between 45-37‰, and was interpreted as forced by changes in glacial meltwater discharge to the Pacific Ocean (Swann et al., 2010). Most recently, Pliocene (2.94-2.52 Ma) $\delta^{18}O_{diatom}$ records from North Pacific IODP Expedition 323 varied between 43-39‰ and documented decreased sea surface temperatures associated with Northern Hemisphere glaciation (Swann et al., 2016).

8.1.6. Aims of this study

To date, no Southern Ocean records of $\delta^{18}O_{diatom}$ have been published using sediments older than Pleistocene age, and no marine records` at all have been published with a robust geochemical assessment of sample purity. The goal of my research was therefore to generate

the first Southern Ocean $\delta^{18}O_{diatom}$ to investigate the applicability of this important, but still relatively untested, diatom-based proxy to Neogene palaeoceanography. A Neogene record of Antarctic freshwater discharge could potentially revolutionise understanding of the behaviour of the Antarctic ice sheets, including their response to past warm periods. To this end, here I will present a high-resolution Pliocene $\delta^{18}O_{diatom}$ record from ODP Site 1165 (Sections 2.6 & 4.4), and Miocene-age pilot analyses from ODP Site 744 (Sections 2.5 & 4.3), alongside a robust geochemical assessment of potential contamination.

8.2. Materials

8.2.1. ODP Site 1165

ODP Site 1165 is located 500 km north of the Prydz Bay coastline and the Amery Ice Shelf; the largest modern ice shelf in East Antarctica (Figure 2). The detailed physical and oceanographic setting, as well as the age model for Site 1165, are presented in Sections 2.6 and 4.4. The 3.75-3.45 Ma interval (39-33 mbsf; 46 samples, providing a temporal resolution of c. 7 ka) was chosen for $\delta^{18}O_{diatom}$ analysis because it encompasses a lithological section of diatom clay (Shipboard Science Party, 2001) with particularly good diatom preservation and high abundance (Chapter 7). The selected interval also crosses an episode of proposed major retreat of the East Antarctic Ice Sheet into the Aurora subglacial basin at 3.55 Ma (Williams et al., 2010), which presumably would have had a large impact on Southern Ocean freshwater dynamics and, therefore, $\delta^{18}O_{diatom}$. Further, the interval contains an episode of abrupt circum-Antarctic warming at c. 3.70 Ma (Escutia et al., 2009), and Site 1165 has published records of SST (Whitehead & Bohaty, 2003), sea ice dynamics (Whitehead et al., 2005) and sedimentology, including IRD accumulation and clay mineralogy (Passchier et al., 2011), providing key data with which to contextualise and constrain $\delta^{18}O_{diatom}$.

8.2.2. ODP Site 744

Five Miocene age samples were analysed from ODP Site 744; the detailed physical and oceanographic setting, as well as the age model for Site 744, are presented in Sections 2.5 and 4.3. The Miocene samples were chosen: (1) to assess how different sediment types may be related to $\delta^{18}O_{diatom}$ (the interval at Site 744 is dominated by biogenic carbonate, whereas terrigenous sediment dominates at Site 1165); and (2) to investigate whether older samples (aged between 15-12 Ma) show substantially different $\delta^{18}O_{diatom}$ values to the younger, Pliocene age samples. To my knowledge, these Miocene samples are the oldest yet analysed for $\delta^{18}O_{diatom}$.

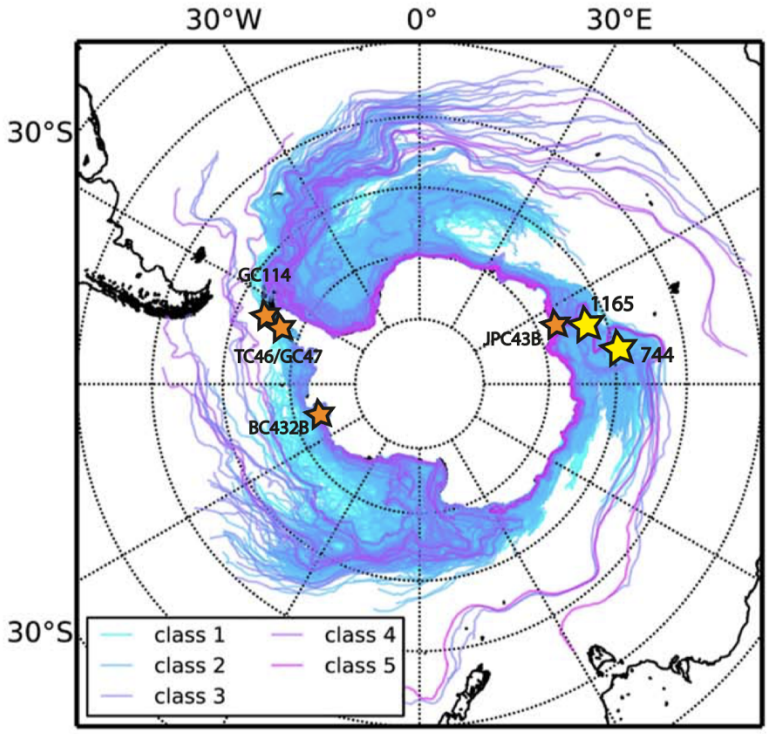

Figure 2. Map of the primary sites discussed in this chapter (ODP Sites 1165 and 744; yellow stars) and the other sites at which data has been provided for this chapter (orange stars) overlaid onto modelled modern Antarctic iceberg trajectories, with icebergs separated by size (class 1 is smallest, class 5 the largest). Background figure is from Rackow et al. (2017).

8.2.3. Other Sites

To date, only one paleoceanographic $\delta^{18}O_{diatom}$ record has been published with geochemical Al/Si data (Bering Sea; Maier et al., 2018). As such, several other unpublished datasets, none older than the Holocene, have been kindly provided by J. Pike (2019); J. Williams (2019); and J. Pike, J. Smith & J. Williams (2019) for discussion in this chapter. All samples were cleaned using the same heavy liquid separation technique as was used for samples from Sites 1165 and 744 (see Section 3.4), and were geochemically analysed using the same XRF instrument at the University of Nottingham. $\delta^{18}O_{diatom}$ and geochemical data are provided from the following sites:

- **Core NBP01-01 JPC43B** (Iceberg Alley, Mac. Roberston Land); unpublished data provided by J. Pike (2019). Isotopes and XRF were analysed using bulk diatom samples. Samples range in age from c. 12 cal yr BP to present.
- **Core TC46 and GC47** (Anvers Shelf, west Antarctic Peninsula); unpublished data provided by J. Williams (2019). Isotopes and XRF were analysed using the 10-38 μm size fraction. Samples range in age from 3912-211 cal yr BP.

- **Core GC114** (Boyd Straight, west Antarctic Peninsula) unpublished data from J. Williams (2019). Isotopes and XRF were performed on the 10-38 μm size fraction. The samples range in age from 3822-76 cal yr BP.
- **Core BC423B** (Amundsen Sea), unpublished data from J. Pike, J. Smith and J. Williams (2019). Isotopes and XRF were analysed using the bulk diatom fraction. Samples range in age from c. 500 years old to modern.

8.3. Results

8.3.1. $\delta^{18}O_{diatom}$ analysis

8.3.1.1. ODP Site 1165

$\delta^{18}O_{diatom}$ at ODP Site 1165 ranged between 46-30‰ (Figure 3). From c. 38-35.5 mbsf, $\delta^{18}O_{diatom}$ fluctuated between 44-37‰, fell to 30‰ between 35.5 and 34.5 mbsf, and increased above 34.5 mbsf. These Site 1165 $\delta^{18}O_{diatom}$ values include some of the lowest documented in any published marine record (<35‰ $\delta^{18}O_{diatom}$). Analytical error (0.33‰), calculated as the mean standard deviation of analytical replicates, is small in proportion to the c. 16‰ $\delta^{18}O_{diatom}$ variability documented within this dataset.

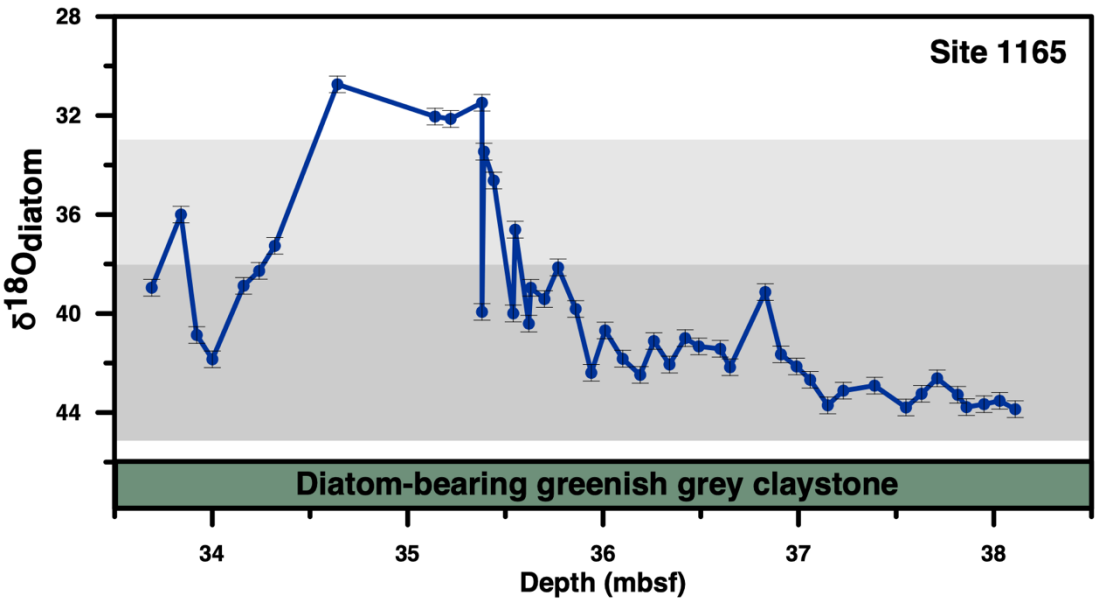

Figure 3. $\delta^{18}O_{diatom}$ at ODP Site 1165. Error bars represent the mean standard deviation of replicate values. The primary lithology of the study interval is shown beneath (Shipboard Science Party, 2001). Shaded grey boxes indicate the range of values previously documented in Antarctic sediments (Swann et al., 2013; Pike et al., 2013) (darker box), and the maximum range of $\delta^{18}O_{diatom}$ values previously documented in any marine sediments (from North Pacific Pliocene

sediments- Swann et al., 2006) (light grey box); values at Site 1165B represent the lowest $\delta^{18}O_{diatom}$ values documented so far in marine sediments between c. 35.5-13.3 mbsf.

8.3.1.2. ODP Site 744

$\delta^{18}O_{diatom}$ in five samples at ODP Site 744 ranged between 44-39‰ (Figure 4), with an analytical error of 0.22‰, calculated, like at Site 1165, as the mean standard deviation of analytical replicates.

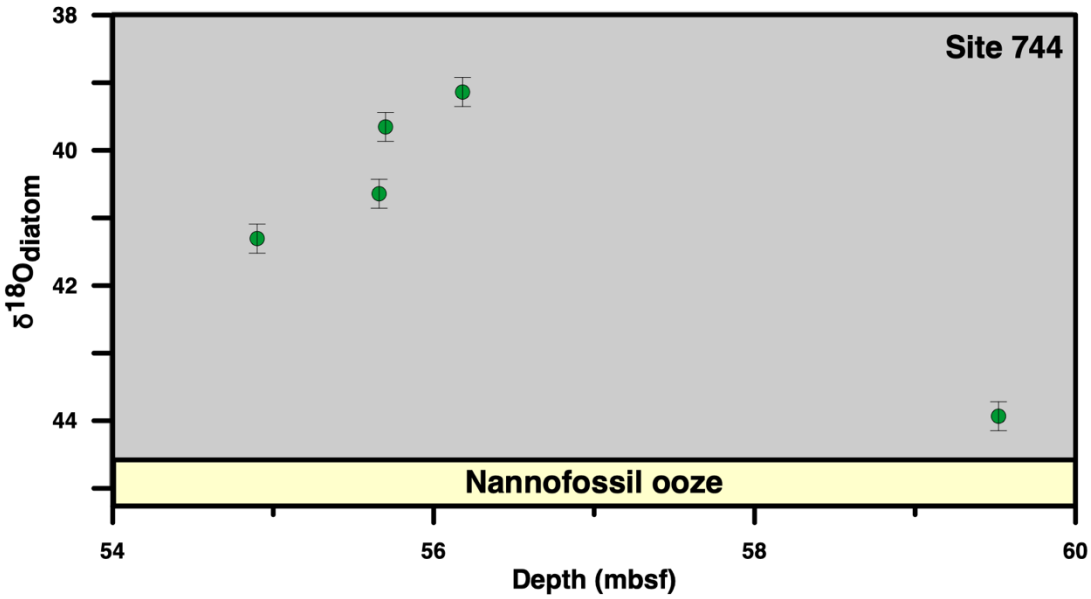

Figure 4. $\delta^{18}O_{diatom}$ at ODP Site 744. Error bars represent the mean standard deviation of replicate values. The primary lithology of the study interval is shown beneath (Shipboard Science Party, 1989). Grey shaded background indicates that $\delta^{18}O_{diatom}$ values at Site 744B fall within the range previously documented in deglacial/Holocene Antarctic sediments (Pike et al., 2013; Swann et al., 2013); see Figure 3.

8.3.2. XRF analysis

XRF geochemical data of cleaned diatom silica samples were examined using univariate (linear regressions) and multivariate (Principal Component Analysis) analysis methods at ODP Site 1165, NBP0101-JPC43B and univariate only (due to a low sample size; n=5) at ODP Site 744. Only the elements above XRF detection limits in more than five samples were included in this analysis.

8.3.2.1. ODP Site 1165

Univariate statistical analysis

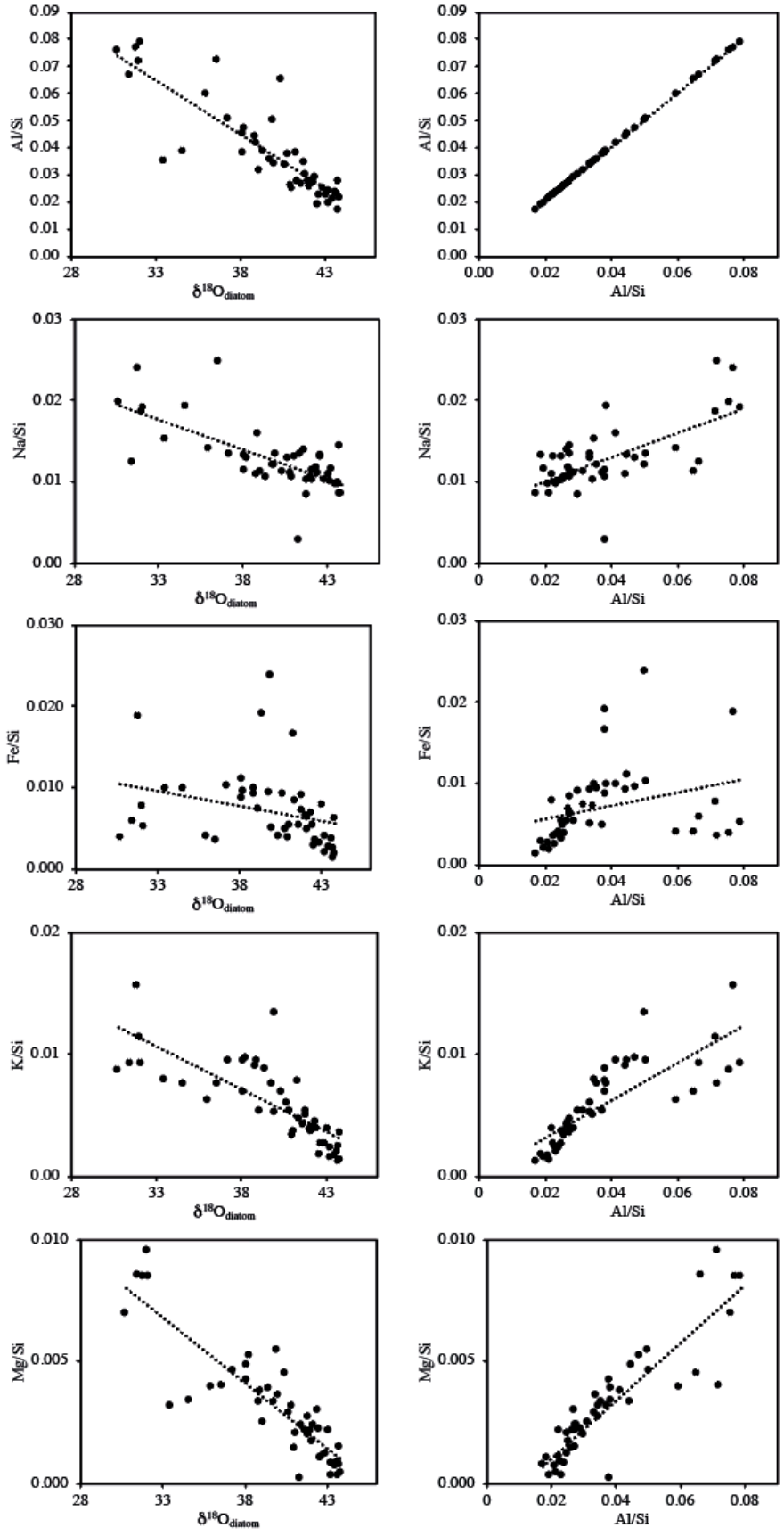
Al/Si
δ18Odiatom
Al/Si
Na/Si
δ18Odiatom
Na/Si
Al/Si
Fe/Si
δ18Odiatom
Fe/Si
Al/Si
K/Si
δ18Odiatom
K/Si
Al/Si
Mg/Si
δ18Odiatom
Mg/Si
Al/Si

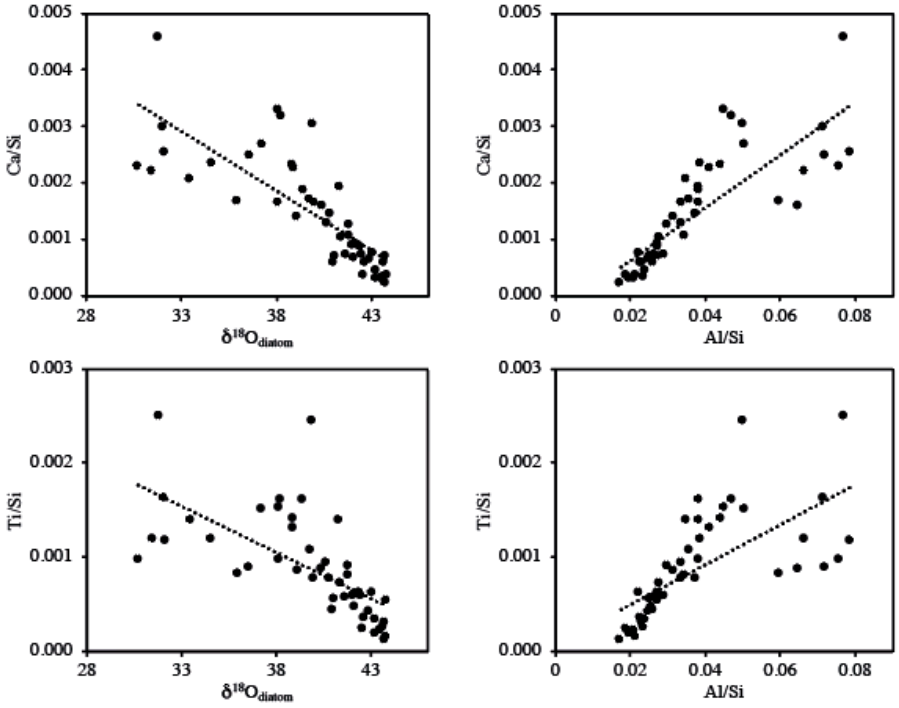

Figure 5. ODP Site 1165 sample elemental ratios plotted against $\delta^{18}O_{diatom}$ (left column) and against Al/Si (right column). Linear regression lines are included. For correlation coefficients and p values see Table 1. Graphs are in order from the most abundant (top) to least abundant (bottom) elements.

Excluding Si, the elements detected at Site 1165, above XRF detection limits, were Al, Na, Mg, Fe, Ca, Ti and K. Linear regression of elemental ratios (element/Si) reveals significant negative correlations with $\delta^{18}O_{diatom}$ for, in order of correlation strength, Mg/Si (r=-0.88, p=<0.01), Al/Si (r=-0.86, p=<0.01), Ca/Si (r=-0.80, p=<0.01), K/Si (r=0.78, p=<0.01), Na/Si (r=-0.70, p=<0.01) and Ti/Si (r=-0.67, p=<0.01) (Figure 5, Table 1). The moderate correlation with Fe (r=-0.30) has a p value of 0.04, which is considered statistically insignificant.

Linear regression of elemental ratios against Al/Si reveals significant positive correlations between, in order of correlation strength, Mg/Si (r=0.90, p=<0.01), Ca/Si (r=0.81, p=<0.01), K/Si (r=0.80, p=<0.01), Ti/Si (r=0.67, p=<0.01) and Na/Si (r=0.66, p=<0.01) (Table 1). As in the regressions against $\delta^{18}O_{diatom}$, the correlation coefficient with Fe is r=0.30, with a p value of 0.04, and thus the relationship between Fe and $\delta^{18}O_{diatom}$ is statistically insignificant at Site 1165.

Table 1. Pearson's correlation co-efficient (Pearson's r) and associated p-values for linear regressions of each ODP Site 1165 element ratio (element/Si) against $\delta^{18}O_{diatom}$ and Al/Si (Figure

5). Red shading indicates insignificant correlation (p-values of <0.01 are considered statistically significant).

	Al	Na	Fe	K	Mg	Ca	Ti
Regression against $\delta^{18}O_{diatom}$							
Pearson's r	-0.86	-0.70	-0.30	-0.78	-0.88	-0.80	0.67
p-value	<0.01	<0.01	0.04	<0.01	<0.01	<0.01	<0.01
Regression against Al/Si							
Pearson's r		0.66	0.30	0.80	0.90	0.81	0.67
p-value		<0.01	0.04	<0.01	<0.01	<0.01	<0.01

Multivariate analysis

Principal component analysis (PCA) of XRF data from ODP Site 1165 was initially performed on unstandardized data. Al is the most abundant element, and accounts for almost all of the data variability within the original dataset at Site 1165 (PCA axis 1 (PCA 1) = 97%; Table 2, Figure 6). As such, analysis of standardized data (Table 2, Figure 7) was also performed; standardization minimises the impact of differences in abundance between elements.

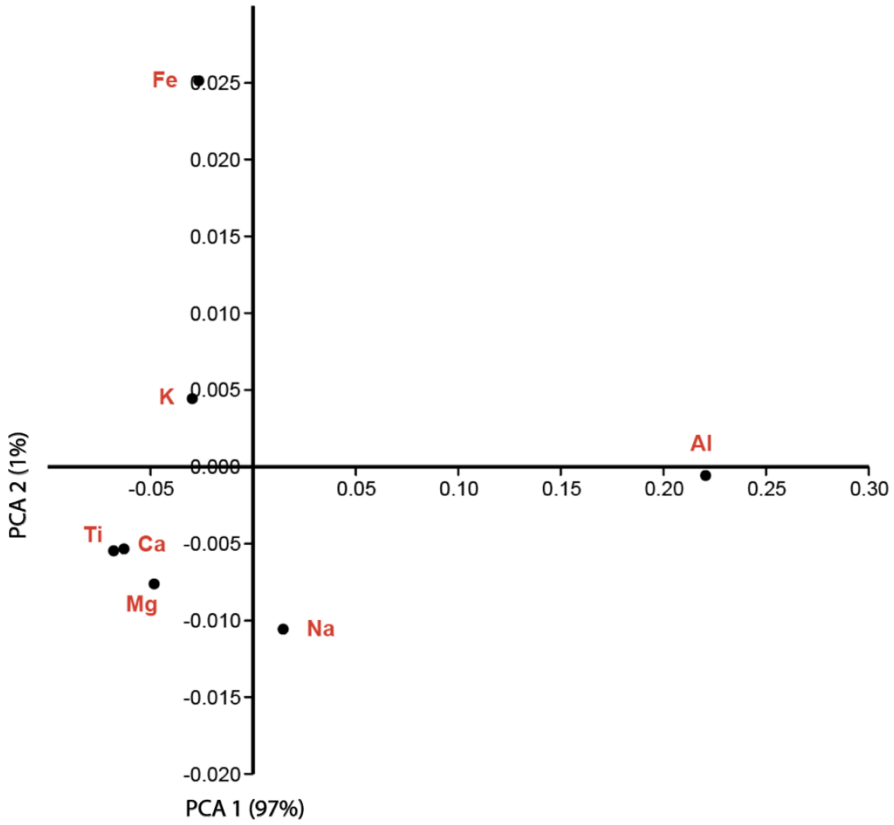

Figure 6. PCA axis 1 (explaining 97% of the data variance) vs. PCA axis 2 (1% variance) of the unstandardized XRF dataset from ODP Site 1165.

PCA 1 accounts for 67% of the variance of the standardized dataset and has positive loadings for Ca, Ti, K and Fe, and negative loadings for Na, Mg and Al (Figure 7). PCA 2, accounting for 20% of the variance, shows high negative loadings for Fe and Na and positive loadings for Al, Mg, Ca, K and Ti (Figure 7).

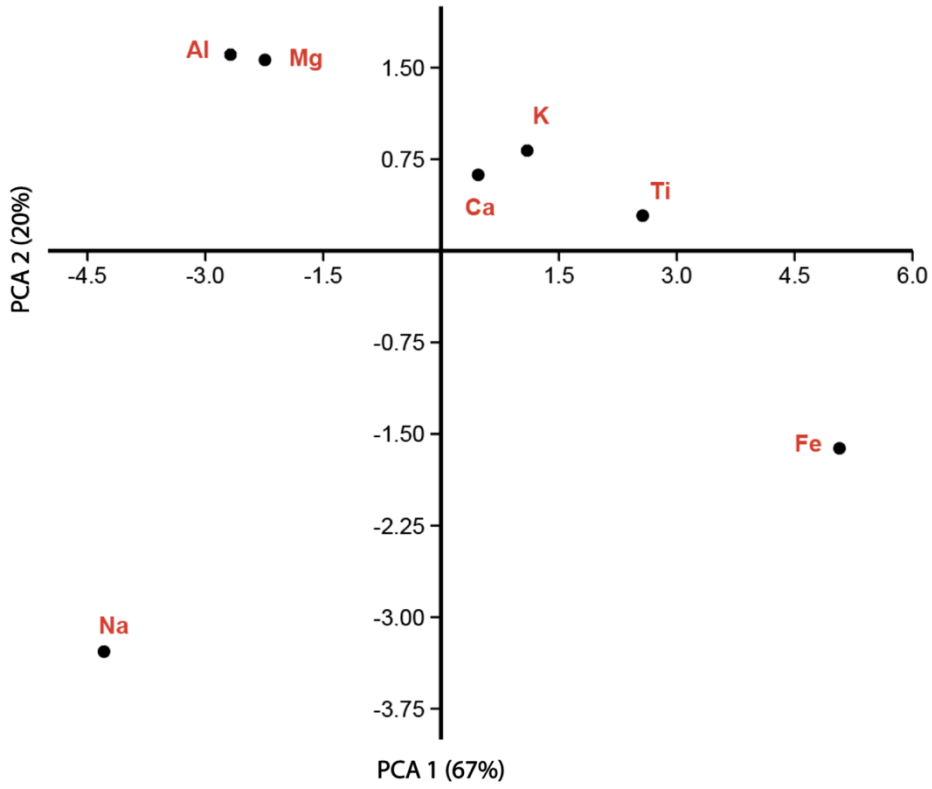

Figure 7. PCA axis 1 (explaining 67% of the data variance) vs. PCA axis 2 (20% of variance) for the standardized XRF dataset from ODP Site 1165.

Table 2. Principal component analysis axes of the unstandardized and standardized datasets at from ODP Site 1165. For the standardized data, only axes that explain greater than 10% of the variance are presented.

Principal component	Eigenvalue	% Variance
PCA 1 (unstandardized data)	0.01	97
PCA 2 (unstandardized data)	<0.01	1
PCA 1 (standardized)	10.7	67

PCA 2 (standardized)	3.3	20

8.3.2.2. ODP Site 744

Univariate statistics

At ODP Site 744 Al, Mg, Na, Fe, Ca, Ti and K were detected above XRF detection limits (excluding Si). Only univariate analysis was performed on the XRF dataset due to the low sample size at this site (n=5). The small sample size also resulted in only one significant correlation, Al/Si versus $\delta^{18}O_{diatom}$, which showed a very strong negative correlation of -0.99 (p=<0.01) (Figure 8, Table 3). However, further significant correlations may be found at the site with a larger sample size.

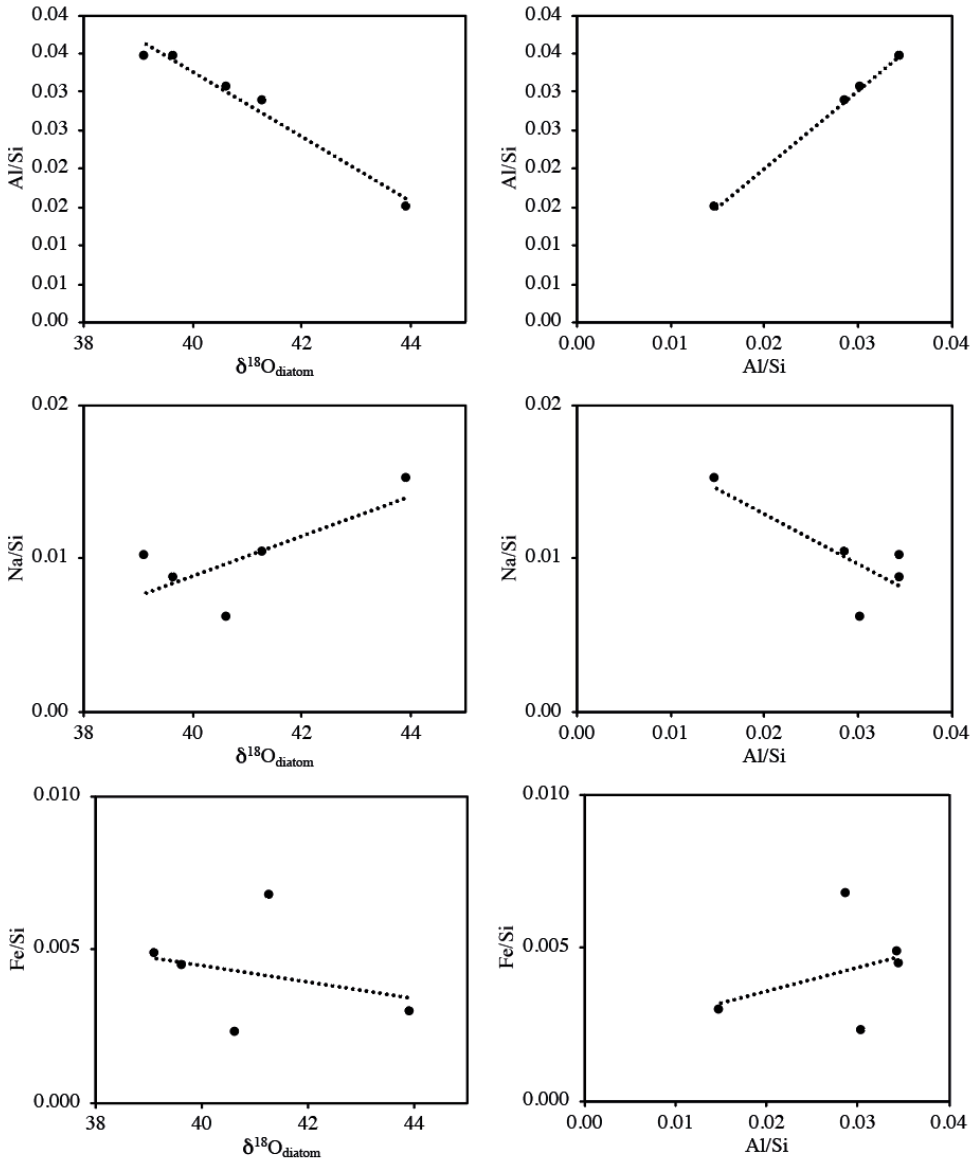

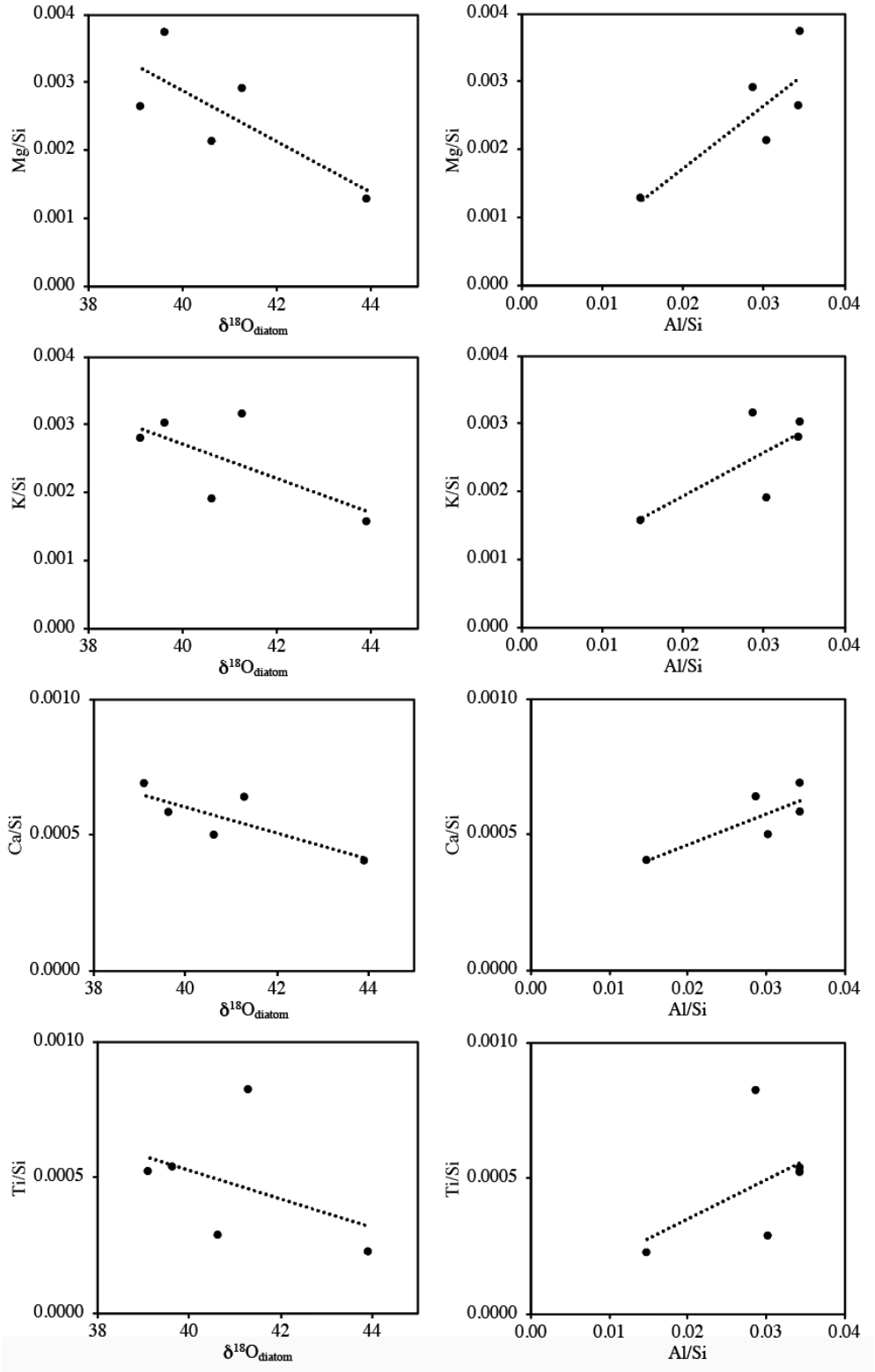

Figure 8. ODP Site 744 elemental ratios plotted against $\delta^{18}O_{diatom}$ (left hand column) and Al/Si (right hand column). Linear regression lines are included. For correlation coefficients and p-values see Table 3. Elements are ordered from the most abundant (top) to least abundant (bottom).

Table 3. Pearson's correlation co-efficient (Pearson's r) and associated p-values for linear regressions of each ODP Site 744 element ratio (element/Si) against $\delta^{18}O_{diatom}$ and Al/Si (see Figure 8). Relationships with p-value of <0.01 are considered statistically significant; values shown in red are not statistically significant.

	Al/Si	Na/Si	Fe/Si	K/Si	Mg/Si	Ca/Si	Ti/Si
Regression against $\delta^{18}O$							
Pearson's coefficient	-0.99	0.74	-0.30	-0.68	-0.76	-0.80	-0.41
p-value	<0.01	0.15	0.62	0.21	0.14	0.10	0.49
Regression against Al/Si							
Pearson's Coefficient		-0.80	0.35	0.73	0.82	0.80	0.49
p-value		0.10	0.56	0.61	0.09	0.10	0.40

8.3.2.3. NBP0101 Site JPC43B

Univariate statistics

At NBP0101 Site JPC43B, only Al, Na, Ti, Ca and K were detected above XRF detection limits. Linear regression of elemental ratios (element/Si) versus $\delta^{18}O_{diatom}$ (Figure 9) reveals significant negative correlations for Ca/Si (-0.063, p=<0.01), Ti/Si (r-0.60, p=<0.01) and K/Si (r=-0.59, p=<0.01) at Site JPC43B, but insignificant correlations between $\delta^{18}O_{diatom}$ Na (r-0.06, p=0.61) and Al (r=-0.14, p=0.24). Linear regressions of elemental ratios (element/Si) against Al/Si reveal significant correlations for Na/Si (r=-0.66, p=<0.01), only (Table 4).

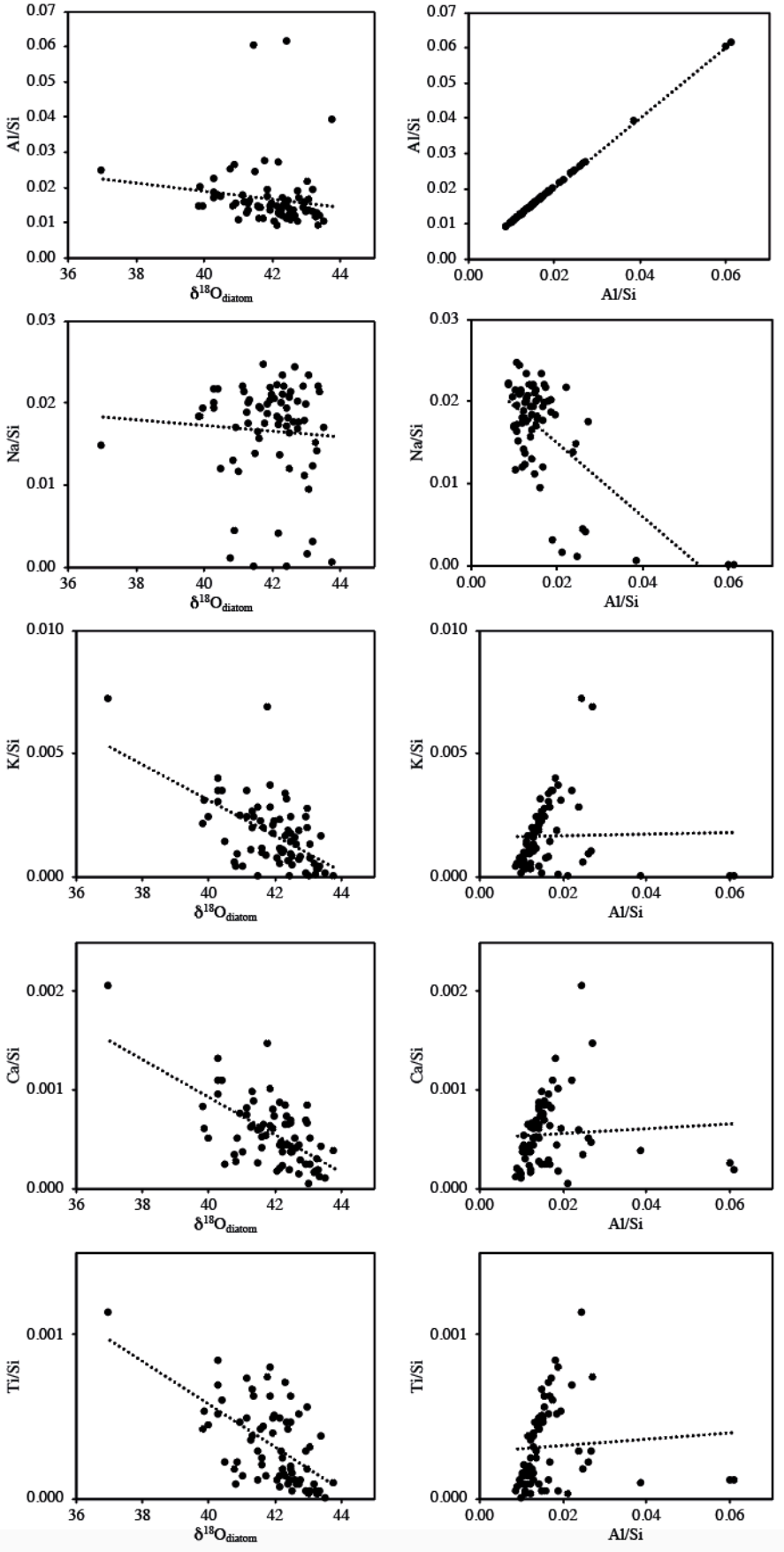
Al/Si
δ18Odiatom
Al/Si
Na/Si
δ18Odiatom
Al/Si
Na/Si
K/Si
δ18Odiatom
Al/Si
K/Si
Ca/Si
δ18Odiatom
Al/Si
Ca/Si
Ti/Si
δ18Odiatom
Al/Si
Ti/Si

Figure 9. NBP0101 Site JPC43B elemental ratios against $\delta^{18}O_{diatom}$ (left hand column) and Al/Si (right hand column). Linear regression lines are included. For correlation coefficients and p-values see Table 4. Elements are ordered from the most abundant (top) to least abundant (bottom).

Table 4. Pearson's correlation co-efficient (Pearson's r) and associated p-values for each NBP0101 Site JPC43B element ratio (element/Si) against $\delta^{18}O_{diatom}$ and Al/Si (Figure 9). Red shading indicates insignificant correlations (p-value of <0.01 is considered significant).

	Al/Si	Na/Si	K/Si	Ca/Si	Ti/Si
Pearson's coefficient	-0.14	-0.06	0.59	-0.63	-0.60
P value	0.24	0.61	<0.01	<0.01	<0.01
Pearson's Coefficient		-0.66	0.02	0.06	0.07
P value		<0.01	0.87	0.62	0.56

Multivariate statistics

Principal component analysis (PCA) of XRF data from NBP0101 Site JPC43B was performed on unstandardized and standardized datasets (Table 5). PCA of the unstandardized data reveals that the first principal component (PCA 1) explains 75% of the variance in the dataset, with strong positive loadings for Na and Al and negative loadings for K, Ca and Ti. The second principal component (PCA 2) explains 25% of the variance, with positive loadings for Na and negative loadings for Al (Figure 10). PCA 1 of the standardized dataset analysis (64% variance) has positive loadings for Na and negative loadings for Al (Figure 11). PCA 2 (27% variance) has positive loadings for Ca, Ti and K and negative loadings for Al and Na (Figure 11).

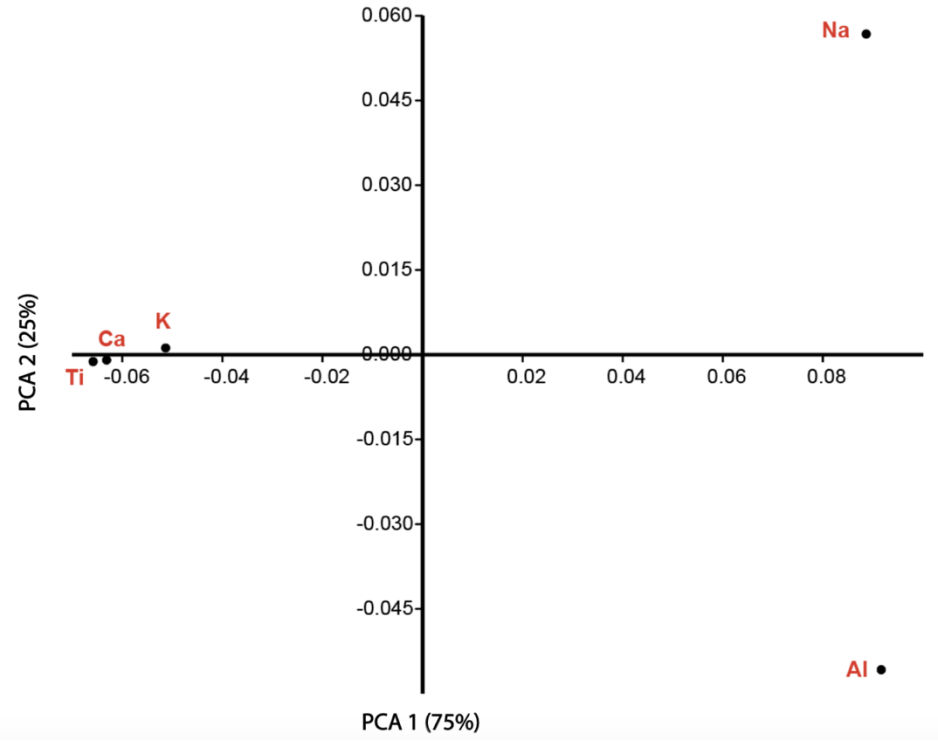

Figure 10. PCA axis 1 (PCA 1 explaining 75% of the data variance) and PCA axis 2 (PCA 2 explaining 25% variance) of the unstandardized XRF dataset from NBP0101 Site JPC43B.

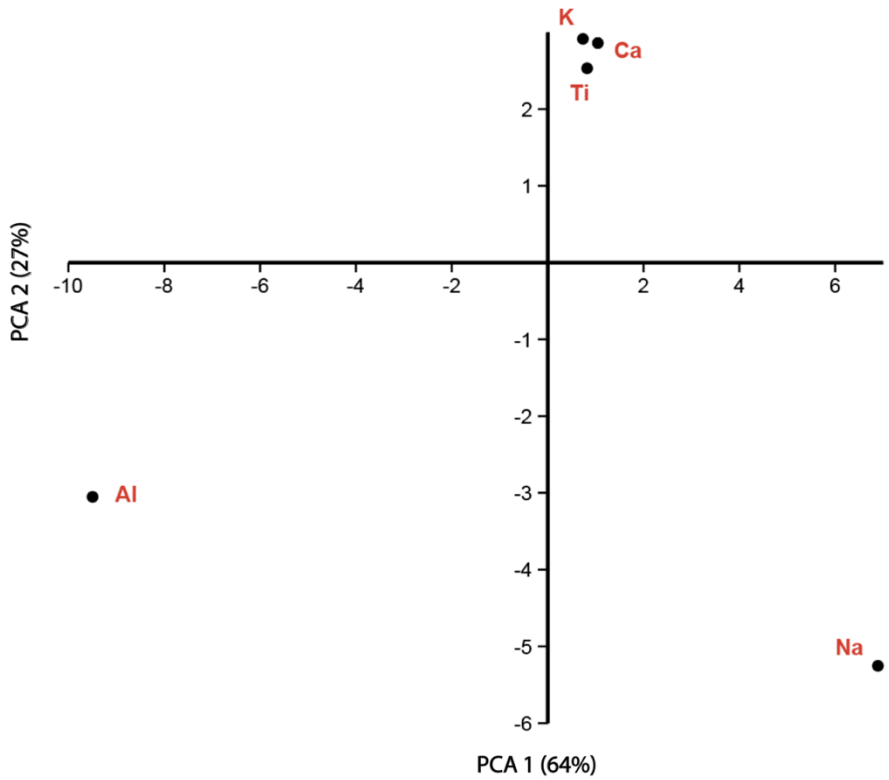

Figure 11. PCA axis 1 (PCA 1 explaining 64% of the data variance) versus PCA axis 2 (PCA 2, 27% of the variance) for NBP0101 43B standardized XRF dataset.

Table 5. Principal Component Analysis of both the unstandardized and standardized XRF datasets from NBP0101 Site JPC43B (only PCA components that explain >10% of data variance are shown).

Principal component	Eigenvalue	% Variance
PCA 1 (unstandardized)	<0.01	75
PCA 2 (unstandardized)	<0.01	25
PCA 1 (standardized)	35	64
PCA 2 (standardized)	15	27

8.3.3. SEM analysis

8.3.3.1. ODP Site 1165

Each sample from ODP Site 1165 was assessed for terrigenous grain and non-diatom siliceous microfossil (sponges, radiolaria, silicoflagellates) contaminants using light microscopy before $\delta^{18}O_{diatom}$ analysis. Several samples were also analyzed using the scanning electron microscope (SEM) (Figures 12-15) to check for contamination. SEM images show that diatoms at ODP Site 1165 are well-preserved with minimal dissolution and, although a small amount of contamination was present in the form of clay particles, sponges, radiolarians and silicoflagellates, the contamination represents a very small proportion of the sample. As such, the source of much of the Al (considered to indicate up to 8% contamination with Al/Si ratios of up to 0.08, Figure 5) is not visible using SEM.

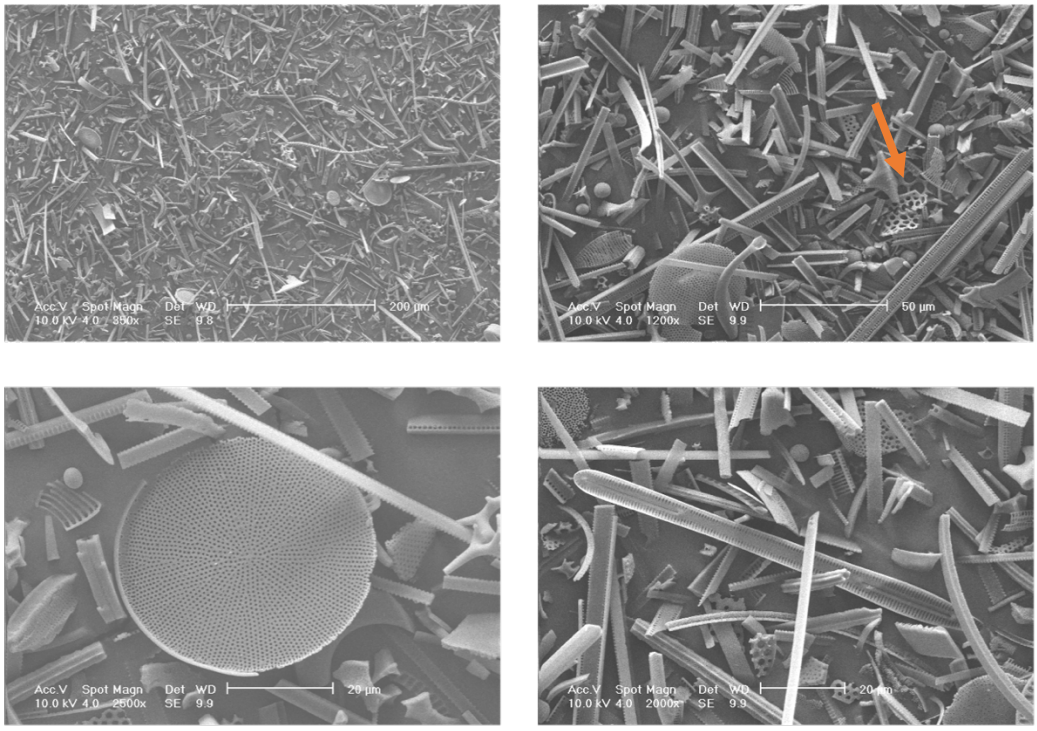

Figure 12. SEM images from Sample ODP Hole 1165B-5H-2W, 107-107 cm. XRF-measured Al/Si is 0.0171 and $\delta^{18}O_{diatom}$ is 43.78‰. Samples show moderate-good preservation a radiolarian fragment (orange arrow), but otherwise good sample purity.

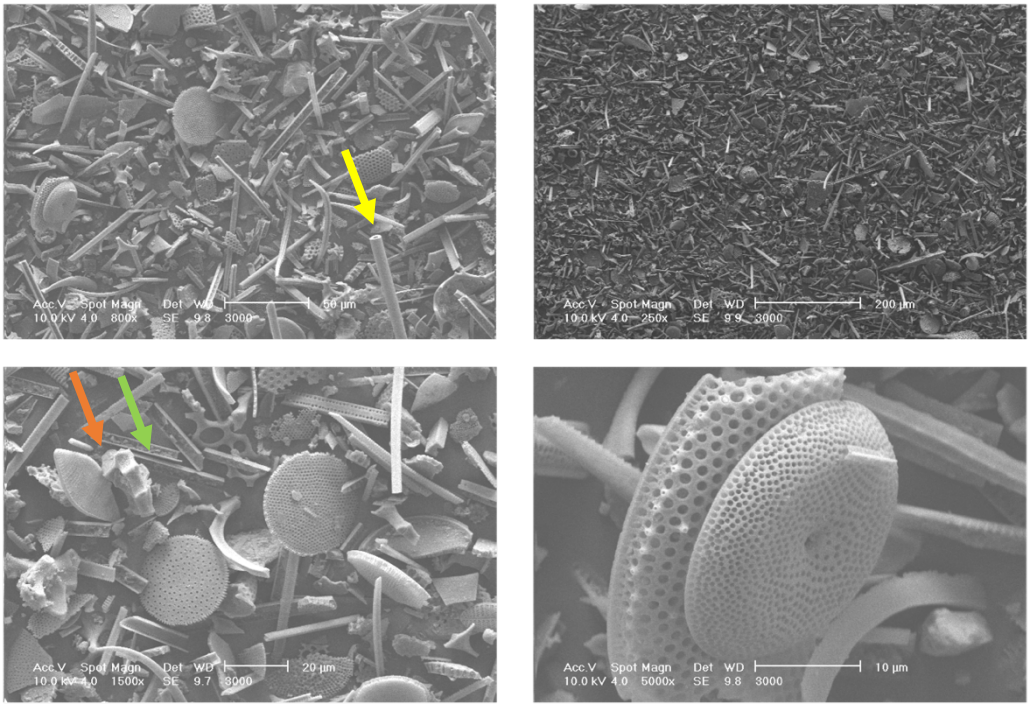

Figure 13: SEM images from ODP Hole 1165B-5H-2W, 56-57 cm. XRF-measured Al/Si is 0.0247 and $\delta^{18}O_{diatom}$ is 42.91‰. Images show moderate-good preservation, with some radiolarian (orange), clay (green) and sponge (yellow) fragments but mostly good sample purity.

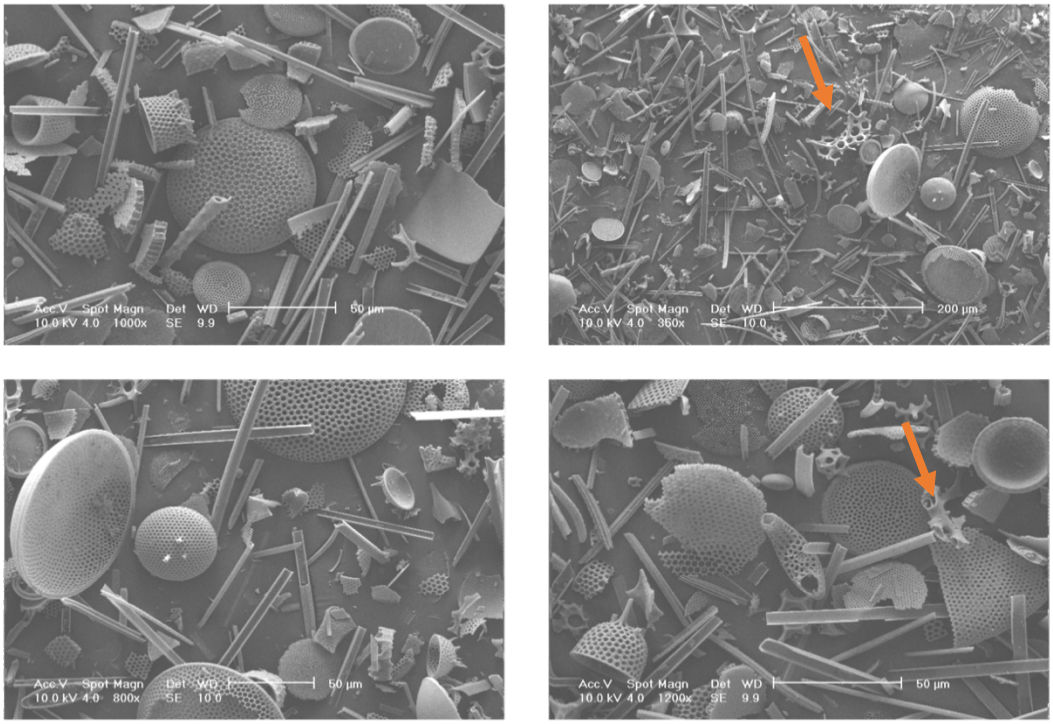

Figure 14. SEM images from ODP Hole 1165B-4H-7W, 49-50 cm. XRF-measured Al/Si is 0.0578 and $\delta^{18}O_{diatom}$ is 33.46‰. Some radiolarian fragments are visible (orange arrows), but sample purity is mostly good.

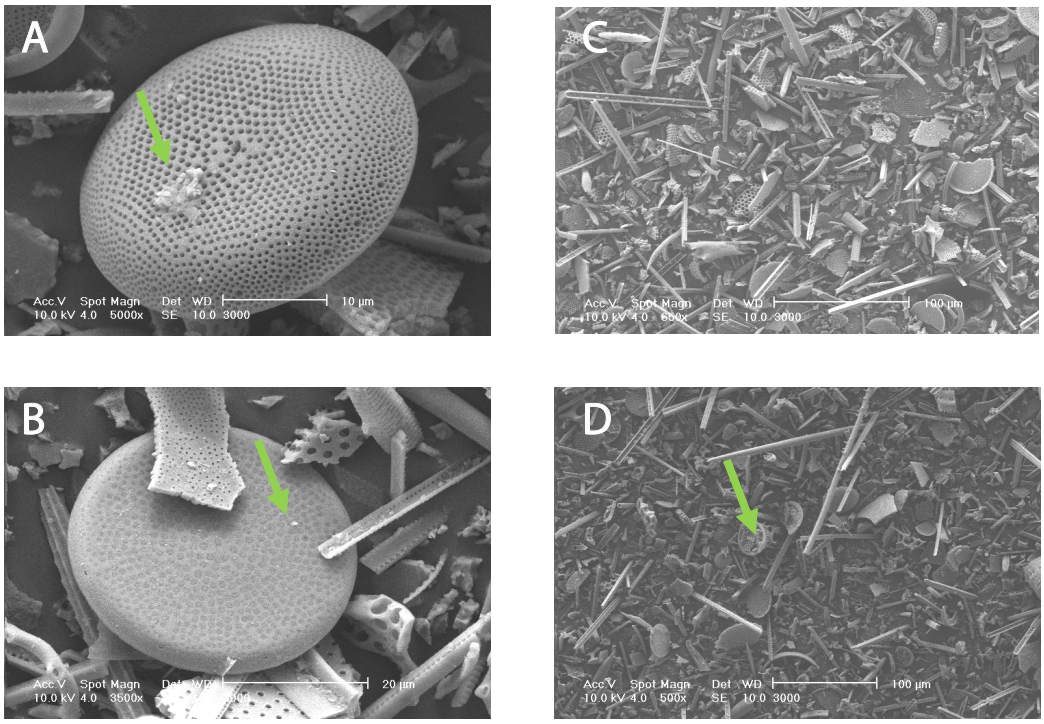

Figure 15. SEM images from ODP Hole 1165B-4H-6W, 134-135 cm. XRF-measured Al/Si is 0.0658 and $\delta^{18}O_{diatom}$ is 30.74‰. Images show moderate preservation and some clay particles (green arrows).

8.3.3.2. ODP Site 744

Samples from Site ODP 744 were investigated prior to analysis for $\delta^{18}O_{diatom}$ using both light microscopy and SEM. SEM images from Site 744 samples show minimal dissolution despite the carbonate parent sediment (Figures 16 and 18). A few clay particles were seen, however, radiolarians, silicoflagellates and sponge spicules were more abundant, particularly in samples with higher Al/Si (Figure 17). Thus, it is possible that non-diatom biogenic silica affected Al/Si and $\delta^{18}O_{diatom}$ at Site 744, but more data and SEM images would be required to explore the hypothesis.

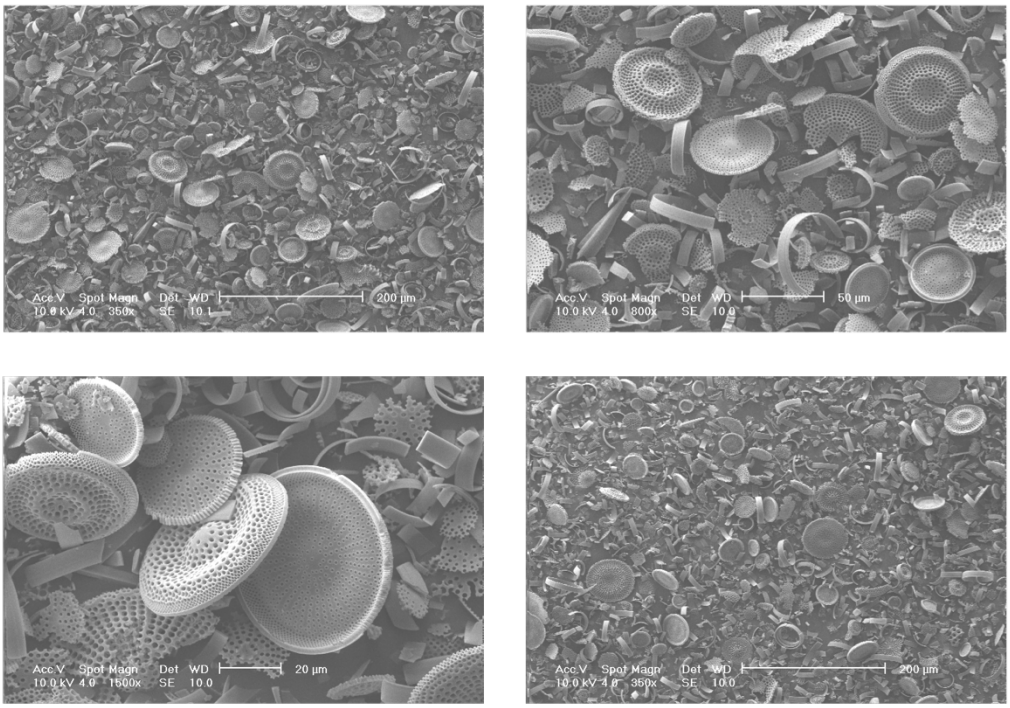

Figure 16. SEM images from ODP Hole 744B-7H-CCW, 2-3 cm. XRF-measured Al/Si is 0.0147 and $\delta^{18}O_{diatom}$ is 43.86‰. Sample purity is very good.

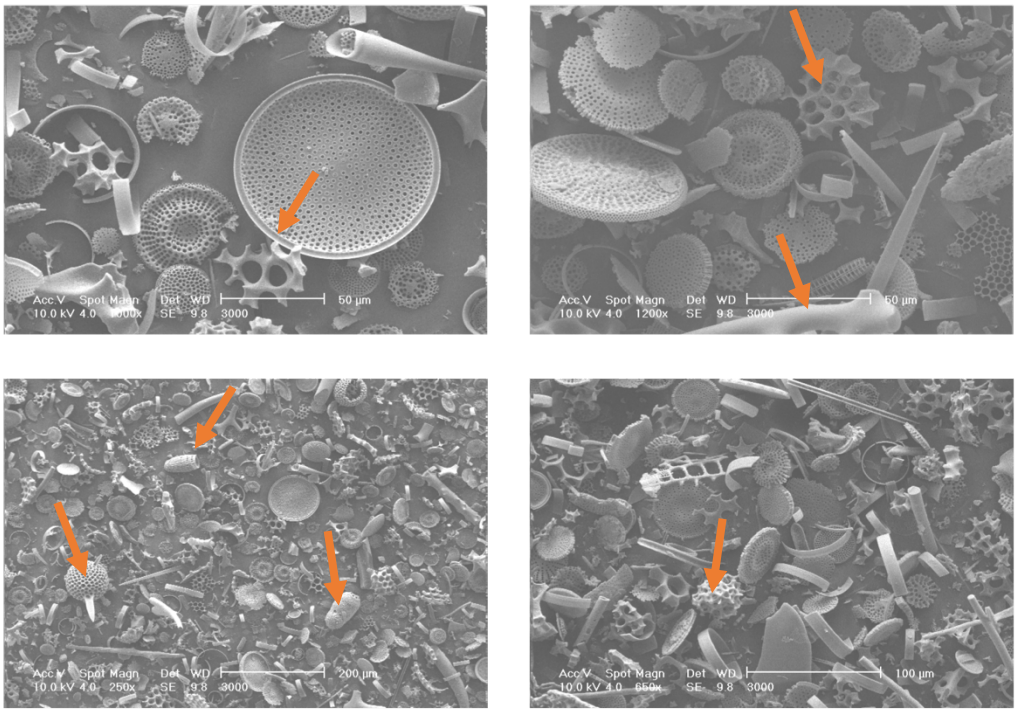

Figure 17. SEM images from ODP Hole 744B-7H-5W, 18-19 cm. XRF-derived Al/Si is 0.0341 and $\delta^{18}O_{diatom}$ is 39.14‰. Some radiolarians are visible (orange arrows) .

8.3.3.3. NBP0101 Site JPC43B

Two samples from NBP0101 Site JPC43B were assessed using the SEM prior to $\delta^{18}O_{diatom}$ analysis. Images revealed a clean, well-preserved diatom assemblage with minimal dissolution or visible contamination (Figures 18-19). Sponge spicules were present (Figure 19) but were not abundant in the samples examined.

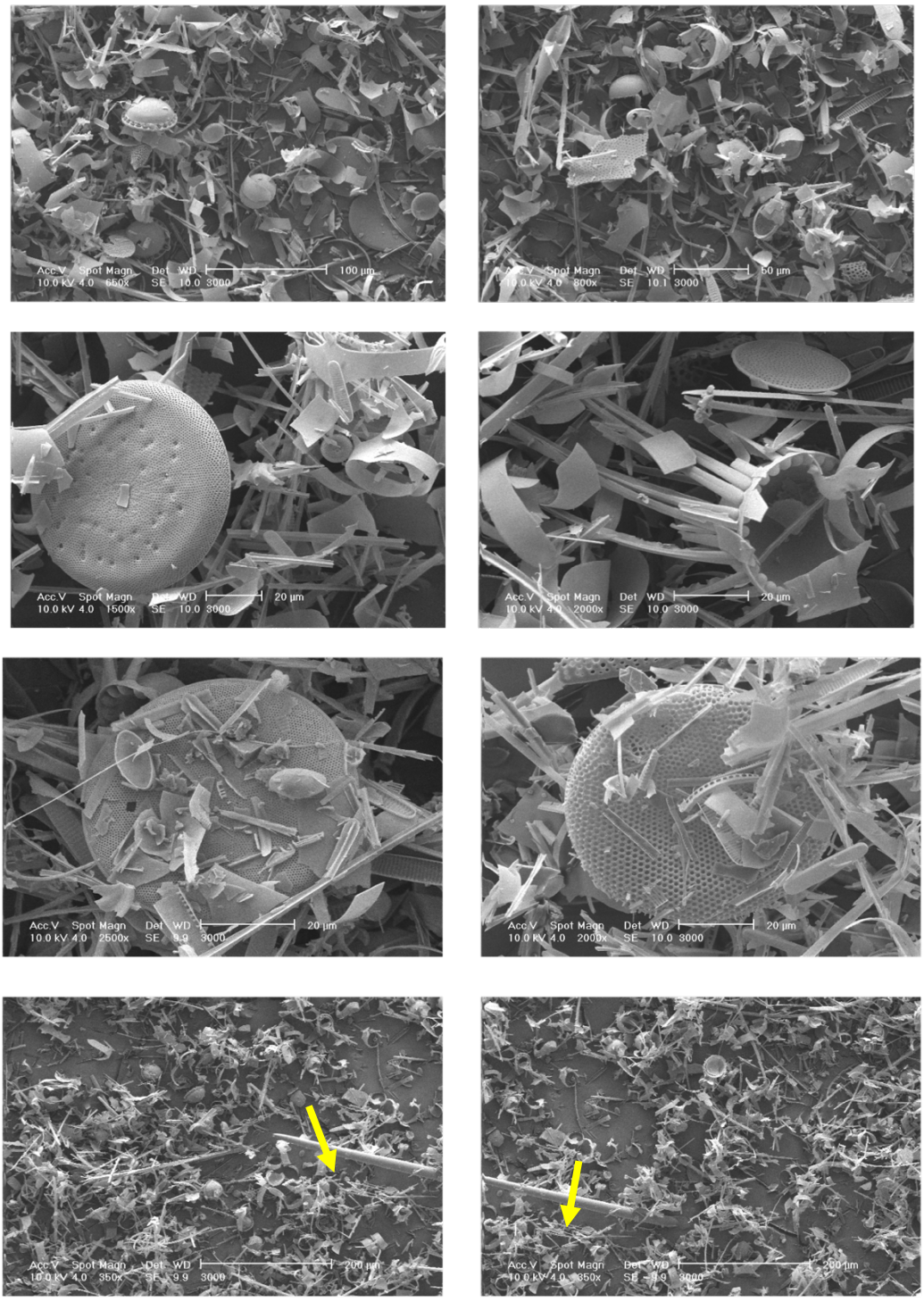

Figure 18. (upper four images) SEM images from NBP0101 JPC43B, 1047-1048 cm. XRF-measured Al/Si is 0.0060and $\delta^{18}O_{diatom}$ is 44.1‰. Diatom preservation was very good, with many *Corethron* setae and girdle bands.

Figure 19. (lower four images) SEM images from NBP0101 JPC43B, 1119-1120 cm. XRF-measured Al/Si is 0.0232 and $\delta^{18}O_{diatom}$ is 33.4‰. Diatom preservation is generally good, with many *Corethron* fragments. A sponge spicule can be seen crossing both lower images (yellow arrows).

8.3.4. Al/Si versus $\delta^{18}O_{diatom}$

Section 8.3.2 demonstrated a strong correlation between Al/Si and $\delta^{18}O_{diatom}$ at both ODP Sites 1165 and Site 744. To contextualise this relationship, unpublished $\delta^{18}O_{diatom}$ and Al/Si datasets have been provided by J. Pike, J. Williams and Pike, J. Smith & Williams (unpublished data, 2019; 12-0 ka, Antarctic margin; see Section 8.2.3). These unpublished data are considered alongside Sites 1165 and 744, and the only published record that includes geochemical data and $\delta^{18}O_{diatom}$ (Maier et al., 2018; 50-5 ka, Bering Sea) (Figure 20; Table 6).

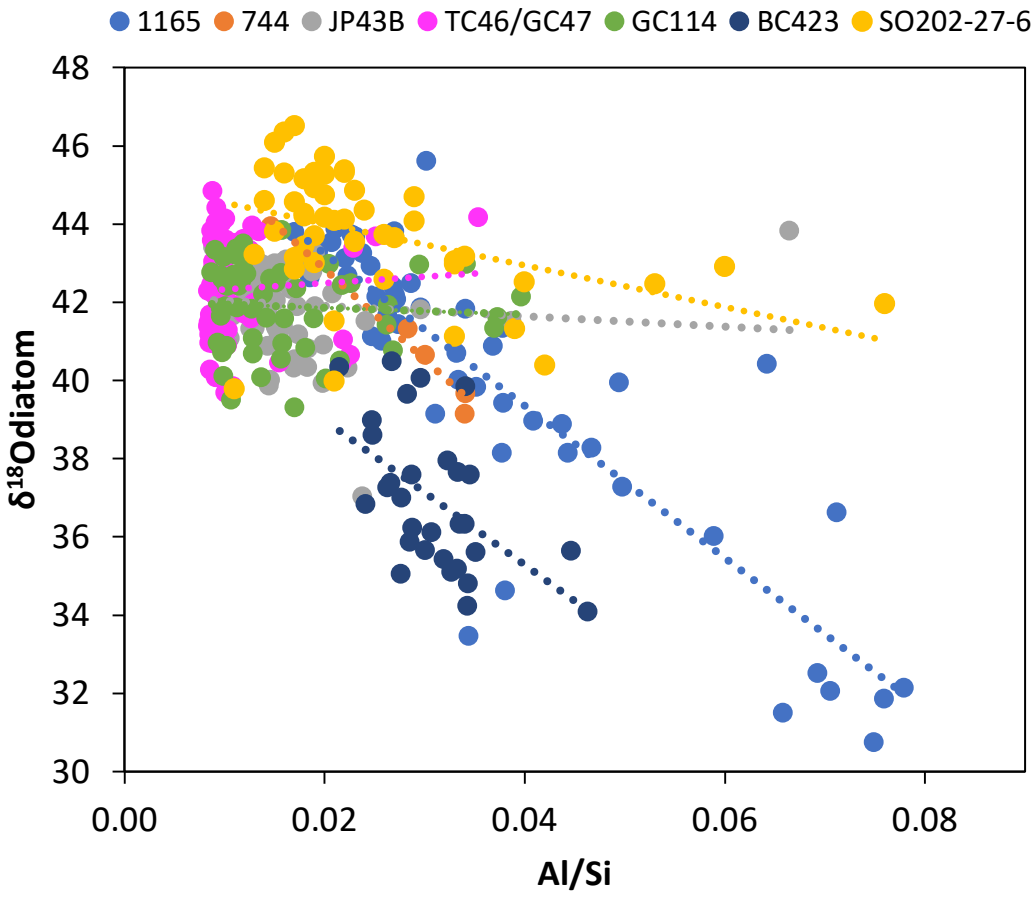

Figure 20. Al/Si versus $\delta^{18}O_{diatom}$ at the different sites considered in this study (Figure 2 for locations, plus Bering Sea site from Maier et al., 2018), including linear regression lines. Correlation coefficients and p-values are given in Table 6.

Table 6. Pearson's r correlation coefficients and associated p-values for Al/Si versus $\delta^{18}O_{diatom}$ linear regressions at unpublished and published sites investigated for this study (Figure 2 for locations, plus Bering Sea site of Maier et al., 2018). Unpublished data were provided by J. Pike and J. Williams (2019) for Sites JPC43B, TC46/GC47, GC114 and BC423B (Section 8.2.3). The only published study for which both $\delta^{18}O_{diatom}$ and Al/Si data are available is Site SO202-27-6 in the Bering sea (Maier et al., 2018). Sites below are listed in order of age, with the oldest samples first. Significant relationships are indicated by p-values of <0.01; red shading indicates statistically insignificant relationships.

Site	Location	Age	Depth (mbsf)	Pearson's r	Al/Si range	P value
744	Kerguelen Plateau	Miocene (12-15 Ma)	54-60	-0.98	0.01-0.04	<0.01
1165	Prydz Bay	Pliocene (3.45-3.75 Ma)	33-39	-0.86	0.01-0.08	<0.01
SO202-27-6	Bering Sea	Pleistocene (55-5 ka)	0-3	0.42	0.01-0.08	<0.01
JPC43B	Iceberg Alley	Holocene (12-0 ka)	0-24	-0.09	0.01-0.07	0.42
TC46/GC47	Anvers Shelf (WAP)	Holocene (3912 - 211 cal yr BP)	0.05-1.67	-0.06	0.01-0.04	0.61
GC114	Boyd Straight (WAP)	Holocene (3822 -76 cal yr BP)	0.05-3.25	-0.06	0.01-0.05	0.69
BC423B	Amundsen Sea	Holocene (594 - -76 cal yr BP)	0-0.3	-0.54	0.01-0.05	<0.01

Presented Al/Si and $\delta^{18}O_{diatom}$ data (Table 6) suggest that Al/Si is significantly negatively correlated with $\delta^{18}O_{diatom}$ at Sites 744 (r=-0.98, p=<0.01), 1165 (r=-0.86, p=<0.01), BC423B (r=-0.54, p=<0.01) and SO202-27-6 (r=-0.42, p=<0.01). Al/Si was found not to be significantly

correlated with $\delta^{18}O_{diatom}$ at Sites JPC43B (r=-0.09, p=<0.42), TC46/GC47 (r=0.06, p=0.61), and GC114 (r=-0.06, p=0.69). Apart from Site BC423B (0-0.3 mbsf, youngest age samples) which is strongly correlated, the strength of the correlation seems to increase with age and/or depth (Table 6). Correlation appears largely unrelated to the range or absolute values of Al/Si at each site.

8.4. Discussion

This discussion will consider whether $\delta^{18}O_{diatom}$ at ODP Site 1165 reflects an environmental signal and, thus, whether $\delta^{18}O_{diatom}$ can be used as a paleoceanographic proxy in Neogene sediments more generally, including implications for the Pliocene climate interval investigated at Site 1165. Finally, the causes for the correlations between Al/Si and $\delta^{18}O_{diatom}$ will be explored, and whether Al/Si can be used as a proxy for sample contamination.

8.4.1. Particulate contamination

The strong correlation (r=-0.86, p=<0.01) between Al/Si and $\delta^{18}O_{diatom}$ at ODP Site 1165 must be investigated before $\delta^{18}O_{diatom}$ can be interpreted as a record of past ocean change. Previous studies have used Al/Si as a measure of particulate contamination (Maier et al., 2018), particularly from clay particles, because these non-diatom particles have low $\delta^{18}O$ and, as such, their unaccounted for presence can artificially reduce the true $\delta^{18}O_{diatom}$ signal. If particulate contamination is affecting the $\delta^{18}O_{diatom}$ signal at Site 1165, it should be possible to remove the contaminated portion of the signal, which can be estimated from the geochemical data, via mass balance modelling (Brewer et al., 2008). The mass-balance equation of Swann & Leng (2009) was therefore applied to $\delta^{18}O_{diatom}$ data from Site 1165:

$$\delta^{18}O_{corrected} = \frac{\delta^{18}O_{measured} - \frac{\%contamination}{100} \bullet \delta^{18}O_{contamination}}{\frac{\%purity}{100}}$$

Different possible contaminant end-member $\delta^{18}O_{diatom}$ were modelled (2-30‰ $\delta^{18}O$) to encompass the maximum possible range of clay mineral $\delta^{18}O$ values, which ranged from 12-21‰ in samples from the Antarctic peninsula (Xu & Gao, 1988) and 13-29‰ in other globally-distributed samples (Savin & Epstein, 1970). Removal of the contaminated outer layer of diatom silica during the SWF process was also accounted for by modelling 50% yields, meaning 50% of material was removed prior to analysis. 50% represents an extreme end-member for the maximum possible amount of material removed during SWF (G. Swann, *personal communication*).

Mass balance modelling does not change the structure and major trends of the $\delta^{18}O_{diatom}$ record at Site 1165 (Figure 21). XRF data suggests that if all of the Al is from particulate aluminosilicate clay contamination, the contaminated material would represent up to 8% of the sample. However, even when yields of 50% and end-member $\delta^{18}O_{contamination}$ values of 2‰ are assumed, 8% contamination cannot account for the 15‰ range in $\delta^{18}O_{diatom}$ values at Site 1165. Further, the SEM images (Figures 12-15) indicate that particulate contamination does not represent up to 8% of the highest Al/Si samples at Site 1165.

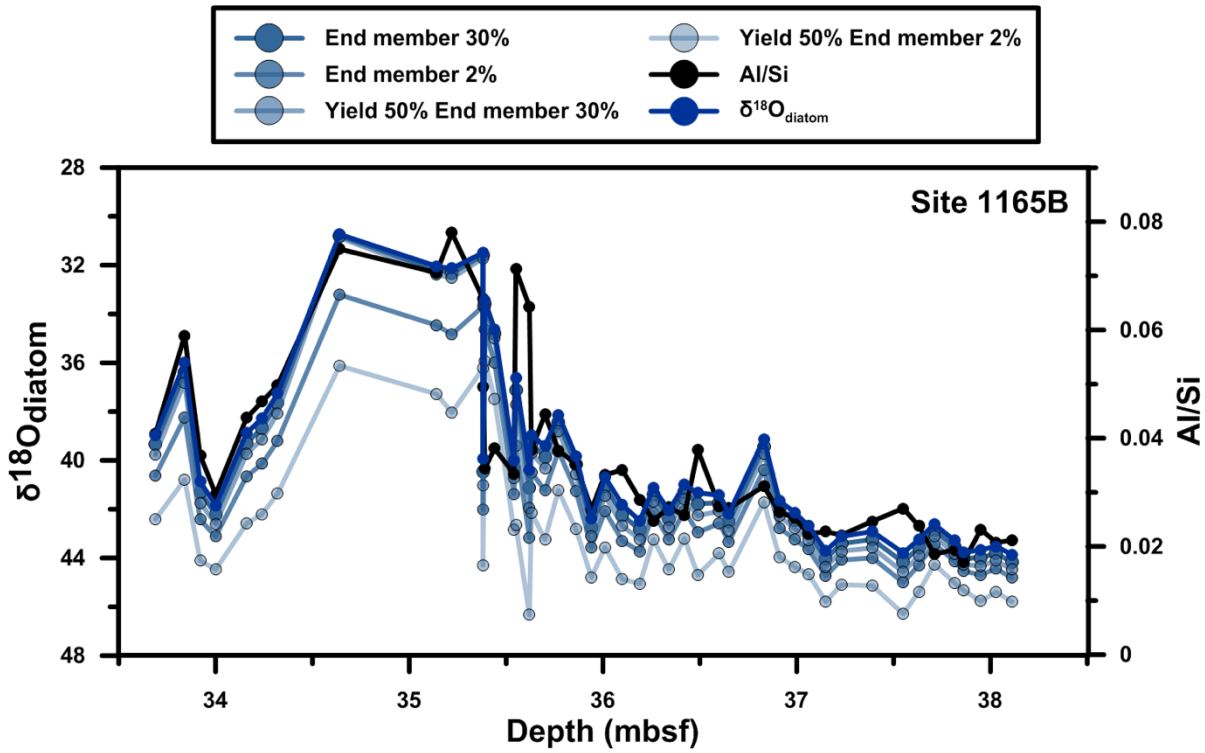

Figure 21. Mass balance modelling of $\delta^{18}O_{diatom}$ at ODP Site 1165 accounting for the most extreme possible end-members for potential particulate contamination of $\delta^{18}O$; 30‰ and 2‰. Maximum (50%) yield (the amount of material removed by stepwise fluorination) is also presented.

Mass balance modelling also did little to change the structure of the Pleistocene Bering Sea record of Maier et al. (2018) (Figure 22), where Al/Si ranged between 0.01-0.08 and an Al/Si versus $\delta^{18}O_{diatom}$ correlation of r=-0.42 (p=<0.01) was documented (Figure 20, Table 6). The inadequacy of mass balance modelling at both of the marine sites (OPD Site 1165 and Site SO202-27-6), as well as the relatively particulate-free SEM images, therefore suggests that particulate contamination alone cannot explain the strong Al/Si versus $\delta^{18}O_{diatom}$ correlation, and cannot account for the range of $\delta^{18}O_{diatom}$. Instead, Al (and potentially the other less abundant

metals), may be incorporated into the diatom silica intrinsically, making them invisible under SEM, thus, a different process (than particulate contamination) must be responsible for the close association between $\delta^{18}O_{diatom}$ and Al/Si.

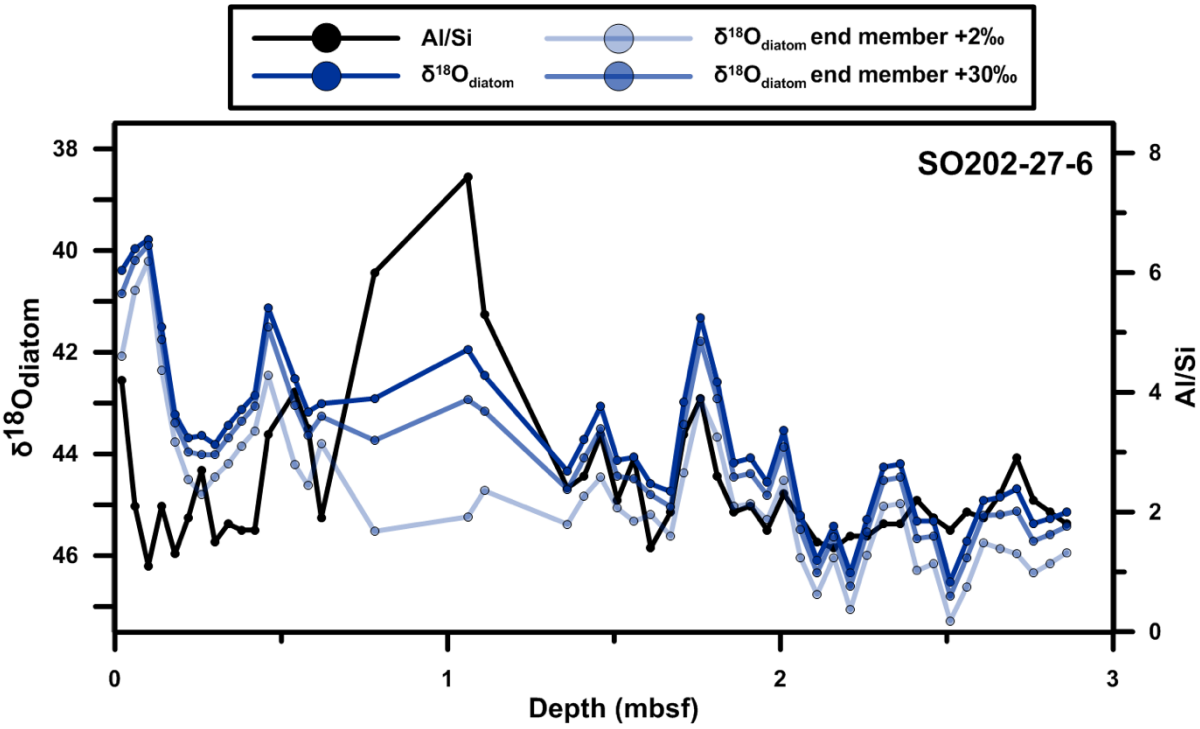

Figure 22. Mass balance modelling of $\delta^{18}O_{diatom}$ at Site SO202-27-6 using the record of Maier et al. (2018). Data have been modelled using the most extreme possible end-members for potential particulate contamination of $\delta^{18}O$, 30‰ and 2‰.

8.4.2. Intrinsic incorporation of metals within diatom silica

Section 8.4.1 concluded that Al/Si is not reflecting particulate contamination, therefore, the Al (and perhaps also other metals) must be intrinsically incorporated in the diatom silica. This section will explore whether the metals could accumulate as a surficial layer via adsorption to the silica lattice, or whether they penetrate more deeply into the silica lattice. I will explore whether accumulation occurs as a result of live processes, perhaps representing a true surface-water environmental signal, or due to post-depositional processes, metal accumulation represents a diagenetic signal.

8.4.2.1. Live bioaccumulation

Diatom silica naturally contains some intrinsic aluminium, which seems to vary by species (Table 7). The amount of Al in diatom silica is also assumed to relate, at least in part, to the

concentration of dissolved Al within the water column (van Benneken et al., 1991). Natural processes largely control the distribution of Al, for example, ice-covered waters contain higher concentrations of dissolved Al (c. 3 nM) than ice-free waters (c.1-1.5 nM) in the Weddell-Scotia Seas (van Bennekom et al., 1991). Glacial discharge also contains glacially-eroded clay minerals and, therefore, clay contamination and $\delta^{18}O_{diatom}$ could co-vary as a result of diatoms incorporating more Al into their frustules (higher Al/Si) when higher amounts of Al are released within glacial discharge (lower $\delta^{18}O_{diatom}$). Alternatively, the incorporation of Al into diatom silica could, hypothetically, increase with temperature although, to my knowledge, no studies have yet investigated the effect of temperature on Al incorporation. The correlation between Al/Si and $\delta^{18}O_{diatom}$ could therefore theoretically result from environmental processes operating in tandem with primary oxygen isotope fractionation and, thus, the Al/Si versus $\delta^{18}O_{diatom}$ correlation could be a true representation of environmental processes and $\delta^{18}O_{seawater}$.

Table 7. Concentrations of Al found in diatom silica. Grey shading indicates the new results from the analysis of ODP Sites 1165 and 744.

Sample type	Location	Species	Al/Si	Reference
Diatom cultures		*Porosira glacialis*	0.00007	Gehlen et al. (2002)
Diatom cultures		*Thalassiosira nordenskjioldii*	0.0013	Gehlen et al. (2002)
Diatom cultures		*Thalassiosira nordenskjioldii*	0.0038	Gehlen et al. (2002)
Diatom cultures		*Lauderia annulata*	0.007	Gehlen et al. (2002)
Diatom cultures		*Thalassiosira punctigera*	0.0012-0.0031	Koning et al. (2007)
Surface water		*Biddulphis spp.*	0.0036	van Bennekom et al. (1989)
Surface water		*Biddulphis spp.*	0.0108	van Bennekom et al. (1989)
Surface water	North Sea	*Biddulphia sinensis*	0.0083	Ren et al. (2013)
Sediment traps at 3444m water depth	Southern Ocean	Multiple species	0.00023	Dixit et al. (2001)

Sediment surface	Wadden Sea tidal flat	Benthic assemblage	0.008	Ren et al. (2013)
Sediment surface	Scotia Sea surface tidal flat	Multiple species	0.021	Rickert et al. (2002)
Sediment surface	Marguerite Bay	Multiple species	0.0021-0.0031	Hendry & Rickaby (2008)
Sediment surface	Marguerite Bay	Multiple species	0.000021-0.0003	Hendry et al. (2010)
Sediment surface	Marguerite Bay	Multiple species	0.007-0.029	Hendry et al. (2010)
Sediment surface	Southern Ocean	Multiple species	0.00014-0.0198	Andersen et al. (2011)
Downcore	Southern Ocean	Multiple species	0.0007-0.0299	Lal et al. (2006)
Downcore	Zaire deep-sea fan	Multiple species	0.13-0.165	van Bennekom et al. (1989)
Downcore	Enderby Basin	Multiple species	0.0027	van Beusekom et al. (1997)
Downcore	Crozet Basin	Multiple species	0.011	Ren et al. (2013)
Downcore	Bering Sea	Multiple species	0.003-0.09	Ren et al. (2013)
Downcore	Bering Sea	Multiple species	0.01-0.08	Maier et al. (2018)
Downcore	Site 1165; Prydz Bay	Multiple species	0.01-0.08	This study
Downcore	Site 744; Kerguelen Plateau	Multiple species	0.01-0.04	This study
Downcore	Iceberg Alley	Multiple species	0.01-0.07	J. Pike (unpublished data, 2019)
Downcore	Marguerite Bay	Multiple species	0.01-0.04	J. Williams (unpublished data 2019)

Downcore	Amundsen Sea	Multiple species	0.02-0.05	J. Williams (unpublished data 2019)
Downcore	Anvers Shelf, West Antarctic Peninsula	Multiple species	0.01-0.04	J. Williams (unpublished data 2019)
Downcore	Boyd Straight, West Antarctic Peninsula	Multiple species	0.01-0.04	J. Williams (unpublished data 2019)

Whilst it is possible that natural processes could explain the correlation between $\delta^{18}O_{diatom}$ and Al/Si in cleaned sedimentary diatom silica samples, for example at Site 1165, the amount of aluminium present in live diatom silica from water column or culture samples is around an order of magnitude lower than what is found in fossil samples (Table 7). Al/Si of <0.008 are found in culture and water column samples (Van Benneken et al., 1991) versus Al/Si of up to 0.08 at Site 1165. The Al/Si of cultured diatom silica does not seem to exceed c. 0.008 even when diatoms are grown in high aluminium sea water, suggesting a biophysical limit to live metal accumulation (Van Beusekom, 1989; Vrieling et al., 1999). As such, live-bioaccumulated aluminium is not likely the source of the Al found in samples at Site 1165, or in the other sedimentary diatom samples investigated in my study and detailed in Table 7.

8.4.2.2. Post-depositional accumulation

If the majority of Al is unlikely to be incorporated into diatom silica during frustule synthesis in the surface waters (Section 4.2.1), it therefore must increase within diatom silica upon burial. Notably, no sample from sedimentary diatoms in Figure 20, or within the published studies detailed in Table 7, has an A/Si of <0.008. Rapid post-mortem accumulation of Al into diatom silica has been suggested to occur once bacteria have broken down the protective diatom cell membranes upon cell-death (Lewin, 1961; Koning et al., 2007). This section will therefore investigate the likely source of post-depositional metals, their mechanistic association with the diatom silica lattice, and their possible impact upon $\delta^{18}O_{diatom}$.

Source of post-depositionally-accumulated metals

Aluminium is the most abundant metal measured by XRF in cleaned diatom samples from ODP Sites 1165 and 744 and Site SO202-27-6 (almost double that of the next most abundant), followed by Na, Fe at Sites 1165 and 744, and Ca, Ti and K at all three sites. A likely potential source of post-depositionally accumulated Al (and possibly other metals) within diatom silica is, therefore, the aluminosilicate clays in which samples are buried. In support of this hypothesis, Al/Si ratios of cleaned diatom silica samples from Pleistocene Bering Sea sediments correlated with the aluminosilicate:opal ratio of bulk sediment (R^2 = 0.57) in the study of Ren et al. (2013), although they did not go on to measure $\delta^{18}O_{diatom}$. In the same record, Mg/Si, Fe/Si and Ca/Si also all exhibited the same patterns as Al/Si, with over a third of the metals measured within samples remaining even after extensive cleaning techniques including density separation, reductive and oxidative processes (Ren et al., 2013). Al/Si ratios of these cleaned Bering Sea samples were between 0.01 and 0.09; directly comparable to those from Site 1165.

Samples from ODP Site 744, where carbonate is the parent sediment, show a maximum of c. 0.04 Al/Si; less than samples from Site 1165, where clay is the parent sediment, and Al/Si ratios reach c. 0.08. However, this is not the case at other sites such as at NBP0101 JPC43B and the West Antarctic Holocene Sites (Table 6), where diatom ooze and terrigenous clay are the parent sediments and maximum Al/Si is lower than at Site 1165. Further, the similarly strong correlations between Al/Si and $\delta^{18}O_{diatom}$ at Sites 1165 (r=-0.88, p=<0.01) and 744 (r=-0.99, p=<0.01), despite stark differences in parent sediment, suggest the associated relationship between metal accumulation and $\delta^{18}O_{diatom}$ is more complicated than simply a linear affect depending on the type of source material/abundance of clays present.

When Al substitutes for Si within the silica lattice, a charge compensation must be provided. The charge can come from Ca and K, with Mg and Na potentially also involved, although this may change depending on the availability of elements in the parent sediment (van Bennekom et al., 1989). This would imply coherent behaviour between the elements, to some extent. However, multivariate analysis of XRF data at Sites 1165 and JPC43B showed Ti, Ca, K plotting together while Al, Mg, Na and Fe plotted separately, and not together (Figures 7 and 11). These distributions suggest distinct sources and/or chemical behaviours for different elements. Thus, the element ratio distributions may represent independent contaminant sources. For example, different areas or lithologies being eroded as erosional/depositional patterns change through time. However, even if auminosilicate clay minerals are the most likely the source of the metals, the nature of the association with diatom silica remains unclear. Further, the question remains

as to whether the metals are absorbed/precipitated at the surface of the diatom, or whether they penetrate more deeply into the silica lattice.

Adsorption onto the surface of the silica lattice

Aluminium, and possibly other metals, can adsorb onto the surface of the silica lattice. This has been demonstrated in the study of Koning et al. (2007), who showed that when the protective organic membrane is removed from pristine cultured diatom silica frustules, which were then exposed to Si and Al concentrations mimicking conditions at the sediment/water interface, a tetrahedral aluminosilicate phase precipitates at the silica surface, remaining even after acid cleaning (Koning et al., 2007). As such, it is possible that the Al (and perhaps also the other metals) documented in samples from my study are only adsorbed onto the surface of the diatom silica. This does not, however, explain the correlation between metal concentrations and $\delta^{18}O_{diatom}$, since measurement of the latter was performed after removal of the outer silica layer during SWF.

Penetration into the silica lattice

In addition to the adsorption/precipitation of metals at the silica surface, post-mortem alteration and the penetration of metals into the inner –Si–O–Si layer of diatom frustules has been documented (van Bennekom et al., 1989; Ren et al., 2013). For example, in sediments from the upper Zaire deep-sea fan, Al has substituted for Si throughout the entire diatom frustule, as well as throughout the skeletons of most other siliceous microfossils (van Bennekom et al., 1989). Some dissolution of diatoms was visible using the SEM, but siliceous sheets and areolation were preserved and minimal clay contamination was observed. Al/Si ranged between 0.13-0.16 in clean, purified Zaire Fan sedimentary diatom samples; approximately double the maximum Al/Si at Site 1165, but Al/Si was only 0.02 in living diatoms from the water column above. Al/Si was also relatively consistent between different siliceous organisms. The source of Al in the Zaire samples was assumed to be the Al-rich clay minerals kaolinite and gibbsite with which the diatom silica was buried (van Bennekom et al., 1989).

The stepwise fluorination (SWF) method used to measure $\delta^{18}O_{diatom}$ at Sites 1165 and 744 is designed to remove the outer layers of diatom silica and should, therefore, also remove any external metal contaminants prior to the analysis of $\delta^{18}O_{diatom}$. The fact $\delta^{18}O_{diatom}$ measured from the internal silica layer correlates with metal ratios measured prior to SWF suggests that the process responsible for incorporating metals into the silica lattice (either surficial adsorption or

more intrinsic penetration) is associated with secondary oxygen isotope exchange within the previously supposed stable inner silica layer. As such, incorporation of metals into the inner layer at Site 1165 seems more likely than merely surficial adsorption.

8.4.3. Secondary isotope exchange associated with metal incorporation

A rapid decrease (up to 5‰) of $\delta^{18}O_{diatom}$ within cultured diatom silica upon experimental sedimentation has been recently documented (Dodd et al., 2017), coincident with a decrease in total silanol group abundance. $\delta^{18}O_{diatom}$ was measured by Dodd et al. (2017) via SWF, the same technique as used in this study, which removes the outer hydroxyls prior to analysis. The decrease in $\delta^{18}O_{diatom}$ must therefore be associated with an exchange of oxygen atoms within the inner, stable silica lattice. Some exchange of oxygen between –OH and Si–O–Si groups has also been demonstrated during the removal of exchangeable oxygen components associated with laboratory processing of raw silica samples (namely, heating to 90°C) by Menicucci et al. (2017). Total silanol dehydroxylation would have occurred within 150 days under the experiential aging conditions of Dodd et al. (2017), while Menicucci et al. (2017) suggest full maturation could take up to 5-6 million years (e.g. samples older than the Late Miocene would be fully mature). However, if age-dependant dehydroxylation was the only process affecting post-depositional isotope exchange, and this process completely overprinted the environmental signature, $\delta^{18}O_{diatom}$ should increase with age. This is not what has been documented in this chapter; at Site 1165, for example, some of the lowest $\delta^{18}O_{diatom}$ values from any Antarctic sediments are documented (up to 30‰ $\delta^{18}O_{diatom}$) during the Pliocene (Figure 3). The correlation between $\delta^{18}O_{diatom}$ and Al/Si does, however, appear to increase with age.

As well as rapid post-depositional changes in $\delta^{18}O_{diatom}$ (Dodd et al., 2017), rapid post-depositional Al-uptake into diatom silica has been observed (Koning et al., 2007). Combined with observed correlations between Al/Si and $\delta^{18}O_{diatom}$, this does suggest a relationship between heavy metal accumulation and secondary isotope exchange, although not necessarily a causative one. Whatever the mechanism, increased frustule Al is associated with decreased $\delta^{18}O_{diatom}$. It is difficult to ascertain whether the relationship is just an association, for example, metal accumulation occurs as a biproduct of whatever process causes secondary isotope exchange, or vice versa, or whether Al and/or other metal incorporation into the silica lattice is playing a more active role in driving post-depositional secondary oxygen isotope exchange.

Potential mechanisms remain speculative, however, it could be that the accumulation of metals, perhaps subject to the abundance and/or mineralogy of clays within the parent sediment, affects dehydroxylation of the silanol layer, which has been shown to cause secondary isotope exchange (Dodd et al., 2017). Alternatively, the presence of aluminium within biogenic silica is also known to substantially reduce the dissolution rate by inducing negative charges on the silica surface, repelling the hydroxyl ions which catalyze silica dissolution (van Benneken et al., 1991). However, since dissolution causes dehydroxylation, which is associated with decreased $\delta^{18}O_{diatom}$, increased Al would therefore be associated with relatively increased $\delta^{18}O_{diatom}$, which is the opposite of what is seen in this study.

The negative correlation (r=-0.54, p=<0.01) between Al/Si and $\delta^{18}O_{diatom}$ at the Holocene Site BC423 (Amundsen Sea) suggests the relationship between metal accumulation and $\delta^{18}O_{diatom}$ could also be site-dependant rather than age-dependant. The correlation between Al/Si and $\delta^{18}O_{diatom}$ is generally strongest at sites that contain detectable levels of Mg (at Sites 1165 and 744); none is detected at the other sites discussed in this record (these data are not available for Site SOS202-27-6). Further, Mg/Si correlates even more strongly with $\delta^{18}O_{diatom}$ than Al/Si at Site 1165 (r=-0.88, p=<0.01; Table 1). As such, it is possible that the presence of a Mg-containing phase, e.g. smectite, could be influencing secondary isotope exchange. Indeed, at Site 1165, 20% of the clay mineral assemblage is smectite (Shipboard Scientific Party, 2001), while at Site 744, although clay minerals are less abundant overall within the carbonate parent sediment, smectite makes up around 70-90% of those present. However, BC423B does not contain significant Mg.

Secondary isotope exchange has previously been documented affecting silicon isotope fractionation within diatom silica (Demarest et al., 2009; Wetzel et al., 2014). Given that siloxane bonds have higher activation energies than silanol bonds, diagenetic isotope fractionation is controlled by siloxane bonds as a rate-limiting step (Wetzel et al., 2014). If activation energies are reduced by changes in pH, for example, isotopic fractionation could change. Changes in pH, perhaps as a result of porewater interactions within parent sediments, therefore provide another mechanism by which secondary isotope exchange could occur. However, the same studies suggested that the effect of pH on silicon isotope fractionation, at least, is small (0.1-0.3‰), although it is likely dependent on Al concentration of the bulk sediment (Wetzel et al., 2014).

8.4.4. What does Al/Si indicate, and is it useful?

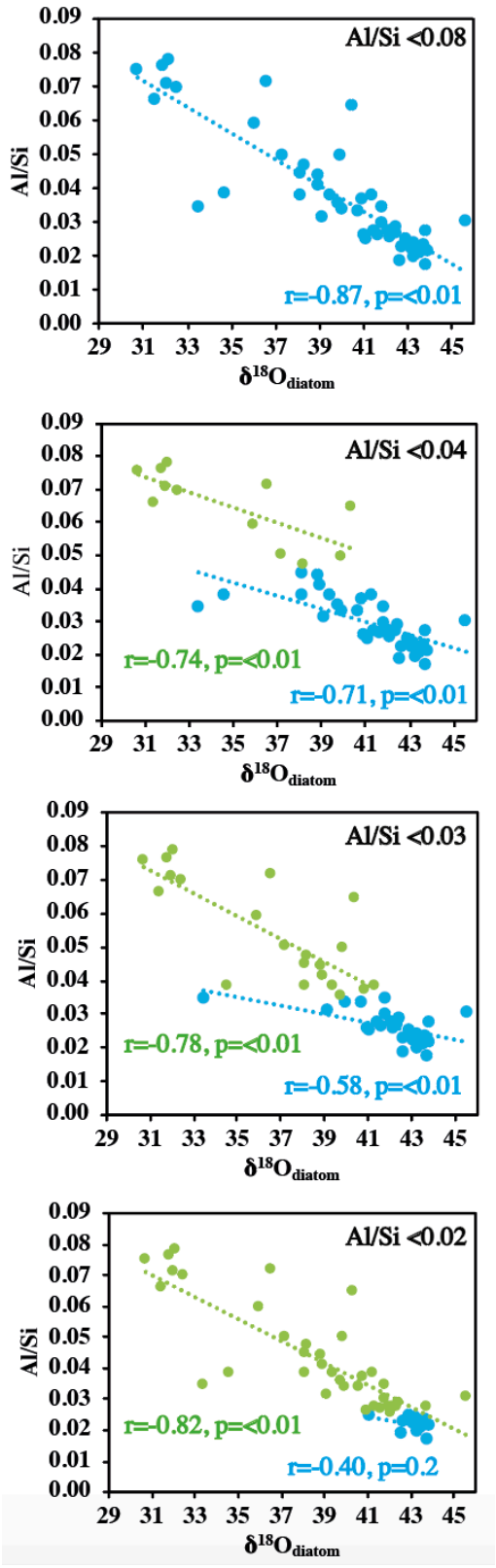

If particulate clay contamination is present in a cleaned, purified sample to be analysed for $\delta^{18}O_{diatom}$, it will be recorded by Al/Si measured by XRF. However, Al/Si may also be recording intrinsic metal accumulation into the silica lattice, associated with secondary isotope exchange if Al/Si and $\delta^{18}O_{diatom}$ are correlated. The way to distinguish between these two scenarios is via microscopy, preferably SEM; if samples appear clean but Al/Si remains high, this indicates intrinsic accumulation. If Al/Si and $\delta^{18}O_{diatom}$ are correlated as well, secondary isotope exchange is implicated, as suggested in this chapter. If this is the case, additional processing and cleaning of the sediment samples will not be able to reduce the Al/Si or to extract a primary environmental signal from the $\delta^{18}O_{diatom}$ record; rather, it will provide a record of environmental variability overprinted by diagenetic processes.

If samples appear clean using the SEM, and Al/Si is low, $\delta^{18}O_{diatom}$ could still record a primary environmental signal. In previous studies, sample contamination of up to a few percent Al/Si has been acceptable for analysis; for example, where the impact of contamination on $\delta^{18}O_{diatom}$ is less than analytical error (e.g. Swann et al., 2006; Abelmann et al., 2015). However, this assumes that Al/Si represents particulate contamination. If Al/Si represents intrinsic metal accumulation and

Figure 25. Al/Si versus $\delta^{18}O_{diatom}$ at ODP Site 1165, with different Al/Si cut-off values. Pearson's r correlation coefficient and p-values are shown for each linear regression. p-values <0.01 are considered significant.

associated secondary isotope exchange, the slope of the linear regression line describing the correlation between Al/Si and $\delta^{18}O_{diatom}$ for the dataset at Site 1165 (y=-0.0038x + 0.191, whereby x= $\delta^{18}O_{diatom}$ and y = Al/Si), which is similar to regression lines for Sites 744 and BC423 (Figure 20), suggests that a 0.01 increase in Al/Si is related to a 2.2‰ isotope exchange-related decrease in $\delta^{18}O_{diatom}$. As such, even a threshold of 0.02 Al/Si (2% contamination) could incorporate an isotope exchange-related decrease of 4.4‰ in $\delta^{18}O_{diatom}$, which is much larger than analytical error (generally around 0.3‰). Only using data with Al/Si <0.02 reduces the slope of the linear regression (Figure 23) and the Al/Si to $\delta^{18}O_{diatom}$ correlation becomes statistically insignificant (Figure 25). However, removing a substantial number of samples from a record would also completely change its structure and resolution.

8.4.5. Implications for the use of $\delta^{18}O_{diatom}$ in Neogene material

I have demonstrated a correlation between $\delta^{18}O_{diatom}$ and Al/Si in cleaned Pliocene samples from ODP Site 1165, and in a pilot study of Miocene samples from ODP Site 744. In the context of other Antarctic sites, the correlation seems to increase with age, being strongest at Miocene Site 744 (r=-0.99, p=<0.01) and lowest in Holocene samples (generally not statistically significant). However, Holocene samples from Site BC423 (Amundsen Sea) do show a moderate correlation (r=-0.54, p=<0.01), suggesting that the correlation could be site-dependant instead of, or in addition to, age-dependant. Further work is needed to confirm the role of sample age, and whether Neogene material is necessarily more problematic. However, it seems most likely that the correlation relates to clay mineral-mediated secondary isotope exchange upon burial of the diatom silica, and possibly to the presence of a Mg-containing phase, e.g. smectite. As such, even if samples appear free from particulate contamination, $\delta^{18}O_{diatom}$ may reflect the diagenetic overprint of an environmental signal rather than a primary surface water signal. Thus, $\delta^{18}O_{diatom}$ should be interpreted with caution, particularly older records where Al/Si and $\delta^{18}O_{diatom}$ correlate but samples appear free from particulate contamination.

8.4.6. Implications for Pliocene climate

The evidence presented in this chapter suggests that the primary environmental signal recorded by $\delta^{18}O_{diatom}$ at IODP Site 1165 is most likely overprinted by clay mineral-mediated secondary isotope exchange. However, I cannot completely rule out that $\delta^{18}O_{diatom}$ reflects, at least to some extent, a primary environmental signal if lithological contamination, measured using Al/Si, increases in tandem with lowered $\delta^{18}O_{diatom}$ via co-dependent processes. For example, substantial glacial discharge that should lower $\delta^{18}O_{seawater}$, thus $\delta^{18}O_{diatom}$, may also increase the

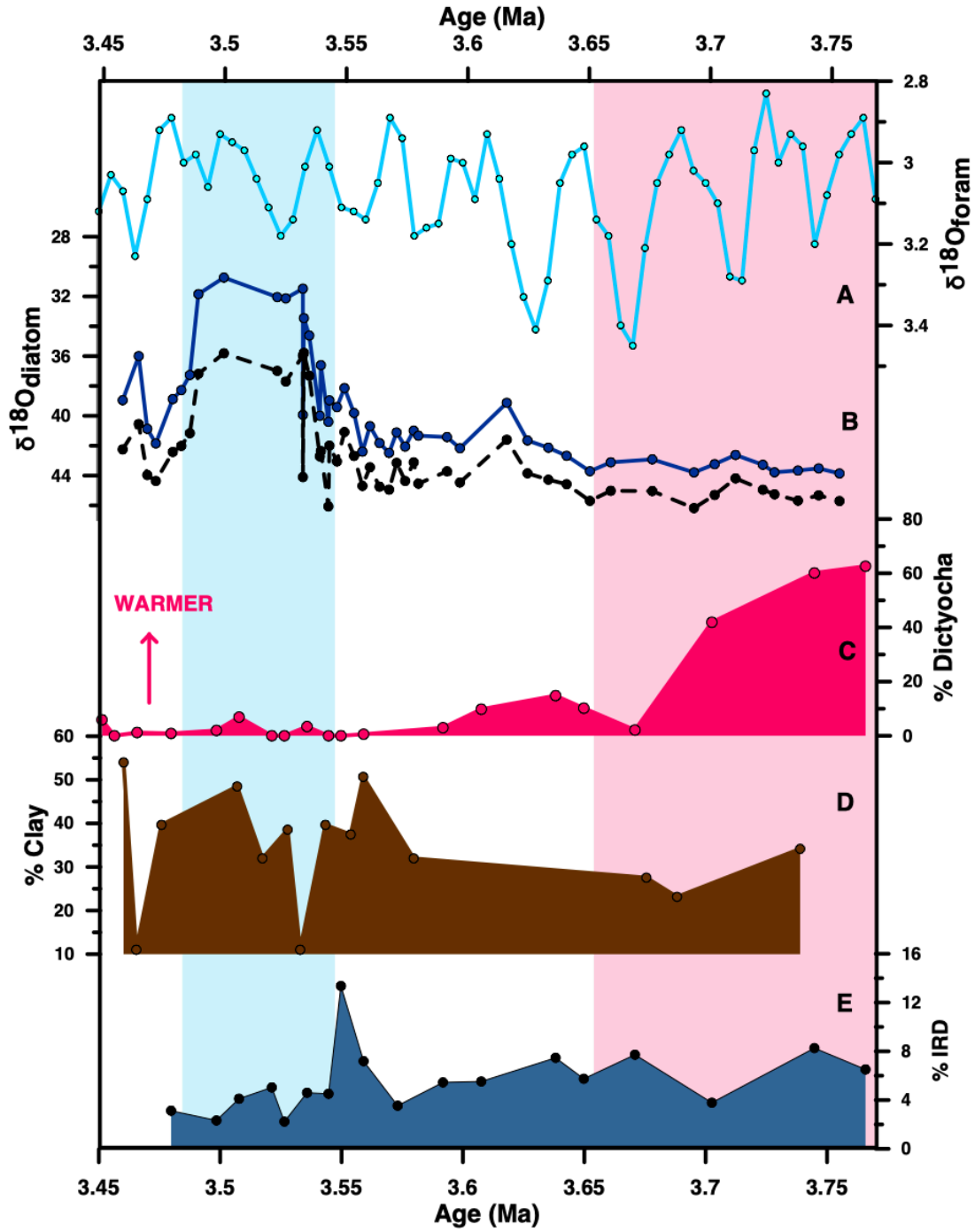

Figure 24. $\delta^{18}O_{diatom}$ at ODP Site 1165 with published climate proxy records. A) $\delta^{18}O_{foram}$ (Lisiecki & Raymo, 2005 benthic stack). B) $\delta^{18}O_{diatom}$ at ODP Site 1165, this study. C) % *Dictyocha* at ODP Site 1165, reflective of sea surface temperature (Whitehead et al., 2003). D) % Clay at ODP Site 1165 (Passchier, 2011). E) % IRD at ODP Site 1165 (Passchier, 2011). All data from ODP Site 1165 are presented using the revised age model (Section 4.4).

amount of glacially-eroded clay released into the Southern Ocean or enhance temperature-dependent Al-incorporation into the silica lattice. As such, I will interpret the $\delta^{18}O_{diatom}$ record

from Site 1165 as an environmental signal of surface water processes, in the context of Pliocene climate and other environmental reconstructions at Site 1165, with the substantial caveat that the primary signal maybe overprinted.

Between 3.75 and 3.55 Ma, $\delta^{18}O_{diatom}$ varies at Site 1165 between 38-46‰ (Figure 24b). $\delta^{18}O_{diatom}$ shows low sensitivity to the proposed circum-Antarctic episode of SST warming prior to 3.7 Ma (Escutia et al., 2009), indicated at Site 1165 by silicoflagellate abundances (Whitehead et al., 2003) (Figure 24). $\delta^{18}O_{diatom}$ decreases slightly (to c. 38‰) at 3.62 Ma, which could have been a response to increased Southern Ocean freshwater release as a result of warming. If the proposed freshwater release affected ocean circulation and/or climate feedbacks, it could have played a role in forcing the transition to lower amplitude glacial cycles after 3.63 Ma (Zachos et al., 2001) (Figure 14a). Following the short trough in $\delta^{18}O_{diatom}$, it returns to higher values until c. 3.56 Ma.

From 3.56 Ma, $\delta^{18}O_{diatom}$ decreases to the lowest levels of the record, c. 30‰ and remains low until 3.48 Ma. These are some of the lowest $\delta^{18}O_{diatom}$ values documented in the Southern Ocean to date, and, if a primary environmental signal, represents freshwater discharge and/or EAIS retreat on a scale not documented during the Holocene or Pleistocene. The freshwater event coincides with, and follows, an episode of increased IRD accumulation at Site 1165 at 3.55 Ma (Passchier, 2011) (Figure 24e), interpreted as the retreat of the EAIS into the Aurora subglacial basin (Williams et al., 2010). The proportion of clay in sediments at Site 1165 also increases after c. 3.57 Ma (Figure 24d), but does not stay high throughout the interval of low $\delta^{18}O_{diatom}$ (Passchier, 2011). The sample resolution of the clay and IRD records is lower than $\delta^{18}O_{diatom}$, so it is difficult to better establish the relationship between clay and $\delta^{18}O_{diatom}$. However, increased glacial discharge (lower $\delta^{18}O_{diatom}$) and clay mineral release could be associated with either a more active hydrological cycle or EAIS retreat between 3.55 and 3.5 Ma.

8.5. Conclusions and further work

The data presented in this chapter indicates either that (1) $\delta^{18}O_{diatom}$ correlates with Al at some Antarctic sites, including Sites 1165 and 744, perhaps because more clay is released alongside glacial discharge; or that, more likely, (2) clay minerals can mediate post-depositional oxygen isotope fractionation within the inner, supposedly stable siloxane layer and, therefore, can cause over-printing of $\delta^{18}O_{diatom}$. This effect may be age and/or site dependent; however, further work is required to delineate and/or to confirm the mechanism by which secondary oxygen

isotope fractionation is affected. For example, a larger dataset of $\delta^{18}O_{diatom}$ with co-analysed XRF data from different sites and of varying ages could confirm whether the Al/Si to $\delta^{18}O_{diatom}$ correlation is age- or site-dependant, and whether the presence of a Mg-phase, for example smectite, enhances the process. Culture studies could confirm whether and/or to what extent frustule Al incorporation is affected by temperature, both live and post-depositionally, while water column samples could be used to investigate the extent to which glacial discharge could affect $\delta^{18}O_{diatom}$ and Al/Si, simultaneously. This chapter also highlights that future $\delta^{18}O_{diatom}$ should be published with Al/Si data and, preferably, geochemical analyses of sample purity, as well as stressing the need for caution when interpreting $\delta^{18}O_{diatom}$ as a primary record of the environment, particularly in Neogene age sediments.

9. Conclusions and further work

This section addresses the "big questions" outlined in the Introduction (Chapter 1, Section 1.5), and will discuss to what extent the work presented in this thesis is able to answer them. I will also recommend ways in which these questions could be further explored in the future.

9.1. How did the Southern Ocean and Antarctic Ice Sheet vary through the Neogene, and is there evidence of substantial warmth and/or retreat?

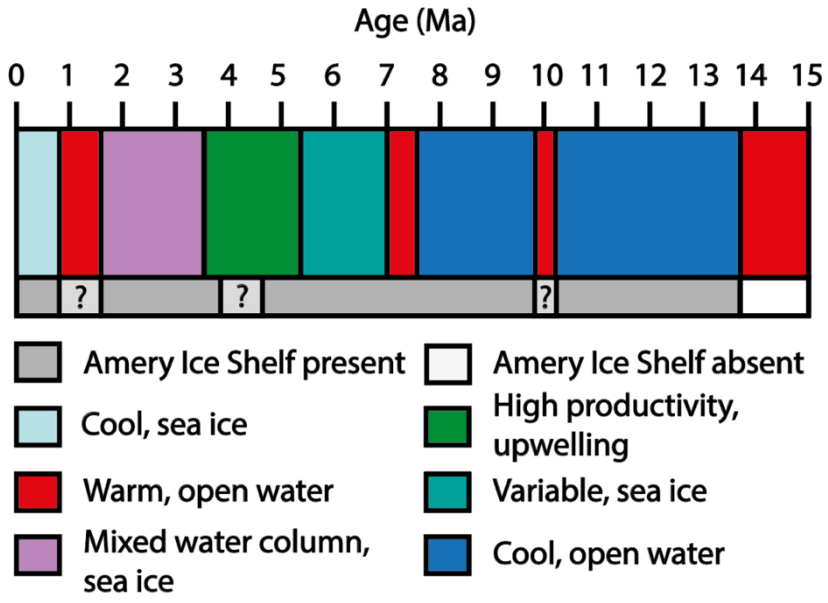

Figure 1. Schematic showing the palaeoceanography at ODP Site 1165 based on diatom assemblages. The inferred presence/absence of the Amery Ice Shelf in Prydz Bay is shown in the lower bar, based on evidence from Site 1165 diatom assemblages and terrestrial outcrops, for example, the Pagodroma Group, surrounding Prydz Bay.

The diatom assemblages from ODP Sites 747, 744 and 1165 that I presented in Chapter 6 indicate that the Southern Ocean was warm and stratified, particularly over Site 1165, prior to the Middle Miocene Climatic Transition (MMCT; Mi3) at c. 13.8 Ma. The abundance of neritic and, especially, benthic diatom species at Site 1165, as well as minimal IRD, indicate a lack of marine ice in Prydz Bay at this time (Chapter 6) (Figure 1).

Following the expansion of the Amery Ice Shelf into Prydz Bay at the MMCT (Figure 1), Southern Ocean diatom assemblages became overwhelmingly dominated by the cool, open water indicator *Denticulopsis simonsenii/vulgaris* until c. 7 Ma. However, within this cool Late

Miocene interval, transient peaks in the warm, open water indicator *Actinocyclus ingens* occurred at 10.20 Ma and c. 7.5 Ma (Chapter 7). I suggest the 10.20 Ma peak may have coincided with deposition of the *Actinocyclus ingens*-dominated, terrestrially-exposed Fisher Bench Formation (Whitehead et al., 2004), implying an associated >300 km retreat of the EAIS at this time (Chapter 7).

During the Messinian period (7.2-5.3 Ma), a transition to generally cool but variable oceanographic conditions occurred at Site 1165, indicated by the simultaneous abundance of warm water species *Thalassionema nitzschioides* var. *parva* and peak abundances of cool, sea ice-indicator species such as *Fragilariopsis praecurta* and *Rouxia peragaalii*. Better characterization of Late Miocene diatom paleoecology (Section 9.4) could further resolve the interpretation of assemblages from this interval, although independent proxy records document decreased Southern Ocean SSTs at this time (Herbert et al., 2016). Based on increased %BSi deposition at some circum-Antarctic sites and hiatuses at others, I infer in Chapter 7 the onset of modern ACC circulation during this period, associated with coincident full-volume NADW upwelling (Billups et al., 2002).

The Early Pliocene (5.3-3.6 Ma) saw the deposition of *Thalassionema nitzschioides*, *Thalassiothrix* and *Trichotoxon* diatoms at high latitude circum-Antarctic sites. My new complete diatom record at Site 1165 demonstrates that these palaeoceanographic conditions, which I interpret as indicative of increased upwelling (Chapter 7), are unique within the last 15 million years. This interval may also coincide with deposition of the *Thalassiothrix/Trichotoxon*-dominated terrestrially-exposed Bardin Bluffs Formation (Whitehead et al., 2004) and/or the Sørsdal Formation in the Vestfold Hills (Harwood et al., 2001), implying a further >250 km retreat of the EAIS in the Prydz Bay region (Figure 1).

I have interpreted higher *Thalassiosira* spp. abundance at Site 1165 as indicating an increasingly well-mixed water column, and higher sea ice diatom abundance as indicating expanded sea ice cover and sea surface cooling during the Late Pliocene (Figure 1 and Chapter 7). Cooling continued through the Pleistocene, although MIS 31 was marked by a climatic amelioration, inferred from increased *Actinocyclus ingens* abundance and the deposition of carbonate at Site 1165, indicating substantial oceanic warmth. A coincident small increase in benthic diatoms at Site 1165 hints at EAIS retreat and/or absence of the Amery Ice Shelf during MIS 31 (Figure 1).

In summary, diatom assemblages at Site 1165 suggest that the Southern Ocean never fully returned to the warm, stratified state that existed prior to the MMCT. Nonetheless, substantial changes in palaeoceanography and episodes of dramatic EAIS retreat are inferred.

9.2. What role did the Southern Ocean play in forcing changes in Neogene climate and the Antarctic Ice Sheet?

Using the records presented in this thesis, I have provided new insight into the role of the Southern Ocean in forcing changes in the EAIS and Neogene climate. For example, diatom assemblage records in Chapter 6 confirm that high latitude Southern Ocean cooling commenced from 14.2 Ma, which would have reduced heat transport to the Antarctic ice sheet and could have played a role in driving ice growth at the MMCT at 13.8 Ma (Chapter 6) and possibly also subsequent Miocene glaciation episodes (Chapter 7). During the Late Miocene, although speculative, I have also suggested that expanded sea ice and invigorated ACC circulation during the Messinian (7.2-5.3 Ma) could have been related to coincident intensification of the Asian monsoon (Ao et al., 2016; Holbourn et al., 2018) (Chapter 7, Section 7.4.2.2).

Following the Messinian, the inferred oceanic upwelling of warm deep waters at the highest latitudes during the Early Pliocene could have provided a source of heat to the EAIS, driving ice sheet retreat. The correspondence I have identified between peak high latitude *Thlx* group abundances and high atmospheric CO_2 also suggests that upwelling, in the context of reduced sea ice cover, could have increased CO_2 outgassing, in turn contributing to increased atmospheric CO_2 and increased global temperatures during this interval. However, further high resolution studies reconstructing atmospheric CO_2 could confirm the structure and timing of the CO_2 increase, while modelling could mechanistically test its association with increased upwelling and potential implications for Early Pliocene global ocean circulation and climate.

As discussed in Section 9.1, I have linked increased *Actinocyclus ingens* abundance at Site 1165, which indicates high SSTs (Chapter 5), with retreat of the EAIS at 10.20 Ma and tentatively during MIS 31 (Figure 1 and Chapter 6). EAIS retreat is also associated with oceanographic conditions (likely increased upwelling) inferred from distinct *Thlx*-dominated diatom assemblages during the Early Pliocene. This highlights that EAIS retreat can be driven by, or occur during, different Southern Ocean forcing modes; and also, that the EAIS is sensitive to relatively transient Southern Ocean SST increases, e.g. at 10.20 Ma.

9.3. How was the Southern Ocean affected by changes in Neogene climate and Antarctic Ice Sheet volume?

Whilst the previous section described how the Southern Ocean has affected the Antarctic Ice Sheet through the Neogene, this thesis also aimed to investigate ways in which the ice sheet has affected the ocean. In Chapter 6, I demonstrated that the surface water warming detected at ODP Sites 1165 and 747 at c. 13.7 Ma (Chapter 6, Section 6.3.4), immediately following the MMCT, was likely driven by wind-mediated warming caused by an expanded EAIS, as proposed by Knorr & Lohmann (2014). Further, the IRD record at Site 1165 demonstrates that this warming event was associated with substantial iceberg discharge. Middle Miocene diatom records at Site 747 (Chapter 6) also document 100 kyr eccentricity-paced fluctuations in SST at Site 747 following Mi3, likely indirectly driven by the impact of an expanded Antarctic ice sheet on the global climate system. This is the first explicit demonstration of eccentricity-paced cyclicity in Southern Ocean temperature palaeoceanographic following Mi3.

Whilst the high resolution diatom records at three Southern Ocean Sites presented in Chapter 6 facilitated identification of the direction of ice/ocean interactions during the Middle Miocene (e.g. whether the ocean was forcing the ice sheet, or vice versa), unpicking this relationship was more difficult through the remainder of the Neogene where only relatively lower resolution records, e.g. at Site 1165, were available (Chapter 7). Higher resolution diatom and other proxy records, perhaps targeting particular intervals, e.g. 11-9 Ma or 6-3 Ma, at additional high latitude sites could help to unpick and determine causative mechanisms, rather than just associations, that explain ice/ocean dynamics during the Late Miocene and Pliocene.

9.4. Did diatoms play a role in carbon drawdown during key episodes of Neogene climate change?

In Chapter 6, I showed that Southern Ocean sedimentary diatom concentrations, and thus diatom productivity, at ODP Sites 747, 744 and 1165 increased following the MMCT rather than playing a role in driving the climate transition. However, I suggest increased siliceous productivity and/or vigorous ACC circulation likely did play a role in carbon drawdown and climate cooling during Mi4 at c. 13 Ma.

Within the last fifteen million years, silicofossil (diatoms/radiolarians/silicoflagellates) concentrations at Site 1165 were highest during the late Middle Miocene and Early Pliocene (Chapter 7). As such, if high latitude siliceous productivity did contribute to atmospheric CO_2

drawdown and climate cooling, it would have been during these periods. However, these intervals generally show opposing trends in atmospheric CO_2, which was lower during the late Middle Miocene and higher during the Early Pliocene. As such, the relationship between high latitude siliceous productivity and atmospheric CO_2 drawdown is clearly complex, and likely modulated by Southern Ocean circulation. The association between Southern Ocean productivity and atmospheric CO_2 could be investigated further using independent proxies for marine productivity, such as barite or silicon isotopes, since sedimentary diatom concentrations can be biased by changes in the supply of other sedimentary components. Further, to better constrain Southern Ocean modulation of the relationship between Neogene Southern Ocean productivity and CO_2, further studies constraining Southern Ocean circulation, as well as numerical modelling, are required.

9.5. To what extent are diatom proxies able to address key questions in Antarctic Neogene paleoclimatology, and how may they be developed in future?

Finally, in this thesis I have substantially developed understanding of both geochemical and assemblage-based Neogene diatom proxies. In Chapter 5 and Appendix 1, I have better characterised extinct Neogene diatom palaeoecologies, providing palaeoecological context for future studies. In Chapters 5, 6 and 7 I have demonstrated that Neogene Southern Ocean diatom assemblages can be as sensitive to environmental parameters as geochemical proxies, for example: the correspondence between % *Actinocyclus ingens* abundance and $\delta^{18}O_{foram}$ at ODP Site 747 during the Middle Miocene (Chapter 5, Figure 2). This correspondence supports the paleoecological interpretation presented in Chapter 5 and Appendix 1, however, many fossil diatom species, predominantly from the Late Miocene, require further investigation and characterisation in order to better resolve their ecological preferences. Better characterisation could be achieved by generating more high-resolution diatom assemblage records alongside independent environmental proxy records. For example, for sea surface temperatures, preferably from the same core samples, which would provide the opportunity to test for statistical correlations with individual diatom species.

Stable oxygen isotopes preserved within biogenic silica ($\delta^{18}O_{diatom}$) have revolutionary potential to track past fluctuations of glacial discharge and meltwater from the Antarctic ice sheets and changes in diatom productivity. However, the correlation between Al/Si and $\delta^{18}O_{diatom}$ at ODP Sites 1165 and 744 (Chapter 8) that I have demonstrated, for the first time, requires that caution be taken when interpreting a palaeoenvironmental signal from the isotope records.

The correlation between Al/Si and $\delta^{18}O_{diatom}$ indicates that post depositional clay mineral-mediated secondary isotope exchange has occurred, causing a diagenetic overprint on the paleoenvironmental signal. Fundamental proxy development work must therefore be carried out before this geochemical diatom proxy can be used to reconstruct past fluctuations in Neogene $\delta^{18}O_{seawater}$ or SST. Additional $\delta^{18}O_{diatom}$ and XRF data from different sites could determine whether the correlation is age-dependant or site-dependant, and future studies could further investigate the mechanism by which metal accumulation is associated with secondary isotope exchange. It is imperative that future $\delta^{18}O_{diatom}$ studies on samples of any age must therefore include a geochemical assessment of elemental concentrations and illustrate the Al/Si versus $\delta^{18}O_{diatom}$ regression before the proxy can be used to interpret the palaeoenvironment.

10. References

Abelmann, A., Gersonde, R., & Spiess, V. (1990). Pliocene—pleistocene paleoceanography in the Weddell Sea—siliceous microfossil evidence. In Geological history of the polar oceans: Arctic versus Antarctic. 729-759. Springer, Dordrecht.

Abrajevitch, A., Roberts, A. P., & Kodama, K. (2014). Volcanic iron fertilization of primary productivity at Kerguelen Plateau, Southern Ocean, through the Middle Miocene Climate Transition. Palaeogeography, palaeoclimatology, palaeoecology, 410, 1-13.

Abrantes, F. (1988). Diatom assemblages as upwelling indicators in surface sediments off Portugal. Marine Geology, 85(1), 15-39.

Allen, C. S., Oakes-Fretwell, L., Anderson, J. B., & Hodgson, D. A. (2010). A record of Holocene glacial and oceanographic variability in Neny Fjord, Antarctic Peninsula. The Holocene, 20(4), 551-564.

Alley, K., Patacca, K., Pike, J., Dunbar, R., & Leventer, A. (2018). Iceberg Alley, East Antarctic Margin: Continuously laminated diatomaceous sediments from the late Holocene. Marine Micropaleontology, 140, 56-68

Anagnostou, E., John, E. H., Edgar, K. M., Foster, G. L., Ridgwell, A., Inglis, G. N., ... & Pearson, P. N. (2016). Changing atmospheric CO_2 concentration was the primary driver of early Cenozoic climate. Nature, 533(7603), 380.

Andersen, M. B., Vance, D., Archer, C., Anderson, R. F., Ellwood, M. J., & Allen, C. S. (2011). The Zn abundance and isotopic composition of diatom frustules, a proxy for Zn availability in ocean surface seawater. Earth and Planetary Science Letters, 301(1-2), 137-145.

Ao, H., Roberts, A. P., Dekkers, M. J., Liu, X., Rohling, E. J., Shi, Z., ... & Zhao, X. (2016). Late Miocene–Pliocene Asian monsoon intensification linked to Antarctic ice-sheet growth. Earth and Planetary Science Letters, 444, 75-87.

Armand, L. K., Crosta, X., Romero, O., & Pichon, J. J. (2005). The biogeography of major diatom taxa in Southern Ocean sediments: 1. Sea ice related species. Palaeogeography, Palaeoclimatology, Palaeoecology, 223(1-2), 93-126.

Armstrong, R. A., Lee, C., Hedges, J. I., Honjo, S., & Wakeham, S. G. (2001). A new, mechanistic model for organic carbon fluxes in the ocean based on the quantitative association of POC with ballast minerals. Deep Sea Research Part II: Topical Studies in Oceanography, 49(1), 219-236.

Arney, J. E., McGonigal, K. L., Ladner, B. C., & Wise Jr, S. W. (2003). Lower Oligocene to middle Miocene diatom biostratigraphy of ODP site 1140, Kerguelen plateau. In Proceedings of the Ocean Drilling Program, Scientific Results, 183, 1-21.

Backman, J., Baldauf, J. G., Ciummelli, M., & Raffi, I. (2016). Data report: a revised biomagnetostratigraphic age model for Site U1338, IODP Expedition 320/321.

Badger, M. P., Lear, C. H., Pancost, R. D., Foster, G. L., Bailey, T. R., Leng, M. J., & Abels, H. A. (2013). CO_2 drawdown following the middle Miocene expansion of the Antarctic Ice Sheet. Paleoceanography, 28(1), 42-53.

Baldauf, J. (1991). Diatom biostratigraphy: Kerguelen Plateau and Prydz Bay regions of the Southern Ocean. In Proc. ODP. Sci. Results. 119, 547-598.

Baldauf, J. G. (2013). Data report: diatoms from sites U1334 and U1338, expedition 320/321. In Proc. ODP. Sci. Results. 320, 321.

Baldauf, J.G. and Barron, J.A. (1991). Diatom biostratigraphy: Kerguelen Plateau and Prydz Bay regions of the Southern Ocean. Proc. ODP. Sci. Results. 119, 547–598.

Barbara, L., Crosta, X., Schmidt, S., & Massé, G. (2013). Diatoms and biomarkers evidence for major changes in sea ice conditions prior the instrumental period in Antarctic Peninsula. Quaternary Science Reviews, 79, 99-110.

Barker, P. F. (2001). Scotia Sea regional tectonic evolution: implications for mantle flow and palaeocirculation. Earth-Science Reviews, 55(1-2), 1-39.

Barker, P. F., & Kennett, J. P. (1988). Leg 113. In Proc. ODP. Sci. Results. 113, 1033.

Barker, P. F., & Thomas, E. (2004). Origin, signature and palaeoclimatic influence of the Antarctic Circumpolar Current. Earth-Science Reviews, 66(1-2), 143-162.

Barrett, P. J. (1989). Antarctic Cenozoic history from the CIROS-1 drillhole, McMurdo Sound. DRIS Publishing.

Barrett, P. J. (2001). Grain-size analysis of samples from Cape Roberts core CRP-3, Victoria Land Basin, Antarctica. Terra Antartica, 8(3), 245-254.

Barrett, P. J. (2013). Resolving views on Antarctic Neogene glacial history–the Sirius debate. Earth and Environmental Science Transactions of the Royal Society of Edinburgh, 104(1), 31-53.

Barron, J. A. (1985). Miocene to Holocene planktic diatoms. Plankton stratigraphy, 763-809.

Barron, J. A. (1992). Pliocene paleoclimatic interpretation of DSDP Site 580 (NW Pacific) using diatoms. Marine Micropaleontology, 20(1), 23-44.

Barron, J. A. (1996). Diatom constraints on the position of the Antarctic Polar Front in the middle part of the Pliocene. Marine Micropaleontology, 27(1-4), 195-213.

Barron, J. A. (2003). Planktonic marine diatom record of the past 18 my: appearances and extinctions in the Pacific and Southern Oceans. Diatom Research, 18(2), 203-224.

Barron, J. A., & Baldauf, J. G. (1986). Diatom stratigraphy of the lower Pliocene part of the Sisquoc Formation, Harris Grade section, California. Micropaleontology, 357-371.

Barron, J. A., & Baldauf, J. G. (1995). Cenozoic marine diatom biostratigraphy and applications to paleoclimatology and paleoceanography. Short Courses in Paleontology, 8, 107-118.

Barron, J. A., Baldauf, J. G., Barrera, E., Caulet, J. P., Huber, B. T., Keating, B. H., ... & Wei, W. (1991). Biochronologic and magnetochronologic synthesis of Leg 119 sediments from the Kerguelen Plateau and Prydz Bay, Antarctica. Proc. ODP. Sci. Results. 119(46), 813-847.

Barron, J., Larsen, B., et al., (1989). Leg 119. In Proc. ODP. Sci. Results. 119. 942.

Barron, J.A., and Gladenkov, A.Y. (1995). Early Miocene to Pleistocene diatom stratigraphy of Leg 145. Proc. ODP. Sci. Results. 119, 3–19.

Bart, P. J., & Iwai, M. (2012). The overdeepening hypothesis: how erosional modification of the marine-scape during the early Pliocene altered glacial dynamics on the Antarctic Peninsula's Pacific margin. Palaeogeography, Palaeoclimatology, Palaeoecology, 335, 42-51.

Bart, P. J., Egan, D., & Warny, S. A. (2005). Direct constraints on Antarctic Peninsula Ice Sheet grounding events between 5.12 and 7.94 Ma. Journal of Geophysical Research: Earth Surface, 110(F4).

Beaufort, L., & Aubry, M. P. (1992). Paleoceanographic implications of a 17-My-long record of high-latitude Miocene calcareous nannoplankton fluctuations. In Proc. ODP. Sci. Results, 120, 539-544.

Benoiston, A. S., Ibarbalz, F. M., Bittner, L., Guidi, L., Jahn, O., Dutkiewicz, S., & Bowler, C. (2017). The evolution of diatoms and their biogeochemical functions. Philosophical Transactions of the Royal Society B: Biological Sciences, 372(1728), 397.

Betzler, C., Eberli, G. P., Kroon, D., Wright, J. D., Swart, P. K., Nath, B. N., ... & Guo, J. A. (2016). The abrupt onset of the modern South Asian Monsoon winds. Scientific reports, 6, 29838.

Bijl, P. K., Houben, A. J., Hartman, J. D., Pross, J., Salabarnada, A., Escutia, C., & Sangiorgi, F. (2018). Paleoceanography and ice sheet variability offshore Wilkes Land, Antarctica-Part 2: Insights from Oligocene-Miocene dinoflagellate cyst assemblages. Climate of the Past, 14(7), 1015-1033.

Billups, K. (2002). Late Miocene through early Pliocene deep water circulation and climate change viewed from the sub-Antarctic South Atlantic. Palaeogeography, Palaeoclimatology, Palaeoecology, 185(3-4), 287-307.

Bo, S., Siegert, M. J., Mudd, S. M., Sugden, D., Fujita, S., Xiangbin, C., ... & Yuansheng, L. (2009). The Gamburtsev mountains and the origin and early evolution of the Antarctic Ice Sheet. Nature, 459(7247), 690.

Bodén, P., & Backman, J. (1996). A laminated sediment sequence from the northern North Atlantic Ocean and its climatic record. Geology, 24(6), 507-510.

Bohaty, S. M., Wise Jr, S. W., Duncan, R. A., Moore, C. L., & Wallace, P. J. (2003). Neogene diatom biostratigraphy, tephra stratigraphy, and chronology of ODP Hole 1138A, Kerguelen Plateau. Proc. ODP. Sci. Results. 183(9), 1-53.

Bowman, V. C., Francis, J. E., & Riding, J. B. (2013). Late Cretaceous winter sea ice in Antarctica? Geology, 41(12), 1227-1230.

Boyd, P. W., & Abraham, E. R. (2001). Iron-mediated changes in phytoplankton photosynthetic competence during SOIREE. Deep Sea Research Part II: Topical Studies in Oceanography, 48(11), 2529-2550.

Boyd, P. W., & Doney, S. C. (2002). Modelling regional responses by marine pelagic ecosystems to global climate change. Geophysical Research Letters, 29(16), 53-1.

Boyd, P. W., & Newton, P. P. (1999). Does planktonic community structure determine downward particulate organic carbon flux in different oceanic provinces? Deep-Sea Research Part I, 46(1), 63-91.

Boyd, P. W., Watson, A. J., Law, C. S., Abraham, E. R., Trull, T., Murdoch, R., ... & Zeldis, J. (2000). A mesoscale phytoplankton bloom in the polar Southern Ocean stimulated by iron fertilization. Nature, 407(6805), 695-702.

Bradbury, J. P., & Krebs, W. N. (1995). The diatom genus *Actinocyclus* in the western United States (No. 1543-AB). US Government Printing Office.

Brandriss, M. E., O'Neil, J. R., Edlund, M. B., & Stoermer, E. F. (1998). Oxygen isotope fractionation between diatomaceous silica and water. Geochimica et Cosmochimica Acta, 62(7), 1119-1125.

Brennan, C. E., Meissner, K. J., Eby, M., Hillaire-Marcel, C., & Weaver, A. J. (2013). Impact of sea ice variability on the oxygen isotope content of seawater under glacial and interglacial conditions. Paleoceanography, 28(3), 388-400.

Brewer, T. S., Leng, M. J., Mackay, A. W., Lamb, A. L., Tyler, J. J., & Marsh, N. G. (2008). Unravelling contamination signals in biogenic silica oxygen isotope composition: the role of major and trace element geochemistry. Journal of Quaternary Science, 23(4), 321-330.

Brewer, T. S., Leng, M. J., Mackay, A. W., Lamb, A. L., Tyler, J. J., & Marsh, N. G. (2008). Unravelling contamination signals in biogenic silica oxygen isotope composition: the role of major and trace element geochemistry. Journal of Quaternary Science, 23(4), 321-330.

Brewster, A. N. (1980). Cenozoic biogenic silica sedimentation in the Antarctic Ocean. Geological Society of America Bulletin, 91(6), 337-347.

Bronselaer, B., Winton, M., Griffies, S. M., Hurlin, W. J., Rodgers, K. B., Sergienko, O. V., ... & Russell, J. L. (2018). Change in future climate due to Antarctic meltwater. Nature, 564(7734), 53.

Buesseler, K. O., Lamborg, C. H., Boyd, P. W., Lam, P. J., Trull, T. W., Bidigare, R. R., ... & Wilson, S. (2007). Revisiting carbon flux through the ocean's twilight zone. Science, 316(5824), 567-570.

Burckle, L. H. (1982). Diatom biostratigraphy of Late Miocene and Pliocene sediments of eastern Java (Indonesia). Marine Micropaleontology, 7(4), 363-368.

Burckle, L. H. & Cooke, D. W. (1983) Late Pleistocene *Eucampia antarctica* abundance stratigraphy in the Atlantic sector of the Southern Ocean. Micropaleontology. 29, 6-10.

Burckle, L. H., Mortlock, R., & Rudolph, S. (1996). No evidence for extreme, long term warming in early Pliocene sediments of the Southern Ocean. Marine Micropaleontology, 27(1-4), 215-226.

Butterworth, B. J., & Miller, S. D. (2016). Air-sea exchange of carbon dioxide in the Southern Ocean and Antarctic marginal ice zone. Geophysical Research Letters, 43(13), 7223-7230.

Cane, M. A., & Molnar, P. (2001). Closing of the Indonesian seaway as a precursor to east African aridification around 3–4 million years ago. Nature, 411(6834), 157.

Cane, M. A., & Molnar, P. (2001). Closing of the Indonesian seaway as a precursor to east African aridification around 3–4 million years ago. Nature, 411(6834), 157.

Carter, A., Riley, T. R., Hillenbrand, C. D., & Rittner, M. (2017). Widespread Antarctic glaciation during the late Eocene. Earth and Planetary Science Letters, 458, 49-57.

Carter, L., McCave, I. N., & Williams, M. J. (2008). Circulation and water masses of the Southern Ocean: a review. Developments in earth and environmental sciences, 8, 85-114.

Carter, S. C., Griffith, E. M., & Penman, D. E. (2016). Peak intervals of equatorial Pacific export production during the middle Miocene climate transition. Geology, 44(11), 923-926.

Cassar, N., DiFiore, P. J., Barnett, B. A., Bender, M. L., Bowie, A. R., Tilbrook, B., ... & Lefevre, D. (2011). The influence of iron and light on net community production in the Subantarctic and Polar Frontal Zones. Biogeosciences, 8(2), 227-237.

Cefarelli, A. O., Ferrario, M. E., Almandoz, G. O., Atencio, A. G., Akselman, R., & Vernet, M. (2010). Diversity of the diatom genus Fragilariopsis in the Argentine Sea and Antarctic waters: morphology, distribution and abundance. Polar biology, 33(11), 1463-1484.

Censarek, B. (2002). The thermal development of the Southern Ocean in the Middle and Upper Miocene - a reconstruction based on diatoms. PhD thesis, Alfred Wergner Institue for polar and marine research.

Censarek, B., & Gersonde, R. (2002). Miocene diatom biostratigraphy at ODP Sites 689, 690, 1088, 1092 (Atlantic sector of the Southern Ocean). Marine Micropaleontology, 45(3-4), 309-356.

Cerling, T. E., Wang, Y., & Quade, J. (1993). Expansion of C4 ecosystems as an indicator of global ecological change in the late Miocene. Nature, 361(6410), 344.

Chow, J. M., & Bart, P. J. (2003). West Antarctic Ice Sheet grounding events on the Ross Sea outer continental shelf during the middle Miocene. Palaeogeography, Palaeoclimatology, Palaeoecology, 198(1-2), 169-186.

Ciesielski, P. F. (1983). The Neogene and Quaternary diatom datum biostratigraphy of subantarctic sediments. Deep Sea Drilling Project Leg 71. Init. Repts. 71, 635-665.

Ciesielski, P. F. (1991). Relative Abundances and Ranges of Select Diatoms and Silicoflagellates from Sites 699 and 704. Subantarctic South Atlantic. In Proc. ODP. Sci. Results, 114, 753-758.

Ciesielski, P. F., & Weaver, F. M. (1974). Early Pliocene temperature changes in the Antarctic seas. Geology, 2(10), 511-515.

Clark, N. A., Williams, M., Hill, D. J., Quilty, P. G., Smellie, J. L., Zalasiewicz, J., ... & Ellis, M. A. (2013). Fossil proxies of near-shore sea surface temperatures and seasonality from the late Neogene Antarctic shelf. Naturwissenschaften, 100(8), 699-722.

Clark, N., Williams, M., Okamura, B., Smellie, J., Nelson, A., Knowles, T., ... & Haywood, A. (2010). Early Pliocene Weddell Sea seasonality determined from bryozoans. Stratigraphy, 7(2), 199.

Cody, R. D., Levy, R. H., Harwood, D. M., & Sadler, P. M. (2008). Thinking outside the zone: high-resolution quantitative diatom biochronology for the Antarctic Neogene. Palaeogeography, Palaeoclimatology, Palaeoecology, 260(1-2), 92-121.

Cody, R., Levy, R., Crampton, J., Naish, T., Wilson, G., & Harwood, D. (2012). Selection and stability of quantitative stratigraphic age models: Plio-Pleistocene glaciomarine sediments in the ANDRILL 1B drillcore, McMurdo Ice Shelf. Global and Planetary Change, 96, 143-156.

Colloni, F., De Santis, L., Siddoway, C. S., Bergamasco, A., Golledge, N. R., Lohmann, G., ... & Siegert, M. J. (2018). Spatio-temporal variability of processes across Antarctic ice-bed–ocean interfaces. Nature communications, 9(1), 2289.

Conway, T. M., Hoffmann, L. J., Breitbarth, E., Strzepek, R. F., & Wolff, E. W. (2016). The growth response of two diatom species to atmospheric dust from the Last Glacial Maximum. PloS one, 11(7), e0158553.

Cook, A. J., Holland, P. R., Meredith, M. P., Murray, T., Luckman, A., & Vaughan, D. G. (2016). Ocean forcing of glacier retreat in the western Antarctic Peninsula. Science, 353(6296), 283-286.

Cook, C. P., Van De Flierdt, T., Williams, T., Hemming, S. R., Iwai, M., Kobayashi, M., ... & McKay, R. M. (2013). Dynamic behaviour of the East Antarctic ice sheet during Pliocene warmth. Nature Geoscience, 6(9), 765.

Cooper, A. K., & O'Brien, P. E. (2004). Leg 188 synthesis: transitions in the glacial history of the Prydz Bay region, East Antarctica, from ODP drilling. In Proc. ODP. Sci. Results. 188, 1-42.

Cornet-Barthaux, V., Armand, L., & Quéguiner, B. (2007). Biovolume and biomass estimates of key diatoms in the Southern Ocean. Aquatic Microbial Ecology, 48(3), 295-308.

Cortese, G., & Gersonde, R. (2008). Plio/Pleistocene changes in the main biogenic silica carrier in the Southern Ocean, Atlantic Sector. Marine Geology, 252(3-4), 100-110.

Coxall, H. K., Wilson, P. A., Pälike, H., Lear, C. H., & Backman, J. (2005). Rapid stepwise onset of Antarctic glaciation and deeper calcite compensation in the Pacific Ocean. Nature, 433(7021), 53.

Cramer, B. S., Miller, K. G., Barrett, P. J., & Wright, J. D. (2011). Late Cretaceous–Neogene trends in deep ocean temperature and continental ice volume: Reconciling records of benthic foraminiferal geochemistry ($\delta^{18}O$ and Mg/Ca) with sea level history. Journal of Geophysical Research: Oceans, 116(12).

Crampton, J. S., Cody, R. D., Levy, R., Harwood, D., McKay, R., & Naish, T. R. (2016). Southern Ocean phytoplankton turnover in response to stepwise Antarctic cooling over the past 15 million years. Proceedings of the National Academy of Sciences, 113(25), 6868-6873.

Crosta, X., Denis, D., & Ther, O. (2008). Sea ice seasonality during the Holocene, Adelie land, east Antarctica. Marine Micropaleontology, 66(3-4), 222-232.

Crosta, X., Pichon, J. J., & Burckle, L. H. (1998). Application of modern analog technique to marine Antarctic diatoms: Reconstruction of maximum sea-ice extent at the Last Glacial Maximum. Paleoceanography and Paleoclimatology, 13(3), 284-297.

Crosta, X., Pichon, J. J., & Labracherie, M. (1997). Distribution of Chaetoceros resting spores in modern peri-Antarctic sediments. Marine Micropaleontology, 29(3-4), 283-299.

Crosta, X., Romero, O., Armand, L. K., & Pichon, J. J. (2005). The biogeography of major diatom taxa in Southern Ocean sediments: 2. Open ocean related species. Palaeogeography, Palaeoclimatology, Palaeoecology, 223(1-2), 66-92.

Crosta, X., Romero, O., Armand, L. K., & Pichon, J. J. (2005). The biogeography of major diatom taxa in Southern Ocean sediments: 2. Open ocean related species. Palaeogeography, Palaeoclimatology, Palaeoecology, 223(1-2), 66-92.

Crowley, T. J. (1991). Modeling pliocene warmth. Quaternary Science Reviews, 10(2-3), 275-282.

de Give, D., Anderson, K., Hew, C., Anderson, B. E., Burckle, L. H., & Anderson, R. F. (2003, December). *Eucampia antarctica* abundance Stratigraphy in the Southern Ocean. In AGU Fall Meeting Abstracts.

De La Rocha, C. L., Nowald, N., & Passow, U. (2008). Interactions between diatom aggregates, minerals, particulate organic carbon, and dissolved organic matter: Further implications for the ballast hypothesis. Global Biogeochemical Cycles, 22(4).

De Vleeschouwer, D., Vahlenkamp, M., Crucifix, M., & Pälike, H. (2017). Alternating Southern and Northern Hemisphere climate response to astronomical forcing during the past 35 my. Geology, 45(4), 375-378.

DeConto, R. M., & Pollard, D. (2003). Rapid Cenozoic glaciation of Antarctica induced by declining atmospheric CO 2. Nature, 421(6920), 245.

DeConto, R. M., & Pollard, D. (2016). Contribution of Antarctica to past and future sea-level rise. Nature, 531(7596), 591.

DeConto, R., Pollard, D., & Harwood, D. (2007). Sea ice feedback and Cenozoic evolution of Antarctic climate and ice sheets. Paleoceanography, 22(3).

Denton, G. H., & Sugden, D. E. (2005). Meltwater features that suggest Miocene ice-sheet overriding of the Transantarctic Mountains in Victoria Land, Antarctica. Geografiska Annaler: Series A, Physical Geography, 87(1), 67-85.

Denton, G. H., Prentice, M. L., Kellogg, D. E., & Kellogg, T. B. (1984). Late Tertiary history of the Antarctic ice sheet: Evidence from the Dry Valleys. Geology, 12(5), 263-267.

Denton, G. H., Sugden, D. E., Marchant, D. R., Hall, B. L., & Wilch, T. I. (1993). East Antarctic Ice Sheet sensitivity to Pliocene climatic change from a Dry Valleys perspective. Geografiska Annaler: Series A, Physical Geography, 75(4), 155-204.

Deppeler, S. L., & Davidson, A. T. (2017). Southern Ocean phytoplankton in a changing climate. Frontiers in Marine Science, 4, 40.

Dickens, G. R., & Barron, J. A. (1997). A rapidly deposited pennate diatom ooze in Upper Miocene-Lower Pliocene sediment beneath the North Pacific polar front. Marine Micropaleontology, 31(3-4), 177-182.

Diekmann, B., Fälker, M., & Kuhn, G. (2003). Environmental history of the south-eastern South Atlantic since the Middle Miocene: Evidence from the sedimentological records of ODP Sites 1088 and 1092. Sedimentology, 50(3), 511-529.

Diekmann, B., Kuhn, G., Gersonde, R., & Mackensen, A. (2004). Middle Eocene to early Miocene environmental changes in the sub-Antarctic Southern Ocean: evidence from biogenic and terrigenous depositional patterns at ODP Site 1090. Global and Planetary Change, 40(3-4), 295-313.

Diester-Haass, L., Billups, K., Gröcke, D. R., François, L., Lefebvre, V. & Emeis, L. K. (2009). Mid-Miocene paleoproductivity in the Atlantic Ocean and implications for the global carbon cycle, Paleoceanography, 24, PA1209.

Diester-Haass, L., Meyers, P. A., & Rothe, P. (1992). The Benguela Current and associated upwelling on the southwest African Margin: a synthesis of the Neogene-Quaternary

sedimentary record at DSDP sites 362 and 532. Geological Society, London, Special Publications, 64(1), 331-342.

Dixit, S., Van Cappellen, P.A., van Bennekom, J. (2001). Processes controlling solubility of biogenic silica and pore water build-up of silicic acid in marine sediments. Marine Chemistry, 73: 333-352.

Dodd, J. P., Sharp, Z. D., Fawcett, P. J., Brearley, A. J., & McCubbin, F. M. (2012). Rapid post-mortem maturation of diatom silica oxygen isotope values. Geochemistry, Geophysics, Geosystems, 13(9).

Dodd, J. P., Wiedenheft, W., & Schwartz, J. M. (2017). Dehydroxylation and diagenetic variations in diatom oxygen isotope values. Geochimica et Cosmochimica Acta, 199, 185-195.

Donegan, D. & Schrader, H. (1982). Biogenic and abiogenic components of laminated hemipelagic sediments in the central Gulf of California. Marine Geology, 48, 215-237.

Donohue, K. A., Tracey, K. L., Watts, D. R., Chidichimo, M. P., & Chereskin, T. K. (2016). Mean antarctic circumpolar current transport measured in drake passage. Geophysical Research Letters, 43(22), 11-760.

Dorn, W. (1991): High-resolution magnetic susceptibility and carbonate records: southern Kerguelen Plateau. In Proc. ODP, Sci. Results , 119, 895-901.

Dowsett, H. J., & Caballero Gill, R. P. (2010). Pliocene climate. Stratigraphy, 7(2-3), 106-110.

Dowsett, H. J., Cronin, T. M., Poore, R. Z., Thompson, R. S., Whatley, R. C., & Wood, A. M. (1992). Micropaleontological evidence for increased meridional heat transport in the North Atlantic Ocean during the Pliocene. Science, 258(5085), 1133-1135.

Dugam, S. S., & Kakade, S. B. (2004). Antarctica sea-ice and monsoon variability. Indian Journal of Radio and Space Physics, 33(5), 306-309.

Dutton, A., Carlson, A. E., Long, A., Milne, G. A., Clark, P. U., DeConto, R., ... & Raymo, M. E. (2015). Sea-level rise due to polar ice-sheet mass loss during past warm periods. Science, 349(6244), 4019.

Egan, K. E., Rickaby, R. E., Hendry, K. R., & Halliday, A. N. (2013). Opening the gateways for diatoms primes Earth for Antarctic glaciation. Earth and Planetary Science Letters, 375, 34-43.

Eppley, R. W., Reid, F. M. H., & Strickland, J. D. H. (1970). The ecology of the plankton off La Jolla, California, in the period April through September 1967. Bull Scripps Institute of Oceanography, 17, 33-42.

Epstein, S., Buchsbaum, R., Lowenstam, H. A., & Urey, H. C. (1953). Revised carbonate-water isotopic temperature scale. Geological Society of America Bulletin, 64(11), 1315-1326.

Escutia, C., & Brinkhuis, H. (2014). From Greenhouse to Icehouse at the Wilkes Land Antarctic Margin: IODP Expedition 318 Synthesis of Results. In Developments in marine geology, 7, 295-328. Elsevier.

Escutia, C., Bárcena, M. A., Lucchi, R. G., Romero, O., Ballegeer, A. M., Gonzalez, J. J., & Harwood, D. M. (2009). Circum-Antarctic warming events between 4 and 3.5 Ma recorded in marine sediments from the Prydz Bay (ODP Leg 188) and the Antarctic Peninsula (ODP Leg 178) margins. Global and Planetary Change, 69(3), 170-184.

Escutia, C., DeConto, R. M., Dunbar, R., Santis, L. D., Shevenell, A., & Naish, T. (2019). Keeping an Eye on Antarctic Ice Sheet Stability. Oceanography, 32(1), 32-46.

Farmer, R. (2011). The Application of Biostratigraphy and Paleoecology at Southern Ocean Drill Sites to Resolve Early to Middle Miocene Paleoclimatic Events. MSc Thesis, University of Nebraska-Lincoln.

Feakins, S. J., Warny, S., & Lee, J. E. (2012). Hydrologic cycling over Antarctica during the middle Miocene warming. Nature Geoscience, 5(8), 557.

Fedorov, A. V., Brierley, C. M., Lawrence, K. T., Liu, Z., Dekens, P. S., & Ravelo, A. C. (2013). Patterns and mechanisms of early Pliocene warmth. Nature, 496(7443), 43.

Ferrario, M. E., Almandoz, G. O., Cefarelli, A. O., Fabro, E., & Vernet, M. (2013). *Stephanopyxis* species (Bacillariophyceae) from shelf and slope waters of the Argentinean Sea: Ultrastructure and distribution. Nova Hedwigia, 96(1-2), 249-263.

Field, C. B., Behrenfeld, M. J., Randerson, J. T., & Falkowski, P. (1998). Primary production of the biosphere: integrating terrestrial and oceanic components. Science, 281(5374), 237-240.

Finkel, Z. V., & Kotrc, B. (2010). Silica use through time: macroevolutionary change in the morphology of the diatom frustule. Geomicrobiology Journal, 27(6-7), 596-608.

Finkel, Z. V., Irwin, A. J., & Schofield, O. (2004). Resource limitation alters the 3/4 size scaling of metabolic rates in phytoplankton. Marine Ecology Progress Series, 273, 269-279.

Flores, J. A., & Sierro, F. J. (2007). Pronounced mid-Pleistocene southward shift of the Polar Front in the Atlantic sector of the Southern Ocean. Deep Sea Research Part II: Topical Studies in Oceanography, 54(21-22), 2432-2442.

Florindo, F., Bohaty, S. M., Erwin, P. S., Richter, C., Roberts, A. P., Whalen, P. A., & Whitehead, J. M. (2003). Magnetobiostratigraphic chronology and palaeoenvironmental history of Cenozoic sequences from ODP sites 1165 and 1166, Prydz Bay, Antarctica. Palaeogeography, Palaeoclimatology, Palaeoecology, 198(1-2), 69-100.

Florindo, F., Farmer, R. K., Harwood, D. M., Cody, R. D., Levy, R., Bohaty, S. M., ... & Winkler, A. (2013). Paleomagnetism and biostratigraphy of sediments from Southern Ocean ODP Site 744

(southern Kerguelen Plateau): Implications for early-to-middle Miocene climate in Antarctica. Global and planetary change, 110, 434-454.

Flower, B. P., & Kennett, J. P. (1994). The middle Miocene climatic transition: East Antarctic ice sheet development, deep ocean circulation and global carbon cycling. Palaeogeography, palaeoclimatology, palaeoecology, 108(3-4), 537-555.

Fogwill, C. J., Phipps, S. J., Turney, C. S. M., & Golledge, N. R. (2015). Sensitivity of the Southern Ocean to enhanced regional Antarctic ice sheet meltwater input. Earth's Future, 3(10), 317-329.

Foster, G. L., Lear, C. H., & Rae, J. W. (2012). The evolution of pCO_2, ice volume and climate during the middle Miocene. Earth and Planetary Science Letters, 341, 243-254

Fourtanier, E. (1991). Diatom biostratigraphy of Equatorial Indian Ocean Site 758. Proceedings of the Ocean Drilling Program, Scientific Results, 121, 189-208: College Station, TX.

Freeman, N. M., & Lovenduski, N. S. (2016). Mapping the Antarctic Polar Front: weekly realizations from 2002 to 2014. Earth System Science Data, 8(1), 191-198.

French, F. W., Hargraves. W., (1980). Physiological characteristics of plankton diatom resting spores. Marine Biology Letters, 1, 185-195.

Fretwell, P., Pritchard, H. D., Vaughan, D. G., Bamber, J. L., Barrand, N. E., Bell, R., ... & Catania, G. A. (2013). Bedmap2: improved ice bed, surface and thickness datasets for Antarctica.

Frigola, A., Prange, M., & Schulz, M. (2018). Boundary conditions for the Middle Miocene Climate Transition (MMCT v1. 0). Geoscientific Model Development, 11(4), 1607-1626.

Frohlich, F. (1989). Deep-sea biogenic silica: new structural and analytical data from infrared analysis – geological implications, Terra Nova, 1, 267–273.

Galeotti, S., DeConto, R., Naish, T., Stocchi, P., Florindo, F., Pagani, M., ... & Sandroni, S. (2016). Antarctic Ice Sheet variability across the Eocene-Oligocene boundary climate transition. Science, 352(6281), 76-80.

Ganopolski, A., & Brovkin, V. (2017). Simulation of climate, ice sheets and CO_2 evolution during the last four glacial cycles with an Earth system model of intermediate complexity. Climate of the Past, 13, 1695-1716.

Gasson, E., DeConto, R. M., & Pollard, D. (2016). Modeling the oxygen isotope composition of the Antarctic ice sheet and its significance to Pliocene sea level. Geology, 44(10), 827-830.

Gehlen, M., Beck, L., Calas, G., Flank, A. M., van Bennekom, A. J., and van Beusekom., J. E. E. (2002). Unraveling the atomic structure of biogenic silica: Evidence of the structural association of Al and Si in diatom frustules, Geochimica et Cosmochimica Acta, 66, 1601– 1609.

Gersonde, R. and Burckle, L.H. (1990). Neogene Diatom biostratigraphy of ODP Leg 113, Weddell Sea Antarctic Ocean, In: Barker, P. F., Kennett, J.P., et al., Proc. ODP, Sci. Results, 113, 761-789.

Gersonde, R., & Bárcena, M. A. (1998). Revision of the Upper Pliocene: Pleistocene diatom biostratigraphy for the northern belt of the Southern Ocean. Micropaleontology, 84-98.

Gersonde, R., & Burckle, L. H. (1990). Neogene diatom biostratigraphy of ODP Leg 113, Weddell Sea (Antarctic Ocean). Proc. ODP, Sci. Results, 113, 779-790.

Gersonde, R., (1990). Taxonomy and morphostructure of Neogene diatoms from the Southern Ocean, Proc. ODP, Sci. Results, 113, 791–802.

Gersonde, R., Abelmann, A., Burckle, L. H., Hamilton, N., Lazarus, D., McCartney, K., ... & Wise Jr, S. W. (1990). Biostratigraphic synthesis of Neogene siliceous microfossils from the Antarctic Ocean, ODP Leg 113 (Weddell Sea). Proc. ODP, Sci. Results, 113, 915-936.

Gersonde, R., & Zielinski, U. (2000). The reconstruction of late Quaternary Antarctic sea-ice distribution—the use of diatoms as a proxy for sea-ice. Palaeogeography, Palaeoclimatology, Palaeoecology, 162(3-4), 263-286.

Gladenkov, A. Y., & Barron, J. A. (1992). Oligocene and early middle Miocene diatom biostratigraphy of Hole 884B. In Proc. ODP, Sci. Results, 21042.

Goldman, J. C. (1993). Potential role of large oceanic diatoms in new primary production. Deep Sea Research Part I: Oceanographic Research Papers, 40(1), 159-168.

Goldner, A., Herold, N., & Huber, M. (2014). Antarctic glaciation caused ocean circulation changes at the Eocene–Oligocene transition. Nature, 511(7511), 574.

Golledge, N. R., Menviel, L., Carter, L., Fogwill, C. J., England, M. H., Cortese, G., Levy, R. H. (2014). Antarctic contribution to meltwater pulse 1A from reduced Southern Ocean overturning. Nature Communications, 5, 5107.

Golledge, N. R., Thomas, Z. A., Levy, R. H., Gasson, E. G., Naish, T. R., McKay, R. M., ... & Fogwill, C. J. (2017). Antarctic climate and ice-sheet configuration during the early Pliocene interglacial at 4.23 Ma. Climate of the Past, 13(7), 959.

Gombos Jr, A. M. (1976). Diatom investigations in the South Atlantic. Antarctic journal of the United States.

Gotelli, N. J. and Colwell, R. K. (2011). Estimating species richness. In: Magurran, A. E. and McGill, B. J. (eds) Biological Diversity: Frontiers in Measurement and Assessment. Oxford, Oxford University Press, 39-54.

Gradstein, F. M., Ogg, J. G., Schmitz, M., & Ogg, G. (Eds.). (2012). The geologic time scale. Elsevier.

Greenop, R., Foster, G. L., Wilson, P. A., & Lear, C. H. (2014). Middle Miocene climate instability associated with high-amplitude CO_2 variability. Paleoceanography and Paleoclimatology, 29(9), 845-853.

Greenop, R., Sosdian, S. M., Henehan, M. J., Wilson, P. A., Lear, C. H., & Foster, G. L. (2019). Orbital Forcing, Ice Volume, and CO_2 Across the Oligocene-Miocene Transition. Paleoceanography and Paleoclimatology, 34(3), 316-328.

Greenwood, D. R., & Wing, S. L. (1995). Eocene continental climates and latitudinal temperature gradients. Geology, 23(11), 1044-1048.

Grigorov, I., Pearce, R. B. and Kemp, A. E. S. (2002). Southern Ocean laminated diatom ooze: mat deposits and potential for palaeo-flux studies, ODP Leg 177, Site 1093. Deep-Sea Research II 49, 3391-3407.

Grover, J. P. (1989). The influence of cell shape and size on algal competitive ability. Journal of Phycology, 25(2), 402-405.

Grützner, J. (2003). Data Report: Multisensor core logging data, coarse-fraction grain-size analyses, and biogenic silica content of upper Miocene, lower Pliocene sediments, ODP Site 1165. In Proc. ODP, Sci. Results, 188, 1-16.

Grützner, J., Hillenbrand, C. D., & Rebesco, M. (2005). Terrigenous flux and biogenic silica deposition at the Antarctic continental rise during the late Miocene to early Pliocene: implications for ice sheet stability and sea ice coverage. Global and Planetary Change, 45(1-3), 131-149.

Gulick, S. P., Shevenell, A. E., Montelli, A., Fernandez, R., Smith, C., Warny, S., ... & Blankenship, D. D. (2017). Initiation and long-term instability of the East Antarctic Ice Sheet. Nature, 552(7684), 225.

Guo, G., Shi, J., Gao, L., Tamura, T., & Williams, G. D. (2019). Reduced Sea Ice Production Due to Upwelled Oceanic Heat Flux in Prydz Bay, East Antarctica. Geophysical Research Letters, 46(9), 4782-4789.

Gupta, K., Yuvaraja, A., Prakasam, M., Clemens, S. C. & Velu, A. (2015). Evolution of the South Asian monsoon wind system since the late Middle Miocene. Palaeogeography, Palaeoclimatology, Palaeoecology, 438, 160-167.

Haimson, M., & Knauth, L. P. (1983). Stepwise fluorination- a useful approach for the isotopic analysis of hydrous minerals. Geochimica et Cosmochimica Acta, 47(9), 1589-1595.

Hain, M. P., Sigman, D. M., & Haug, G. H. (2010). Carbon dioxide effects of Antarctic stratification, North Atlantic Intermediate Water formation, and subantarctic nutrient drawdown during the

last ice age: Diagnosis and synthesis in a geochemical box model. Global Biogeochemical Cycles, 24(4).

Hale, M. S., & Mitchell, J. G. (2001). Functional morphology of diatom frustule microstructures: hydrodynamic control of Brownian particle diffusion and advection. Aquatic Microbial Ecology, 24(3), 287-295.

Hall, I. R., McCave, I. N., Zahn, R., Carter, L., Knutz, P. C., & Weedon, G. P. (2003). Paleocurrent reconstruction of the deep Pacific inflow during the middle Miocene: Reflections of East Antarctic Ice Sheet growth. Paleoceanography and Paleoclimatology, 18(2).

Hambrey, M. J., Ehrmann, W., & Larsen, B. (1991). Cenozoic glacial record of the Prydz Bay continental shelf, East Antarctica. In: Barron, J; Larsen, B, et al.(eds.), Proc. ODP, Sci. Results, 119, 77-132.

Hamon, N., Sepulchre, P., Lefebvre, V., & Ramstein, G. (2013). The role of eastern Tethys seaway closure in the Middle Miocene Climatic Transition (ca. 14 Ma). Climate of the Past, 9(6), 2687-2702

Hansen, M. A., & Passchier, S. (2017). Oceanic circulation changes during early Pliocene marine ice-sheet instability in Wilkes Land, East Antarctica. Geo-Marine Letters, 37(3), 207-213.

Haq, B. U., Hardenbol, J., & Vail, P. R. (1987). The new chronostratigraphic basis of Cenozoic and Mesozoic sea level cycles. Special Publication, Cushman Foundation for Foraminiferal Research, 24, 7-13.

Hartman, J. D., Sangiorgi, F., Salabarnada, A., Peterse, F., Houben, A. J., Schouten, S., ... & Bijl, P. K. (2018). Paleoceanography and ice sheet variability offshore Wilkes Land, Antarctica-Part 3: Insights from Oligocene-Miocene TEX86-based sea surface temperature reconstructions. Climate of the Past, 14(9), 1275-1297.

Harwood, D. M., McMInn, A. & Quilty, P. G. (2000). Diatom biostratigraphy and age of the Pliocene Sørsdal Formation, Vestfold Hills, East Antarctica. Antarctic Science, 12(4), 443-462.

Harwood, D. M. (1989). Siliceous microfossils. Antarctic Cenozoic history from the CIROS-1 drillhole, McMurdo Sound. DSIR Bulletin, 245, 67-97.

Harwood, D. M., & Maruyama, T. (1992). Middle Eocene to Pleistocene diatom biostratigraphy of Southern Ocean sediments from the Kerguelen Plateau, Leg 120. Proc. ODP, Sci. Results, 120, 683-733.

Harwood, D. M., Bohaty, S., & Scherer, R. (1998). Lower Miocene diatom biostratigraphy of the CRP-1 drillcore, McMurdo Sound, Antarctica. Terra Antartica, 5(3), 499-514.

Harwood, D., & Bohaty, S. (2007). Late Miocene sea ice diatoms indicate a cold polar East Antarctic ice sheet event. In EGU Annual meeting.

Harwood, D.M. (1986). Diatoms. In: Barrett, P.J. ed., Antarctic Cenozoic History from the MSSTS-1 Drillhole. McMurdo Sound: DSIR Bulletin, 237, 69–107.

Harwood, D.M. and Bohaty, S.M., (2002). Early Oligocene siliceous microfossil biostratigraphy of Cape Roberts project Core CRP-3, Victoria Land Basin, Antarctica:Terra Antartica, 8(4) 315-338.

Hasle, G. R. (1976, April). The biogeography of some marine planktonic diatoms. In Deep Sea Research and Oceanographic Abstracts, 23(4), 319.

Hasle, G. R. (2001). The marine, planktonic diatom family Thalassionemataceae: morphology, taxonomy and distribution. Diatom Research, 16(1), 1-82.

Hasle, G. R., & Semina, H. J. (1987). The marine planktonic diatoms Thalassiothrix longissima and Thalassiothrix antarctica with comments on *Thalassionema* spp. and *Synedra reinboldii*. Diatom Research, 2(2), 175-192.

Hasle, G. R., Medlin, L. K., & Syvertsen, E. E. (1994). *Synedropsis* gen. nov., a sea ice associated araphid diatom genus. Phycologia, 33, 248-270.

Hasle, G. R., Syvertsen, E. E., Steidinger, K. A., Tangen, K., & Tomas, C. R. (1996). Identifying marine diatoms and dinoflagellates. Elsevier.

Haug, G. H., & Tiedemann, R. (1998). Effect of the formation of the Isthmus of Panama on Atlantic Ocean thermohaline circulation. Nature, 393(6686), 673.

Haug, G.H., Ganopolski, A., Sigman, D.M., Rosell-Mele, A., Swann, G.E.A., Tiedemann, R., Jaccard, S., Bollmann, J., Maslin, M.A., Leng, M.J., Eglinton, G. (2005). North Pacific seasonality and the glaciation of North America 2.7 million years ago. Nature 433, 821–825.

Hauptvogel, D. W., Pekar, S. F., & Pincay, V. (2017). Evidence for a heavily glaciated Antarctica during the late Oligocene warming (27.8–24.5 Ma): Stable isotope records from ODP Site 690. Paleoceanography, 32(4), 384-396.

Hayashi, T., Krebs, W. N., Saito-Kato, M., & Tanimura, Y. (2018). The turnover of continental planktonic diatoms near the middle/late Miocene boundary and their Cenozoic evolution. PloS one, 13(6), e0198003.

Hayes, C. T., Anderson, R. F., & Fleisher, M. Q. (2011). Opal accumulation rates in the equatorial Pacific and mechanisms of deglaciation. Paleoceanography, 26(1), 299-325.

Haywood, A. M., & Valdes, P. J. (2004). Modelling Pliocene warmth: contribution of atmosphere, oceans and cryosphere. Earth and Planetary Science Letters, 218(3-4), 363-377.

Haywood, A. M., Hill, D. J., Dolan, A. M., Otto-Bliesner, B. L., Bragg, F., Chan, W. L., ... & Kamae, Y. (2013). Large-scale features of Pliocene climate: results from the Pliocene Model Intercomparison Project. Climate of the Past, 9(1), 191-209.

Haywood, A. M., Smellie, J. L., Ashworth, A. C., Cantrill, D. J., Florindo, F., Hambrey, M. J., ... & Lear, C. H. (2008). Middle Miocene to Pliocene history of Antarctica and the southern ocean. Developments in Earth and Environmental Sciences, 8, 401-463.

Haywood, A. M., Valdes, P. J., & Peck, V. L. (2007). A permanent El Niño–like state during the Pliocene? Paleoceanography and Paleoclimatology, 22(1).

Heider, F., Leitner, B., & Inokuchi, H. (1992). High southern latitude magnetostratigraphy and rock magnetic properties of sediments from Sites 747, 749 and 751. Proc. ODP, Sci. Results, 120, 205-216.

Heinrich, S., Zonneveld, K. A., Bickert, T., & Willems, H. (2011). The Benguela upwelling related to the Miocene cooling events and the development of the Antarctic circumpolar current: evidence from calcareous dinoflagellate cysts. Paleoceanography, 26(3).

Hendry, K. R., & Rickaby, R. E. (2008). Opal (Zn/Si) ratios as a nearshore geochemical proxy in coastal Antarctica. Paleoceanography and Paleoclimatology, 23(2).

Hendry, K. R., Meredith, M. P., Measures, C. I., Carson, D. S., & Rickaby, R. E. (2010). The role of sea ice formation in cycling of aluminium in northern Marguerite Bay, Antarctica. Estuarine, Coastal and Shelf Science, 87(1), 103-112.

Herbert, T. D., Lawrence, K. T., Tzanova, A., Peterson, L. C., Caballero-Gill, R., & Kelly, C. S. (2016). Late Miocene global cooling and the rise of modern ecosystems. Nature Geoscience, 9(11), 843.

Hernández-Molina, F. J., Larter, R. D., & Maldonado, A. (2017). Neogene to Quaternary stratigraphic evolution of the Antarctic Peninsula, Pacific Margin offshore of Adelaide Island: Transitions from a non-glacial, through glacially-influenced to a fully glacial state. Global and Planetary Change, 156, 80-111.

Heywood, K. J., Sparrow, M. D., Brown, J., & Dickson, R. R. (1999). Frontal structure and Antarctic bottom water flow through the Princess Elizabeth Trough, Antarctica. Deep Sea Research Part I: Oceanographic Research Papers, 46(7), 1181-1200.

Hill, D. J., Haywood, A. M., Valdes, P. J., Francis, J. E., Lunt, D. J., Wade, B. S., & Bowman, V. C. (2013). Paleogeographic controls on the onset of the Antarctic circumpolar current. Geophysical Research Letters, 40(19), 5199-5204.

Hillenbrand, C. D., & Cortese, G. (2006). Polar stratification: a critical view from the Southern Ocean. Palaeogeography, Palaeoclimatology, Palaeoecology, 242(3-4), 240-252.

Hillenbrand, C. D., & Ehrmann, W. (2001). Distribution of clay minerals in drift sediments on the continental rise west of the Antarctic Peninsula, ODP Leg 178, Sites 1095 and 1096. In Barker, PF, Camerlenghi, A., Acton, GD, and Ramsay, ATS (Eds.), Proc. ODP, Sci. Results, 178.

Hillenbrand, C. D., Smith, J. A., Hodell, D. A., Greaves, M., Poole, C. R., Kender, S., ... & Klages, J. P. (2017). West Antarctic Ice Sheet retreat driven by Holocene warm water incursions. Nature, 547(7661), 43.

Hodell, D.A., Kanfoush, S.L., Shemesh, A., Crosta, X., Charles, C.D., Guilderson, T.P. (2001). Abrupt cooling of Antarctic surface waters and sea ice expansion in the South Atlantic sector of the Southern Ocean at 5000 cal yr BP. Quaternary Research 56, 191–198.

Holbourn, A. E., Kuhnt, W., Clemens, S. C., Kochhann, K. G., Jöhnck, J., Lübbers, J., & Andersen, N. (2018). Late Miocene climate cooling and intensification of southeast Asian winter monsoon. Nature communications, 9(1), 1584.

Holbourn, A., Kuhnt, W., Clemens, S., Prell, W., & Andersen, N. (2013). Middle to late Miocene stepwise climate cooling: Evidence from a high-resolution deep water isotope curve spanning 8 million years. Paleoceanography, 28(4), 688-699.

Holbourn, A., Kuhnt, W., Frank, M., & Haley, B. A. (2013). Changes in Pacific Ocean circulation following the Miocene onset of permanent Antarctic ice cover. Earth and Planetary Science Letters, 365, 38-50.

Holbourn, A., Kuhnt, W., Kochhann, K. G., Andersen, N., & Sebastian Meier, K. J. (2015). Global perturbation of the carbon cycle at the onset of the Miocene Climatic Optimum. Geology, 43(2), 123-126.

Holbourn, A., Kuhnt, W., Lyle, M., Schneider, L., Romero, O., & Andersen, N. (2014). Middle Miocene climate cooling linked to intensification of eastern equatorial Pacific upwelling. Geology, 42(1), 19-22.

Holbourn, A., Kuhnt, W., Schulz, M., & Erlenkeuser, H. (2005). Impacts of orbital forcing and atmospheric carbon dioxide on Miocene ice-sheet expansion. Nature, 438(7067), 483.

Honjo, S., Manganini, S. J., Krishfield, R. A., & Francois, R. (2008). Particulate organic carbon fluxes to the ocean interior and factors controlling the biological pump: A synthesis of global sediment trap programs since 1983. Progress in Oceanography, 76(3), 217-285.

Hoppema, M., Klatt, O., Roether, W., Fahrbach, E., Bulsiewicz, K., Rodehacke, C., & Rohardt, G. (2001). Prominent renewal of Weddell Sea Deep Water from a remote source. Journal of marine research, 59(2), 257-279.

Huang, X., Stärz, M., Gohl, K., Knorr, G., & Lohmann, G. (2017). Impact of Weddell Sea shelf progradation on Antarctic bottom water formation during the Miocene. Paleoceanography, 32(3), 304-317.

Ishman, S. E., & Rieck, H. J. (1992). A Late Neocene Antarctic Glacio-Eustatic Record, Victoria Land Basin Margin, Antarctica. The Antarctic Paleoenvironment: A Perspective on Global Change: Part One, 56, 327-348.

Jacobs, S. S., Jenkins, A., Giulivi, C. F., & Dutrieux, P. (2011). Stronger ocean circulation and increased melting under Pine Island Glacier ice shelf. Nature Geoscience, 4(8), 519.

Jena, B., Kumar, A., Ravichandran, M., & Kern, S. (2018). Mechanism of sea-ice expansion in the Indian Ocean sector of Antarctica: Insights from satellite observation and model reanalysis. PloS one, 13(10), e0203222.

Ji, S., Nie, J., Lechler, A., Huntingdon, K. W., Heitmann, E. O. & Breecker, D. O. (2018). A symmetrical CO_2 peak and asymmetrical climate change during the middle Miocene. Earth and Planetary Science Letters, 499, 134-144.

Jiménez-Moreno, G. (2006). Progressive substitution of a subtropical forest for a temperate one during the middle Miocene climate cooling in Central Europe according to palynological data from cores Tengelic-2 and Hidas-53 (Pannonian Basin, Hungary). Review of Palaeobotany and Palynology, 142(1-2), 1-14.

John, C. M., Karner, G. D., Browning, E., Leckie, R. M., Mateo, Z., Carson, B., & Lowery, C. (2011). Timing and magnitude of Miocene eustasy derived from the mixed siliciclastic-carbonate stratigraphic record of the northeastern Australian margin. Earth and Planetary Science Letters, 304(3-4), 455-467.

Jones, T. D., Bown, P. R., Pearson, P. N., Wade, B. S., Coxall, H. K., & Lear, C. H. (2008). Major shifts in calcareous phytoplankton assemblages through the Eocene-Oligocene transition of Tanzania and their implications for low-latitude primary production. Paleoceanography, 23(4).

Joughin, I., Alley, R. B., & Holland, D. M. (2012). Ice-sheet response to oceanic forcing. Science, 338(6111), 1172-1176.

Joughin, I., Das, S. B., King, M. A., Smith, B. E., Howat, I. M., & Moon, T. (2008). Seasonal speedup along the western flank of the Greenland Ice Sheet. Science, 320(5877), 781-783.

Jordan, R. W., & Stickley, C. E. (2010). Diatoms as indicators of paleoceanographic events. The Diatoms: Applications for the Environmental and Earth Sciences. Cambridge University Press, Cambridge.

Juillet-Leclerc, A., Labeyrie, L. (1987). Temperature dependence of the oxygen isotopic fractionation between diatom silica and water. Earth and Planetary Science Letters 84, 69–74.

Kato, Y., Onodera, J., Suto, I., Teraishi, A., & Takahashi, K. (2016). Pliocene and Pleistocene paleoceanography in the western subarctic Pacific based on diatom analyses of ODP Leg 145

Hole 884B and IODP Expedition 323 Holes U1341B and U1343E. Deep Sea Research Part II: Topical Studies in Oceanography, 125, 29-37.

Keller, G., & Barron, J. A. (1983). Paleoceanographic implications of Miocene deep-sea hiatuses. Geological Society of America Bulletin, 94(5), 590-613.

Kemp, A. E. S. (1995). Origins and paleoceanographic significance of laminated diatom ooze from the eastern equatorial Pacific Ocean. In Proc. ODP Sci. Res. (Vol. 138, pp. 641-645).

Kemp, A. E. S., Grigorov, I., Pearce, R. B., & Garabato, A. N. (2010). Migration of the Antarctic Polar Front through the mid-Pleistocene transition: evidence and climatic implications. Quaternary Science Reviews, 29(17-18), 1993-2009.

Kemp, A. E., & Baldauf, J. G. (1993). Vast Neogene laminated diatom mat deposits from the eastern equatorial Pacific Ocean. Nature, 362(6416), 141.

Kemp, A. E., Pike, J., Pearce, R. B., & Lange, C. B. (2000). The "Fall dump"—a new perspective on the role of a "shade flora" in the annual cycle of diatom production and export flux. Deep Sea Research Part II: Topical Studies in Oceanography, 47(9-11), 2129-2154.

Kender, S., Bogus, K. A., Cobb, T. D., & Thomas, D. J. (2018). Neodymium evidence for increased Circumpolar Deep Water flow to the North Pacific during the middle Miocene climate transition. Paleoceanography and Paleoclimatology, 33(7), 672-682.

Kennett, J. P. (1977). Cenozoic evolution of Antarctic glaciation, the circum-Antarctic Ocean, and their impact on global paleoceanography. Journal of geophysical research, 82(27), 3843-3860.

Kennett, J. P., & Barker, P. F. (1990). Climatic and oceanographic developments in the Weddell Sea, Antarctica, since the latest Cretaceous: An ocean-drilling perspective. Kennett, JP, and Barker, PF, et al., Proc. ODP, Sci. Results, 113, 937-962.

Key, T., McCarthy, A., Campbell, D. A., Six, C., Roy, S., & Finkel, Z. V. (2010). Cell size trade-offs govern light exploitation strategies in marine phytoplankton. Environmental microbiology, 12(1), 95-104.

Knauth, L. P. (1973). Oxygen and hydrogen isotope ratios in cherts and related rocks. Doctoral dissertation, California Institute of Technology.

Knorr, G., & Lohmann, G. (2014). Climate warming during Antarctic ice sheet expansion at the Middle Miocene transition. Nature Geoscience, 7(5), 376.

Koç, N., and Scherer, R.P. (1996). Neogene diatom biostratigraphy of the Iceland Sea Site 907. In Thiede, J., Myhre, A.M., Firth, J.V., Johnson, G.L., and Ruddiman, W.F. (Eds.), Proc. ODP, Sci. Results, 151, 61–74.

Koizumi, I. (1990). Successional changes of middle Miocene diatom assemblages in the northwestern Pacific. Palaeogeography, Palaeoclimatology, Palaeoecology, 77(3-4), 181-193.

Kominz, M. A., Browning, J. V., Miller, K. G., Sugarman, P. J., Mizintseva, S., & Scotese, C. R. (2008). Late Cretaceous to Miocene sea-level estimates from the New Jersey and Delaware coastal plain coreholes: An error analysis. Basin Research, 20(2), 211-226.

Koning, E., Gehlen, M., Flank, A-M., Calas, G., Epping, E. (2007). Rapid post-mortem incorporation of aluminium in diatom frustules: evidence from chemical and structural analyses. Marine Chemistry, 103, 97-111.

Krylov, A. A., Andreeva, I. A., Vogt, C., Backman, J., Krupskaya, V. V., Grikurov, G. E., ... & Shoji, H. (2008). A shift in heavy and clay mineral provenance indicates a middle Miocene onset of a perennial sea ice cover in the Arctic Ocean. Paleoceanography and Paleoclimatology, 23(1).

Kuhnert, H., Bickert, T., & Paulsen, H. (2009). Southern Ocean frontal system changes precede Antarctic ice sheet growth during the middle Miocene. Earth and Planetary Science Letters, 284(3-4), 630-638.

Kumar, N., Anderson, R. F., Mortlock, R. A., Froelich, P. N., Kubik, P., Dittrich-Hannen, B., & Suter, M. (1995). Increased biological productivity and export production in the glacial Southern Ocean. Nature, 378(6558), 675.

Kuwata, A. (1993). Ecophysiological characterization of two life forms, resting spores and resting cells, of a marine planktonic diatom Chaetoceros pseudocurvisetus, formed under nutrient depletion. Marine Ecological Progress Series, 102, 245-255.

Kwiek, P. B., & Ravelo, A. C. (1999). Pacific Ocean intermediate and deep water circulation during the Pliocene. Palaeogeography, Palaeoclimatology, Palaeoecology, 154(3), 191-217.

Labeyrie, L. (1979). Oxygen isotopic ratio of the diatom siliceous valves: development of a new method in quantitative paleoclimatology.

Labeyrie, L. D., & Juillet, A. (1980). Isotopic exchange of the biogenic silica oxygen. Comptes rendus des séances de la academie des sciences serie D, 290(18), 1185-1188.

Labeyrie, L. D., & Juillet, A. (1982). Oxygen isotopic exchangeability of diatom valve silica; interpretation and consequences for paleoclimatic studies. Geochimica et Cosmochimica Acta, 46(6), 967-975.

Labeyrie, L. J. (1974). New approach to surface seawater palaeotemperatures using $^{18}O/^{16}O$ ratios in silica of diatom frustules. Nature, 248(5443), 40.

Lal, D., Charles, C., Vacher, L., Goswami, J. N., Jull, A. T., McHargue, L., & Finkel, R. C. (2006). Paleo-ocean chemistry records in marine opal: Implications for fluxes of trace elements, cosmogenic nuclides (10Be and 26Al), and biological productivity. Geochimica et cosmochimica acta, 70(13), 3275-3289.

Lamb, A. L., Brewer, T. S., Leng, M. J., Sloane, H. J., & Lamb, H. F. (2007). A geochemical method for removing the effect of tephra on lake diatom oxygen isotope records. Journal of Paleolimnology, 37(4), 499-516.

Lampitt, R. S. (1985). Evidence for the seasonal deposition of detritus to the deep-sea floor and its subsequent resuspension. Deep Sea Research Part A. Oceanographic Research Papers, 32(8), 885-897.

LaRiviere, J. P., Ravelo, A. C., Crimmins, A., Dekens, P. S., Ford, H. L., Lyle, M., & Wara, M. W. (2012). Late Miocene decoupling of oceanic warmth and atmospheric carbon dioxide forcing. Nature, 486(7401), 97.

Latorre, C., Quade, J., & McIntosh, W. C. (1997). The expansion of C4 grasses and global change in the late Miocene: stable isotope evidence from the Americas. Earth and Planetary Science Letters, 146(1-2), 83-96.

Lavaud, J., Strzepek, R. F., & Kroth, P. G. (2007). Photoprotection capacity differs among diatoms: Possible consequences on the spatial distribution of diatoms related to fluctuations in the underwater light climate. Limnology and Oceanography, 52(3), 1188-1194.

Lawver, L. A., & Gahagan, L. M. (2003). Evolution of Cenozoic seaways in the circum-Antarctic region. Palaeogeography, Palaeoclimatology, Palaeoecology, 198(1-2), 11-37.

Lawver, L.A., Coffin, M.F., Dalziel, I.W.D., Gahagan, L.M., and Campbell, D.A. (2003). The PLATES 2003 Atlas of Plate Reconstructions (750 Ma to Present Day), PLATES Progress Report No. 260, 83.

Lazarus, D. B. 1994. Neptune: A marine Micropaleontology Database. Mathematical Geology, 26(7): 817-832.

Lazarus, D., Barron, J., Renaudie, J., Diver, P., & Türke, A. (2014). Cenozoic planktonic marine diatom diversity and correlation to climate change. PLoS One, 9(1), 84857.

Lear, C. H., Coxall, H. K., Foster, G. L., Lunt, D. J., Mawbey, E. M., Rosenthal, Y., ... & Wilson, P. A. (2015). Neogene ice volume and ocean temperatures: Insights from infaunal foraminiferal Mg/Ca paleothermometry. Paleoceanography, 30(11), 1437-1454.

Lear, C. H., Coxall, H. K., Foster, G. L., Lunt, D. J., Mawbey, E. M., Rosenthal, Y., ... & Wilson, P. A. (2015). Neogene ice volume and ocean temperatures: Insights from infaunal foraminiferal Mg/Ca paleothermometry. Paleoceanography and Paleoclimatology, 30(11), 1437-1454.

Lefebvre, V., Donnadieu, Y., Sepulchre, P., Swingedouw, D., & Zhang, Z. S. (2012). Deciphering the role of southern gateways and carbon dioxide on the onset of the Antarctic Circumpolar Current. Paleoceanography, 27(4).

Leng, M. J., & Barker, P. A. (2006). A review of the oxygen isotope composition of lacustrine diatom silica for palaeoclimate reconstruction. Earth-Science Reviews, 75(1-4), 5-27.

Leng, M. J., & Sloane, H. J. (2008). Combined oxygen and silicon isotope analysis of biogenic silica. Journal of Quaternary Science: Published for the Quaternary Research Association, 23(4), 313-319.

Leng, M., Barnker, P., Greenwood, P., Roberts, N., & Reed, J. (2001). Oxygen isotope analysis of diatom silica and authigenic calcite from Lake Pinarbasi, Turkey. Journal of Paleolimnology, 25(3), 343-349.

Leventer A., Crosta, X. and Pike, J. (2010). Holocene marine diatom records of environmental change. In: Smol, J. P. and Stoermer, E. F. (eds) The Diatoms: Applications for the Environmental and Earth Sciences. Cambridge, Cambridge University Press, 401-423.

Leventer, A., Domack, E., Barkoukis, A., McAndrews, B., & Murray, J. (2002). Laminations from the Palmer Deep: A diatom-based interpretation. Paleoceanography and Paleoclimatology, 17(3).

Leventer, A., Domack, E., Dunbar, R., Pike, J., Stickley, C., Maddison, E., ... & McClennen, C. (2006). Marine sediment record from the East Antarctic margin reveals dynamics of ice sheet recession. GSA Today, 16(12), 4.

Leventer, A., Dunbar, R. B., & DeMaster, D. J. (1993). Diatom evidence for late Holocene climatic events in Granite Harbor, Antarctica. Paleoceanography, 8(3), 373-386.

Levy, R., Harwood, D., Florindo, F., Sangiorgi, F., Tripati, R., Von Eynatten, H., ... & Fielding, C. (2016). Antarctic ice sheet sensitivity to atmospheric CO_2 variations in the early to mid-Miocene. Proceedings of the National Academy of Sciences, 113(13), 3453-3458.

Levy, R., Harwood, D., Florindo, F., Sangiorgi, F., Tripati, R., Von Eynatten, H., ... & Fielding, C. (2016). Antarctic ice sheet sensitivity to atmospheric CO2 variations in the early to mid-Miocene. Proceedings of the National Academy of Sciences, 113(13), 3453-3458.

Lewin, J.C. (1961). The dissolution of silica from diatom walls. Geochimica et Cosmochimica Acta, 21, 182–198.

Lewis, A. R. & Ashworth, A. C. (2016). An early to middle Miocene record of ice-sheet and landscape evolution from the Friis Hills, Antarctica. GSA Bulletin, 128 (5-6), 719–738.

Lewis, A. R., Marchant, D. R., Ashworth, A. C., Hedenäs, L., Hemming, S. R., Johnson, J. V., ... & Willenbring, J. K. (2008). Mid-Miocene cooling and the extinction of tundra in continental Antarctica. Proceedings of the National Academy of Sciences.

Lewis, A. R., Marchant, D. R., Ashworth, A. C., Hemming, S. R., & Machlus, M. L. (2007). Major middle Miocene global climate change: Evidence from East Antarctica and the Transantarctic Mountains. Geological Society of America Bulletin, 119(11-12), 1449-1461.

Li, X., Jiang, D., Zhang, Z., Zhang, R., Tian, Z., & Yan, Q. (2015). Mid-Pliocene westerlies from PlioMIP simulations. Advances in Atmospheric Sciences, 32(7), 909-923.

Liebrand, D., de Bakker, A. T., Beddow, H. M., Wilson, P. A., Bohaty, S. M., Ruessink, G., ... & Huck, C. E. (2017). Evolution of the early Antarctic ice ages. Proceedings of the National Academy of Sciences, 114(15), 3867-3872.

Lisiecki, L. E., & Raymo, M. E. (2005). A Pliocene-Pleistocene stack of 57 globally distributed benthic δ18O records. Paleoceanography, 20(1).

Litchman, E., Klausmeier, C. A., & Yoshiyama, K. (2009). Contrasting size evolution in marine and freshwater diatoms. Proceedings of the National Academy of Sciences, 106(8), 2665-2670.

Lücke, A., Moschen, R., & Schleser, G. H. (2005). High-temperature carbon reduction of silica: a novel approach for oxygen isotope analysis of biogenic opal. Geochimica et Cosmochimica Acta, 69(6), 1423-1433.

Lunt, D. J., Foster, G. L., Haywood, A. M., & Stone, E. J. (2008). Late Pliocene Greenland glaciation controlled by a decline in atmospheric CO 2 levels. Nature, 454(7208), 1102.

Lunt, D. J., Valdes, P. J., Haywood, A., & Rutt, I. C. (2008). Closure of the Panama Seaway during the Pliocene: implications for climate and Northern Hemisphere glaciation. Climate Dynamics, 30(1), 1-18.

Lyle, M., & Baldauf, J. (2015). Biogenic sediment regimes in the Neogene equatorial Pacific, IODP Site U1338: Burial, production, and diatom community. Palaeogeography, Palaeoclimatology, Palaeoecology, 433, 106-128.

Lyle, M., Gibbs, S., Moore, T. C., & Rea, D. K. (2007). Late Oligocene initiation of the Antarctic circumpolar current: evidence from the South Pacific. Geology, 35(8), 691-694.

Mackay, A. W., Swann, G. E., Fagel, N., Fietz, S., Leng, M. J., Morley, D., ... & Tarasov, P. (2013). Hydrological instability during the Last Interglacial in central Asia: a new diatom oxygen isotope record from Lake Baikal. Quaternary Science Reviews, 66, 45-54.

Maddison, E. J., Pike, J., & Dunbar, R. (2012). Seasonally laminated diatom-rich sediments from Dumont d'Urville Trough, East Antarctic margin: Late-Holocene neoglacial sea-ice conditions. The Holocene, 22(8), 857-875.

Maier, E., Zhang, X., Abelmann, A., Gersonde, R., Mulitza, S., Werner, M., ... & Stein, R. (2018). North Pacific freshwater events linked to changes in glacial ocean circulation. Nature, 559(7713), 241.

Majewski, W. (2002). Mid-Miocene invasion of ecological niches by planktonic foraminifera of the Kerguelen Plateau, Antarctica. Marine Micropaleontology, 46(1-2), 59-81.

Majewski, W., & Bohaty, S. M. (2010). Surface-water cooling and salinity decrease during the Middle Miocene climate transition at Southern Ocean ODP Site 747 (Kerguelen Plateau). Marine Micropaleontology, 74(1-2), 1-14.

Malinverno, E., Maffioli, P., & Gariboldi, K. (2016). Latitudinal distribution of extant fossilizable phytoplankton in the Southern Ocean: Planktonic provinces, hydrographic fronts and palaeoecological perspectives. Marine Micropaleontology, 123, 41-58.

Marinov, I., Gnanadesikan, A., Toggweiler, J. R., & Sarmiento, J. L. (2006). The Southern Ocean biogeochemical divide. Nature, 441(7096), 964-967.

Marlow, J. R., Lange, C. B., Wefer, G., & Rosell-Melé, A. (2000). Upwelling intensification as part of the Pliocene-Pleistocene climate transition. Science, 290(5500), 2288-2291.

Martin, J. H., Fitzwater, S. E., & Gordon, R. M. (1990). Iron deficiency limits phytoplankton growth in Antarctic waters. Global Biogeochemical Cycles, 4(1), 5-12.

Martínez-Botí, M. A., Foster, G. L., Chalk, T. B., Rohling, E. J., Sexton, P. F., Lunt, D. J., ... & Schmidt, D. N. (2015). Plio-Pleistocene climate sensitivity evaluated using high-resolution CO_2 records. Nature, 518(7537), 49.

Martínez-Garcia, A., Rosell-Melé, A., Jaccard, S. L., Geibert, W., Sigman, D. M., & Haug, G. H. (2011). Southern Ocean dust–climate coupling over the past four million years. Nature, 476(7360), 312.

Martinson, D. G. (2011). Transport of warm upper circumpolar deep water onto the Western Antarctic Peninsula Continental Shelf. Ocean Science Discussions, 8(6), 2479.

Maruyama, T. (2000). Middle Miocene to Pleistocene diatom stratigraphy of Leg 167. In Lyle, M., Koizumi, I., Richter, C., and Moore, T.C., Jr. (Eds.), Proc. ODP, Sci. Results, 167, 63-110.

Maruyama, T., & Shiono, M. (2003). Middle Miocene to Pleistocene diatom biostratigraphy of the northwest Pacific at Sites 1150 and 1151. Proc. ODP, Sci. Results, 186, 1–38.

Maslin, M. A., Li, X. S., Loutre, M. F., & Berger, A. (1998). The contribution of orbital forcing to the progressive intensification of Northern Hemisphere glaciation. Quaternary Science Reviews, 17(4-5), 411-426.

Matheney, R. K., & Knauth, L. P. (1989). Oxygen-isotope fractionation between marine biogenic silica and seawater. Geochimica et Cosmochimica Acta, 53(12), 3207-3214.

Mazloff, M. R., Heimbach, P., & Wunsch, C. (2010). An eddy-permitting Southern Ocean state estimate. Journal of Physical Oceanography, 40(5), 880-899.

McCave, I. N., Crowhurst, S. J., Kuhn, G., Hillenbrand, C. D., & Meredith, M. P. (2014). Minimal change in Antarctic Circumpolar Current flow speed between the last glacial and Holocene. Nature geoscience, 7(2), 113.

McCollum, D.W. (1975). Diatom stratigraphy of the Southern Ocean. In: Hayes, D.E., Frakes, L.A., et al., Initial Reports of the Deep Sea Drilling Project, 28, 515-571.

McKay, R. M., Barrett, P. J., Levy, R. S., Naish, T. R., Golledge, N. R., & Pyne, A. (2016). Antarctic Cenozoic climate history from sedimentary records: ANDRILL and beyond. Philosophical Transactions of the Royal Society A: Mathematical, Physical and Engineering Sciences, 374(2059), 20140301.

McKay, R., Naish, T., Carter, L., Riesselman, C., Dunbar, R., Sjunneskog, C., ... & Schouten, S. (2012). Antarctic and Southern Ocean influences on Late Pliocene global cooling. Proceedings of the National Academy of Sciences, 109(17), 6423-6428.

McKelvey, B. C. (1991). The Cainozoic glacial record in South Victoria Land: A geological evaluation of the McMurdo Sound drilling projects. The Geology of Antarctica. Clarendon Press, Oxford, 434-454.

McLean, A. J. (2011). Morphological change and evolution of the marine diatom Thalassiosira torokina from upper Miocene to lower Pleistocene Antarctic marine sediments, Doctoral dissertation, Northern Illinois University.

Meehl, G. A., Arblaster, J. M., Chung, C. T., Holland, M. M., DuVivier, A., Thompson, L., ... & Bitz, C. M. (2019). Sustained ocean changes contributed to sudden Antarctic sea ice retreat in late 2016. Nature communications, 10(1), 14.

Meinshausen, M., Smith, S. J., Calvin, K., Daniel, J. S., Kainuma, M. L. T., Lamarque, J. F., ... & Thomson, A. G. J. M. V. (2011). The RCP greenhouse gas concentrations and their extensions from 1765 to 2300. Climatic change, 109(1-2), 213.

Mejía, L. M., Méndez-Vicente, A., Abrevaya, L., Lawrence, K. T., Ladlow, C., Bolton, C., ... & Stoll, H. (2017). A diatom record of CO_2 decline since the late Miocene. Earth and Planetary Science Letters, 479, 18-33.

Menicucci, A. J., Spero, H. J., Matthews, J., & Parikh, S. J. (2017). Influence of exchangeable oxygen on biogenic silica oxygen isotope data. Chemical Geology, 466, 710-721.

Meredith, M. (2019). The importance of the Southern Ocean and the key role of its freshwater cycle. Ocean Challenge, 23-32.

Mikkelsen, N., Labeyrie Jr, L., & Berger, W. H. (1978). Silica oxygen isotopes in diatoms: A 20,000 yr record in deep-sea sediments. Nature, 271(5645), 536.

Miller, K. G., Wright, J. D., & Fairbanks, R. G. (1991). Unlocking the ice house: Oligocene-Miocene oxygen isotopes, eustasy, and margin erosion. Journal of Geophysical Research: Solid Earth, 96(B4), 6829-6848.

Miller, K. G., Wright, J. D., Browning, J. V., Kulpecz, A., Kominz, M., Naish, T. R., ... & Sosdian, S. (2012). High tide of the warm Pliocene: Implications of global sea level for Antarctic deglaciation. Geology, 40(5), 407-410.

Mitchell, B. G., & Holm-Hansen, O. (1991). Observations of modeling of the Antartic phytoplankton crop in relation to mixing depth. Deep Sea Research Part A. Oceanographic Research Papers, 38(8), 981-1007.

Mitchell, B. G., Brody, E. A., Holm-Hansen, O., McClain, C., & Bishop, J. (1991). Light limitation of phytoplankton biomass and macronutrient utilization in the Southern Ocean. Limnology and Oceanography, 36(8), 1662-1677.

Mithal, R. and Becker, D. G. (2006). The Janus database: providing worldwide access to ODP and IODP data, Geol. Soc. Lond. Spec. Publ., 267, 253–259.

Montade, V., Kageyama, M., Combourieu-Nebout, N., Ledru, M. P., Michel, E., Siani, G., & Kissel, C. (2015). Teleconnection between the Intertropical Convergence Zone and southern westerly winds throughout the last deglaciation. Geology, 43(8), 735-738.

Moore, C. M., Seeyave, S., Hickman, A. E., Allen, J. T., Lucas, M. I., Planquette, H., ... & Poulton, A. J. (2007). Iron–light interactions during the CROZet natural iron bloom and EXport experiment (CROZEX) I: phytoplankton growth and photophysiology. Deep Sea Research Part II: Topical Studies in Oceanography, 54(18), 2045-2065.

Mopper, K., & Garlick, G. D. (1971). Oxygen isotope fractionation between biogenic silica and ocean water. Geochimica et Cosmochimica Acta, 35(11), 1185-1187.

Morche, W., Hubberten, H. W., Mackensen, A. & Keller, J. (1992). Geochemistry of Cenozoic ash layers from the Kerguelen Plateau (Leg 120) a first step toward a tephrostratigraphy of the southern Indian Ocean. Proceedings ODP, Sci Results, 120, 151-160.

Morley, D. W., Leng, M. J., Mackay, A. W., Sloane, H. J., Rioual, P., & Battarbee, R. W. (2004). Cleaning of lake sediment samples for diatom oxygen isotope analysis. Journal of Paleolimnology, 31(3), 391-401.

Moschen, R., Lücke, A., & Schleser, G. H. (2005). Sensitivity of biogenic silica oxygen isotopes to changes in surface water temperature and palaeoclimatology. Geophysical Research Letters, 32(7).

Mudelsee, M., & Raymo, M. E. (2005). Slow dynamics of the Northern Hemisphere glaciation. Paleoceanography, 20(4).

Nair, A., Mohan, R., Manoj, M. C., & Thamban, M. (2015). Glacial-interglacial variability in diatom abundance and valve size: Implications for Southern Ocean paleoceanography. Paleoceanography, 30(10), 1245-1260.

Naish, T., Powell, R., Levy, R., Wilson, G., Scherer, R., Talarico, F., ... & Carter, L. (2009). Obliquity-paced Pliocene West Antarctic ice sheet oscillations. Nature, 458(7236), 322.

Nakayama, Y., Timmermann, R., Rodehacke, C. B., Schröder, M., & Hellmer, H. H. (2014). Modeling the spreading of glacial meltwater from the Amundsen and Bellingshausen Seas. Geophysical Research Letters, 41(22), 7942-7949.

Nelson DM, Treguer P, Brzezinski MA, Leynaert A, Queguiner B. (1995). Production and dissolution of biogenic silica in the ocean: Revised global estimates, comparison with regional data and relationship to biogenic sedimentation. Global Biogeochemical Cycles, 9, 359–372.

Núñez-Riboni, I., & Fahrbach, E. (2009). Seasonal variability of the Antarctic Coastal Current and its driving mechanisms in the Weddell Sea. Deep Sea Research Part I: Oceanographic Research Papers, 56(11), 1927-1941.

O'Brien, P. E., Cooper, A. K., Florindo, F., Handwerger, D. A., Lavelle, M., Passchier, S., ... & Whitehead, J. M. (2004). Prydz Channel Fan and the history of extreme ice advances in Prydz Bay. In Proc. ODP, Sci. Results, 188, 1-32.

Ohneiser, C., & Wilson, G. S. (2018). Eccentricity-Paced Southern Hemisphere Glacial-Interglacial Cyclicity Preceding the Middle Miocene Climatic Transition. Paleoceanography and Paleoclimatology, 33(7), 795-806.

Olney, M. P., Bohaty, S. M., Harwood, D. M., & Scherer, R. P. (2009). *Creania lacyae* gen. nov. et sp. nov. and *Synedropsis cheethamii* sp. nov., fossil indicators of Antarctic sea ice? Diatom Research, 24(2), 357-375.

Olney, M. P., Scherer, R. P., Bohaty, S. M., & Harwood, D. M. (2005). Eocene–Oligocene paleoecology and the diatom genus Kisseleviella Sheshukova-Poretskaya from the Victoria Land Basin, Antarctica. Marine Micropaleontology, 58(1), 56-72.

Orejola, N., Passchier, S., & Expedition, I. O. D. P. (2014). Sedimentology of lower Pliocene to Upper Pleistocene diamictons from IODP Site U1358, Wilkes Land margin, and implications for East Antarctic Ice Sheet dynamics. Antarctic Science, 26(2), 183-192.

Orsi, A. H., & Whitworth III, T. (2005). Hydrographic Atlas of the World Ocean Circulation Experiment (WOCE) Volume 1: Southern Ocean.

Orsi, A. H., Whitworth III, T., & Nowlin Jr, W. D. (1995). On the meridional extent and fronts of the Antarctic Circumpolar Current. Deep Sea Research Part I: Oceanographic Research Papers, 42(5), 641-673.

Pagani, M., Freeman, K. H., & Arthur, M. A. (1999). Late Miocene atmospheric CO_2 concentrations and the expansion of C4 grasses. Science, 285(5429), 876-879.

Pahlow, M., Riebesell, U., & Wolf-Gladrow, D. A. (1997). Impact of cell shape and chain formation on nutrient acquisition by marine diatoms. Limnology and Oceanography, 42(8), 1660-1672.

Pälike, H., Norris, R. D., Herrle, J. O., Wilson, P. A., Coxall, H. K., Lear, C. H., ... & Wade, B. S. (2006). The heartbeat of the Oligocene climate system. Science, 314(5807), 1894-1898.

Parkinson, C. L., & Cavalieri, D. J. (2012). Antarctic sea ice variability and trends, 1979-2010, Cryosphere Discuss. 6, 931–956.

Parslow, J. S., Boyd, P. W., Rintoul, S. R., & Griffiths, F. B. (2001). A persistent subsurface chlorophyll maximum in the Interpolar Frontal Zone south of Australia: Seasonal progression and implications for phytoplankton-light-nutrient interactions. Journal of Geophysical Research: Oceans, 106(C12), 31543-31557.

Passchier, S. (2011). Linkages between East Antarctic Ice Sheet extent and Southern Ocean temperatures based on a Pliocene high-resolution record of ice-rafted debris off Prydz Bay, East Antarctica. Paleoceanography and Paleoclimatology, 26(4).

Patterson, M. O., McKay, R., Naish, T., Escutia, C., Jimenez-Espejo, F. J., Raymo, M. E., ... & Klaus, A. (2014). Orbital forcing of the East Antarctic ice sheet during the Pliocene and Early Pleistocene. Nature Geoscience, 7(11), 841.

Pearson, P. N. (2012). Oxygen isotopes in foraminifera: Overview and historical review. The Paleontological Society Papers, 18, 1-38.

Petersen, S. V., & Schrag, D. P. (2015). Antarctic ice growth before and after the Eocene-Oligocene transition: New estimates from clumped isotope paleothermometry. Paleoceanography and Paleoclimatology, 30(10), 1305-1317.

Pfuhl, H. A., & McCave, I. N. (2005). Evidence for late Oligocene establishment of the Antarctic Circumpolar Current. Earth and Planetary Science Letters, 235(3-4), 715-728.

Pierce, E. L., van de Flierdt, T., Williams, T., Hemming, S. R., Cook, C. P., & Passchier, S. (2017). Evidence for a dynamic East Antarctic ice sheet during the mid-Miocene climate transition. Earth and Planetary Science Letters, 478, 1-13.

Pike, J., Swann, G. E., Leng, M. J., & Snelling, A. M. (2013). Glacial discharge along the west Antarctic Peninsula during the Holocene. Nature Geoscience, 6(3), 199.

Pokras, E. M. (1991). A displaced neritic diatom (Delphineis karstenii) in pelagic sediments of the southeast Atlantic. Marine Micropaleontology, 17(3-4), 311-317.

Pollard, D., & DeConto, R. M. (2005). Hysteresis in Cenozoic Antarctic ice-sheet variations. Global and Planetary Change, 45(1-3), 9-21.

Pollard, D., & DeConto, R. M. (2009). Modelling West Antarctic ice sheet growth and collapse through the past five million years. Nature, 458(7236), 329.

Pollard, D., DeConto, R. M., & Alley, R. B. (2015). Potential Antarctic Ice Sheet retreat driven by hydrofracturing and ice cliff failure. Earth and Planetary Science Letters, 412, 112-121.

Pound, M. J., Haywood, A. M., Salzmann, U., & Riding, J. B. (2012). Global vegetation dynamics and latitudinal temperature gradients during the Mid to Late Miocene (15.97–5.33 Ma). Earth-Science Reviews, 112(1-2), 1-22.

Prabhu, A., Mahajan, P., Khaladkar, R., & Bawiskar, S. (2009). Connection between Antarctic sea-ice extent and Indian summer monsoon rainfall. International Journal of Remote Sensing, 30(13), 3485-3494.

Prebble, J. G. et al. (2013) An expanded modern dinoflagellate cyst dataset for the Southwest Pacific and Southern Hemisphere with environmental associations. Marine Micropaleontology. 101, 33–48.

Primeau, F. W., Holzer, M., & DeVries, T. (2013). Southern Ocean nutrient trapping and the efficiency of the biological pump. Journal of Geophysical Research: Oceans, 118(5), 2547-2564.

Queguiner, B. (2013). Iron fertilization and the structure of planktonic communities in high nutrient regions of the Southern Ocean. Deep Sea Research Part II: Topical Studies in Oceanography, 90, 43-54.

Quilty, P. G., Kerry, K. R., & Marchant, H. J. (1985). A seasonally recurrent patch of Antarctic planktonic diatoms. Search, 16(1), 48-51.

Rackow, T., Wesche, C., Timmermann, R., Hellmer, H. H., Juricke, S., & Jung, T. (2017). A simulation of small to giant Antarctic iceberg evolution: Differential impact on climatology estimates. Journal of Geophysical Research: Oceans, 122(4), 3170-3190.

Ravelo, A. C., & Andreasen, D. H. (2000). Enhanced circulation during a warm period. Geophysical Research Letters, 27(7), 1001-1004.

Ravelo, A. C., & Hillaire-Marcel, C. (2007). Chapter eighteen the use of oxygen and carbon isotopes of foraminifera in paleoceanography. Developments in Marine Geology, 1, 735-764.

Ravelo, A. C., Andreasen, D. H., Lyle, M., Lyle, A. O., & Wara, M. W. (2004). Regional climate shifts caused by gradual global cooling in the Pliocene epoch. Nature, 429(6989), 263.

Raymo, M. E., Kozdon, R., Evans, D., Lisiecki, L., & Ford, H. L. (2018). The accuracy of mid-Pliocene $\delta^{18}O$-based ice volume and sea level reconstructions. Earth-Science Reviews, 177, 291-302.

Raymo, M. E., Rind, D., & Ruddiman, W. F. (1990). Climatic effects of reduced Arctic sea ice limits in the GISS II general circulation model. Paleoceanography and Paleoclimatology, 5(3), 367-382

Reinardy, B. T. I., Escutia, C., Iwai, M., Jimenez-Espejo, F. J., Cook, C., van de Flierdt, T., & Brinkhuis, H. (2015). Repeated advance and retreat of the East Antarctic Ice Sheet on the

continental shelf during the early Pliocene warm period. Palaeogeography, Palaeoclimatology, Palaeoecology, 422, 65-84.

Rembauville, M., Blain, S., Armand, L., Quéguiner, B., & Salter, I. (2014). Export fluxes in a naturally fertilized area of the Southern Ocean, the Kerguelen Plateau: ecological vectors of carbon and biogenic silica to depth (Part 2). Biogeosciences Discuss, 11, 17089-17150.

Ren, H., Brunelle, B. G., Sigman, D. M., & Robinson, R. S. (2013). Diagenetic aluminum uptake into diatom frustules and the preservation of diatom-bound organic nitrogen. Marine Chemistry, 155, 92-101.

Renaudie, J. (2016). Quantifying the Cenozoic marine diatom deposition history: links to the C and Si cycles. Biogeosciences, 13(21), 6003-6014.

Rickert, D., Schlüter, M., & Wallmann, K. (2002). Dissolution kinetics of biogenic silica from the water column to the sediments. Geochimica et Cosmochimica Acta, 66(3), 439-455.

Rignot, E., Mouginot, J., Scheuchl, B., van den Broeke, M., van Wessem, M. J., & Morlighem, M. (2019). Four decades of Antarctic Ice Sheet mass balance from 1979–2017. Proceedings of the National Academy of Sciences, 116(4), 1095-1103.

Rigual-Hernández, A. S., Trull, T. W., Bray, S. G., Closset, I., & Armand, L. K. (2015). Seasonal dynamics in diatom and particulate export fluxes to the deep sea in the Australian sector of the southern Antarctic Zone. Journal of Marine Systems, 142, 62-74.

Rind, D., & Chandler, M. (1991). Increased ocean heat transports and warmer climate. Journal of Geophysical Research: Atmospheres, 96(D4), 7437-7461.

Rintoul, S. R. & da Silva, C. E. (2019) Antarctic Circumpolar Current. In Encyclopaedia of Ocean Sciences (Third Edition). (3) 248-261.

Rocchi, S., LeMasurier, W. E., & Di Vincenzo, G. (2006). Oligocene to Holocene erosion and glacial history in Marie Byrd Land, West Antarctica, inferred from exhumation of the Dorrel Rock intrusive complex and from volcano morphologies. Geological Society of America Bulletin, 118(7-8), 991-1005.

Romero, O. E., Rixen, T., & Herunadi, B. (2009). Effects of hydrographic and climatic forcing on diatom production and export in the tropical southeastern Indian Ocean. Marine Ecology Progress Series, 384, 69-82.

Romero, O., Armand, L. K., Crosta, X. & Pichon, J. J. (2005). The biogeography of major diatom taxa in Southern Ocean sediments: 3. Tropical/Subtropical species. Palaeogeography, Palaeoclimatology, Palaeoecology 223(1-2), 49-65.

Romero, O. E., Swann, G. E. A., Hodell, D. A., Helmke, P., Rey, D., & Rubio, B. (2011). A highly productive Subarctic Atlantic during the Last Interglacial and the role of diatoms. Geology, 39(11), 1015-1018.

Rovere, A., Raymo, M. E., Mitrovica, J. X., Hearty, P. J., O'Leary, M. J., & Inglis, J. D. (2014). The Mid-Pliocene sea-level conundrum: Glacial isostasy, eustasy and dynamic topography. Earth and Planetary Science Letters, 387, 27-33.

Sancetta, C., & Silvestri, S. (1986). Pliocene-Pleistocene evolution of the North Pacific Ocean-Atmosphere system, interpreted from fossil diatoms. Paleoceanography, 1(2), 163-180.

Sancetta, C., Heusser, L., Labeyrie, L., Sathy Naidu, A., Robinson, S.W. (1985). Wisconsin – Holocene paleoenvironment of the Bering Sea: evidence from diatoms, pollen, oxygen isotopes and clay minerals. Marine Geology, 62, 55–68.

Sangiorgi, F., Bijl, P. K., Passchier, S., Salzmann, U., Schouten, S., McKay, R., ... & Levy, R. (2018). Southern Ocean warming and Wilkes Land ice sheet retreat during the mid-Miocene. Nature communications, 9(1), 317.

Scambos, T. A., Bohlander, J. A., Shuman, C. U., & Skvarca, P. (2004). Glacier acceleration and thinning after ice shelf collapse in the Larsen B embayment, Antarctica. Geophysical Research Letters, 31(18).

Scher, H. D., Bohaty, S. M., Smith, B. W., & Munn, G. H. (2013). Isotopic interrogation of a suspected late Eocene glaciation. Paleoceanography, 29(6), 628-644.

Scher, H. D., Whittaker, J. M., Williams, S. E., Latimer, J. C., Kordesch, W. E., & Delaney, M. L. (2015). Onset of Antarctic Circumpolar Current 30 million years ago as Tasmanian Gateway aligned with westerlies. Nature, 523(7562), 580.

Scherer R.P., Bohaty S.M., and Harwood D.M. (2001). Oligocene and Lower Miocene Siliceous Microfossil Biostratigraphy of Cape Roberts Project Core CRP-2/2A, Victoria Land Basin, Antarctica. In: Studies from the Cape Roberts Project, Ross Sea, Antarctica, Scientific Report of CRP-2/2A, Barrett P.J. and Ricci C.A., eds., Terra Antartica 7(4), 417-442.

Scherer, R. P. (1994). A new method for the determination of absolute abundance of diatoms and other silt-sized sedimentary particles. Journal of Paleolimnology, 12(2), 171-179.

Scherer, R. P., Aldahan, A., Tulaczyk, S., Possnert, G., Engelhardt, H., & Kamb, B. (1998). Pleistocene collapse of the West Antarctic ice sheet. Science, 281(5373), 82-85.

Scherer, R. P., DeConto, R. M., Pollard, D., & Alley, R. B. (2016). Windblown Pliocene diatoms and East antarctic ice sheet retreat. Nature communications, 7, 12957.

Scherer, R. P., Sjunneskog, C. M., Iverson, N. R., & Hooyer, T. S. (2004). Assessing subglacial processes from diatom fragmentation patterns. Geology, 32(7), 557-560.

Schiff, C. J., Kaufman, D. S., Wolfe, A. P., Dodd, J., & Sharp, Z. (2009). Late Holocene storm-trajectory changes inferred from the oxygen isotope composition of lake diatoms, south Alaska. Journal of Paleolimnology, 41(1), 189-208.

Schmidt, M., Botz, R., Rickert, D., Bohrmann, G., Hall, S. R., & Mann, S. (2001). Oxygen isotopes of marine diatoms and relations to opal-A maturation. Geochimica et Cosmochimica Acta, 65(2), 201-211.

Schmidt, M., Botz, R., Stoffers, P., Anders, T., & Bohrmann, G. (1997). Oxygen isotopes in marine diatoms: A comparative study of analytical techniques and new results on the isotope composition of recent marine diatoms. Geochimica et Cosmochimica Acta, 61(11), 2275-2280.

Schmidtko, S., Heywood, K. J., Thompson, A. F., & Aoki, S. (2014). Multidecadal warming of Antarctic waters. Science, 346(6214), 1227-1231.

Schrader, H. J. (1974). Cenozoic marine planktonic diatom stratigraphy of the tropical Indian Ocean. Initial Reports of the Deep Sea Drilling Project, 24, 887-968.

Schrader, H. J. (1976). Cenozoic planktonic diatom biostratigraphy of the southern Pacific Ocean. Initial Reports of the Deep Sea Drilling Project., 35, 605-671.

Seeberg-Elverfeldt, I. A., Lange, C. B., Arz, H. W., Pätzold, J., & Pike, J. (2004). The significance of diatoms in the formation of laminated sediments of the Shaban Deep, Northern Red Sea. Marine Geology, 209(1-4), 279-301.

Seki, O., Foster, G. L., Schmidt, D. N., Mackensen, A., Kawamura, K., & Pancost, R. D. (2010). Alkenone and boron-based Pliocene pCO_2 records. Earth and Planetary Science Letters, 292(1-2), 201-211.

Serreze, M. C., & Stroeve, J. (2015). Arctic sea ice trends, variability and implications for seasonal ice forecasting. Philosophical Transactions of the Royal Society A: Mathematical, Physical and Engineering Sciences, 373(2045), 20140159.

Shakun, J. D., Corbett, L. B., Bierman, P. R., Underwood, K., Rizzo, D. M., Zimmerman, S. R., ... & Hay, C. C. (2018). Minimal East Antarctic Ice Sheet retreat onto land during the past eight million years. Nature, 558(7709), 284.

Shao, A. E., Gille, S. T., Mecking, S., & Thompson, L. (2015). Properties of the Subantarctic Front and Polar Front from the skewness of sea level anomaly. Journal of Geophysical Research: Oceans, 120(7), 5179-5193.

Shemesh, A., Burckle, L. H., & Hays, J. D. (1995). Late Pleistocene oxygen isotope records of biogenic silica from the Atlantic sector of the Southern Ocean. Paleoceanography, 10(2), 179-196.

Shemesh, A., Burckle, L.H., Hays, J.D. (1994). Meltwater input to the Southern Ocean during the Last Glacial Maximum. Science, 266, 1542–1544.

Shemesh, A., Charles, C. D., & Fairbanks, R. G. (1992). Oxygen isotopes in biogenic silica: global changes in ocean temperature and isotopic composition. Science, 256(5062), 1434-1436.

Shepherd, A., Gilbert, L., Muir, A. S., Konrad, H., McMillan, M., Slater, T., ... & Engdahl, M. (2019). Trends in Antarctic Ice Sheet Elevation and Mass. Geophysical Research Letters.

Shevenell, A. E., & Kennett, J. P. (2004). Paleoceanographic change during the middle Miocene climate revolution: an Antarctic stable isotope perspective. The Cenozoic Southern Ocean: Tectonics, Sedimentation, and Climate Change Between Australia and Antarctica, Geophys. Monogr. Ser, 151, 235-252.

Shevenell, A. E., Kennett, J. P., & Lea, D. W. (2004b). Middle Miocene Southern Ocean cooling and Antarctic cryosphere expansion. Science, 305(5691), 1766-1770.

Shevenell, A. E., Kennett, J. P., & Lea, D. W. (2008). Middle Miocene ice sheet dynamics, deep-sea temperatures, and carbon cycling: A Southern Ocean perspective. Geochemistry, Geophysics, Geosystems, 9(2).

Shipboard Scientific Party (2001), Leg 188 summary: Prydz Bay-Cooperation Sea, Antarctica, Proc. Ocean. Drill. Program, Sci. Results, 188, 1-65.

Shipboard Scientific Party (2001). Site 1165, Proc. ODP, Init. Repts, 188, 1–193.

Shipboard Scientific Party (1989). Site 744. Proc. ODP, Init. Repts., 119, 477–504.

Shipboard Scientific Party (1989). Site 747. Proc. ODP, Init. Repts., 120, 89–156.

Shipboard Scientific Party (2000). Site 1138. Proc. ODP, Init. Repts., 183, 1–205.

Shoenfelt, E. M., Winckler, G., Lamy, F., Anderson, R. F., & Bostick, B. C. (2018). Highly bioavailable dust-borne iron delivered to the Southern Ocean during glacial periods. Proceedings of the National Academy of Sciences, 115(44), 11180-11185.

Silvano, A., Rintoul, S. R., & Herraiz-Borreguero, L. (2016). Ocean-ice shelf interaction in East Antarctica. Oceanography, 29(4), 130-143.

Sims, P. A., Fryxell, G. A., & Baldauf, J. G. (1989). Critical examination of the diatom genus Azpeitia: Species useful as stratigraphic markers for the Oligocene and Miocene Epochs. Micropaleontology, 293-307.

Sjunneskog, C., & Winter, D. (2012). A diatom record of late Pliocene cooling from the Ross Sea continental shelf, AND-1B, Antarctica. Global and Planetary Change, 96, 87-96.

Smedsrud, L. H., Jenkins, A., Holland, D. M., & Nøst, O. A. (2006). Modeling ocean processes below Fimbulisen, Antarctica. Journal of Geophysical Research: Oceans, 111(C1).

Smetacek, V., Klaas, C., Strass, V. H., Assmy, P., Montresor, M., Cisewski, B., ... & Bathmann, U. (2012). Deep carbon export from a Southern Ocean iron-fertilized diatom bloom. Nature, 487(7407), 313.

Smith, A. C., Leng, M. J., Swann, G. E., Barker, P. A., Mackay, A. W., Ryves, D. B., ... & Hems, M. (2015). An experiment to assess the effects of diatom dissolution on oxygen isotope ratios. Rapid Communications in Mass Spectrometry, 30(2), 293-300.

Sniderman, J. K., Woodhead, J. D., Hellstrom, J., Jordan, G. J., Drysdale, R. N., Tyler, J. J., & Porch, N. (2016). Pliocene reversal of late Neogene aridification. Proceedings of the National Academy of Sciences, 113(8), 1999-2004.

Sokolov, S., & Rintoul, S. R. (2007). On the relationship between fronts of the Antarctic Circumpolar Current and surface chlorophyll concentrations in the Southern Ocean. Journal of Geophysical Research: Oceans, 112(C7).

Solheim, A., Forsberg, C. F., & Pittenger, A. (1991). Stepwise consolidation of glacigenic sediments related to the glacial history of Prydz Bay, East Antarctica. In Proc. ODP, Init. Repts., 119, 169-182.

Sosdian, S. M., Greenop, R., Hain, M. P., Foster, G. L., Pearson, P. N., & Lear, C. H. (2018). Constraining the evolution of Neogene ocean carbonate chemistry using the boron isotope pH proxy. Earth and Planetary Science Letters, 498, 362-376.

Spero, H. J., Bijma, J., Lea, D. W., & Bemis, B. E. (1997). Effect of seawater carbonate concentration on foraminiferal carbon and oxygen isotopes. Nature, 390(6659), 497.

Stevens Goddard, A. L., & Carrapa, B. (2018). Using basin thermal history to evaluate the role of Miocene–Pliocene flat-slab subduction in the southern Central Andes (27°S–30°S). Basin Research, 30(3), 564-585.

Stickley, C. E., Brinkhuis, H., McGonigal, K. L., Chaproniere, G. C. H., Fuller, M., Kelly, D. C., ... & Suzuki, N. (2004). Late Cretaceous–Quaternary biomagnetostratigraphy of ODP Sites 1168, 1170, 1171, and 1172, Tasmanian Gateway. In Proc. ODP, Init. Repts., 189, 1-57.

Stickley, C. E., Brinkhuis, H., Schellenberg, S. A., Sluijs, A., Röhl, U., Fuller, M., ... & Williams, G. L. (2004). Timing and nature of the deepening of the Tasmanian Gateway. Paleoceanography, 19(4).

Stickley, C. E., St John, K., Koç, N., Jordan, R. W., Passchier, S., Pearce, R. B., & Kearns, L. E. (2009). Evidence for middle Eocene Arctic sea ice from diatoms and ice-rafted debris. Nature, 460(7253), 376.

Strass, V. H., Garabato, A. C. N., Pollard, R. T., Fischer, H. I., Hense, I., Allen, J. T., ... & Smetacek, V. (2002). Mesoscale frontal dynamics: shaping the environment of primary production in the

Antarctic Circumpolar Current. Deep Sea Research Part II: Topical Studies in Oceanography, 49(18), 3735-3769.

Sugden, D. E. (1996). The East Antarctic ice sheet: unstable ice or unstable ideas? Transactions of the Institute of British Geographers, 443-454.

Sugden, D. E., Marchant, D. R., & Denton, G. H. (1993). The case for a stable East Antarctic ice sheet: the background. Geografiska Annaler: Series A, Physical Geography, 75(4), 151-154.

Sugden, D. E., Summerfield, M. A., Denton, G. H., Wilch, T. I., McIntosh, W. C., Marchant, D. R., & Rutford, R. H. (1999). Landscape development in the Royal Society Range, southern Victoria Land, Antarctica: stability since the mid-Miocene. Geomorphology, 28(3-4), 181-200.

Sugden, D., & Denton, G. (2004). Cenozoic landscape evolution of the Convoy Range to Mackay Glacier area, Transantarctic Mountains: onshore to offshore synthesis. Geological Society of America Bulletin, 116(7-8), 840-857.

Super, J. R., Thomas, E., Pagani, M., Huber, M., O'Brien, C., & Hull, P. M. (2018). North Atlantic temperature and pCO_2 coupling in the early-middle Miocene. Geology, 46(6), 519-522.

Suto, I. (2004). Taxonomy of the diatom resting spore form genus Liradiscus Greville and its stratigraphic significance. Micropaleontology, 50(1), 59-79.

Swann, G. E., & Leng, M. J. (2009). A review of diatom $\delta^{18}O$ in palaeoceanography. Quaternary Science Reviews, 28(5-6), 384-398.

Swann, G. E., Leng, M. J., Juschus, O., Melles, M., Brigham-Grette, J., & Sloane, H. J. (2010). A combined oxygen and silicon diatom isotope record of Late Quaternary change in Lake El'gygytgyn, North East Siberia. Quaternary Science Reviews, 29(5-6), 774-786.

Swann, G. E., Leng, M. J., Sloane, H. J., & Maslin, M. A. (2008). Isotope offsets in marine diatom δ18O over the last 200 ka. Journal of Quaternary Science: Published for the Quaternary Research Association, 23(4), 389-400.

Swann, G. E., Pike, J., Snelling, A. M., Leng, M. J., & Williams, M. C. (2013). Seasonally resolved diatom δ18O records from the west Antarctic Peninsula over the last deglaciation. Earth and Planetary Science Letters, 364, 12-23.

Swann, G. E., Snelling, A. M., & Pike, J. (2016). Biogeochemical cycling in the Bering Sea over the onset of major Northern Hemisphere Glaciation. Paleoceanography, 31(9), 1261-1269.

Tamsitt, V., Drake, H. F., Morrison, A. K., Talley, L. D., Dufour, C. O., Gray, A. R., ... & Weijer, W. (2017). Spiraling pathways of global deep waters to the surface of the Southern Ocean. Nature communications, 8(1), 172.

Tang, Z., Shi, X., Zhang, X., Chen, Z., Chen, M. T., Wang, X., ... & Ge, S. (2016). Deglacial biogenic opal peaks revealing enhanced Southern Ocean upwelling during the last 513 ka. Quaternary international, 425, 445-452.

Taylor-Silva, B. I., & Riesselman, C. R. (2018). Polar frontal migration in the warm late Pliocene: Diatom evidence from the Wilkes Land margin, East Antarctica. Paleoceanography and Paleoclimatology, 33(1), 76-92.

Taylor, F., & Sjunneskog, C. (2002). Postglacial marine diatom record of the Palmer deep, Antarctic Peninsula (ODP Leg 178, site 1098) 2. Diatom assemblages. Paleoceanography and Paleoclimatology, 17(3).

Teitler, L., Florindo, F., Warnke, D. A., Filippelli, G. M., Kupp, G., & Taylor, B. (2015). Antarctic Ice Sheet response to a long warm interval across Marine Isotope Stage 31: A cross-latitudinal study of iceberg-rafted debris. Earth and planetary science letters, 409, 109-119.

Tremblay, J. E., Lucas, M. I., Kattner, G., Pollard, R., Strass, V. H., Bathmann, U., & Bracher, A. (2002). Significance of the Polar Frontal Zone for large-sized diatoms and new production during summer in the Atlantic sector of the Southern Ocean. Deep Sea Research Part II: Topical Studies in Oceanography, 49(18), 3793-3811.

Tyler, J. J., Leng, M. J., Sloane, H. J., Sachse, D., & Gleixner, G. (2008). Oxygen isotope ratios of sedimentary biogenic silica reflect the European transcontinental climate gradient. Journal of Quaternary Science: Published for the Quaternary Research Association, 23(4), 341-350.

Tyler, J. J., Sloane, H. J., Rickaby, R. E., Cox, E. J., & Leng, M. J. (2017). Post-mortem oxygen isotope exchange within cultured diatom silica. Rapid Communications in Mass Spectrometry, 31(20), 1749-1760.

van Bennekom, A.J., Buma, A.G.J., Nolting, R.F. (1991). Dissolved aluminum in the Weddell-Scotia confluence and effect of Al on the dissolution kinetics of biogenic silica. Marine Chemistry, 35: 423-434.

Venables, H., & Moore, C. M. (2010). Phytoplankton and light limitation in the Southern Ocean: Learning from high-nutrient, high-chlorophyll areas. Journal of Geophysical Research: Oceans, 115(C2), 199-221.

Verdy, A., Follows, M., & Flierl, G. (2009). Optimal phytoplankton cell size in an allometric model. Marine Ecologial Progress Series, 379, 1-12.

Villa, G., Fioroni, C., Persico, D., Roberts, A. P., & Florindo, F. (2014). Middle Eocene to Late Oligocene Antarctic glaciation/deglaciation and Southern Ocean productivity. Paleoceanography and Paleoclimatology, 29(3), 223-237.

Vincent, E., & Berger, W. H. (1985). Carbon dioxide and polar cooling in the Miocene: The Monterey hypothesis. The carbon cycle and atmospheric CO_2: Natural variations Archean to present, 32, 455-468.

Vivier, F., Park, Y. H., Sekma, H., & Le Sommer, J. (2015). Variability of the Antarctic Circumpolar Current transport through the Fawn Trough, Kerguelen Plateau. Deep Sea Research Part II: Topical Studies in Oceanography, 114, 12-26.

Wang, C. H., & Yeh, H. W. (1985). Oxygen isotopic compositions of DSDP Site 480 diatoms: Implications and applications. Geochimica et Cosmochimica Acta, 49(6), 1469-1478.

Ward, P., Whitehouse, M., Meredith, M., Murphy, E., Shreeve, R., Korb, R., ... & Cunningham, N. (2002). The southern antarctic circumpolar current front: physical and biological coupling at South Georgia. Deep Sea Research Part I: Oceanographic Research Papers, 49(12), 2183-2202.

Warny, S., Askin, R. A., Hannah, M. J., Mohr, B. A., Raine, J. I., Harwood, D. M., ... & SMS Science Team. (2009). Palynomorphs from a sediment core reveal a sudden remarkably warm Antarctica during the middle Miocene. Geology, 37(10), 955-958.

Watson, A. J., Bakker, D. C. E., Ridgwell, A. J., Boyd, P. W., & Law, C. S. (2000). Effect of iron supply on Southern Ocean CO2 uptake and implications for glacial atmospheric CO2. Nature, 407(6805), 730-733.

Weaver, F. M., & Gombos Jr, A. M. (1981). Southern high-latitude diatom biostratigraphy. SEPM Special Publication, The DSDP: a decade of progress. 32.

Webb, P. N., Harwood, D. M., McKelvey, B. C., Mercer, J. H., & Stott, L. D. (1984). Cenozoic marine sedimentation and ice-volume variation on the East Antarctic craton. Geology, 12(5), 287-291.

Wefer, G. (2015). Paleoceanographic proxies. Encyclopedia of Marine Geosciences, 1-9.

Westerhold, T., Bickert, T., & Röhl, U. (2005). Middle to late Miocene oxygen isotope stratigraphy of ODP site 1085 (SE Atlantic): new constrains on Miocene climate variability and sea-level fluctuations. Palaeogeography, Palaeoclimatology, Palaeoecology, 217(3), 205-222.

Wetzel, F., De Souza, G. F., & Reynolds, B. C. (2014). What controls silicon isotope fractionation during dissolution of diatom opal? Geochimica et Cosmochimica Acta, 131, 128-137.

Whitehead, J. M., & Bohaty, S. M. (2003). Pliocene summer sea surface temperature reconstruction using silicoflagellates from Southern Ocean ODP Site 1165. Paleoceanography, 18(3).

Whitehead, J. M., & McMinn, A. (2002). Kerguelen Plateau Quaternary–late Pliocene palaeoenvironments: from diatom, silicoflagellate and sedimentological data. Palaeogeography, Palaeoclimatology, Palaeoecology, 186(3-4), 335-368.

Whitehead, J. M., Harwood, D. M., McKelvey, B. C., Hambrey, M. J., & McMinn, A. (2004). Diatom biostratigraphy of the Cenozoic glaciomarine Pagodroma Group, northern Prince Charles Mountains, East Antarctica. Australian Journal of Earth Sciences, 51(4), 521-547.

Whitehead, J. M., Quilty, P. G., Harwood, D. M., & McMinn, A. (2001). Early Pliocene paleoenvironment of the Sørsdal Formation, Vestfold Hills, based on diatom data. Marine Micropaleontology, 41(3-4), 125-152.

Whitehead, J. M., Quilty, P. G., McKelvey, B. C., & O'Brien, P. E. (2006). A review of the Cenozoic stratigraphy and glacial history of the Lambert Graben—Prydz Bay region, East Antarctica. Antarctic Science, 18(1), 83-99.

Whitehead, J. M., Wotherspoon, S., & Bohaty, S. M. (2005). Minimal Antarctic sea ice during the Pliocene. Geology, 33(2), 137-140.

Williams, G. D., Herraiz-Borreguero, L., Roquet, F., Tamura, T., Ohshima, K. I., Fukamachi, Y., ... & Harcourt, R. (2016). The suppression of Antarctic bottom water formation by melting ice shelves in Prydz Bay. Nature Communications, 7, 12577.

Williams, T., van de Flierdt, T., Hemming, S. R., Chung, E., Roy, M., & Goldstein, S. L. (2010). Evidence for iceberg armadas from East Antarctica in the Southern Ocean during the late Miocene and early Pliocene. Earth and Planetary Science Letters, 290(3-4), 351-361.

Wilson, D. S., Pollard, D., DeConto, R. M., Jamieson, S. S., & Luyendyk, B. P. (2013). Initiation of the West Antarctic Ice Sheet and estimates of total Antarctic ice volume in the earliest Oligocene. Geophysical research letters, 40(16), 4305-4309.

Winter, D., & Iwai, M. (2002). Data report: Neogene diatom biostratigraphy, Antarctic Peninsula Pacific margin, ODP Leg 178 rise sites. In Proc. ODP, Sci. Results (Vol. 178, pp. 1-25).

Winter, D. (2001). Data report: diatom biostratigraphic data and plates from ODP Leg 172, Hole 1063D, with brief discussion of present ecological affinities of taxa. Proc. ODP, Sci. Results, 172, 1–49.

Winter, D., Sjunneskog, C., & Harwood, D. (2010). Early to mid-Pliocene environmentally constrained diatom assemblages from the AND-1B drillcore, McMurdo Sound, Antarctica. Stratigraphy, 7(2), 207.

Winter, D., Sjunneskog, C., Scherer, R., Maffioli, P., Riesselman, C., & Harwood, D. (2012). Pliocene–Pleistocene diatom biostratigraphy of nearshore Antarctica from the AND-1B drillcore, McMurdo Sound. Global and Planetary Change, 96, 59-74.

Wolfe, C. L., & Cessi, P. (2011). The adiabatic pole-to-pole overturning circulation. Journal of Physical Oceanography, 41(9), 1795-1810.

Woodruff, F., & Savin, S. (1991). Mid-Miocene isotope stratigraphy in the deep sea: High-resolution correlations, paleoclimatic cycles, and sediment preservation. Paleoceanography, 6(6), 755-806.

Wright, J. D., Miller, K. G., & Fairbanks, R. G. (1991). Evolution of modern deepwater circulation: Evidence from the late Miocene Southern Ocean. Paleoceanography, 6(2), 275-290.

Wright, N. M., Scher, H. D., Seton, M., Huck, C. E., & Duggan, B. D. (2018). No change in Southern Ocean circulation in the Indian Ocean from the Eocene through late Oligocene. Paleoceanography and Paleoclimatology, 33(2), 152-167.

Xiong, Z., Li, T., Crosta, X., Algeo, T., Chang, F., & Zhai, B. (2013). Potential role of giant marine diatoms in sequestration of atmospheric CO2 during the Last Glacial Maximum: $\delta^{13}C$ evidence from laminated Ethmodiscus rex mats in tropical West Pacific. Global and Planetary Change, 108, 1-14.

Yanagisawa, Y. & Akiba, F. (1990). Taxonomy and phylogeny of the three marine diatom genera, Crucidenticula, Denticulopsis and Neodenticula. Bulletin of the Geological Survey of Japan, 41(5): 197-301

Zachos, J. C., Dickens, G. R., & Zeebe, R. E. (2008). An early Cenozoic perspective on greenhouse warming and carbon-cycle dynamics. Nature, 451(7176), 279.

Zachos, J. C., Quinn, T. M., & Salamy, K. A. (1996). High-resolution (104 years) deep-sea foraminiferal stable isotope records of the Eocene-Oligocene climate trasition. transition. Paleoceanography and Paleoclimatology, 11(3), 251-266.

Zachos, J., Pagani, M., Sloan, L., Thomas, E., & Billups, K. (2001). Trends, rhythms, and aberrations in global climate 65 Ma to present. science, 292(5517), 686-693.

Zhang, Y. G., Pagani, M., Liu, Z., Bohaty, S. M., & DeConto, R. (2013). A 40-million-year history of atmospheric CO2. Philosophical Transactions of the Royal Society A: Mathematical, Physical and Engineering Sciences, 371(2001), 20130096.

11. Appendix 1: Assignment of Neogene diatom species' palaeocological preferences

1. Group 1: warm water species

1.1.1. Extant taxa

Actinocyclus ehrenbergii* (maximum observed abundance at ODP Site 1165 <1%; documented at ODP Site 1165 between 10.62 - 9.32 Ma): A. ehrenbergii* has been found with brackish species in outcrops from Arizona (Bradbury & Krebbs, 1995). However, it is primarily a planktonic cosmopolitan diatom species (Winter, 2001) and, as such, is included in the warm group at Site 1165.

***Actinoptychus senarius* (<1%; 14.73 - 7.52 Ma):** *A. senarius* is generally considered a long-ranging, cosmopolitan diatom (Winter, 2001) and, between 15-12 Ma, is more abundant at Site 747 (4%) than at Site 1165 (<1%). I have included it in the warm water group, however, it has also been suggested that *A. senarius* could be meroplanktonic (Winter, 2001; Abrantes, 1988).

Coscinodiscus marginatus* (1%; present prior 2.50 Ma): Coscinodiscus marginatus* is a cosmopolitan diatom (Barron, 1985) and is more abundant at Site 747 (13%) than at Site 1165 (1%), at least during the Middle Miocene. It is frequently documented in equatorial regions (Lyle & Baldauf, 2015) and, therefore, likely indicates relatively warm waters in the Southern Ocean.

Dactyliosolen antarcticus* (valves <1%, but girdle bands are more numerous; present throughout the 15 Ma record): D. antarcticus* is assigned a warm, open-ocean ecology based on its previous use as a warm-water indicator in Antarctic Pliocene diatom assemblage records (Sjunneskog & Winter, 2012; Whitehead et al., 2001; Whitehead & McMinn, 2002). Considering silicoflagellate sea surface temperature (SST) associations (Whitehead & McMinn, 2002), *D. antarcticus* is assumed to proliferate at SSTs of c. 4°C. Unfortunately, valves are rarely preserved. Girdle bands are preserved, however, girdle bands were not included in quantitative diatom assemblage analysis because the number of girdle bands per valve varies, and so an accurate quantification of valve numbers using girdle bands is impossible.

***Fragilariopsis pseudonana* (<1%; 10.12 Ma - present)**: *F. pseudonana* is a cosmopolitan diatom species which, within the Southern Ocean, is most abundant north of the Subantarctic Front,

proliferating at SSTs of between –1.33°C and 14.06°C (Cefarelli et al., 2010). It is first documented at Site 1165 at 10.12 Ma, although its early appearances may represent an ancestor or early form, rather than the true first appearance of *F. pseudonana*.

***Fragilariopsis rhombica* (<1%*;* only documented in one sample at 0.25 Ma)**: *F. rhombica* is an endemic Southern Ocean species documented at SSTs of between –1.6 to 13.35°C (Cefarelli et al., 2010). It is found throughout the Southern Ocean north of the sea ice edge, however, its higher relative abundance within the subantarctic zone (Cefarelli et al., 2010) is the reason for its inclusion in the warm group.

Hemidiscus cuneiformis* (1%; 9.79 - 5.21 Ma)*, Hemidiscus karstenii* (& *karstenii f.1)* (1%; 9.04 - 5.66 Ma)*, Hemidiscus ovalis* (<1%; only documented in one sample at 5.21 Ma)*, Hemidiscus triangularis* (<1%; only documented in two samples between 7.30 - 6.91 Ma)*: The *Hemidiscus* spp. group occur at low abundances at Site 1165. *H. karstenii* and *H. triangularis* are endemic to the Southern Ocean, however, Censarek (2002) inferred warm water preferences for all *Hemidiscus* species given the usual association of the modern taxa with warmer waters (Hasle et al., 1996). *H. karstenii* is more abundant in the Southern Ocean during Pleistocene interglacials than glacials (Burckle, 1982), while *H. triangularis* has been documented in the Southwest Pacific (Ciesieski, 1983). Censarek (2002) also documented the co-occurrence of *H. triangularis* and *Azpeitia tabularis* at subantarctic ODP Sites 1092 and 1088. As such, I have included the *Hemidiscus* spp. group within the warm species group.

***Shionodiscus tetraoestrupii* (19%; 5.23 Ma - present)**: *S. tetraoestrupii* is a modern subantarctic species generally associated with SSTs of 5 to 20°C (Winter et al., 2010). It also co-occurs with *Stellarima stellaris*, *Thalassiosira teres*, *Fragilariopsis laqueata* and *Fragilariopsis bohatyii* in the late Pliocene ANDRILL core (Sjunneskog & Winter, 2012) and was assigned a warm, summer ecology. This species was also noted to be less tolerant of fresher water than some others (namely *Thalassiosira vulnifica* and *Rouxia antarctica*) (Sjunneskog & Winter, 2012), but is likely most strongly associated with warm waters at Site 1165.

Shionodiscus tetraoestrupii* var. *reimerii* (1%; 2.41 Ma - 1.30 Ma)*: Based on the palaeo-occurrences of *S. tetraoestrupii* var. *remerii* (Sjunneskog & Winter, 2012), this species is more abundant north of the Polar Front and so represents warmer water at Site 1165. It has also

been linked to water column stratification (Winter et al., 2010) but, for this study, I keep this species in the warm group.

Stellarima stellaris* (2%; 9.86 Ma - present): S. stellaris* is a modern subantarctic (Winter et al., 2010) and, even, cosmopolitan (Winter, 2001) diatom species. Within Pliocene records, based on its co-occurrence with *Shionodiscus tetraoestrupii* and *Thalassiosira teres* in the ANDRILL core (Winter et al., 2010), Sjunneskog & Winter (2012) assigned *S. stellaris* to temperate summer conditions.

***Thalassionema nitzschioides* var. *parva* (6%; present throughout the entire 15 Ma record):** *T. nitzschioides* var. *parva* was documented at the equatorial Pacific IODP Site U1338 throughout the Neogene (Lyle & Baldauf, 2015), where it was linked to warm SSTs. In my records, It is more abundant at ODP Site 747 (15%) than Site 1165 (<6%) between 15-12 Ma and, as such, is assigned to the warm water group.

1.1.1.1. Extinct taxa

***Actinocyclus ingens* (54%; present from 15 Ma until 0.89 Ma):** *A. ingens* is a cosmopolitan diatom frequently documented in low latitude regions (Lazarus, 1994; Barron, 1985). It is more abundant at Site 747 (up to 83%) than Site 1165 (up to 54%) and is, thus, assumed to indicate warm waters at Site 1165 (Figure 2 in Chapter 5 for additional support for warm-associated interpretation).

***Actinocyclus ingens* var. *nodus* (15%; 14.63 - 10.41 Ma):** Including *A. ingens* var. *nodus* within the '*A. ingens* group' improves the comparison with $\delta^{18}O_{foram}$ at Site 747 (Figure 2, Chapter 5). *A. ingens* var. *nodus* is also much more abundant at Site 747 (up to 72%) than at Site 1165 (15%) and, as such, can be considered a relatively warm water indicator species.

Actinocyclus ingens* var. *ovalis* (2%; 8.76 - 5.87 Ma): A. ingens* var. *ovalis* is an endemic Southern high latitude species (Censarek, 2002), however, it co-occurs with other varieties of *A. ingens* which prefer warmer waters (Gersonde & Burkle, 1990). Further, it was suggested by Gersonde (1990) that *A. ingens* var. *ovalis* was, in fact, *Hemidiscus karstenii* f. 1 (Ciesielski, 1983), which has a subantarctic distribution. As such, *A. ingens* var. *ovalis* has been described as a warm associated diatom (Censarek (2002).

Actinocyclus* sp. nov #2 (1%; 14.10 - 6.20 Ma, although the younger occurrences may represent reworking)*: This is a new species (see Appendix 2 for full description) and is assigned to the warm group because it is more abundant at Site 747 (5%) than at Site 1165 (<1%) from 15-12 Ma.

***Azpeitia* species (<2%; present for the entire 15 Ma interval):** Species of *Azpeitia* are generally assumed to indicate relatively warm waters (Sims et al., 1989). The *Azpeitia* spp. group is more abundant at Site 747 (17%) than Site 1165 (<2%) and, as such, the unidentified (to species level) *Azpeitia* species that comprise this group are assigned a warm water ecology.

***Azpeitia tabularis* group *(Azpeitia endoi* and *Azpeitia tabularis*) (27%; present for the entire 15 Ma interval):** *A. endoi* and *A. tabularis* are combined here (see Appendix 2), however, *A. tabularis* is extant, while *A. endoi* is extinct. In terms of palaeoecology, *A. tabularis* is associated with the subantarctic zone in the modern Southern Ocean (Nair et al., 2015; Crosta et al., 2005). Based on morphological and taxonomic similarities between the two, as well as common low latitude occurrences of *A. endoi* in fossil assemblages (e.g. Schrader, 1974)*, A. endoi* is also assumed to prefer warmer conditions. Futher, the group is generally more abundant between 15-12 Ma at Site 747 (>13 %) than at Site 1165 (<4 %, except for one anomalous Site 1165 sample at 13.44 Ma which contains >27%).

Caviatus jouseanus* (1%; present from the beginning of the record to 14.17 Ma)*: *C. jouseanus* is considered a cosmopolitan Neogene diatom (Barron, 1985) and is more abundant at Site 747 (25%) than at Site 1165 (1%).

***Crucidenticula nicobarica* (2%; 14.30 - 12.65 Ma):** *Crucidenticula* is generally considered a low latitude genus, where it can comprise up to 50% of the diatom assemblage (Yanagisawa & Akiba, 1990). *C. nicobarica* is much more abundant at Site 747 (38 %) than at Site 1165 (2%), so is included in the warm group.

Fragilariopsis interfrigidaria* (3%; 3.80 - 2.18 Ma)*: *F. interfrigidaria* was associated with relatively high-nutrient, warm sea surface temperature conditions based on its co-occurrence with *Thalassionema nitszchioides* in the Late Pliocene AND-1B core (Winter et al., 2010). It is also common in the northern Southern Ocean (Lazarus, 1994).

***Fragilariopsis matuyamae* (<1%; documented in only one sample at 2.50 Ma):** *F. matuyamae* is found in the upper Pliocene of northern Southern Ocean sites and, thus, is assumed to be a relatively warm-water *Fragliariopsis* species (Gersonde & Barcena, 1998).

Nitzschia porteri* (<1%; 14.01 - 9.66 Ma)*: *N. porteri* has a cosmopolitan distribution (Barron, 1985) and has been documented in the equatorial Pacific Ocean (Baldauf, 2013).

Fragilariopsis praeinterfrigidaria* (10%; 6.91 - 2.82 Ma)*: *F. praeinterfrigidaria* likely had similar ecological preferences to its descendant, *F. interfrigidaria*, and has been described as a warm species based on its co-occurrence with *Thalassiosira inura* in the Late Pliocene AND-1B core (Winter et al., 2010) and its occurrences in the northern Southern Ocean (Lazarus, 1994).

***Fragilariopsis weaveri* (2%; 3.22 - 2.41 Ma):** Most *Fragliariopsis* species are associated with cold water or sea ice (Crosta et al., 2005; Armand et al., 2005), however, *F. weaveri* is interpreted as a subantarctic species that proliferates north of the Polar Front and has been used to reconstruct movements of the Polar Front during the Pliocene (Taylor-Silva & Riesselman, 2018). The first occurrence of this species in the Southern Ocean is between 4.31 and 3.1 Ma (3.22 Ma at Site 1165), during the relatively warm Pliocene (Cody et al., 2008).

***Fragilariopsis clementia* (<1%; 5.35 - 2.41 Ma)**: *F. clementia* first occurs at IODP Site U1361 (situated at 64°S; a similar latitude to Site 1165) during a Pliocene interglacial at 3.15 Ma, and is used to infer the incursion of warmer waters (and a poleward shift of the Polar Front) at that site (Taylor-Silva & Riesselman 2018). It also co-occurs with *Fragilariopsis weaverii* in the same record and, as such, is assigned warm water preferences. At Site 1165, *F. clementia* appears earlier at 5.35 Ma, in line with its proposed first occurrence (FO) in the Southern Ocean, which is at 8.85 Ma at slightly lower latitudes (Sangiorgi et al., 2018), and indicates the southward migration of warm waters during the Pliocene.

***Fragilariopsis miocenica* (1%; 8.71 - 6.10 Ma):** *F. miocenica* is a cosmopolitan diatom found at low latitudes, for example, in the equatorial Pacific (Baldauf, 2013).

Fragilariopsis reinholdii* (3%; 5.23 - 3.06 Ma)*: *F. reinholdii* exhibits a warm water ecology. This interpretation is based on its cosmopolitan distribution (Barron, 1985) and highest abundances within warmer water masses (Sancetta and Silvestri, 1986; Barron, 1992). Censarek (2002) also

documented *F. reinholdii* only at their northern-most Southern Ocean ODP sites (Sites 1088 and 1092, not at Sites 689 and 690).

***Rouxia californica* (3%; 9.04 - 3.96 Ma):** *R. californica* has a lower latitude distribution compared to other *Rouxia* species found at Site 1165 (Lazarus, 1994), and is used as a biostratigraphic marker in mid-latitude records, e.g. in the California Basin (Barron, 1985).

***Rouxia peragalli* (13%; 8.65-5.23 Ma):** *R. peragalli* is a cosmopolitan species documented from equatorial regions and the northern mid-high latitudes as well as in the Southern Ocean (Lazarus, 1994).

***Shionodiscus praeoestrupii* (2%; 8.35 - 4.39 Ma)**: *S. praeoestrupii* likely has a warm-associated ecology based on its palaeo-occurrences and the preferences of its descendent *S. oestrupii*, which is most abundant at ODP Sites underlying relatively warm waters (Sjunneskog & Winter, 2012).

***Thalassiosira complicata* (4%; 5.77 - 2.52 Ma)**: *T. complicata* is inferred to be a warm-associated species based on its co-occurrence with *Thalassiosira inura* in the Late Pliocene AND-1B core, within units assumed to be deposited under a warm, wind-mixed and unstable water column (Winter et al., 2010).

***Thalassiosira convexa* var. *aspinosa* (4%; documented in one sample only at 6.10 Ma):** *T. convexa* var*. aspinosa* is a cosmopolitan diatom species common at low latitudes (Lazarus, 1994).

***Thalassiosira elliptipora* (1%; 4.27 - 3.18 Ma):** *T. elliptipora* is an endemic Southern Ocean species (Barron, 1985), however, it is most frequently documented at sites north of the Polar Front (Lazarus, 1994) and as such likely represents relatively warm waters at Site 1165.

***Thalassiosira insigna* (33%; 5.07 - 2.34 Ma):** The biogeography and palaeoecological preferences of *T. insigna* are not well known, however, it is commonly documented north of the Subantarctic Front, for example, from ODP Sites 1171, 1170, 1088, 1090, 1089, 699, 751 (Lazarus, 1994) and, as such, is assumed to prefer relatively warm waters. Its first appearance

at Site 1165 is documented earlier (5.07 Ma) than in the literature (4.22 Ma; Sangiorgi et al., 2018), evolving during the warm Early Pliocene.

Thalassiosira inura* (8%; 5.07 - 2 Ma): T. inura* is generally found in warmer, more northern Southern Ocean waters within the subantarctic zone (Sjunneskog & Winter, 2012; Winter et al., 2010).

***Thalassiosira miocenica* (9%; 6.38 - 5.87 Ma):** *T. miocenica* is a cosmopolitan diatom and has been documented from, and provides biostratigraphic constraints in, the equatorial Pacific, for example at IODP Sites U1338 and U1334 (Baldauf, 2013).

***Thalassiosira nativa* (5%; 9.79 - 4.21 Ma):** *T. nativa* is a cosmopolitan diatom species documented throughout the low latitudes, for example in the Indian monsoon gyres, California upwelling regions and at the Pacific equatorial divergence, as well as in the Southern Ocean (Lazarus, 1994). Thus, it indicates warmer waters at Site 1165, but potentially also upwelling conditions.

***Thalassiosira torokina* (7%; 8.96 - 1.77 Ma):** *T. torokina* is documented throughout the Southern Ocean, however, its frequent occurrence within the subantarctic zone, for example, offshore of New Zealand (Lazarus, 1994), suggests it is tolerant of relatively warm SSTs.

***Thalassiosira vulnifica* (28%; 3.22-2.41 Ma):** This species generally co-occurs with *T. insigna* at Site 1165, assigned warm water preferences, and becomes an important and abundant biostratigraphic marker in the Middle Pliocene. It has been suggested that *T. vulnifica* can tolerate fresh waters better than other species (Sjunneskog & Winter, 2012), however, its palaeo-occurrences suggest it is most abundant within or just north of the Polar Frontal Zone (Sjunneskog & Winter, 2012), and, as such, it is assigned warm water preferences.

***Trinacria excavata* (9%; present for the entire 15 Ma interval):** *T. excavata* is a cosmopolitan marine species frequently observed alongside *Actinocyclus ingens*, *Coscinodiscus marginatus* and *Rouxia peragaalii* (McCollum, 1972), and it is much more abundant prior to the Middle Miocene Climate Transition (c. 13.8 Ma) at Site 1165. As such, I have assigned *T. excavata* to the warm species group for my study. However, this species is only seen at Site 1165, and not at ODP Sites 747 or 744, for at least the Middle Miocene interval (12-15 Ma), and generally co-

occurs with benthic species at Site 1165, so further study may uncover either a neritic ecology and/or an association with conditions different to the species groups used in my study.

2. Group 2: Cool water species

1.1.1.1. Extant taxa

***Coscinodiscus oculus-iridus/asteromphalus* (1%; present prior to 3.29 Ma):** This species group is only documented at Site 1165 and not at ODP Sites 747 or 744. Both *C. oculus-iridus* and *C. asteromphalus* are primarily documented south of the Polar Front in the modern Southern Ocean (Watanabe, 1982; Garrison et al., 1987; Ishikawa et al., 2001).

Eucampia antarctica* var. *recta* (4%; present throughout the entire 15 Ma record)*: *E. antarctica* has two varieties in the modern Southern Ocean; a symmetrical, southerly form (*E. antarctica* var. *recta*) and an asymmetrical, northerly form (*E. antarctica* var. *antarctica*) (Leventer, 2002). Only the symmetrical, southerly form was observed at Site 1165 and, as such, indicates cool waters. *E. antarctica* is also more abundant in Southern Ocean sediments during Pleistocene glacial periods, such that its abundance can be used as a stratigraphic tool (Burckle & Cook, 1983).

***Fragilariopsis kerguelensis* (76%; early form present from 2.55 Ma, modern form from 1.88 Ma)**: The modern form of *F. kerguelensis* is an endemic Southern Ocean species that comprises up to 80% of the Southern Ocean sedimentary diatom assemblage between the sea ice edge and the Subantarctic Front, and is the major contributor to the Southern Ocean opal belt (Crosta et al., 2005). It is most abundant in sea surface temperatures of 1-8°C and has been documented surviving in SSTs of up to c. 18°C (Crosta et al., 2005), but is most abundant south of the Polar Front.

***Fragilariopsis separanda* (2%; 1.31 Ma - present)**: *F. separanda* first appears at Site 1165 at 1.31 Ma. It is most abundant south of the Polar Front in SSTs of between –1.15 and 4.33°C (Cefarelli et al., 2010) and, as such, both the extant species and its early form likely indicate cool waters at Site 1165. A few valves that morphologically similar to *F. separanda* were also observed at Site 1165 as early as 4.85 Ma, but it is unclear whether these represent a true first appearance, an early ancestor or laboratory contamination. I included these early appearances in the *Fragilariopsis* spp. group which is also assigned to the cool water group.

***Thalassiosira lentiginosa* (11%; 3.55 Ma - present)**: *T. lentiginosa* shows similar distribution patterns to *F. kerguelensis* in the Southern Ocean, peaking in abundance between the sea ice edge and the Subantarctic Front, but most abundant south of the Polar Front (Crosta et al., 2005).

***Thalassiosira oliveriana* (7%; 8.71 Ma - present):** *T. oliveriana* is an ice-tolerant extant species generally associated with cold, open waters south of the Polar Front (Winter et al., 2010; Whitehead & McMinn, 2002).

1.1.1.2. Extinct taxa

***Actinocyclus karstenii (*16%; 10.88 Ma – present)*:** *A. karstenii* is more abundant south of the Polar Front during the Pliocene (Sjunneskog & Winter, 2012).

***Denticulopsis crassa* (4%; 13.86 - 4.12 Ma):** *D. crassa* has been described as having a mid-high latitude distribution, and is related to other cool water *Denticulopsis* species (Yanagisawa & Akiba, 1990). On average, *D. crassa* is slightly more abundant at ODP Site 747 (5%) than Site 1165 (1%), however, its abundance peak (4%) occurs at Site 1165 at c. 9 Ma.

***Denticulopsis delicata* (37%; 13.91 - 2.93 Ma):** *D. delicata* is an endemic Southern Ocean species (Yanagisawa & Akiba, 1990). It first appears at Site 1165 during major Middle Miocene cooling and is not documented at all at ODP Site 747 between 15-12 Ma.

Denticulopsis dimorpha* (48%; 12.57 - 10.62 Ma, with some likely reworked younger occurrences)*: Like *Denticulopsis hyalina* and *Denticulopsis praedimorpha, D. dimorpha* is more abundant at ODP Site 747 (69%) than at Site 1165 (48%) from 15-12 Ma. However, its abundance does not peak at Site 1165 until 11.05 Ma. *D. dimorpha* is also considered a middle-high latitude species and evolves following major Middle Miocene cooling (Yanagisawa & Akiba, 1990). Based on my data and published records, within the Southern Ocean *D. dimorpha* may be concentrated at the Polar Frontal Zone.

***Denticulopsis dimorpha* var. *areolata* (1%; 10.71 - 10.41 Ma; sporadic reworked specimens occur until 5.21 Ma)**: *D. dimorpha* var. *areolata* has a relatively high latitude distribution (Yanagisawa & Akiba, 1990). Along with its morphologically-close relative, *D. dimorpha*, I have assigned this variety a cool water ecology.

Denticulopsis hustedtii* (1%; 10.06 - 5.07 Ma)*: *D. hustedtii* is a mid-high latitude species (Yanagisawa & Akiba, 1990). It is present only sporadically in low abundances at Site 1165 during the Late Miocene, and is present in only one sample at ODP Site 747 at 12.26 Ma.

***Denticulopsis hustedtii* var. *aspera* (3%; 9.16 - 8.65 Ma):** *D. hustedtii* var. *aspera* is a short-lived Late Miocene species documented at Site 1165, and is included in the cool water group based on its palaeo-occurences and relationship with cool-assigned *D. hustedii* (Yanagisawa & Akiba, 1990). However, further discussion of this variety is presented in Appendix 2, and it likely should be transferred to a species category (e.g. *Denticulopsis aspera*).

Denticulopsis hyalina* (17%; 14.43 - 13.90 Ma)*: *D. hyalina* is considered a middle- to high-latitude species (Yanagisawa & Akiba, 1990), and is more abundant at ODP Site 747 (27%) than at Site 1165 (17%) between 15-12 Ma. However, *D. hyalina* only appears during peak Middle Miocene cooling, associated with cool SSTs (Shevenell et al., 2004).

***Denticulopsis lauta* (22%; present from the beginning of the record to 13.42 Ma, with sporadic younger occurrences assumed to represent reworking):** *D. lauta* has been documented at low abundances in equatorial regions, but is generally considered a middle-high latitude species (Yanagisawa & Akiba, 1990). It is more abundant at Site 1165 (22%) than at Site 747 (4%).

***Denticulopsis maccollumii* (16%; present from the beginning of the record until 14.14 Ma, with a few sporadic younger appearances likely reworked):** *D. maccollumii* has a relatively high latitude global distribution (Yanagisawa & Akiba, 1990). Between 15-12 Ma *D. maccollumii* is more abundant at Site 744 (77%) than at Sites 747 (18%) or 1165 (16%). This may be because *D. maccollumii* was strongly concentrated around the latitude of Site 744, perhaps associated with a proto-Southern Antarctic Circumpolar Current Front.

Denticulopsis maccollumii* var. A (1%; present from the beginning of the record until 13.96 Ma)*: Showing an almost identical abundance distribution to its relative *D. maccollumii*, I have recognized a new variety (following Bohaty, unpublished plates 2013), *D. maccollumii* var. A, distinguished by punctuation on the valve face. *D. maccollumii* var. A is present in low abundances at Site 1165 prior to 13.96 Ma but relatively high abundances at Site 744 (22%).

The distinctive punctuation of this variety could occur as a result of either phenotypic plasticity or genetic adaptation, possibly in response to an environmental trigger.

***Denticulopsis ovata* (49%; 11.05 - 10.31 Ma):** *D. ovata* is a short-ranging but abundant species at Site 1165. It is endemic to the Southern Ocean, and is likely a descendent of *D. dimorpha* var. *areolata*; a relatively cool water species (Yanagisawa & Akiba, 1990), and is assigned to the cool water group based on its relative abundance at higher latitude ODP Sites 689/689 vs. lower latitide Sites 1092/1088 in the study of Cansarek (2002).

***Denticulopsis praedimorpha* (28%; 12.87 - 10.83 Ma):** *D. praedimorpha*, like *D. dimorpha*, is more abundant at ODP Site 747 (44%) than at Site 1165 (28%) from 15-12 Ma, with peak Site 1165 abundance occuring at 12.46 Ma. However, like *D. dimorpha,* it is generally considered a cool-associated, mid-high latitude species (Censarek, 2002) and evolved following major Middle Miocene cooling (Yanagisawa & Akiba, 1990).

***Denticulopsis simonsenii/vulgaris* (70%; 14.30 - 4.24 Ma):** *D. simonsenii* has a relatively cosmopolitan global distribution, however, it is more abundant, and has a longer stratigraphic range, at higher latitudes (Yanagisawa & Akiba, 1990). It was probably introduced to the low latitudes as a result of Middle Miocene cooling (Barron, 1986). *D. vulgaris* shows a similar distribution to *D. simonsenii* (Yanagisawa & Akiba, 1990). The distinction between *D. simonsenii* and *D. vulgaris* in the Southern Ocean is unclear; many transitional specimens exist between the two species and the punctation on the valve face that distinguishes the two can be affected by dissolution and is not always easy to identify using a light microscope. Thus, in my study I did not separate *D. simonsenii* and *D. vulgaris,* following Gulick et al. (2017). *Denticulopsis simonsenii/vulgaris* is substantially more abundant at Site 1165 (70%) than Site 747 (20%) between 15-12 Ma and, as such, likely prefers cooler waters. The species group first occurs at 14.30 Ma, but is most dominant between 14-7 Ma.

***Denticulopsis sp. 3* (2%; 13.85 - 5.22 Ma):** I have distinguished *Denticulopsis* sp. 3 **(**described in Appendix 2) from *D. simonsenii/vulgaris* by its centrally flared valve outline. It is only identified at Site 1165, not at Sites 747 and 744 and, as such, likely preferred cooler SSTs, like its morphologically-close relative *D. simonsenii/vulgaris*.

***Eucampia antarctica var. twista* (3%; present from the beginning of the record until 12.85 Ma):** *E. antarctica* var. *twista* is distinguished from the extant *Eucampia antarctica* var. *recta* by its twisted valve morphology. *E. antarctica* var. *twista*, which is most abundant at Site 1165 when *Chaetoceros (Hyalochaete)* species resting spores are also most abundant (prior to the Middle Miocene Climate Transition at c.13.8 Ma), could indicate seasonal stratification of the water column. However, given its increased abundance at Site 1165, absence at Site 747 and appearance in only one sample at Site 744, as well as the cool ecological preferences of *E. antarctica* var. *recta*, I have included *E. antarctica* var. *twista* in the cool water paleoecological group.

***Fragilariopsis arcula* (3%; 7.80 - 3.96 Ma)**: Like *Fragilariopsis aurica, F. arcula* evolved earlier, and is more abundant, in the high latitude Southern Ocean (e.g. at ODP Sites 690/689) than further north (e.g. at ODP Sites 1088/1092) (Censarek, 2002), and as such is placed in the warm group. However, it is more abundant during the warm Early Pliocene.

***Fragilariopsis aurica* (5%; 8.65 - 3.29 Ma)**: Like *Fragilariopsis arcula*, *F. aurica* evolved earlier, and is more abundant, in the high latitude Southern Ocean (e.g. at ODP Sites 690/689) than further north (e.g. at ODP Sites 1088/1092) (Censarek, 2002). However, I note, also like *F. arcula*, it is most abundant during the warm Early Pliocene.

***Fragilariopsis barronii* (23%; 3.96 - 1.31 Ma)**: As an ancestor of, and showing similar distributional patterns to, *Fragilariopsis kerguelensis* (Lazarus, 1994), and due to the existence of many transitional specimens between the two, *F. barronii* likely had similar ecological preferences to *F. kerguelensis*. However, although I include it in the cool water group with *F. kerguelensis*, based on its occurrence in the early Pliocene when SSTs at Site 1165 were slightly higher than present (Whitehead & Bohaty, 2003), *F. barronii* probably preferred slightly warmer SSTs than *F. kerguelensis*.

***Fragilariopsis claviceps* (3%: 14.10 - 9.87 Ma):** *F. claviceps* is present in relatively low abundances at Site 1165. Between 15-12 Ma, it is not documented at ODP Site 747, and only a few valves were identified at Site 744.

***Fragilariopsis donahuensis* (5%; 14.30 - 5.77 Ma):** *F. donahuensis* first appeared during the onset of Middle Miocene cooling (Shevenell et al., 2004). At Site 1165, peak abundance

occurred at 10.62 Ma. Between 15-12 Ma it is slightly more abundant and more consistently present at Site 1165 (2%) than at Site 747 (1%).

***Fragilariopsis efferans* (1%: 14.07 - 9.03 Ma):** *F. efferans* is morphologically similar to *Fragilariopsis claviceps*. *F. efferans* is also more abundant at Site 1165 than at Site 747, where no more than 3 valves were identified within any one sample.

***Fragilariopsis januaria* (11%; 14.14 - 5.77 Ma):** *F. januaria* is slightly more abundant at ODP Site 747 (2%) than Site 1165 (<1%) between 15-12 Ma. However, together with *Fragilariopsis efferans*, *Fragilariopsis claviceps* and *Fragilariopsis pseudokerguelensis*, *F. januaria* is part of a radiation of the *Fragilariopsis* genus the occurred at the onset of Middle Miocene cooling (Chapter 6). Peak abundances of *F. januaria* at Site 1165 occurs at 6.38 Ma; a documented interval of particularly low Southern Ocean surface temperatures (Herbert et al. (2016).

***Fragilariopsis januaria* var. A (3%; 9.71 - 5.21 Ma):** This is a new variety of *F. januaria,* described in Appendix 2, following Bohaty (unpublished plates). This Late Miocene variety is closely related to *F. januaria* and co-occurs with *F. januaria*. As such, it is assigned similar ecological preferences.

***Fragilariopsis lacrima* (<1%; 4.85 - 3.64 Ma):** *F. lacrima* is an endemic Southern Ocean species, with palaeo-occurrences at high latitude Southern Ocean Sites, for example, ODP Site 1095 (Winter & Iwai, 2002). It is not abundant at Site 1165, but has been included in the cool water group based on its taxonomic relationship to the generally cool-water *Fragilariopsis* genus and its presence at Antarctic Peninsula Site 1095 (Iwai & Winter, 2002).

***Fragilariopsis pseudokerguelensis* (<1%; 14.07 - 13.17 Ma):** This short-ranging species is rare at Site 1165 and Site 747 (1%). I have included it in the cool water group on the basis of its morphological resemblance to *Fragilariopsis kerguelensis*, one of the most abundant extant Southern Ocean cool-water species. *F. pseudokerguelensis* is also part of the group of *Fragilariopsis* species that evolved around the time of peak Middle Miocene cooling (Shevenell et al. (2004, Chapter 6).

***Fragilariopsis* sp. nov #1 (most abundant prior to 13.66 Ma; later occurences may be reworked, 2%), *Fragilariopsis* sp. A (14.39-13.73 Ma, <1%), *Fragilariopsis* sp. nov # 2 (present**

in one sample at 6.66 Ma, <1%), *Fragilariopsis* sp. nov #3 (9.79-5.07 Ma, <1%), *Fragilariopsis* sp. nov #4 (13.07-12.83, Ma, <1%): These five new *Fragilariopsis* species (after Bohaty, unpublished plates 2013) occur in low abundances at Site 1165, and are described in Appendix 2. Due to their sporadic low abundances, range estimates may not be entirely accurate since it is diffuclt to distinguish last appearances from reworking. I have grouped them palaeoecologically here based on morphological similarity; all are relatively small (<25 µm in length) and finely silicified. They are included in the cool water group because the majority of *Fragilariopsis* species, particularly those that occur in the Southern Ocean, are associated with relatively cool waters (Cefarelli et al., 2010). Further, none of the five species are documented at Sites 747 or 744, at least between 15-12 Ma. However, it is possible that some could also be associated with sea ice.

***Fragilariopsis* spp. (7%)**: This group includes *Fragilariopsis* species not yet described, as well as *Fragilariopsis* valves that were encountered as fragments, recognisable as *Fragilariopsis* but not to species level. This group has been included within the cool water group because *Fragilariopsis* is generally considered a cool water genus. Many of the valves counted as part of this group were morphologically similar to the extinct *F. aurica* and *F. arcula* that are included in the cool water group, as well as to sea ice taxa such as *Fragilariopsis curta, Fragilariopsis praecurta* and *Fragilariopsis cylindrus,* but morphologically different to the warm water *Fragilariopsis* such as *Fragilariopsis interfrigidaria* and *Fragilariopsis weaveri* that tend to be more robustly silicified. It is possible that at least some of the *Fragliariopsis* species I have included in the *Fragilariopsis* spp. group represent sea ice at Site 1165, however, this group is relatively low in abundance at Site 1165 (up to 7% but generally <3%) and, as such, an incorrect paleoecological assignment should not greatly bias conclusions.

***Nitzschia denticuloides* (7%; 13.96 - 12.71 Ma):** *N. denticuloides* is an endemic Southern Ocean species (Yanagisawa & Akiba, 1990; Barron & Baldauf, 1995) and first appears during peak Middle Miocene cooling (Shevenell et al., 2004). It is more abundant at ODP Site 747 (32%) than Site 1165 (7%), however, I include it in the cool water group because Censarek (2002) assigned this group a PFZ distribution.

***Nitzschia* sp. 17 (1%; 13.95 - 13.44 Ma):** This variety exhibits several small holes or pores in the hyaline middle section of the valve face but generally co-occurs with *Nitzschia denticuloides* at

Site 1165, as well as at Sites 744 and 747, thus, is assigned to the cool water group alongside *N. denticuloides*.

***Nitzschia grossepunctata* (5%; 14.60 - 12.79 Ma):** *N. grossepunctata* is an endemic Southern Ocean species (Lazarus, 1994). *Nitzschia denticuloides* and *N. grossepunctata* have similar distribution patterns, were both more abundant at Site 747 (19%) than Site 1165 (5%), and seem to be concentrated within the PFZ (Censarek, 2002).

***Rouxia isopolica* (9%; 9.89 - 2.46 Ma):** *R. isopolica* co-occurs with *Rouxia antarctica* and *Rouxia naviculoides* in Pleistocene records from the southern Kerguelen region (Whitehead & McMinn, 2002). However, *R. isopolica* was less abundant during intervals associated with pack ice (Whitehead & McMinn, 2002), so I have included it in the cool water group rather than the sea ice group.

***Rouxia* spp. (6%):** This group includes valves identifiable to the *Rouxia* genus but not to species level. They have been included in the cold water paleoecological group on the basis that *Rouxia* species are generally cold-water associated in the Southern Ocean, with the exception of *Rouxia californica and Rouxia peragallii*. The *Rouxia* spp. group is more abundant at Site 1165 (5%) than Site 747 (1%).

***Thalassiosira kolbei* (1%; 3.80 - 2.41 Ma):** *T. kolbei* is ice-tolerant, but generally prefers cool, open waters (Winter et al., 2010).

***Thalassiosira mahoodii* (5%; 9.36 - 5.96 Ma):** *T. mahoodii* has been documented from south of the Polar Front, for example, at ODP Leg 178 sites offshore of the Antarctic Peninsula (Iwai & Winter, 2002) and at ODP Site 746 on the southern Kerguelen Plateau (Baldauf & Barron, 1991), and is therefore likely tolerant of cooler waters.

***Thalassiosira oliveriana* var. *sparsa* (13%; 9.50 - 1.77 Ma):** *T. oliveriana* var. *sparsa* has a close taxonomic relationship to *Thalassiosira oliveriana* and palaeo-occurrences of *T. oliveriana* var. *sparsa* largely mirror those of its cool water (Winter et al., 2010; Whitehead & McMinn, 2002) relative, *T. oliveriana* (Lazarus, 1994).

***Thalassiosira striata* (<1%; 4.27 - 3.22 Ma):** *T. striata* has been associated with cold sea surface temperatures but not sea ice (Winter et al., 2010). It has been suggested that this species is an ancestor of the extant cool water-associated *Thalassiosira lentiginosa* (Winter et al., 2010).

***Thalassiosira torokina* (7%; 8.96 - 1.77 Ma)**: *T. torokina* has been associated with cold, nutrient-rich waters (Winter et al., 2010).

***Thalassiosira cf. antarctica* (3%: 9.76 - 3.39 Ma):** This species is morphologically similar to, and may be the ancestor of, *Thalassiosira antarctica*; an ice-tolerant, cool water, extant species (Armand et al., 2005).

3. Group 3: High productivity species

Extant species

***Chaetoceros (Hyalochaete*) species resting spores (CRS) (36%; present throughout the 15 Ma record):** *Chaetoceros (Hyalochaete)* are found throughout the global oceans associated with high nutrient conditions because their relatively small size and large surface area provides a physiological advantage in nutrient uptake (Donegan & Schrader, 1982; Armand et al., 2005). Resting spores (CRS) are produced towards the end of the vegetative bloom in response to nutrient depletion (Crosta et al., 1997). Vegetative *Chaetoceros (Hyalochaete)* are rarely preserved in the sediments, but CRS are most abundant in sediments where over-lying water column nutrient concentrations were highest, for example, along the Antarctic margin where sea ice melt and glacial discharge create ideal high-nutrient conditions for blooms to occur (e.g. Sjunneskog & Taylor, 2002; Allen et al., 2010).

***Liradiscus* species resting spores (6%; sporadically present throughout the record but consistently present prior to 14 Ma)**: *Liradiscus* resting spores are most abundant at Site 1165 where CRS are also most abundant – prior to c. 14 Ma. *Liradiscus* resting spores often co-occur with CRS at other sites, thus it has been suggested that *Liradiscus* species flourish in a similar environmental niche to CRS (Suto, 2004).

***Thalassionema nitzschioides* (28%; present throughout the entire 15 Ma record):** *T. nitzschioides* is a cosmopolitan diatom commonly associated with high productivity, upwelling conditions in equatorial regions (Romero et al., 2009; Baldauf & Lyle, 2015).

***Thalassiothrix/Trichotoxon* spp. (33%; present throughout the 15 Ma record):** Species of *Thalassiothrix* and *Trichotoxon* are morphologically similar, both having long, thin, needle-shaped valves. As such, I have grouped them together. *Thalassiothrix* species are generally associated with areas of high productivity in the modern ocean. For example, *Thalassiothrix longissima* accumulates beneath upwelling regions of high biological productivity in the equatorial Pacific (Lyle & Baldauf, 2015), while increased *T. longissima* abundance coincided with relatively high $\delta^{30}Si_{diatom}$, indicating increased siliceous productivity, during the last interglacial in a core from the North Atlantic (Romero et al., 2011). In the Southern Ocean, *Thalassiothrix antarctica* is documented in both the subantarctic and Antarctic zones, but is most abundant within the PFZ where upwelling is strongest (Hasle, 2001). High concentrations of *Thalassithrix* species can also occur in sediments as a result of physical oceanographic processes rather than surface, nutrient-fuelled blooms (Kemp et al., 2009). High concentrations of *T. antarctica* have been observed at depth south of the Polar Front, being advected northwards at rates of 1 cms^{-1} to the Polar Front region, and deposited to the sediment as *Thalassiothrix* mats (Parslow et al., 2001; Strass et al., 2002). However, strong evidence exists for an association between *Thalassiothrix* species and high productivity upwelling regions and, as such, I have assigned this species group high productivity palaeoecological preferences.

Trichotoxon reinboldii, the only species described within the *Trichotoxon* genus, is endemic to the Southern Ocean and is closely related to *Thalassionema* and *Thalassiothrix* (Hasle, 2001). Although its association with high productivity conditions is less well documented, *T. reinboldii* is included in the high productivity group on the basis that it generally co-occurs with *Thalassiothrix* species in the Southern Ocean, for example, in the Holocene sediments of Palmer Deep (Leventer, 2002).

3.1.1. Group 4: sea ice species

3.1.1.1. Extant species

***Actinocyclus actinochilus* (2%; 1.88 Ma - present):** *A. actinochilus* is closely associated with areas of seasonal sea ice cover in the modern Southern Ocean (Armand et al., 2005). It was also included in the sea ice assemblage group in the Late Pliocene AND-1B record, where it had a similar distribution to *Stellarima microtrias,* also a sea ice species (Winter et al., 2010).

***Fragilariopsis* cf. *curta* (4%; 12.17 Ma – present)**: The modern form of *F. curta* has been documented from waters of between –1.6 and 13.35°C (Cefarelli et al., 2010) and is most abundant south of the winter sea ice edge, in waters with SSTs of between –0.5 and 1°C and 9-11 months of sea ice cover per year (Armand et al., 2005). *F. curta* is commonly used as a sea ice indicator within Holocene diatom paleoenvironmental reconstructions (e.g. Taylor & Sjunneskog, 2002; Crosta et al. 2008; Allen et al., 2010; Alley et al., 2018). Specimens resembling *F. curta* have been included in this study as *F.* cf. *curta* (see Appendix 2 for details). However, this brings the first appearance of the species much earlier than previously documented (4.8 Ma, Cody et al., 2012), although given its similar ecological niche to *F. vanheurckii*, the first appearance of which has also been suggested to be much earlier than conventionally thought (Harwood & Boahty, 2007), it seems likely that the same may be true for *F. curta.*

***Fragilariopsis cf. linearis* (1%; 10.71 - 3.45 Ma).** *F. cf. linearis* and *Fragilariopsis curta* have a close taxonomic relationship and are morphologically similar (Cefarelli et al., 2010), thus, I have included *F. cf. linearis* in the sea ice group. However, this species is rare at Site 1165.

***Fragilariopsis* cf. *vanheurkii* (2%; 14.58 Ma - present)**: In the modern Southern Ocean, *F. vanheurckii* has been found at SSTs of between –1.60 and –0.17°C, often associated with the brownish underside of sea ice (Cefarelli et al., 2010). It has been described as a littoral species (Hasle, 1965), and is frequently included within sea ice groups in Holocene sea ice reconstructions (e.g. Taylor & Sjunneskog, 2002; Barbara et al., 2013). *F. vanheurckii* has also been described from terrestrial Antarctic outcrops of Late Miocene age (Harwood & Bohaty, 2007), suggesting it could have evolved in the cooler Late Miocene and survived in refugia through the warm Early Pliocene. At Site 1165, specimens resembling *F. vanheurckii* occur in low abundances throughout the record, as far back as 14.58 Ma. If these are true *F. vanheurckii*, they would represent its earliest known occurrence. However, these specimens could also represent an ancestor or early form of *F. vanheurckii*, in the same way that early forms of *Fragilariopsis kerguelensis* are documented.

***Fragilariopsis obliquecostata* (1%; 3.80 Ma - present)**: *F. obliquecostata* is most abundant in the vicinity of the Southern Ocean summer sea edge, in waters with temperatures of between –1 and 0°C and which experience >7 months of sea ice cover per year (Armand et al., 2005). It

is frequently used as a sea ice indicator in Holocene diatom assemblage reconstructions, in particular as an indicator for the summer sea ice edge (Allen et al., 2011).

***Fragilariopsis ritscheri* (3%; 4.12 Ma - present)**: Highest abundances of *F. ritscheri* in the modern Southern Ocean have been documented from waters between 0 and 3°C and covered by sea ice for between 2-10.5 months per year, although even here relative abundances of *F. ritscheri* within planktonic samples generally do not exceed c. 4% (Armand et al., 2005).

***Fragliariopsis sublinearis* (4%; 5.23 Ma - present)**: *F. sublinearis* has been found in waters with temperatures of between –1.60 and 4.33°C (Cefarelli et al., 2010), and is associated with sea ice in the modern Southern Ocean (Armand et al., 2005).

***Stellarima microtrias* (5%; present throughout the entire 15 Ma record)**: *S. microtrias* is most abundant in the Southern Ocean within a temperature range of –0.5 to 0.5°C, and where seasonal sea ice cover, including land-fast ice and pack ice, exceeds 7.5 months per year (Armand et al., 2005).

***Thalassiosira tumida* (3%; 4.52-2.80 Ma):** In the modern Southern Ocean, *T. tumida* is a sea ice associated diatom that thrives in waters with SSTs of 0 to 0.5°C and >8.5 months of sea ice cover (Armand et al., 2005). Although it is an extant species, *T. tumida* is not seen after 2.80 Ma at Site 1165.

3.1.1.2. Extinct species

Fragilariopsis praecurta* (20%; 14.79 - 3.39 Ma)*: *F. praecurta* is abundant in the high latitude Southern Ocean (Censarek, 2002). It is likely an ancestor of *Fragilariopsis curta* (Gersonde, 1991), an extant sea ice-associated diatom (Armand et al., 2005), although is distinct from the forms grouped as *F. cf. curta*. At Site 1165, *F. praecurta* occurs earlier than its published first Southern Ocean occurrence of either between 8.77-10.11 Ma (Cody et al., 2008) or closer to 11.2 Ma (Barron, 2010). As with other *Fragilariopsis* species that I have documented occurring earlier at Site 1165 than in the published literature, for example, *F. curta* and *F. vanheurckii*, the earliest occurrences may represent an early form of *F. praecurta*.

***Fragilariopsis pusilla* (5%; present from the beginning of the record until 6.63 Ma):** *F. pusilla* is an endemic Southern Ocean species (Censarek, 2002) that had its peak abundance at Site

1165 at 13.98 Ma, during the Middle Miocene Climate Transition and, again, at 10.62 Ma. Between 15-12 Ma it is more abundant at Site 1165 (5%) than at Site 747 (1%). As such, it is included in the sea ice group on the basis that it resembles modern sea-ice associated *Fragilariopsis curta* and the sea-ice associated extinct *Fragilariopsis trunctata*. The last appearance of *F. pusilla* has previously been documented in the literature at around 15 Ma (Sangiorgi et al., 2018) but, after careful checking with images and descriptions of *F. pusilla*, the younger specimens documented at Site 1165 seem to be true specimens. Since the abundance of this species co-varies with other sea-ice and cool water species, these appearances are not likely reworking and, instead, represent a longer range for the species than previously described.

Fragilariopsis robusta* (4%; 4.52 - 1.81 Ma): F. robusta* is the ancestor of *Fragilariopsis obliquecosta* (Sjunneskog et al., 2012), a modern sea ice species that has been used to reconstruct the summer sea ice edge (Allen et al., 2011). *F. robusta* evolved during the establishment of widespread sea-ice cover during Late Pliocene cooling (it peaks in abundance at c. 3 Ma) (McKay et al., 2012).

***Fragliariopsis bohatyii* (1%; 4.12 - 1.88 Ma)**: *F. bohatyii* is present in only four samples at Site 1165. Its evolution was linked to Late Pliocene cooling in the AND-1B core, where it co-occurred with another potentially sea-ice associated diatom, *Fragilariopsis robusta*, with transitional specimens existing between the two species (Sjunneskog et al., 2012).

***Fragliariopsis truncata* (<1%; 14.44 - 12 Ma):** *F. truncata* is very rare at Site 1165, and was not seen at ODP Sites 747 or 744 between 15-12 Ma. The species was used to infer sea ice during the Middle Miocene at the ANDRILL coresite (Levy et al., 2016), and closely resembles modern sea ice-associated *Fagilariopsis curta*.

***Nitzschia maleinterpretaria* (1%; present from the beginning of the record until 12.61 Ma):** *N. maleinterpretaria* has been interpreted as a sea-ice associated diatom at ODP Site 744 (Farmer, 2011). As such, I have also included in the sea ice group for my study.

***Rouxia antarctica* (5%; 6.30 - 1.88 Ma):** *R. antarctica* is an endemic Southern Ocean species abundant south of the Polar Front (Abelmann et al., 1990). Within the Pliocene section of the AND-1B core, *R. antarctica* co-occurs with extant sea ice species (Winter et al., 2010) and is

most abundant during intervals of inferred pack-ice in Pleistocene sediments from the southern Kerguelen region (Whitehead & McMinn, 2002). However, *R. antarctica* also survived during the warm Pleistocene interglacials so may be tolerant of a wide range of conditions (Whitehead & McMinn, 2002). The first occurrence *of R. antarctica* at Site 1165, 6.30 Ma, is earlier than its previously documented first appearance of 4.95 Ma (Cody et al., 2012).

***Rouxia diploneides* (23%; 6.20 - 2.41 Ma):** *R. diploneides* co-occurs with extant sea ice diatoms in the Late Pliocene AND-1B core (Winter et al., 2010).

***Rouxia naviculoides* (8%; 10.71 - 1.88 Ma):** *R. naviculoides* is a Southern Ocean species which, like *Rouxia antarctica*, is more abundant south of the Polar Front (Abelmann et al., 1990). It is most abundant during cold, pack-ice associated intervals in Pleistocene sediments from the southern Kerguelen region where it co-occurs with *R. antarctica* (Whitehead & McMinn, 2002). *R. naviculoides* also survived during the warm Pleistocene interglacials and, like *R. antarctica*, may be therefore be tolerant of a wide range of conditions (Whitehead & McMinn, 2002).

***Synedropsis* sp. A, *Synedropsis* sp. B., *Synedropsis* sp. C., *Synedropsis* sp. 1 and *Synedropsis* spp. (specimens unidentifiable to species level). (4%; sporadically present throughout the record):** The entire *Synedropsis* genus has been assigned to the sea ice category on the basis that modern *Synedropsis* are mostly sea ice-associated (Hasle et al., 1994). Extinct *Synedropsis* species were also used to infer sea ice presence in the Eocene Arctic, coinciding with IRD (Stickely et al., 2009). Further, the morphological similarities between *Synedropsis* sp. A and *Crania lacyae*, a proposed sea-ice associated diatom (Olney et al., 2009), suggest that the two may in fact be synonymous. See appendix 2 for descriptions of each *Synedropsis* species, most of which have not previously been formally described.

3.1.2. Group 5: Stratification species

Extant Species

***Corethron pennatum* (1%; 10.73 Ma - present)**: *C. pennatum* is an endemic extant Southern Ocean species, commonly found in shelf sediments along the Antarctic margin where it has been documented forming sedimentary laminations during the Holocene (Alley et al., 2018; Maddison et al., 2012). The ability of *Corethron* to adjust their buoyancy and, therefore, to sink deeper within the water column to access available nutrients makes them especially well-adapted to highly stratified water conditions (Leventer et al., 2002; Alley et al., 2018).

***Rhizosolenia costata* (1%; 3.29 - 3.18 Ma), *Rhizosolenia harwoodii* (2%; 3.60 - 2.80 Ma), *Rhizosolenia hebetata* (5%; present throughout the entire 15 Ma record), *Rhizosolenia hebetata* var. *hiemalis* (4%; present throughout the entire 15 Ma record), *Rhizosolenia styliformis* (12%; present throughout the entire 15 Ma record), plus *Rhizosolenia*. sp. 1 (<2%; 9.58-5 Ma), *Rhizosolenia*. sp. 2 (<1%; 10.02-6.12 Ma), *Rhizosolenia*. sp. 3 (3%; 3.96 Ma), *Rhizosolenia*. sp. A (1%; 13.79-3.15 Ma) & *Rhizosolenia* spp. (specimens not identifiable to species level) (combined abundance 29%):** Like *Corethron pennatum* that is also included within the stratification group, *Rhizosolenia* are capable of moving vertically within the water column in order to access nutrients at depth and sunlight in the surface water. Their large surface area:volume ratio may restrict their ability to acquire nutrients in comparison to smaller diatoms, putting them at a disadvantage under high nutrient conditions in the surface water (Alley et al., 2018). As such, it has been suggested that *Rhizosolenia* indicate a stratified water column (Seeberg-Elverfeldt et al., 2004), perhaps associated with glacial meltwater events (Leventer et al., 2002) or relatively high sea surface temperatures. *Rhizosolenia* species comprise up to 35% of the diatom assemblage at Site 1165, although may be slightly over-represented on account of their strongly silicified, easily recognizable (to genus level) rimoportulae.

3.1.3. Group 6: reworked species

***Hemiaulus spp. (1%)*:** The *Hemiaulus* genus is Oligocene or older in age and therefore represent reworking at Site 1165.

Rocella gelida (<1%): *Rocella gelida* is an Oligocene species and therefore represents reworking at Site 1165.

Pyxilla spp. (<1%): Paleocene age *Pyxilla* spp. are reworked into the 15 myr record at Site 1165.

3.1.4. Group 7: other species

It was not possible to assign a number of species to paleoecological groups based on existing evidence, however, none of these species make up >6% of the assemblage and their exclusion does not preclude the paleoceanographic interpretation of the diatom assemblage records that I have presented in this thesis. The species included in this group are:

***Actinocyclus fasciculatus* (2%; 2.80 - 1.88 Ma), *Actinocyclus maccollumii* (1%; 2.80 Ma), *Actinocyclus octonarius var. asteriscus* (<1%; 9.04 Ma), *Actinocyclus spp.* (6%; present throughout the entire 15 Ma interval), *Asteromphalus kenettii* (1%; 10.31 - 9.16 Ma), *Asteromphalus cf. parvalus* (<1%; 14.08 - 6.20 Ma), *Cavitatus miocenicus* (1%; present from the beginning of the record until 4.52 Ma), *Entopyla* spp. (<1%; present from the beginning of the record until 14.36 Ma), *Eurossia* spp. (<1%; 14.53 - 14.30 Ma), *Lisitzinia ornata* (<1%; 9.04 Ma), *Nitzschia* cf. *challengerii* (<1%; 14 - 13.98 Ma), *Proboscia praebarboi/barboi* (<1%; 10.73 - 3.39 Ma), *Thalassiosira* sp. nov (<1%; 9.40 - 3.11 Ma), *Thalassiosira gersondeii* (2%; 9.16 - 4.39 Ma), *Thalassiosira jacksonii* (<1%; 5.21 - 3.11 Ma), *Thalassiosira maculata* (1%; 8.81 Ma - present), *Thalassiosira nansenii* (<1%; 10.66 Ma), *Thalassiosira praelineata* (3%; 9.10 - 5.77 Ma), *Actinocyclus* sp. nov #1 (<1%; 13.92 - 13.78 Ma), *Thalassiosira* spp. (4%).**

3.2. Neritic/Shelfal Diatoms

3.2.1. Extant

***Delphineis* spp. (<1%):** Although not identified to species level, *Delphineis karstenii* is a widely documented benthic species (Pokras, 1991). *Delphineis* have also been documented growing on sand grains (Round et al., 1990), but are likely primarily neritic rather than benthic.

***Ellerbeckia sol* (2%; present throughout the 15 Ma record):** Designated a neritic species by Kato et al. (2016) based on a subarctic record.

***Paralia sulcata* (2%; present throughout the 15 Ma record):** This species has been designated a coastal species because its abundance correlates with high nutrient availability and high salinities (McQuoid & Nordberg, 2003).

***Stephanopysis turris* (19%; present throughout the 15 Ma record):** Designated meroplanktonic based on samples from the Antarctic terrestrial-exposed Sørsdal Formation (Harwood et al., 2002), this extant species is also frequently documented in coastal environments, for example, the Argentine shelf (Ferrario et al., 2012).

3.2.2. Extinct

***Stephanopyxis* sp. B (Harwood & Bohaty, 2000; 14%; present prior to 11.01 Ma).** This species was only documented at ODP Site 1165, not Sites 747 or 744, between 12-15 Ma. Given that

many *Stephanopyxis* spp. are neritic, for example *Stephanopyxis turris*, I have designated *Stephanopyxis* sp. B as neritic.

***Actinocyclus* sp. nov #2, described in Appendix 2 (18%; present prior to 10.98 Ma):** I found this new species only in Site 1165 samples. Whilst its exclusive appearance at Site 1165 could be explained by cooler sea surface temperature (SST) conditions than existed at Sites 747 or 744, the fact that the species was most abundant when Southern Ocean SSTs were higher (Shevenell et al., 2004) and other neritic and benthic species were most abundant, prior to the Middle Miocene Climate Transition at 13.8 Ma, suggests *Actinocyclus* sp. Nov #2 is also neritic.

3.3. Benthic diatoms

Benthic diatom species require stretches of ice-free coast to survive, since they need ice-free water in order to photosynthesize. Site 1165 is located on the continental rise offshore of Prydz Bay, so benthic species are transported to the site rather than deposited in-situ. Possible benthic diatom transport mechanisms to Site 1165 include delivery via bottom currents, attached to the undersides of anchor sea ice (formed as ice freezes to the sea floor at the coast and then rises to the surface as sea ice), and/or attached to macroalgae which float either in isolation or attached to icebergs or sea ice. The appearance of benthic diatoms at Site 1165 likely represent periods when marine ice was reduced, or absent, in Prydz Bay, allowing benthic diatoms to flourish along the coastline. Occurrence ranges at Site 1165 are not provided for benthic species because almost all are so rare at Site 1165 that true ranges cannot accurately be gauged.

3.3.1. Extant

Arachnodiscus spp. (<1%): This genus consists of epiphytic discoid cells that live on seaweeds. It is particularly common along the tropical Pacific coastline (Round et al., 1990).

Cocconeis spp. (2%): I grouped *Cocconeis* species at genus level due to the many undescribed species and the low abundance of the genera overall; however, *C. costata* and *C. californica* were observed. The *Cocconeis* spp. group has previously been described as benthic at Site 1165 (Whitehead & Bohaty, 2003), and in Antarctic terrestrially-exposed samples from the Pagodroma Group (Whitehead et al., 2004) and Sørsdal Formation (Harwood et al., 2002).

Cymatosira spp. (<1%): A small marine benthic genus that forms filamentous colonies; *Cymatosira* have been collected in inshore plankton but may also grow in the epipsammon (Round et al., 1990).

Diploneis spp. (<1%): *Diploneis* species were included as benthic in previous studies at Site 1165 **(**Whitehead & Bohaty, 2003), and in Antarctic terrestrially-exposed samples from the Pagodroma Group (Whitehead et al., 2004) and Sørsdal Formation (Harwood et al., 2002).

***Entopyla spp*. (<1%):** *Entoyla* species were described as benthic in samples from the Antarctic terrestrially-exposed Sørsdal Formation (Harwood et al., 2002; Prasad & Frxyell, 1991).

Grammatophora spp. (<1%): *Grammatophora* species were described as benthic in Antarctic terrestrially-exposed samples from the Pagodroma Group (Whitehead et al., 2004).

***Melosira spp.* (<1%):** *Melosira* species were described as benthic in Antarctic terrestrially-exposed samples from the Pagodroma Group (Whitehead et al., 2004) and Sørsdal Formation (Harwood et al., 2002).

***Navicula spp.* (<1%):** *Navicula* species were described as benthic in previous studies at Site 1165 (Whitehead & Bohaty, 2003) and in Antarctic terrestrially-exposed samples from the Pagodroma Group (Whitehead et al., 2004).

Pleurosigma spp. (1%): Usually found in brackish or marine waters as epipelic on sand or silt. Occasional planktonic occurrences have been documented, but *Pleurosigma* is generally considered a benthic genus (Round et al.,1990).

***Raphoneis spp*. (<1%):** Raphoneis species were described as benthic in Antarctic terrestrially-exposed samples from the Pagodroma Group (Whitehead et al., 2004).

***Rhabdonema japonicum* (<1%):** *R. japonicum* was described as benthic in Antarctic terrestrially-exposed samples from the Pagodroma Group (Whitehead et al., 2004) and Sørsdal Formation (Harwood et al., 2002).

***Rhabdonema* spp. (2%):** Unidentified *Rhabdonema* species were described as benthic in Antarctic terrestrially-exposed samples from the Pagodroma Group (Whitehead et al., 2004) and Sørsdal Formation (Harwood et al., 2002).

***Synedra spp.* (<1%):** *Synedra* species were described as benthic in Antarctic terrestrially-exposed samples from the Pagodroma Group (Whitehead et al., 2004).

***Trigonium antarcticum* (<1%; 6.20 and 3.18 Ma):** *T. antarcticum* was described as benthic in Antarctic terrestrially-exposed samples from the Sørsdal Formation (Harwood et al., 2002).

3.3.2. Extinct

***Isthmia* spp. (<1%):** *Isthmia* species were described as benthic in Antarctic terrestrially-exposed samples from the Sørsdal Formation (Harwood et al., 2002).

Kisseleviella* spp. (<1%)*: *Kisseleviella* is a fossil genus that is morphologically similar to the extant benthic genus *Cymatosira*, is typically documented in neritic Antarctic environments and is likely tychopelagic (Olney et al., 2005).

Lithodesmium* cf. *minusculum* (<1%)*: *L. cf. minusculum* has been described as a Lower Pliocene benthic species (Barron & Baldauf, 1986).

Sphynctolethus spp.: In an Oligocene Antarctic record *Sphynctolethus* was designated a benthic genus (Barron & Mahood, 1993).

12. Appendix 2: Taxonomy

A taxonomic list of all diatom species encountered in my study is presented here, including taxonomic references where available. Four new species are also presented from 15-12 Ma at ODP Sites 747, 744 and 1165. Bold, square brackets refer to Plates 1-5 presented in Chapter 5.

Actinocyclus actinochilus (Ehrenberg) Simonsen, 1982, pp. 101-116, pl. 1-4; Villareal and Fryxell, 1983, p. 461, figs. 21-32.

Actinocyclus ehrenbergii Ralfs in Pritchard, 1861, p. 834; Hustedt, 1928, p. 525, fig. 298.
Synonym: *Actinocyclus octonarius* Ehrenberg, 1838, p. 173, pl. 21, fig. 7.

Actinocyclus fasciculatus Harwood and Maruyama, 1992, p. 700, pl. 13, figs. 14, 15; Censarek and Gersonde, 2002, p. 350, pl. 1, fig. 5.

Actinocyclus ingens **[Plate 1, Fig 1]** Rattray**.** Akiba, 1982, p. 42, pl. 5, figs. 7-14; Gersonde, 1990, pp. 791, 792, pl. 1, figs. 1, 3-5; pl. 3, figs. 8, 9; pl. 4, fig. 1.

Actinocyclus ingens **var. *nodus* [Plate 1, Figs 2-3].** Baldauf in Baldauf and Barron, 1980, p. 104, pl. 1, figs. 5-9; Gersonde, 1990, p. 792, pl. 1, fig. 6; pl. 3, figs. 4-7; Censarek and Gersonde, 2002, p. 350, pl. 1, fig. 4**.**

Actinocyclus ingens **var. *ovalis* [Plate 1, Fig. 16].** Gersonde, 1990, p. 792, pl. 1, fig. 7; pl. 3, figs. 1-3; pl. 5, figs. 4, 7; pl. 6, figs. 1, 4-5; Censarek and Gersonde, 2002, p. 350, pl. 1, figs. 6, 8 (Pl. 1, figs. 2, 3)**.**

Actinocyclus karstenii **[Plate 4, fig. 10].** Van Heurck; Harwood and Maruyama, 1992, p. 700, pl. 13, figs. 1, 2, 6-8, 10, 11, 13; Mahood and Barron, 1996b, p. 288, pl. 3, fig. 5; Zielinski and Gersonde, 2002, p. 253, pl. 3, figs. 4, 5, 7-9, 12(?).
Synonym: *Actinocyclus fryxellae* Barron, in Baldauf and Barron, 1991, pl. 1, figs. 1–2, 4.

Actinocyclus maccollumii Harwood and Maruyama, 1992, p. 700, pl. 17, fig. 29.

Actinocyclus octonarius **var. *asteriscus* [Plate 1, Fig. 4].** Barron 1975; Harwood et al. 2000, p. 459, pl. 7, fig l.

***Actinocyclus* sp. nov - #1 [Plate 2, Fig. 6].**

Synonym: *Actinocyclus* sp. in Bohaty, unpublished plates 2013 - Figure 5, Plate 1.

Description: Valve circular, slightly convex and 25-45 µm in diameter. Curved mantle and prominent ribbed margin. Areolae on the valve face decrease in size away from the center, arranged in tangential rows focused towards 10-12 marginal strutted processes. Areolae become disordered closer to the large hyaline area in the center of the valve.

Remarks: Differs from *Actinocyclus* sp. nov #2 due to its larger size, larger hyaline area in the centre of the valve, ribbed margin and marginal strutted processes. Differs from *Thalassiosira lentiginosa* due to the absence of a prominent labiate process and scattered strutted process across the valve face.

Stratigraphic occurrence: Based on the magnetostratigraphic record at ODP Hole 747A, where the species is most abundant and chronologically calibrated using the robust magnetostratigraphic age/depth curve, *Actinocyclus* sp. nov #1 first appears at 14.18 Ma (72.62 mbsf), peaks in abundance at 13.47 Ma (5%) (67.68 mbsf), and is not seen after 13.26 Ma (66.31 mbsf), making it a relatively short-ranging and, therefore, biostratigraphically useful species. The species is also seen at ODP Hole 744B, where it first occurs at 57.52 mbsf, peaks in abundance (1.2%) at 54.54 mbsf, and disappears at 53.10 mbsf. At ODP Hole 1165B, it first appears at 291.45 mbsf, and peaks in abundance (1.2%) at 283.36 mbsf, used as a tie-point in the age model, after which the species disappears at 282.76 mbsf.

***Actinocyclus* sp. nov. #2 - [Plate 2, Figs. 13-15]**

Description: Valve circular, flat and 12-25 µm in diameter. Slightly curved mantle and minimal margin. Areolae on the valve face show a slightly disordered fasciculation pattern, particularly towards the hyaline central area which can appear slightly off-centre, along with the central rimoportula.

Remarks: Differs from *Actinocyclus* sp. nov #1 in its smaller size, reduced margin and less prominent hyaline central area which may appear off-centre. Differs from *Thalassiosira lentiginosa* in its smaller size and lacking a prominent marginal labiate process or strutted processes scattered across the valve face. Differs from *Actinocyclus endoi/tabularis* in showing punctation right to the mantle, whilst *A. tabularis/endoi* generally shows a hyaline gap between the valve face and mantle.

Stratigraphic occurrence: *Actinocyclus* sp. Nov. #2 is only recognised at ODP Hole 1165B, where it appears throughout the record (15.06-12.12 Ma) but is most abundant prior to Mi3 at

13.8 Ma, peaking in abundance (18%) at 14.70 Ma. Its stratigraphic utility remains unknown and, as such, I have not used it in any of the age models in my study.

Actinoptychus senarius **[Plate 2, fig. 4]** (Ehrenberg) Ehrenberg; Akiba, 1986, pl. 29, fig. 2.

Araniscus lewisianus **[Plate 1, Fig. 17]** Greville, Komura, 1998, pp. 6-8, figs. 20-22, 87-104, and text fig. 1.
Basionym: *Coscinodiscus lewisianus* Greville; Schrader, 1973, p. 703, pl. 8, figs. 1-6, 10, 15; Schrader, 1976, p. 631, pl. 14, fig. 3; Harwood and Maruyama, 1992, p. 702, pl. 6, fig. 13.

Arachnodiscus Bailey ex. Ehrenberg, 1849.

Asteromphalus hookeri Ehrenberg; Akiba, 1982, p. 42, pl. 1, fig. 1; Bohaty et al., 1998, pl. 2, fig. 5.
Notes: *A. parvulus* and *A. hookeri* were grouped together in Bohaty et al. (2003).

Asteromphalus kennettii Gersonde, 1990, p. 793, pl. 2, fig. 1; pl. 6, fig. 2; Harwood and Maruyama, 1992, p. 701, pl. 11, fig. 3; Censarek and Gersonde, 2002, p. 350, pl. 1, fig. 2.

Asteromphalus cf. parvulus Karsten; Fenner et al., 1976; p. 769, pl. 4, figs. 20, 21.

Azpeitia endoi **[Plate 1, Figs 11-12]** Sims and Fryxell in Fryxell et al. of Baldauf and Barron, 1991, p. 586; Gladenkov and Barron, 1995, p. 31.
Synonym: *Coscinodiscus endoi* Kanaya, 1959; McCollum, 1975, pl. 4, figs. 5, 6; Schrader, 1976, pl. 11, figs. 8–10, 12; Gombos, 1977, pl. 2, figs. 6, 7; *Azpeitia tabularis* (Grunow) Fryxell and Sims in Fryxell et al., 1986; Harwood and Maruyama, 1992, p. 701, pl. 11, fig. 5.
Notes: Transitional species were noted between *A. endoi* and *A. tabularis* when the central depression was not easily distinguished. These specimens were grouped here as *A. endoi* unless unambiguously *A. tabularis.*

Azpeitia harwoodii **[Plate 1, Fig. 18]** Bohaty and Shiono n. sp. (Pl. P1, fig. 10; Pl. P3, figs. 1-6, 10-13).
Synonym: *Azpeitia* sp. B of Shiono, 2000a (doctoral thesis), pl. 34, figs. 1-6; pl. 35, figs. 1-6.

***Azpeitia tabularis* (Grunow) [Plate 1, Fig. 8].** Fryxell and Sims in Fryxell et al., 1986, pp. 16-18, figs. XIV, XV, XXX-I; Censarek and Gersonde, 2002, p. 350, pl. 1, fig. 7.

***Cavitatus jouseanus* [Plate 5, figs. 19-21]** (Sheshukova) Williams; Akiba et al., 1993, pp. 20-22, figs. 6-19, 6-20; Censarek and Gersonde, 2002, p. 350, pl. 5, fig. 12.

***Cavitatus miocenicus* [Plate 5, figs. 15-16]** (Schrader) Akiba and Yanagisawa in Akiba et al., 1993, p. 28, figs. 9-1 through 9-11.

Chaetoceros* (*Hyalochaete), Ehrenberg, 1884. Subgenera *Hyalochaete,* Priddle and Fryxell, 1985.
Notes: The *Chaetoceros* genus is split into two subgenera: *Hyalochaete* and *Phaeoceros,* based on their ability to form resting spores. All *Chaetoceros* resting spores identified are therefore of the subgenus *Chaetoceros* (*Hyalochaete).*

***Cocconeis* spp. [Plate 6, figs. 1-9]** Ehrenberg, 1838, Harwood 1998, p. 511, Pl. 3-6, figs 1-4.

***Corethron pennatum* [Plate 4, fig. 14]** Castracane; Krebs, 1983, p. 285, pl. 2, fig. 4a, b; Harwood and Maruyama, 1992, p. 701, pl. 19, figs. 8-11; pl. 5, fig. 15.

***Coscinodiscus marginatus* [Plate 2, figs 8-10]** Ehrenberg; Schrader, 1973, p. 703, pl. 20, figs. 7, 10, 12, 13; Schrader, 1976, p. 631, pl. 12, fig. 2.

***Coscinodiscus oculus-iridus/asteromphalus* [Plate 2, fig. 1-2].** This species group combines *Coscinodiscus asteromphalus* Ehrenberg, 1844, p. 77; Ehrenberg, 1854, pi. 18, fig. 45; pi. 33, fig. 15; Hustedt, 1928, p. 452, figs. 250 a-c., Arney et al. (2003), p. 8, pl. P3, fig. 3; Suto et al. (2013), p. 32, pl. P2, figs. 1, 2 (no illustrations) with *Coscinodiscus oculus-iridis* (Ehrenberg) Ehrenberg 1840, 67, Yang and Chao, 1996, 1-7, figs. 1-20.

***Coscinodiscus radiatus* [Plate 2, figs. 3 & 5]** Ehrenberg; Fenner, 1978, p. 516, pl. 7, fig. 6.

***Coscinodiscus* sp. A**
Notes: Morphologically similar to *Coscinodiscus marginatus*, but distinguished by its smaller size and much less prominent margin.

Crucidenticula ikebei Akiba and Yanagisawa, 1986, pp. 485, 486, pl. 1, figs. 1, 2; Yanagisawa and Akiba, 1990, pp. 228, 229, pl. 1, figs. 10-12; pl. 8, figs. 8-13.

Crucidenticula nicobarica **[Plate 2, figs. 30-32]** Akiba and Yanagisawa, 1986, pp. 486, 487, pl. 1, fig. 9; pl. 2, figs. 1-7; pl. 5, figs. 1-9; Yanagisawa and Akiba, 1990, p. 232, pl. 1, figs. 23-29; Censarek and Gersonde, 2002, p. 351, pl. 2, figs. 25, 26.
Notes: Another variety of *C. nicobraica* was possibly recognised occurring at Site 747 only, which is identical to *C. nicobarica* but asymmetrical along the apical axis (see Plate 3, fig. 31). However, this was grouped here as *C. nicobarica*.

Cymatosira **spp. [Plate 6. Fig. 23]** Grunow, 1862. Suto and Uramoto, 2015, p. 21, Pl 5, figs 17-19.

Dactyliosolen antarcticus Castracane; Hasle, 1975, pp. 119-121, figs. 90-100, 109-112; Harwood and Maruyama, 1992, p. 702, pl. 18, fig. 12.

Delphineis **spp.** Andrews, 1977.

Denticulopsis "hustedtii **var.** ***aspera"*** Maruyama in Harwood and Maruyama, 1992, p. 702, pl. 10, figs. 8-11, 15, 16.
Remarks: Bohaty et al. (2003) noted that because of taxonomic revisions in the *Denticulopsis* group by Yanagisawa and Akiba (1990), this form should be renamed, or the variety name *"aspera"* should be elevated to species status. However, this has not yet occurred, so it remains *D. hustedii* var. *aspera* here.

Denticulopsis crassa **[Plate 2, fig. 23]** Yanagisawa and Akiba, 1990, pp. 248, 249, pl. 3, figs. 21-27; pl. 12, figs. 1-8; Censarek and Gersonde, 2002, p. 351, pl. 2, fig. 12.

Denticulopsis delicata **[Plate 2, fig. 33]** Yanagisawa & Akiba, 1990. pp. 246, pl. 7, figs. 1-4.

Denticulopsis dimorpha **[Plate 2, figs. 34, 41-45]** Schrader (Simonsen) var. *dimorpha* Yanagisawa and Akiba, 1990, pp. 254, 255, pl. 4, figs. 42-49; pl. 7, figs. 14-16.

Denticulopsis dimorpha* var. *areolata Yanagisawa and Akiba, 1990, p. 257, pl. 4, figs. 40, 41, 50-54; pl. 5, figs. 13-17; pl. 6, figs. 1-5, 15-23; pl. 12, figs. 15, 16.

Denticulopsis hustedtii Simonsen, 1979. Yanagisawa & Akiba, 1990, p. 246 Pl. 3, figs 14-19, Pl. 11, figs. 11-13.

***Denticulopsis hyalina* [Plate 2, figs. 24-26]** (Schrader) Simonsen; Yanagisawa and Akiba, 1990, pp. 240, 241, pl. 2, figs. 14, 33, 34; pl. 9, figs. 8, 9.

***Denticulopsis* cf. *lauta* [Plate 2, figs. 1-6, 8-12]** (Bailey) Simonsen, 1979, p. 64; Maruyama, 1984a, p.14, figs. 1a-8b, p. 785; Akiba, 1986, pl. 26, fig. 15; Akiba and Yanagisawa, 1986, p. 489, pl. 7, fig. 29, pl. 9, figs. 2-9, non pl. 9, fig. 1.
Notes: Species resembling *Denticulopsis* cf. *lauta* have been grouped here. A new variety was possibly identified in addition to classical *D. lauta* valves at Site 1165 only; featuring a more rounded valve outline and less pronounced valve deck (Plate 3, Figs 1-5). However, both varieties are grouped here.

Denticulopsis maccollumii Simonsen; Yanagisawa and Akiba, 1990, pp. 264, 265, pl. 2, figs. 39-41; Harwood and Maruyama, 1992, p. 702, pl. 6, fig. 22; pl. 7, fig. 17; pl. 9, fig. 27; Censarek and Gersonde, 2002, p. 351, pl. 2, figs. 32-34.

***Denticulopsis maccollumii* var. A [Plate 2, figs. 27-28]**
Notes: This variety is distinguished in this study from *D. maccollumii* by punctation on the valve face; usually 1-3 punctae, following Bohaty (unpublished plates, 2013).

***Denticulopsis maccollumii* sp. 1 [Plate 2, fig. 29]**
Notes: This variety is distinguished from *D. maccollumii* following Bohaty (unpublished plates, 2013) due to its more prominent marginal ribs, smaller size (not larger than c. 40 µm) and fewer pseudosepta.

***Denticulopsis ovata* [Plate 2, fig. 46]** (Schrader) Yanagisawa and Akiba, 1990, pp. 257, 258, pl. 6, figs. 6-14, 24-32; Censarek and Gersonde, 2002, p. 351, pl. 2, figs. 13-20.
Synonym: *Denticulopsis meridionalis* Harwood and Maruyama, 1992, pp. 702, 703, pl. 6, figs. 1-4; pl. 7, figs. 1-4, 6-9, 11-13; pl. 9, figs. 1-4, 10-14; pl. 10, fig. 7.

Denticulopsis praedimorpha Barron ex Akiba var. *praedimorpha* Yanagisawa and Akiba, 1990, pp. 251, 252, pl. 4, figs. 3-5, 10, 12-17, 39; pl. 5, figs. 4-12; Censarek and Gersonde, 2002, p. 351, pl. 2, figs. 1-7.

Denticulopsos praelauta **[Plate 2, fig. 7]** Akiba & Koizumi, 1986, p. 439, p. 26, figs. 10-14; Akiba and Yanagisawa, 1986, p. 490, pl. 7, figs 1-15, pl. 8, figs. 1-9; Yanagisawa et al., 1989, pl. 6, figs. 3-4, Yanagisawa & Akiba, 1990, Pl. 2, figs. 3-5, 16-18.

Denticulopsis praehyalina **[Plate 2, fig. 14-15]** Tanimura emend. 1989, p. 172-174, p. 1, figs. 1-4, 6-9b; pl. 2, figs 1-3b, 5-7, non pl. 1, fig. 5, pl. 2, figs 4a, 4b. Yanagisawa & Akiba, 1990, Pl. 2, figs 28-32, Pl. 9, figs. 5-6.

Denticulopsis simonsenii/vulgaris **[Plate 2, figs. 16-22]** Yanagisawa and Akiba, 1990, pp. 242, 243, pl. 3, figs. 1-3; pl. 11, figs. 1, 5; Censarek and Gersonde, 2002, p. 351, pl. 2, figs. 21-24. Remarks: *D. simonsenii* was separated from *Denticulopsis vulgaris* following the taxonomic indications of Yanagisawa and Akiba (1990). In this study, I do not distinguish *D. simonsenii* from its descendent *D. vulgaris*, following Gulick et al. (2017). The primary distinguishing feature between these two species is punctation of the valve face (increased in *D. simonsenii*, reduced in *D. vulgaris*; Yanagisawa & Akiba, 1990). However, valve punctation was not always visible due to dissolution of the valves, and several intermediate forms were observed, making it difficult to separate the two species. As such, diatom assemblage diversity at Site 1165 may be underestimated, particularly where *D. simonsenii/ vulgaris* is abundant. However, *D. vulgaris* abundance is thought to have remained low until the *D. dimorpha* diatom zone (NPD 5D) in the North Pacific at least (Yanagisawa & Akiba, 1990), suggesting most of the *D. simonsenii/vulgaris* valves documented in this study during the Middle Miocene are likely *D. simonsenii*. Substantial variation other than valve punctation was also observed within the *Denticulopsis simonsenii/vulgaris* species complex, for example in terms of density of pseudosepta or width of the valve deck, which may allow it to be further split in later studies. However, I have followed Bohaty (unpublished plates, 2013) in separating *Denticulopsis* sp. 3, distinguished by its centrally-flared valve outline.

Denticulopsis **sp. 3**

Synonym: Bohaty unpublished plates (Pl. 1, figs. 1-12).

Description: Frustule rectangular with rounded corners in girdle view, valve elongated but centrally flared, 20-50 µm long. Transapical striae finely punctated. Primary and secondary pseudosepta present, equally spaced. Short marginal ribs between each pseudosepta.
Remarks: This species is very similar to *Denticulopsis simonsenii,* but is distinguished by its distinctive centrally flared valve outline.
Stratigraphic occurrence: This species co-occurs with *Denticulopsis simonsenii/vulgaris* at ODP Site 1165 during the Middle-Late Miocene.

Denticulopsis vulgaris (Okuno) Yanagisawa and Akiba, 1990, pp. 243, 244, pl. 3, figs. 4-8; pl. 11, figs. 2, 6-10.
Remarks: See notes under *Denticulopsis simonsenii.*

Diploneis Ehrenberg, 1845.

Ellerbeckia sol (Ehrenberg) R.M.Crawford & P.A.Sims 2006, 151.

***Entopyla* spp.** Bohaty et al. (2003) Pl. P2, fig. 19).

***Eucampia antarctica* [Plate 4, fig. 15]** (Castracane) Mangin; Krebs, 1983, p. 285, pl. 3, figs. 3a, b; Mahood and Barron, 1996b, p. 290, pl. 1, figs. 1-3; pl. 7, figs. 1, 2.

Eucampia antarctica* var. *"twista" Bohaty, Wise, Duncan, Moore & Wallace
Notes**:** This variety of *E. antarctica* has not been formally described, but is characterized by rotation (up to 90°) on the valvar plane, similar to the Paleogene species *Hemiaulus rectus* var. *twista* Fenner. I have followed Bohaty et al. (2003) in separating it from *E. antarctica* var. *recta*

Eurossia spp. Mahood, Baron and Sims, 1993., p.254-255, figs. 31-36.

Fragilariopsis arcula (Gersonde) Gersonde and Bárcena, 1998, p. 92; Censarek and Gersonde, 2002, p. 351, pl. 3, figs. 15-18.
Basionym: *Nitzschia arcula* Gersonde, 1991, pp. 143, 144, pl. 2, fig. 4; pl. 4, fig. 4; pl. 5, figs. 1-6.

Fragilariopsis aurica (Gersonde) Gersonde and Bárcena, 1998, p. 92; Censarek and Gersonde, 2002, p. 351, pl. 3, figs. 9-12; Zielinski and Gersonde, 2002, p. 257, pl. 1, figs. 13-15.
Basionym: *Nitzschia aurica* Gersonde, 1991, pp. 144-146, pl. 1, figs. 18-25; pl. 3, fig. 5; pl. 4, figs. 5, 6; pl. 7, fig. 6.

Fragilariopsis barronii (Gersonde) Gersonde and Bárcena, 1998, p. 92; Zielinski and Gersonde, 2002, p. 257, pl. 1, figs. 29-31.
Basionym: *Nitzschia barronii* Gersonde, 1991, pp. 146, 147, pl. 3, fig. 6; pl. 4, figs. 1-3; pl. 5, figs. 7-17.

Fragilariopsis bohatyii Sjunneskog in Sjunneskog et al., 2012., p. 284-285, pl. 3, figs. a-q.

Fragilariopsis claviceps (Schrader) Censarek & Gersonde, 2002.
Basionym: *Nitzschia claviceps*, Schrader, 1976, 633, pl. 2, figs. 2, 4.

Fragilariopsis clementia (Gombos) Zielinski and Gersonde, 2002, p. 33; Censarek and Gersonde, 2002, p. 351, pl. 3, figs. 7, 8.
Basionym: *Nitzschia clementia* Gombos, 1977, p. 595, pl. 8, figs. 18, 19; Gersonde and Burckle, 1990, p. 779, pl. 2, figs. 22, 23, Bohaty et al., 2003, Pl. 2, figs 8 and 9.

Fragilariopsis cf. curta (Van Heurck) Hustedt; Hasle, 1965, pp. 32, 33, pl. 6, fig. 6; pl. 12, figs. 2-5; pl. 13, figs. 1-6; pl. 16, fig. 6; pl. 17, fig. 5.
Basionym: *Fragilaria curta* Van Heurck, 1909, p. 24, pl. 3, fig. 37.
Synonym: *Nitzschia curta* (Van Heurck) Hasle, 1972, p. 115; Krebs, 1983, p. 286, pl. 4, fig. 4; Hasle and Medlin, 1990, p. 181, pl. 24.6, figs. 2-5.
Notes: specimens that resemble *Fragilariopsis curta* have been grouped here as *F. cf. curta*. In some specimens, the asymmetric poles characteristic of *F. curta* are not as obvious, and/or the poles are more rounded. However, this varies, and using light microscopy some of these specimens are otherwise indistinguishable from *F. curta*.

Fragilariopsis cylindrus (Grunow) Krieger in Helmcke and Krieger; Hasle, 1965, pp. 34-37, pl. 12, figs. 6-12; pl. 14, figs. 1-10; pl. 17, figs. 2-4.
Synonym: *Nitzschia cylindrus* (Grunow) Hasle, 1972, p. 115; Hasle and Medlin, 1990, p. 181, pl. 24.6, figs. 6-11.

***Fragilariopsis donahuensis* [Plate 5, fig. 12]** (Schrader) Censarek and Gersonde, 2002, p. 350, pl. 3, figs. 13, 14.
Basionym: *Nitzschia donahuensis* Schrader, 1976, p. 633, pl. 2, fig. 30; Gersonde and Burckle, 1990, p. 780, pl. 1, figs. 16-18.

Fragilariopsis efferans (Schrader) Censarek and Gersonde, 2002, p. 350.
Basionym: *Nitzschia efferans* Schrader, 1976, p. 633, pl. 2, figs. 1, 3, 5-7.

Fragilariopsis interfrigidaria (McCollum) Gersonde and Bárcena, 1998, p. 92; Zielinski and Gersonde, 2002, p. 259, pl. 1, figs. 20, 21.
Basionym: *Nitzschia interfrigidaria* McCollum, 1975, p. 535, pl. 9, figs. 7-9; Ciesielski, 1983, p. 655, pl. 1, figs. 11-18; Gersonde and Burckle, 1990, p. 780, pl. 1, figs. 1-3 Bohaty et al., 2003, Pl. P2, figs 15-18).

Fragilariopsis januaria (Schrader) Bohaty n. comb. 2003.
Basionym: *Nitzschia januaria* Schrader, 1976, p. 634, pl. 2, figs. 25-29, Ciesielski 1986, pl. 3, fig. 5; Baldauf and Barron, 1991, pl. 5, fig. 10.
Remarks: Following the taxonomic revisions of Gersonde and Bárcena (1998), Zielinski and Gersonde (2002), and Censarek and Gersonde (2002), this taxon was transferred to the genus *Fragilariopsis* by Bohaty et al. (2003).

***Fragilariopsis januaria* var. A**
Synonym: *Fragliariopsis januaria* var. A (Bohaty, unpublished plates 2013); pl. 4, figs. 46-49.
Notes: This new variety, first recognised by Bohaty (unpublished plates, 2013), is distinguished from *F. januaria* by larger punctation on the valve face and a shorter, wider valve outline.

Fragilariopsis kerguelensis (O'Meara) Hustedt; Hasle, 1965, pp. 14-18, pl. 3, figs. 4, 5; pl. 4, figs. 11-18; pl. 5, figs. 1-11; pl. 6, figs. 2-4; pl. 7, fig. 9; pl. 8, fig. 10; pl. 16, figs. 3-5.
Notes: *Fragilariopsis barronii* grades into *F. kerguelensis* in the upper part of its range (see illustrations of transitional forms in Zielinski and Gersonde, 2002, pl. 1, figs. 25-28). Early forms of *F. kerguelensis* have smaller areolae than typical modern forms of *F. kerguelensis.*
Synonym: *Nitzschia kerguelensis* (O'Meara) Hasle, 1972, p. 115; Fenner et al., 1976, p. 776, pl. 2, figs. 19-30; Hasle and Medlin, 1990, p. 181, pl. 24.2, figs. 11-18, Bohaty et al., 2003, Pl2, fig. 13.

Fragilariopsis lacrima (Gersonde) Gersonde and Bárcena, 1998, p. 92; Censarek and Gersonde, 2002, p. 351, pl. 3, figs. 5, 6; Zielinski and Gersonde, 2002, p. 259, pl. 1, figs. 8, 9.
Basionym: *Nitzschia lacrima* Gersonde, 1991, p. 148, pl. 1, figs. 1-6, 26; pl. 2, figs. 1-3, Bohaty bet al., 2003, P2, figs. 10, 11.

Fragilariopsis* cf. *linearis (Castrane) Frenguelli, 1943, p. 244, pl. 1, fig. 16.
Synonym: *Nitzschia lineata* (Castracane) Hasle, 1972, p 115.

Fragilariopsis matuyamae Gersonde and Bárcena, 1998, p. 93, pl. 1, figs. 1-9, 13-16; pl. 2, figs. 1, 4, 5, 7-9; Zielinski and Gersonde, 2002, p. 259, pl. 1, figs. 10, 11.

Fragilariopsis miocenica (Burckle) Censarek & Gersonde (2002).

Fragilariopsis obliquecostata (Van Heurck) Heiden in Heiden and Kolbe; Hasle, 1965, pp. 18-20, pl. 7, figs. 2-7.
Basionym: *Nitzschia obliquecostata* (Van Heurck) Hasle, 1972, p. 115; Fenner et al., 1976, pp. 776, 777, pl. 2, figs. 15-18.

Fragilariopsis praecurta (Gersonde) Gersonde and Bárcena, 1998, p. 92; Censarek and Gersonde, 2002, pp. 351, 352, pl. 3, figs. 19-21.
Basionym: *Nitzschia praecurta* Gersonde, 1991, pp. 148, 149, pl. 1, figs. 7-17; pl. 2, figs. 5, 6; pl. 3, figs. 3, 4; pl. 10, fig. 7.

Fragilariopsis praeinterfrigidaria (McCollum) Gersonde and Bárcena, 1998, p. 92; Zielinski and Gersonde, 2002, p. 259, pl. 1, figs. 22, 23; Censarek and Gersonde, 2002, p. 352, pl. 3, figs. 22, 23.
Basionym: *Nitzschia praeinterfrigidaria* McCollum, 1975, p. 535, pl. 10, fig. 1; Ciesielski, 1983, p. 655, pl. 2, figs. 1-8, 13-16; pl. 3, fig. 5.
Notes: Intermediate forms between *F. praeinterfrigidaria* and *Fragilariopsis interfrigidaria* were noted in the Pliocene section of ODP Hole 1165B. These forms possessed light silicification between the transapical costae, also noted by Bohaty et al. (2003) at ODP Site 1138, but are included in *F. praeinterfrigidaria* unless unambiguloisly *F. interfrigidaria*.

Fragilariopsis pseudokerguelensis **[Plate 5, fig. 13]** Schrader, 1976, p. 634, pl. 15, figs. 13–15. Gersonde and Burckle, 1990, pl. 2, fig. 2, Censarek & Gersonde, 2002, Pl. 2, fig. 39.
Basionym: *Niztschia pseudokerguelensis* Schrader, 1976, Censarek & Gersonde, 2002.

Fragilariopsis pseudonana Hasle; Hasle, 1965, pp. 22-24, pl. 1, figs. 7-14; pl. 4, figs. 20, 21; pl. 8, figs. 1-9; pl. 17, fig. 6.
Basionym: *Nitzschia pseudonana* Hasle, 1974, p. 427; Fenner et al., 1976, p. 777, pl. 2, figs. 6-11; Hasle and Medlin, 1990, p. 181, pl. 24.1, figs. 7-14.
Remarks: See Hasle and Syvertsen (1996) for comments on the taxonomy of this species.

Fragilariopsis pusilla (Schrader) Censarek and Gersonde, 2002, p. 350, pl. 3, fig. 25.
Basionym: *Nitzschia pusilla* Schrader, 1976, p. 634, pl. 2, fig. 20.

Fragliariopsis robusta Sjunneskog & Reisselman in in Sjunneskog *et al.* 2012: 277; pl. 5,6.
Basionym: *Nitzschia robusta* Hustedt, 1949.

Fragilariopsis rhombica (O'Meara) Hustedt; Hasle, 1965, pp. 24-26, pl. 1, fig. 6; pl. 4, fig. 19; pl. 6, fig. 5; pl. 8, fig. 11; pl. 9, figs. 1-6; pl. 10, figs. 2-6.
Synonym: *Nitzschia angulata* Hasle, 1972, p. 115; Fenner et al., 1976, p. 775, pl. 1, figs. 17-39; Hasle and Medlin, 1990, p. 181, pl. 24.1, fig. 6; pl. 24.2, fig. 19; pl. 24.4, figs. 1-6.

Fragilariopsis ritscheri Hustedt; Hasle, 1965, pp. 20, 21, pl. 1, fig. 20; pl. 3, fig. 3; pl. 4, figs. 1-10; pl. 5, figs. 12, 13; pl. 6, fig. 1; pl. 7, fig. 8.
Synonym: *Nitzschia ritscheri* (Hustedt) Hasle, 1972, p. 115; Fenner et al., 1976, p. 777, pl. 3, figs. 1-12; Hasle and Medlin, 1990, p. 181, pl. 24.1, fig. 20; pl. 24.2, figs. 1-10; pl. 24.3, fig. 9.

Fragilariopsis separanda Hustedt; Hasle, 1965, pp. 26, 27, pl. 9, figs. 7-10; pl. 10, fig. 1; Zielinski and Gersonde, 2002, p. 259, pl. 1, figs. 16, 17.
Synonym: *Nitzschia separanda* (Hustedt) Hasle, 1972, p. 115; Fenner et al., 1976, p. 777, pl. 1, figs. 1-16; Hasle and Medlin, 1990, p. 181, pl. 24.2, figs. 7-10.

Fragilariopsis truncata H. T. Brady ex M. P. Olney in Olney et al., 2007, Pl 1., figs 6-11, Pl 2., figs 23-28.

Synonyms: *Nitzschia truncata* Brady 1978, p. 123-123, no illustration; Brady 1979, p.130, Brady, 1980, pp. 10-12, Pl. 6, figs 11-14.
Notes: Olney et al. (2007) note that this species may be an ancestor of *Fragilariopsis vanheurckii* and/or other *Fragliariopsis* species that evolved in the Middle/Late Miocene. As such, it is also morphologically similar to some specimens included in *Fragilariopsis cf. curta* group in this study and is, at times, difficult to separate from *Fragilariopsis curta* likely due to transitional species between the two. Brady et al. (1983) note that the main difference between *F. curta* and *F. truncata* are a greater striae density and single arrangement of pores in *F. truncata*, but this is difficult to view using light microscopy and may only become apparent under SEM.

Fragilariopsis sublinearis (Van Heurck) Heiden and Kolbe, 1943, p. 241, figs 12, 13-15.

Fragilariopsis weaveri (Ciesielski) Gersonde and Bárcena, 1998, p. 93; Zielinski and Gersonde, 2002, p. 260, pl. 1, figs. 18, 19.
Basionym: *Nitzschia weaveri* Ciesielski, 1983, p. 655, pl. 1, figs. 1-10.

Fragilariopsis cf. vanheruckii (Peragallo) Hustedt, 1958: 166, pl. 12, figs 154-156.
Notes: Valves resembling *Fragliariopsis vanheurckii* have been grouped here as *F. cf. vanheurckii*.

***Fragliariopsis* sp. nov #1**
Synonym: Bohaty, unpublished plates (2013), plate 5, figs 39-40.

***Fragliariopsis* sp. nov #2**
Synonym: Bohaty, unpublished plates (2013), plate 5, fig 38
Notes: Morphologically similar to *F. januaria*, but distinguished by its symmetrical outline.

***Fragliariopsis* sp. nov #3**
Synonym: Bohaty, unpublished plates (2013), plate 5, fig 41.
Notes: Small, length 5-20 µm. Strongly pointed valve ends, flared towards the centre. Morphologically resembles *F. rhombica*, and may represent an ancestor; further investigation by SEM microscopy is required to fully distinguish.

***Fragliariopsis* sp. nov #4**

Synonym: Bohaty, unpublished plates (2013), plate 5, fig 51-52.

Notes: Valves approximately 10-20 µm in length. Distinguished from *F. praecurta* by its narrower valve shape and isopolar ends, and also distinguished from *F. curta* by its isopolar ends.

***Fragilariopsis* sp. A** Harwood, Harwood, Bohaty, S. and Scherer, R. 1998.

Basionym: Niztschia sp. A (Harwood, Sherwood and Webb, 1989, pl. 4, figs 12-14), Kellogg and Kellogg, 1986, pl. 2., fig 23.

Grammatophora spp. [Plate 6, figs. 25-26] Ehrenberg 1840.

Hemiaulus Heiberg, 1863.

Notes: species of *Hemiaulus* are assumed to be reworked in the study interval at Site 1165.

Hemidiscus cuneiformis Wallich; Fenner, et al., 1976, p. 774, pl. 11, fig. 17; Harwood and Maruyama, 1992, pl. 11, fig. 11. Iwai & Winter, 2002, Pl. P21, fig. 2.

***Hemidiscus karstenii* f. 1** of Ciesielski, 1983, p. 656, pl. 4, figs. 2-5, but not pl. 4, fig. 1.

Remarks: This form is described with widely spaced areolae in the central area (Ciesielski, 1983). I have followed Bohaty et al. (2003) in strictly applying this definition and excluding specimens with closely packed areolae in the central area (Ciesielski, 1983, pl. 4, fig. 1). In contrast, Zielinski and Gersonde (2002, p. 260) apply "*H. karstenii* f. 1" to specimens with closely packed areolae in the central area.

Hemidiscus karstenii Jousé; Abbott, 1974, p. 313, pl. 1, figs. D-F; Fenner, 1991, p. 108, pl. 1, fig. 2; Censarek and Gersonde, 2002, p. 352, pl. 3, fig. 27.

Hemidiscus ovalis Lohman, 1938. P. 91, Pl. 22, fig. 9.

Hemidiscus* sp. cf. *H. cuneiformis Wallich; Schrader, 1973, p. 706, pl. 24, fig. 14; Fenner et al., 1976, p. 774, pl. 11, fig. 17; Harwood and Maruyama, 1992, p. 703, pl. 11, fig. 11; Censarek and Gersonde, 2002, p. 352, pl. 4, fig. 5.

Hemidiscus triangularus (Jousé) Harwood and Maruyama, 1992, p. 703; Censarek and Gersonde, 2002, p. 352, pl. 4, figs. 1-4.
Basionym: *Cosmiodiscus insignis* f. *triangula* Jousé; Ciesielski, 1983, p. 656, pl. 5, figs. 1-10; Ciesielski, 1986, p. 876, pl. 4, figs. 5, 6.

***Isthmia* spp**. Agardh, 1832.

***Kisseleviella* spp.** Sheshukova-Poretzkaya, 1962.

Liradiscus spp. Greville, 1985.

Lithodesmium minisculum Grunow in Van Heurck; Schrader, 1973, p. 706, pl. 12, figs. 7(?), 15, 17.

Lisitzinia ornata Jousé, 1978, 47, tabl. 10, fig. 1-6.

***Macrora barbadensis* [Plate 4, fig. 2]** (Deflandre) Bukry, 1977.

***Melosira* spp. [Plate 6, fig. 14]** Agardh, 1824

***Navicula* spp.** Bory, 1822

***Nitzschia cf. challengerii* [Plate 5, fig. 14]** Schrader, 1973, p. 754-755, Pl. 5, Figs 10-14.

***Nitzschia denticuloides* [Plate 5, figs. 1-2]** Schrader, 1976, p. 633, pl. 3, figs. 7, 8, 10, 12, 18-24; pl. 15, fig. 22; Harwood and Maruyama, 1992, p. 704, pl. 8, figs. 5-8, 17; pl. 9, figs. 24-26; pl. 10, fig. 1; Censarek and Gersonde, 2002, p. 352, pl. 2, figs. 27-31.

***Nitzschia grossepunctata* [Plate 5, figs. 5-7]** Schrader, 1976, pp. 633, 634, pl. 3, figs. 1-4; Harwood and Maruyama, 1992, p. 704, pl. 10, fig. 2; Censarek and Gersonde, 2002, p. 352, pl. 2, figs. 37, 38.

Nitzschia maleinterpretaria Schrader, 1976, p. 634, pl. 2, figs. 9, 11-19, 21, 24.

Synonym: *Fragilariopsis maleinterpretaria* (Schrader) Censarek and Gersonde, 2002, p. 351, pl. 3, fig. 26.

Nitzschia miocenica Burckle; Ciesielski, 1983, p. 656, pl. 2, figs. 9-12; Akiba, 1986, p. 443, pl. 23, figs. 10, 14; Akiba and Yanagisawa, 1986, p. 496, pl. 39, figs. 7-15; pl. 41, figs. 1, 2.
Synonym: *Fragilariopsis miocenica* (Burckle) Censarek and Gersonde, 2002, p. 351.

Nitzschia porteri Frenguelli, 1949. 116, Pl. 1, figs. 33, 34.

Nitzschia reinholdii Kanaya ex Schrader, 1973, p. 708, pl. 4, figs. 12-16; pl. 5, figs. 1-9; Akiba, 1986, pp. 443, 444, pl. 22, figs. 4, 5; Akiba and Yanagisawa, 1986, p. 496, pl. 40, figs. 8, 9; pl. 41, figs. 3, 4.
Synonym: *Fragilariopsis reinholdii* (Kanaya) Zielinski and Gersonde, 2002, p. 259, pl. 1, figs. 3, 4; Censarek and Gersonde, 2002, p. 352, pl. 3, figs. 1, 2.

***Nitzschia* sp. 3 [Plate 5, fig. 9]** Farmer, 2011. Pl. 4, figs. 12, 16.

***Nitzschia* sp. 17 [Plate 5, fig. 3-4]** of Schrader, 1976, p. 634, pl. 3, figs. 13-15, 17; pl. 2, fig. 10.

Paralia sulcata (Ehrenberg) Cleve, 1873.
Synonym: *Melosira sulcata* (Ehrenberg) Kützing; Schrader, 1973, p. 706, pl. 20, fig. 9.

Pleurosigma* spp.** Smith, 1852.***

Proboscia barboi (Briin) Jordan el Priddle, 1991, p. 56, figs. 1-2; Fenner, 1991, pi. 3, figs. 1, 3.
Basionym: *Pyxilla (Rhizosolenia) barboi* Briin, 1894, p. 87, pi. 5, figs. 16, 17, 23.
Synonyms: *Rhizosolenia barboi* (Brim) Tempere et Peragallo, 1908, p. 26, no. 47; *Rhizosolenia curviostris* var. *inermis* Jouse, 1971, p. 15, pi. 2, figs. 1, 2; *Simonseniella barboi* (Brtin) Fenner, 1991, p. 108, pi. 3, figs. 1,3.

Pyxilla Greville, 1865, p1-10, Pl. 1-2.
Notes: assumed to be reworked in samples aged 15 Ma or younger from ODP Sites 747, 744 and 1165.

Raphidodiscus marylandicus Christian; Andrews, 1978, p. 400, pl. 5, figs. 23, 24; Schrader, 1976, p. 635, pl. 5, fig. 19; pl. 15, fig. 16.

Rhabdonema japonicum **[Plate 6, fig. 27-28]** Tempère and Brun; Scherer et al., 2000, p. 436, pl. 5, fig. 10., Harwood et al. 2000, p. 460, pl. 9, fig. K, fig 5.16.

Rhabdonema **spp. [Plate 6, figs. 15-22]** Kützing 1844; e.g. Whitehead et al., 2004, p. 536, fig. 5.16.

Rhaphoneis **spp.** Ehrenberg 1845; e.g. Whitehead et al., 2004, p. 536, fig. 5.19.

Rhizosolenia costata Gersonde, 1991, pp. 149, 150, pl. 9, figs. 1-6; pl. 10, figs. 1-6; Harwood and Maruyama, 1992, p. 705, pl. 18, figs. 1, 2.

Rhizosolenia harwoodii sp. nov. Winter, in Winter et al., 2012, p.66, Pl 5, fig 18.
Synonym: *Rhizosolenia* sp. D Harwood et Maruyama, 1992, Pl. 18, Figs. 7–10; *Rhizosolenia* sp. A. of Akiba, 1986, Pl. 18, Fig. 11; *Rhizosolenia* sp. A of Koizumi, 1968, Pl. 34, Figs. 2a–b.

Rhizosolenia hebetata **[Plate 4, fig. 19]** Bailey; Scherer et al., 2000, p. 436, pl. 3, figs. 6, 7.

Rhizosolenia hebetata **f.** ***hiemalis*** **[Plate 4, fig. 16-17]** Gran sensu Schrader, 1973, p. 709, pl. 9, figs. 11, 13-17, 19-21, 24, 25; Schrader, 1976, p. 635, pl. 9, figs. 1-3; Akiba, 1986, p. 444, pl. 17, figs. 10, 11; pl. 18, figs. 9, 10; Harwood and Maruyama, 1992, p. 11, fig. 7.
Remarks: *Rhizosolenia hebetata* f. *hiemalis* and *Rhizosolenia hebetata* f. *hiemalis-spinosa* identified by Schrader (1976) are included together here.

Rhizosolenia styliformis **[Plate 4, fig. 20]** Brightwell; Schrader, 1973, p. 710, pl. 9, fig. 9(?); pl. 10, figs. 1, 18-21.

Rhizosolenia **sp. 1 [Plate 4, fig. 18]**.
Synonym: Bohaty, unpublished plates (2013), Pl. 16, fig 3-4.

Rhizosolenia **sp. A**
Synonym: Bohaty, unpublished plates (2013), Pl. 16, figs. 9-11.

Rocella gelida (Mann) Bukry; Gombos and Ciesielski, 1983, p. 604, pl. 6, figs. 1-6; pl. 26, fig. 1.

Rouxia antarctica Heiden in Heiden and Kolbe; Schrader, 1976, p. 635, pl. 5, figs. 1-8; Mahood and Barron, 1996b, p. 292, pl. 2, figs. 5, 6; pl. 7, figs. 18, 19; Zielinski and Gersonde, 2002, p. 261, pl. 2, fig. 10.

Rouxia californica Peragallo; Schrader, 1973, p. 710, pl. 3, figs. 18-20, 22(?), 26; Baldauf and Barron, 1991, p. 590, pl. 5, fig. 6.

Rouxia diploneides Schrader, 1973, p. 750-751, Pl. 3, figs 24-25.
Synonym: *Navicula rouxiodiea* Sheshukova-Poretskaya (1976) (partim) p. 284, pl. XLVI, figs. 6a, 6b.

Rouxia heteropolara Gombos; Gombos, 1977, p. 597, pl. 7, figs. 14, 15.

Rouxia isopolica Schrader, 1976, pp. 635, 636, pl. 5, figs. 9, 14, 15, 20.

Rouxia naviculoides Schrader, 1973, p. 710, pl. 3, figs 27-32; Zielinski and Gersonde, 2002, p. 261, pl. 2, figs. 8, 9.

Rouxia peragalli Brun and Héribaud sensu Baldauf and Barron, 1991, p. 590, pl. 5, figs. 7, 8.

Shionodiscus praeoestrupii (Dumont, Baldauf & Barron) Alverson, Kang & Theriot

Shionodiscus tetraoestrupii Bodén, 1993, p. 63, pl. 1, figs. A-G; pl. 2, figs. A, B, H, J; Mahood and Barron, 1995, figs. 9-19, 25, 26, 28-46.
Remarks: Following Bohaty et al. (2003), this group includes several species that possess a central strutted process and a labiate process on the valve face. *Thalassiosira tetraoestrupii* var. *reimeri* was recorded separately.

Shionodiscus tetraoestrupii* var. *reimeri Mahood and Barron, 1995, p. 2, figs. 1-8, 20-24, 27.
Remarks: *T. tetraoestrupii* var. *reimeri* has a narrow, consistent range in the upper Pliocene of ODP Site 1165 (Bohaty et al., 2003). A few rare specimens were also identified in the lower

Pleistocene; these occurrences may indicate a longer total range for this taxon, or they may be reworked.

***Sphyntolethus* spp.** Hanna, 1927.

***Stellarima microtrias* [Plate 4, fig. 13]** (Ehrenberg) Hasle and Sims; Hasle et al., 1988, pp. 196-198, figs. 1-25.

Stellarima stellaris (Roper) Hasle and Sims; Hasle et al., 1988, pp. 198-200, figs. 26-38.

***Stephanopyxis turris* [Plate 4, figs. 6-8]** (Greville et Arnott) Ralfs; Schrader et Fenner, 1976, pi. 30, figs. 1-10, 14; pi. 37, figs. 17-19.

***Stephanopyxis* sp. B [Plate 4, fig. 11-12]** in Harwood and Bohaty, 2000, Pl 2., Fig. F.

***Syndera* spp.** Ehrenberg 1832.

Synedropsis sp. A

Synonym: Bohaty, unpublished plates (2013). Pl. 6, Fig. 3.

***Synedropsis* sp. B** Bohaty in Bohaty et al., 2003, p. 51, Pl. 2, fig 12.

Synonym: "*Tigeria*" sp. B of Scherer et al., 2000, p. 440, pl. 2, fig. 15 (Pl. P2, fig. 12).

***Synedropsis* sp. C**

Synonym: Bohaty, unpublished plates (2013), Pl. 6, fig. 8.

***Synedropsis* sp. 1**

Synonym: Bohaty, unpublished plates (2013). Pl. 6, fig. 2.

Thalassionema nitzschioides (Grunow) Mereschkowsky; Hasle, 2001, pp. 9-16, figs. 1-3, 5-25, 27.

***Thalassionema nitzschioides* var. 1** Bohaty et al. (2003).

Notes: Separation of this form from *Thalassionema nitzschioides* follows Bohaty et al. (2003) at Site 1138, where this form is present in the upper Miocene- lower Pliocene section. *Thalassionema nitzschioides* var. 1 is distinguished from T. *nitzschioides* by one apical end that is inflated.

***Thalassionema nitzschioides* var. *parva* [Plate 5, fig. 11]** Heiden; Hasle, 2001, pp. 9-16, figs. 4, 26.

Thalassiothrix/Trichotoxon [Plate 5, fig. 10]

Notes: species of *Thalassiothrix* and *Trichotoxon* are grouped together in this thesis. However, *Trichotoxon reinboldii* (Van Heurck) F. M. H. Reid & Round 1988: 224, is the only species in the *Trichotoxon* genus, and the *Thalassiothrix* species in this record likely consist of *Thalassiothrix longissima* Cleve and Grunow, 1880; Hustedt, 1958, p. 247, fig. 726, *Thalassiothrix antarctica* Schimper ex Karsten 1905: 124, pl. 17: fig. 12 and/or *Thalassiothrix miocenica* Schrader, 1973, p. 713, pl. 23, figs. 2–5 (Plate V, 15).

***Thalassiosira cf. antarctica* [Plate 4, fig. 5]** Comber, 1896.

Synonym: *Thalassiosira antarctica* Comber; Krebs, 1983, p. 286, pl. 5, fig. 4a-f; Johansen and Fryxell, 1985, p. 158, figs. 15-17, 37-39.

Notes: Specimens resembling *T. antarctica* are grouped as *T. cf. antarctica*. However, these specimens occur much earlier at Site 1165 than in the published literature and, as such, may represent an earlier form of *T. antarctica*.

Thalassiosira complicata Gersonde, 1991, pp. 150, 151, pl. 1, figs. 1, 2; pl. 5, figs. 18-20; pl. 6, figs. 1-6; pl. 7, figs. 1-5.

Thalassiosira convexa* var. *aspinosa Schrader, 1974. pi. 2, figs. 8, 9, 13-21.

Synonym: *Thalassiosira convexa* Koizumi 1975a, pi. 4, figs. 15-18.

Thalassiosira elliptipora (Donahue) Fenner ex Mahood and Barron, 1996b, pp. 292-294, pl. 4, fig. 3; pl. 5, figs. 4a-7c; pl. 8, fig. 6.

Thalassiosira fasciculata Harwood and Maruyama, 1992, p. 707, pl. 15, figs. 4-6; Mahood and Barron, 1996a, p. 287, figs. 15-24, 27, 28.

Thalassiosira gersondei Barron in Barron and Baldauf, 1991, Pl. 2, Figs. 1, 2; Pl. 3, Figs. 1, 3, 5, 6; Pl. 5, Fig. 4.

Thalassiosira gracilis (Karsten) Hustedt; Johansen and Fryxell, 1985, pp. 168-170, figs. 8, 58, 59.
Remarks: *T. gracilis* var. *gracilis* and *T. gracilis* var. *expecta* are grouped together in this thesis.

Thalassiosira insigna (Jousé) Harwood and Maruyama, 1992, p. 707, pl. 14, figs. 3-5; Zielinski and Gersonde, 2002, p. 264, pl. 5, figs. 14, 15 (Pl. P1, fig. 4).
Notes: From Bohaty et al. (2003): "The current usage of "*Thalassiosira insigna*" for Pliocene specimens from the Southern Ocean is incorrect (D. Harwood, pers. comm., 2002). The basionym for this taxon, *Cosmiodiscus insignis* Jousé, was described from the North Pacific samples (Jousé, 1977) and is better placed within the family Hemidiscaceae, not Thalassiosiraceae, based on the presence of a marginal ring of labiate processes and the absence of strutted processes. The Southern Ocean forms, however, possess strutted processes and, therefore, should be given a separate name within the Thalassiosiraceae (pers. comm. I. Makarova to D. Harwood, 1999)." In this thesis I have followed Bohaty et al. (2003) in applying the taxonomy of Harwood and Maruyama (1992) and continued the (incorrect) usage of *T. insigna.* Only specimens with an entirely hyaline central area (i.e., nonperforated) are included as *T. insigna.*

Thalassiosira inura Gersonde, 1991, p. 151, pl. 6, figs. 7-14; pl. 8, figs. 1-6; Gersonde and Burckle, 1990, p. 782, pl. 3, figs. 15-17; pl. 5, fig. 14; Harwood and Maruyama, 1992, p. 707, pl. 14, figs. 12-16.

Thalassiosira jacksonii Koizumi and Barron in Koizumi; Baldauf and Barron, 1991, p. 591, pl. 6, fig. 7.

Thalassiosira kolbei (Jousé) Gersonde, p. 793, pl. 1, fig. 2; pl. 5, figs. 3, 5, 6; Fenner, 1991, p. 108, pl. 1, figs. 1, 4; pl. 2, figs. 3, 4; Mahood and Barron, 1996b, p. 294, pl. 4, figs. 1, 2; pl. 8, fig. 1a, b.

Thalassiosira lentiginosa (Janisch) Fryxell; Mahood and Barron, 1996b, p. 294, pl. 4, figs. 4a, b, 5; pl. 8, fig. 2a, b.

Notes: As at ODP Site 1138 (Bohaty et al., 2003), the first occurrence of *T. lentiginosa* could not be determined with certainty at ODP Site 1165; early forms appear to intergrade with *Thalassiosira striata.* As noted by Bohaty et al. (2003); "both *T. lentiginosa* and *T. striata* possess strutted processes scattered across the valve face, and some lower to middle Pliocene specimens of *T. striata* possess a large labiate process that is radially oriented on the valve margin—a diagnostic feature of *T. lentiginosa.* SEM work is needed to clarify the taxonomic differences between *T. lentiginosa* and *T. striata."*

Thalassiosira maculata Fryxell and Johansen in Johansen & Fryxell, 1985, p. 170, figs 13, 69, 70, 72-74, 77-80.

Thalassiosira mahoodii Barron, Baldauf and Barron, 1991, p. 585; pl. 2, fig. 3-5, pl. 3, fig. 2, 4, pl. 4, fig. 1-6.

Thalassiosira miocenica Schrader; Barron, 1985a, p. 445, pl. 5, fig. 6; Barron, 1985b, p. 792, fig. 11.11; Gersonde and Burckle, 1990, p. 782, pl. 3, figs. 4, 5; Baldauf and Barron, 1991, p. 591, pl. 6, fig. 2.

Thalassiosira nansenii Scherer and Koç, 1996, p. 89, pl. 4, figs. 1-5.

Thalassiosira nativa Sheshukova-Poretzkaya (1959), p. 41, pl. 1, fig. 8; pl. 4, fig. 5; Schrader (1976), p. 636, pl. 12, figs. 8–11; Baldauf and Barron (1991), p. 591, pl. 6, fig. 5; Iwai and Winter (2002), p. 13, pl. P19, fig. 9, 10 (Pl. P11, figs. 3, 4).

Thalassiosira oliveriana (O'Meara) Makarova and Nikolaev; Mahood and Barron, 1996b, pl. 5, figs. 1-3; pl. 8, figs. 3-5.

Notes: Specimens identified as *T. oliverana* represent a complex group of morphologies with both coarse and fine areolation. Forms with a central dimple (Harwood and Maruyama, 1992, pl. 14, figs. 11, 17) and small diameter (≤40 µm) are included here as *T. oliveriana.* Specimens of *Thlassiosira oliveriana* var. *sparsa* (see Harwood and Maruyama, 1992, p. 708, pl. 16, fig. 13) were recorded separately.

Thalassiosira oliveriana* var. *sparsa Harwood and Maruyama, 1992, p. 708, pl. 16, fig. 13; Censarek and Gersonde, 2002, p. 353, pl. 5, figs. 1, 2.

Thalassiosira praefraga Gladenkov and Barron, 1995, pp. 30, 31, pl. 2, figs. 3-6, 9; Scherer et al., 2000, p. 440, pl. 2, figs. 3, 7.

Thalassiosira praelineata Jousé, 1977. Harwood and Maruyama, 1992, pl. 5, figs. 6–9 (Plate V, 6–7).
Synonym: *Coscinodiscus praelineatus* Jousé as synonyms of *Thalassiosira leptopus* (Grun.) Hasle and G. Fryx in Hasle and Syversten, 1982, pl. 1, fig. 6.

Thalassiosira striata Harwood and Maruyama, 1992, p. 708, pl. 15, figs. 7-9; Zielinski and Gersonde, 2002, p. 264, pl. 4, fig. 7.
Notes: See discussion under *Thalassiosira lentiginosa.*

Thalassiosira torokina Brady, 1977, p. 123, figs. 1-5; Scherer, 1991, pl. 2, fig. 4; Mahood and Barron, 1996b, p. 296, pl. 6, figs. 1-3; pl. 8, fig. 8.

Thalassiosira tumida (Janisch) Hasle in Hasle et al.; Fenner et al., 1976, p. 780, pl. 10, figs. 6, 7; Johansen and Fryxell, 1985, pp. 176, 177, figs. 28-32.

Thalassiosira vulnifica (Gombos) Fenner, 1991, p. 108, pl. 2, fig. 2; Mahood and Barron, 1996a, pp. 285-287, figs. 1-14, 25, 26.

***Thalassiosira* sp. nov [Plate 2, Fig. 5]**
Synonym: *Thalassiosira cf. eccentrica* Bohaty, unpublished plates (2013), Pl. 9, fig. 1; Fryxell and Hasle, 1972, p. 300, figs. 1-18 (Pl. P1, fig. 6).
Description: Valve circular, convex and 31-40 µm in diameter with a prominent fultoportula, ribbed margin and strutted processes around the edge of the valve face. Coarse hexagonal striation of the valve occurs in a near-straight tangential arrangement.
Remarks: This species is morphologically similar to *Thalassiosira eccentrica*, but shows larger areolae, no central arrangement of pores around the fultoportula and a distinctive near-straight tangential striation pattern, whilst *T. eccentrica* can often exhibit curved tangential striation.

Stratigraphic occurrence: This species was present at ODP Sites 747, 744 and 1165 at low abundances. Based on stratigraphic occurrences at ODP Hole 747A constrained by magnetostratigraphy, the first appearance of *Thalassiosira* sp. nov within the 15-12 Ma interval was at 13.72 Ma at 69.78 mbsf, with its last appearance at 13.35 Ma at 66.35 mbsf. At ODP Hole 1165B, it first appears at 283.56 mbsf and disappears at 276.16 mbsf. At ODP Hole 744B, it first appears at 55.58 mbsf and disappears at 53.80 mbsf. In this thesis, the last appearance of this species at 13.35 Ma is used in the age models at ODP Holes 744B and 1165B.

Trinacria excavata **[Plate 6, figs. 10]** Heiberg 1863, Figure 6.22, Harwood, 1989, p. 82, pl. 3, fig. 1.

Trigonium arcticum (Brightwell) Cleve 1868.

13. Appendix 3: alternative age model at Site 1165.

Two age models were considered at Site 1165, discussed in detail in Chapter 4, section 4.4. One features a hiatus at Site 1165 between 14.3-13.4 Ma, whilst one interprets relatively continuous sedimentation during this section (as was interpreted by previous age models for this interval; Shipboard Science Party, 2001; Florindo et al., 2003). The age model without the hiatus is used in the text of the thesis, for reasons outlined in Section 4.4. However, three figures from Chapter 6 using the alternative age model (including the hiatus) are presented here for reference.

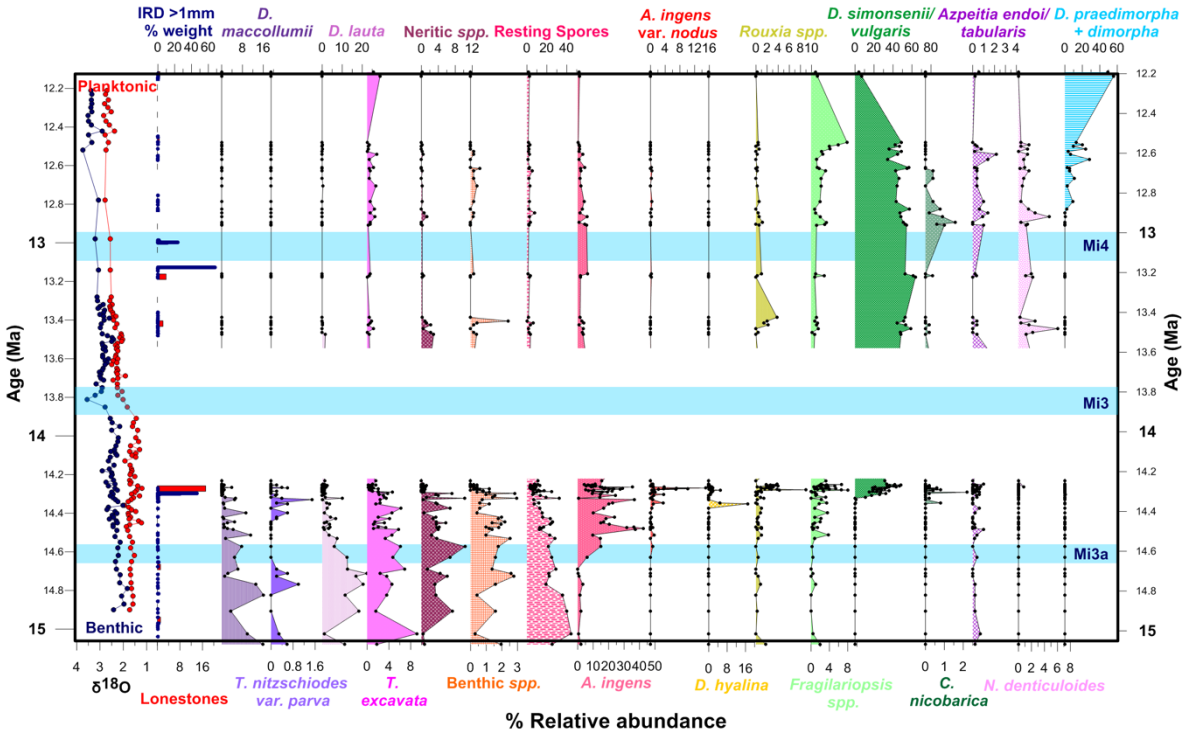

Figure 1. Alternative to Figure 3 in Chapter 6. Diatom relative abundance at ODP Site 1165 between 15-12 Ma. Planktonic and benthic $\delta^{18}O$ is from Site 747 (Majewski & Bohaty, 2010), and IRD at Site 1165 is from this study (purple bars) and lonestones from the Shipboard Scientific Party (2001) (red bars). Blue and pink horizontal shading indicates Miocene glaciation events (Mi3a, Mi, Mi4) and the transient increase in SSTs following Mi3, respectively.

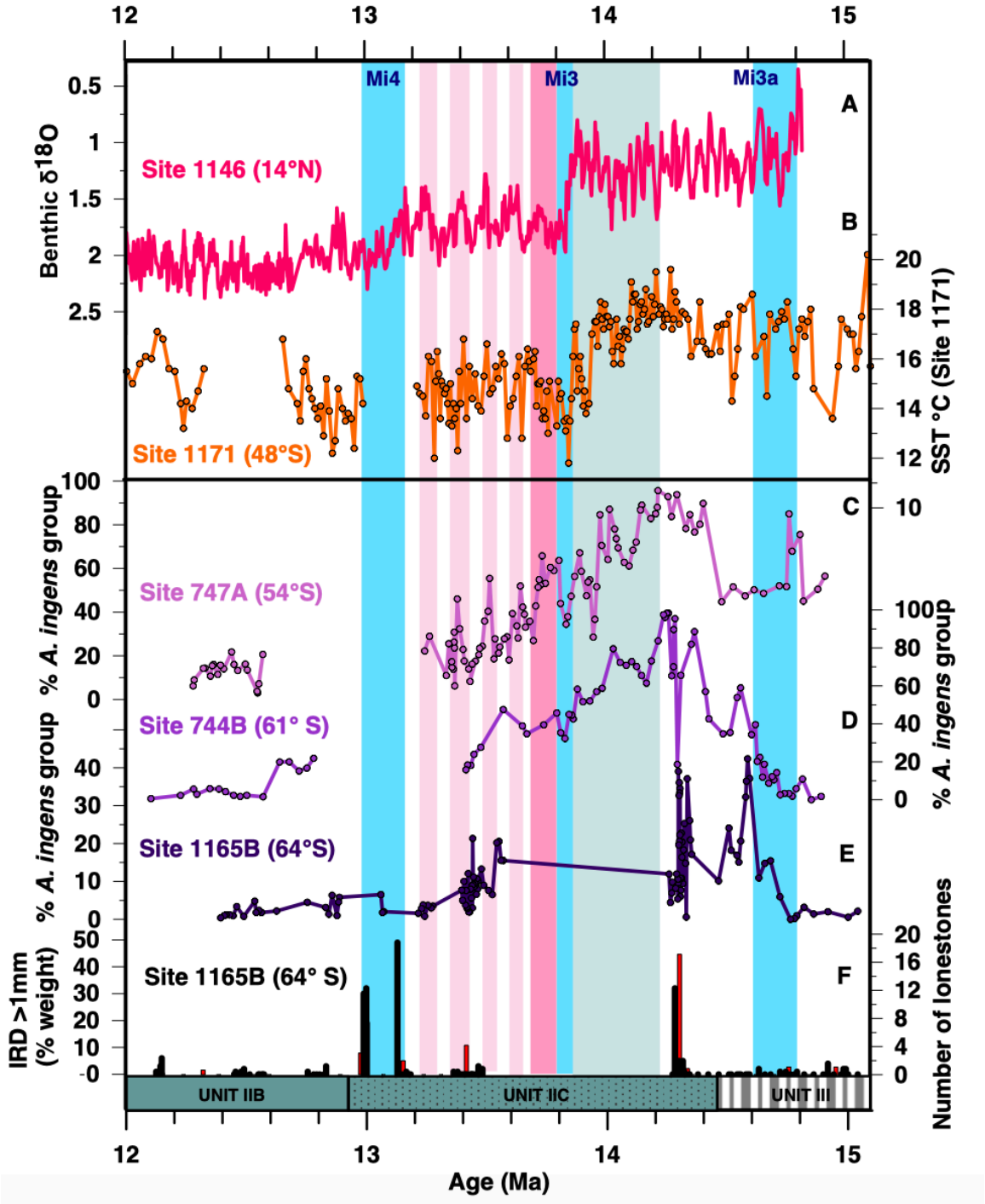

Figure 2. Alternative to Figure 7, Chapter 6. A) ODP Site 1146 benthic oxygen isotopes (Holbourn et al., 2013); B) ODP Site 1171 SST record (Shevenell et al., 2004), C-E: % *A. ingens* group abundances at ODP Sites 1165, 744 and 747. F) IRD at Site 1165. Black bars= this study, red bars= lonestones (Shipboard Science Pary, 2001). Vertical blue shaded bars indicate Miocene isotope glaciation events. Vertical dark pink shaded box represents SST warming following Mi3. Pale pink shaded bars indicate four subsequent interglacials that seem to be paced by 100 kyr-eccentricity cycles. The bottom panel shows the lithological transitions at Site 1165 from Unit II (thinly

bedded, laminated fissile claystones with minimal bioturbation) to Unit III (moderately bioturbated structureless clays with increased clay mineral content, shelf-derived foraminifers and glauconite).

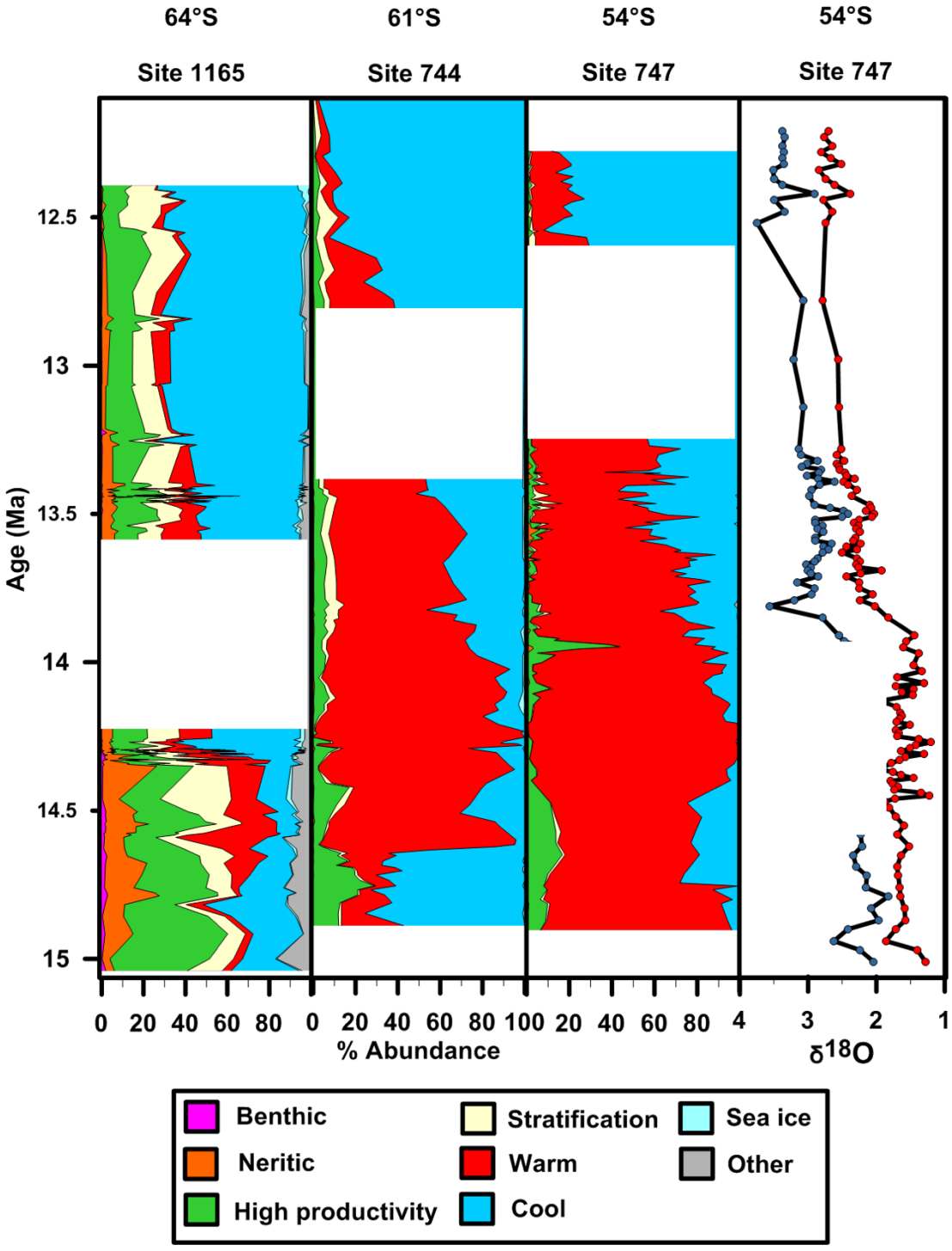

Figure 3. Alternative to Figure 8, Chapter 6. Diatom species at ODP Sites 747, 744 and 1165, group by inferred palaeoecological preferences (see Chapter 5 and Appendix 1). In the right-

hand panel, benthic (blue) and planktonic (red) Site 747 stable oxygen isotope records are shown (Majewski & Bohaty, 2010).